Behaviour of buried water supply pipelines in earthquake zones

A thesis submitted to the University of London
For the degree of Doctor of Philosophy and for the Diploma of the
Imperial College of Science, Technology and Medicine
by

Iain Tromans
Department of Civil and Environmental Engineering
Imperial College of Science, Technology and Medicine
London, SW7 2AZ

January 2004

ABSTRACT

Earthquakes can cause extensive damage to buried water supply pipelines, resulting in major financial losses for water utility operators and lengthy disruption of an essential service for whole communities. This thesis focuses on the behaviour of buried water supply pipelines subject to earthquake effects; particularly the transient ground strains caused by the passage of seismic waves.

Existing empirical relations for the prediction of earthquake-induced pipeline damage are reviewed, with specific emphasis on identifying the reliability of the datasets used. Improvements are made to an existing dataset and areas of uncertainty in the characterisation of the seismic action highlighted.

New predictive relationships are derived for strong-motion peaks from a substantial database of strong-motion records obtained from fifty-one significant European earthquakes. The sensitivity of each dataset to the record processing technique is investigated. The peak ground velocity estimations are particularly useful for prediction of earthquake-induced pipeline damage rates.

Results are presented of a post-earthquake investigation into water pipeline damage in the town of Düzce, Turkey, caused by the Kocaeli and Düzce earthquakes in 1999. Temporal variations in pipeline repair statistics before and after the earthquakes are analysed to identify earthquake-related pipe breaks. In the absence of detailed geological data, site conditions in Düzce are characterised using microtremor measurements. GIS-based analysis reveals no clear correlations between spatial distributions of pipeline damage and site characteristics. A reasonable correlation *is* observed between pipeline damage and building damage. The spatial variation in pipeline damage rates as a result of the Kocaeli earthquake is used to infer the spatial distribution of peak ground velocity based on an existing pipeline fragility relationship. Interpretation of pipeline damage rates caused by the Düzce earthquake is obscured by the effects of the earlier Kocaeli earthquake.

ACKNOWLEDGEMENTS

This research was jointly funded by EPSRC, DTI, WRc Plc and Kubota Corporation under the PTP (Postgraduate Training Partnership) initiative.

Firstly, I would like to thank my supervisor, Dr Julian Bommer for giving me the opportunity to work on such an interesting project, for his continued direction and support, and for his patient endurance, especially in the closing stages of the thesis.

I have enjoyed my time based at Imperial College and have benefited much from discussions with various members of the academic staff and fellow students. In particular, I am grateful to Dr Sarada Sarma and Dr John Douglas and to other fellow members of the Soil Mechanics Research Group.

On the WRc side, I would like to thank Dr Dave Marlow and Hitoshi Inada for their help with the field-work in Turkey and all subsequent assistance. Staff in the GIS Section were responsible for digitising several large maps for the Düzce case study - for which I am very grateful. Dr Ian Walker, Dr Gerald Jones, Professor Nigel Graham (of Imperial College), Dave Landon, Stephen Russell, Dr Jon Morris and Julia Trew all helped me at various stages in the project.

The fieldwork in Turkey would not have happened without the initial support of Dr Julian Bommer and Professor Amr Elnashai, who put me in contact with the right people on the ground. I wish to thank Dr Cansen Guralp and his colleagues at Guralp Systems Ltd. for lending us seismometers for the microtremor survey and for their technical support. Municipality staff in Düzce provided us with data relating to building and pipeline damage and gave much practical assistance during the fieldwork. Murat Şahin & Klaus Tadday, UNICEF staff involved in the post-earthquake reconstruction of Düzce, also gave us much help and advice. Professor Mustafa Erdik and colleagues at Boğaziçi University, Professor Haluk Sucuoğlu and colleagues at METU, Professor Ozer and colleagues at Kocaeli University and Professor Hasan Sarikaya at ITU all gave of their time to assist in the fieldwork. Dr Chris Menkiti of Geotechnical Consulting Group and Roberto Rossetti of Astaldi S.p.A gave us the benefit of their local geological expertise and provided us with much useful information.

I would like to thank Magdalina for her wisdom and care and for the many sacrifices she has made to help me complete this thesis. Thanks to my family for constant encouragement and to the Thacks, Steve, David, Michael, Vik, Peter, Andi, Miyuki, the Hicks, the Tweeddales and all at the Grove for coming to my rescue at critical moments.

Above all, thanks to God for His faithfulness.

"The end of a matter is better than its beginning," Ecclesiastes 7:8a.

TABLE OF CONTENTS

ABBREVIATIONS

AIJ	Architectural Institute of Japan
ALA	American Lifelines Alliance
ASCE/TCLEE	American Society of Civil Engineers/Technical Council on Lifeline Earthquake Engineering
ASME	American Society of Mechanical Engineers
AU	Ankara Üniversitesi (Ankara University)
CAE	Centre for Advanced Engineering, University of Canterbury, New Zealand
CERI	Center for Earthquake Research and Information, the University of Memphis, Tennessee
COSMOS	Consortium of Organisations for Strong-Motion Observation Systems
CRAAG	Centre de Recherche en Astronomie, Astrophysique et Géophysique, Alger, Algeria
CSOES	California State Office of Emergency Services
ESEE	Engineering Seismology and Earthquake Engineering
EERI	Earthquake Engineering Research Institute
FEMA	Federal Emergency Management Agency
GD_p	Permanent ground deformation
GD_t	Transient ground deformation
IAHS	International Association for Housing Services
IASPEI	International Association of Seismology and Physics of the Earth's Interior
ICBO	International Conference of Building Officials
ISESD	Internet Site for European Strong-Motion Data (Ambraseys *et al.*, 2002)
ITU	Istanbul Technical University
IWSA	International Water Services Association
JDIPA	Japan Ductile Iron Pipe Association
JSCE	Japanese Society of Civil Engineers
JWWA	Japan Water Works Association
KOERI	Kandilli Observatory and Earthquake Research Institute
LEAS	Bureau d'études électroniques, Saint Ismier, Cedex, France
MCEER	Multidisciplinary Center for Earthquake Engineering Research (formerly NCEER)
MTA	Maden Tetkik ve Arama Genel Müdürlügü (General Directorate of Mineral Research and Exploration, Turkey)
NCEER	National Center for Earthquake Engineering Research (now MCEER)
NEIC	National Earthquake Information Centre, World Data Center for Seismology, Denver, Colorado, US
NERC	Natural Environment Research Council
NIBS	National Institute of Building Sciences
OECD	Organisation For Economic Co-Operation And Development
OFWAT	Office of Water Services, UK

PEER	Pacific Earthquake Engineering Research Centre
PWA	Pacific Water Association
SPT	Standard Penetration Test
TC4/ISSMGE	Technical Committee for Earthquake Geotechnical Engineering of the International Society for Soil Mechanics and Geotechnical Engineering
TDV	Türkiye Deprem Vakfı (Turkish Earthquake Foundation)
TMG	Tokyo Metropolitan Government
TRRL	Transport and Road Research Laboratory
UNICEF	United Nations Children's Fund
USAID	United States Agency for International Development

LIST OF SYMBOLS

a	regression coefficient
a_p	peak particle acceleration
a_{rms}	root-mean-square acceleration
$a(t)$	acceleration
A	area of fault rupture surface
A_0	ground-motion amplification at frequency, f_0
$A_{0.5\text{-}2}$	average HVSR amplification (0.5 to 2 Hz)
$A_{2\text{-}5}$	average HVSR amplification (2 to 5 Hz)
$A_{5\text{-}10}$	average HVSR amplification (5 to 10 Hz)
A_{fp}	HVSR amplitude at soil predominant frequency
A_g	amplitude of ground motion
A_{loop}	area of hysteresis loop
A_p	cross-sectional area of pipeline annulus
A_{PGV}	relative amplification factor for PGV
$A_r^{NHV}(f)$	horizontal-to-vertical spectral ratio of noise at rock site
$A_s(f)$	horizontal-to-vertical spectral ratio due only to surface waves
A_{seis}	seismogram trace amplitude
$A_s^{NHV}(f)$	horizontal-to-vertical spectral ratio of noise at soil site
$\mathrm{AHSA}_{\mathrm{f\_0.5\text{-}2.5}}$	average horizontal spectral amplification (0.5 to 2.5 Hz)
$\mathrm{AHSA}_{\mathrm{T\_0.4\text{-}2.0}}$	average horizontal spectral amplification (0.4 to 2.0 s)
b	regression coefficient
B	embankment height
B_i	modification factors (Isoyama *et al.,* 2000 pipeline fragility relationships)
c	apparent propagation velocity
c_{ave}	average apparent propagation velocity
c_P, c_S, c_R	apparent propagation velocity of P-waves, S-waves and R-waves respectively
c_{ph}	phase velocity of R-waves
C	impedance contrast
C_i	coefficients of regression (different for different regressions)
C_{PL}	pipe length adjustment factor
d_e	epicentral distance
d_{eff}	effective duration (of strong-motion)
d_f	fault distance
d_h	hypocentral distance
d_r	distance to closest point on rupture plane
d_s	distance to location on fault plane of largest slip
d_{seis}	distance to closest point on seismogenic rupture plane
D	displacement
D_1, D_2	building damage index

D_0	external diameter of pipeline
D_H	horizontal (permanent) ground displacement
D_{max}	maximum displacement on fault rupture surface
$\overline{D}$	average displacement on fault rupture surface
E	Young's modulus of elasticity
E_d	energy density
$E(f)$	source function
f	frequency
f_0	fundamental frequency
f_B	building fundamental frequency
f_c	corner frequency
f_{eq}	frequency of equivalent harmonic wave
f_{H0}	fundamental frequency (horizontal direction)
f_n	frequency of nth harmonic
f_p	predominant frequency
f_L	lower frequency filter cut-off
f_U	upper frequency filter cut-off
F_l	limit-state force causing pipeline failure or loss of serviceability
F_{m1}	maximum pipeline axial force
F_{m2}	maximum frictional force between pipeline and surrounding soil
g	acceleration due to gravity (= 9.81 m/s^2)
G	shear modulus
$\overline{G}$	average shear modulus (over several soil layers)
G_{max}	maximum shear modulus
G_{sec}	secant shear modulus
G_{tan}	tangent
h	focal depth
h_0	regression coefficient
H	total thickness of soil layer(s)
H_B	building height
H_i	thickness of ith soil layer
H_{liq}	thickness of liquefied layer
H_{sand}	thickness of sandy layer(s)
$H(f)$	soil transfer function
$H^T(f)$	true site-amplification function (horizontal component)
HVSR	horizontal-to-vertical spectral ratio
I_0	epicentral intensity (MSK)
I_a	Arias intensity
I_{Duzce}	intensity (MSK) experienced in town of Düzce
I_{EMS-98}	European Macroseismic Scale Intensity
I_{JMA}	Japanese Meteorological Agency Intensity

I_{MM}	Modified Mercalli Intensity
I_{MSK}	Medvedev-Spoonheuer-Karnik Intensity
$I(f)$	instrument response function
k_0	lateral earth pressure coefficient at rest
K_1	modification factor (Eidinger *et al.*(1995) pipeline fragility relationship)
K_{1ALA}	modification factor (ALA (2001) pipeline fragility relationship)
L	mean seismic wavelength (JWWA seismic design code)
L_p	pipe length
L_{rup}	fault rupture length
L_s	separation distance (for determination of ground strain)
LSI	liquefaction severity index
m_b	body-wave magnitude
M	magnitude (unspecified scale)
M_0	seismic moment
M_{JMA}	Japanese Meteorological Agency magnitude
M_L	local (Richter) magnitude
M_s	surface-wave magnitude
M_w	moment magnitude
n, N	integer
N_{Btot}	total number of buildings (per district)
N_{Di}	number of buildings classified at damage level i (per district)
N_{si}	number of buildings with i storeys (per district)
N_{SPT}	SPT N-value
$O_s(f)$	Fourier spectrum of seismogram recorded at a soil site
$O_r(f)$	Fourier spectrum of seismogram recorded at a rock site
p_f	frictional force per unit length of pipe between pipe and soil
$P(f)$	path function
PGA	peak ground acceleration
PGA_A	peak ground acceleration (arithmetic mean of two horizontal components)
PGA_G	peak ground acceleration (geometric mean of two horizontal components)
PGA_L	peak ground acceleration (largest of two horizontal components)
PGA_V	peak ground acceleration (square root of sum of squares of two horizontal components)
PGD	peak ground displacement
PGV	peak ground velocity
r^2, R^2	coefficient of determination
$R_b^H(f)$	horizontal spectrum of body wave portion of noise at a rock reference site
$R_b^V(f)$	vertical spectrum of body wave portion of noise at a rock reference site
R_0	standard pipeline damage rate (Isoyama *et al.,* 2000 pipeline fragility relationship)
R30_pre	average pre-earthquake pipeline repair rate per km length of pipe adjusted to a 30-day average (based on 7 months of pre-earthquake data)

$R30\_pK18$	average post-earthquake pipeline repair rate per km length of pipe adjusted to a 30-day average (based on 18 months of post Kocaeli data)
R_D	damage modification factor for pipeline diameter (Hwang & Lin, 1997 pipeline fragility relationship)
R_pD2	post-earthquake pipeline repair rate per km length of pipe (aggregated post Düzce earthquake 2 months)
R_pK3	post-earthquake pipeline repair rate per km length of pipe (aggregated post Kocaeli earthquake 3 months)
R_pK5	post-earthquake repair rate per km length of pipe (aggregated post Kocaeli earthquake 5 months)
R_R	pipeline repair rate (per unit length of pipe)
S_b	spatial density of buildings
S_p	spatial density of pipelines
$S(f)$	site function
$S^{NH}(f)$	Fourier spectrum of noise (horizontal component)
$S^{NV}(f)$	Fourier spectrum of noise (vertical component)
$S_r(f)$	spectral amplitude at bedrock level
$S_s(f)$	spectral amplitude at ground surface level
S_v'	"design velocity response" (JWWA seismic design code)
SA	spectral acceleration
SD	spectral displacement
SI	spectral intensity
SV	spectral velocity
t	time
t_0	start time (used for calculation of d_{eff})
t_r	total duration of strong-motion record
t_{rup}	fault rupture duration
T	period
T_0	fundamental period
T_B	fundamental period of building
T_{eq}	period of equivalent harmonic wave
T_i	natural period of ith soil layer
T_p	predominant period
$U_1(t)$, $U_2(t)$	ground displacement at time t at locations 1 and 2 respectively
$U_h(z)$	horizontal (transient) ground displacement at depth z below ground surface
UFW	unaccounted-for water
v_p	peak particle velocity
v_{pP}, v_{pS}, v_{pR}	peak particle velocity caused by P-waves, S-waves and R-waves respectively
v_{rup}	fault rupture velocity
v_S	shear-wave velocity
$\overline{v}_S$	average shear-wave velocity
v_{Si}	shear-wave velocity of ith soil layer

v_{S30}	average shear-wave velocity over a depth of 30m
v_{SQ}	average shear-wave velocity over a depth of one-quarter wavelength for a 1-second period wave
v_{scaled}	scaled velocity (O'Rourke & Jeon, 1999)
v_{Ssoil}	shear-wave velocity of soil layer
v_{Srock}	shear-wave velocity of bedrock
$v(t)$	velocity
$V^T(f)$	true site-amplification function (vertical component)
W_B	volume of water billed or consumed
W_D	dissipated energy
W_i	weighting coefficient (for calculation of building damage index)
W_P	volume of water produced and introduced to the distribution network
W_S	maximum strain energy
x	space coordinate
X	strong-motion parameter
X_i	estimated fundamental mode shape at lower boundary of soil layer i
y	dependent variable
$\overline{y}$	mean of y
$\hat{y}$	predicted value of y
z	depth below ground surface
z_i	depth below surface of ith soil layer
z_p	depth below ground surface of pipe centreline
$\beta(f)$	relative proportion of surface waves to body waves (measured on the vertical component)
γ	soil unit weight
γ_c	shear strain amplitude
γ_S	angle of incidence of body waves with respect to vertical
δ	friction angle between pipe and soil
δ_1, δ_2	ground settlement
δ_f	angle of fault dip
ε	strain
ε_p	peak ground strain
ε_y	pipeline yield strain
θ	max [slope of base of liquefied layer, slope of ground surface]
κ_p	peak ground curvature
λ	wavelength
λ_f	fault rake
μ	rigidity of Earth's crust
ν	Poisson's ratio
ξ	damping ratio
ρ	density

$\overline{\rho}$	average density (over several soil layers)
σ, $\sigma_{\log X}$, $\sigma_{\ln X}$	standard deviation
σ_y	pipeline yield stress
φ	angle of incidence of seismic wave with respect to pipe axis
φ_s	angle of fault strike
φ_v	predominant direction of ground motion with respect to the vertical
ω_i	natural circular frequency of ith soil layer

1.1 Background

Water distribution systems are one of six broad categories of infrastructure grouped under the heading 'lifelines' (O'Rourke, 1998). Together with electric power, gas and liquid fuels, telecommunications, transportation and wastewater facilities, they provide the basic services and resources upon which modern communities have come to rely, particularly in the urban context. Disruption of these lifelines through earthquake damage can therefore have a devastating impact, threatening life in the short term and a region's economic and social stability in the long term.

The field of lifeline earthquake engineering is a relatively new one. Its formal recognition came in the 1970's with the establishment in the United States of ASCE's Technical Council on Lifeline Earthquake Engineering (Duke & Matthiesen, 1973). In 1975, Council Members, C.M. Duke and D.F. Moran commented that the state-of-the-art for lifeline earthquake engineering was 10 to 20 years behind that of buildings (Duke & Moran, 1975). A concerted research effort since then has made up much of the lost ground, but many challenges remain.

Damage to a city's water distribution system will affect the whole post-earthquake recovery operation. Lack of clean piped mains supply for basic drinking and sanitation needs in the immediate aftermath of an earthquake constitutes a fresh threat to the lives of those who have survived the initial devastation.

The water distribution system in Nicaragua's capital, Managua, sustained considerable damage as a result of an earthquake in 1972. The restoration of supply was held up by problems at the city's main reservoir where an earthquake-induced landslide had blocked the water pump inlets and electricity supply to the pump house had been cut off. Once power had been restored, 9 hours after the earthquake, water supply was only re-established in the region closest to the reservoir due to a severely fragmented distribution network. The authorities decided to evacuate the worst hit areas in the short term until water supply and other essential infrastructure were repaired. In the interim period, water was conveyed by truck to temporary distribution centres to meet emergency needs (Cajina, 1973; CSOES, 1973).

A damaged water distribution system can also increase the severity of secondary disasters such as conflagration or flooding. Fire losses, in particular, can be greater than the losses directly due to the earthquake. The fire that followed the 1906 San Francisco earthquake is perhaps the most striking example. Reduced fire-fighting capabilities as a result of rupture of the city's three principal water transmission pipelines and breaks in the trunk line system contributed to the destruction by fire of almost 500 blocks of the city, resulting in the worst fire loss in US history (O'Rourke *et al.*, 1992).

Table 1.1 gives an overview of water supply system damage in Kobe City following the 1995 Hyogoken-Nanbu earthquake in Japan. The total cost of damage caused by this earthquake approached US$100bn and a significant proportion of this (5%) was lifelines-related (Hamada, 1997). A similar pattern was observed in the Kocaeli and Düzce earthquakes in Turkey in 1999, with the cost of lifelines damage estimated at US$1bn out of a total of US$16bn (Erdik, 2000). Of the damage caused to lifelines in Kobe and its surrounding area, around one tenth was damage to water distribution facilities (Katayama, 1996). The cost of damage to distribution mains alone accounted for almost half of the total system damage.

Table 1.1 Break down of damage to the water supply system in Kobe City (after Matsushita *et al.*, 1998)

Facility	Total system composition	Damage level	Repair cost (US$m)
Dams	3	1	70
Purification plants	7	2	
Trunk mains	43km	2 lines	
Principal feeder mains	260km	6 lines	
Distribution reservoirs	119	1	19
Distribution mains	4 002km	1 757 failures	135
Service connections	650 000 lines	89 584 failures	25
Miscellaneous	Various components	Several buildings including Waterworks Bureau Head Office	41
Total			**290**

Buried water supply pipelines can be subject to both transient ground deformation and permanent ground deformation in the event of an earthquake. Transient ground deformation is caused by the passage of seismic waves (ground shaking). Permanent ground deformation is caused by surface faulting or secondary effects which give rise to localised ground failure (liquefaction, landslides and densification of surface soil layers).

The relative impact of different effects on buried pipelines varies from earthquake to earthquake. Transient effects are common to all earthquakes and are felt over a wide geographical area and associated pipeline damage tends to be spread over the whole of a water supply system. Resulting damage rates (in terms of breaks per unit length of pipe) are relatively low but the total number of pipe breaks can be high. Surface faulting or secondary earthquake effects can give rise to very high ground strains. Where these phenomena coincide with buried pipelines, relatively high pipeline damage rates are observed but in localised areas.

In the current research, the behaviour of buried pipelines subject to various earthquake effects has been investigated, with particular emphasis on ground shaking. Key factors affecting transient ground motion and pipeline vulnerability have been identified from both theory and evidence from the field. An outline of the work covered is given in the following section.

1.2 Thesis outline

Chapter 2 is a summary of earthquake effects, explaining the mechanisms of earthquake-induced ground movements and their interactions with buried pipelines. The chapter considers surface fault rupture, the ground shaking which accompanies seismic energy release and collateral earthquake effects. Emphasis is placed on transient ground movements, the factors that influence these and ways for quantifying their effects.

Chapter 3 constitutes a detailed treatment of the behaviour of buried pipelines subject to ground shaking. The key factors influencing both the seismic action and pipeline vulnerability are explained. A detailed review is presented of existing pipeline fragility relations. These use pipeline damage statistics from previous earthquakes to quantify seismic action and pipeline vulnerability. In the review, particular emphasis is placed on identifying the size, origin and reliability of the datasets from which the fragility relations were derived. Improvements are made to an existing dataset using newly available data and suggestions are made regarding future improvements to predictions of pipeline damage.

Post-earthquake investigation of factors influencing pipeline damage and prediction of future earthquake damage both require characterisation of the spatial variation in ground shaking. In Chapter 4, a summary is presented of some common methods used to characterise site effects, which can significantly influence ground shaking. Detailed consideration is given to the microtremor approach which is based on ambient noise measurements. This is the method subsequently used to characterise site effects during field work carried out in Turkey (described in chapters 6 to 8).

Prediction of damage in future earthquakes requires reliable estimation of the level of ground shaking, as characterised using various strong-motion parameters. In Chapter 5, new predictive relationships are derived for three different strong-motion parameters, based on data from European earthquakes. The equations are of use in seismic hazard analysis and earthquake-resistant design of structures. The sensitivity of the datasets to the record processing technique is investigated.

Chapters 6, 7 and 8 constitute a detailed investigation into earthquake damage to buried water pipelines in the town of Düzce, Turkey, caused by two destructive earthquakes in 1999. Data were collected during field investigations conducted as part of the current research. Chapter 6 describes the earthquakes in their historical and physical contexts and explains significant features of the effects caused. In Chapter 7, the microtremor investigation used for estimation of site effects is presented. The influence of various factors on the spatial distribution of pipeline damage is investigated in Chapter 8 using a Geographical Information System (GIS).

Chapter 9 summarises the main contributions of this research to understanding the behaviour of buried pipelines in past earthquakes and improving damage prediction in the event of a future earthquake. Various recommendations are made for future work, in the light of these conclusions.

CHAPTER 2. EARTHQUAKE EFFECTS

The direct effects of earthquakes are surface faulting and ground shaking. Secondary or "collateral" effects include liquefaction, landslides, densification and tsunami. The first three of these effects are briefly characterized in this chapter. Although potentially damaging to water supply systems, tsunami are not considered.

Earthquake effects on buried pipelines are best understood by considering the displacements induced in the surrounding soil. Damage may be caused by transient ground deformation (GD_t), or permanent ground deformation (GD_p), or a combination of the two. O'Rourke (1998) defines the distinction between these two effects, "*GD_p involves the irrecoverable movement of the ground that often is the result of ground failure, but also may result from modest levels of volumetric strain and shear distortion. GD_t involves ground waves and soil strains associated with strong shaking. Although ground cracks and fissures may result from GD_t, the magnitude of this residual deformation will normally be less than the maximum GD_t during strong shaking."* All of the collateral earthquake effects, plus faulting, can give rise to permanent ground deformation.

The relative impact of different effects on buried pipelines varies from earthquake to earthquake. Transient effects are common to all earthquakes and are felt over a wide geographical area and associated pipeline damage tends to be spread over the whole of a water supply system. Resulting damage rates (in terms of breaks per unit length of pipe) are relatively low but the total number of pipe breaks can be high. Surface fault rupture and collateral earthquake effects can give rise to very high ground strains. Where these phenomena coincide with buried pipelines, relatively high pipeline damage rates are observed but in localised areas.

Water pipeline damage data from the 1999 Ji-Ji (Taiwan) earthquake reveals the relative impact of different earthquake effects (Table 2.1). In this case, ground shaking was directly responsible for almost half of the total damage. The proportion of fault-induced damage was also high, due to the extensive faulting and large fault displacements that characterised this earthquake. Liquefaction-induced damage was relatively insignificant. However, because the earthquake-affected area was mountainous, landslide-induced damage was significant.

Table 2.1 Damage to water pipelines in the 1999 Ji-Ji (Taiwan) earthquake (Shih *et al.,* 2000; Miyajima & Hashimoto, 2001)

Cause of damage to water pipelines	% of total damage
Ground shaking	48
Faulting	35
Landslides	11
Liquefaction	2
Other (unspecified)	4

In contrast to the Taiwanese data, pipeline damage statistics from the 1906 San Francisco earthquake were dominated by liquefaction-induced failures. Even though zones of liquefaction-induced lateral spreading accounted for only 5% of the built-up area affected by strong ground shaking, approximately 52% of pipeline breaks occurred within one city block of these zones. The other breaks were attributed to ground-shaking effects (O'Rourke & Liu, 1999).

The relative impact of the various earthquake effects on buried pipelines depends on the geological conditions in which surface faulting and collateral effects occur and the coincidence of these regions with the buried infrastructure. Even in the absence of surface faulting, landslides, liquefaction or ground settlement, pipeline damage can be severe, as observed in the 1985 Michoacan (Mexico) earthquake (Ayala & O'Rourke, 1989).

2.1 Faulting

Most earthquakes occur as a result of the build up of stresses at tectonic plate boundaries. When these stresses exceed the rock's ability to resist them, rupture occurs along a fault, releasing the stored strain energy in the form of seismic waves and heat. The fault rupture usually coincides with a pre-existing discontinuity in the Earth's crust. The extent of faulting is linked closely with earthquake magnitude. Large earthquakes can produce faults of several hundred kilometres length with widths of tens of kilometres and offsets of several metres. There are many ways to quantify earthquake magnitude. Definitions of magnitude scales referred to in the current work are presented in Appendix A, together with a comparison among the scales.

In most earthquakes, the fault rupture plane does not have a surface expression (*blind faulting*) (Reiter, 1990). A surface fault trace is usually only observed for large earthquakes occurring at shallow depth. The extent of surface faulting depends chiefly on the length and amount of offset of the subsurface faulting, the attitude of the fault plane, the direction of the fault movement and the type and thickness of the surficial geology (Taylor & Cluff, 1977). Faults can be classified according to the movement of the two sides of the fault relative to each other (Figure 2.1). Faulting is termed *strike-slip* when the movement is predominantly horizontal. It is known as *dip-slip* when the movement is predominantly in the direction of dip of the fault plane. Dip-slip movement where the horizontal component is compressional is called *reverse faulting*. Where the horizontal component is extensional, the faulting is termed *normal*. A combination of dip-slip and strike-slip movement is referred to as *oblique faulting*

Not all fault-like features observed at the surface are related to tectonic rupture. Fractures may be formed by ground shaking, landslides or triggered slip on surface faults not related to the primary fault plane (e.g. slip on bedding plane faults or near-surface slip on adjacent faults). These secondary 'faults' are sometimes difficult to distinguish from primary faults, especially for smaller magnitude earthquakes (surface-wave magnitude, $M_s < 6$) (Wells & Coppersmith, 1994).

As illustrated in Figure 2.1, fault-induced ground-strain is most severe at the intersection between the fault plane and the ground surface. However, the crustal deformation that accompanies earthquake faulting (*coseismic deformation*) can be significant at considerable distances from the surface rupture.

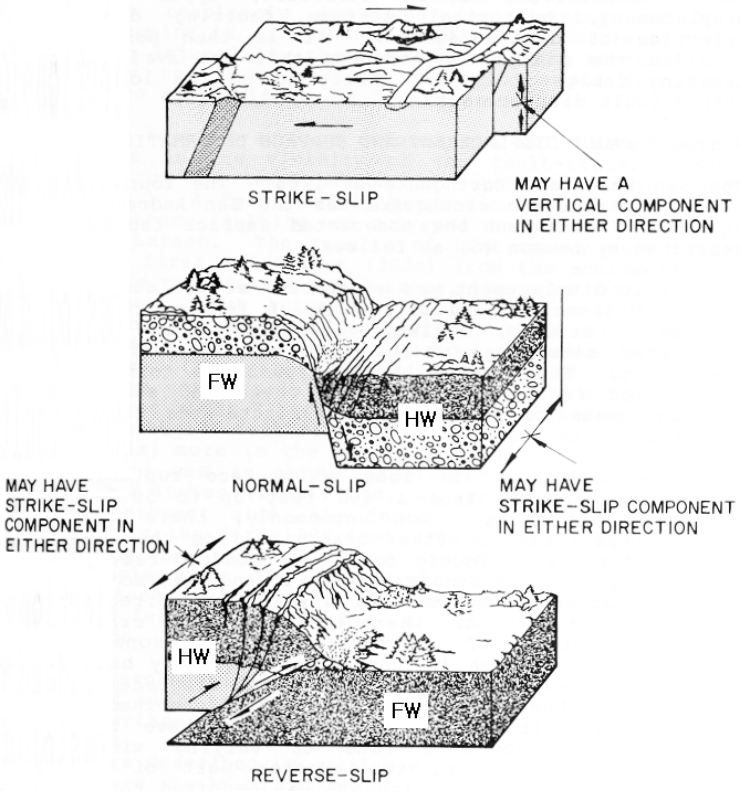

Figure 2.1 Surface expression of different types of faulting (Taylor & Cluff, 1977). FW – foot wall; HW – hanging wall.

Figure 2.2 shows the vertical displacements either side of the normal fault which ruptured at Borah Peak, Idaho in 1983 (M_s 7.3). The black dots are measurement points along the line of a road that intersects the fault. The elevation changes were found by comparing the results of levelling surveys taken before and after the earthquake. It can be seen that the uplift and subsidence reduce to negligible values at a distance from the fault similar to the down-dip fault width, which in this case is about 15km. The amplitude at the ground surface of the permanent fault offset is dependent on the amount of slip on the fault plane. These wavelength and amplitude characteristics of the coseismic displacement field are typical of all strike-slip and dip-slip faulting.

Mansinha & Smylie (1971) derived analytical expressions for the displacement fields of inclined faults by considering dislocations in an elastic half-space. These expressions are useful for estimating the likely displacement field for a given fault width, length and slip. They can also be differentiated to obtain strain and stress fields. This kind of model is based on a number of simplifying assumptions, including constant slip across the fault and constant material properties throughout the region affected by the fault. The thin black line in Figure 2.2 is the fit from an elastic dislocation model of fault slip using the parameters listed. These parameters are consistent

with values obtained from seismological measurements. In spite of the model simplifications, calculated displacement fields can correspond closely with those observed in actual earthquakes.

In the last decade or so, sophisticated satellite-based geodetic techniques have become commonplace. Jackson (2001) describes their application to understanding the deformation and relative movements of tectonic plates. Global Positioning System (GPS) observations allow the relative positions of points on the Earth's surface to be measured at sub-centimetre precision. Comparison of pre- and post-earthquake measurements therefore gives coseismic displacement. Synthetic Aperture Radar (SAR) interferometry cannot achieve such precision but offers much higher spatial resolution than GPS, allowing coseismic displacements to be mapped over the whole of an earthquake-affected region. Reilinger *et al.* (2000) use both GPS and SAR techniques to obtain the displacement field and fault slip distribution for the 17 August 1999 Izmit, Turkey earthquake. Ayhan *et al.* (2001) use GPS measurements to estimate the geometry and slip distribution of the 12 November 1999 Düzce, Turkey earthquake.

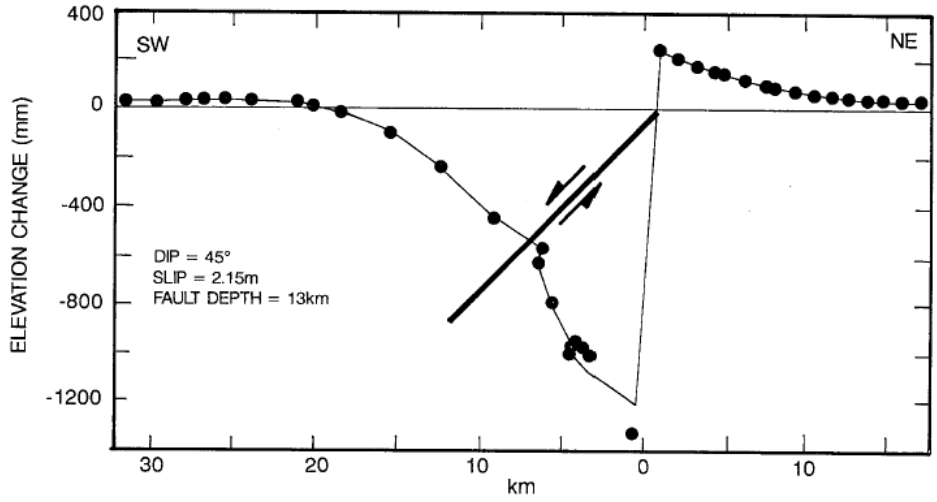

Figure 2.2 Elevation change along a road projected onto a section perpendicular to the surface fault rupture of the 1983 Borah Peak, Idaho earthquake (Jackson, 2001).

The large permanent ground deformations associated with faulting can present a very severe hazard to structures on or near to active faults. Where potentially active faults can be identified, "no-build" zones can be designated, to avoid unnecessary damage in the event of an earthquake. In the case of water pipelines, crossing active faults is often unavoidable, since pipeline location is dictated by the locations of supply and demand areas. It is therefore useful to be able to estimate the amount of permanent ground displacement that might occur in the event of an earthquake of a given magnitude on a particular fault.

Numerous studies have been carried out to investigate the connection between earthquake magnitude and various characteristics of the fault rupture. Wells & Coppersmith (1994) compiled a worldwide database of 244 earthquakes covering the moment magnitude range $5.6 \leq M_w \leq 8.1$. Observed fault displacements ranged from 0.05 - 8.0 m for strike-slip faults, 0.08 - 2.1 m for

normal faults and 0.06 - 1.5 m for reverse faults. From this database, empirical relationships were derived among magnitude, rupture length, rupture width, rupture area and surface displacement. These expressions can be used to predict likely fault rupture characteristics given a specific magnitude of event. Of most interest for the prediction of pipeline damage are expressions for expected surface fault displacement as a function of magnitude:

$$\log \overline{D} = C_1 + C_2 M_w \tag{2.1}$$

where: $\overline{D}$ is the average surface fault displacement (m),
M_w is the moment magnitude,
C_1 and C_2 are coefficients derived from the regression. Values for different categories of fault slip type are presented in Table 2.2.

Table 2.2 Regression coefficients for different categories of fault slip type for use in Equation (2.1) (Wells & Coppersmith, 1994).

Fault slip type	C_1	C_2	Standard deviation	Correlation coefficient	Magnitude range
Strike-slip	-6.32	0.90	0.28	0.89	5.6 – 8.1
Reverse	-0.74	0.08	0.38	0.10	5.8 – 7.4
Normal	-4.45	0.63	0.33	0.64	6.0 – 7.3
All	-4.80	0.69	0.36	0.75	5.6 – 8.1

Coefficients were also derived for the *maximum* surface fault displacement, D_{max} with the observation that on average, $D_{\max} / \overline{D} \approx 2$. Based on the correlation coefficients obtained from each regression, the investigators suggested use of the all-slip-type relationship for predictive purposes unless strike-slip faulting in particular is expected.

Where data were available (for 32 events), Wells & Coppersmith (1994) compared average slip on the fault-plane with average displacement observed at the ground surface. The ratios of these values had a wide range, varying from 0.25 to 6.0. However, the mode of the distribution of ratios was quite distinct, being 1.32. The indication here is that, for this subset of earthquakes showing surface rupture, most slip on the fault plane at seismogenic depths *was* manifested at the surface.

Even for earthquakes without a surface fault expression, coseismic strains induced in the epicentral region may still be large enough to cause damage to buried pipelines. O'Rourke (1999) has likened a water supply system to a giant buried strain gauge, pipe failures giving an indication of regions of high strain.

The response of a buried pipe to surface faulting depends to a large extent on its orientation with respect to the fault. Bending, buckling due to axial compression or pull-out due to axial extension are all possible responses. For similar ground displacements, the mechanism of dip-slip faulting tends to be more damaging to pipelines than strike-slip faulting, because the bearing pressure on an embedded object moving downwards in soil is greater than the resistance to movement in the lateral direction. Analytical models of buried pipe behaviour subject to earthquake faulting are summarised in O'Rourke & Liu (1999).

2.2 Ground shaking

Ground shaking is caused by two different kinds of seismic waves: *body waves* and *surface waves*. Body waves are generated by earthquake faulting and are responsible for the radiation of seismic energy from the rupture zone at depth to the surface of the Earth. Body wave disturbances are of two types: *P-waves* (primary waves) and *S-waves* (secondary) (Figure 2.3). P-waves (compression waves) are characterised by disturbance parallel to the direction of wave propagation whereas S-waves (shear waves) cause a disturbance perpendicular to the direction of travel. The direction of particle movement can be used to divide S-waves into two components: SV (vertical) and SH (horizontal).

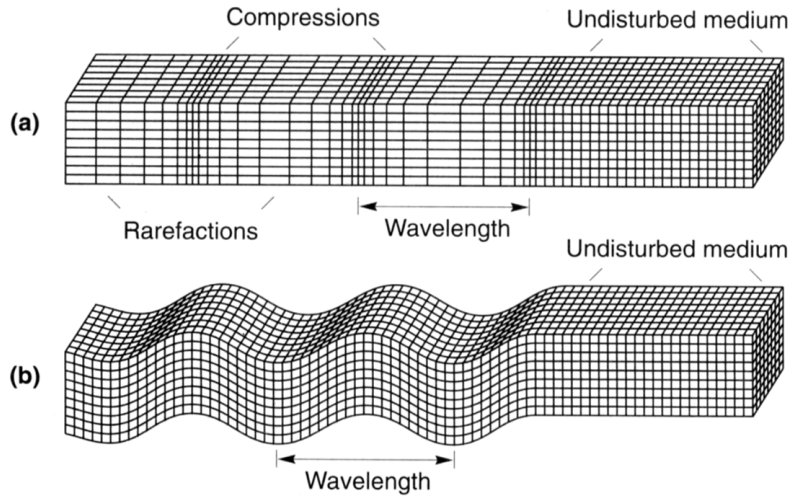

Figure 2.3 Deformations produced by body waves: (a) p-wave; (b) SV-wave (Bolt, 1993).

The interaction of body waves with the surface of the Earth causes surface waves, the most important of which, for engineering purposes, are *R-waves* (Rayleigh waves) and *L-waves* (Love waves) (Figure 2.4). For R-waves, the particle motion traces an ellipse in a vertical plane, the size of the ellipse decreasing with depth below the ground surface. R-waves also have a horizontal component, which is parallel to the direction of propagation. For L-waves, the particle motion is in the horizontal plane, perpendicular to the direction of propagation, with the amplitude decreasing with depth below the ground.

Both types of waves are of interest when considering the response of buried pipelines to seismic ground shaking. For body waves, only S-waves are normally considered as they carry more energy than P-waves. In the case of surface waves, it is R-waves which are most important, inducing axial strains in buried pipelines of much more significance than the bending strains induced by L-waves (O'Rourke & Liu, 1999).

Seismic wave propagation theory indicates significant differences between the transient ground motions associated with body waves and those associated with surface waves. Analytical models of soil-pipeline interaction and strong-motion data from the field also indicate that there are significant differences in the way in which the two types of seismic waves affect buried pipelines.

In order to predict earthquake damage to pipeline systems or design a new pipeline for earthquake resistance, it is therefore important to define the predominant effects at the site or region of interest.

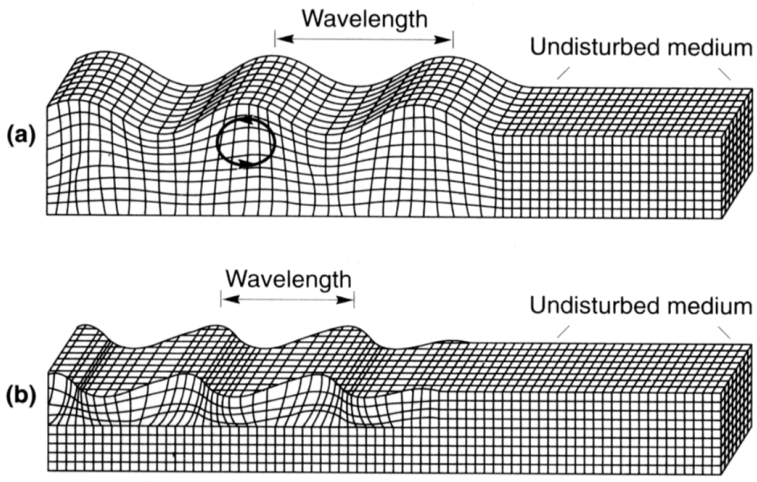

Figure 2.4 Deformations produced by surface waves: (a) R-wave; (b) L-wave (Bolt, 1993).

The ground shaking felt at a given location will be made up of a combination of body waves and surface waves. In the immediate locality of the fault rupture, body waves will dominate the motion. The amplitude of ground motion reduces with distance from the source of seismic energy release. This is due to a combination of geometric attenuation, which accounts for the spread of the wavefront as it moves away from the source, and anelastic attenuation, which is caused by material damping. Geometric attenuation is different for body waves than for surface waves. Assuming that the earthquake rupture zone can be represented as a point source and R is the distance from the rupture zone, the amplitude of body waves decreases in proportion to $1/R$, while the amplitude of surface waves decreases in proportion to $1/\sqrt{R}$. This explains why ground motion at large epicentral distances is generally dominated by surface waves.

Nakamura (1988), cited by Kamiyama *at al.* (1992), defined criteria for the domination of surface waves at a given site based on earthquake magnitude (M), focal depth (h) and epicentral distance (d_e). Kamiyama e*t al.* (1992) used these criteria to distinguish between conditions in which body waves are likely to predominate and conditions in which surface waves are likely to predominate. Conditions for the domination of surface waves are defined by expressions (2.2) and (2.3):

$$M > 6.0 \text{ and } \frac{d_e}{h} > 1.5 \tag{2.2}$$

$$6.0 \geq M > 5.0 \text{ and } \frac{d_e}{h} > 6.0 \tag{2.3}$$

In Chapter 3, methods for approximating the transient strains induced in buried pipelines are described. These methods differ according to the seismic wave type. Criteria like those shown above allow the appropriate method to be used for a given situation.

The response of buried pipelines to seismic waves differs substantially from that of most above-ground structures. For a building, the ratio of its weight (inertia) to the restoring forces (stiffness) in the structural elements is high, causing significant relative motion between the building and the ground on which it stands. A fluid-filled pipeline typically has less weight than the soil it replaces. Inertial forces are therefore low with respect to the stiffness of the surrounding soil. The response of the pipeline to ground shaking depends on the level of strain induced in the ground, the stiffness of the soil, the stiffness of the pipeline and the frictional resistance at the pipeline-soil interface.

Transient strains and curvatures are induced in buried pipelines as a result of incoherent, or out-of-phase ground motion along their length. These effects are significant for pipelines because of their extent, whereas for most above-ground structures, the ground motion at the foundation can be considered as coherent. This effect helps to explain why pipelines oriented parallel to a radial line extending away from an earthquake source tend to suffer more damage than pipelines which are perpendicular to the wave passage (O'Rourke *et al.*, 1980; Takada *et al.* 2002).

O'Rourke (1998) identifies four distinct categories of transient ground shaking effects of relevance to pipelines and other lifelines:

a) *Travelling ground waves*.

b) *Surface-wave generation in large sedimentary basins* (typically several kilometres wide with depths less than 1 km). Significant long-period motions are caused by surface waves generated by the trapping and focussing of obliquely incident S-waves in large sedimentary basins. Analytical modelling of the Los Angeles basin during a large earthquake has indicated that such displacements can reach a maximum amplitude of metres in places (Teng *et al.*, 1996).

c) *Vibration of sediments in relatively narrow valleys* (several hundreds of metres wide by several tens of metres deep). For smaller basins, mass shear deformation in the valley sediments is more important than wave scattering effects. In such cases, large strains are induced near valley margins.

d) *Liquefaction-induced ground oscillation* (dealt with in Section 2.4.1).

The last three phenomena are examples of long-period ground motion. It is only large earthquakes, with extended fault ruptures that give sufficiently strong excitation in the long-period range to be of engineering interest.

2.2.1 Effects of surface topography

Destructive earthquakes have often caused higher concentrations of building damage on the tops of hills than at their bases. Bard & Riepl-Thomas (2000) cite a number of examples, including the 1976 Friuli (Italy) earthquake, the 1980 Irpinia (Italy) earthquake and the 1985 Chile earthquake.

Instrumental and theoretical evidence supports the hypothesis that surface topography can significantly modify the amplitude and frequency content of ground motion. However, few systematic investigations have been conducted into this phenomenon and there is, as yet, no general consensus.

Geli *et al.* (1988) made a compilation of eleven individual studies of topographic effects, including both instrumental and theoretical results. Their conclusions are summarised below:

a) The amplification of ground motions on a hilltop and its de-amplification at the foot of a hill is supported, at least qualitatively, by observations and theory. In general, amplification is more pronounced for the horizontal components of ground motion than for the vertical component. For ridge-like topographies, amplification is often larger perpendicular to the ridge axis.

b) Amplification on a hilltop is roughly related to the sharpness of the topography. The steeper the terrain, the greater the amplification at the peak.

c) The frequencies most significantly modified by surface topography are those which correspond to wavelengths comparable to the horizontal dimension of the topographic feature.

d) Numerical models of topographic effects confirm the general trends observed in measurements made in the field. Sophisticated numerical models have been seen to correspond closely with field data only in cases where amplifications observed at ridge crests have been small. However, current numerical models have not consistently been able to explain the numerous instances where topographic amplification has been more significant.

In view of the current lack of understanding of topographic modification of earthquake ground motion, Bard & Riepl-Thomas (2000) suggest the need for more detailed studies of this phenomenon involving dense arrays of strong-motion instruments and detailed geotechnical characterisation of the study area. In particular, this will enable more reliable prediction of ground motions in mountainous regions, which are susceptible to landslides.

2.2.2 Effects of soft surface layers

It is well recognised that earthquake-induced ground motions are strongly influenced by the nature of near-surface geological materials. Earthquake damage to structures situated on soft soil is consistently greater than damage to structures on firm soil or bedrock outcrops. Research into this phenomenon has been motivated by the fact that most large population centres, seismic areas not excepted, have grown up on fertile, alluvial or volcanic soils often characterised by their softness and therefore their susceptibility to ground-motion amplification.

Detailed reviews of the effects of soft soil layers on strong ground-motion have been carried out by Aki (1993), Simpson (1996) and Bard & Riepl-Thomas (2000). Key features of their findings are included here, with reference to a case study in San Salvador.

The amplification of ground motion in soft soils is caused by the trapping of seismic waves within the soft layers because of the contrast in properties between the soft overlying material and the firmer underlying bedrock. In the simplest case of horizontally layered sediments, this trapping affects only the vertical propagation of body waves. However, any real soil structure will also have lateral heterogeneities which trap horizontally propagating surface waves. The trapped waves interfere with each other, giving rise to resonance effects whose spatial distribution and frequency content depend on the characteristics of the incident seismic wave form and the geometrical and mechanical characteristics of the geological structure.

Resonance effects at a given strong-motion measurement location can be identified by considering frequency domain representation of the ground motion. Fourier or response spectral plots (see Section 2.3.2.3) will peak at resonant frequencies. The location of these peaks will depend on the thickness and seismic velocities of the soil layers. For a simplified single layer 1-D structure, the fundamental frequency, f_0 and its harmonics, f_n are given by the expressions below:

$$f_0 = v_s / 4H \tag{2.4}$$

$$f_n = (2n+1) f_0 \tag{2.5}$$

where: v_s is the shear-wave velocity of the surface soil layer,
H is the layer thickness, and
n is an integer.

Very thick deposits or very soft soils (of low-shear wave velocity) are therefore characterised by low fundamental frequencies (~0.2Hz), whereas very thin or stiff layers have much higher fundamental frequencies (~10Hz).

The amplitude of resonant peaks depends mainly on the contrast between the soil layers and the underlying bedrock, on the material damping in the sediments and, to a lesser extent, on the characteristics of the incident wave field (type of waves, incidence angle, and distance from fault rupture). In the case of a single homogeneous layer impinged by vertically propagating plane S-waves, the amplification, A_0 of the fundamental peak is given by:

$$A_0 = \frac{1}{(1/C) + 0.5\pi\xi_1} \tag{2.6}$$

with:

$$C = \rho_2 v_{s2} / \rho_1 v_{s1} \tag{2.7}$$

where: C is the impedance contrast,

ρ_i is the density of the ith medium (i=1 for sediments; i=2 for bedrock), and

ξ_1 is the material damping of the sediments

For very low damping values ($\xi_1 \approx 0$), the amplification is simply equal to the impedance contrast.

Figure 2.5 shows the variation of spectral response across the city of San Salvador (El Salvador), recorded during the M_s 5.4 10 October 1986 earthquake. There is a general reduction of spectral ordinates with distance from the fault due largely to attenuation of the ground motion. However, from east to west, there is also a reduction in the fundamental period of ground motion. This is equivalent to an increase in the fundamental frequency and is evidence of the decreasing thickness of volcanic ash layers from around 30 m in the east at site IGN to around 10 m in the west at site HSH.

In comparing acceleration response spectra recorded on rock with those recorded on soil sites, Aki (1993) observed that, above a 'cross-over' period of about 0.2 s, soil sites tend to show higher amplification than rock sites by a factor of two to three, whereas the relation is the opposite for periods below this cross-over value.

The effects of soft surface layers are not only evident in spectra of earthquake motions. Time domain characteristics of ground motion are also modified, including peak ground acceleration (PGA), peak ground velocity (PGV) and strong-motion duration. In Mexico City, records from the 1985 Michoacan earthquake showed PGA values on the soft lakebed sediments around four times higher than on nearby bedrock outcrops overlooking the city, even though source distances were almost identical for both areas.

An important characteristic of the dynamic behaviour of soils is its non-linearity. As strain increases, the shear modulus of the soil decreases and the material damping increases. Laboratory tests have revealed that this non-linear behaviour can occur at strains as low as 10^{-4}. Non-linearity has the effect of reducing the fundamental frequency of motion due to a decrease in the shear-wave velocity. Increase in material damping results in a decrease in the spectral amplification and peak acceleration, especially at high frequencies.

Many different methods have been developed to predict the effects of soft surface layers on strong ground motion. As the main focus of the current research is on strong ground-shaking, a more detailed treatment of methods is included in Chapter 4 in the context of microzonation of ground shaking for application to damage prediction of buried pipelines.

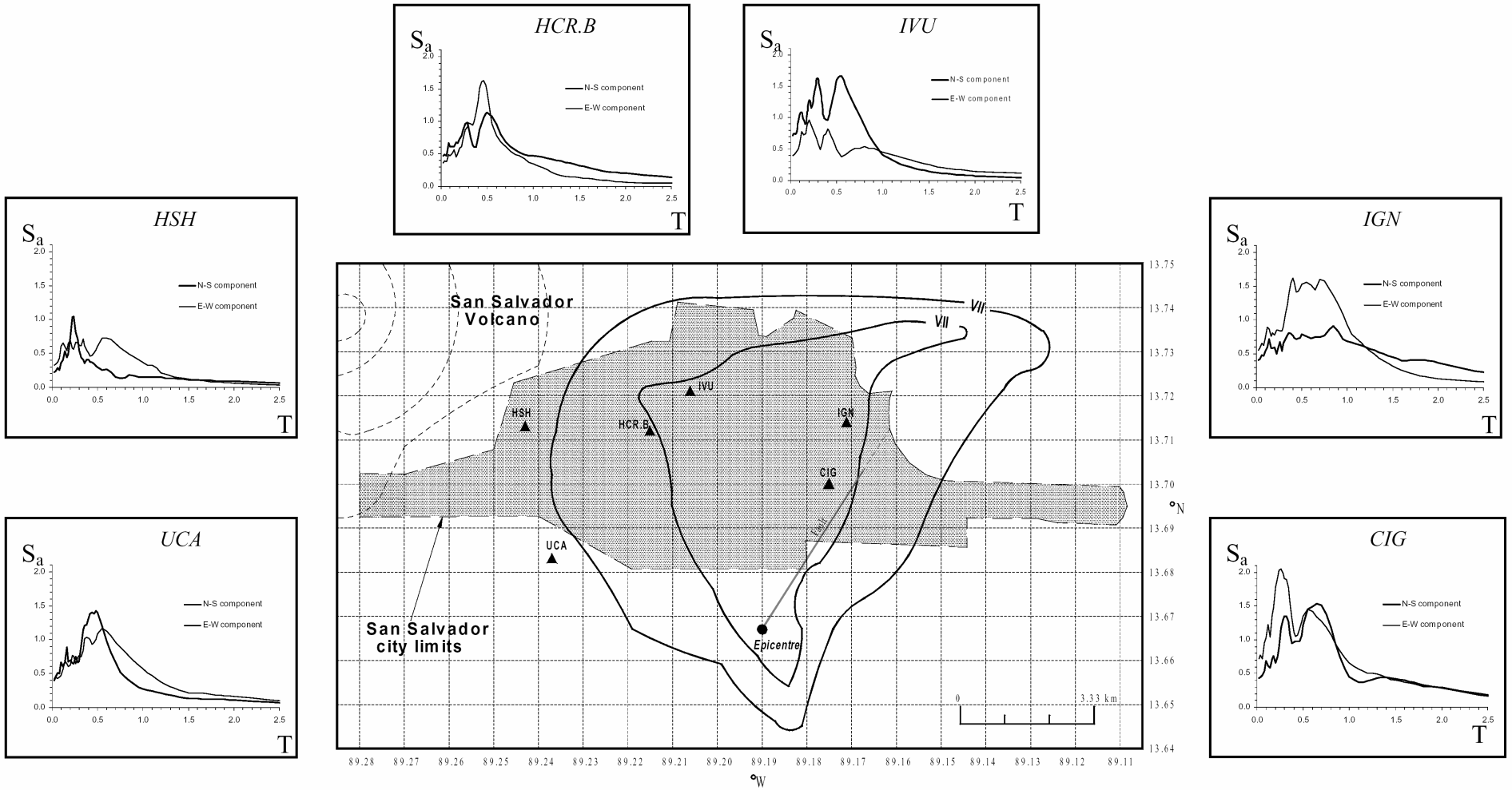

Figure 2.5 Location of accelerograph stations that recorded the 1986 San Salvador earthquake and their 5% damped acceleration response spectra (Bommer *et al.*, 2001)

2.2.3 Near-field effects

In the immediate vicinity of a fault, ground motion exhibits various characteristics that can be attributed to the orientation, direction and other features of propagation of the fault rupture. These are termed "near-field" effects; for a detailed treatment of near-field ground motions, see Martinez-Pereira (1999).

If a rupture front propagates towards a site, which is aligned with the direction of slip on the fault, most of the seismic energy will arrive in a single large pulse of motion which occurs near the beginning of the record. This is because the shear-wave velocity and the fault rupture velocity are very similar. Conversely, rupture propagation away from a site gives rise to long-duration motions having low amplitudes.

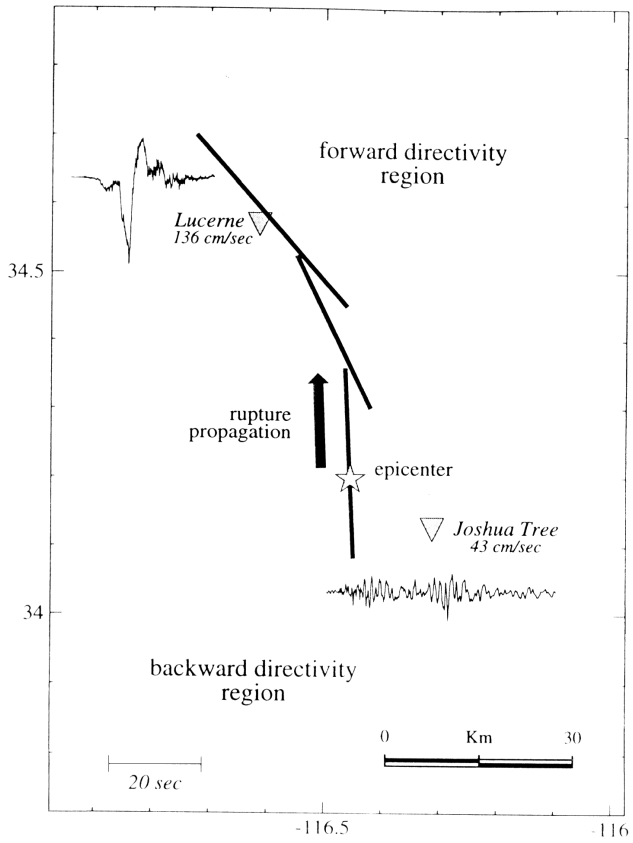

Figure 2.6 Near-field directivity effects illustrated using records from the 1992 Landers earthquake (Somerville *et al.*, 1997).

Figure 2.6 illustrates this directivity effect using the strike-normal components of ground velocity recorded at two stations during the M_s 7.3 Landers (California) earthquake of 1992. The Lucerne record was made about 1km from the surface fault rupture and consists of a large, short duration pulse of motion. This is typical of a site experiencing forward directivity effects. The Joshua Tree record, on the other hand, located near the earthquake epicentre, had a longer duration and lower amplitude, features typical of a site subject to backward directivity effects.

Attempts have been made to quantify these forward and backward directivity effects for predictive purposes. Somerville *et al*. (1997) developed modifications that can be applied to any empirical attenuation relationships for spectral ordinates to account for these effects. The ground-motion parameters modified include the duration of the acceleration time-history, the ratio of strike-normal to strike-parallel spectral acceleration and the actual amplitude of the spectral ordinates.

Sommerville *et al*. (1997) suggest that modification factors need only be considered for earthquakes of at least M_w 6.5. Bommer *et al.* (2001) highlight significant near-field effects in events of lower magnitude. In particular, they carry out 1-D ground response analysis of strong-motion records from the M_s 5.4 1986 San Salvador earthquake in order to decouple the site effects mentioned in the previous section from other factors which may have influenced the motion. They show how soil amplification at station CIG in particular (Figure 2.5) cannot fully account for the high spectral ordinates present in the recorded motion. It is suggested that this and various other features of the strong ground-motion in San Salvador are evidence of rupture directivity effects.

The issue of predicting near-field effects for a future earthquake is still very much in a state of flux. The 1997 edition of the Uniform Building Code (UBC-97) is the only seismic design code to formally consider near-field earthquake effects (ICBO, 1997). Near-source factors are defined which modify the response spectral ordinates for different period ranges depending on source-to-site distance and fault type. However, in order to correctly apply these factors to the design of a structure at a location near to an active fault requires the assumptions that the nearby fault will indeed rupture and that it will rupture in such a way as to produce forward directivity effects at the site. If forward directivity effects cannot be predicted with sufficient confidence, the application of near-source factors will inevitably give rise to over-conservative designs.

For dipping faults, differences have been noticed in the near-field between strong motion on the foot wall and strong motion on the hanging wall. This is a result of the geometry of the fault (see Figure 2.1). For a given distance from the surface projection of the fault, a site on the hanging wall will be closer to the fault as a whole than a site on the foot wall. This gives rise to a systematic increase in ground motions on the hanging wall side (Somerville, 1998b). This feature of near-field motions has been termed “the hanging-wall effect”.

2.3 Strong-motion parameters

2.3.1 Macroseismic intensity

Macroseismic intensity is a subjective measure of the severity of earthquake effects at a particular location. It is defined according to an index scale, each level having a qualitative description of earthquake effects based on human perceptions, effects on construction and effects on natural surroundings. A widely used scale, the Modified Mercalli Intensity (MMI) scale alludes specifically to the level of response of various aspects of water supply systems (see Appendix B).

At the lower intensity levels (up to VI), the effects are unlikely to be damaging to intact components of the water supply system, although sloshing effects can disrupt water treatment processes and cause structural damage to water storage tanks. Significant damage is associated with levels of VII or more.

Estimates of intensity at individual locations are combined to create isoseismal maps where contours delineate regions within which the intensity is approximately the same. The level of correlation between macroseismic intensity and damage to the water supply system depends on the weighting given to water supply system-related criteria and the level of smoothing applied when defining the isoseismals.

Due to its subjective definition, there is considerable uncertainty associated with macroseismic intensity levels and the compilation of intensity maps. Caution should therefore be exercised in the use of intensity maps for the definition of the variation in earthquake hazard from place to place or their use as a basis for the estimation of future losses. However, in the absence of instrumental data, macroseismic data is often the best available (Coburn & Spence, 1992).

Various different intensity scales exist, each with its own qualitative descriptions of earthquake effects at different intensity levels. Approximate conversions can be made between different scales, as illustrated in Figure 2.7. The recently defined European Macroseismic Intensity Scale, EMS-98 (Grunthal, 1998) (not shown) is another 12-point intensity scale, approximately equivalent to the MMI and MSK scales.

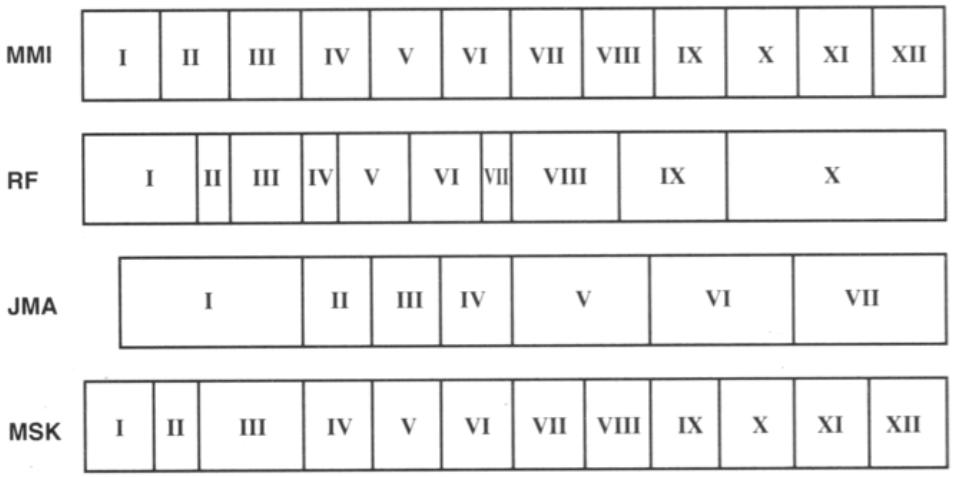

Figure 2.7 Comparison between various intensity scales. MMI – Modified Mercalli; RI – Rossi-Forel; JMA – Japanese Meteorological Agency; MSK – Medvedev-Spoonheuer-Karnik (Kramer, 1996).

2.3.2 Instrumental parameters

To completely characterise earthquake ground motion at a point, time histories would be required of the amplitude of oscillation in three mutually perpendicular directions plus torsional movements about each of the three axes. However, in order to be of use to the engineer, the severity of ground motion must be quantified concisely whilst retaining the important damage-inducing characteristics of the earthquake record. There are many ways of doing this, based on time histories of ground motion, although no single parameter is considered sufficient to accurately describe all of the key ground-motion characteristics (Kramer, 1996; Bommer & Martinez-Pereira, 2000). For earthquake engineering applications, amplitude, duration, frequency content and energy are the strong-motion characteristics of most interest.

2.3.2.1 Amplitude parameters

The commonest measure of the amplitude of earthquake motion is the peak ground acceleration, PGA. Although accelerations are related directly to inertial forces, PGA itself is not a particularly good measure of damage to structures, except in certain special cases (i.e. very stiff structures). Relatively small magnitude earthquakes, for example, can give rise to large peak accelerations but have very little impact on structures because the duration of ground shaking is so transient and the peak accelerations are at frequencies too high to be of engineering interest. As far as pipelines are concerned, regions of high PGA have been seen to correlate with pipeline damage where this damage has been due to permanent ground deformations (O'Rourke & Toprak, 1997). This is testimony to the fact that slope movements and ground cracking are generally caused by inertial forces.

Velocity is a parameter less sensitive to high frequency components of the ground motion. As such, the peak ground velocity, PGV is a useful indicator of the effect of ground motion on structures such as tall or flexible buildings, which are sensitive to intermediate frequencies. Velocity parameters in general are closely linked to the energy associated with an earthquake record, so may be better indicators of structural damage potential (Newmark & Hall, 1982). As will be elaborated upon in Chapter 3, PGV correlates well with transient strains induced in the ground. As such, it is a very useful parameter for understanding the seismic behaviour of buried pipelines.

Peak ground displacements (PGD) are related more to the low-frequency content of strong ground-motion. Where displacements are calculated from the integration of acceleration time-histories, their reliability in characterising aspects of the true ground motion is significantly limited by inaccuracies in processing the raw data and by the presence of long-period noise. These issues are dealt with in detail in Chapter 5. It is worth noting that the acronym PGD is sometimes used in the literature to refer to permanent ground deformation, which, in the current study is designated GD_p.

PGA, PGV or PGD normally refer to the maximum amplitudes of motion as measured in the horizontal plane. The peak ground-motion amplitudes in the vertical plane are usually lower than those measured in the horizontal plane. PGA, PGV and PGD have been defined in various ways in different studies. Some of these definitions are compared in Section 5.1.3.

2.3.2.2 Duration parameters

The level of earthquake damage is often strongly influenced by the duration of strong ground-motion. In the presence of certain ground conditions (e.g. liquefiable deposits), repeated stress or load cycles of moderate amplitude, over an extended period, can cause more damage than higher amplitude motion over a shorter period.

Bommer & Martinez-Pereira (1999) review almost thirty different definitions of strong-motion duration, which have been proposed by various researchers since 1962. They identify three generic groups: bracketed duration, uniform duration and significant duration. They show that the use of different definitions can give rise to very different duration values for any given strong-motion record. Selection of a specific definition should therefore depend on purpose.

2.3.2.3 Frequency-content parameters

The earthquake response of structures and the ground is highly influenced by the frequency content of the input motion. Frequency content is significant for buried structures in as much as the response of the soil layers in which they are embedded is sensitive to frequency content. It is therefore important to consider how the amplitude of ground motion is distributed among the range of frequencies.

Plots of response and Fourier spectra are both commonly used to identify dominant components of ground motion that might have an over-riding influence on the response of certain structures or soil types. The response spectrum describes the maximum response of a single-degree-of-freedom (SDOF) system to a given input motion as a function of the natural frequency (or natural period) and damping ratio of the SDOF system. The response may be expressed in terms of displacement, velocity or acceleration. The maximum system response values are referred to as the spectral displacement (SD), spectral velocity (SV) and spectral acceleration (SA) respectively. The spectral acceleration at zero natural period (which corresponds to an infinite natural frequency) is equal to PGA

The Fourier amplitude spectrum of strong ground-motion shows how the amplitude of the motion is distributed with frequency (or natural period). It allows clear visualisation of the frequency content of motion. As with response spectra, Fourier spectra can be expressed in terms of displacement, velocity or acceleration. Important characteristics of the ground motion can be

extracted from the spectra using simple scalar parameters such as predominant period and bandwidth.

The peak velocity and the peak acceleration values are related to the high and intermediate frequency components of strong ground-motion respectively. The ratio PGV/PGA is therefore a measure of the relative importance of these frequency ranges in the motion. Since for simple harmonic motion, (PGV/PGA).2π is equal to the period, T, the same quantity for a multi-frequency content motion can give a measure of the effective period of the ground motion (Tso *et al.*, 1992; Kramer, 1996).

2.3.2.4 Other parameters

A number of parameters are particularly useful in that they embody more than one of the key earthquake characteristics of amplitude, duration and frequency content. Arias intensity (Arias, 1970), I_a embodies both the amplitude and duration characteristics. It is defined as

$$I_a = \frac{\pi}{2g} \int_0^{t_r} [a(t)]^2 \, dt \tag{2.8}$$

where *a(t)* is the variation of acceleration with time, g is the acceleration due to gravity and t_r is the total duration of the record.

The energy density, E_d (Sarma, 1971) also includes characteristics of both amplitude and duration. Its definition is similar to I_a but it is obtained from the velocity time-history, $v(t)$, rather than the acceleration time-history:

$$E_d = \int_0^{t_r} [v(t)]^2 \, dt \tag{2.9}$$

The root-mean-square acceleration, a_{rms} is a measure of equivalent constant level of acceleration defined over an extended interval, $t_d = t_2 - t_1$ of the strong-motion record:

$$a_{rms} = \sqrt{\frac{1}{t_d} \int_{t_1}^{t_2} [a(t)]^2 \, dt} \tag{2.10}$$

Unlike peak acceleration, this parameter is not unduly influenced by the high-frequency content of the ground motion, although it is sensitive to the value of t_d selected.

The response spectral intensity, SI is the area under the pseudo-velocity spectrum between periods of 0.1 s and 2.5 s, a period range which covers the response of many structures. Of particular interest is the fact that the pipeline network shut-down system operated by Tokyo Gas Company uses this parameter to define its threshold ground-motion level (Nakane *et al.*, 1992; Molas & Yamazaki, 1994).

2.4 Collateral effects

2.4.1 Liquefaction

Liquefaction is a term used to describe a variety of complex phenomena involving soil deformations characterized by the generation of excess pore-water pressure under undrained loading conditions.

Previous earthquakes have produced spectacular examples of liquefaction-induced damage in all types of structure, above and below the ground. The term *liquefaction* has been used to describe a number of different, though related phenomena. For engineering purposes, Kramer (1996) divides liquefaction phenomena into two main groups: *flow liquefaction* and *cyclic mobility*.

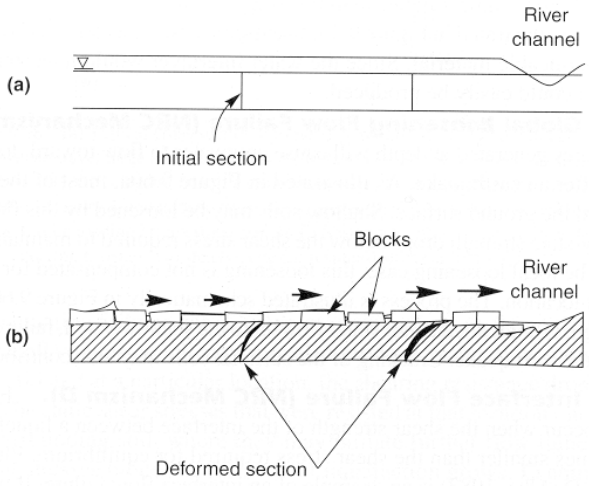

Figure 2.8 Lateral spreading caused by liquefaction of subsurface layer (a) before and (b) after an earthquake (Kramer, 1996)

Flow liquefaction failures are characterized by their sudden, catastrophic nature and the speed and extent of movement of the liquefied materials. The occurrence of flow liquefaction requires an undrained disturbance to bring the soil to an unstable state. Once initiated, it is actually the static shear stresses that drive the failure and give rise to the often large deformations observed. The effects of flow liquefaction on buried pipelines is discussed in Section 2.4.2.

Cyclic mobility occurs under a broader range of soil and site conditions than flow liquefaction. As a result, it is observed in the field much more frequently although its effects are generally less severe. Cyclic mobility occurs when the static shear stress is smaller than the shear strength of the liquefied soil. Deformations are not sudden as in the case of flow liquefaction, but develop incrementally over the duration of ground shaking. The deformations to which it gives rise are termed *lateral spreads* and can be up to several metres if the earthquake is large enough or of sufficient duration. Lateral spreading can occur on very gently sloping ground or even on flat ground adjacent to a free face, as illustrated in Figure 2.8. In this case, lateral movement of the liquefied subsurface soil has broken the surface layer into distinct blocks which move differentially both horizontally and vertically. A pipeline embedded in the non-liquefied surface layer may be

pulled apart or sheared. A pipeline passing through the liquefied layer would be subject to horizontal and vertical forces due to the flow of soil around it, plus an uplift force due to buoyancy.

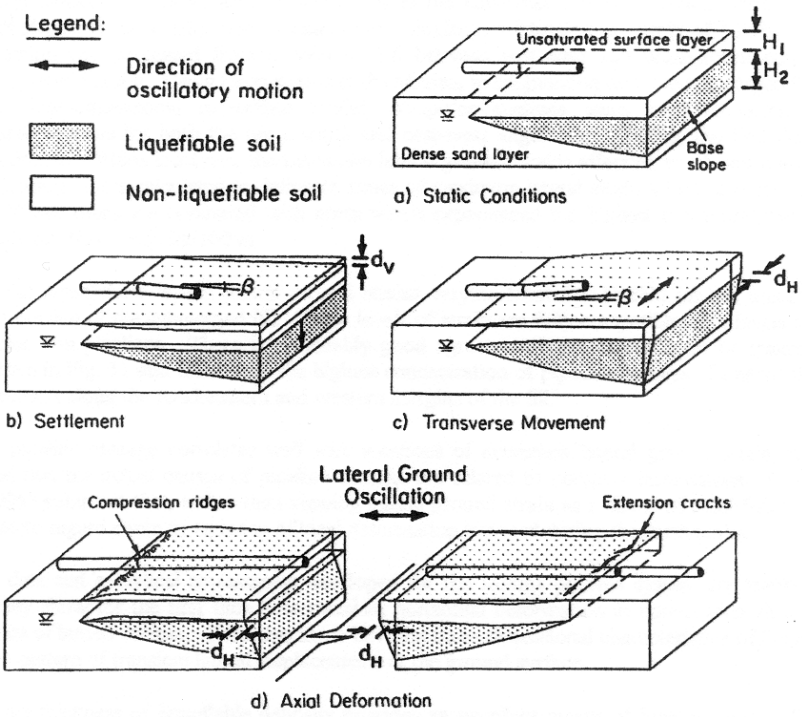

Figure 2.9 Behaviour of pipelines embedded in a competent surface layer overlying a liquefied subsoil (O'Rourke, 1996)

A special case of cyclic mobility, termed ground oscillation, has been observed in areas of virtually level ground where surface soils oscillate on top of a liquefied layer. Unlike other liquefaction phenomena, ground oscillation is essentially transient. Pease & O'Rourke (1997) confirmed its significance for buried pipelines in an investigation of damage caused during the 1989 Loma Prieta earthquake. Figures 2.9 (c) and (d) illustrate pipeline response to ground oscillation. The situation has been simplified by considering transverse and axial components of movement separately. The potential for damage is greatest where the liquefiable layer thins out, forming a boundary with more competent material. Figure 2.9 (b) illustrates permanent vertical deformation in a non-liquefiable soil caused by consolidation of the liquefied sub-layer.

Soil liquefaction has caused significant damage to buried lifelines in past earthquakes. Zonation of liquefaction hazard is therefore of particular importance to lifeline earthquake engineers. Not all soils are susceptible to liquefaction, so the first stage of liquefaction hazard evaluation must be determination of liquefaction susceptibility. For any given soil, liquefaction susceptibility can be judged according to various historical, geological, compositional or soil state criteria. Once it has been established that soil has the potential for liquefaction, the next stage is to determine the likelihood that an earthquake will cause a disturbance strong enough to initiate the phenomenon. The criteria necessary for liquefaction susceptibility and the conditions required to trigger

liquefaction are complex and beyond the scope of the current study. A detailed treatment of these issues can be found in Kramer (1996).

Given that liquefaction is likely at a particular location, of most importance from an engineering perspective is to predict the amount of permanent ground displacement associated with the liquefaction. Hamada *et al.* (1986), for example, proposed a formula to predict the horizontal ground displacement caused by liquefaction-induced lateral spreads, based on failures observed in the 1964 Niigata and 1983 Nihonkai-Chubu earthquakes. From a comparison of pre-earthquake and post-earthquake aerial photographs, ground deformation patterns were identified. Lateral spreads were divided into discrete blocks. The amount of horizontal displacement, the thickness of the inferred liquefied layer and the severity of ground slope were then averaged within each block to give the following expression:

$$D_H = 0.75\sqrt{H_{liq}}\cdot\sqrt[3]{\theta} \tag{2.11}$$

where: D_H is the horizontal ground displacement (m),
H_{liq} is the thickness of the liquefied layer (m)
θ is the maximum of slope of base of liquefied layer and slope of ground surface (%)

H_{liq} is a parameter which indirectly accounts for the amount of ground shaking (a function of earthquake magnitude and distance) as well as the soil conditions at the site.

Youd & Perkins (1987) introduced the idea of a Liquefaction Severity Index (LSI) to predict the maximum ground displacement expected at a given liquefaction site. From observations made during six earthquakes in the western US, they suggested that ground displacement is primarily a function of the amplitude and duration of strong ground-motion. However, due to lack of strong-motion records for many of the sites studied, they defined LSI in terms of earthquake magnitude and distance as follows:

$$\log LSI = -5.09 - 1.86\log d_f + 0.98M_w \tag{2.12}$$

where: LSI is the maximum expected permanent horizontal displacement (m), arbitrarily truncated at 100 inches (2.54 m),
d_f is the shortest horizontal distance measured from the surface projection of the seismic energy source or fault rupture to the site of interest (km),
M_w is the moment magnitude.

Both of these empirical relationships give useful estimates of the amount of ground deformation but are limited in their range of applicability. Bartlett & Youd (1992) showed that equation 2.11 produces reasonable estimates of permanent ground deformation for earthquakes with magnitude around 7.5 and at epicentral distances between about 20 and 30 km. The Youd & Perkins (1987) relationship is only strictly valid for the western US since it describes the attenuation characteristics of strong motion with distance for that particular region.

Pipeline response to liquefaction-induced lateral spreading is strongly influenced by the shape and spatial extent of the liquefied area (O'Rourke & Liu, 1999). However, analytical or empirical methods for their prediction are not yet available.

2.4.2 Landslides

The importance of earthquake-induced landslides is well-recognized (Keefer, 1984; Rodriguez *et al.*, 1999). In many earthquakes the economic and social impact of landslide damage alone has exceeded the combined impact of all other seismic hazards (Kramer, 1996).

The term *landslide* covers a broad range of phenomena involving gravity-driven movements of earth materials downslope. Various classification schemes have been proposed based on morphology, material, mechanism of initiation or other criteria (Keefer, 1984). The classification developed by Varnes (1978) is one of the most widely used and has been adopted by Keefer (1984) to classify earthquake-induced landslides according to material type (soil or rock), character of movement (disrupted or coherent) and other secondary attributes (water content, velocity of movement and depth). The full scheme is included in Appendix C. Three main categories are identified: disrupted slides and falls, coherent slides, and lateral spreads and flows.

Disrupted slides and falls are the most catastrophic types of failures, occurring in steep terrain and characterized by high velocities. This category includes a range of phenomena, from individual rock falls, the most abundant type of earthquake-induced landslide, to rock avalanches, uncommon but incredibly destructive events involving volumes of material $\sim 10^6$ m^3, translated over large distances (~km). All of the landslides in this category, whether in rock or soil, are characterized by 'high' or 'very high' levels of internal disruption (see Appendix C for definitions).

Coherent slides generally involve deep-seated translational movements of blocks of intact material sliding on a basal shear surface. Failures occur on moderate to steep slopes and tend to have much lower velocities than disrupted slides.

The landslide phenomena in the category *lateral spreads and flows* generally occur in saturated conditions, although rapid soil flows may occur in dry soils (Keefer, 1984). Lateral spreads are translational movements on basal zones of liquefied gravel, sand, silt or weakened sensitive clay. They are more disrupted than soil slumps or soil block slides, containing many internal fissures and grabens. Rapid soil flows exhibit fluid-like behaviour and can involve large volumes of soil travelling significant distances. All phenomena in this category can occur even on very shallow slopes because of the low residual strength of the materials involved. Liquefaction-induced lateral spreads and flows, a subset of this category have been described in section 2.4.1.

A slope that is stable under static gravitational loading may fail under seismic loading due to the additional dynamic forces. The instabilities that cause seismic slope failure may be grouped into two categories: *inertial instabilities* and *weakening instabilities* (Kramer, 1996). Inertial

instabilities involve temporary exceedances of the strength of the earth material due to the earthquake loading. The strength of the material remains almost constant. Weakening instabilities are related to changes in the inherent strength of the material caused by a combination of pore pressure generation and structural disturbance. Any specific instance of earthquake-induced landslide will generally have been caused by a combination of these two instabilities. In general terms, the more coherent the landslide, the less significant the weakening instability.

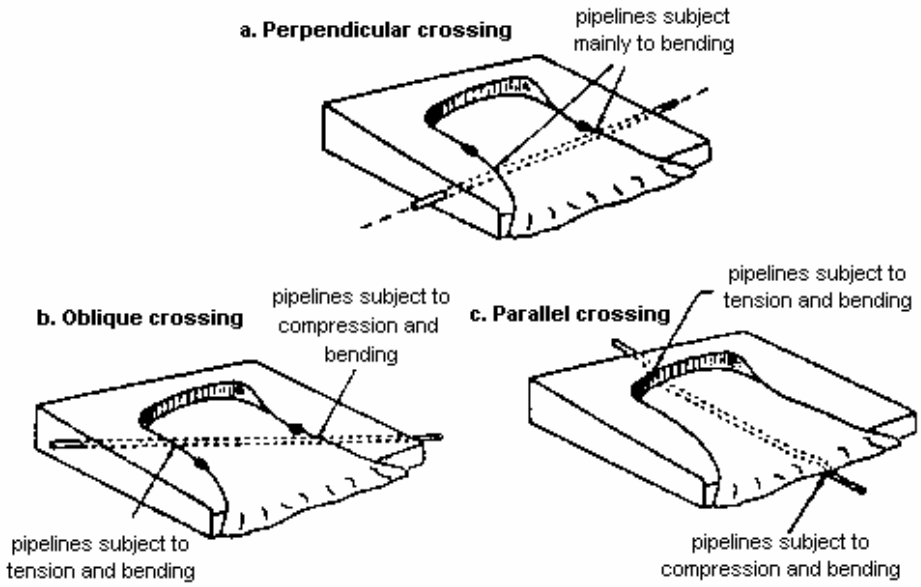

Figure 2.10 Principal effects of landslides on pipelines according to their orientation (O'Rourke, 1998)

Studies of past earthquakes have indicated the relative abundance of the different types of landslides over a broad range of earthquakes and geological environments (see Appendix C). This gives a global indication of the relative importance of each hazard to the built environment, as more abundant types of landslides are more likely to cause damage to engineered structures. However, the relative abundance of each landslide phenomenon may vary significantly between earthquakes.

Buried pipelines are vulnerable to differential movements in the surrounding soil. Pipeline damage will therefore depend on the amount, extent and abruptness of permanent ground deformation associated with a landslide. The soil-pipe interaction is affected chiefly by the stiffness of the soil. All other things being equal, a coherent slide will therefore be more damaging than a landslide in disrupted or liquefied material. The significance of pipeline orientation with respect to landslide movement is illustrated in Figure 2.10.

The routing of pipelines through regions susceptible to landslides is often unavoidable. This is particularly true for bulk water transmission pipelines that convey water from mountain sources to

population centres. The zonation of landslide hazards is therefore an important step in the identification of vulnerable portions of the water supply system.

Pitilakis *et al.* (1995) described an approach for the zonation of landslide hazard specifically for the vulnerability assessment of buried pipelines. The region of interest is divided into square cells, each cell being characterised by a number of factors which affect susceptibility to earthquake-induced landslides. These include geotechnical parameters and information on surface geology, topography and hydrology. The cell dimensions are defined to be commensurate with the level of detail of data available to characterise each cell. The seismic hazard is defined for each cell in terms of a peak strong-motion parameter. The landslide hazard can then be defined for each cell in terms of a dynamic factor of safety, allowing the stable and potentially unstable areas to be readily distinguished.

2.4.3 Densification

Earthquake-induced strong ground-shaking can cause densification of both cohesive and cohesionless soils (O'Rourke & Liu, 1999). This process manifests itself as settlement at the ground surface and is therefore potentially damaging to buried infrastructure, as illustrated in Figure 2.9b. Seismic densification of clays has been observed, but it is the densification of sands, either saturated or dry, which is of greater consequence.

Settlement of dry sands is normally complete by the end of strong ground-shaking. However, the process in saturated sands occurs only as earthquake-induced excess pore water pressures dissipate. This will depend on the permeability and compressibility of the soil and on the drainage path length and therefore may not be complete until some hours after the earthquake. Following the 1995 Hyogoken-Nanbu (Kobe) earthquake, post-liquefaction settlements of up to 1 m were observed in the loose artificial fill materials on reclaimed land in the Osaka Bay area.

Formulae for the estimation of ground settlement during earthquakes have been developed by Takada & Tanabe (1988) based on the regression analysis of 404 instances of ground settlement from five major Japanese earthquakes ($7.4 \leq M_{JMA} \leq 7.9$). The expressions were derived specifically for the purpose of earthquake design of lifeline facilities, motivated by the high levels of settlement-induced pipeline damage observed in the earthquakes under investigation. Two expressions are given - the first for settlement of an embankment (δ_1) and the second for settlement of a plain (level) site (δ_2). δ_2 and δ_2 are both measured in cm.

$$\delta_1 = \frac{C_1 B H_{sand} a_p}{N_{SPT}} + C_2 \tag{2.13}$$

$$\delta_2 = \frac{C_3 H_{sand} a_p}{N_{SPT}} + C_4 \tag{2.14}$$

where: B is the embankment height (m),
H_{sand} is the thickness of the sandy layer (m),
N_{SPT} is the Standard Penetration Test (SPT) N-value of the sandy layer,
a_p is the PGA (in cm/s^2), and
C_i are coefficients of regression. C_1 has dimensions of s^2/m^2; C_2 and C_4 have dimensions of cm; C_3 has dimensions of s^2/m.

For both expressions, coefficients were derived for two different datasets: settlements in liquefied soil, and settlements in both liquefied and non-liquefied soil. Coefficients are summarised in Table 2.3.

Table 2.3 Regression coefficients for calculation of δ_1 and δ_2 according to Equations (2.13) and (2.14) respectively.

Quantity predicted	Type of site	Dataset	C_1	C_2	Correlation coefficient	Size of dataset
δ_1	Embankment	Liquefied soil	0.123	19.3	0.88	35
δ_1	Embankment	Liquefied and non-liquefied soil	0.118	19.9	0.88	42
Quantity predicted	**Type of site**	**Dataset**	C_3	C_4	**Correlation coefficient**	**Size of dataset**
δ_2	Plain site	Liquefied soil	0.339	3.79	0.81	41
δ_2	Plain site	Liquefied and non-liquefied soil	0.332	4.86	0.82	43

Two sets of regressions were carried out using two different PGA datasets (calculated using two different, unspecified attenuation relationships). The coefficients quoted in Table 2.3 are, in each case, the values associated with the PGA dataset which gave the best correlation coefficient. Separate coefficients were presented for expressions which used PGV and PGD instead of PGA, although the investigators recommend use of the PGA expressions for predictive purposes.

The expressions indicate that ground settlement increases with the thickness of the sandy soil layer and with PGA but decreases with increasing SPT N-value of the sandy layer. Settlements in liquefied soil were greater than settlements in non-liquefied soil, all other factors being equal. No ground settlement was observed for PGA below 50 cm/s^2.

In the current Chapter, the behaviour of buried pipelines subject to earthquake-induced ground shaking is considered in some detail. In the first Section, a distinction is made between pipeline behaviour subject to different types of seismic waves. The influence of ground conditions on pipeline response is considered in Section 3.2.

Factors affecting the earthquake vulnerability of buried pipelines are discussed in Section 3.3, including a detailed review of empirical relations for the estimation of pipeline damage caused by seismic ground shaking.

3.1 Earthquake-induced ground and pipe strain using a travelling-wave model

In order to evaluate the effect of seismic wave propagation on buried pipelines, it is important first to quantify the ground strain. If the seismic excitation at the surface is treated as a simple travelling wave of constant shape, it can be shown that the peak horizontal soil strain, ε_p in the direction of propagation is related to the peak horizontal particle velocity, v_p (also in the direction of wave propagation) by the relationship

$$\varepsilon_p = \frac{v_p}{c} \tag{3.1}$$

where c is the apparent propagation velocity of the waves with respect to the ground surface (Newmark, 1967; Newmark & Rosenblueth, 1971). The derivation of Equation (3.1) is given in Appendix D.

St John & Zahrah (1987) used Newmark's approach to develop solutions for ground strains and curvatures as a result of P-waves, S-waves and R-waves. These results give free-field deformations, which ignore the interaction between the ground and the pipeline. However, they can be used to provide a first-order estimate of the anticipated deformation of a buried structure. A summary of the results for longitudinal strain, taken from Hashash *et al.* (2001), is given in Table 3.1. Figure 3.1 shows the wave orientation, ϕ, with respect to the pipeline axis.

Hashash *et al.* (2001) give additional expressions derived by St John & Zahrah (1987) for normal strain, shear strain and curvature, as a result of P-waves, S-waves and R-waves. However, other than for very large diameter pipelines and tunnels, it is the longitudinal deformations which dominate under seismic action.

Equations (3.3), (3.5) and (3.7) in Table 3.1 give the maximum longitudinal strain together with the corresponding value of ϕ. For P-waves and R-waves, the maximum longitudinal strain occurs when the direction of propagation is parallel to the pipe axis. For S-waves, the maximum strain occurs when propagation is oblique to the pipeline axis (ϕ = 45°).

Table 3.1 Ground strains induced by seismic waves propagating along a pipeline (St John & Zahrah, 1987). v_{pP} is peak particle velocity caused by P-waves, c_p is the apparent P-wave propagation velocity, v_{pS} is the peak particle velocity caused by S-waves, c_S is the apparent S-wave propagation velocity, v_{pR} is the peak particle velocity caused by R-waves, c_R is the apparent R-wave propagation velocity and ϕ is the angle of incidence of the wave with respect to the tunnel axis. The term "apparent propagation velocity" refers to the velocity of a seismic wave with respect to the ground surface.

Wave type	Longitudinal strain	Maximum longitudinal strain
P-wave	$\varepsilon = \frac{v_{pP}}{c_P}\cos^2\phi$ (3.2)	$\varepsilon_p = \frac{v_{pP}}{c_P}$ for ϕ = 0° (3.3)
S-wave	$\varepsilon = \frac{v_{pS}}{c_S}\sin\phi\cos\phi$ (3.4)	$\varepsilon_p = \frac{v_{pS}}{2c_S}$ for ϕ = 45° (3.5)
R-wave (compressional component)	$\varepsilon = \frac{v_{pR}}{c_R}\cos^2\phi$ (3.6)	$\varepsilon_p = \frac{v_{pR}}{c_R}$ for ϕ = 0° (3.7)

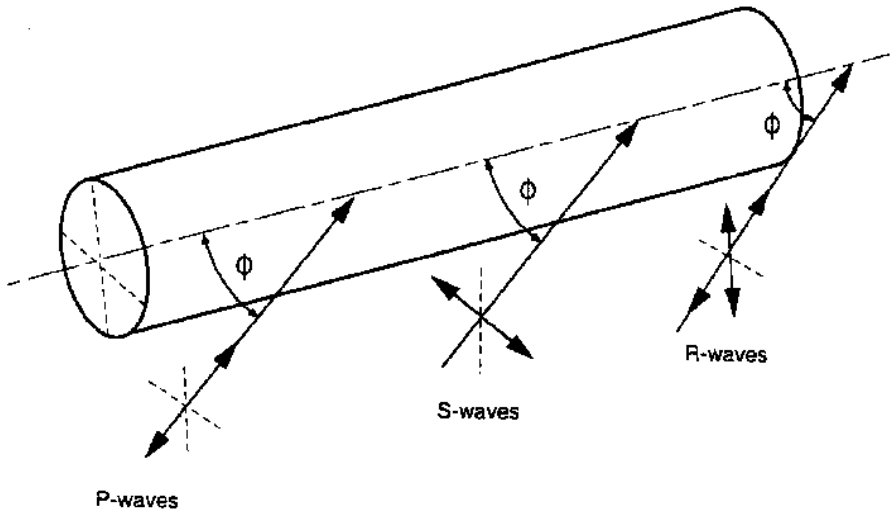

Figure 3.1 Definition of angle of incidence of seismic waves with respect to pipeline axis, as defined in Table 3.1 (Hashash *et al.*, 2001). ϕ is measured in the horizontal plane in the case of R-waves and in the vertical plane in the case of body waves.

For the purposes of back-analysis or design, v_{pP}, v_{pS} and v_{pR} in Table 3.1 are equivalent to PGV obtained from strong-motion time-histories or attenuation relationships (see Chapter 5). The variation of PGV with depth, as observed in data from various downhole arrays (eg. Sykora & Bastani, 1998) is generally not significant for typical pipeline burial depths (0.5-3 m). Values recorded at the ground surface can therefore be used unmodified. If a site-specific seismic hazard analysis is available for a given design scenario, both PGA and PGV for a particular return period are likely to be available. However, for less critical facilities, PGA might be the only parameter available. In such cases, it has been suggested (O'Rourke & El Hmadi, 1988; Hashash *et al.*, 2001) that PGV be approximated from PGA using established relationships for the ratio PGA/PGV (eg. Seed *et al.*, 1976; Hashash *et al.*, 2001).

Whether surface waves or body waves are likely to dominate the strong motion at a given site is important for calculation of the apparent propagation velocity, c, which is different for different wave types. Conditions for the domination of surface waves at a given location have been summarised in Equations (2.5) and (2.6), based on earthquake magnitude, epicentral distance and focal depth. Methods for approximating c in order to calculate ground strain are explained in Sections 3.1.1 and 3.1.2.

3.1.1 Estimation of ground strain caused by body waves

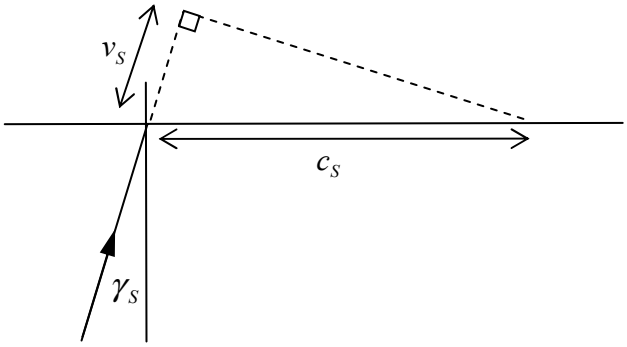

Figure 3.2 Apparent propagation velocity of S-waves, c_S (vertical plane).

As body waves travel upwards towards the ground surface, they are refracted towards the normal due to increasingly soft strata of geological materials. By the time they reach the surface, the angle of incidence is usually very small. In fact, most ground response models (eg. ProShake) assume vertical S-wave arrival. The apparent propagation velocity of a vertically-incident body wave (γ_S = 0) is infinite. In other words, the motion at the ground surface is in-phase. In reality, body-wave arrival is sub-vertical, giving rise to high values of apparent velocity with respect to the ground surface. As illustrated in Figure 3.2, the apparent propagation velocity of S-waves, c_S is given by

$$c_S = \frac{v_S}{\sin \gamma_S} \tag{3.8}$$

where: v_S is the shear wave velocity of surface materials and
γ_S is the angle of incidence of S-waves

Without modification for angle of incidence, the shear-wave velocity in the soil, v_s significantly underestimates the apparent propagation velocity, c_S. The angle of incidence of body waves is not easy to determine for a given location. However, O'Rourke *et al.* (1982) developed a technique for approximating its value from time-histories of strong motion and knowledge of material properties of the surface soil layer. The technique involves the calculation of the predominant direction of

ground motion from a ground motion intensity tensor for a set of three mutually perpendicular ground accelerations. Accounting for the reflection of waves at the free surface, an approximate relationship is derived between the predominant direction of ground motion with respect to the vertical, ϕ_v and the angle of incidence of body waves with respect to the vertical, γ_S. Assuming a Poisson's ratio for bedrock of 0.25, this relationship is:

$$\gamma_S = 0.87\phi_v \tag{3.9}$$

For small angles of incidence (γ_S and ϕ_v not exceeding about 25°), $\sin\alpha \approx \alpha$. Equation (3.8) can therefore be rewritten as:

$$c_S = \frac{v_S}{0.87\phi_v} \tag{3.10}$$

O'Rourke *et al.* (1982) calculate ϕ_v from the P-wave portion of the accelerogram. They then use this result to calculate the apparent propagation velocity of S-waves since S-waves carry more energy and tend to generate greater ground strains than P-waves. The method of O'Rourke *et al.* (1982) assumes that the ground motion at a given site is dominated by S-waves. Any contribution from surface waves is assumed to be negligible.

The investigators applied the technique to data from the 1971 San Fernando and 1979 Imperial Valley earthquakes and found values of c_s of 2.1 km/s and 3.7 km/s respectively. These values are comparable to values obtained using more direct, cross-correlation techniques at sites in Japan. c_S can also be approximated from wave arrival times if the relevant information is available.

During the M_w 6.7 1994 Northridge earthquake, velocity pulses of up to 177 cm/s were observed in the near-field. O'Rourke *et al.* (2001) use values of v_{pS} and c_S of 100 cm/s and 2.5 km/s respectively to estimate typical maximum body-wave induced strains for this event, based on Equation (3.5). Even for such a high PGV, strain is only of the order of 2 x 10^{-4}. Because of high apparent propagation velocities, ground strains induced by travelling body waves are generally only large enough to cause damage to pipes already weakened by corrosion and/or stress concentrations (O'Rourke *et al.*, 2001).

3.1.2 Estimation of ground strain caused by surface waves

The most significant surface-wave motions are those caused by Rayleigh waves. These induce alternating tensile and compressive strains in the direction of propagation. Since R-waves always travel parallel to the ground surface, the apparent velocity of propagation is equal to the phase velocity, c_{ph}. The phase velocity is defined as the velocity at which a transient vertical disturbance at a given frequency, originating at the ground surface, propagates across the surface of the medium (O'Rourke & Liu, 1999). The wavelength, λ, and the frequency, f, are related to c_{ph} by

$$c_{ph} = \lambda f \tag{3.11}$$

This frequency dependence can be quantified by means of a dispersion curve. Curves have been derived by various researchers for layered soil profiles (eg. Haskell, 1953). O'Rourke *et al.* (1984) developed a simple procedure for determining the dispersion curve of layered soil profiles. Figure 3.3 shows a normalised dispersion curve for a uniform layer of thickness, H, with shear-wave velocity v_{Ssoil} (km/s) and Poisson's ratio, υ_{soil}, overlying a half space with shear-wave velocity v_{Srock} (km/s) and Poisson's ratio, υ_{rock}. Curves are shown for two values of the shear velocity ratio. Densities of the soil layer and half space do not have a significant effect on the form of the dispersion curve.

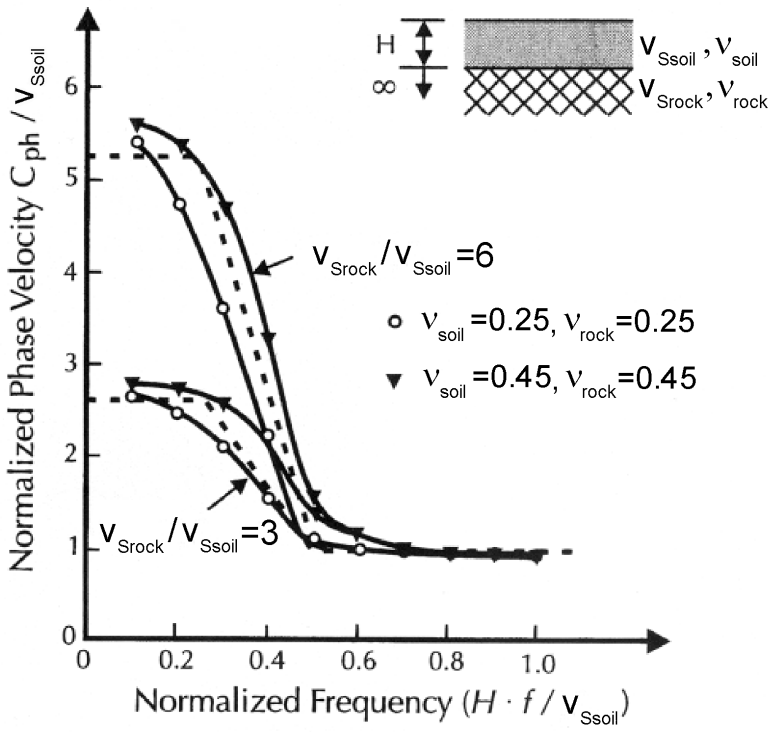

Figure 3.3 Normalised dispersion curve for single layer over half space (O'Rourke *et al.*, 1984)

O'Rourke *et al.* (1984) showed that at low frequencies ($Hf/v_{Ssoil} \leq 0.25$), c_{ph} is just below the shear wave velocity of the half space. There is no appreciable dependency on the properties of the overlying soil layer because the wavelength is large compared to the thickness of the soil layer. For high frequencies ($Hf/v_{Ssoil} > 0.5$), the wavelength is comparable to or smaller than the thickness of the surface layer. The phase velocity is therefore governed by the properties of the surface layer. For intermediate frequencies, the properties of both the soil layer and the half-space need to be considered. O'Rourke *et al.* (1984) simplified the relationship between phase velocity and frequency for a single layer overlying a half space to the tri-linear relationship shown in Figure 3.3 (dashed line). The method can be extended to multiple layered soil profiles.

The fact that the phase velocity of R-waves is an increasing function of wavelength raises the problem of identifying an appropriate wavelength for calculation of an effective R-wave propagation velocity, c_R, for determining ground strain. O'Rourke *et al.* (1984) analysed ground displacement time-histories recorded during the 1971 San Fernando earthquake at eight pairs of strong-motion stations and showed that maximum strains due to R-waves could be modelled by a fundamental mode R-wave with a phase velocity having a wavelength equal to four times the separation distance, L_s between the points. A combination of Equation (3.11) and a dispersion curve for the site of interest can therefore be used to find a value of c_R for use in estimating maximum longitudinal strain in Equation (3.7).

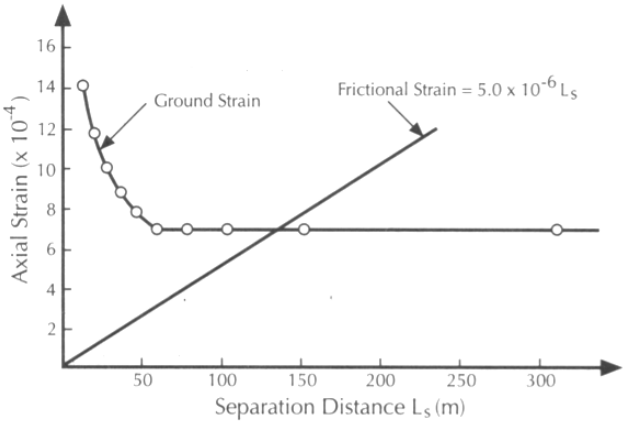

Figure 3.4 Variation of frictional strain and ground strain with separation distance (O'Rourke & El Hmadi, 1988)

O'Rourke & El Hmadi (1988) developed a procedure for estimating the maximum pipe strain caused by R-waves in a continuous pipe. For a given set of ground conditions, they calculate the ground strain for a range of values of L_s using the procedure described above. They then calculate the ground strain which would result in frictional slippage between the pipe and the surrounding soil based on an elastic model of the pipeline surrounded by equivalent soil springs. As illustrated in Figure 3.4, they show that the ground strain is a decreasing function of L_s whereas the maximum pipeline strain due to friction is an increasing function of L_s. At a particular separation distance (that is, for a particular value of quarter wavelength of R-waves), the friction strain matches the ground strain. O'Rourke & El Hmadi (1988) suggest that this is the peak strain which could be induced in a continuous pipeline by R-wave propagation and propose use of the procedure for design purposes. As noted by O'Rourke & Liu (1999), this procedure conservatively assumes that PGV corresponds to all frequencies of R-wave propagation and that all frequencies are present in the record.

Ayala & O'Rourke (1989) used the procedure to back-analyse a pipeline failure observed in Mexico City during the 1985 Michoacan earthquake. Use of the R-wave model was deemed appropriate as strong-motion records indicated that peak velocities were associated with surface waves rather than body waves. The pipeline under investigation was a 1070 mm diameter welded

steel pipeline, 9 km in length with the pipe centreline 1.94 m below the ground surface. The top 40 m of soil consisted of very soft clay (v_s = 40 m/s). Below this were two stiffer strata with thicknesses of 80 m and 400 m and shear wave velocities of 300 m/s and 500 m/s respectively. Shear wave velocity of the bedrock was estimated to be about 1250 m/s. Maximum estimated pipe strain based on a diagram similar to Figure 3.4 for the set of ground conditions present at the study site was around 0.0023. Ayala & O'Rourke (1989) calculated the corresponding pipeline stress to be about 282 MPa, around 96% of the theoretical value required to cause local buckling failure, which was indeed the failure mode observed in the pipeline. Such high wave-propagation-induced ground strains are exceptional and are related to the extremely soft soil encountered in the Mexico City region. However, the case study does illustrate the vulnerability of buried pipelines to the effects of surface waves. The apparent R-wave propagation velocity, c_R, giving rise to the maximum strain observed in this case was around 150 m/s. Even though the PGV at the Mexico City site (34.8 cm/s) was significantly less than for the Northridge example cited in Section 3.1.1, peak ground strains predicted by the travelling wave model for surface waves were about a factor of ten greater in Mexico City. In summary, for the same PGV, ground strain induced by surface-wave dominated ground-motion is significantly greater than ground-strain induced by body-wave dominated ground motion.

O'Rourke (1996) proposed an alternative procedure for assessing the damage potential of transient wave propagation to buried pipelines based on damage threshold values for v_p and T_p (the predominant period of the soil surrounding the pipeline). The method uses a travelling wave assumption and is derived in a similar way to the method of Ayala & O'Rourke (1989). For R-waves, assuming that longitudinal pipeline strain and ground strain are equal, the maximum axial force, F_{m1} in a pipeline, using Equation (3.6) is given by:

$$F_{m1} = \frac{EA_p v_p \cos^2 \phi}{c} \tag{3.12}$$

where: E is the Young's modulus of the pipeline material, and
A_p is the cross-sectional area of the pipe annulus.

The maximum frictional force, F_{m2}, between the pipeline and soil caused by the propagation of a wave of wavelength λ is approximated by:

$$F_{m2} = \frac{p_f \lambda}{4 \cos \phi} \tag{3.13}$$

where: p_f is the frictional force per unit length of pipe, given by:

$$p_f = \left(\frac{1 + k_0}{2} \right) \gamma . z_p . \pi . D_0 . \tan \delta \tag{3.14}$$

where: k_0 is the lateral earth pressure co-efficient at rest,
γ is the soil unit weight,
z_p is the depth below ground surface of the pipe centreline,
δ is the friction angle between pipe and soil, and
D_o is the external pipe diameter.

Recognising that $\lambda = cT_p$, (where T_p is the predominant period of the ground), Equation (3.13) becomes:

$$F_{m2} = \frac{p_f c T_p}{4\cos\phi} \tag{3.15}$$

If F_l is the limit state force which causes pipeline failure or loss of serviceability, Equations (3.12) and (3.15) can be rewritten to express the threshold values of v_p and T_p for pipeline damage as functions of the apparent wave propagation velocity, c:

$$v_p \geq \frac{F_l c}{EA_p \cos^2\phi} \tag{3.16}$$

$$T_p \geq \frac{4F_l \cos\phi}{p_f c} \tag{3.17}$$

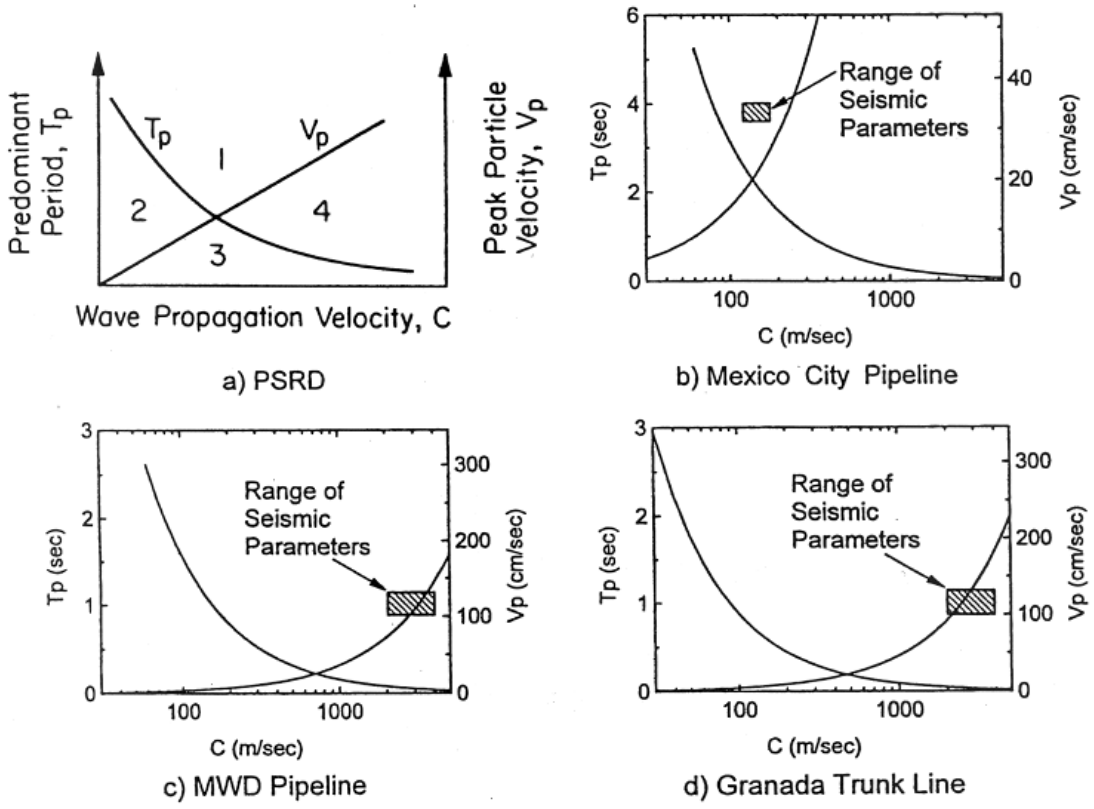

Figure 3.5 Pipeline seismic response diagram (O'Rourke, 1996). Zone 1 - pipeline is vulnerable to damage; Zone 2 - v_p exceeds the limit conditions but small c results in a wavelength insufficient to mobilise shear forces to exceed the limit state force; Zone 3 - neither v_p nor T_p exceed the limit conditions; Zone 4 - the wavelength is sufficiently large to mobilise the appropriate force, but v_p is too small to develop enough axial force to damage the pipe

Similar expressions can be written for the case of body-waves. These conditions can be conveniently expressed in a pipeline seismic response diagram (PSRD) (Figure 3.5 (a)). The pipeline is vulnerable to damage only if the combination of T_p , v_p and c plot in zone 1. The procedure was carried out for three separate case studies where earthquake damage was observed in pipelines, including the Mexico City example from Ayala & O'Rourke (1989). As shown in Figures 3.5 (b), (c) & (d), the seismic characteristics relevant to each case plot in an area overlapping the vulnerable zone. This indicates that v_p and T_p are effective parameters to use in the prediction of seismic pipeline damage. It also shows the usefulness of pipeline seismic response diagrams for identifying critical transient motion conditions for non-segmented pipes.

3.1.3 Discussion of the travelling wave model

Zerva (2000) shows that the travelling wave model expressed by Equation (3.1) gives a valid approximation of the ground strains caused by spatial variability of ground motions for apparent propagation velocities in the range associated with surface waves. At higher values of c, which are associated with body waves, the ground strains become controlled by incoherence caused by spatially variable delays in upward travelling wave fronts due to differences in travel paths from bedrock to different points on the ground surface. The effect of c on ground strain is illustrated in Figure 3.6, in which the root-mean-square (rms) value of strain is normalised with respect to the rms value of the particle velocity and is plotted against the apparent propagation velocity. Initially, the curve shows normalised seismic ground strains varying inversely with c, as anticipated from Equation (3.6). For higher values of c, strains tend to a constant value which is no longer significantly affected by c. This behaviour has been confirmed from analytical models for spatial variability (Zerva, 2000) and is consistent with the observations of O'Rourke *et al.* (1980) using data from the 1971 San Fernando earthquake.

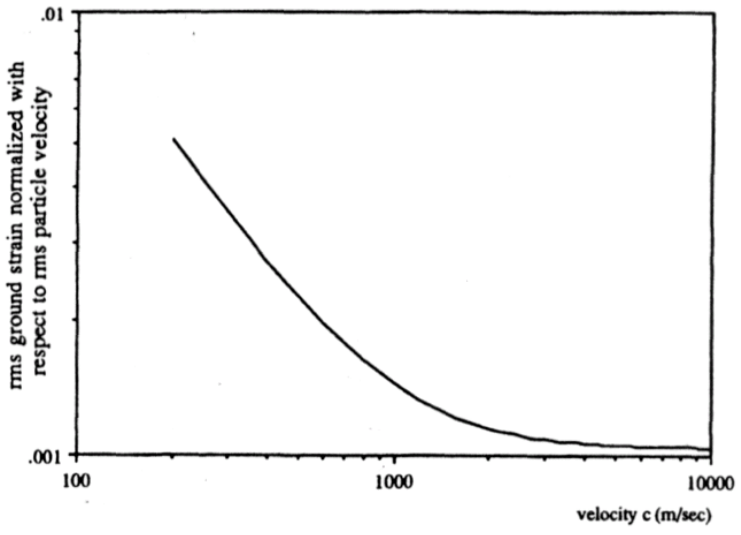

Figure 3.6 Variation of normalised rms ground strain with apparent propagation velocity (Zerva, 2000)

The travelling wave model gives reasonable first-order approximations of ground strains and as such, is useful for predicting likely values of buried pipeline strain. The approach gives best results for the range of apparent propagation velocities associated with surface waves. For a given value of PGV, surface waves will induce significantly higher ground strains than body waves. The travelling wave model is therefore useful for estimating the ground strains which will govern pipeline design. The model is nevertheless also used for calculating body wave-induced strains for the design of pipelines, subways and tunnels (Hashash *et al.,* 2001).

More reliable estimation of ground strains has to consider the full range of physical causes for spatial variability of ground motion ('incoherence'): source effects, wave passage of the waveforms on the ground surface, scattering along the path of the waves from source to site and local site conditions. Data obtained from dense instrument arrays such as the SMART-1 array (Strong Motion ARray in Taiwan) (eg. Abrahamson *et al.*, 1991) and the Parkfield, California array operated by EPRI (Electric Power Research Institute) (eg. Schneider *et al.*, 1990) during the last 15 to 20 years has helped the development of empirical and semi-empirical models for coherency of seismic motions. In reviewing some of these models, Zerva (2000) recognises that the majority of existing models are event-specific and cannot be reliably extrapolated to different events and sites. A suitable model for application in earthquake engineering is unfortunately not yet available.

3.2 Influence of site effects on the seismic response of buried pipelines

The influence of site conditions on the seismic response of buried pipelines has been implied in Section 3.1 by the dependency of strain on the apparent propagation velocity of seismic waves, which in turn is related to the shear-wave velocity of the ground. For both body waves and surface waves, for a fixed value of PGV, ground strain will generally be greater in soft soils (i.e. low v_s value) than stiffer soils. This has been confirmed by Nakajima *et al.* (1998) in a series of field measurements using strain gauges and accelerographs. As shown in Figure 3.7, for the same value of PGV, maximum ground strain observed in soft ground (Shimonaga) is on average 3 to 4 times that observed in hard ground (Kansen). In this case, the predominant period of the soft ground was 1.3 s whilst the predominant period of the hard ground was around 0.4 s.

One of the earliest investigations into the effect of geological environment on pipeline damage was by Kachadoorian (1976). Using data mainly from the 1964 Alaska and 1971 San Fernando earthquakes, he considered three broad geological categories: bedrock, fine-grained sediments and coarse-grained sediments. For each category, he identified the relative occurrence of various potentially damaging earthquake effects. He then assigned relative pipeline damage intensities to each earthquake effect for all three geological categories. For the earthquakes studied, across all earthquake effects (which included ground shaking, landslides, faulting, seismic settlement and others), pipeline damage intensity was greatest in fine-grained soils, and least in bedrock. Kachadoorian (1976) suggested that this reflected the greater abundance of damaging earthquake

effects in fine-grained soils compared to the other two geological environments. For ground shaking alone, slightly more pipeline damage was observed in fine-grained soils than coarse-grained soils.

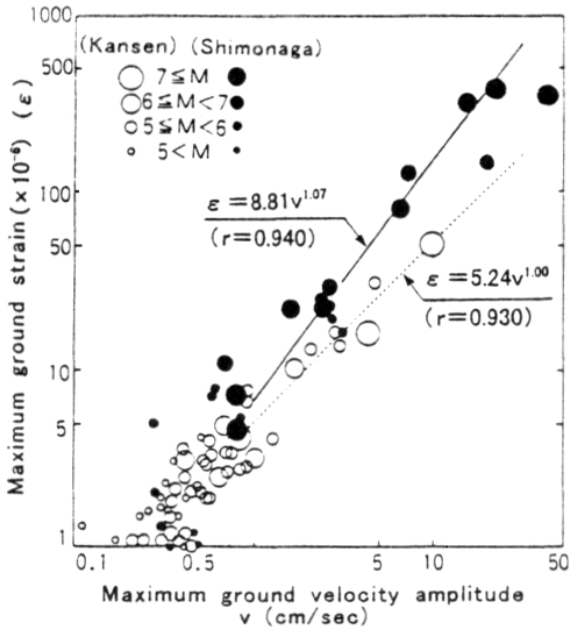

Figure 3.7 Field measurements of PGV and peak ground strain at sites in Japan with different ground conditions (Nakajima *et al.*, 1998)

The pipeline seismic response diagrams in Figure 3.5 illustrate the significance of the predominant period of the ground, T_p, to the vulnerability of buried pipelines. A pipeline embedded in ground having a high value of T_p is more vulnerable to damaging seismic motions than the same pipeline buried in soil with a lower value of T_p.

The importance of ground conditions for the seismic behaviour of buried pipelines is illustrated in the Japanese code for pipeline design (JWWA, 1997) in which the ground strain, ε_p, along the pipe axis is related to T_p through the following expressions:

$$\varepsilon_p = \frac{\pi U_h(z)}{L} \tag{3.18}$$

$$U_h(z) = \frac{2}{\pi^2} S'_v T_p \cos\frac{\pi z}{2H} \tag{3.19}$$

where: $U_h(z)$ is the horizontal ground displacement for a 'level 2' seismic motion (equivalent to ground motion caused by the 1995 Hyogoken-nanbu earthquake) at burial depth, z. The expression comes from solution of the equation of motion of a soil layer subject to vertically-incident S-waves (Takada, 1991),
S'_v is the "design velocity response" (Figure 3.8),
T_p is the natural period of the uppermost soil layer,
H is the thickness of the uppermost soil layer , and
L is an average wavelength term calculated from the harmonic mean of L_1 and L_2:

$$L = \frac{2L_1 L_2}{L_1 + L_2} \tag{3.20}$$

with:

$$L_1 = v_{Ssoil} T_p \tag{3.21}$$

$$L_2 = v_{Srock} T_p \tag{3.22}$$

where: v_{Ssoil} is the average shear-wave velocity in the surface layers, and
v_{Srock} is the shear-wave velocity of the basement layer

The expressions given are based upon a simple travelling wave model, which was discussed in Section 3.1. Equations (3.18) and (3.19) suggest that the ground strain is directly proportional to T_p. However, because L in Equation (3.19) is also proportional to T_p through Equations (3.20) to (3.22), the direct dependency of ground strain on T_p drops out. Equation (3.18) then becomes:

$$\varepsilon_p = \frac{S_v'(v_{Ssoil} + v_{Srock})\cos\left(\frac{\pi z}{2H}\right)}{\pi v_{Ssoil} v_{Srock}} \tag{3.23}$$

in which the effect of ground conditions is present in the value of S_v', which is an increasing function of T_p for $0.1 < T_p \leq 0.7$ s (Figure 3.8) and in the shear-wave velocity terms. The relationship between maximum ground strain and shear-wave velocity for a range of values of H is illustrated in Figure 3.9a. For a given soil layer thickness, ε_p will decrease with increasing v_{Ssoil}. For a given v_{Ssoil}, ε_p will be greater for greater soil layer thickness up to a certain limit. This limit is a result of the fact that S_v' is constant for $T_p > 0.7$ s and is observed in Figure 3.9 for $H \geq 50$ m and $v_{Ssoil} < 290$ m/s. Figure 3.9b shows the inter-relationship between ε_p, v_{Ssoil} and T_p for the case $H = 50$ m. The maximum ground strain is seen to increase with increasing T_p (for a given value of H).

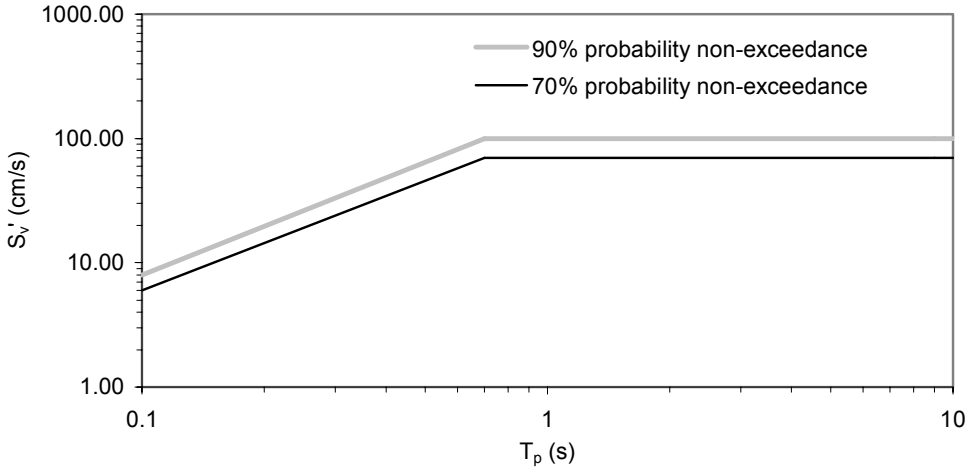

Figure 3.8 Design response velocity spectrum for "Level 2" seismic motion from the Japanese design code.

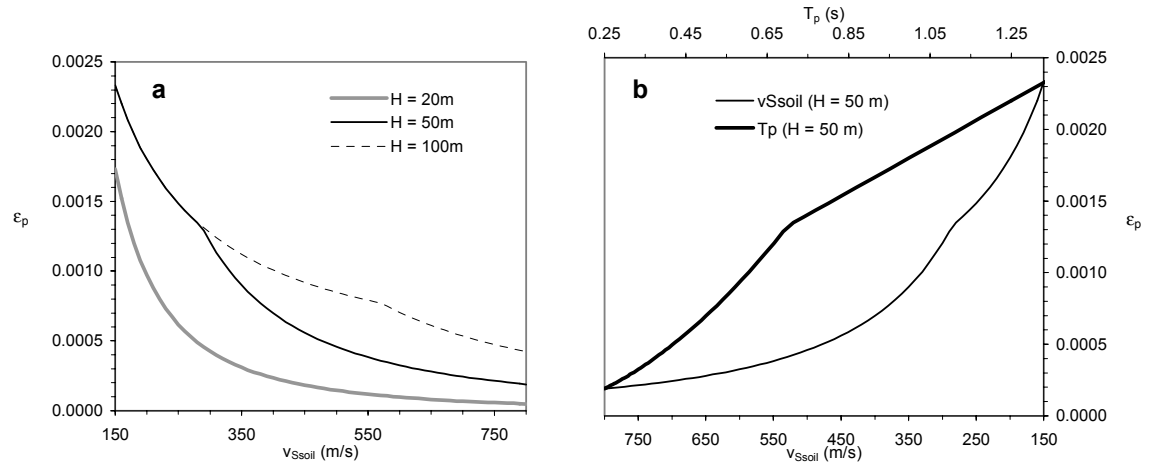

Figure 3.9 Variation of peak ground strain, ε_p, parallel to pipeline as a function of ground conditions according to Equation (3.23), with z = 1 m, v_{Srock} = 1500 m/s and S_v' defined by the 90% non-exceedance probability spectrum in Figure 3.8. (a) Variation of ε_p with v_{Ssoil} for three different values of soil layer thickness, H. (b) Variation of ε_p with v_{Ssoil} and T_p for the case of H = 50 m (note change in direction of v_{Ssoil} axis to allow T_p to be plotted increasing from left to right)

In the preceding discussion, earthquake-induced pipe strains are shown to be strongly influenced by the average properties of the soil in which they are laid, whether that be characterised by the shear-wave velocity or the natural period. Many field observations and theoretical studies have shown, however, that for transient earthquake effects, the level of non-uniformity of ground conditions is also extremely important in the seismic behaviour of buried pipelines (Liang & Sun, 2000). Lateral variation of ground conditions has been shown to cause strain concentrations during ground shaking due to significant differences in ground-motion characteristics even over short distances. Strong-motion array measurements have shown variations by a factor of five in velocity over a distance of 200 m and by a factor of two in acceleration over the same distance, all caused by variable site conditions (Zerva, 2000). Ground non-uniformity significant to the seismic behaviour of buried pipelines includes lateral variation in surface soil type, variation in surface topography and sloping subsurface strata. The features responsible for ground non-uniformity can be large scale, as in the case of major geological boundaries between surface soil types or small scale such as man-made cut-and-fill boundaries.

Nishio *et al.* (1988) investigated the effect of lateral variations in ground conditions on earthquake-induced ground and pipe strain using an instrumented arc-welded steel pipeline at Tama New Town in a western suburb of Tokyo. The pipeline under observation passed through a boundary between stiffer cut ground and softer fill material. Observations made during twelve earthquakes, with magnitude values $4.2 \leq M_{JMA} \leq 6.7$, always showed greater peak accelerations in the filled ground than the cut ground. Maximum pipe strains, as measured using an array of strain gauges, were also much greater where the pipe was embedded in the fill material. Maximum strains generally coincided with the shoulder of the embankment, which was assumed to be a topographic effect. Other than this, an additional strain concentration was observed at the cut-and-fill boundary due to lateral variation in ground stiffness. Nishio *et al.* (1988) found that these ground strains were much

greater than those calculated from a simple travelling wave model. Liang & Sun (2000) point out that the observations of Nishio *et al.* (1988) are all for relatively low values of strain. Further research is required to verify similar behaviour at levels of strain outside the linear range.

Ando *et al.* (1992) used a finite element model to calculate the lateral variation of ground strains for the set of ground conditions found at the Tama New Town site (Figure 3.10a). Using an accelerogram from the 1978 Miyagiken-oki earthquake (input at the base of the site as a vertically propagating body wave), they found peak ground strain to be greatest in the fill material at location PA3X, above which the original ground surface is inclined (Figure 3.10b). The peak ground strain at this location is around ten times that calculated for the original uniform ground. Similarly high strains were calculated for the ground in line with the shoulder of the fill material. The numerical results of Ando *et al.* (1992) confirm the observations made by Nishio *et al.* (1988).

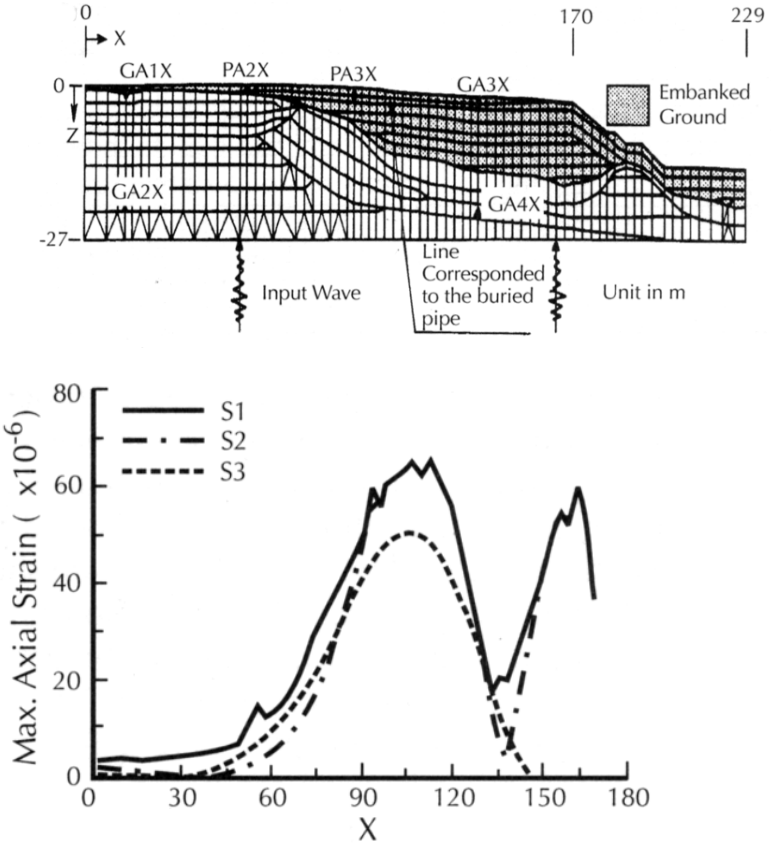

Figure 3.10 (a) Site profile and finite element model used by Ando *et al.* (1992).
(b) Lateral variation of ground strains using an accelerogram obtained from the 1978 Miyagiken-oki earthquake as base input motion. S1 is the peak horizontal ground strain; S2 is the horizontal ground strain when the maximum value occurred; S3 is the axial pipe strain

O'Rourke & Liu (1999) and Takada *et al.* (2000) present simplified approaches to calculating ground strain for ground with an inclined soil-rock interface. Research by Kobayashi *et al.* (2000) into the effects of irregular surface layers on earthquake-induced ground strain suggests that a value of 0.3% should be used as the peak ground strain for pipeline design purposes for such ground conditions.

Shinozuka & Kawakami (1977) proposed a method for evaluating elastic surface strains from the spatial variability of the ground fundamental frequency. A reasonable correlation was reported between strains found using this approach and pipeline damage statistics collected following the 1923 Kanto earthquake. Nishio (1994) presented a method for predicting earthquake-induced pipeline damage which accounted for not only the stiffness of the ground but also its non-uniformity.

3.3 Factors affecting earthquake vulnerability of pipelines

For succinctness in the discussion which follows, a few useful abbreviations are defined in Table 3.2.

Table 3.2 Some commonly-used pipeline-related abbreviations, together with typical yield stress and yield strain values for common pipe barrel materials (from O'Rourke & Liu, 1999).

Abbreviation	Term	Typical yield stress, σ_y (Mpa)	Typical yield strain, ε_y
AC	asbestos cement	†	†
C	concrete	2 – 28	0.0001-0.0013
CI	cast iron	97 – 290	0.001-0.003
DI	ductile Iron	290 – 360	0.0018-0.0022
PE	polyethylene	15 – 17	0.022-0.025
PVC	polyvinyl chloride	35 – 45	0.017-0.022
S	steel	227,289,358,448,517*	0.00134, 0.00231**
SG	steel (threaded joint)	-	-
WS	welded steel	-	-
WSAWJ (A,B)	welded steel arc-welded joints (Grades A & B steel)	-	-
WSAWJ (X)	welded steel arc-welded joints (Grade X steel)	-	-
WSCJ	welded steel caulked joints	-	-
WSGWJ	welded steel gas welded joints	-	-

† AC does not have yield values due to its brittleness. Its strength is normally characterised using transverse crushing strength or beam strength.
* Values are quoted for five different grades of steel: B, X-42, X-52, X-65 & X-70 respectively.
** Values are given for X-42 and X-65 grades of steel.

Many studies have been done on the factors affecting pipeline vulnerability under non-catastrophic (aseismic) operating conditions. Due to the difficulty in characterising the condition of buried pipelines, much of the work has been inconclusive. However, several important factors influencing pipe leakage and break rates (per unit length of pipe) have been identified. In a literature review covering the period 1948 to 1991, Wengstrom (1993) investigated the influence of pipe age, installation method, material type, pipe dimensions (diameter and thickness), joint type, previous damage history, operating pressure, soil conditions, land use and seasonal variations of external environment. Many of these factors are important in understanding pipeline vulnerability under seismic conditions.

Three of these factors (pipe type, joint type and pipe diameter) have been considered in a rating scheme developed by Ballantyne (1995) for earthquake vulnerability of pipelines. Ballantyne (1995) assessed the seismic performance of pipelines based on four qualitative parameters: *ruggedness* - a function of pipe material strength and ductility; *bending* – a measure of resistance of

the pipe barrel to bending failure; *joint flexibility* – a measure of the pipe's ability to extend, compress or bend and rotate around the joint without breaking the joint's water-tight seal; *restraint* – a measure of the ability of the pipe-joint system to hold together in extension. The scheme was derived mainly with permanent ground deformation effects in mind, although is just as useful for identifying pipeline vulnerability to transient ground deformations. The rating scheme for seventeen pipe-joint systems is given in Table 3.3. For each parameter, the pipe-joint system is graded out of 5, with 1 representing the worst performance and 5 representing the best performance.

The scheme highlights the influence of joint type on the overall pipeline vulnerability. A pipe-joint system is only as strong as its weakest element. A gas-welded joint renders a steel pipe as vulnerable to damage as a CI or AC pipe, even though the tensile strength of a steel barrel is much greater than that of CI or AC (Table 3.2). For a given joint type, however, steel and ductile iron (DI) pipes are less vulnerable than more brittle pipe types (eg. PVC, AC, CI). The derivation of the pipeline performance parameters is not explained in any detail. Nevertheless, the scheme gives a useful relative measure of pipeline vulnerability which can aid pipeline selection.

Table 3.3 Relative earthquake vulnerability of water pipes (Ballantyne, 1995). Joint types: B&S - bell & spigot; RG - rubber gasket; R – restrained; UR – unrestrained.

Material type/diameter	Joint type	Ruggedness	Bending	Joint flexibility	Restraint	Total
LOW VULNERABILITY						
ductile iron	B&S,RG,R	5	5	4	4	18
polyethylene	Fused	4	5	5	5	19
steel	arc welded	5	5	4	5	19
steel	Riveted	5	5	4	4	18
steel	B&S, RG, R	5	5	4	4	18
LOW/MODERATE VULNERABILITY						
concrete cylinder	B&S, R	3	4	4	3	14
ductile iron	B&S, RG, UR	5	5	4	1	15
PVC	B&S, R	3	3	4	3	13
steel	B&S, RG, UR	5	5	4	1	15
MODERATE VULNERABILITY						
AC>200mm Φ	Coupled	2	4	5	1	12
cast iron > 200mm Φ	B&S, RG	2	4	4	1	11
PVC	B&S, UR	3	3	4	1	11
concrete cylinder	B&S, UR	3	4	4	1	12
MODERATE/HIGH VULNERABILITY						
AC < 200mm Φ	Coupled	2	1	5	1	9
cast iron < 200mm Φ	B&S, RG	2	1	4	1	8
steel	gas welded	3	3	1	2	9
HIGH VULNERABILITY						
cast iron	B&S, rigid	2	2	1	1	6

Observations of pipeline damage in Kobe, Ashiya and Nishinomiya cities, caused by the 1995 Hyogoken-nanbu earthquake are consistent with the rating scheme given in Table 3.3. A summary of data collected by Shirozu *et al.* (1996) is given in Figure 3.11. The worst affected category of pipes was steel with threaded joints (SG). However, this failure rate is unrealistically high, representing localised damage averaged over a very short length of pipe. The highest reliable

damage rate was observed in AC pipes, followed by CI, PVC and DI, with steel pipes showing the best overall performance.

The importance of joint type is illustrated with reference to the performance of pipes having "S-type" or "S II type" joints. DI pipes having these specially-designed anti-seismic joints (not included in Table 3.3), suffered no damage as a result of the Hyogoken-nanbu earthquake. These types of pipe-joint systems constituted about 270 km of the total water distribution network, 100 km of which coincided with areas experiencing significant liquefaction-induced permanent ground deformation (Shirozu *et al.*, 1996). In the Ashiyama District, for example, a 500mm diameter pipe with S type joints remained intact after a lateral ground movement of about 2m. A 300 mm diameter pipeline with SII type joints at the Egeyama distribution reservoir also suffered no damage, in spite of subsidence of around 1.3 m (Inada, 2000).

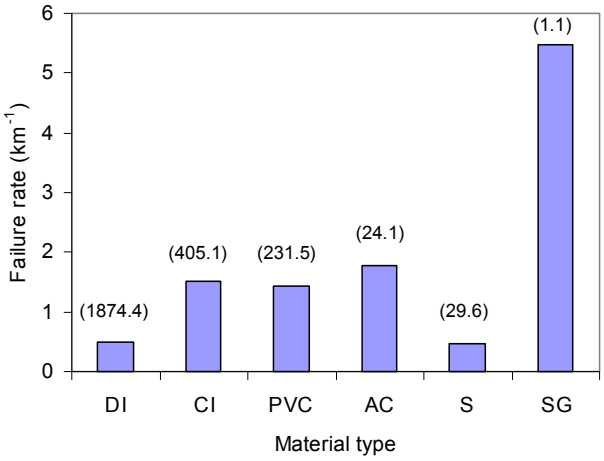

Figure 3.11 Pipeline failure rate for various pipe types from the study by Shirozu *et al.* (1996). Pipe lengths are given for each category (km).

These S and S II type anti-seismic joints are illustrated in Figure 3.12. S II type joints are for smaller diameter pipes (in the range 75 - 450 mm), whilst S type joints are for larger diameter pipes (500 - 2600 mm). The lock-ring provides a restraining force of $3D_0$ kN, where D_0 is the nominal pipeline diameter in mm. Both joint types allow for expansion and contraction at the joint equal to 1% of pipe length. Allowable deflection angles range from 1.5° for the largest diameter pipes to 4° for the smallest diameter pipes (JDIPA, 1998). A run of several anti-seismic pipe lengths can therefore tolerate significant permanent ground deformations. For example, eleven 6 m lengths of 1000mm diameter pipe with S type joints can theoretically absorb a lateral displacement of about 7m (Nakajima *et al.,* 1998). Due to the high costs involved, installation of anti-seismic joints is only warranted in locations likely to experience significant permanent ground deformation as a result of liquefaction, landslides or faulting.

Seismic loading of pipelines can cause a number of different failure modes. The principal failure modes for corrosion-free continuous pipelines (e.g. steel pipe with welded joints) are rupture due to axial tension, local buckling due to axial compression and flexural failure. For shallow burial

depths, continuous pipelines in compression can also fail by beam buckling. For corrosion-free segmented pipelines with bell and spigot type joints, the main failure modes are axial pull-out at the joints, crushing at the joints and round flexural cracks in pipe segments away from the joints. Failure criteria for each of these modes are given by O'Rourke & Liu (1999).

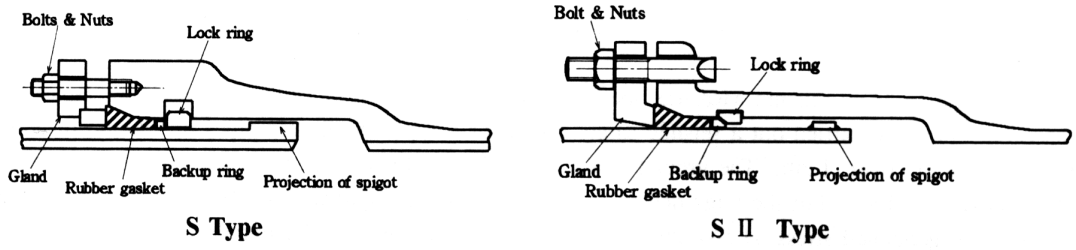

Figure 3.12 Cross-sections of anti-seismic pipe joints (Nakajima *et al.,* 1998)

The presence of corrosion in CI, DI or steel pipes increases the likelihood of failure by decreasing pipe wall thickness. The occurrence of corrosion is linked to pipeline age but is significantly influenced by the prevailing soil conditions (as characterised by pH, soil resistivity and soil aeration). Isenberg (1979) investigated the role of corrosion in pipeline performance during three US earthquakes. In the San Fernando Valley, Los Angeles, an inspection of pipeline repair reports showed that over half the leaks attributed to the destructive 1971 earthquake were related to corrosion. Most leaks in steel and galvanised steel mains caused by the 1969 Santa Rosa earthquake occurred at points weakened by corrosion. The pipes which leaked as a result of the earthquake had a normal leakage rate about ten times higher than the system as a whole. However, data were unavailable to establish whether there were other areas with high normal leakage rates which were relatively unaffected by the earthquake.

Approximately 60% of the total number of pipe breaks and leaks attributed to the 1965 Puget Sound earthquake were in steel and galvanised steel mains and service pipes which had been weakened by corrosion. Water pressure monitoring during the time of the earthquake revealed another factor which may have contributed to pipe failures. Pressure surges observed in one of the regions of the distribution system exceeded normal levels by at least 100%. These surges were attributed to the ground shaking.

Earthquake-induced pipe failure rate has been seen to increase with pipe age (Eidinger *et al.,* 1995, 1998); this is certainly influenced by pipe deterioration. For CI, DI or steel pipes, corrosion is the deterioration mechanism. AC pipes are weakened due to softening caused by leaching of lime (decalcification) and PVC pipes are weakened by fatigue. The influence of pipe age, however is also connected to environmental changes and the changes over time of pipe installation and material specification and selection practices.

Certain elements of a pipeline network have increased vulnerability to earthquake damage due to stress concentrations induced by the passage of seismic waves. Stresses at pipeline elbows and at pipe intersections can significantly exceed stresses in adjacent portions of straight pipe (Stuart *et al.*, 1996; Datta, 1999). Portions of pipe connecting to manholes, tanks or buildings can be vulnerable due to their propensity for differential movements.

For seismic risk analysis of water distribution systems, pipeline repair rates need to be related to earthquake effects as well as factors affecting pipeline vulnerability. Since the 1970's, attempts have been made to correlate earthquake intensity and various peak ground motion parameters with pipeline damage rates (given in terms of numbers of repairs per unit length of pipe). The resulting *fragility* relations can then be used for predictive purposes in estimating likely damage in the event of a future earthquake. These are discussed in the next section.

3.3.1 Fragility relations for buried pipes subject to ground shaking

Separate pipeline fragility relations exist for permanent ground deformation and ground shaking effects. The focus of the current review is on ground shaking effects. A discussion of fragility relations for permanent ground deformation can be found in O'Rourke & Liu (1999), with more recent developments given by ALA (2001).

A total of seventeen studies have been found relating pipeline damage to ground shaking effects from data culled from past earthquakes. A summary of these studies, fifteen of which present fragility relationships, is given in Table 3.4a. The strong-motion parameter(s) used to define the level of ground shaking/earthquake effects for each study are summarised in Table 3.4b. The table also indicates the earthquakes from which data have been obtained in each study, and wherever known, the number of data points used. Fragility curves, including the datasets from which they are derived are included wherever available. The dependent variable is given variously as "repair rate", "damage rate" or "damage ratio"; other studies use the term "failure rate". These terms are used interchangeably in the literature. In the following sections, specific emphasis is placed on identifying the size, origin and reliability of the data for each study.

3.3.1.1 Katayama *et al.* (1975)

One of the first attempts to correlate observed seismic damage in pipelines with any strong-motion parameter was when Katayama *et al.* (1975) considered damage rate in terms of PGA. The study is based on pipeline failure rates obtained for six earthquakes, as indicated in Table 3.4a. Figure 3.13 shows the data of Katayama *et al.* (1975) as presented by Bresko (1980). This figure has been reproduced in several publications (e.g. O'Rourke & Liu, 1999) although the original report (Bresko, 1980) was not available. Numbers of data points indicated in Table 3.4a refer to the original dataset of Katayama *et al.* (1975). Where the numbers of data points presented by Bresko

Table 3.4a Summary of pipeline fragility studies for ground shaking effects according to earthquake data used.

Event ID	Date	Earthquake Name	Country	Magnitude	Katayama *et al.* (1975)	Isoyama & Katayama (1982)	Eguchi (1983)	Barenberg (1988)	Ballantyne *et al.* (1990)	Eguchi (1991)	ASCE/TCLEE (1991)	O'Rourke *et al.* (1991)	Hamada (1991)	Tiedemann (1992)	O'Rourke & Ayala (1993) [HAZUS]	Eidinger (1995, 1998)	Kitaura & Miyajima (1996)	Hwang & Lin (1997)	O'Rourke *et al.* (1998)	Isoyama *et al.* (2000)	ALA (2001)
1	18-Apr-06	San Francisco	US	7.9																	
2	01-Sep-23	Kanto	Japan	7.9 (M_{JMA})	2						2			1							2
3	11-Mar-33	Long Beach	US	6.5																	1
4	28-Jun-48	Fukui	Japan	7.1 (M_{JMA})	1						1										GD_p
5	13-Apr-49	S Puget Sound	US	6.7																	2
6	16-Jun-64	Niigata	Japan	7.5 (M_{JMA})	1						1			1			1				1
7	29-Apr-65	Puget Sound	US	6.5 (M_L)				1							1	1					2
8	16-May-68	Tokachi-oki	Japan	7.9 (M_{JMA})	11 (9)						8										GD_p
9	01-Oct-69	Santa Rosa	US	5.6 [5.7] (M_L)			1	1	1	1		1			1	1					a-s
10	09-Feb-71	San Fernando	US	6.6	19			3			19			2	2	2			2		13
11	23-Dec-72	Managua	Nicaragua	6.3	3 (1)		1			1	1										GD_p
12	28-Jul-76	Tangshan	China	7.6 (M_S)										2							
13	12-Jun-78	Miyagiken-oki	Japan	7.4 (M_{JMA})									1								
14	15-Oct-79	Imperial Valley	US	6.5																	1
15	02-May-83	Coalinga	US	6.4							1	1			2	1					1
16	26-May-83	Nihonkai-chubu	Japan	7.7 (M_{JMA})									3								
17	19-Sep-85	Michoacan	Mexico	8 [7.5]											3	5					a-s
18	01-Oct-87	Whittier	US	5.9 [5.3]															1		a-s
19	25-Apr-89	Tlahuac	Mexico	6.9 (M_S)											2	1					1
20	18-Oct-89	Loma Prieta	US	7										1		9	5		1		13
21	28-Dec-94	Sanriku Haruka-oki	Japan	7.7													1				
22	17-Jan-94	Northridge	US	6.7															7		35
23	16-Jan-95	Hyogoken-nanbu	Japan	6.9													3			19	9
	TOTAL NO. EARTHQUAKES				**6**	**1**	**4**	**3**	**6**	**4**	**7**	**7**	**2**	**7**	**6**	**7**	**5**	**15**	**4**	**1**	**12**

Notes for Table 3.4a Magnitudes are M_w unless otherwise stated and are mostly taken from ISESD (Ambraseys *et al.,* 2002) or TMG (1995). Studies highlighted in grey present fragility curves; other studies show the range of data observed but do not define fragility curves. Shaded boxes in the main table indicate the use of data from a given earthquake. For each study, the number of separate data points from a given earthquake is given where known. For the ALA (2001) study, GD_p refers to to data points considered but excluded due to likely effects of permanent ground deformation; a-s refers to data points considered in the study but excluded due to the occurrence of an aftershock of similar magnitude to the main event, leading to difficulties in associating damage to a single event. Aftershock magnitudes are indicated in square brackets. For this study, PGD refers to the transient peak ground displacement, rather than permanent ground displacement.

Table 3.4b Strong-motion parameters considered by each study. Studies highlighted in grey present fragility curves; other studies show the range of data observed but do not define fragility curves (as Table 3.4a).

Strong-motion parameter	Katayama *et al.* (1975)	Isoyama & Katayama (1982)	Eguchi (1983)	Barenberg (1988)	Ballantyne *et al.* (1990)	Eguchi (1991)	ASCE TCLEE (1991)	O'Rourke *et al.* (1991)	Hamada (1991)	Tiedemann (1992)	O'Rourke & Ayala (1993) [HAZUS]	Eidinger (1995, 1998)	Kitaura & Miyajima (1996)	Hwang & Lin (1997)	O'Rourke *et al.* (1998)	Isoyama *et al.* (2000)	ALA (2001)
I_a																	
I_{MM}																	
PGA																	
PGV																	
PGD																	
SA																	
SI																	

Table 3.4c Summary of earthquakes used in studies given in Table 3.4a

Location	No of earthquakes
US	11
Japan	8
Mexico/Central America	3
China	1

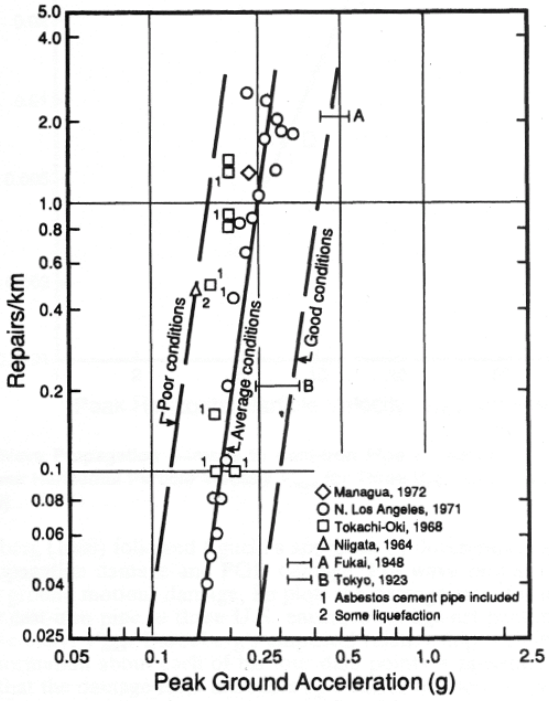

Figure 3.13 Pipeline fragility data of Katayama *et al.* (1975) as presented by O'Rourke & Liu (1999). This graph presents the data in a more comprehensive manner than the graph included in the original study and includes trends suggested by Bresko (1980).

(1980) differ, these are given in brackets. The small differences are due to different ways of aggregating the pipeline damage statistics.

PGA values in the vicinity of each damaged pipeline system were estimated from the few strong-motion records available for these earthquakes. For the 1923 Kanto (Tokyo) and 1948 Fukui earthquakes, no records were available so ranges of values were assigned from earthquake effects, as shown in Figure 3.13. Eight separate data points are shown for different localities affected by the 1968 Tokachi-oki earthquake. PGA values appear to have been estimated from values of JMA intensity given for each locality although the conversion method used is not known. Nineteen separate data points were obtained for the 1971 San Fernando earthquake by dividing a map of pipeline failures in Northern Los Angeles into 19 strips, each of width 0.48 km. A PGA value for each strip was found by estimating PGA at the northern and southern extremities of the mapped area (probably based on strong-motion recorded nearby, although details are not specified) and interpolating values using a strong-motion attenuation relationship. The PGA values given in Figure 3.13 for the San Fernando earthquake cover the range 0.18 – 0.34 g whereas those in Katayama *et al.* (1975) for the same earthquake cover the range 0.27 – 0.50 g. This represents a discrepancy between the Bresko (1980) and Katayama *et al.* (1975) studies. Another discrepancy is found in the PGA value for the 1972 Managua earthquake, which Katayama *et al.* (1975) estimate at 0.41 g ± 0.05 g but which Bresko (1980) plots below 0.25 g. PGA for the 1964 Niigata earthquake is not specified by Katayama *et al.* (1975) and may be an addition from Bresko (1980) based on either intensity or strong-motion values. The scatter in the dataset presented by Bresko (1980) is considerable, although it would be greater if the original PGA values of Katayama *et al.*

(1975) had been used. Such large scatter is typical of pipeline fragility relations, although in this case is undoubtedly influenced by heightened damage rates due to permanent ground deformation in certain cases (*eg.* liquefaction-induced damage during the Niigata earthquake and damage due to faulting in the case of the Managua earthquake). Most of the data presented in Figure 3.13 is for CI pipes although the data from the 1968 Tokachi-oki earthquake includes damage to AC pipes. The fragility relationship makes no distinction between different pipe diameters or joint types, both of which are known to influence damage rates, as discussed in Section 3.3. However, Katayama *et al.* (1975) do comment on the tendency for damage to increase with increasing pipe diameter. The fragility relations indicated in Figure 3.13 are those suggested by Bresko (1980) and expressed in Equation (3.28) (Table 3.9). *b* is a parameter which depends on a range of factors including soil conditions and pipe age. It has a value of 4.75, 3.65 or 2.20 for "poor", "average" or "good" conditions respectively (Ayala & O'Rourke, 1989).

3.3.1.2 Eguchi (1991)

The work of Eguchi (1991) was a modification of an earlier study (Eguchi, 1983) in the light of data from more recent (unspecified) earthquakes. Both sets of fragility relations give pipeline repair rate as a function of I_{MM} (see Appendix B). The earlier study was the first time a fragility relationship had been derived which explicitly separated out wave propagation damage from permanent ground deformation damage (O'Rourke & Liu, 1999).

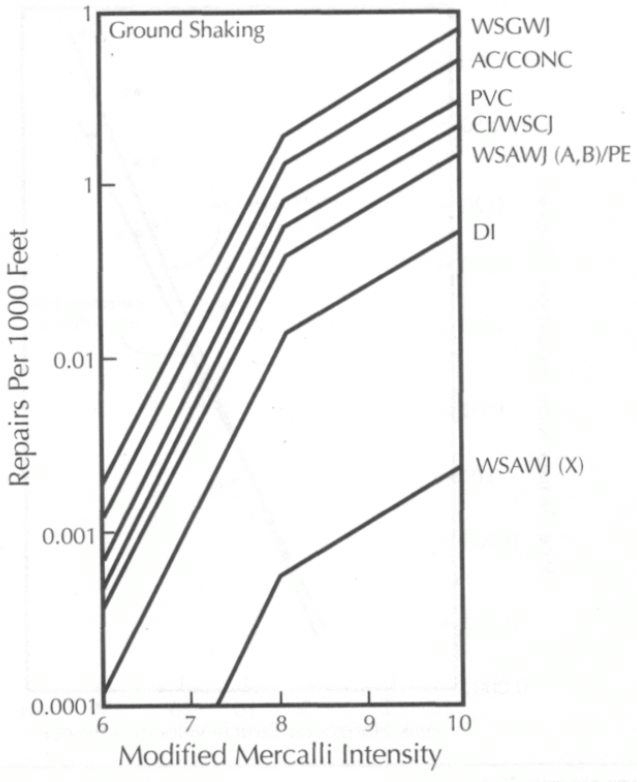

Figure 3.14 Bilinear pipeline fragility relations of Eguchi (1991). See Table 3.2 for abbreviations. Note that repair rate is given per 1000 ft.

The relations derived by Eguchi (1983) were based on detailed pipe damage data from four earthquakes (indicated in Table 3.4a) plus less complete data from an additional (unspecified) 21 earthquakes (Hwang & Lin, 1997). The modified relations are shown in Figure 3.14. The amount of scatter associated with these relations is not possible to determine as individual data points are not presented. Distinction is made between different pipe and joint types, with greatest damage rates observed in steel pipes with gas-welded joints. AC and concrete pipes were found to be more vulnerable than PVC pipes, which in turn were more vulnerable than CI pipes and welded steel pipes with caulked joints. DI pipes experienced on average about ten times fewer repairs per unit length than the worst performing pipes. The repair rate of X grade steel pipes with arc-welded joints was approximately ten times smaller than that of DI pipes. The relationships shown in Figure 3.14 are bilinear, with damage rates increasing by about a factor of ten for unit increase in I_{MM} for $I_{MM} < 8$, and doubling for unit increase in I_{MM} above I_{MM} 8.

3.3.1.3 O'Rourke & Ayala (1993)

Barenberg (1988) plotted the damage rate for CI pipe against PGV using data from three US earthquakes (Table 3.4a). O'Rourke & Ayala (1993) subsequently added data from the 1983 Coalinga and two Mexican earthquakes (1985 Michoacan and 1989 Tlahuac). The fragility relations defined by both investigations are shown in Figure 3.15.

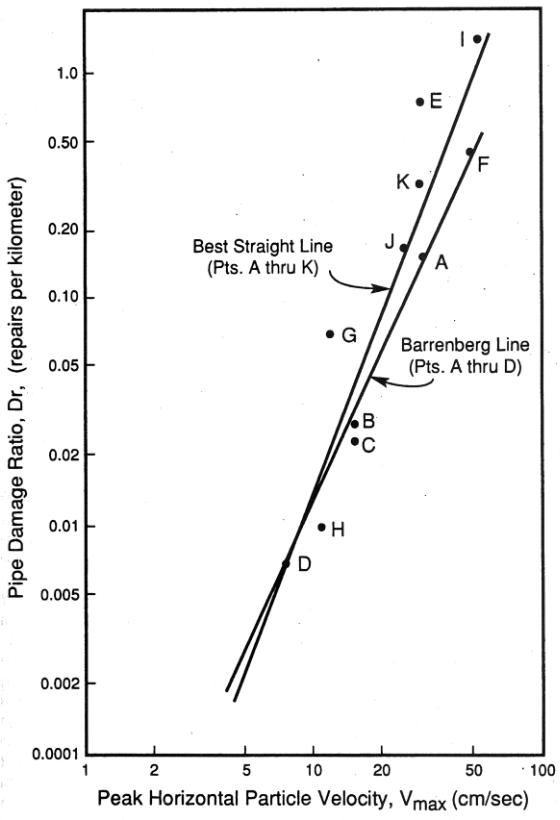

Figure 3.15 Fragility relations of Barenberg (1988) (derived from data points A – D), and O'Rourke & Ayala (1993) (derived from data points A-K).

The Barenberg (1988) relationship was derived from four data points (A to D) whilst the relationship of O'Rourke & Ayala (1993) was derived from eleven data points (A to K). A detailed description of how PGV and pipeline damage rates were calculated is not included in the studies. However, details for data obtained from Mexico City during the Michoacan earthquake are given in a report by Ayala & O'Rourke (1989). The pipeline damage in Mexico City was divided up according to three distinct geological regions: the lake zone, consisting primarily of soft lacustrine clays; the hill zone, consisting of volcanic rocks that surround the lake bed; and a transition zone between the two. PGV values were obtained by averaging the peak values from all strong-motion stations within each zone. Four records were available from the hill zone, one from the transition zone and five from the lake zone. Further information concerning most of the other earthquakes can be found in a report by O'Rourke (1985), which was not available for the current study.

The fragility relationship of Barenberg (1988) suggests that a doubling of PGV will lead to an increase in the pipeline damage rate by a factor of about 4.5. The same increase in PGV for the modified relationship results in a 6-fold increase in pipeline damage rate. Two outlying points, E and G are largely responsible for this change. O'Rourke & Ayala (1993) explain the unusually high damage rate for point E, representing CI pipe damage during the 1983 Coalinga earthquake, by corrosion effects. Point G represents damage to AC, CI and concrete pipes in the transition zone during the 1985 Michoacan earthquake. It is suggested that the relatively high damage level in this case is largely due to abrupt changes in the subsurface conditions which characterise this region (O'Rourke & Ayala, 1993). The data scatter in Figure 3.15 is significantly less than that observed in Figure 3.13. The dataset of O'Rourke & Ayala is more consistent than that of Katayama *et al.* (1975). Pipeline failures are not influenced by permanent ground deformation effects and PGV values are more reliable due to greater availability of strong-motion records for these later earthquakes. The improved correlation observed in Figure 3.15 is also almost certainly due to the close relationship between PGV and ground strain, as explained in the early part of this chapter. Katayama *et al.* (1975) and Barenberg (1988) both comment on the inadequacy of PGA for determining ground shaking intensity.

The fragility relationship of O'Rourke & Ayala (1993) has been incorporated into the national loss estimation methodology used in the US, HAZUS (FEMA, 1999). The relationship, given in Equation (3.32) (Table 3.10) is used for brittle pipes only as it is based on data from AC, concrete and CI pipes. For more ductile pipe types (steel, DI or PVC), HAZUS (FEMA, 1999) suggests this relation be multiplied by 0.3. Steel pipes with arc-welded joints are classified as ductile whereas steel pipes with gas-welded joints are classified as brittle. In the absence of joint information, pre-1935 steel pipes are classified as brittle pipes. The HAZUS methodology does not consider pipe diameter as a factor.

3.3.1.4 Eidinger *et al.* (1995, 1998)

Eidinger *et al.* (1995) presented a fragility relationship for PGV based on data from seven earthquakes. A more detailed description of this investigation is given in Eidinger *et al.* (1998). The dataset is similar to the one used by O'Rourke & Ayala (1993) but includes an additional nine data points from the 1989 Loma Prieta earthquake.

The pipeline repair rates for the Loma Prieta earthquake were obtained from GIS-based analysis using pipeline data digitised from 1:12,000 scale maps provided by the East Bay Municipal Utility District (EBMUD). Pipeline repair locations were obtained from repair records made in the two weeks immediately following the earthquake. The pipeline data included a number of factors of interest from the point of view of pipeline vulnerability: diameter, pipe material, lining, coating and date of installation. Some unspecified problems with the pipeline inventory led to omission of about 10% of the network from the analysis. A map of relative soil corrosivity based on pre-earthquake pipe repair rates and expert opinion was included in the GIS model.

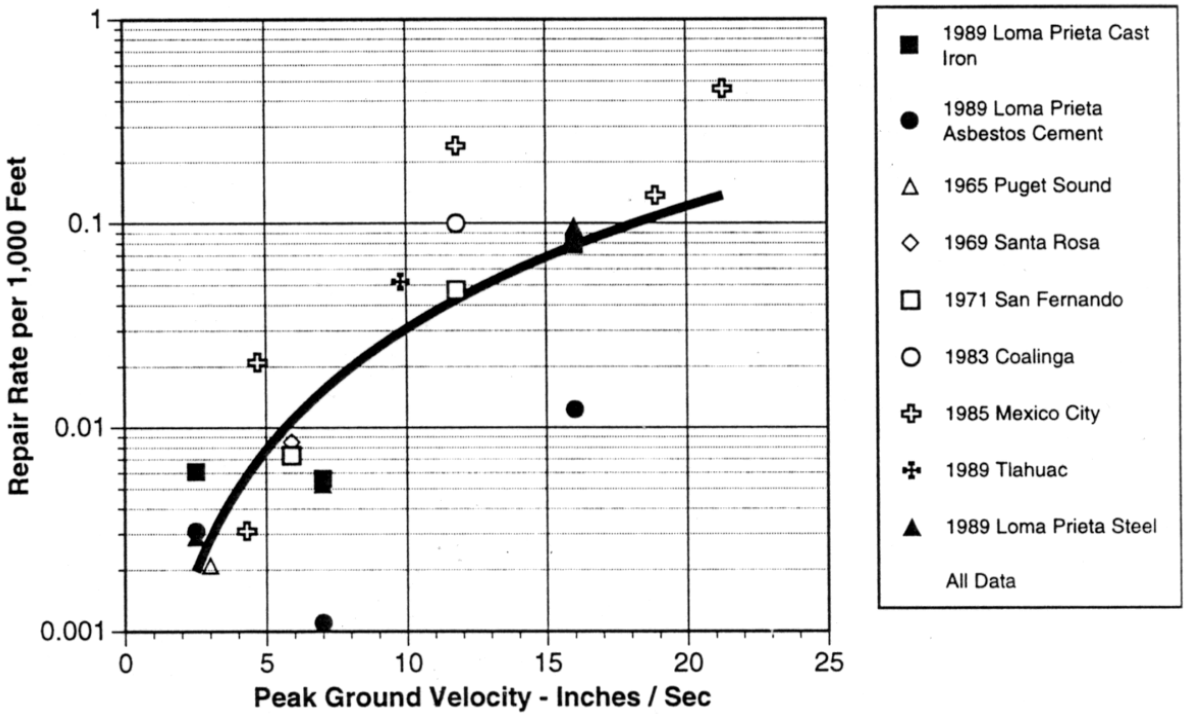

Figure 3.16 Data set and fragility relations of Eidinger *et al.* (1995, 1998). Repair rate and PGV are both measured in Imperial units.

PGV at each repair location was estimated using strong-motion attenuation relations and soil amplification data specific to the EBMUD service area. A total of 24 recordings of horizontal strong ground-motion were used from within the study area, which extended over an area of approximately 1,200 km^2. Specific details on how pipeline lengths, repair locations and calculations of PGV were combined to obtain average repair rates are not given. The fragility

relation defined by Eidinger *et al.* (1995, 1998) assumes a power relationship between pipe repair rate, R_R, and PGV.

The data set and best-fit line through data from all seven earthquakes is shown in Figure 3.16. The fragility relationship is expressed by Equation (3.32), which has also been plotted for comparison with other pipeline fragility relations for PGV in Figure 3.24. This has been converted to SI units as the original fragility relation is based on PGV in inches/s and R_R in repairs/1000 ft. Eidinger *et al.* (1995, 1998) specify a modification factor, K_1, to account for different combinations of pipe material, joint type and soil type. Values of K_1 are summarised in Table 3.5.

Table 3.5 Values of modification factor, K_1 for different combinations of pipe material, joint type, soil type and pipe diameter, for use with the pipeline fragility relations of Eidinger *et al.* (1995, 1998). Constants K_{1ALA} are for the fragility relations of ALA (2001), described in Section 3.3.1.9. Shaded cells indicate where ALA (2001) constants are different to those of Eidinger *et al.* (1995, 1998).

pipe material	joint type	soils *	diameter	K_1	K_{1ALA}	Quality index**
CI	cement	unknown	small	0.8	1.0	B
	cement	corrosive	small	1.1	1.4	C
	cement	non corrosive	small	0.5	0.7	B
	rubber gasket	unknown	small	0.5	0.8	D
WS	arc welded single lap	unknown	small	0.5	0.6	C
	arc welded single lap	corrosive	small	0.8	0.9	D
	arc welded single lap	non corrosive	small	0.3	0.3	B
	arc welded single lap	all	large	0.15	0.15	B
	rubber gasket	unknown	small	0.7	0.7	D
	screwed	all	small	-	1.3	-
	riveted	all	small	-	1.3	-
AC	rubber gasket	all	small	0.5	0.5	C
	cement	all	small	1.0	1.0	B
	cement	all	large	2.0	-	D
C	welded	all	large	1.0	0.7	D
	cement	all	large	2.0	1.0	D
	rubber gasket	all	large	-	0.8	-
PVC	rubber gasket	all	small	0.5	0.5	C
DI	rubber gasket	non corrosive	all	0.3	-	C
	rubber gasket	all	small	-	0.5	-

* For the Eidinger *et al.* (1995, 1998) study, "small" refers to pipe diameter, D_0 < 30.48 cm (12 inches); "large" refers to $D_0 \geq$ 30.48 cm. For the ALA (2001) study, the "small" category includes pipes of 30.48 cm diameter, whereas "large" refers to D_0 > 30.48 cm.

** The quality index refers to K_1 only and is described beneath this table.

Each relationship is classified according to a data quality index, which describes the confidence in the current empirical data set. Each level has an approximate qualitative description:

B - "there is a reasonable amount of backup empirical data and study"
C - "limited empirical data and study"
D - "based largely on extrapolation and judgement, with very limited empirical data"

The absence of any 'A' rating in this study is an indicator of how much work still needs to be done in defining pipeline fragility relationships.

3.3.1.5 Hwang & Lin (1997)

The fragility relation of Hwang & Lin (1997) gives pipeline failure rate as a function of PGA and is based on a review of data drawn from six previous studies (Katayama *et al.*, 1975; Eguchi, 1991; ASCE/TCLEE, 1991; O'Rourke *et al.*, 1991; Hamada, 1991; Kitaura & Miyajima, 1996). The fragility curve of Hwang & Lin (1997) is shown in Figure 3.17 along with the relations upon which it is based. This curve was not found from regression analysis of the combined datasets of the named studies but rather represents an average trend. It therefore indirectly makes use of data from 15 different earthquakes, the most used by any of the studies summarised in Table 3.4a.

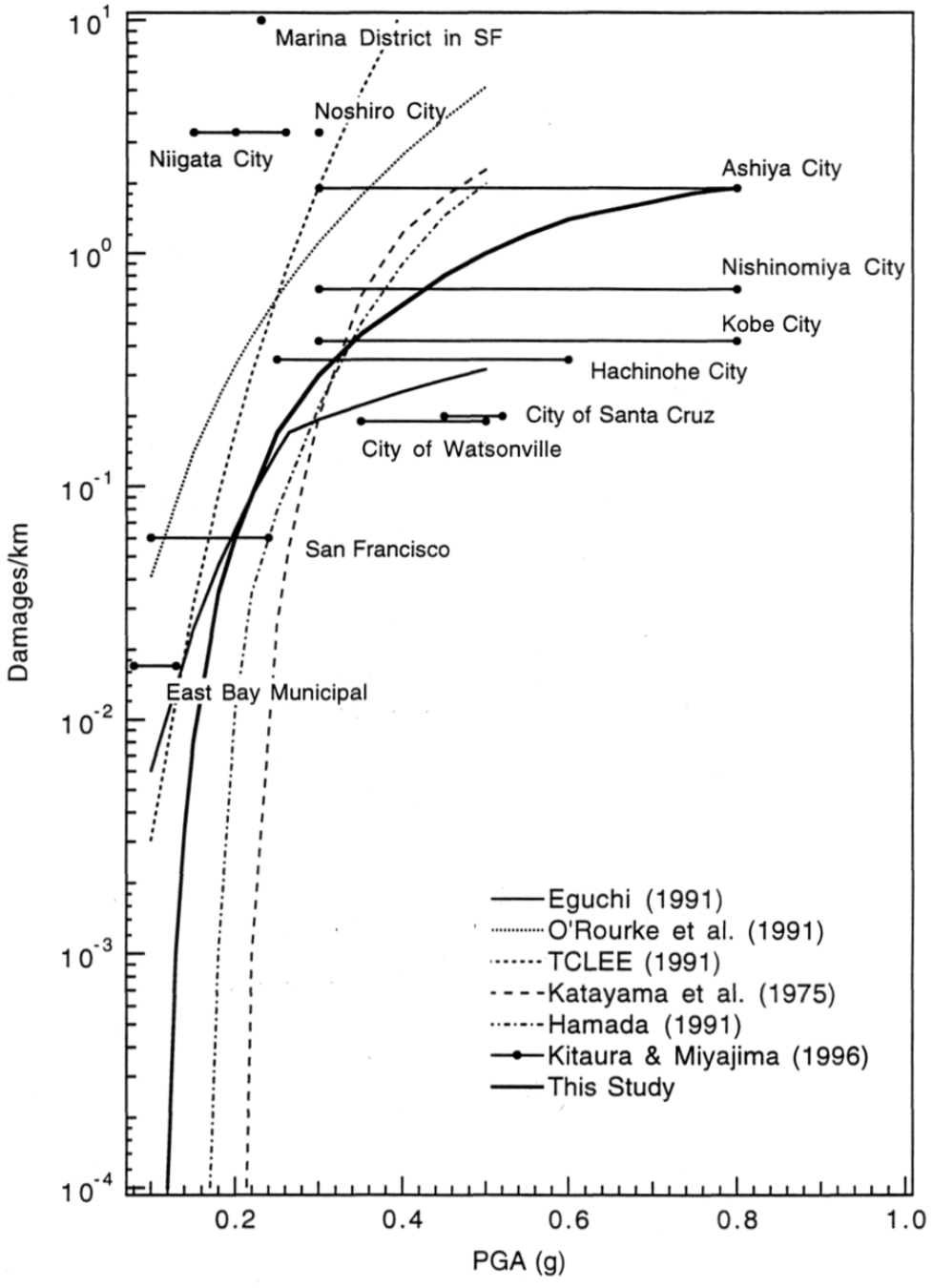

Figure 3.17 A comparison between the fragility curve of Hwang & Lin (1997) ("This Study") with other fragility curves for PGA (1993)

A number of points concerning some of the datasets are worth mentioning. The relationships of Eguchi (1991) and O'Rourke *et al.* (1991) were originally defined for I_{mm} and so were converted to PGA using equations suggested by Trifunac & Brady (1975). The study by ASCE/TCLEE (1991) was a re-analysis of the dataset of Katayama *et al.* (1975) to include data from the 1983 Coalinga earthquake. The relation of Hamada (1991) is based on the pipeline damage observed during the 1971 San Fernando and 1978 Miyagiken-Oki earthquakes. Data from Kitaura & Miyajima (1996) is also included in Figure 3.17; although these researchers do not derive fragility relations *per se*, they plot pipeline failure rates observed at various locations along with the range of PGA values experienced. The Kitaura & Miyajima (1996) study includes data from five earthquakes, including the 1995 Hyogoken-nanbu earthquake. Figure 3.17 highlights how great the differences are between different fragility relationships. The basic curve established by Hwang & Liu (1997) is for CI pipes with diameters of around 300 mm. The pipe diameter factor, R_D, which is defined based on data from the 1995 Hyogoken-nanbu earthquake (Kitaura & Miyajima, 1996; Shirozu *et al.*, 1996), is shown in Figure 3.18.

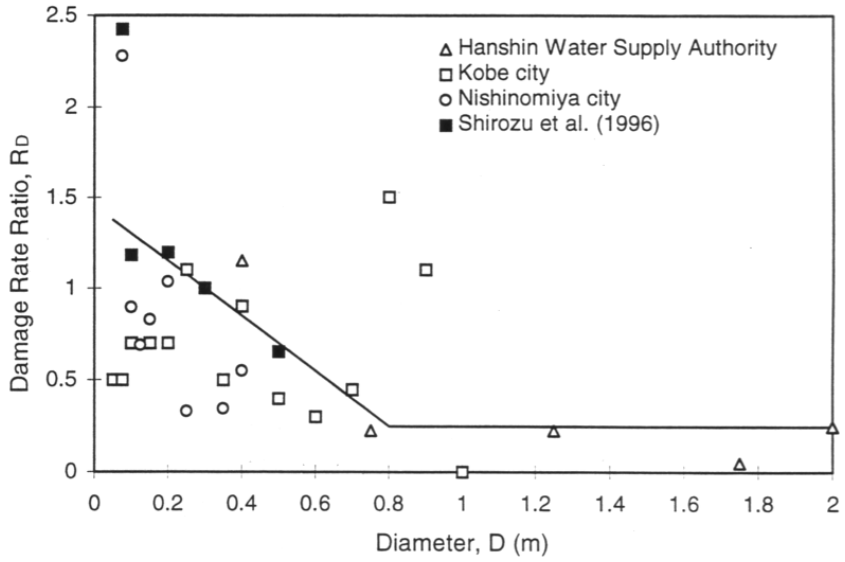

Figure 3.18 Damage rate ratio for different pipe diameters (Hwang & Lin, 1997)

3.3.1.6 O'Rourke *et al.* (1998)

O'Rourke *et al.* (1998) used a GIS database to investigate factors affecting water supply system damage caused by the 1994 Northridge earthquake. All Los Angeles Department of Water and Power (LADWP) and Metropolitan Water District (MWD) trunk lines within the LADWP system were digitised from 1:12,000 maps provided by LADWP. The trunk line repair database was assembled from statistics provided by LADWP and MWD and the distribution line repair database came from statistics developed for the State of California Office of Emergency Services (OES). Of 1,405 original OES repair records, 1,013 were deemed valid for investigation into damage to

distribution mains and hydrants. Of these, reliable information about pipe composition could be found for 964 repairs, most of which (944) also had information concerning pipe diameter.

The strong-motion database incorporated into the GIS analysis was the same as that described by Chang *et al.* (1996), consisting of records obtained from over 230 stations covering an area of around 6000 km^2 in and around Northridge. Most of these stations were concentrated within a smaller (approximately 1200 km^2) region corresponding with the extent of earthquake-induced damage to Northridge's water distribution network. Such an extensive strong-motion dataset allowed reliable contour maps to be drawn for various different strong-motion parameters, including PGA, PGV, PGD, SA, I_a and SI (defined in Chapter 2). The I_{MM} maps of Dewey *et al.* (1995) were also incorporated into the GIS model.

Pipeline repair rate contours were calculated for CI pipes, which constituted approximately 76% of the distribution network. The contours were found by dividing the Northridge area into a grid of 2 x 2 km squares and determining the length of CI pipe and number of CI pipeline repairs in each square. Figure 3.19 shows the repair rate contours for CI pipes superimposed on a contour map of PGV. No pipeline damage was observed in regions with PGV < 10 cm/s. Highest repair rates were shown to coincide reasonably well with zones of highest PGV. Similar correlations were found for other strong-motion parameters. Concentrated areas of damage were generally found to coincide with occurrences of ground failure due to liquefaction or landslides.

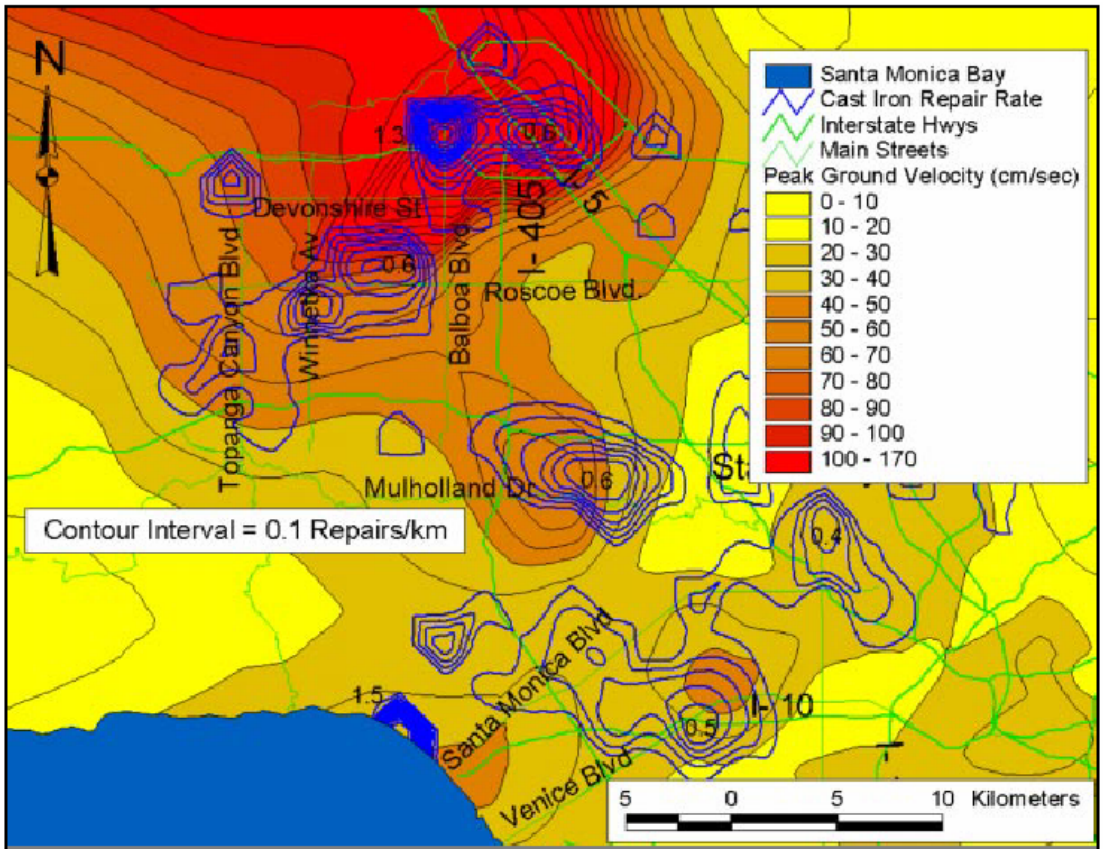

Figure 3.19 Pipeline repair rate contours for CI pipe vs. PGV for the Northridge earthquake (O'Rourke & Toprak, 1997)

Various regression analyses were carried out between strong-motion parameters and pipeline repair rates. O'Rourke & Jeon (2000) specify that of the 241 3-component strong-motion records available, 164 were used in the regression analyses. Data points for the regression were obtained by summing pipeline lengths within zones of equal value of a given parameter as delineated from the corresponding contour map. The value assigned to each zone was the mid-range value. Only those zones containing pipe lengths greater than 150 km (2% of the total length of CI pipes) were included in the correlation in order to reduce bias due to local erratic effects. It was found that the most statistically significant strong-motion parameter was PGV (O'Rourke & Jeon, 1999). The screening process tended to omit from the dataset damage associated with PGV ≥ 70 cm/s. For the Northridge earthquake, these regions often corresponded to locations where permanent ground deformation had occurred. The screening technique was therefore useful in minimising the influence of landslide or liquefaction-induced damage on the fragility relations.

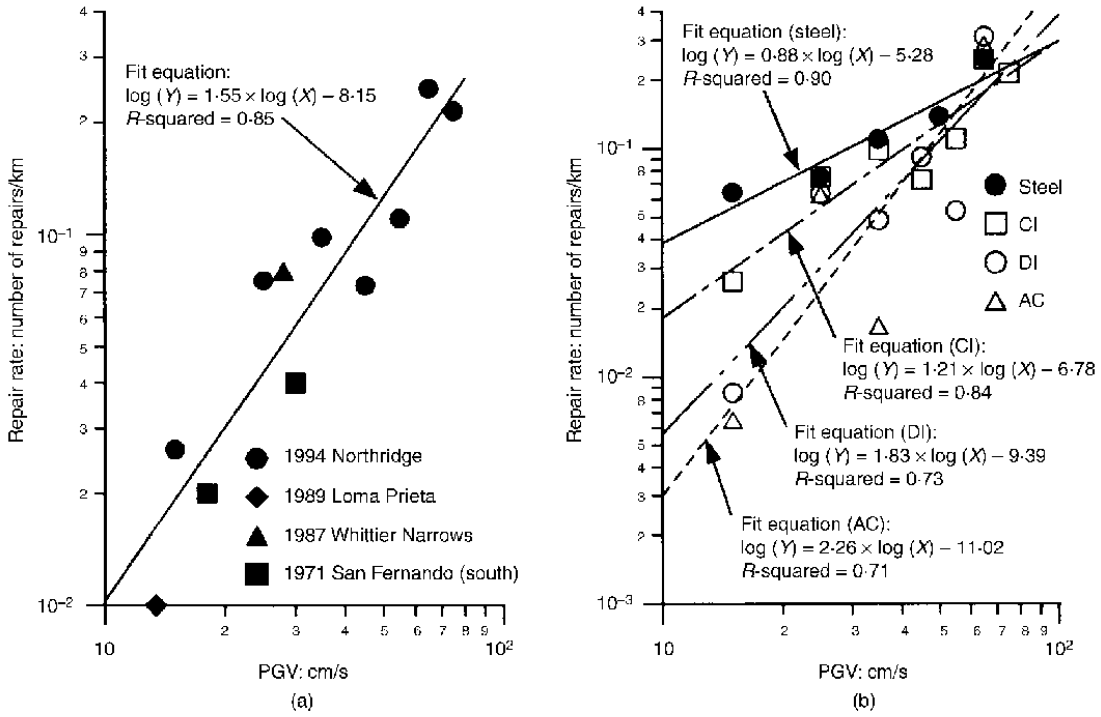

Figure 3.20 Pipeline repair rate correlation with PGV for steel, CI, DI and AC distribution lines: (a) CI distribution lines; and (b) steel, CI, DI and AC distribution lines (O'Rourke *et al.*, 2001)

The study by O'Rourke *et al.* (1998) includes pipeline fragility relations for I_{MM} and SI (derived from the 20% damped velocity spectrum as described in Section 2.3.2.4) based only on Northridge data and relations for PGA and PGV which also use data from three other US earthquakes (Table 3.4 (a)). Relations for the other parameters indicated in Table 3.4 (a) were not presented. The relation shown in Figure 3.20 (a) is for PGV for CI pipes of all diameters. The best-fit line in this case is taken from a more recent publication (O'Rourke *et al.,* 2001) and has slightly different coefficients than the ones given in O'Rourke *et al.* (1998). The trend of O'Rourke *et al.* (2001) is expressed in Equation (3.35) and has been plotted in Figure 3.24 for subsequent comparison with

fragility relations by other investigators. The PGA fragility relation of O'Rourke *et al.* (1998) is expressed in Equation (3.30) and plotted in Figure 3.23.

Figure 3.20 (b) shows repair rate correlations for steel, CI, DI and AC pipes, all obtained from GIS analysis of the Northridge data. The relative vulnerabilities of CI and DI pipes implied by these trends confirm the findings of previous studies. The low damage rates observed for AC pipes and the high damage rates observed for steel pipes are, however, surprising. No explanation is given for the relatively impressive performance of AC pipes. O'Rourke *et al.* (2001) suggest that the poor performance of steel distribution pipelines may have been influenced by the high water pressures associated with steel distribution pipelines in the Los Angeles area, and also by their vulnerability to corrosion.

O'Rourke & Jeon (1999) also developed a fragility relationship for *scaled velocity*, a parameter based on peak ground velocity but normalised for the effects of pipe diameter. This showed a better correlation with pipeline repair rate than the unscaled parameter did with repair rates for each pipe diameter category plotted separately. The expression for scaled velocity, v_{scaled} is given as:

$$R_R = 0.050\left(v_{scaled}\right)^{0.865} \tag{3.24}$$

$$v_{scaled} = \frac{PGV}{D_0^{1.138}} \tag{3.25}$$

where: R_R is the pipeline repair rate (per km length of pipe),
PGV is the peak ground velocity (cm/s^2),
D_0 is the pipeline diameter (cm).

3.3.1.7 Isoyama *et al.* (2000)

Isoyama *et al.* (2000) extended the GIS-based investigation of the Japan Water Works Association (JWWA) (Shirozu *et al.,* 1996) to establish pipeline fragility relations for PGA and PGV. Shirozu *et al.* (1996) established a GIS database to analyse factors influencing water pipeline damage caused by the 1995 Hyogoken-nanbu earthquake. This database consisted of distribution pipes digitised from 1:5000 or 1:6000 maps for the whole of Kobe City and neighbouring Ashiya City (except for Okuyama and Okuike Districts) and Nishinomiya City, all of which suffered extensive earthquake damage. The location of each pipeline repair, including data on pipe material, pipe diameter, failure mode and year of installation, was entered into the database. Topographical and geological data was digitised from 1:10000 maps developed by the Geographical Survey Institute (1996) and areas affected by liquefaction were identified from a study of permanent ground deformation effects from aerial photos (Hamada *et al.,* 1995*)*. Macroseismic intensity data was included from a study by Chuo Kaihatsu Co Ltd (1995).

Shirozu *et al.* (1996) analysed the data set for the whole of Kobe, Ashiya and Nishinomiya, using a grid with cell dimensions of about 290 x 230 m, chosen to conform to the Japanese national land

standard mesh. Isoyama *et al.* (2000) carried out a more detailed investigation focusing on Ashiya and Nishinomiya Cities. For this region, 50 m grid cells were defined in order to better represent "narrow valleys" and other topography types. The topographical category types of the Geographical Survey Institute were simplified to the five given in Table 3.6, and within the "alluvial plain" category three sub-categories were defined based on the occurrence of liquefaction (Table 3.6). A multivariate analysis was carried out to quantify the influence of the various factors on pipeline damage rate, establishing empirical correction factors to account for pipe material, pipe diameter, ground topography and liquefaction (Table 3.6). The method of analysis included a weighting scheme according to the length of pipe within each category. Correction factors for some of the categories shown in Table 3.6 were considered less reliable due to the relatively small values of pipe length upon which they were based.

A separate analysis was performed using strong-motion data from across the whole Kobe-Osaka region to establish standard damage rate curves, to which the correction factors could be applied. For details concerning the strong-motion dataset, Isoyama *et al.* (2000) cite a separate Japanese study (Isoyama *et al.,* 1998) not seen for the current study. Records used in the analysis were probably a subset of the database presented by Ohno *et al.* (1996). Out of a total of 53 records, 17 are likely to have been within the heavily damaged region located within about 20 km of the surface fault rupture. Some of the many additional records not available in the public domain may also have been used in the GIS study. The pipeline fragility relationships were derived according to the form given in Equations (3.26) and (3.27).

$$R_R(X) = B_p B_d B_g B_L R_0(X) \tag{3.26}$$

$$R_0(X) = a(X - X_{\min})^b \tag{3.27}$$

where: R_R (X) is the pipeline repair rate per km of pipe as a function of the strong-motion parameter, X. Fragility relations have been derived for PGA and PGV.
B_i are modification factors defined in Table 3.6,
R_0 is the standard pipeline damage rate, defined for CI pipe of diameter range 100 - 150 mm located in alluvial soil with no liquefaction (coefficients $B_i = 1.0$ in Table 3.6)
a and b are regression coefficients,
X_{min} is the minimum value of strong ground-motion for which damage is considered to occur (100cm/s^2 in the case of PGA and 15cm/s in the case of PGV).

The basic repair rate algorithms for PGA and PGV are shown in Figures 3.21a and 3.21b respectively, along with data points used in the regression.

The fragility relations were based on 19 data points and 16 data points, respectively (estimated from Figure 3.21). In each case, several additional outlying points were excluded due to extreme instances of liquefaction or topographic effects. As a result of the size and quality of the data set,

the work of Isoyama *et al.* (2000) represents a major improvement on a previous pipeline fragility relation for PGA developed by Isoyama & Katayama (1982); both relations are plotted in Figure 3.23 for comparison. The algorithms are expressed in Equations (3.29) and (3.31) respectively. The basic repair rate algorithm of Isoyama *et al.* (2000) for PGV is given by Equation (3.34) and plotted in Figure 3.24.

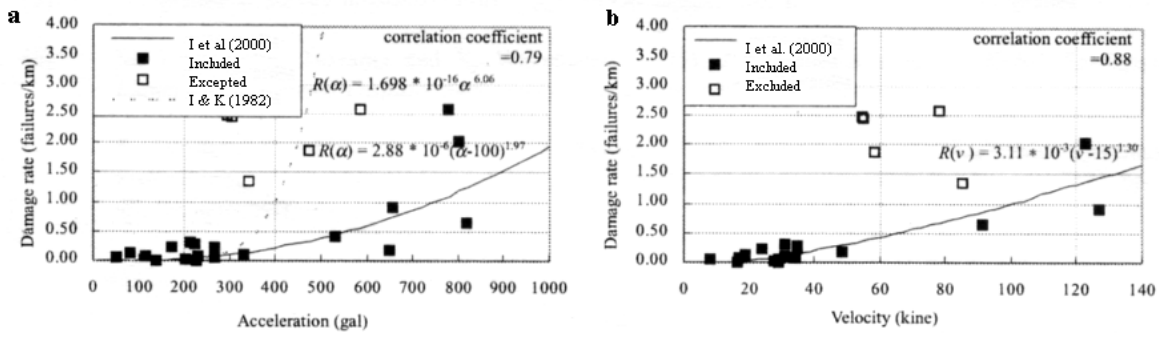

Figure 3.21 Data sets and fragility relations of Isoyama *et al.* (2000). Acceleration scale is PGA (1 gal = 1 cm/s^2); Velocity scale is PGV (1 kine = 1 cm/s). Solid squares indicate data points included in the regression. Open squares indicate data points excluded due to their association with extreme instances of liquefaction-induced permanent ground deformation or topographic effects, leading to excessive pipeline failure rates.

Table 3.6 Correction factors for application to the fragility relations of Isoyama *et al.* (2000). Values in brackets are less reliable due to small sample size.

Pipe material correction factor, B_p		**Pipe diameter correction factor, B_d**		**Ground topography correction factor, B_g**		**Ground liquefaction correction factor, B_L**	
DI	0.3	75 mm	1.6	Disturbed hill	1.1	No liquefaction	1.0
CI	1.0	100-150 mm	1.0	Terrace	1.5	Partial liquefaction	2.0
PVC	1.0	200-400 mm	0.8	Narrow valley	3.2	Total liquefaction	2.4
Steel	(0.3)	> 500 mm	(0.5)	Alluvial	1.0		
AC	(1.2)			Stiff alluvial	0.4		

3.3.1.8 ALA (2001)

In 2001 the American Lifelines Alliance (ALA), a public-private partnership between FEMA and ASCE, published a set of detailed procedures to evaluate the probability of damage from earthquake effects to various components of water supply systems (ALA, 2001). The work covered water conveyance systems (pipelines, tunnels and canals), above-ground cylindrical storage tanks and portions of the conveyance control and data acquisition system (SCADA) that are located along the conveyance system, and flow control mechanisms (*e.g.* valves and gates). For each component, the likely damage states and corresponding fragility functions were presented. For buried pipelines, fragility relations were developed separately for permanent ground deformation effects and ground shaking effects.

The database developed for ground shaking effects included pipeline damage rates from 18 earthquakes spanning the period 1923-1995. Data were obtained from a number of sources, as detailed in Table 3.7.

The data of Katayama *et al.* (1975), O'Rourke & Ayala (1993), Eidinger *et al.* (1995) and Shirozu *et al.* (1996) had already been used separately in developing previous fragility relations, as outlined above. The dataset included from Toprak (1998) was part of that used by O'Rourke *et al.* (1998). As indicated in the table, an additional ALA report was cited for some of the data from the 1989 Loma Prieta and 1994 Northridge earthquakes. Details of this report, however, were not specified. The full ALA (2001) database was homogenised as much as possible. Where data were based on I_{MM} or PGA, conversions to PGV were made using the equations of Wald *et al.* (1999). The database was then screened for duplicate points. Data from three earthquakes were excluded due to excessive and unquantifiable influence of permanent ground deformation effects on pipeline failure rates (Table 3.4a). Data from a further three earthquakes were excluded as these events had aftershocks deemed significant enough to have caused additional pipeline damage. These events, together with their aftershock magnitudes, are indicated in Table 3.4a. Two data points were excluded because of excessive corrosion effects (one point each from the 1979 Imperial Valley and 1983 Coalinga earthquakes).

Table 3.7 Summary of data sources used to develop the ALA (2001) database of pipeline damage caused by ground shaking.

Source	1923 Kanto	1933 Long Beach	1948 Fukui	1949 S Puget Sound	1964 Niigata	1965 Puget Sound	1968 Tokachi oki	1969 Santa Rosa	1971 San Fernando	1972 Managua	1979 Imperial Valley	1983 Coalinga	1985 Michoacan	1987 Whittier Narrows	1989 Tlahuac	1989 Loma Prieta	1994 Northridge	1995 Hyogoken-nanbu
ALA report (unspecified)																■	■	
Eidinger *et al.* (1995)																■		
Katayama *et al.* (1975)	■		■		■		■		■	■								
O'Rourke & Ayala (1993)						■		■	■			■	■		■			
Shirozu *et al.* (1996)																		■
Toprak (1998)		■		■		■		■	■		■			■		■	■	

Various different definitions exist for PGV based on the use of the two horizontal components of motion; an issue addressed in some detail in Chapter 5. The ALA (2001) investigators selected to use the geometric mean of the two horizontal velocity components (PGV_G) in their definition of PGV, as used in the attenuation relations of Sadigh & Egan (1998) (Table 5.1). Peak velocities from the Northridge and Hyogoken-nanbu earthquakes appeared in the database as PGV_L, the maximum of the two horizontal components, so were converted to PGV_G using multiplication factors of 0.90 and 0.83 respectively, determined by averaging numerous instrumental values

obtained from these two earthquakes. For some of the other earthquakes, the data sources did not specify the PGV definition used, leading to possible inconsistencies in the ALA (2001) database.

ALA (2001) has published its full dataset as an appendix along with its report. For each data point, pipe material, pipe repair rate *(R_R),* pipe diameter, PGV and any adjustments made are specified. Where available, the numbers of repairs and length of pipe used to calculate R_R are given. Pipe material and pipe diameter categories are summarised in Table 3.8.

Table 3.8 Pipe material and pipe diameter categories included in the dataset for the ALA (2001) fragility relation (percentages subject to rounding errors).

Pipeline characteristic	Category	Description	Percentage of total database
Material type	AC	Asbestos Cement	12.3
	CI	Cast Iron	46.9
	CP	Concrete	2.5
	DI	Ductile Iron	11.1
	MX	Mixed (CI & DI combined)	11.1
	S	Steel	16.0
Diameter	DS	Distribution system (mainly small diameter)	70.3
	LG	Large diameter (> 30.48 cm)	9.9
	SM	Small diameter (≤ 30.48 cm)	19.8

A total of 81 data points remained following the screening procedure outlined above. The distribution of data for different pipeline categories is summarised in Table 3.8. The full ALA (2001) dataset is plotted in Figure 3.22.

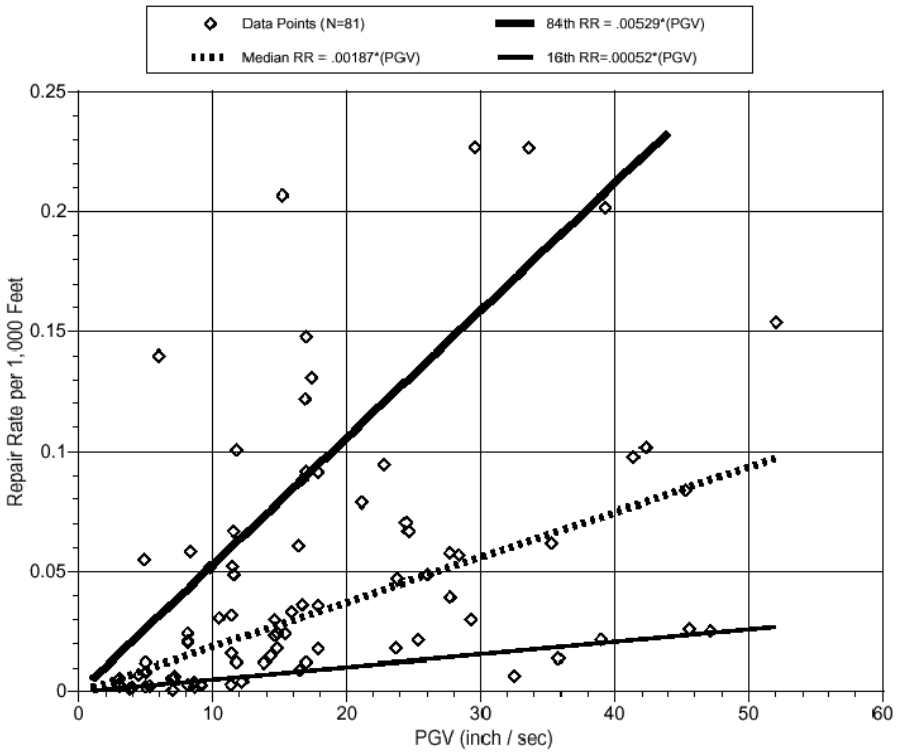

Figure 3.22 Data set used by ALA (2001) to derive pipeline vulnerability function for PGV. Median repair rate (R_R) line defines standard "backbone" curve. Lines defining the 16th and 84th percentiles are included to illustrate the scatter.

This includes the standard "backbone" fragility relationship based on a single-parameter linear model and lines representing the 16th and 84th percentiles of the data set. The "backbone" line defines the median slope of all 81 data points and has the property of having equal numbers of points above and below it. This approach was chosen in preference to a least-squares best-fit line due to the amount of scatter in the data set. The line of median slope is a description of central tendency less sensitive to data outliers. The "backbone" fragility relation is expressed in Equation (3.36) and plotted in Figure 3.23.

Additional analyses were performed to assess the influence of earthquake magnitude, pipe material and pipe diameter on the pipe failure rate. In each case, the relative repair rate for a given category was quantified by taking ratios of slope coefficients for different subsets of the database. Earthquake magnitude was taken as a surrogate measure for duration of ground shaking, with the implication that for a given value of PGV, pipe damage rate would be higher in regions experiencing longer duration of ground shaking. However, no meaningful relationship was identified from the available data. The identification of a duration effect would require several datasets similar to that of O'Rourke *et al.* (1998), consisting of a reliable pipeline inventory and a high density of strong-motion records; this remains to be done.

The relative vulnerabilities of different pipe diameter ranges and material types were quantified by fragility curve modification factors, K_{1ALA}. These are shown in Table 3.5, alongside the modification factors derived by Eidinger *et al.* (1995, 1998). Notable differences between the two sets of factors are highlighted in the table. The influence of soil corrosivity for metal pipes was quantified based on expert opinion as relevant data was not available for most of the dataset. The "backbone" fragility relation of ALA (2001) was defined for small diameter CI pipes with cement joints installed in soils with unknown corrosivity.

The ALA (2001) investigation included details on application of the fragility relations for different pipe-joint-diameter-soil types and a discussion of scatter in the dataset, which is considerable.

3.3.1.9 Lessons learned

The majority of pipeline fragility relations use either PGA or PGV as the predictor parameter. A selection of available relations for PGA are given in Table 3.9 and are plotted for comparison purposes in Figure 3.23, along with an indication of the range of applicability of each relation, where this could be estimated.

The predictions of Bresko (1980), based on the data of Katayama *et al.* (1975) are significantly greater than any of the other predictions for PGA above about 200 cm/s^2. Extrapolation of repair rates for PGA values much beyond this is, however, not warranted from the dataset. The high values predicted reflect both the influence of permanent ground deformation effects and large uncertainties in the derivation of repair rates. The curves of Isoyama & Katayama (1982) and

Isoyama *et al.* (2000) give similar predictions to each other in the range 120 - 300 cm/s^2. Much beyond this, the earlier study predicts significantly larger values of repair rate. Details of the dataset used by Isoyama & Katayama (1980) were unavailable for the current study, although the likely reason for over-prediction is lack of data for large values of PGA. The Isoyama & Katayama (1982) study is based on data from the San Fernando earthquake (Table 3.4a), which according to Bresko (1980), yielded pipeline repair rate data for the PGA range 170-330 cm/s^2 (Figure 3.23). Data from the Hyogoken-nanbu earthquake used by Isoyama *et al.* (2000) included data for PGA up to about 800 cm/s^2 and so is more reliable in the range 330 < PGA < 800 cm/s^2. In any case, the Isoyama *et al.* (2000) study is based on a much more reliable and comprehensive database than that of the earlier study.

Table 3.9 Pipeline fragility relations for PGA derived by several investigators. R_R denotes repair rate. PGA is measured in cm/s^2.

Investigators	R_R = f(PGA)		Notes
Katayama *et al.* (1975)	$10^{b+6.39\log_{10} PGA}$	(3.28)	Mainly CI pipes. Data is from Katayama *et al.* (1975) Trend is as suggested by Bresko (1980) for "average conditions" (b = 3.65)
Isoyama & Katayama (1982)	$1.698\times10^{-16}\,PGA^{6.06}$	(3.29)	CI pipes
O'Rourke *et al.* (1998)	$10^{1.25\log_{10} PGA-0.63}$	(3.30)	CI pipes
Isoyama *et al.* (2000)	$2.88\times10^{-6}\left(PGA-100\right)^{1.97}$	(3.31)	CI pipes

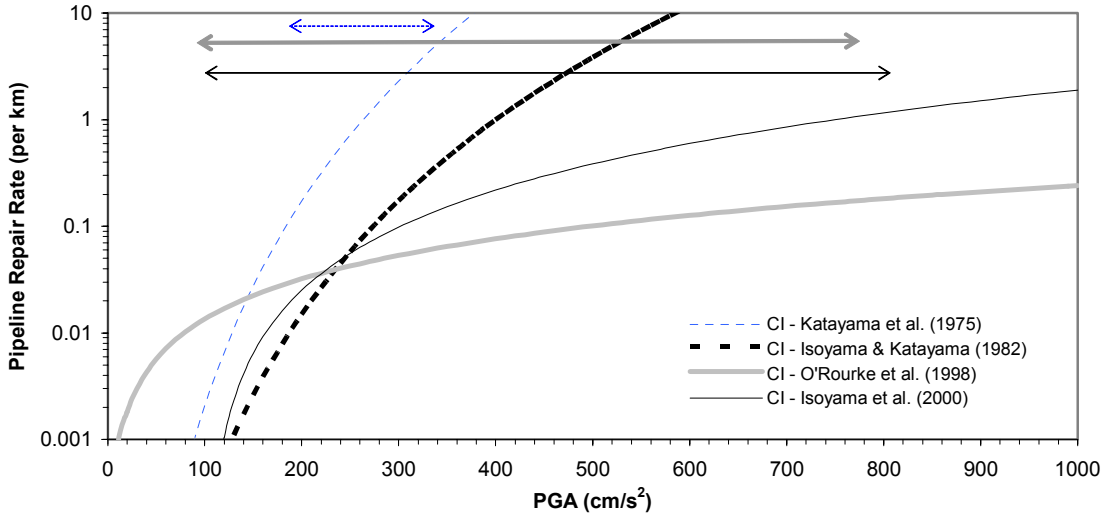

Figure 3.23 Comparison of the pipeline fragility relations for PGA expressed in Table 3.9. Arrows refer to the range of applicability of a given relation, approximated from knowledge of the dataset from which it was derived.

The relation derived by O'Rourke *et al.* (1998) predicts high repair rates for low values of PGA. However, application of the relation to PGA values below about 90 cm/s^2 requires extrapolation beyond the limits of the dataset. Differences at low PGA with the relation of Isoyama *et al.* (2000) are largely due to the functional form assumed in the Japanese study, in which the minimum PGA

to cause pipeline damage was set to 100 cm/s^2, although some damage was observed below this value (Figure 3.21). For PGA greater than around 220 cm/s^2, the O'Rourke *et al.* (1998) relation predicts lower repair rate values than the Japanese study. The two curves diverge significantly: the ratio of repair rates for the two relations at 400 and 800 cm/s^2 are 2.9 a 6.4 respectively. The reasons for this difference are not clear without more information on how the relations were derived.

Various PGV fragility relations are expressed in Table 3.10 and compared graphically in Figure 3.24. The range of applicability for each relation is indicated in the Figure, estimated from the range of PGV values used to derive each study.

Table 3.10 Pipeline fragility relations for PGV derived by several investigators. R_R denotes repair rate. PGV is measured in cm/s.

Investigators	R_R = f(PGV)		Notes
Eidinger *et al.* (1995, 1998)	$K_1 0.0001658 PGV^{1.98}$	(3.32)	"best-fit" fragility relation (K_1 = 1), converted from Imperial units to SI units
O'Rourke & Ayala (1993) HAZUS (FEMA, 1999)	$0.0001 PGV^{2.25}$	(3.33)	"brittle pipes" fragility relation
Isoyama *et al.* (2000)	$3.11\times10^{-3}(PGV-15)^{1.30}$	(3.34)	CI pipes "standard curve"
O'Rourke *et al.* (2001)	$e^{1.55\ln PGV-8.15}$	(3.35)	CI pipes
ALA (2001)	$K_{1ALA} 0.002416 PGV$	(3.36)	"backbone" fragility relation (K_{1ALA} = 1), converted from Imperial units to SI units

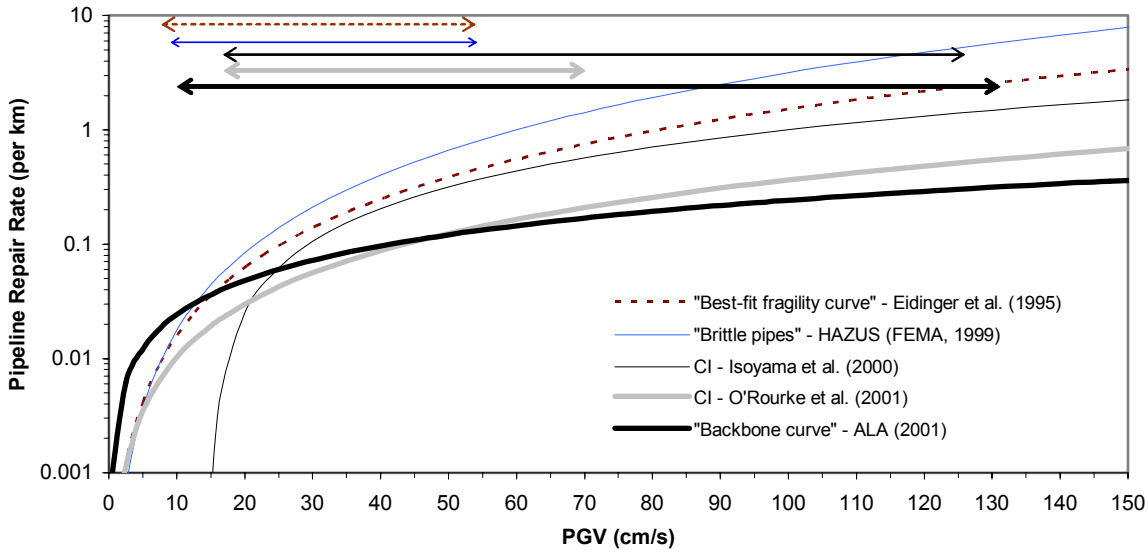

Figure 3.24 Comparison of the pipeline fragility relations for PGV expressed in Table 3.10. Arrows refer to the range of applicability of a given relation, approximated from knowledge of the dataset from which it was derived.

The HAZUS curve, based on the data of O'Rourke & Ayala (1993) gives the highest predictions of pipeline repair rate for PGV greater than 15 cm/s. O'Rourke (1999) considers this fragility relation

to be over-conservative, with pipeline repair rates being unduly affected by the long durations of ground shaking experienced during the Michoacan earthquake.

The Eidinger *et al.* (1995, 1998) and Isoyama (2000) relations predict repair rates within about a third of each other over the range 35 < PGV < 70 cm/s. These predictions are remarkably close for fragility relations, especially considering the fact that completely different data sets were used in each case. The disagreement at lower levels of PGV is largely due to the assumption by Isoyama *et al.* (2000) of a lower PGV threshold for pipeline damage. The Eidinger *et al.* (1995, 1998) relation has a much more limited range than that of Isoyama *et al.* (2000) and probably should not be extrapolated much beyond about 55 cm/s. The HAZUS relation is based on a dataset with a similarly restricted range.

The curves of O'Rourke *et al.* (2001) and ALA (2001) are remarkably similar over a wide range of PGV values. Much of any differences observed is due to the difference in functional form. ALA (2001) derived an alternative power relationship using the same dataset as was used for the linear relationship shown in the Figure and this agrees more closely with the O'Rourke *et al.* (2001) relation. The similarity between the O'Rourke *et al.* (2001) and ALA (2001) relations is strongly connected to the large proportion of Northridge earthquake data in both datasets (7 out of 11 data points in the former study; 35 out of 81 data points in the latter).

For the range of strong-motion values typically associated with destructive earthquakes, the variation in repair rate obtainable using different fragility relations is generally less for PGV than PGA (Figures 3.13 and 3.14). This suggests that PGV may be a better predictor of earthquake-induced pipeline damage than PGA. However, many factors have contributed to the scatter observed among the various fragility relations and a more quantitative investigation is required to draw more firm conclusions.

In Table 3.11, a summary is given of r^2 values for a selection of fragility relations for which either r^2 was quoted or could be calculated from the original dataset. r^2 is the coefficient of determination and measures the proportion of the total variation in the dependent variable, y (in this case, pipeline repair rate) that can be accounted for by the regression equation:

$$r^2 = \frac{\sum_{i=0}^{n} (\hat{y}_i - \bar{y})^2}{\sum_{i=0}^{n} (y_i - \bar{y})^2} \tag{3.37}$$

where: $\bar{y}$ is the mean of the measured values,
$\hat{y}$ is the predicted value using the regression equation and
n is the number of data points.

Comparison of r^2 for different fragility relations can give an indication of which parameter is most effective in predicting pipeline damage. A linear regression on the PGA dataset of Katayama *et al.*

(1975) gives the least convincing fit of all. However, the r^2 value is not much lower than that calculated for the original PGV dataset of ALA (2001). Both investigations involved the collection of pipeline repair rates for as many earthquakes as possible, drawing from a wide range of sources. The ALA (2001) investigators applied a careful screening process to all their data in order to reduce the heterogeneity of their database. However, the retention of data points having PGV values derived indirectly from PGA, I_{MM} or I_{JMA} introduces additional uncertainty into the dataset. At the time of the investigation, ALA (2001) only had pipeline repair rates for the Hyogoken-nanbu earthquake in terms of PGA, as provided by Shirozu *et al.* (1996). The data presented by Isoyama *et al.* (2000) includes pipeline repair rates for PGV, providing an opportunity to update the ALA (2001) dataset.

Table 3.11 Comparison of r^2 values for various fragility relation datasets. r^2 is the coefficient of determination, defined by Equation (3.37). Shaded values indicate values computed by the current author from original data.

	Investigation	EQ[1]	Pipe Material	Parameter	Data points	r^2	Regression equation
1	Katayama *et al.* (1975)	V	MX	PGA	37	0.12	Linear (non-zero intercept)
2	ALA1	V	MX	PGV	81	0.18	Linear (non-zero intercept)
3	ALA2	V	MX	PGV	88	0.26	Linear (non-zero intercept)
4	ALA3	V	MX	PGV	69	0.29	Linear (non-zero intercept)
5	O'Rourke & Ayala (1993)	V	MX	PGV	11	0.68	Linear (non-zero intercept)
6	O'Rourke *et al.* (1998)	N	CI	SI	9	0.68	Logarithmic
7	O'Rourke & Jeon (1999)	N	CI	PGV	7	0.85	Logarithmic – Eqn (3.39)
8	O'Rourke *et al.* (1998)	N S,W,L	CI	PGA	12	0.81	Logarithmic – Eqn (3.30)
9	O'Rourke *et al.* (2001)	N S,W,L	CI	PGV	11	0.85	Logarithmic – Eqn (3.35)
10	Isoyama *et al.* (2000)	H	CI	PGA	17	0.62	Power – Eqn (3.31)
11	Isoyama *et al.* (2000)	H	CI	PGV	15	0.77	Power – Eqn (3.32)
12	Isoyama *et al.* (2000)	H	DI	PGA	16	0.64	Power
13	Isoyama *et al.* (2000)	H	DI	PGV	12	0.96	Power

1 - EQ refers to earthquakes from which data are included in a given dataset: V-Various (see Table 3.4a); N-1994 Northridge; S-1971 San Fernando; W-1987 Whittier Narrows; L-1989 Loma Prieta; H-1995 Hyogoken-nanbu.
2 - ALA1 is the full dataset of ALA (2001) as presented in the original study.
3 - For ALA2, the nine PGA-derived data points for the Hyogoken-nanbu earthquake have been updated with PGV data from Isoyama *et al.* (2000).
4 - ALA3 is the ALA2 dataset with any remaining data points derived from I_{MM} or PGA values removed.

This has been done in the current investigation and is seen to lead to a marked improvement in the r^2 value as well as an increase in the size of database (Table 3.11, item 3). However, subsequent removal of any remaining data points having their PGV values calculated indirectly from PGA or earthquake intensity has little additional effect on the r^2 value (Table 3.11, item 4). The scatter in the remaining data set (ALA3) is notably less than the scatter of the Katayama e*t al.* (1975) dataset, but is nevertheless still considerable, as illustrated in Figure 3.25.

The ALA3 dataset includes pipeline repair rates for a range of pipe materials, pipe diameters and soil conditions, not to mention other unrecorded attributes which are likely to have influenced pipeline earthquake vulnerability. Further refinement to the strong-motion values used (assuming this were possible) is therefore unlikely to lead to significant additional improvement in the r^2 value. The much greater r^2 value observed in the data of O'Rourke & Ayala (1993) is largely due to a smaller, more homogeneous data set.

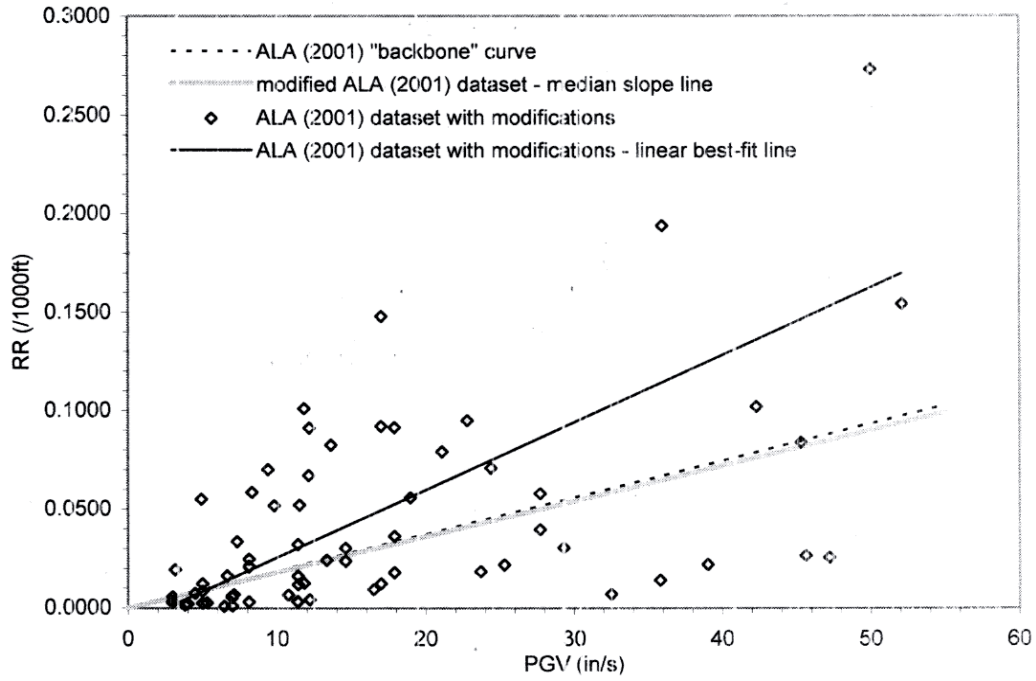

Figure 3.25 Comparison between "backbone" curve of ALA (2001) and median slope line of modified ALA (2001) dataset. Modified ALA (2001) dataset is expressed as ALA3 in Table 3.11. It has PGA derived data for Hyogoken-nanbu earthquake updated with PGV data of Isoyama *et al.*. (2000). In addition, any remaining data points derived from I_{MM} or PGA values have been removed.

In order to compare the relative success of different strong-motion parameters in predicting pipeline damage, separate regressions must be performed for different instrumental strong-motion values for the same pipeline damage dataset. To reduce the scatter due to other factors, it is helpful to only include data from a restricted number of pipeline attribute categories. The detailed GIS-based analyses carried out by O'Rourke *et al.* (1998, 2001) and Isoyama *et al.* (2000) are the only known studies which come close to meeting these criteria.

O'Rourke *et al.* (1998, 2001) and O'Rourke & Jeon (1999) compared fragility relations for CI pipes using data from the 1994 Northridge earthquake. For each regression performed, the pipeline repair rate for a given strong-motion value was calculated from a weighted average repair rate over a range of pipe diameters, with weighting based on pipe length (O'Rourke & Jeon, 1999). Approximately 97% of the pipes had a diameter in the range 10.2 - 20.3 cm (4-8 in). Out of the seven parameters indicated in Table 3.4 (b), the most statistically significant was stated to be PGV (O'Rourke & Jeon, 1999), although regression equations, datasets and r^2 values were only presented for SI and PGV. r^2 values for these strong-motion parameters are given in Table 3.11 and suggest that PGV is the better predictor variable. It should be noted that some of this difference in r^2 is probably due to the difference in size of the datasets. Even though the two datasets were obtained from the same set of strong-motion records and the same pipeline damage database, the method of spatial analysis used (summarised in Section 3.3.1.6) will inevitably have created different-sized datasets for different strong-motion parameters, although these differences can be minimised by careful selection of strong-motion parameter bins used in the zoning procedure.

O'Rourke and his colleagues combined data from the Northridge earthquake with data from other US earthquakes and carried out additional regressions, as specified in Table 3.11 (Items 8 and 9). For the combined dataset, PGV again proved to be the best predictor parameter, in this case compared with PGA, although the difference here was minimal.

The investigation by Isoyama *et al.* (2000) using data from the Hyogoken-nanbu earthquake yielded four separate fragility relations: PGA and PGV relations for both CI and DI pipes. r^2 values obtained from these regressions were significantly higher for PGV in both cases. The Hyogoken-nanbu dataset discriminates between the predictive capabilities of PGA and PGV more than the Northridge dataset.

The investigations of O'Rourke *et al*. (1998, 2001) and Isoyama *et al.* (2000) suggest that PGV is more effective than PGA for the prediction of pipeline damage caused by earthquake-induced ground shaking. That this should be the case has been suspected for a long time. Newmark (1967) highlighted the close connection between ground strain and PGV and this served as the motivation for the first PGV fragility relation (Barenberg, 1983). Measures of ground acceleration (although not necessarily the *peak* ground acceleration) are of more relevance in predicting damage to above-ground structures, for which inertial forces are much more important.

O'Rourke & Jeon (1999) mentioned that regression was performed between pipeline repair rate and PGD for the Northridge data. Any correlation was, however, masked by the inherent uncertainty of this strong-motion parameter (O'Rourke, 1999). PGD is obtained from double-integrated accelerograms, which, as is shown in Chapter 5, are very sensitive to the correction method applied. PGD values from routinely-processed strong-motion data are therefore not particularly reliable. Even if the PGD values used were reliable, it is unlikely that they would show a close correlation with damage to buried pipelines. Although pairs of displacement time-histories can be used to

approximate ground strain using Equation (3.38) (see for example Villacis & Katayama, 1992 or O'Rourke *et al.*, 1980), the *peak* ground displacement is not necessarily connected to ground strain. Two nearby locations can experience very high values of PGD but relatively low strains because motion at the two locations is coherent:

$$\varepsilon = \frac{U_1(t) - U_2(t)}{L_s} \tag{3.38}$$

where: ε is the ground strain,
$U_1(t)$ and $U_2(t)$ are the ground displacements at the two stations, at time t and
L_S is the separation distance between the two stations.

The work of O'Rourke and his colleagues was the only investigation found which considered strong-motion parameters other than PGA, PGV or macroseismic intensity. There is therefore much room for further research, although at present, further investigation appears to be restricted to the two existing GIS-based datasets. ALA (2001) investigated the possibility of strong-motion duration influencing pipeline damage rates, but were unable to draw any firm conclusions due to limitations in their dataset. More data would be needed to isolate such an effect if indeed it existed.

The Northridge and Hyogoken-nanbu studies have independently shown close correlation between PGV and pipeline repair rate. However, the resulting fragility relations predict very different damage rates for a given value of PGV. This is illustrated in Figure 3.26, in which the relation of Isoyama *et al.* (2000), derived purely from data obtained from the Hyogoken-nanbu earthquake and expressed by Equation (3.34) is compared with the relation of O'Rourke & Jeon (1999), derived purely from data obtained from the Northridge earthquake and expressed by Equation (3.39):

$$R_R = e^{1.22 \ln PGV - 6.82} \tag{3.39}$$

The ratio of the Isoyama *et al.* (2000) curve to that of O'Rourke & Jeon (1999) exceeds 2 for PGV > 40 cm/s and 3 for PGV above about 70 cm/s. For lower values of PGV, the ratio tails off due to the functional form assumed by Isoyama *et al.* (2000). It is suggested that the large differences observed between the two curves cannot be explained solely in terms of pipe vulnerability. The two fragility relations predict damage for approximately the same categories of pipe type and diameter and it is unlikely that the pre-earthquake vulnerability of the pipe networks was very dissimilar. A more feasible explanation is found in Equation (3.1). The travelling wave model shows that peak strain induced in the ground will increase with increasing value of PGV. However, it also implies that the same level of PGV would induce different levels of ground strain due to different values of the apparent propagation velocity of the seismic wave. The higher rates of CI pipe damage observed in Kobe during the Hyogoken-nanbu earthquake could be evidence of lower average apparent propagation velocities, c_{ave}, compared to Northridge. A greater predominance in Kobe than Northridge of surface waves over body waves in the areas experiencing pipeline damage would help explain this phenomenon.

Predominance of surface waves in Mexico City during the 1985 Michoacan earthquake caused unusually high pipeline damage rates, as discussed in Section 3.1.2. For a better understanding of the seismic wave fields experienced in Kobe and Northridge, a detailed analysis of strong-motion records and earthquake source processes would be required, which is beyond the scope of the current investigation. From the information given in Figure 3.26, however, it might not be unreasonable to suggest that the value of c_{ave} experienced in Northridge exceeded that in the Kobe area by a factor of between 2 and 3. Such a difference could readily be explained by differences in c_{ave} of body waves. Data summarised by O'Rourke & Liu (1999) from seven US and Japanese earthquakes between 1968 and 1979 show a range of values for c_{ave} for S-waves between 2.6 - 5.3 km/s.

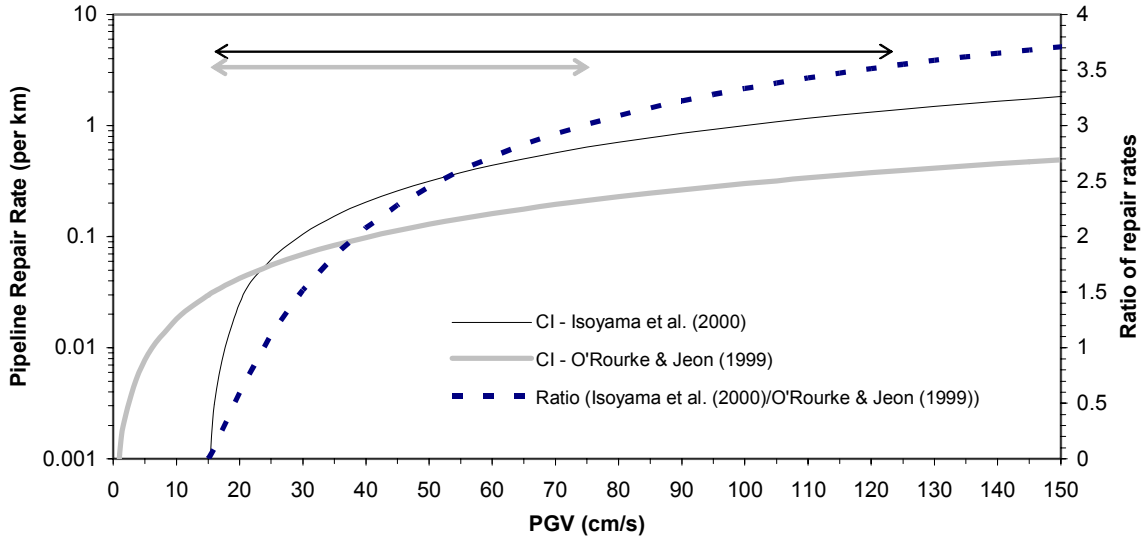

Figure 3.26 Comparison of pipeline fragility relations for O'Rourke & Jeon (1999) and Isoyama *et al.* (2000). The ratio of the two relations is also plotted on a separate y-axis. The fragility relation of O'Rourke & Jeon (1999) is expressed in Equation (3.39).

The suggested effect of c_{ave} on pipeline fragility relations adds extra uncertainty to prediction of pipeline damage rates in future earthquakes. Estimates based on the O'Rourke & Jeon (1999) relation assume a value of c_{ave} similar to that observed in Northridge during the 1994 earthquake. However, as stated by Trifunac & Lee (1996), the value of c_{ave} will be different for every earthquake, as it depends on the type of waves, the properties of the local soil and the underlying rock, and on the direction of wave arrival. Todorovska & Trifunac (1996) propose a method for hazard mapping of peak seismic ground strains in which strain estimates are based on scaling in terms of PGV and the proportionality factor is the phase velocity with which the wave energy is propagating. The method is of particular interest in that it forms part of a wider investigation by the same research team into strong-motion and damage patterns observed during the Northridge earthquake (Trifunac *et al.* 1996; Trifunac & Todorovska, 1998a), including treatment of pipeline damage (Trifunac & Todorovska, 1997). Detailed comparison between these studies and the studies of O'Rourke and his colleagues is therefore warranted, although beyond the limits of the current investigation.

Pipeline fragility relations have improved considerably over recent years and are useful for damage prediction. For general application, the PGV relation of ALA (2001) is recommended as it is derived from a global database. Although the scatter in the data is large, the relation allows many of the contributors to this scatter to be accounted for using modification factors. Detailed guidelines on its application are included in the original publication. In Figure 3.25, a modified backbone curve calculated for the modified dataset, ALA3 (Table 3.11) is seen to be almost identical to the one defined for the original dataset. This adds weight to the reliability of the backbone curve derived in the original study.

For Japan, the Isoyama *et al.* (2000) relations are suggested. Application to other locations is made difficult by the topographic classification scheme (see Table 3.6) which is not normally used outside of Japan. The fragility relations of O'Rourke *et al.* (1998, 2001) are of particular relevance to the US as data from other locations have not been included. The O'Rourke *et al.* (1998) relation is only strictly applicable to CI pipes and should be used accordingly.

Although it has been shown that PGV is a better predictor parameter for pipeline damage than PGA, it is nevertheless useful to have PGA fragility relations because of the widespread use of this parameter in earthquake risk assessment. It should be stressed, however, that wherever possible, predictions of pipeline damage should be made from PGV estimates.

3.3.1.10 Implications for future development

As noted previously, the ALA (2001) fragility relationship is the best currently available for broad application. It is unlikely that significant improvements can be made on the strong-motion estimates used, other than the ones already suggested here, due to the scarcity of relevant strong-motion records for most of the earthquakes.

The future development of pipeline fragility relations will depend very much on data availability from future earthquakes. Extending the existing dataset will require both reliable strong-motion data and reliable pipeline repair data. The number of strong-motion records generated by destructive earthquakes has increased dramatically in recent years as numbers of strong-motion recording stations in seismically active regions have increased (Trifunac & Todorovska, 2001). This trend will continue as long as earthquakes continue to occur. The availability of such data has also increased, with the establishment of online public-access databases such as ISESD (Ambraseys *et al.,* 2002) and COSMOS (http://db.cosmos-eq.org/).

Experience has shown that pipeline repair data is seldom recorded in a systematic manner following an earthquake and even more seldom reported in the literature. In the immediate aftermath of an earthquake, the emergency repair of buried water pipelines for the re-establishment of a basic water supply has generally taken precedence over detailed documentation of earthquake damage. This situation is, however, likely to change as many water utility operators are currently

investing significantly in GIS-based asset management tools. These tools assist reliable record keeping and, as illustrated by examples in Northridge and Kobe, help in the determination of factors influencing earthquake-related pipeline damage.

As more data becomes available, current fragility relations can be updated. The ALA (2001) database was compiled in as transparent a way as possible to make subsequent updating simple. The study includes suggestions about future improvements to the reliability of pipeline damage predictions using Bayesian inference.

Water supply systems are characterised by their spatial extent. In the event of an earthquake, different system elements are therefore exposed to different levels of the various earthquake effects. In order to understand the distribution of damage throughout a water supply system, the spatial variation of the various earthquake effects must be mapped. Earthquakes effects must also be mapped in order to predict the likely damage in the event of a future earthquake.

In the current chapter, an overview is presented of methods used to map the spatial distribution of earthquake effects. Emphasis is placed on the mapping of transient ground deformation, with only passing reference to other earthquake effects. Section 4.1 is concerned with the mapping of earthquake effects in post-earthquake investigation of damage to water supply pipes. In Section 4.2, an overview is given of methods used to predict the spatial distribution of ground shaking for a future earthquake event. Section 4.3 is a detailed consideration of the microtremor method, used to help interpret the spatial distribution of ground motions. This approach is subsequently used to characterise site effects in the case study of earthquake damage to buried pipelines presented in Chapters 6 to 8.

4.1 Post-earthquake mapping of earthquake effects

Post-earthquake mapping of earthquake effects involves a combination of field investigation and desk study. The field investigation should ideally take place promptly after the earthquake event as data relating to many of the permanent ground deformation features is highly perishable. If it is not lost in the post-earthquake reconstruction, then it soon degrades by weathering. Field investigation can take the form of 'walk-about' surveys, topographic surveys, questionnaires, air photography, satellite image interpretation. This is supplemented with existing surface geological maps and information on damage distribution from previous earthquakes.

Mapping of the transient components of ground motion is based on strong-motion data retrieved from instruments situated in the region of strong ground-shaking. Following any given earthquake event, recordings of ground motion will generally only be available for a few distinct points within the area of strong ground shaking. In order to correlate observed damage to a water utility network with characteristics of the ground motion, known data must be extrapolated/interpolated to any other locations of interest. For some earthquakes (*eg*. 1994 Northridge or 1995 Hyogoken-nanbu), this is fairly straightforward, owing to the availability of extensive databases of strong-motion records and well-documented damage to the water distribution system. As demonstrated in Chapter 3, GIS-based spatial analysis of such a dataset allows the identification of earthquake damage patterns and their causes, even yielding new empirically-derived pipeline fragility relations for subsequent use in earthquake risk analysis. This procedure is illustrated in Figure 4.1.

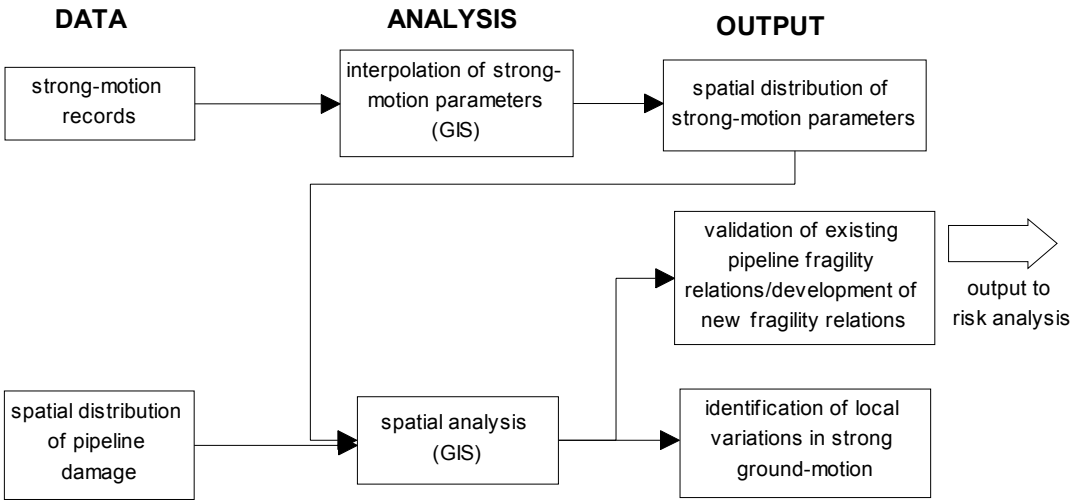

Figure 4.1 Post-earthquake investigation of water supply system damage

For most earthquakes, strong-motion data is much sparser. In these cases, strong ground shaking may be estimated from macroseismic data and/or through the use of microzonation methods (see Section 4.2). Many of the studies described in the previous chapter involved estimation of PGV from only a handful of strong-motion records supplemented with information on site conditions.

The distribution of earthquake damage to engineered structures can be used to infer characteristics of strong motion and other earthquake effects at a resolution greater than the resolution of strong-motion sampling, as defined by the spatial density of strong-motion instruments. Trifunac & Todorovska (1999), for example, used the spatial density of breaks in buried water pipes and the spatial density of severely-damaged buildings to infer the spatial distribution of PGV as a result of the 1994 Northridge earthquake. The resolution of these maps was even greater than could be obtained from the high density of strong-motion stations which recorded the Northridge earthquake. Yamaguchi & Yamazaki (2001) used building damage data from the 1995 Hyogoken-nanbu earthquake to infer strong-motion distribution in Kobe at the district level.

4.2 Prediction of ground shaking

The most important factors influencing earthquake ground motion and its duration at a particular location are (Mohraz & Elghadamsi, 1989):

a) earthquake magnitude
b) distance from the source of energy release
c) local soil conditions
d) variation in geology and propagation velocity of seismic waves along the travel path
e) earthquake source conditions and mechanism (fault type, stress conditions, stress drop)

The prediction of ground motion during a future earthquake event therefore depends upon characterisation of all of these factors in some way. The earthquake magnitude (and sometimes

fault type) and the source-to-site distance are defined by the seismic hazard study (Section 4.2.1). Attenuation relationships are then used to predict the decrease of a strong-motion parameter with distance. These relationships are derived from regression analyses of strong-motion data. The strong-motion parameter, X is generally expressed in terms of magnitude, distance, and sometimes other variables, as indicated below:

$$X = f(M, R, P_i) \tag{4.1}$$

where: X is the strong-motion parameter,
M is the earthquake magnitude,
R is a measure of the distance from earthquake source to the site of interest,
P_i are various other parameters used to characterise earthquake source, wave propagation path, and local site conditions.

A large number of attenuation relationships have been developed for various different geographic and tectonic environments. Most are for the prediction of PGA, for the same reason that PGA is the most commonly used strong-motion parameter (see Chapter 2). However, relationships have been defined for other parameters such as PGV, PGD, SA and I_a. A review of the available predictive relationships for PGV and PGD is presented in Chapter 5, alongside new predictive relationships for PGA, PGV and PGD derived by the author.

The characterisation of site effects used in attenuation relations is usually quite crude. The same seismic response is often assumed at sites representing a broad range of geological conditions. This level of detail is often sufficient for prediction of ground shaking on a regional basis. However, for more detailed seismic zonation, other methods give improved characterisation of site effects. Some commonly used methods are explained in Section 4.2.2.

4.2.1 Overview of seismic hazard analysis for water supply systems

Seismic hazard analysis involves the quantitative estimation of ground-shaking hazard at a particular site. The hazard may be quantified deterministically, by assuming a scenario earthquake, or probabilistically, in which uncertainties in the earthquake size and location in both time and space are considered explicitly.

Deterministic hazard analysis for a specific site consists of four main steps (Reiter, 1990):

1. Identification and characterisation of all earthquake sources capable of producing significant ground motion at the site of interest, based on geological evidence and the distribution of previous earthquakes. Source characterisation includes definition of the source's geometry and earthquake potential.
2. Selection of a source-to-site distance parameter for each source zone. This will depend on the measure of distance used in the predictive relationship used in the following step.

3. Selection of the controlling earthquake (i.e. the earthquake that is expected to produce the strongest level of ground shaking), usually expressed in terms of some ground-motion parameter at the site. The selection is made by comparing the levels of shaking produced by earthquakes defined in step 1 assumed to occur at the distances identified in step 2. The controlling earthquake is then described in terms of magnitude and distance from the site.

4. Formal definition of the hazard at the site in terms of the ground motions produced at the site by the controlling earthquake. Ground-motion characteristics are described by one or more ground-motion parameters obtained from predictive relationships.

The procedure is shown schematically in Figure 4.2.

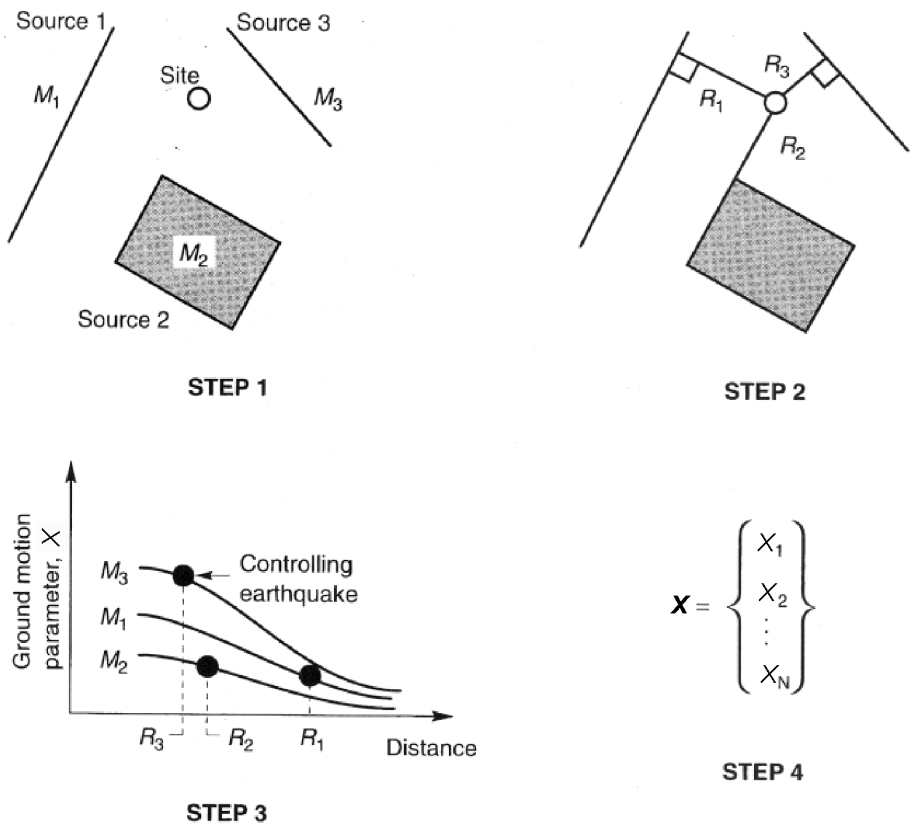

Figure 4.2 Main aspects of a deterministic seismic hazard analysis (Kramer, 1996)

For a spatially distributed system, such as a water distribution system, the variation of hazard over an extended region must be mapped out for each potential seismic source defined in step 1. The controlling earthquake is the one that causes the most severe ground motions over the whole system area or the one which causes most damage to certain critical components of the system.

A deterministic approach to earthquake hazard analysis is particularly appropriate for any lifeline system since it is important to consider the amalgamated effect of damages to the whole system. For site-specific analysis of individual critical facilities (*eg.* a raw water transmission main or a major pump station), probabilistic or deterministic hazard assessments can both be used.

Probabilistic seismic hazard models (*e.g.* Selcuk & Yucemen, 2000) are being developed for use in the assessment of reliability of lifeline systems. However, although these methods consider all potential seismogenic sources explicitly, they do not allow the definition of an actual system damage state. The deterministic approach, by using a small number of scenario-based loss estimates, will not consider the losses from a large number of other potential earthquake scenarios. However, particularly in highly seismic areas, with clearly defined earthquake sources, expert knowledge can be used to define the critical scenarios.

In practice, utility operators tend to use the scenario-based approach (Savage, 2000). This allows identification not only of the likely extent of physical damage for a given scenario, but also the loss of functionality of the system. Examples of seismic upgrade of water supply systems based on a scenario approach to earthquake hazard include East Bay Municipal Utility District, California (Taylor *at al.*, 1998) and Wellington Regional Council, New Zealand (CAE, 1991).

4.2.2 Characterisation of site effects

Quantitative models exist for the prediction of both soil amplification effects and secondary effects. The ISSMGE (International Society for Soil Mechanics and Geotechnical Engineering) Technical Committee for Geotechnical Earthquake Engineering has compiled a manual which describes in detail a selection of methods available for quantifying various geotechnical earthquake hazards (TC4/ISSMGE, 1999). The outcome of each method is generally in the form of a hazard zonation map in which areas with different levels of hazard potential are identified. The manual grades methods according to the input data requirements and the level of detail of the output, as summarised in Table 4.1.

Table 4.1 Use of data for different levels of zonation (TC4/ISSMGE, 1999)

	Grade-1	Grade-2	Grade-3
Scale of mapping	1:1 000 000 - 1:50 000	1:100 000 - 1:10 000	1:25 000 - 1:5 000
Ground motions	• historical earthquakes and existing information • geological maps • interviews with local residents (i.e. macroseismic data)	• microtremor • simplified geotechnical study	• geotechnical investigation • ground response analysis
Slope instability	• historical earthquakes and existing information • geological and geomorphological maps	• air photos and remote sensing • field studies • vegetation and precipitation data	• geotechnical investigation • analysis
Liquefaction	• historical earthquakes and existing information • geological and geomorphological maps	• air photos and remote sensing • field studies • interviews with local residents	• geotechnical investigation • analysis

In general, Grade-1 methods predict site effects based purely on empirical relationships and data collected from the literature or from on-site observation (e.g. geological maps and recorded motions and damage from previous earthquakes). They are suitable for an initial assessment of hazard on a large scale (typically 1:1,000,000 to 1:50,000) and form the basis of more detailed investigation. Grade-2 methods rely on *in situ* measurements to predict soil effects, either directly, through the use of microtremor investigation, or indirectly, through the use of empirical relationships defined for pertinent soil properties. Grade-2 studies allow mapping of earthquake effects at a scale most appropriate for water supply or other lifeline systems (typically 1:10,000). Grade-3 methods involve ground response analysis using data from detailed geotechnical investigation. For water supply systems, Grade-3 site specific investigation might be warranted for critical facilities such as water treatment works or large diameter transmission lines but would be too costly for characterisation of site effects across the whole of a water supply system.

The focus of the current section is on methods which allow estimations of ground shaking at a level of detail most appropriate for water supply systems. An overview of methods used to predict secondary earthquake effects, such as landslides and liquefaction is beyond the limits of the current study but can be found in TC4/ISSMGE (1999).

Numerous observations of the seismic response of different ground conditions have permitted the development of empirical relations between various measures of ground-motion and characteristics of the surface geology.

On the regional or urban scale, empirical relations between surface geology and macroseismic intensity can be used to create intensity anomaly maps. The relations of Medvedev (1962) and Evernden & Thompson (1985) have been used extensively for seismic zonation in Eastern Europe and Western Europe/the United States respectively. The relations of Evernden & Thompson are summarised in Table 4.2, from TC4/ISSMGE (1999).

Table 4.2 Intensity increments for different geological units (Evernden & Thompson, 1985)

Geological unit	Intensity increment (Modified Mercalli Intensity scale)
Granitic and metamorphic rocks	0
Paleozoic rocks	0.4
Early Mesozoic rocks	0.8
Cretaceous to Eocene rocks	1.2
Undivided Tertiary rocks	1.3
Oligocene to middle Pliocene rocks	1.5
Pliocene to Pleistocene	2.0
Tertiary volcanic rocks	0.3
Quaternary volcanic rocks	0.3
Alluvium (water table < 30 ft)	3.0
Alluvium (30 ft < water table < 100 ft)	2.0
Alluvium (100 ft < water table)	1.5

Similar relations have been developed between various geological units and the spectral amplification of ground motion for different frequency ranges. Borcherdt & Gibbs (1976), for

example, found a strong correlation between generalised classifications of surface geology in the San Francisco area and the average horizontal spectral amplification in the frequency range 0.5 to 2.5 Hz, $AHSA_{f\_0.5\text{-}2.5}$. Relative amplification factors for various geological units with respect to a granite reference site are given in Table 4.3 (TC4/ISSMGE, 1999).

Table 4.3 Relative site amplification for various geological units according to Borcherdt & Gibbs (1976).

Geological unit	Relative amplification factor
Bay mud	11.2
Alluvium	3.9
Santa Clara Formation	2.7
Great Valley sequence	2.3
Franciscan Formation	1.6
Granite	1.0

These geological units are very region-specific, making these particular amplification factors difficult to apply to other locations. TC4/ISSMGE (1999) presents other similar empirical relations which use different definitions of spectral amplification and which are defined for different geological categories. The scheme of Midorikawa (1987), which predicts the average spectral amplification in the frequency range 0.4 to 5 Hz relative to ground motion on Pre-Tertiary rocks, is of more general application as it uses broader geological categories (Table 4.4).

Table 4.4 Relative site amplification for various geological units according to Midorikawa (1987).

Geological unit	Relative amplification factor
Holocene	3.0
Pleistocene	2.1
Quaternary volcanic rocks	1.6
Miocene	1.5
Pre-Tertiary	1.0

The importance of the shear-wave velocity, v_s, of the near-surface layers of soil to its dynamic behaviour has already been illustrated in Chapters 2 and 3. Various researchers have proposed empirical relations between the average shear-wave velocity of surficial deposits (averaged over a given depth) and relative amplification of ground motion. TC4/ISSMGE (1999) presented a comparison of three such studies (Joyner & Fumal, 1984; Midorikawa, 1987 and Borcherdt *et al.*, 1991). The expressions derived are summarised in Table 4.5 and compared graphically in Figure 4.3. All of the relations show the same general trend of increasing relative amplification with reduction in the average shear-wave velocity. Such relations allow reference zones to be identified in which the local ground-shaking hazard is expected to be equal to the regional ground-shaking hazard, as defined by the regional seismic hazard study. These reference zones are characterised by a relative amplification factor of 1.0. The reference ground conditions for the relations of Joyner & Fumal (1984) and Midorikawa (1987) are very similar (having an average shear-wave velocity of around 1100 m/s), although the relations use slightly different definitions of average shear-wave velocity. The reference value of v_{s1} for the Borcherdt *et al.* (1991) relations is 700 m/s

in the case of weak-motion and 600 m/s in the case of strong-motion. This difference is evidence of the non-linear dynamic behaviour of soil (Chapter 2). The relations of Borcherdt *et al.* (1991) and Joyner & Fumal (1984) not only imply amplification of ground shaking in regions with ground conditions less favourable than the reference conditions, but also imply de-amplification of ground shaking in the presence of more favourable ground conditions (i.e. greater average shear-wave velocity).

Table 4.5 Empirical relations between average shear-wave velocity and relative amplification (TC4/ISSMGE).

Study	Proposed empirical relationship	Notes
Joyner & Fumal (1984)	$A_{PGV} = 23 v_{SQ}^{-0.45}$ (4.2)	-
Midorikawa (1987)	$A_{PGV} = 68 v_{S30}^{-0.6}$ (4.3)	for $v_{S30} < 1100$ m/s
	$A_{PGV} = 1.0$ (4.4)	for $v_{S30} > 1100$ m/s
Borcherdt *et al.* (1991)	$AHSA_{T\_0.4-2.0} = 700/v_{s1}$ (4.5)	for weak motion
	$AHSA_{T\_0.4-2.0} = 600/v_{s1}$ (4.6)	for strong motion

A_{PGV} is the relative amplification factor for *PGV*; $AHSA_{T\_0.4\text{-}2.0}$ is the average horizontal spectral amplification in the period range 0.4 to 2.0 s; v_{S30} is the average shear-wave velocity over a depth of 30m; v_{SQ} is the average shear-wave velocity over a depth of one-quarter wavelength for a one-second period wave; v_{S30} and v_{SQ} are both in m/s.

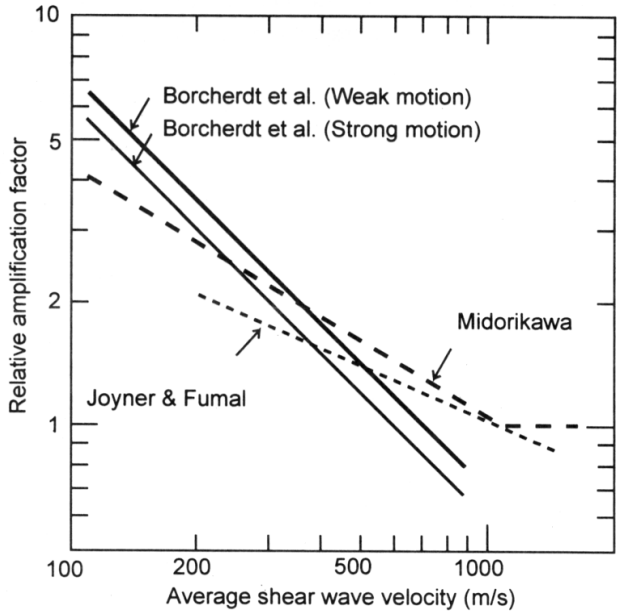

Figure 4.3 Comparison between various empirical relations giving relative amplification factor as a function of the average shear-wave velocity (TC4/ISSMGE, 1999).

The usefulness of such empirical relations is limited by the availability of shear-wave velocity data for the region under study. Various geophysical methods exist which allow direct measurement of the shear-wave velocity of the ground. Some of these methods, such as cross-hole logging and down-hole logging require boreholes to be drilled and are costly and time-consuming. Other

surface-based techniques have been developed which are less costly and are therefore more appropriate for characterisation of ground conditions over a wide area. The spectral-analysis-of-surface-waves method (SASW) (Nazarian & Stokoe, 1984; Brown *et al.*, 2000) is particularly appropriate for rapid shear-wave velocity profiling along lifelines (Andrus, 1997).

In the absence of direct measurements of the shear-wave velocity, estimations can be made from the results of standard penetration tests (SPT) or cone penetration tests (CPT), which are much more widely available, being commonly used in a number of geotechnical engineering applications. Many empirical relations exist between the SPT blow count, N_{SPT} and v_s for various types of soil (*eg.* Ohta & Goto, 1978; Raptakis *et al.*, 1995 and Baziar *et al.,* 1998). CPT results can be used to estimate v_s through their correlation with N_{SPT} (*e.g.* Robertson *et al.*, 1983).

The methods outlined so far allow site effects to be characterised in a fairly simple way, requiring only a few soil parameters. When more detailed geotechnical information is available, site effects can be estimated through numerical analysis. Numerical methods are often only feasible for site-specific studies, for individual buildings or critical lifeline facilities. However, in some urban areas, sufficient geotechnical data can sometimes be compiled to allow characterisation of site effects using numerical methods at a scale appropriate for whole lifeline systems.

If a given site can be approximated to a simple one-layer structure over bedrock, Equations (2.4) and (2.6) can be used to estimate the fundamental frequency, f_0 and the corresponding amplification at the fundamental frequency, A_0, based on the shear-wave velocity and depth of the soil layer, the impedance contrast between the soil and underlying bedrock and the sediment damping.

For multi-layered soil profiles, hand calculations can provide satisfactory estimates of f_0, or its reciprocal, T_0. Dobry *et al.* (1976) presented a number of simplified procedures for estimating the fundamental period, T_0 (or T_p) of a layered soil profile. Some of these procedures have been summarised by Bard (1997) and are presented in Table 4.6, with the relevant notation illustrated in Figure 4.4.

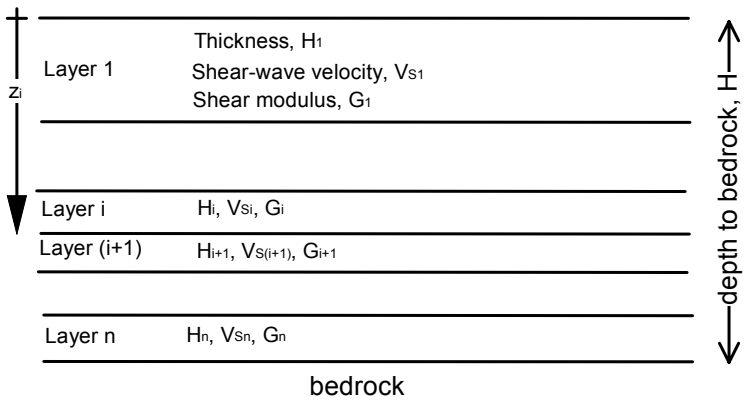

Figure 4.4 Layered soil profile

Table 4.6 Summary of approximate methods for estimating the fundamental period, T_0 of a horizontally layered soil profile (Bard, 1997).

Method	Description	Mathematical formulation	Comments
1	Weighted average of S-wave velocities	$\bar{v}_S = \frac{1}{H}\sum_{i=1}^{n} v_{Si} H_i$ $T_0 \approx T_1 = \frac{4H}{\bar{v}_S}$	Slight mean overestimating: 10 to 15% Precision: about 30% Limitation: No significant velocity jump between two contiguous layers ($1.5 > v_{Si}/v_{S(i+1)} > 0.5$)
2	Weighted average of shear moduli and densities	$\bar{G} = \frac{1}{H}\sum_{i=1}^{n} G_i H_i$ $\bar{\rho} = \frac{1}{H}\sum_{i=1}^{n} \rho_i H_i$ $T_0 \approx T_2 = \frac{4H}{\sqrt{\bar{G}/\bar{\rho}}}$	Very slight mean overestimation: 5% Precision: about 30%
3	Sum of natural periods of each layer	$T_0 \approx T_3 = \sum_{i=1}^{n} \frac{4H_i}{v_{Si}}$	Large mean overestimation: 25 to 30% Precision: about 40%
4	Linear approximation of the fundamental mode shape	$\omega_4^2 = \frac{3}{H^3}\sum_{i=1}^{n} v_{Si}^2 H_i$ $T_0 \approx T_4 = \frac{2\pi}{\omega_4}$	Very slight underestimation: 5% Precision: 25 to 30%
5*	Simplified version of Rayleigh approach	$X_{i-1} = X_i + \frac{z_i + z_{i-1}}{v_{Si}^2} H_i \; ; X_n = 0$ $\omega_5^2 = \frac{4\sum_{i=1}^{n} \frac{(z_i + z_{i-1})^2}{v_{Si}^2} H_i}{\sum_{i=1}^{n} (X_i + X_{i-1})^2 H_i}$ $T_0 \approx T_5 = \frac{2\pi}{\omega_5}$	No bias Precision: about 5% No limitations

* X_i and X_{i+1} are the estimated fundamental mode shapes at the lower and upper boundary of layer i.

In most cases, these methods only require the thickness and shear-wave velocity of each soil layer. Method 2 also requires the density, ρ_s of each soil layer, and the shear modulus, G, which can be calculated using the expression:

$$G = \rho . v_s^2 \tag{4.7}$$

Comments about the reliability and limitations of each method are included in Table 4.6. Method 5, which is a simplified version of the Rayleigh procedure, gives the best results, although assumes a constant density soil profile. A recently proposed method by Hadjian (2002) allows estimation of the fundamental period and mode shape of layered soil profiles which incorporates different layer densities.

In order to estimate ground-motion amplification as well as the fundamental period of vibration, more complex numerical methods are required. One method which is commonly used in ground response studies and which has been applied to the seismic zonation of water supply systems (*eg.* Ichihara & Yamada, 1982), is the theoretical transfer function model. This is based on one-dimensional linear wave propagation theory *i.e.* soil deposits are idealised as discrete horizontal strata and seismic shear waves are assumed to be vertically incident. Surface response is found by solving the simplified equations of motion in the frequency domain. The linear transfer function, *H(f)* is defined as the ratio of soil surface amplitude to the bedrock outcrop amplitude. *H(f)* effectively describes how soil layers filter the frequency content of seismic waves which is dependent upon the soil's viscoelastic properties. Transfer function models can be used to express modification of various spectral ordinates. The general form of the equation describing the surface spectrum is:

$$S_s(f) = H(f) S_r(f) \tag{4.8}$$

where: $S_s(f)$ is the spectral amplitude at the ground surface level,
$S_r(f)$ is the spectral amplitude at the bedrock level and
f is the frequency (Hz)

The transfer function approach relies on the principle of superposition. As such, it is limited to the analysis of linear systems. Soil, however, is well recognised for its non-linear stress-strain behaviour. The method is therefore generally modified by means of an equivalent linear approximation of the non-linear response, whereby the soil properties are adjusted iteratively to be compatible with the level of shear strain induced in the soil. In order to set up the analysis, the soil must be discretised into layers. Profiles down to and including bedrock are required of soil unit weight ($\gamma = \rho.g$) and either the maximum shear modulus, G_{max} or shear-wave velocity, v_s.

For the equivalent linear analysis, modulus reduction and damping ratio curves are needed for each material type. These describe the ways in which equivalent linear approximations of the soil's stiffness and damping characteristics change with the level of strain. In the modulus reduction curve, the normalised value of the secant shear modulus, G_{sec} is plotted against strain. G_{sec} is an approximation of the true hysteretic behaviour of the soil over one complete loading cycle (see Figure 4.5).

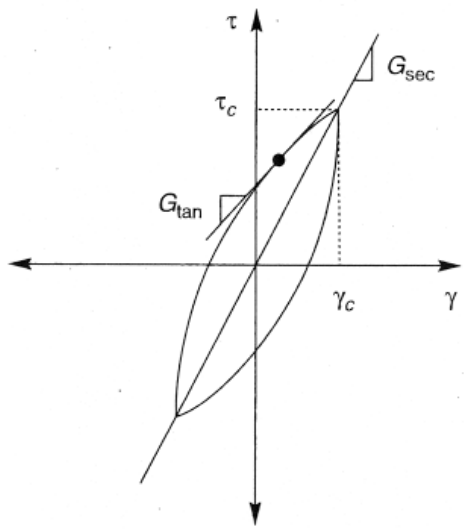

Figure 4.5 Linear approximation of hysteretic soil behaviour (Kramer, 1996)

The damping ratio curve shows the strain-dependency of the equivalent linear damping ratio, ξ. This is the damping ratio that produces the same energy loss in a single cycle as characterised by the actual hysteresis loop and is defined by (Kramer, 1996):

$$\xi = \frac{W_D}{4\pi W_s} = \frac{1}{2\pi}\frac{A_{loop}}{G_{\sec}\gamma_c^2} \tag{4.9}$$

where: W_D is the dissipated energy,
W_S is the maximum strain energy,
A_{loop} is the area of the hysteresis loop and
γ_c is the shear strain amplitude.

The nature of the modulus reduction and damping ratio curves has been well established for a range of soil and rock types.

The equivalent linear approach is a convenient method of approximating some of the key aspects of soil's non-linear, inelastic behaviour. However, it remains a linear method and is incapable of representing the changes that actually occur in the soil stiffness during an earthquake. In addition, permanent strains and pore water pressures cannot be computed. The method has been used in the analysis of soil response in a wide variety of geological conditions. As such, problems associated with the model are well-documented, allowing their effects to be taken into consideration in the analysis. Ho (1991) summarises some of the model's main limitations:

- Over-simplification of the true ground response by assuming that shear waves propagate vertically and that the soil layers are discrete and horizontal.
- Attenuation of the high-frequency content of ground motions (above around 5 to 10 Hz). This is thought to be because of the linearisation process.

- Unrealistic soil amplification at the resonant period when the predominant period of the soil profile and the input motion coincide.

Furthermore, equivalent linear analysis is only considered applicable at strains up to about 0.5%. This has been confirmed by comparison with strong-motion data taken from a vertical accelerograph array (Yoshida & Iai, 1998). In spite of these limitations, the model has been shown to produce reasonable estimations of soil response under many conditions of practical importance.

4.3 Characterisation of site effects using the microtremor technique

Increasingly, measurements of low-amplitude ambient ground noise ("microtremors") are being used in the characterisation of local site effects. These can be carried out at any time and location, relatively cheaply. Bard (1998), in his state-of-the-art report on microtremors, identifies the 1985 Michoacan, Mexico earthquake as a landmark event in western interest in microtremor techniques due to the consistency between microtremor measurements taken after the earthquake and strong-motion observations (Lermo *et al.*, 1988).

Microtremors have been used in four main ways for understanding site effects:

a) Absolute Fourier spectra,
b) Spectral ratios with respect to a reference (rock) site,
c) Single station HVSR (Horizontal to Vertical Spectral Ratio),
d) Shear wave velocity structure inversion through array measurements.

This section will consider the first three methods. The fourth method is essentially a geophysical approach which provides Rayleigh wave dispersion curves which can be inverted to obtain an estimation of the shear-wave velocity profile down to bedrock (eg. Tokimatsu *et al.*, 1996; Kudo *et al.,* 2002). Discussion of this approach is beyond the limits of the current study.

Before looking in more detail at the methods used, it is useful first to consider the nature of the noise wave field. Much of the early work on microtremors was done in Japan starting in the 1950s. One of the first studies (Kanai & Tanaka, 1961) was based on the assumption that microtremors consisted mainly of vertically-incident S-waves. The spectrum of the wave field prior to modification by site effects was assumed to be flat (i.e. white noise) and hence any deviation was interpreted as representing only the site response.

Subsequent investigations (eg. Toksoz & Lacoss, 1968) have shown that microtremors consist of a number of different wave-types and have characteristics that can vary with frequency and time. Long-term noise observations (eg. Seo *et al.*, 1996; Nakajima *et al.,* 2000) have clarified some of the key characteristics of ambient ground noise.

At short frequencies (below about 0.5 Hz), microtremors are thought to originate predominantly from distant oceanographic disturbances. Spectral amplitudes are generally very stable over

periods of several hours. Variations have been seen to correlate with large- scale meteorological changes which affect the oceans.

At intermediate frequencies (0.5 to 1 Hz), microtremors are mainly generated by nearby sea waves and by the wind. Spectral amplitudes can therefore vary significantly with time (typically by a factor of 1.5 to 2 during the course of a day).

Above about 1 Hz, microtremors are mainly anthropogenic (generated by human activity). Nearby sources dominate the noise wave-field. Spectral amplitudes vary according to human activity. In urban areas, daytime values can exceed night-time values by a factor of 3 to 4.

In the literature, a distinction is often made between long-period *microseisms* (T > 1 s), chiefly of natural origin and short-period *microtremors* (T < 1 s), which are mainly artificially generated.

Figure 4.6 shows Fourier spectra of acceleration for noise measurements at soil sites in and around Düzce, Turkey.

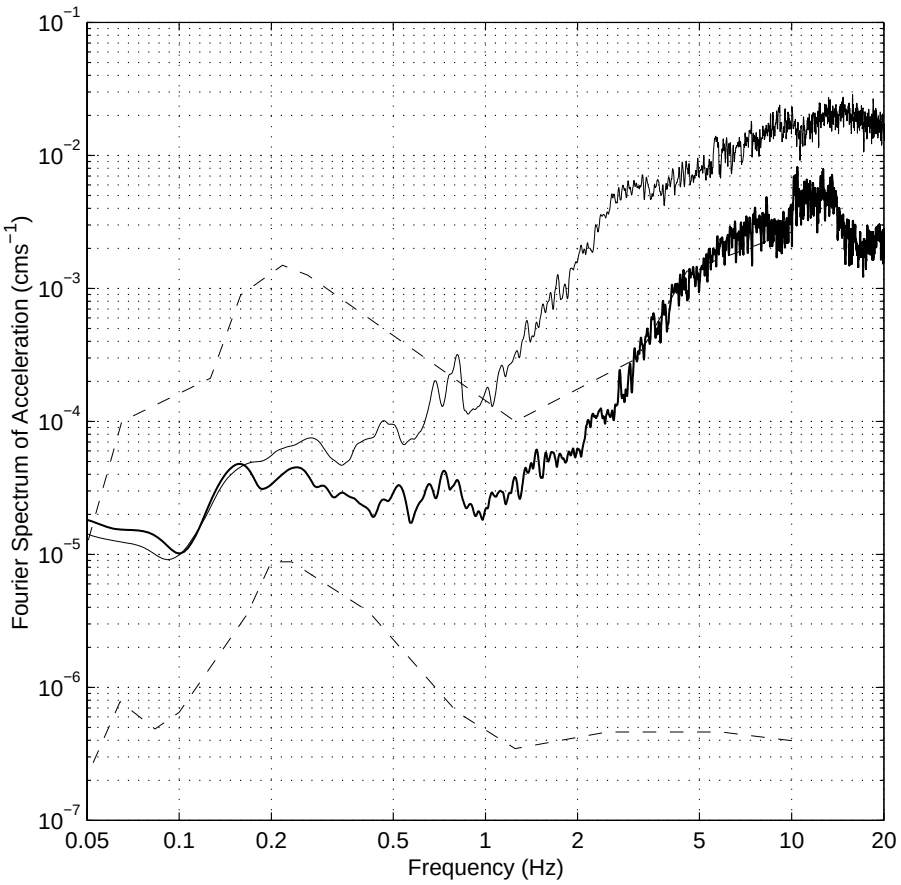

Figure 4.6 Comparison of Fourier spectra of acceleration for microtremor records. Thick solid line - quiet rural site, thin solid line – urban site. Measurements were made in and around Düzce, Turkey during daytime as part of field-work described in Chapter 8. Instrument used is a Guralp CMG-3ESP broadband seismometer (flat response from 0.0333 to 50 Hz). Spectra are for vertical motions, calculated using the procedure explained in Chapter 7. Spectra are not smoothed in order to preserve long-period amplitudes. Dotted lines are the high and low noise models (HNM & LNM) of Peterson (1993).

Spectra are compared for an urban and a rural site, both measured during day time. Below about 0.2 Hz, the spectra are very similar, even though the measurements are separated in time by about

2½ hours and in space by about 5 km. This illustrates the stability of long-period microtremors. Above 0.2 Hz, higher amplitudes for the urban site are due partly to different soil conditions and partly to increased anthropogenic noise. The dotted lines in Figure 4.6 show the high and low noise models derived by Peterson (1993). These are generalised spectra of Earth noise for hypothetical quiet and noisy station sites. The spectra are based on seismic data from 75 stations around the world and update earlier models such as Brune & Oliver (1957). The curves show characteristic peaks at around 0.07 Hz and 0.20 Hz. The first peak is believed to be caused by the action of ocean waves along the coastline and the second larger peak has been ascribed to pressure caused by standing ocean waves (Trifunac & Todorovska, 2000). These features are visible in the Turkey data. The spectrum at the quieter rural site is seen to follow the general form of the noise models quite closely.

The relative contributions from different wave types in any given microtremor record are generally not known. In order to quantify the relative proportions of Love, Rayleigh, P and S waves, dense array measurements are needed from sites covering a range of geological conditions. Bard (1998, 2001) identifies the systematic investigation of this issue as one of the most urgent needs in microtremor (and indeed strong-motion) research at this time.

4.3.1 Absolute spectra

On their own, absolute Fourier spectra of microtremor records are of limited use in the estimation of site response. As has been explained, amplitudes are often dominated by source and path effects; site effects are not easily decoupled from the ground motion. In their study of the response of deposits in Imperial Valley, California, Udwadia & Trifunac (1973) concluded that microtremor measurements for the El Centro area gave details of the exciting function rather than the transfer function of the ground.

Bard (1998), in a review of more recent studies, suggests that absolute Fourier spectra can reflect site response if one or both of the following are true:

a) Impedance contrast between soil and bedrock at depth is high. This leads to trapping of surface and/or body waves giving rise to a conspicuous spectral peak at the resonant frequency.

b) Soil layers are very deep, giving rise to a low fundamental frequency. Long-period microseisms are relatively stable in time due to their natural origin.

In Mexico City, Lermo *et al.* (1988) were able to identify the soil fundamental frequency from Fourier spectra of microtremor records due to the presence of very soft soil. The same is true for studies carried out by Field *et al.* (1990) and Shinoara *et al.* (1996) for sites in New York and Kushiro City, Japan respectively.

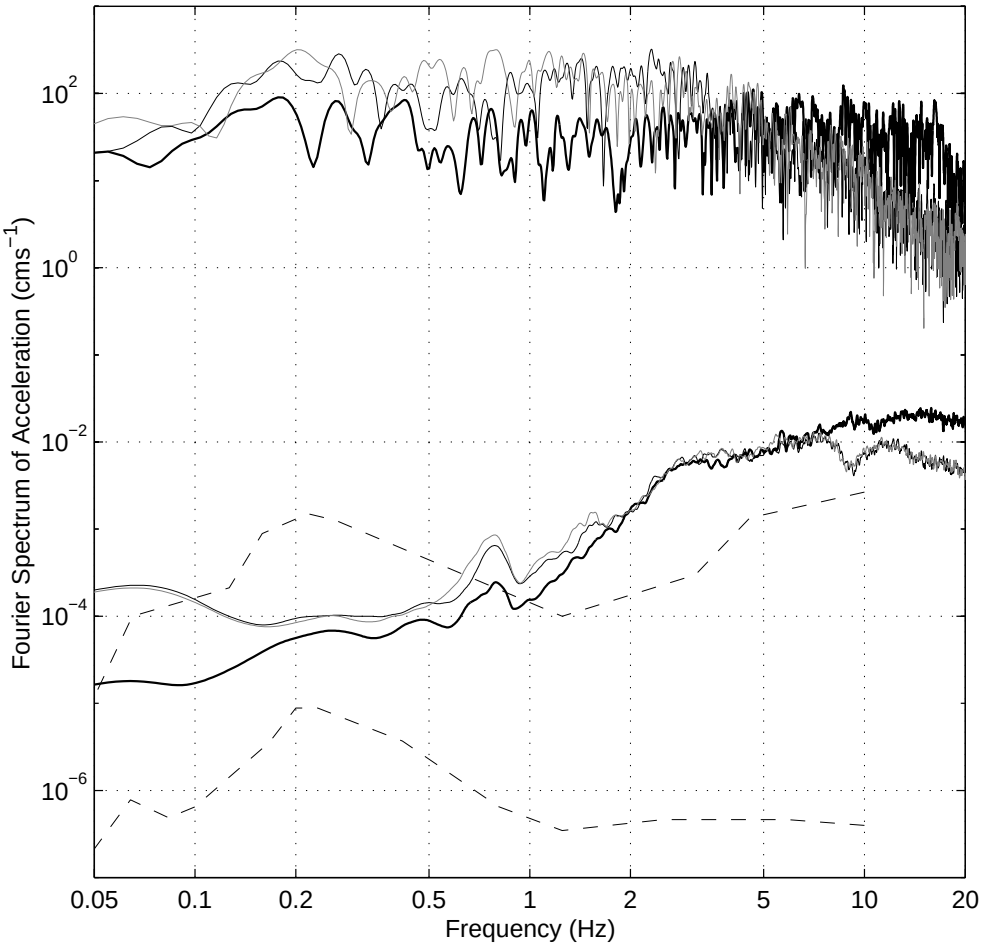

Figure 4.7 Comparison of Fourier spectra of acceleration for microtremor and earthquake records recorded at the same location. Thick black line - vertical component; thin black line – E-W component; thin grey line – N-S component. Measurements were made at Düzce strong-motion station (DZC). Earthquake shown is the M_s 7.3 Duzce event of 12/11/1999 (epicentral distance, d_e = 9 km). Data are unfiltered. Microtremor data were recorded during fieldwork in summer 2001. Processing details are explained in Chapter 7. Spectra are not smoothed in order to preserve long-period amplitudes. Dotted lines are the high and low noise models (HNM & LNM) of Peterson (1993).

In Figure 4.7, Fourier spectra of microtremor measurements taken at the strong-motion station in Duzce, Turkey are compared with Fourier spectra of strong-motion data from the same site. A systematic comparison between strong-motion data and noise data in and around Düzce is reserved for Chapter 7. However, this figure does illustrate how the fundamental resonant frequency of a site (at around 0.7 Hz) can be identified from absolute Fourier spectra of noise. Peaks in strong-motion spectra are often less distinct, especially in the case of a near-field record. However, the 0.7 Hz peak is visible in the fault-normal (N-S) component.

4.3.2 Reference site method

Computing a point-by-point ratio of a ground-motion spectrum at a soil site of interest with respect to a spectrum obtained simultaneously at a reference site can, under specific conditions, yield a reasonable approximation of the site response function.

Assuming that the soil behaves linearly, Borcherdt (1970) showed that if the Fourier spectrum as a function of frequency, *f*, at a given site, *O(f)* is represented as the convolution of the source function *E(f)*, the path function *P(f)*, the site function *S(f)* and the instrument response function, *I(f)* (Equation. 4.10), the ratio of the absolute value of the Fourier spectrum of a seismogram recorded at a soil site ($O_s(f)$) to that recorded from the same source at a nearby reference station ($O_r(f)$) reduces to the expression given in Equation (4.11).

$$O(f) = E(f) * P(f) * S(f) * I(f) \tag{4.10}$$

$$\frac{|O_s(f)|}{|O_r(f)|} = \frac{|S_s(f)|}{|S_r(f)|} \tag{4.11}$$

Using records from distant nuclear explosions, Borcherdt (1970) obtained site response functions at various locations in the San Francisco Bay area based on Equation (4.11). Path effects could be considered constant for all sites in the study area because the distance between any reference site-soil site pair was considerably less than the distance between the seismic source and the study area. In addition, the direction of wave arrival (azimuth) was almost identical for all sites.

Numerous studies have been performed to find site response functions from earthquake data using the reference-site approach (eg. Darragh & Shakal, 1991; Atakan & Figueroa, 1993). Steidl *et al.* (1996) stress the importance of not only finding soil-reference-site pairs with similar path functions for the records being analysed, but also ensuring that the reference site itself does not have a marked characteristic response that would lead to underestimation of spectral ratios for certain frequency bands. They find that near-surface weathering and cracking of bedrock can affect recorded ground motions at frequencies of engineering interest, even at sites apparently located on competent crystalline rock.

The use of the reference-site approach with microtremor data also depends on the ability to separate source, path and site effects. In a review of some of the many investigations carried out using this approach, Bard (1998) finds some favourable and some less favourable results.

The favourable results tend to come from investigations in which the soil-site-to-reference-site distance is small and/or the emphasis is on spectral ratios at long periods, where path effects are likely to be similar between pairs of nearby sites because of the distant origin of long-period microseisms.

Bard (1998) recognizes the validity of the microtremor reference-site technique for both qualitative and quantitative estimation of site transfer functions (eg. Gaull *et al.*, 1995). However, he stresses the importance of great care in both measurement and processing of the data and gives some basic procedural guidelines:

a) Select at the very least one site for continuous measurement for the whole duration of the survey in order to check time variations of noise characteristics.

b) Ensure soil-site-to-reference-site distance is suitable for the frequency band of interest. For frequencies greater than 1 Hz, this should not exceed 500 m.

c) Select a few sites for which earthquake data are available to allow comparison between noise and strong-motion spectral ratios.

Having a minimum inter-station distance clearly limits the use of the method to those soil sites which are adjacent to outcrop exposures, although some researchers have made use of temporary non-rock reference sites to try to overcome this limitation.

4.3.3 Single-station HVSR

Although commonly referred to as the "Nakamura technique", the single-station HVSR method using microtremor observations was first introduced by Nogoshi and Igarashi in the early 1970s (Nogoshi & Igarashi, 1971). It was subsequently popularized by Nakamura (1989) and has since been used extensively for the mapping of site effects. The widespread use of the technique is due to its ability to estimate site effects without the need for a simultaneous reference-site measurement. The HVSR (ratio of horizontal to vertical Fourier amplitude spectra) has been shown to be effective for the estimation of fundamental frequency and even spectral amplification factors in a range of geological environments. In spite of its popularity, a satisfactory theoretical explanation has yet to be agreed upon in the scientific community. In-depth literature reviews on the microtremor HVSR technique have been carried out by Kudo (1995) for the period 1990 – 1995 and Bard (1998) for the period 1995 – 1998. A summary of the two popular interpretations of the method is given below, adapted from Bard (1998).

4.3.3.1 Surface wave interpretation

Nogoshi and Igarashi (1971) originally explained the technique by assuming that the incident noise wave-field was predominantly made up of Rayleigh waves. Many authors, (eg. Lachet & Bard, 1994; Konno & Ohmachi, 1998; Bard 1998) have since investigated the validity of this assumption, through both field measurements and numerical simulation and support the original interpretation.

The ellipticity of Rayleigh waves is frequency-dependent, as illustrated in Figure 4.8. In the fundamental mode, the ellipticity has a sharp peak which corresponds closely with the fundamental site frequency, f_0, at sites with a high enough impedance contrast between the surface layers and deeper layers. This peak is the result of a vanishing of the vertical component of motion as the sense of particle orbit changes from retrograde (opposite to the direction of wave propagation) at low frequencies to prograde at intermediate frequencies. This is a feature of Rayleigh waves not only for simple 1-D structures, as illustrated in Figure 4.8, but has also been confirmed for more complex, multi-layered soil profiles (Konno & Ohmachi, 1998).

The presence of Love waves in the wave-field does not interfere with the location of the Rayleigh-wave ellipticity peak as Love waves have no vertical component. The presence of a significant proportion of body waves, however, causes the Rayleigh wave explanation to break down as P and SV waves do affect the vertical component of motion.

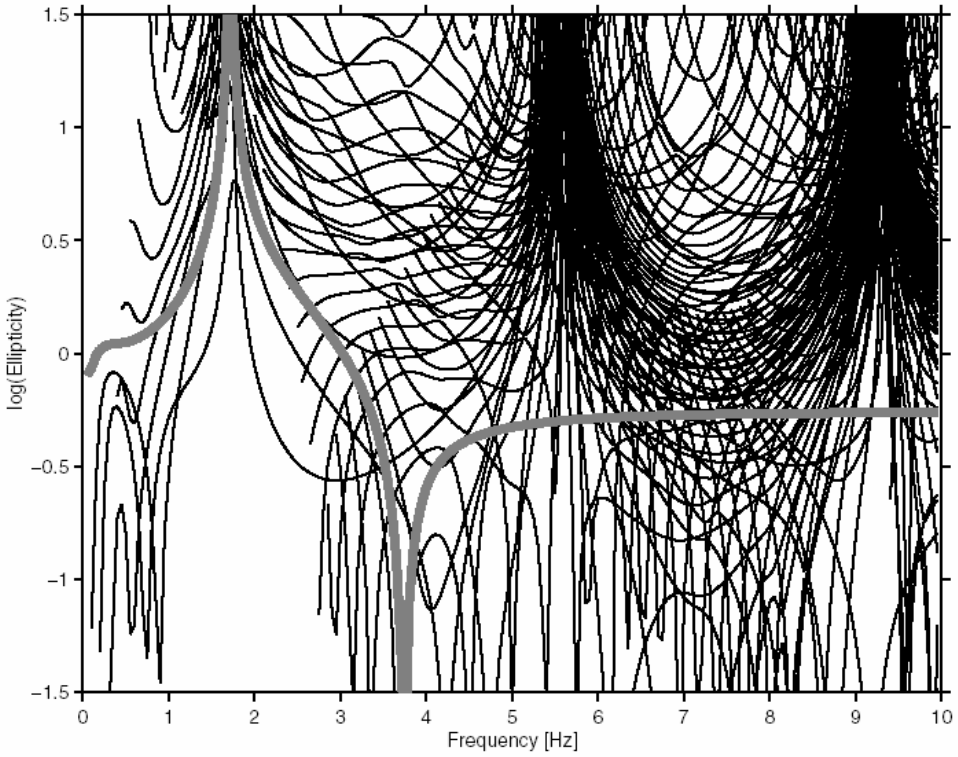

Figure 4.8 Ellipticity of the fundamental mode Rayleigh wave (thick grey line) and its higher modes (thin black lines) for a single layered soil profile with v_s = 222 m.s^{-1} and a thickness of 30 m (Fah *et al.*, 2001). f_0 for this profile coincides with the fundamental mode Rayleigh wave peak (between 1.7 and 1.85 Hz).

Various researchers have suggested impedance contrast thresholds, below which Rayleigh wave ellipticity peaks are not expected to be conspicuous. Nogoshi & Igarashi (1971) suggest a value between 2.5 and 3; Konno & Ohmachi (1998) give a value of 2.5. Bard recommends using a threshold of around 3.

Assuming the validity of the surface wave interpretation, Konno & Ohmachi (1998) point out that, even if a measured HVSR does not have a conspicuous peak (for example, in the presence of low impedance contrast soils), an estimation of f_0 may still be possible from the location of a conspicuous trough. This is the result of the vanishing of the horizontal component of motion as the Rayleigh wave particle orbit changes from prograde at intermediate frequencies back to retrograde at higher frequencies. For many soil profiles, this trough will occur at very close to twice the frequency of the peak, as illustrated in Figure 4.8.

A surface-wave interpretation gives a compelling explanation for the existence of an HVSR peak at the fundamental frequency of a site. However, it does not so readily explain how the amplitude of this peak might relate to the S-wave amplification. For impedance contrasts above a certain value,

the amplitude of the HVSR peak for fundamental-mode Rayleigh waves becomes infinite. However, Konno & Ohmachi (1998) suggest that this difficulty can be overcome by applying a specially-developed smoothing function to the horizontal and vertical spectra prior to calculation of the HVSR. The resulting HVSR peaks for a number of soil profiles are shown to correlate reasonably well with the S-wave amplification at f_o. However, as pointed out by Bard (1998), the peak values, denoted R_B, depend significantly on both the selected smoothing parameter and the Poisson ratio. Once an appropriately smoothed ellipticity curve has been obtained, there is a further complication: in order to relate R_B to an HVSR peak measured in the field, the relative proportions of Rayleigh and Love waves present must be taken into account. Konno & Ohmachi (1998) propose a simple multiplication factor based on the assumption that Love waves account for 60% of the wave-field whilst Rayleigh waves account for 40%. Bard (1998) stresses the need for further justification of this method and particularly for verification of whether the proportion of Rayleigh and Love waves is frequency-dependent or not.

4.3.3.2 Body wave interpretation

An alternative interpretation is the one advocated by Nakamura, based on the assumption that surface waves can be neglected, leading to a direct relationship between the HVSR and the S-wave transfer function. In fact, Nakamura terms the HVSR, the "Quasi-Transfer Spectrum" (QTS). Nakamura modified his initial explanation (Nakamura, 1989) as a result of criticisms concerning his assumptions. The summary given here is based on this modified explanation (Nakamura, 1996) and uses the notation of Bard (1998).

The noise wave-field is separated into body wave and surface wave components (denoted by subscripts *b* and *s* respectively):

$$S^{NH}(f) = S_b^H(f) + S_s^H(f) = H_T(f).R_b^H(f) + S_s^H(f) \tag{4.12}$$

$$S^{NV}(f) = S_b^V(f) + S_s^V(f) = V_T(f).R_b^V(f) + S_s^V(f) \tag{4.13}$$

where: $S^{NH}(f)$ and $S^{NV}(f)$ are Fourier spectra of noise for the horizontal and vertical components respectively,

$H_T(f)$ and $V^T(f)$ are the true, frequency-dependent site amplification functions for the horizontal and vertical components respectively,

$R_b^H(f)$ and $R_b^V(f)$ are horizontal and vertical spectra of the body wave portion of noise at a rock reference site.

The HVSR, denoted $A^{NHV}(f)$, is simply the ratio of Equation (4.12) to Equation (4.13). By introducing three more definitions (Equations 4.14 – 4.16), $A^{NHV}(f)$ can be written as Equation (4.17):

$$A_r^{NHV}(f) = \frac{R_b^H(f)}{R_b^V(f)} \tag{4.14}$$

$$\beta(f) = \frac{S_s^V(f)}{R_b^V(f)} \tag{4.15}$$

$$A_s(f) = \frac{S_s^H(f)}{S_s^V(f)} \tag{4.16}$$

$$A^{NHV}(f) = \frac{H_T(f).A_r^{NHV}(f) + \beta(f).A_s(f)}{V_T(f) + \beta(f)} \tag{4.17}$$

where: $A_r^{NHV}(f)$ is the HVSR of noise at a rock site,

$\beta(f)$ is the relative proportion of surface to body waves (measured on the vertical component),

$A_s(f)$ is the HVSR due only to surface waves.

Nakamura's assertion is that at the fundamental resonant frequency in the horizontal direction, f_{H0}, Equation (4.17) can be simplified to the following form:

$$A^{NHV}(f_{H0}) = H_T(f_{H0}) \tag{4.18}$$

This however requires at least the following assumptions:

a) The vertical component is not amplified at f_{H0} : $V^T(f_{H0}) = 1$

b) The HVSR on rock is equal to 1 at f_{H0}: $A_r^{NHV}(f_{H0}) = 1$

c) $\beta(f_{H0}) << 1$

d) $\beta(f_{H0}).A_s(f_{H0}) << 1$

Bard (1998) suggests that the first two assumptions are reasonable without qualification. Assumption (c) is reasonable for high-impedance contrast soil profiles because $S_s^V(f)$ in Equation (4.15) vanishes around f_{H0}, as explained in Section 4.3.3.1. However, Bard (1998) questions the validity of assumption (d) because the quantity $A_s(f_{H0})$ has been shown to be very large. In any case, the product $\beta(f_{H0}).A_s(f_{H0})$, from Equations (4.15) and (4.16) is actually equivalent to the ratio of horizontal amplitude of surface waves to the vertical amplitude of body waves on rock. There is no obvious reason why this should be small compared with the S-wave amplification.

Some studies have extended the assertion of Equation (4.18) to all frequencies, requiring that all four assumptions be valid at all frequencies. For this more general case, Bard (1998) does not

accept assumptions (c) and (d), based simply on the appearance of Rayleigh wave ellipticity curves (eg. Figure 4.3). He also questions the validity of assumptions (a) and (b).

In a recent paper, Nakamura (2000) maintained his original idea that the HVSRs in the peak frequency range are not affected by the fundamental-mode Rayleigh wave, allowing a direct comparison with the S-wave transfer function. However, a subsequent study by Fah *et al.* (2001) contradicted Nakamura's conclusion and indeed added more weight to the surface wave interpretation supported by Bard (1998). It is the current author's belief that the surface wave interpretation has a stronger theoretical basis than the body wave interpretation.

The inadequacy of using solely peak ground acceleration (PGA) as a strong-motion parameter for seismic design has been recognised for some time (McGuire, 1978). In the area of lifeline earthquake engineering, as has been shown in Chapter 3, the behaviour of buried pipelines is controlled by the ground strain, which is closely related to peak ground velocity (PGV). Peak ground displacement (PGD) is of particular importance for structures with multiple supports such as above-ground pipelines and bridges, or other large-scale structures with long-period response (Gregor, 1995). Different parameters are therefore appropriate for different types of structure. The three ground-motion parameters together can also be used to define the elastic response spectrum (Bommer *et al.*, 2000). The unified derivation of predictive relationships for PGA, PGV and PGD is therefore desirable.

In this chapter, attenuation relationships are derived for horizontal PGA, PGV and PGD by regression analysis of European strong-motion data. The database is based on that used by Bommer *et al.* (1998) to derive attenuation relationships for ordinates of spectral displacement, but is updated to include recent significant crustal earthquakes. The full data set consists of 249 strong-motion records obtained from 51 European earthquakes with surface-wave magnitudes between 5.5 and 7.9. These newly-derived equations are presented in Section 5.2.

There is an abundance of relationships for PGA and spectral acceleration (SA) in the published literature, but relatively few for PGV and PGD. Douglas (2001a) has compiled a comprehensive worldwide summary of attenuation relationships for PGA and SA. In Section 5.1, a review is made of significant attenuation relationships for PGV and PGD.

Peak values of ground motion can be significantly affected by the strong-motion processing method used. This is particularly true of PGV and PGD. As such, section 5.3 explores the effects of filtering and correction methods on the strong-motion parameters.

5.1 Review of predictive relationships for PGV and PGD

Following the comprehensive summary by Douglas (2001a) of predictive relationships for PGA, a search was conducted to find previously derived predictive equations for PGV and PGD. Important characteristics of these equations are summarised in Table 5.1. The functional form, regression coefficients, details of site characterisation and other pertinent information for each predictive equation are given in Appendix E. Relationships for PGA are only included where they have been derived for the same study as the relationships for PGV and (in some cases) PGD.

Information has been compiled from 13 studies in all. In seven of these, all three peak ground-motion parameters are derived together, as in the current study. Four of the studies entail joint derivation of PGA and PGV. One study, that of Gregor & Bolt (1997), following on from an

earlier investigation (Gregor, 1995), concentrated solely on the derivation of predictive relationships for PGD.

5.1.1 Applicability of relationships

Table 5.1 gives various information indicating the applicability of each relationship. The applicability of a given relationship depends chiefly on the range of data in terms of magnitude and distance. The table gives minimum and maximum values of magnitude and distance but no indication of the distribution of the dataset within magnitude-distance space.

As stated by Ambraseys *et al.* (1997), individual tectonic regions should ideally have their own predictive relationships for strong-motion parameters, although this is limited by data availability. Different tectonic environments might be expected to exhibit different attenuation characteristics because of the prevailing geological conditions and the predominance of a particular earthquake mechanism and/or range of focal depths. However, in their comparison of attenuation relationships for PGA for use in Europe, Ambraseys & Bommer (1995) point out that differences between selected relationships for Europe (Ambraseys, 1995) and western North America (Joyner & Boore, 1988) are less than the scatter in either relationship. Greater differences might be evident in comparison with relationships from other regions, such as Japan. However, it remains to be seen how much regional attenuation characteristics can be distinguished when comparing predictive relationships whose form is strongly dependent on other factors such as the regression model employed.

The geographical coverage of each study is indicated in Table 5.1, although it should be pointed out that regionalisations based on political boundaries are artificial and are more likely due to data availability rather than any seismological considerations. Six of the 13 studies were based solely on data from North America. Two of the studies concentrated on Japanese data. The Campbell (1997) data included records from around the world although for both PGA and PGV, data from regions other than N. America amounted to only 5% of the total dataset. The only studies that have used a significant proportion of European records are Sabetta & Pugliese (1987), Theodulidis & Papazachos (1992), Rinaldis *et al.* (1998) and Bommer *et al.* (2000), and of these, only two include relationships for PGD. Of all of the studies with a European focus, the study by Bommer *et al.* (2000) uses the largest (183 records) and most evenly distributed dataset (in magnitude-distance space). Geographical restrictions on datasets in the other studies have unnecessarily limited the numbers of records used for analysis. Sabetta & Pugliese (1987) use only Italian records (95) whilst Theodulidis & Papazachos (1992) use mainly Greek records (105), supplemented with selected records (16) from Japanese and Alaskan earthquakes to extend the upper magnitude limit from M_s 7.0 to 7.5. Rinaldis *et al.* (1998) use a combination of Greek and Italian records for their attenuation relationship (a total of 137 records).

Table 5.1 Summary of predictive equations for PGV and PGD (including PGA where it has been derived in the same study). See following page for notes and explanation.

Study	Appendix E Reference	Geographical coverage	Dependent variable(s) defined			No. of records, earthquakes	M_{min}, M_{max}	M scale	d_{min},d_{max} (km)	d	Site class	Comp	Other predictor variable
McGuire (1974)[1]	**E1**	W. USA	U	U	PGD	U	U	U	U	U	U	U	-
Trifunac (1976), Trifunac & Brady (1976)[2]	**E2**	W. USA	PGA*	PGV*	PGD*	181, 57	3.8, 7.7	Mostly M_L	6, 400	d_e	3	B	-
McGuire (1978)[3]	**E3**	W. USA	PGA	PGV	PGD	70, 17+	4.5, 7.7	M_s, M_L, m_b	11, 210	d_h	2	B	-
Joyner & Boore (1981)[4]	**E4**	W.N.America	PGA	PGV	-	182, 23	5.0, 7.7	M_w (M_L)	0.5, 370	d_f	2	L	-
Kawashima *et al.* (1986)[5]	**E5**	Japan	PGA	PGV	PGD	197, 90	5.0, 7.9	M_{JMA}	5, 550	d_e	3	R	-
Sabetta & Pugliese (1987)[6]	**E6**	Italy	PGA	PGV	-	95, 17	4.6, 6.8	M_s, M_L	1.5, 180	d_f, d_e	2	L	-
Kamiyama *et al.* (1992)[7]	**E7**	Japan	PGA	PGV	PGD	357, 82	4.1, 7.9	M_{JMA}	3.4, 413	d_h	C, I	B	-
Theodulidis & Papazachos (1992)[8]	**E8**	Greece	PGA	PGV	PGD	105, 36 (16, 4)	4.5, 7.0 (7.2, 7.5)	M_s	1, 128 (48, 236)	d_e	2	B	-
Gregor & Bolt (1997)[9]	**E9**	California	-	-	PGD*	338, 12	5.4, 7.2	M_w	6, 224	d_s	2	S	Fault mechanism
Campbell (1997)[10]	**E10**	World-wide	PGA*	PGV*	-	645, 47 (225, 26)	4.7, 8.0 (4.7, 8.1)	M_w	3, 60 (3, 60)	d_{seis}	3	G	Fault mechanism
Rinaldis *et al.* (1998)[11]	**E11**	Italy, Greece	PGA	PGV	-	137, 24	4.5, 7.0	M_s or M_w	7, 138	d_e	2	U	Fault mechanism
Sadigh & Egan (1998)[12]	**E12**	California	PGA	PGV	PGD	960, 119 (4, 2)	3.8, 7.4	M_w	0.1, 305	d_r	2	G	Fault mechanism
Bommer *et al.* (2000)[13]	**see 5.2**	Europe	PGA	PGV	PGD	183, 43	5.5, 7.9	M_s	3, 260	d_f	3	L	-
This study	**see 5.2**	Europe	PGA	PGV	PGD	249, 51	5.5, 7.9	M_s	1, 359	d_f	3	L	-

Notes to accompany Table 5.1

U in any column indicates "Unknown"

Dependent variable(s) defined: Horizontal components of motion only unless parameter is asterisked, in which case, expressions are also derived for vertical motion

M scale: Magnitude scale used:
m_b Body-wave magnitude
M_{JMA} Japanese Meteorological Agency magnitude
M_L Local magnitude
M_s Surface-wave magnitude
M_w Moment magnitude

d: Source-to-site distance definition used:
d_e epicentral distance
d_f distance to closest point on surface projection of fault
d_h hypocentral distance
d_r distance to closest point on rupture plane
d_s distance to location on fault plane of largest slip
d_{seis} distance to closest point on seismogenic rupture plane (assuming fault rupture within the upper 2 to 4km of the fault zone is primarily non-seismogenic)

Site class: Number or type of site classification scheme used:
C Continuous classification
I Individual classification for each site

Comp: Use of the two horizontal components of each accelerogram:
B Both components
G Geometric mean
L Larger component
R Resolved component (i.e. the maximum resolved value over all possible azimuths)
S Single horizontal component of motion resolved perpendicularly to a line connecting the site to the location of largest slip on the fault plane

Additional notes for references in the Table (see 1st column):
1 The study may have included PGA and PGV but information was unavailable
2 *d*-range only stated as valid for $d \geq 20$ km.
See Table E2 for more details on magnitude ranges for each individual peak parameter
3 Idriss (1978) reports that magnitudes used are a mixture of M_L, m_b and M_s
d-range only stated as valid for $d \geq 200$ km.
4 In the few cases where M_w was not available, M_L was used
6 Magnitude taken as M_s when both M_s and $M_L \geq 5.5$; M_L otherwise
7 Continuous site classification based on SPT N-value profile only given for PGV since the focus of the study was on PGV. Site classification for PGA and PGD was on a site-by-site basis.
8 Due to the lack of strong-motion data from large shallow earthquakes in Greece, selected records were added from Japanese and Alaskan earthquakes (statistics given in brackets)
9 Separate equations have been derived for different combinations of site category, component orientation and fault mechanism. Different magnitude and distance ranges are relevant for each equation, as summarised in Table E12.
10 Figures in the table refer to the dataset used for PGA equations. Figures in brackets refer to the dataset used for equations for vertical motion. Numbers of records and earthquakes in the PGV dataset are 226,30 (173,22); *M*-range for the PGV dataset is 4.7 - 8.1 (4.7 - 8.1). PGV equation uses M_L for M_s<6 and M_s for $M_s \geq 6$. *d*-range for the PGV dataset is 3.0 - 30.0 km for $M < 6.25$ and 3.0 - 50.0 km for $M_s \geq 6.25$ (for both vertical and horizontal motion).
12 Dataset includes records from 2 foreign earthquakes to improve representation from large magnitude events. Data in brackets refer to foreign records. Equations stated to be useful for the distance range 1-100km. For smaller earthquakes, d_h is used due to poorly defined fault rupture plane. Dataset statistics are for PGA. PGV and PGD datasets are smaller, but unspecified.
13 relationship for PGA is quoted from Ambraseys *et al.* (1996) who use the same regression method but a larger dataset. d_e was used for some smaller events for which the fault-plane was poorly-defined.

5.1.2 Site classification

There is no common definition of site classification among the different studies, reflecting the lack of consensus that exists in the engineering community regarding the effects of near-surface foundation materials on strong ground-motion. The various site classification schemes used in the studies in Table 5.1 are explained in more detail in Appendix E. Most of the relationships distinguish between either two or three different site classes. Rock and soil sites are usually in different classes. Soil sites are then sometimes subdivided into two distinct categories (eg. 'deep soil' and 'shallow soil' or 'soft soil' and 'stiff soil'). In the Sabetta & Pugliese (1987) relationships, the site classification schemes for PGA and PGV are different. For PGA, 'stiff' and 'deep' soil sites showed similar amplification and were grouped together to form a single category, whereas for PGV, 'deep' soil and 'shallow' soil sites showed similar amplification characteristics and so were grouped together.

5.1.3 Use of components

There are various ways to make use of the two horizontal components of ground motion in deriving a predictive relationship. The relationships in Table 5.1 use a total of five different approaches, all explained in the accompanying notes.

The choice of method can have a significant effect on the predicted values of strong-motion peaks. Kawashima *et al.* (1986) use the maximum resolved peak values over all possible azimuths of the horizontal components of motion for their relationships for PGA, PGV and PGD. However, in a previous study (Kawashima *et al.* 1983) they show that this gives peak values around 8% greater than selecting the larger of the two orthogonal horizontal components.

In order to investigate the effect of different uses of the two horizontal components on the predicted values of strong motion, Douglas (2001b) derived seven separate attenuation relationships for PGA from the same set of 180 near-field records, each regression being based on a different use of the horizontal components. For each separate equation, PGA was calculated for all records represented in the dataset. The effect of the use of horizontal components was then quantified by comparing predicted PGAs for each pair of relationships, noting the maximum and minimum ratios in each case. For any given pair of relationships, the ratios are stable for the magnitude and distance ranges considered. Systematic differences in PGAs between the various methods are summarised in Table 5.2. Ratios are given with respect to PGA_L, which is from the relationship that uses the larger of the two horizontal components of motion, as used in the current study. It can be seen that use of the larger component is conservative when compared to most other approaches. It is only the 'resolved'

and 'vectorial' methods which give systematically greater values of PGA (by about 21% and 7% respectively).

Table 5.2 Comparison of values of PGA obtained using different methods for selecting/combining the two components of horizontal motion (modified from Douglas, 2001b). In each case, the numerator is PGV_L, the largest of the two horizontal components of motion. 'Vectorially' resolved means the square root of the sum of the squares of the two components

Ratio	PGA_L/PGA_V	PGA_L/PGA_R	PGA_L/PGA_C	PGA_L/PGA_A	PGA_L/PGA_G	PGA_L/PGA_B
Meaning of denominator subscript	Vectorial	Resolved	Randomly selected	Arithmetic mean	Geometric mean	Both
minimum value	0.78	0.93	1.10	1.12	1.13	1.13
maximum value	0.80	0.94	1.24	1.15	1.18	1.18

5.1.4 Comparison of predictive relationships

Direct comparison between the predictive relationships summarised in Appendix E is complicated by differences in parameterisation. Some of the key differences are listed below:

- Most of the equations use different combinations of five different magnitude scales and six different source-to-site distance measures.
- Site classification schemes are different in most of the studies.
- There are a total of five different ways of using the two horizontal components of motion to obtain the dependent variables.
- Some of the studies make a distinction between different fault mechanisms and one of the studies (Sadigh & Egan, 1998), due to a particularly large dataset, has separate equations for different magnitude ranges.

Table 5.3 Additional studies not included in the current review

Study	Features of study	Reason for exclusion
Boore *et al.* (1980)	Simple expressions derived for PGA, PGV and PGD as a function of source-to-site distance. 25 records from Californian earthquakes divided into two separate magnitude categories ($5.3<M_L<5.7$ and $M_L = 6.4$)	Dataset too small
Wang & Li (1986)	Expressions for PGA, PGV and PGD based on 133 records from China and other (unspecified) countries. Site classification scheme according to predominant period	Study only available in Chinese
Lee *et al.* (1995)	Expressions for PGA, PGV and PGD based on a large dataset of records from the US. Strong-motion parameters are given in terms of M, d, fault-length, type of propagation path (P), fraction of epicentral distance travelled through basement rocks (r) and site conditions	Path-dependent parameters P and r are not generally available for regions outside of the USA. Furthermore, they cannot be realistically assessed for future earthquakes, restricting the use of the relationships for predictive purposes

A detailed comparison of all the relationships is beyond the scope of the current study. However, comparisons are later made between the predictive relationships derived for the current study and a selection of the relationships summarised above.

Three other investigations were found in which relationships were derived for PGA, PGV and PGD. However, they are not included in the current study for reasons outlined in Table 5.3.

5.2 Development of new predictive relationships for PGA, PGV and PGD

In this section, new predictive relationships are derived for PGA, PGV and PGD. The dataset, regression method, results and inspection of regression residuals are presented in separate sub-sections.

5.2.1 Data

The original dataset of Bommer *et al.* (1998) consisted of 183 accelerograms generated by 43 shallow earthquakes from Europe and the immediate surrounding region. In the current study, an additional 69 accelerograms from 8 more recent earthquakes have been added. A full list of the supplementary records, together with station and earthquake parameters is given in Table F1, Appendix F. Two records were obtained from the M_s 5.6 Konitsa (Greece) earthquake of 5 August 1996. However, the recording site classifications were not available so they were not included in the analysis. Various sources were used for the data presented. The sources are summarised in Appendix F, Table F2.

The new records have been added subject to the same magnitude criterion as Bommer *et al.* (1998) in their derivation of predictive equations for spectral displacement *i.e.* only earthquakes with $M_s \geq 5.5$ are considered, in recognition of the fact that small earthquakes produce very little long-period radiation, making it particularly difficult to separate out long-period noise in the record processing. As will be shown in Section 5.3, the ability to distinguish between long-period noise and genuine signal is of particular importance for PGV and even more so for PGD.

The selection of M_s in the original dataset was due in part to the lack of M_L determinations for earthquakes in some parts of the study area (Algeria, Iran, Turkey and the former USSR). M_s on the other hand was available for all events in the database due to the large number of teleseismic data available for its assessment. In western North America, M_L is commonly used for earthquakes with magnitudes less than 6.0. However, the seismicity of Europe is generally evaluated in terms of M_s (Ambraseys *et al.* 1996). For the supplementary earthquakes, the ISESD (Ambraseys *et al,* 2002) determinations of M_s, focal depth and

epicentral co-ordinates have been used when available, verified against the values from various special studies. For events 44 and 45, ISC determinations have been used.

The source-to-site distance measure used in the current study is the shortest horizontal distance to the surface projection of the fault rupture (d_f), as defined by Joyner & Boore (1981). The use of epicentral distance, d_e for earthquakes of $M_s > 6.0$ is not realistic because for all but the most distant records, the earthquake source dimensions will be a significant proportion of (if not greater than) the source-to-station distance. Having said this, there are a few events in the original dataset for which d_f could not be evaluated because of a poorly-defined rupture surface; most of these earthquakes had $M_s < 6.0$.

Assessment of source-to-station distance requires accurate determination of the locations of both source and station. Station co-ordinates have been obtained from more than one source wherever possible and checked using a web-based mapping package [http://www.mapblast.com]. In some cases, significant errors in station co-ordinates have been found, often due to typographical errors in published data. Fault plane projections have been estimated for all of the new earthquakes in the database from published studies of aftershocks and source mechanisms. Distances have been calculated using a FORTRAN program, Flt_dis (Douglas, 2001b) which finds the co-ordinates of the surface projection of a fault from the dip angle and strike. In some cases (eg. for the Kocaeli and Duzce earthquakes), detailed information on surface fault rupture have allowed the identification of several distinct fault segments. Figure 5.1 shows surface projections for the various segments of the Kocaeli earthquake fault together with strong-motion recording stations in the immediate vicinity of the fault. Lines joining stations to the fault projection represent d_f. Source parameters used were from MCEER (2000) and are summarised in Table 7.2. Each fault segment was assumed to have the same dip angle and width.

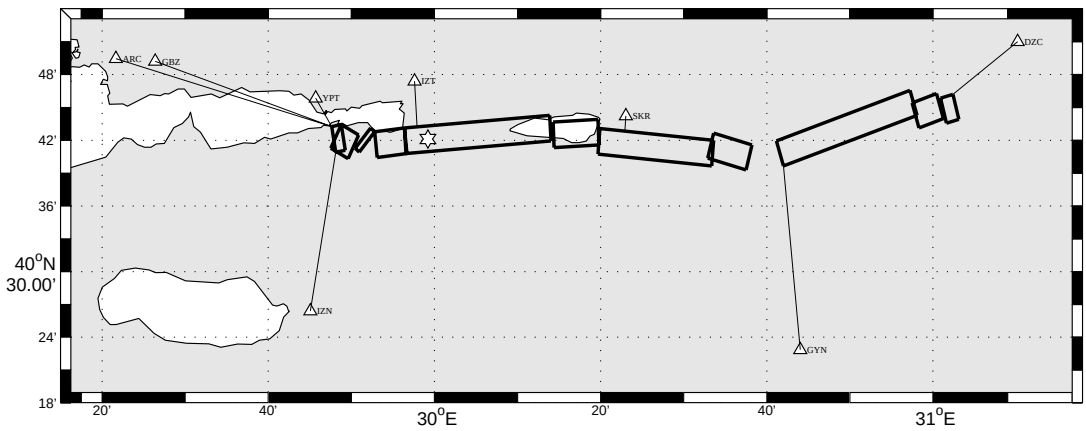

Figure 5.1 Surface projection of segments of fault rupturing during the 17/08/1999 Kocaeli earthquake. Triangles represent strong-motion recording stations. The epicentre is shown as a star.

The recording site geology is classified according to the average shear-wave velocity, v_{s30} over the upper 30m. For $v_{s30} \leq 360$ m/s, sites are classified as soft soil (S); for $v_{s30} \geq 750$ m/s, sites are classified as rock (R); for v_{s30} in between these levels, sites are classified as stiff soil (A). For stations lacking explicit information on v_{s30}, agency classifications have been used. For the 1999 Athens earthquake, site conditions were defined from qualitative descriptions given in Papadopoulos *et al.* (2000) and Psycharis *et al.* (1999) and the classification system of Wills & Silva (1998). For stations lacking site classifications, records were excluded from the analysis, reducing the supplementary data from 90 records down to 69. Three records from the original dataset also had to be excluded for this reason.

The distribution of records in magnitude-distance space is shown in Figure 5.2. The new data has contributed significantly to the large-magnitude region and for the whole range of distances; representation from near-field records has been improved. The magnitude and distance ranges are $5.5 \leq M_s \leq 7.9$ and $1 \leq d \leq 359$ km respectively. The full dataset consists of 249 records, distributed amongst the three site categories R, A and S in the ratio 25:50:25. This is almost identical to the distribution of the original dataset, which is 25:51:24. The distribution in magnitude-distance space of records in each site category is shown in Figure 5.3. The distributions are similar for categories A and S. However, there are few category R records for earthquakes of $M_s > 7.0$. The geographical distribution of records is summarised in Table 5.4. Italian and Turkish records together make up around 62% of the total dataset.

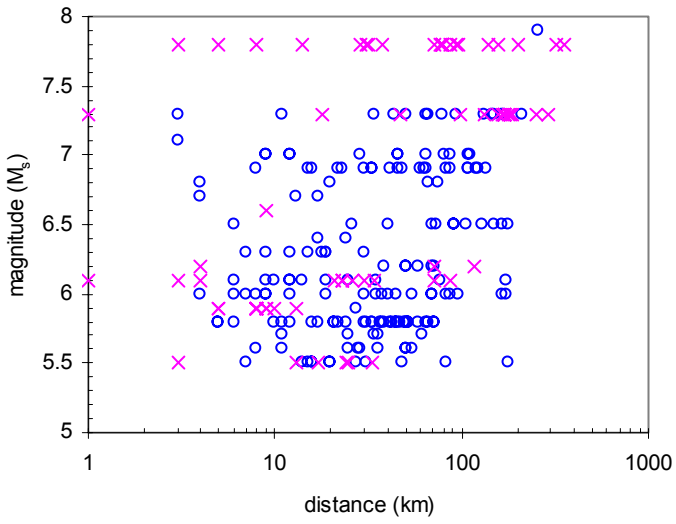

Figure 5.2 Distribution of the dataset with respect to magnitude, M_s and distance. Circles denote data from the 1998 dataset; crosses denote new data for this study

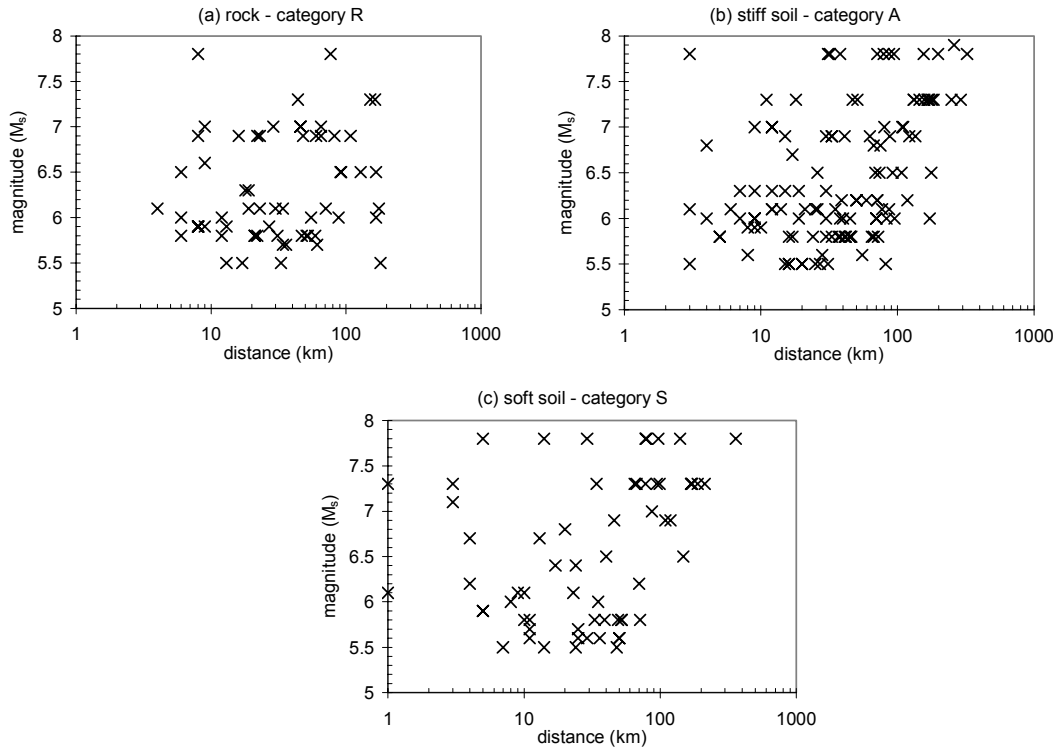

Figure 5.3 Distribution in magnitude-distance space of the data subsets grouped according to site geology

Table F1, Appendix F gives instrument types for all of the supplementary records. 44 of the 69 records are from digital instruments. Instrument types were not available for all of the original dataset. None of these records however are thought to have been recorded on digital instruments.

Table 5.4 Regional distribution of records in dataset

Country/region	Number of records	% of total dataset
Algeria	1	0.4%
Azores	1	0.4%
Greece	31	12.4%
Iran	18	7.2%
Italy	98	39.4%
Portugal	1	0.4%
Turkey	56	22.5%
Former USSR	10	4.0%
Former Yugoslavia	33	13.3%

Values of PGA, PGV and PGD were obtained from time-histories of earthquake motion following record processing. Processing of strong-motion records was carried out uniformly for the whole dataset using a band-pass filter to remove high and low-frequency noise. The filtering was carried out using an elliptical filter (Shyam Sunder & Connor, 1982) as

implemented by Menu (1986) in the FORTRAN program ELLICOR. The new records were processed using the same procedure that Bommer *et al.* (1998) used on the original dataset. Since velocity and displacement time-histories are particularly sensitive to the selection of the low-frequency filter cut-off, f_L, each record was filtered separately. The procedure is summarised below:

Filter the record with as low a value of f_L as possible and plot velocity and displacement time-histories.

1. If, on visual inspection, these time-histories are judged to be contaminated by noise, increase f_L by a small increment and plot the newly filtered record.
2. Continue this process until the resulting velocity and time displacement time histories are deemed to be acceptable and furthermore no significant improvement is observed by further increase in f_L.

A standard value (25 Hz) was used for the upper-frequency filter cut-off, f_U. Upper and lower roll-off frequencies were selected to minimise the width of the transition bands separating stop bands and pass band. These were set to $1.04f_U$ and $f_L/1.04$ respectively. Spectral leakage was minimised by fixing pass-band and stop-band ripple levels to 0.002 and 0.00001 respectively, based on guidelines given by Menu (1986).

Once all records were processed, the larger value of PGA, PGV and PGD was selected from the two horizontal components of each accelerogram. For two of the recordings, only a single component of horizontal motion was available.

5.2.2 Regression method

Following processing, regression analyses were performed on the maximum PGA, PGV and PGD values using the FORTRAN program ATTEN (Sarma, 1994). The input file containing the whole dataset is included in Appendix G. The regression method was identical to that employed by Ambraseys *et al.* (1996) and Bommer *et al.*(1998) for spectral ordinates. The equation has the form:

$$\log(X) = C_1 + C_2 M_S + C_4 \log(r) + C_A S_A + C_S S_S + \sigma.P \tag{5.1}$$

$$r = \sqrt{d^2 + h_0^2} \tag{5.2}$$

where: X is the strong-motion parameter: PGA (cm/s^2), PGV (cm/s) or PGD (cm),
M_S is the surface-wave magnitude,
d is the source-to-site distance (km),
S_A and S_S are dummy variables taking into account the site conditions (S_A is 1 for stiff soil sites or 0 otherwise; S_S is 1 for soft soil sites or 0 otherwise),

σ is the standard deviation of log (y) with P being a variable that takes the value of 0 for median values of y and 1 for 84-percentile values,
C_1, C_2, C_4, C_A, C_S and h_0 are coefficients determined by the regression.

Parameter h_0 does not explicitly represent the effect of depth on the ground motion. It does however allow for the fact that the peak motion may not necessarily be caused by the closest point on the fault rupture.

5.2.3 Results

Regression coefficients for all three strong-motion parameters are summarised in Table 5.5, along with coefficients for PGA from Ambraseys *et al.* (1996) and coefficients of PGV and PGD from Bommer *et al.* (2000).

Table 5.5 Summary of regression coefficients for existing and updated attenuation relationships

X	Units	Reference	C_1	C_2	h_0	C_4	C_A	C_S	σ
PGA	cm/s^2	Ambraseys *et al.* (1996)	1.512	0.266	3.50	-0.922	0.117	0.124	0.25
		Updated	2.080	0.214	7.27	-1.049	0.058	0.085	0.27
PGV	cm/s	Bommer *et al.*(2000)	-0.195	0.390	4.50	-1.074	0.142	0.185	0.27
		Updated	0.003	0.356	6.06	-1.058	0.138	0.233	0.28
PGD	cm	Bommer *et al.*(2000)	-1.757	0.526	3.50	-1.135	0.114	0.217	0.32
		Updated	-2.128	0.597	6.18	-1.144	0.133	0.268	0.36

The magnitude-dependence of strong-motion peaks, given by coefficient C_2 increases markedly from PGA to PGV and from PGV to PGD. This variation is more significant for the updated equations than for the other equations quoted in the table. The predictive relationships of Sabetta and Pugliese (1987) show a similar increase in magnitude dependence from PGA to PGV (they do not include PGD in their analysis). Other investigations which have included PGD have shown a similar trend, including those by Trifunac (1976), Kawashima *et al.* (1986) and Kamiyama *et al.* (1992).

The distance terms in Equation (5.1), C_4 are almost identical for each parameter, being slightly less than -1.0. In deriving predictive equations for the Western USA, McGuire (1978) found that the attenuation of PGD was less than that for PGV, which in turn was less than that for PGA. This accords with the expectation from theory that the longer period content of motion attenuates less rapidly than the shorter period content of motion. However, because of the oversimplified character of the model, firm conclusions about frequency-dependent attenuation are difficult to make with any confidence (Joyner & Boore, 1981). It is worth noting that values of C_4 should theoretically be no smaller than –1.0, but here allowance is made because the separate term for anelastic attenuation has been removed.

The dependency of peak strong-motion on site conditions is obtained from coefficients C_A and C_S. Comparing updated values with the other values quoted in Table 5.5, the amplifying effects of both stiff and soft soils on PGA have reduced. For PGD, these effects have both increased. In the case of PGV, the amplifying effect of stiff soil is practically unchanged but the effect of soft soil has increased.

In Figures 5.4 to 5.6, strong-motion peaks from the updated equations are compared with values calculated from the other predictive relationships quoted in Table 5.5. Comparison is also made with at least one additional well-established predictive relationship for each strong-motion parameter. In each case, the equations are plotted for an event of magnitude M_s 7.0 for both rock and soft soil sites. Extra plots for stiff soil sites are excluded because some of the equations used for comparison are only defined for two distinct site categories.

Peak Ground Acceleration

In Figure 5.4, accelerations from the updated relationship for PGA are presented alongside accelerations predicted by the equations of Ambraseys *et al.* (1996), Boore *et al.* (1993) and Sabetta & Pugliese (1987). All relationships use the same definition for source-to-site distance. The equation of Sabetta & Pugliese was selected because it is based on European data (even though this is limited to Italian records and strictly only valid for earthquakes up to magnitude M_s 6.8) and because it was derived together with a predictive equation for PGV, which is plotted in Figure 5.5. Boore *et al.* (1993) was selected because of its widespread use; it is based on accelerograms from western North America.

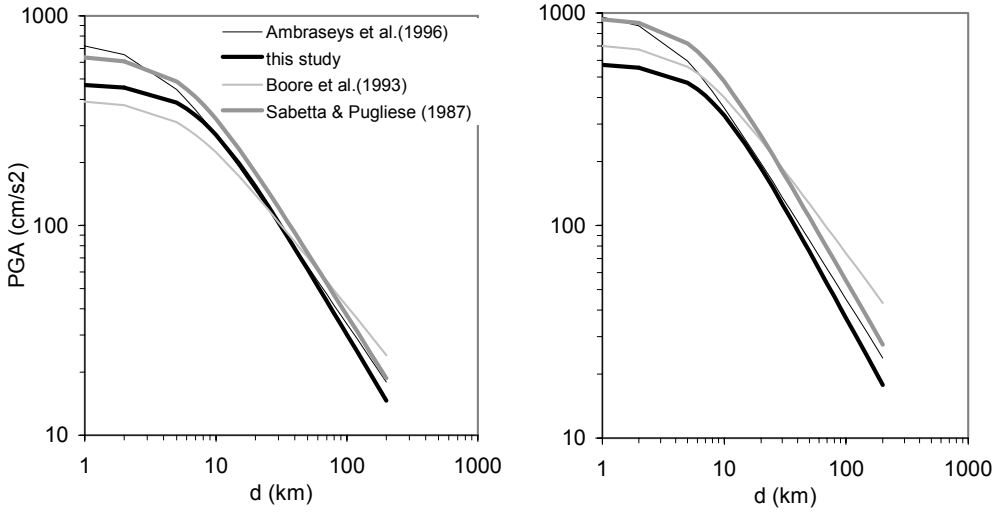

Figure 5.4 Predicted values of PGA for rock sites (left) and soft soil sites (right) from the equations quoted in Table 5.5 for an earthquake of magnitude M_s 7.0. Comparisons are made with the predictions of Boore *et al.* (1993) for the same site categories and Sabetta & Pugliese (1987) for 'rock' (left) and 'soil' (right).

The updated equation predicts very similar values of PGA to the equation of Ambraseys *et al.* (1996) for all distances but the near-field, whether for rock sites or for soft soil sites. The disparity is almost solely due to the difference in h_0. The equation of Sabetta & Pugliese (1987) predicts consistently higher PGA values than the updated equation. The Sabetta & Pugliese (1987) equation appears to exhibit greater site-dependency than the other European equations. However, this is partly due to the fact that the Italian equation distinguishes between only two site categories. For rock sites, the relationship of Boore *et al.* (1993) predicts lower accelerations than the updated relationship up to about d = 30km. For soft soil sites, the Boore *et al.* (1993) relationship predicts greater values at all distances. The predictive relationships derived from European data all exhibit similar attenuation with distance. The lower attenuation rate observed for the American relationship may reflect differences in regional attenuation characteristics.

The standard deviation of the updated relationship (Table 5.5) is slightly greater than that of Ambraseys e*t al.* (1996). The standard deviations of the equations of Boore *et al.* (1993) and Sabetta & Pugliese (1987) are 0.205 and 0.173 respectively.

Peak Ground Velocity

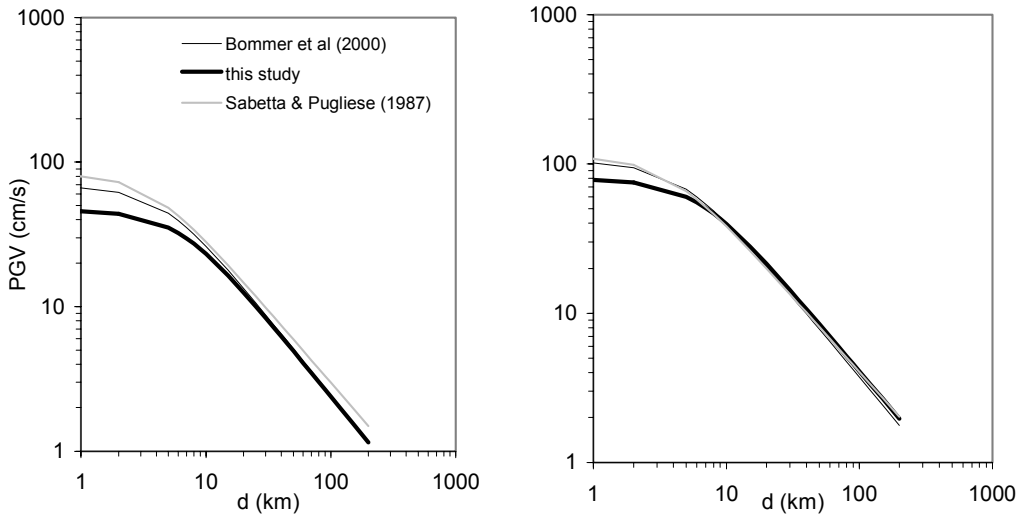

Figure 5.5 Predicted values of PGV for rock sites (left) and soft soil sites (right) from the equations quoted in Table 5.5 for an earthquake of magnitude M_S 7.0. Comparisons are made with the predictions of Sabetta & Pugliese (1987) for 'rock' (left) and 'soil' (right).

In Figure 5.5, PGV from the updated relationship is presented along with the Bommer *et al.* (2000) relationship and the PGV relationship derived from Italian data by Sabetta & Pugliese (1987). As seen in Figure 5.4, attenuation with distance is almost identical for all three

relationships, which are based on European data. As with PGA, significant differences are only observed for $d < 10\,\text{km}$. Again, the differences are almost solely due to differences in h_0 (the corresponding coefficient in the Italian relationship being 3.60). The amplifying effect of soil is less for the Sabetta & Pugliese (1987) relationship than for the other two. It should be noted that the distinction between 'rock' and 'soil' categories for the Sabetta & Pugliese (1987) relationship for PGV differs from the distinction used for PGA. The standard deviation of the Sabetta & Pugliese (1987) relationship is 0.215.

Peak Ground Displacement

Predictive relationships for PGD are far less common than those for PGA and PGV. A handful of relationships have been derived from North American data (eg. McGuire, 1974; Trifunac, 1976; McGuire, 1978; Gregor & Bolt, 1997; Sadigh & Egan, 1998) and Japanese data (eg. Kawashima *et al.,* 1986; Kamiyama *et al.*, 1992). However, to the author's knowledge, only two relationships have yet been derived with an emphasis on data from European earthquakes: Theodulidis & Papazachos (1992) and Bommer *et al.* (2000).

The updated relationships for PGD are presented in Figure 5.6 alongside relationships from Gregor & Bolt (1997), based on Californian data and Theodulidis & Papazachos (1992). The Gregor & Bolt (1997) relationship, although based on data from a different part of the world, was selected because it was derived taking into consideration a number of issues of particular importance to PGD which other studies have not addressed; some of these issues are mentioned later.

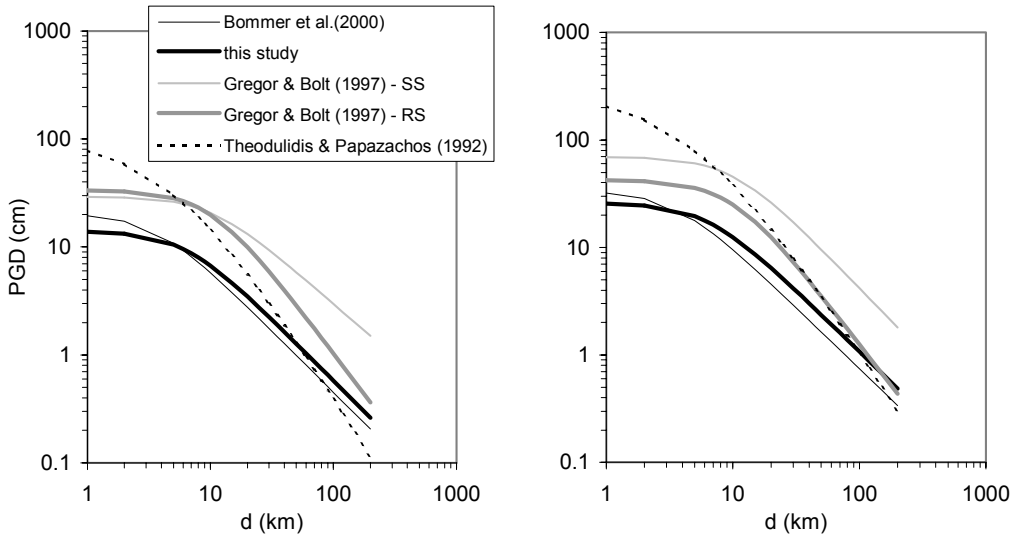

Figure 5.6 Predicted values of PGD for rock sites (left) and soft soil sites (right) from the equations quoted in Table 5.5 for an earthquake of magnitude M_S 7.0. Comparisons are made with the predictions of Theodulidis & Papazachos (1992) for 'rock' sites (left) and 'alluvium' sites (right) and the predictions of Gregor & Bolt (1997) for 'rock' sites (left) and 'soil' sites (right) distinguishing between strike-slip (SS) and reverse-slip (RS) earthquakes

Considering first the relationships derived from European data, it can be seen that the updated relationship corresponds closely with that of Bommer *et al.* (2000). The curves intersect because the updated relationship has both greater magnitude-dependence and greater h_0.

The equation of Theodulidis & Papazachos (1992) generally predicts significantly greater PGD values than the equation derived in the current study. Although the Theodulidis & Papazachos (1992) equation includes a coefficient to account for near-field saturation of PGD, the near-field values are still very large. This is because of their use of epicentral distance in the regression and because of the distribution of their dataset in M-d space. For small epicentral distances, the shape of the curve is dictated largely by small magnitude earthquakes (M_s < 5.5). Indeed, for M_s > 6.5, the dataset has no records within 30km of the epicentre. For epicentral distances greater than about 90km, there are no records from events smaller than M_s 6.8.

Gregor & Bolt (1997) derived two separate relationships for PGD, dependent on fault mechanism. The strike-slip attenuation model was regressed on data from earthquakes in the range $5.4<M_w<7.2$. The reverse-slip attenuation model was based on a more restricted range of magnitudes ($5.6<M_w<6.7$). It is worth noting that for magnitudes of about 7, M_w and M_s are similar.

The Gregor & Bolt (1997) relationships give significantly greater values of PGD than the updated European relationship for both rock and soil sites. The difference is rather less in the RS model, which in fact for distances approaching 100km gives very similar results to the updated European relationship. The European data includes records from both types of earthquake, so might be expected to predict values somewhere between the two Gregor & Bolt (1997) curves. However direct comparisons between the European and American relationships are complicated by several factors:

- The source-to-site distance used by Gregor & Bolt (1997) is H_{slip}, the straight-line distance from the recording site to the location on the fault plane of largest slip. This parameter is used because of the association of PGD with long wavelengths of motion which are likely to have been generated by a much larger patch of slip on the fault plane than both PGA and PGV. In all of the earthquakes investigated by Gregor & Bolt (1997), the location of the largest slip never coincided with either the initial hypocentre or the closest part of the fault plane to the site. For predictive purposes, H_{slip} cannot be found so Gregor & Bolt (1997) suggest using an alternative distance measure such as the shortest distance from the site to the causative fault.
- PGD values were measured only from the S wave portion of the strong-motion records after discrimination of the seismic wave types. Gregor & Bolt (1997) point

out that PGD can occur in the surface wave train of a record even though PGA and PGV occur in the body wave portion of the same record. They stress that, since the attenuation of surface waves is proportional to the inverse of the square root of the distance from the source, while the attenuation of S waves is proportional to the inverse of the distance from the source, PGD values from S wave pulses should not be mixed with peak surface wave values in the same analysis. For most of the European records, the selection of filter parameter f_L was such that PGD coincided with the same portion of time-history as the PGA and PGV values. The predictive relationship derived here is therefore unlikely to have been influenced much by the surface wave related behaviour of PGD.

- The equations derived by Gregor & Bolt (1997) do not use the same site classification scheme as the current study, based on v_{s30} values, because the amplitude of seismic waves responsible for PGD (which have a characteristic wavelength of the order of 3000m, being equal to c/f where c = wave velocity (~3km/s) and f = characteristic frequency (~1 Hz)) is unlikely to be influenced significantly by the geological structure of the upper 30m. v_{s30} values are more important for the analysis of PGA which is associated with shorter wavelengths. In the current study, v_{s30} was used for site classification for all three peak strong-motion parameters for consistency.

In spite of the careful treatment outlined above, standard deviations for the relationships of Gregor & Bolt (1997) are still large when compared to standard deviations in other strong-motion parameters. For the SS models for rock and soil, σ is 0.37 and 0.30 respectively. For the RS models, the standard deviations are 0.32 and 0.27. Standard deviation for the updated European relationship compares favourably with these values, even though it represents an increase with respect to the Bommer *et al.* (2000) relationship.

5.2.4 Inspection of Residuals

Residuals of log(y) with respect to Equation (5.1) are plotted against distance and magnitude for all three parameters, together with linear best-fit relations (Figures 5.7, 5.8). No significant trends are observed for the full dataset with respect to magnitude or distance. The distribution of residuals about distance or magnitude is a function of both the dataset and the regression method employed. The predictive equations presented in Appendix E are derived from a variety of different regression models. As stated by Ambraseys *et al.* (1996), each method has its limitations and there is no ideal method, different approaches working better for different datasets. There is scope for testing different methods on the current dataset, but that is beyond the limits of the current study.

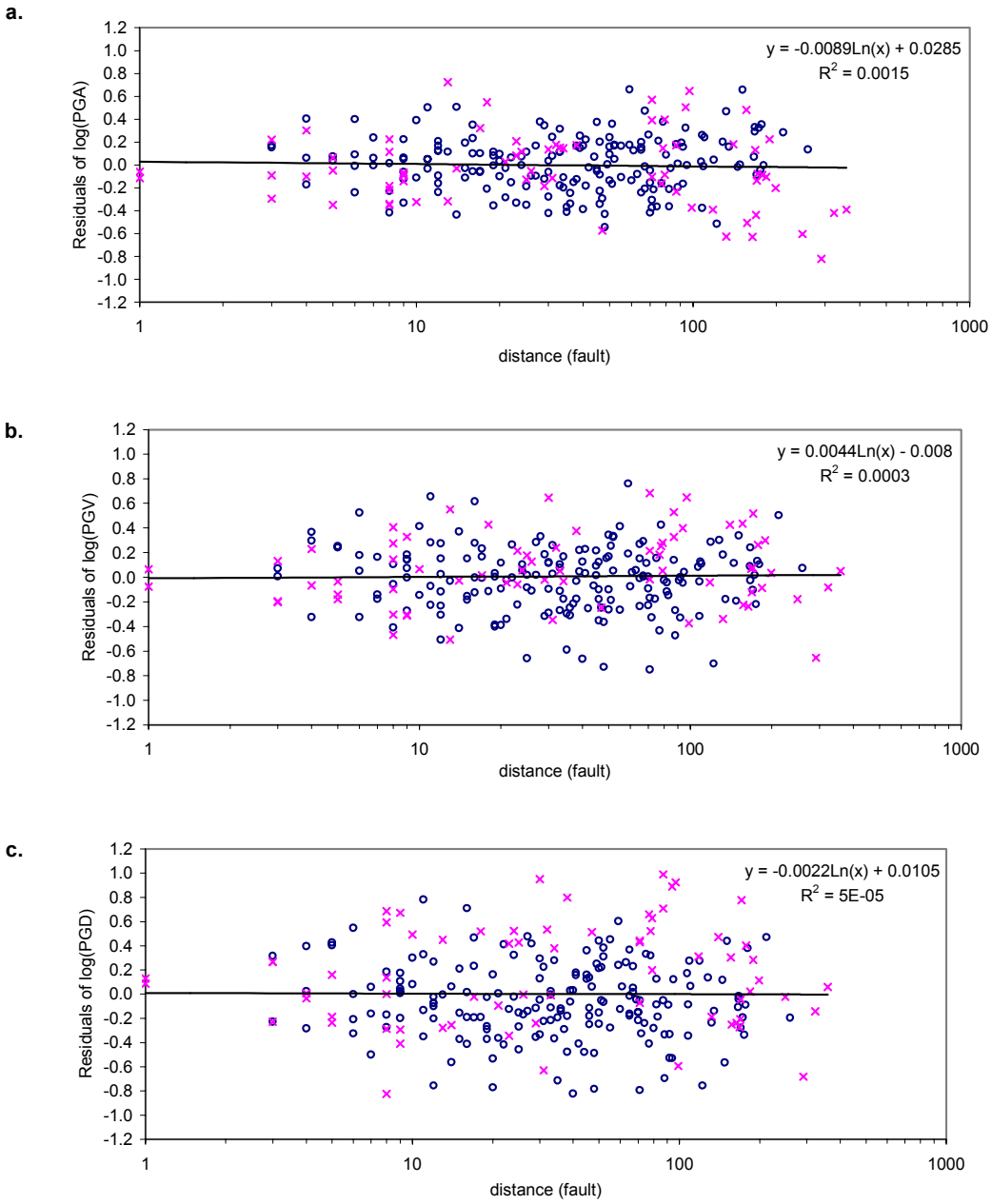

Figure 5.7 Distance dependence of log (observed peak value) – log (predicted peak value). (o indicates 1998 dataset; x indicates new records)

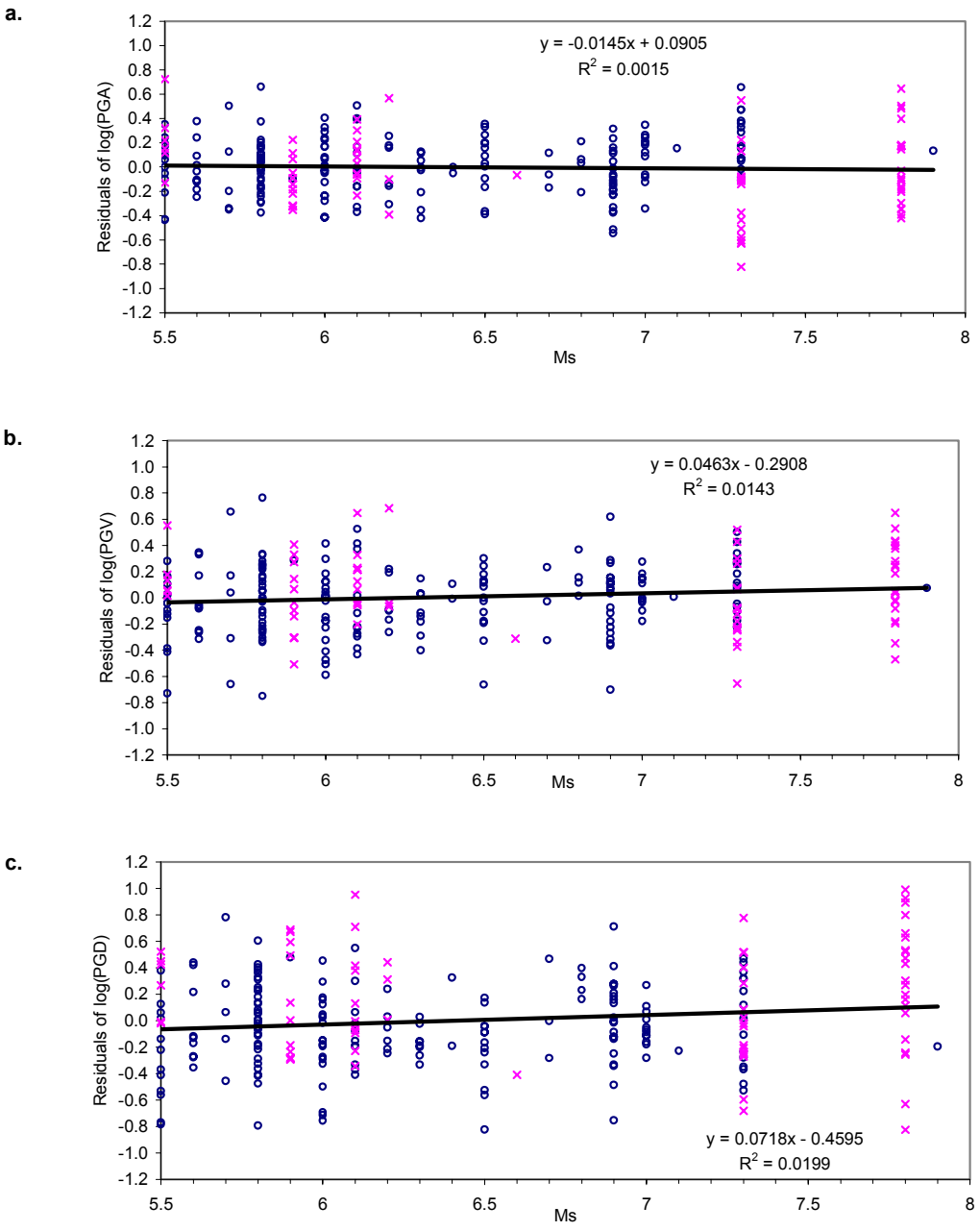

Figure 5.8 Magnitude dependence of log (observed peak value) – log (predicted peak value). (o indicates 1998 dataset; x indicates new records)

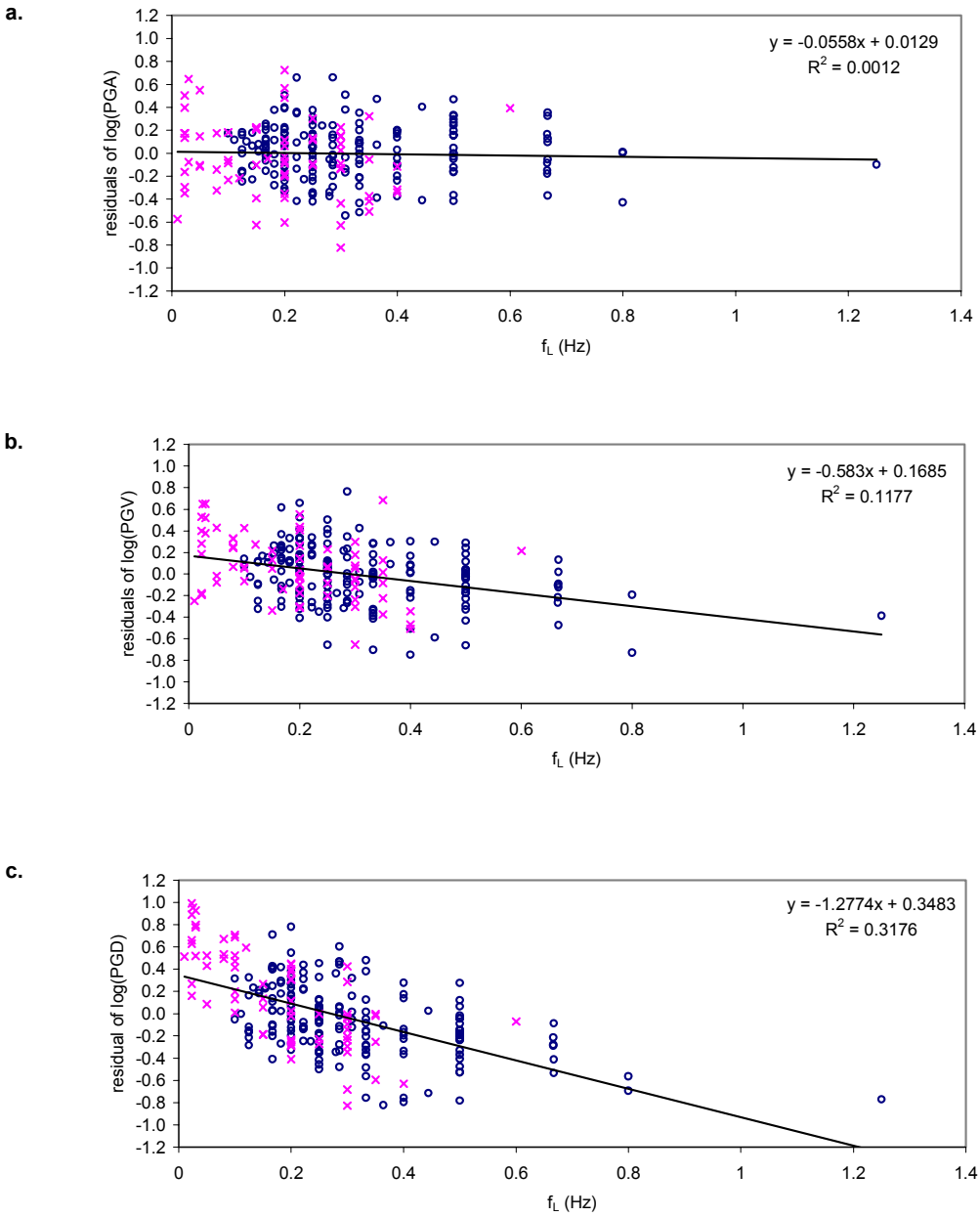

Figure 5.9 Dependence of (log (observed peak value) – log (predicted peak value)) on lower frequency cut-off, f_L. (o indicates 1998 dataset; x indicates new records)

In Figure 5.10, residuals of PGA, PGV and PGD are plottted against each other to investigate whether the derived relationships tend to 'overpredict' or 'underpredict' for the same records for different pairs of variables. The figures show that residuals of PGV and PGD correlate with each other more closely than either of the other two pairings of variables. A detailed examination of the residuals from individual records, as performed by Ambraseys & Bommer (1991) in their study of attenuation of PGA, has not been carried out and is reserved for future study.

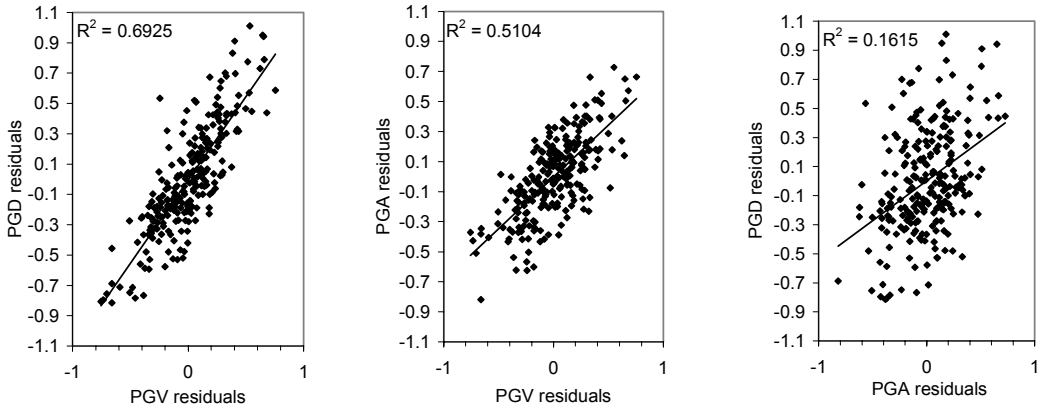

Figure 5.10 Comparison of residuals between different pairs of variables

Figures 5.7 and 5.8 both show a systematic increase in scatter from PGA to PGV and from PGV to PGD. This trend is apparent from the values of standard deviation given in Table 5.5. These values of σ however conceal the intrinsic uncertainty associated with each of the variables in the regression. Care has been taken to minimise errors in magnitude and distance estimation and through individual selection of the lower frequency filter cut-off; care has also been taken to minimise the difference between the peak strong-motion parameters obtained from the processed record and the true ground motion peaks. However, in many cases, identification of an appropriate f_L was hampered by the difficulty in distinguishing between signal-related long-period motion and noise-related long-period motion. The f_L-selection procedure has resulted in an apparent trend in the residuals of log (PGD) when plotted against f_L (Figure 5.9). Records 'under-predicted' by the equation (i.e. having a positive residual in Figure 5.9) tend to have been processed using a low f_L. This trend is less evident for log(PGV) residuals and not apparent at all for log (PGA) residuals, which is evidence of the increasing influence of f_L on strong-motion peaks from PGA to PGV to PGD. This is the focus of the next section.

5.3 The effects of filtering and correction on strong-motion peaks

In their derivation of a relationship for spectral displacement ordinates, Bommer *et al.* (1998) show that reliable values can be obtained up to a clearly defined maximum period (about 3 s). However, peak values of strong-motion are much more sensitive to record processing.

Errors in strong-motion records are most significant when dealing with analogue instruments. The sources of error have been investigated in detail by Trifunac *et al.* (1973, 1999).

In transferring accelerograms from paper or film into digital format, there are two main sources of error:

1. High-frequency errors of significance to instrument correction procedures and
2. Low-frequency errors influencing the baseline correction

Of these, it is the second that has the most significant effect on strong-motion records, especially on the integrated velocity and displacement time-histories. Low-frequency noise is caused by uncertainty in the location of the baseline, imperfections in the digitising systems and other factors such as warping and transverse play of the film. High-frequency errors generally have very little engineering significance, except in certain specialised areas.

Schiff & Bogdanoff (1967) argued that the accuracy of digitised uncorrected accelerograms was too limited for the double-integrated displacement curves to be of much use. Trifunac *et al.* (1973) demonstrated that, by careful digitisation and appropriate processing of the digitised data, strong-motion accelerograms can give accurate information about the ground motion over a frequency range 0.07 Hz - 25 Hz. The processing method used involved instrument correction (Trifunac, 1972) and base-line correction (Trifunac, 1971) using an Ormsby filter. As stated by Trifunac & Lee (1974), in routine processing of large amounts of strong-motion data, an average lower frequency is generally used. For ISESD, this has been selected as 0.20 Hz. However, for specialised research applications, the optimal f_L should be determined separately for each record, as has been done in the current study.

Several records from the data set were processed for a broad range of f_L to investigate its effect on strong-motion peaks. In Figure 5.11, PGA, PGV and PGD are plotted against f_L for two pairs of horizontal components of ground motion from the Duzce-Bolu earthquake of 12/11/1999. The records from station BOL were recorded using a GSR-16 digital accelerograph whereas those records from station DZC were recorded using an analogue SMA-1 accelerograph.

PGA values exhibit stability until at least f_L = 0.4 Hz for the selected records. PGV is more sensitive to f_L, especially from the analogue records. PGV for the digital records does not vary much for f_L up to around 0.5 Hz for the N-S component and 0.2 Hz for the E-W

component. The variation of PGD with selection of f_L is quite dramatic for the analogue records shown. However, for the digital records, PGD is considerably more stable. In the processing of records for the database, selection of an appropriate f_L was generally easier in cases where the strong-motion peaks exhibited stability over a broad range of f_L. This was more likely for digital records than for analogue records. As shown in Table F1, Appendix F, the majority of the supplementary records added to the database (i.e. 44 of 69) were from digital instruments. However, for the complete dataset, records from analogue instruments predominate.

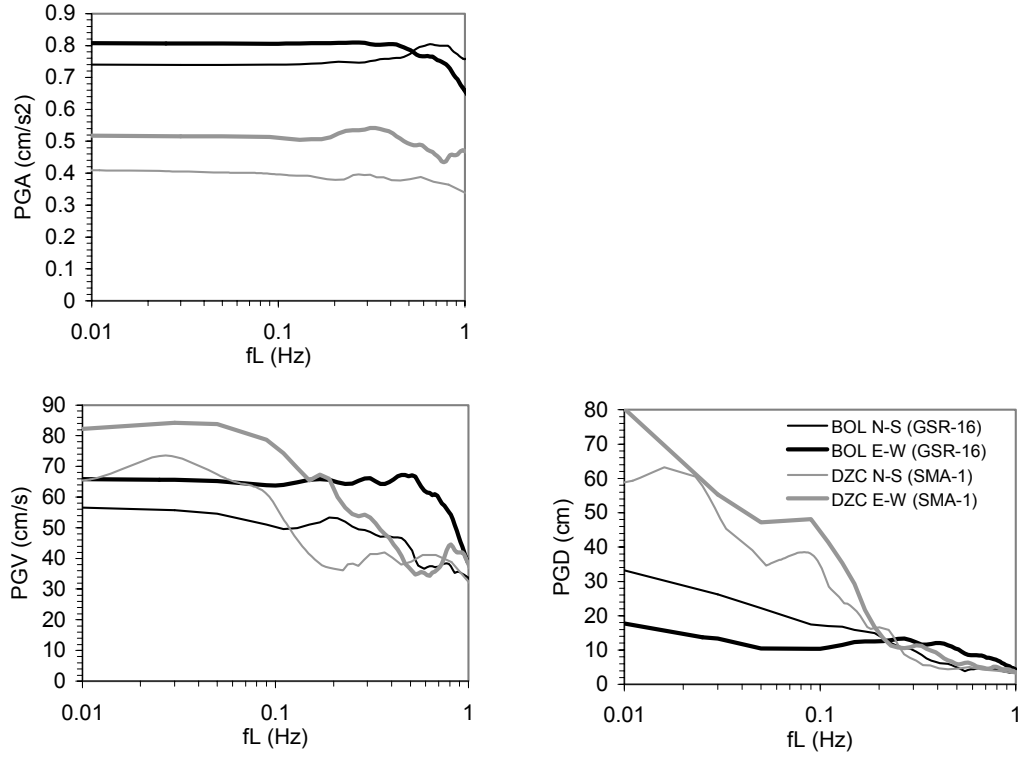

Figure 5.11 The effect of f_L on PGA, PGV and PGD for records from the Duzce-Bolu earthquake of 12 November 1999

It is useful to consider which records may have been filtered too harshly, causing significant parts of the signal to be lost, and which ones may have been filtered using values of f_L so low as to leave significant noise in the record and result in overestimation of PGD (and, to a lesser extent, PGV). Record-independent approximations of f_L can be found based on the assumption that an earthquake will not produce ground motions with a period longer than the time it takes for the entire fault to rupture (assuming a unilateral rupture process). Rupture duration (t_{rup}) will simply be the ratio of earthquake fault rupture length (L_{rup}) - calculated from the equations of Wells & Coppersmith (1994) - to the fault rupture velocity (v_{rup}) (typical values of 2, 2.5 and 3 km/s assumed). This will suggest a 'lower-bound' frequency

$f_{L1} = 1/t_{rup}$ that could be expected to be present in a strong-motion record. The 'corner-frequency' (f_c) provides another record-independent measure that can be used to approximate a lower-bound f_L (Joyner & Boore, 1988). The corner frequency is a characteristic of the far-field earthquake displacement spectrum, being defined as the frequency at the intersection of the low- and high-frequency asymptotes (Brune, 1970). Figure 5.12 gives estimations of f_{L1} and f_c in terms of earthquake magnitude and compares them with the values of f_L selected for each record in the database. Further explanations of the method are given in the figure caption.

Points lying above the lines represent records that may have been filtered using too high a value of f_L, thereby underestimating the true value of PGD. This is most likely for the distant records in the database whose signal-to-noise ratios are considerably higher than those closer to the earthquake source.

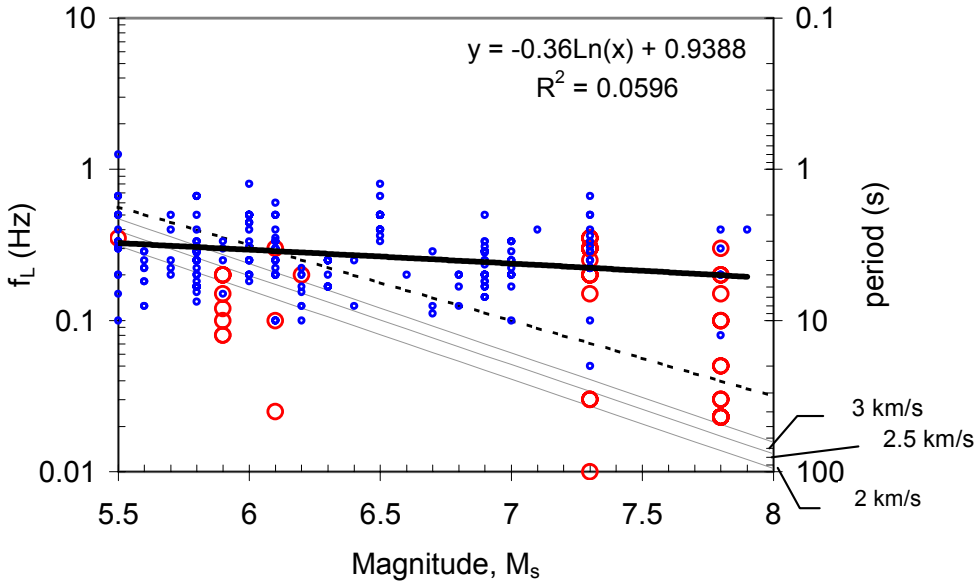

Figure 5.12 Distribution of lower frequency cut-off, f_L with earthquake magnitude

- Small circles represent analogue records; larger circles represent digital records.
- Bold line shows the trend for these variables (equation and scatter given).
- Solid grey lines show the lowest anticipated frequency (f_{L1}) present in a record as a function of magnitude, assuming: $f_{L1} = v_{rup}/L_{rup}$, where v_{rup} is average fault rupture velocity and L_{rup} is the subsurface rupture length from Wells & Coppersmith (1994): $log(L_{rup}) = -2.44 + 0.59M_w$.
- M_w is assumed equal to M_s for the range of magnitudes considered. f_{L1} is given for three different values of v_{rup}. Dotted line gives the corner frequency, f_c, where $log(f_c) = -(M_w-5)/2$, as reported in Joyner & Boore (1988).

Points lying below the f_{L1} or f_c lines represent possible over-estimations of true PGD, assuming that long-period noise levels are appreciable. However, because f_L was selected for each record as the lowest value to give acceptable time-histories of acceleration, velocity and displacement (i.e. not being over-influenced by long-period noise), the PGD values are probably reasonable approximations to true PGD.

It is important to note that obtaining 'true' displacements in the near-field is complicated by the effect of permanent tectonic deformations on the strong-motion records. This is the 'tectonic fling' phenomenon described in Chapter 2. Band-pass filtering, as employed in the current study, removes any trace of permanent displacement from a record. However, the amplitudes observed in a filtered record are not completely unaffected by the presence of 'fling' effects. This is illustrated in Figure 5.13, in which time-histories of velocity and displacement are plotted for the strike-parallel component of motion at station SKR during the Kocaeli earthquake. A comparison is made between the time-histories obtained using a technique which allows permanent displacements to be retained (Graizer, 1979) and time-histories that have been band-pass filtered using different values of f_L. The acceleration time-histories have not been included because there was no appreciable difference between the three curves. The lowest value of f_L permitted by the ELLICOR filtering program with the combination of filter parameters given in Section 5.2.1 was 0.023 Hz. The velocity trace in this case follows the Graizer velocity trace very closely. The PGV of the filtered record is only slightly less than the PGV of the Graizer-corrected record. Increasing f_L to 0.2 Hz has the effect of removing the long-period 'spike' between 6 and 12 s. This causes a significant reduction of PGV. The differences in the three displacement traces are greater than those observed in the velocity traces. Peak values vary by up to an order of magnitude.

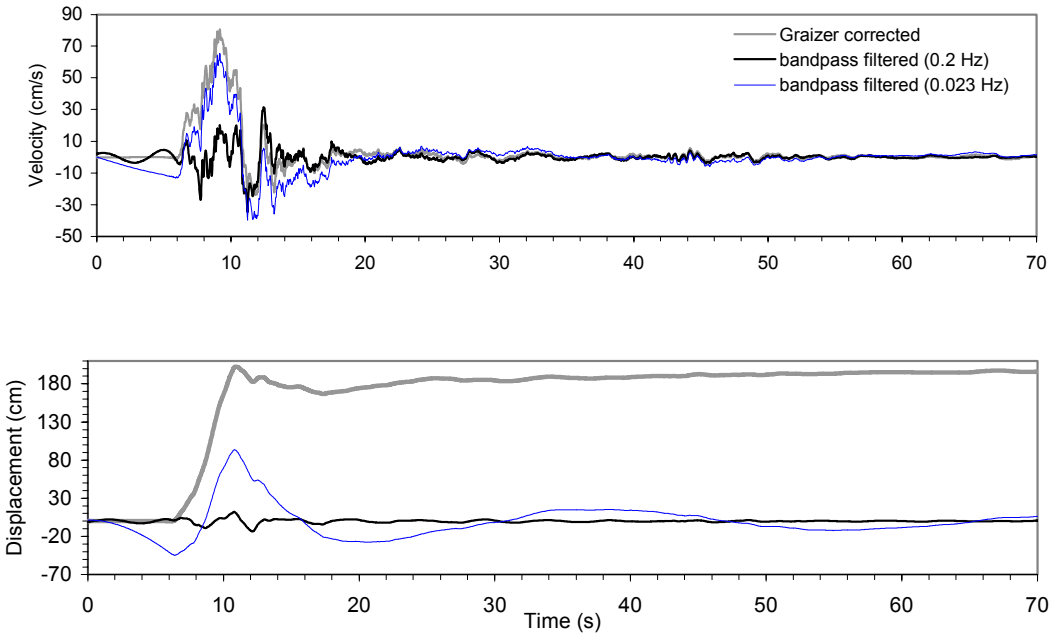

Figure 5.13 Comparison of velocity and displacement time-histories obtained using two different record processing methods. The record shown is the EW (strike-parallel) component of motion recorded at the Sakarya station (SKR) during the 17 August 1999 Kocaeli, Turkey earthquake (d_f = 3 km).

For the strong-motion dataset developed for the current study, the SKR EW record was filtered using f_L = 0.023 Hz. Because the record was obtained from a digital instrument, with a high signal-to-noise ratio, use of a greater f_L was considered unnecessary. Indeed, doing so would have removed significant parts of the signal in the frequency domain, reducing velocity and displacement amplitudes in the time domain.

The predictive relationships developed in the current study assume attenuation of PGD as r^{C_4} (from Equation 5.1), where $C_4 \approx -1$. However, in the near-field, the true PGD is often dominated by the fault dislocation amplitude. Lee *et al.* (1995) cite Haskell's (1969) expression for elastic displacements in a homogeneous medium to show that the amplitude of the permanent displacement will initially decay as d^{-4} and then as d^{-2} (where d is distance away from the surface fault rupture). PGD (i.e. the sum of transient and permanent/tectonic components of displacement) will only decay as d^{-1} at large distances ($d >> A^{1/2}$, where A is the fault rupture area) from the surface fault rupture, where the tectonic component is small compared to the transient component.

In order to model the attenuation of PGD more precisely, changes could be made to the record processing technique and/or the functional form of the predictive relationship. Two possible approaches are outlined below:

1. Process all records (for which tectonic displacement is likely to be significant) using a polynomial baseline correction technique such as Graizer (1979). Derive an attenuation relationship with a distance-dependent coefficient C_4.

2. Use a combination of filtering and polynomial correction to separate out transient and tectonic components of displacement. Retain the form of equation used in the current study but only include the transient components of displacement in the regression.

Both methods rely on the effectiveness of the polynomial correction technique in giving accurate displacement time-histories that retain any permanent offset. Trifunac & Todorovska (2001) show that reliable permanent displacements cannot be obtained without knowledge of the rotations about each of the three orthogonal component axes. Such measurements are not routinely carried out. However, as pointed out by Douglas (2001b), obtaining reliable measurements of permanent ground displacement might be possible for accelerograms in which contributions from tilting and angular accelerations are negligible. Comparison between permanent offsets from digital strong-motion data and GPS measurements taken before and after the 1999 Chi-Chi, Taiwan earthquake suggests that realistic values can be obtained from strong-motion data if care is taken in selecting the various correction parameters (Boore, 2001; Douglas, 2001b). However, application of polynomial correction requires pre-event data and low digitisation noise levels, neither of

which are available for records obtained from analogue instruments (Trifunac & Todorovska, 2001). Currently, the vast majority of European strong-motion records are analogue, although many of the more recent (post-1994) records added to the database for the current study are digital. The database of usable records is currently too sparse to adequately constrain the first model suggested above, which, because of its greater complexity, would require a dataset somewhat larger than the one used in the current study.

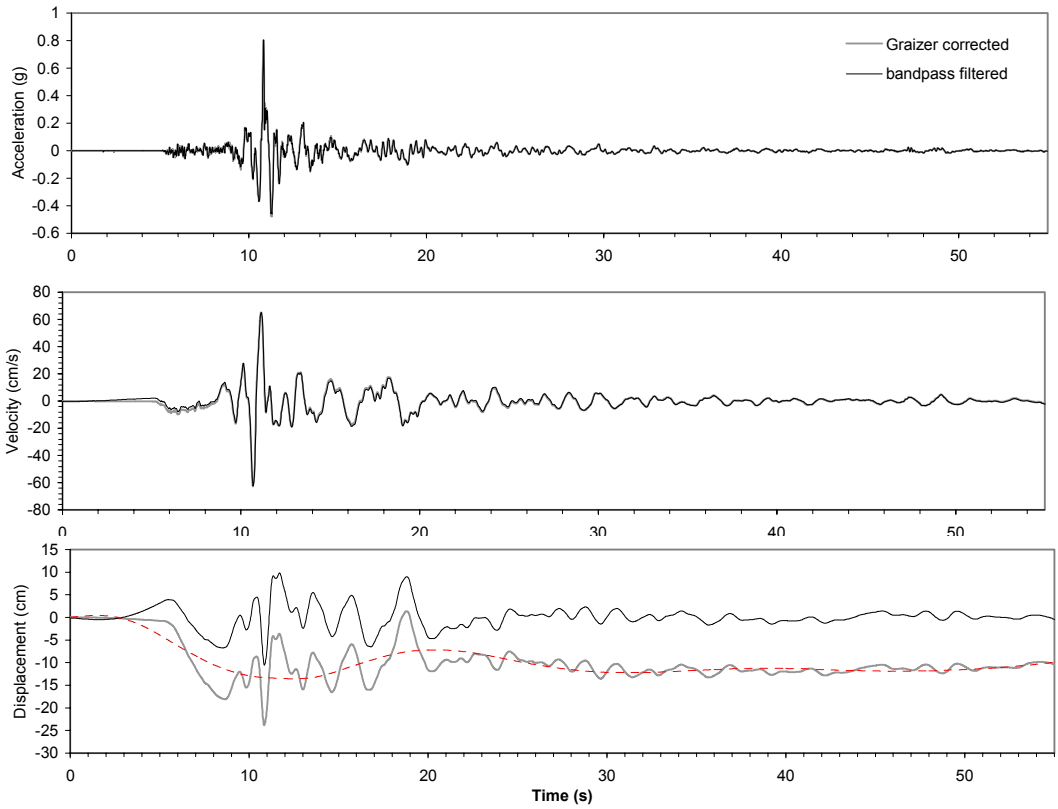

Figure 5.14 Comparison of strong-motion time-histories obtained using two different record processing methods. The record shown is the EW (strike-parallel) component of motion recorded at the Bolu station (BOL) during the 12/11/1999 Duzce-Bolu, Turkey earthquake (d_f =18 km). The third (red) line in the displacement time-history represents the bandpass-filtered record subtracted from the Graizer-corrected record.

The second approach suggested above requires a method for separating out the fling effect from strong-motion records. This has recently been investigated by Abrahamson (2001) using records from the 1992 Landers, 1999 Chi-Chi and 1999 Kocaeli earthquakes. In Figure 5.14, an attempt has been made to distinguish between transient and tectonic displacements from the EW (strike-parallel) component of motion recorded at the Bolu (BOL) station during the Duzce-Bolu earthquake. The transient component has been obtained by application of a bandpass filter with f_L = 0.05 Hz (as used for this record in the current study). The permanent component has been obtained by subtracting the transient component from the Graizer-corrected displacement trace. The BOL EW record is less sensitive to the selection of f_L than

the SKR EW record. This is evident from both the velocity and displacement time-histories in Figures 5.13 and 5.14. The high level of stability in PGA, PGV and PGD values for BOL EW has been illustrated in Figure 5.11. The amplitudes of transient displacement in the bandpass-filtered record are therefore considered to be a reasonably accurate representation of the true ground motion. The sense of permanent displacement (towards the West) agrees with the expected offset for a site located to the south of a right-lateral strike-slip fault with a strike of around 90^o. Furthermore, GPS measurements before and after the earthquake at a site on the same side of the fault as the BOL strong-motion station show tectonic displacement of around 12cm to the west (Ayhan *et al.*, 2001). This is close to the value shown in Figure 5.14, although it should be noted that the GPS station and strong motion station are approximately 21km apart.

5.4 Conclusions

Supplementary records added to the database of European records have constrained the predictive relationships better for large magnitude earthquakes ($M_s > 7$) and for distances less than 10 km. Changes have been noted in the magnitude-dependence, site-dependence and h_0 values. However, the overall effect on the original equations of Bommer *et al.*(2000) has not been large. Changes in scatter are negligible in the equations for PGA and PGV, although there is an increase in the scatter associated with the new PGD equation. This is most likely related to slight differences in the criteria used for selection of the low-frequency filter cut-off when processing the supplementary strong-motion records, as compared to the original strong-motion dataset.

The new unified equations provide useful estimates of PGA, PGV and PGD with particular application to Europe. Values of PGV and PGD are inherently more uncertain than values of PGA due to problems related to record processing.

The database could be extended to include additional records now available from the Grevena, Umbria-Marche and Kocaeli earthquakes. However, based on the experience of the current investigation, this is unlikely to have a major effect on the new equations. In order to improve the new predictive relationships markedly, more digital records would be needed to permit more reliable PGV and PGD determinations. This could also allow the decomposition of displacement traces into permanent and transient components.

As pointed out by Abrahamson (2001), the effect of seismic fling on different classes of structure is a little-known area. In the case of buried pipelines, the tectonic displacement is likely to be of some significance, adding an additional component of strain to the transient strain caused by the ground shaking.

In 1999, Turkey experienced two major, destructive earthquakes separated by fewer than 90 days and having epicentres closer than 100 km. The M_s 7.8 17/08/1999 Kocaeli and M_s 7.3 12/11/1999 Düzce earthquakes caused significant damage in an area stretching from Istanbul in the west to Bolu in the east (Figure 6.1).

These two events provided the most extensive strong ground-motion data set ever recorded in Turkey (Durukal, 2002). Strong-motion stations operated by the General Directorate of Disaster Affairs (ERD), the Kandilli Observatory and Earthquake Research Institute of Bogazici University (KOERI) and Istanbul Technical University (ITU) produced at least 27 strong-motion records within 200 km of the fault for the Kocaeli earthquake alone. Such coverage is rare for any earthquake outside of the USA, Japan and Taiwan.

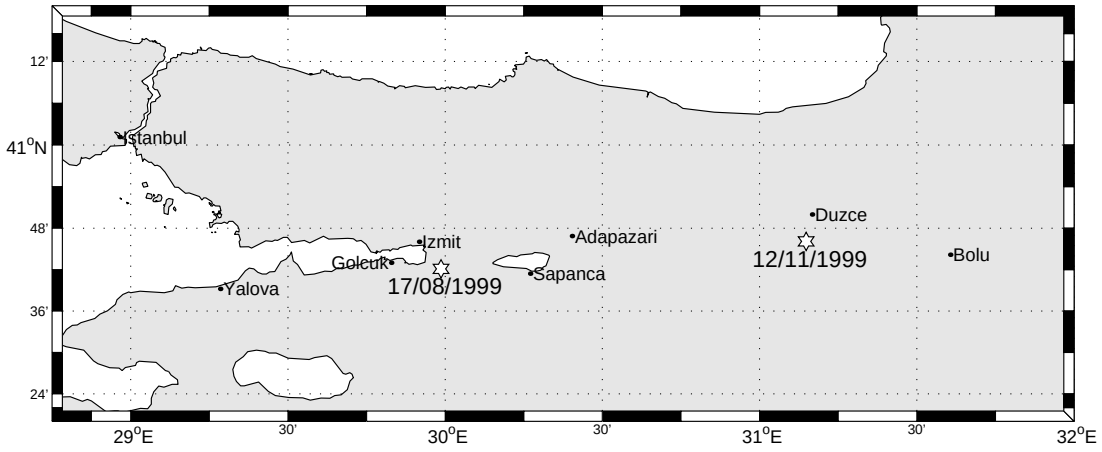

Figure 6.1 Area worst affected by the 17/08/1999 Kocaeli and 12/11/1999 Düzce earthquakes. Epicentres are indicated by stars.

Both earthquakes were characterised by extensive surface faulting and numerous examples of ground failure, including liquefaction, slumping and settlement. Many researchers around the world have recognised the significance of these earthquakes and the important opportunity afforded by them to understand earthquake effects. In February/March 2000, the author carried out a review of existing studies containing information on the performance of water supply systems and their components during the two earthquakes. Brief accounts of both good and bad performance were found for the towns of Izmit, Golcuk, Yalova, Adapazari and Düzce in a range of publications (ASCE/TCLEE, 1999a & 1999b; EERI, 1999; EQE International, 1999; Falconer, 1999; Sarikaya *et al.*, 1999; Scawthorn, 1999; Sellars, 1999; Water UK Magazine, 1999). However, at this stage, the only detailed investigation available was that of Sarikaya *et al.* (1999) for the town of Sapanca, whose water supply system suffered extensive damage during the Kocaeli earthquake.

As highlighted in Chapter 3, understanding the relative importance of factors contributing to earthquake damage of buried pipelines is completely dependent upon the amount and quality of data available. A field visit was therefore conducted in May 2000 to gather relevant information.

The time spent in the field focussed on six main areas, as laid out in the ASCE TCLEE post-earthquake investigation guidelines (ASCE TCLEE, 1997):

1. Documenting performance of facilities (good and bad)
2. Identifying failure modes
3. Determining factors contributing to damage/failure
4. Determining impacts of damage/failure (to the water supply system, the emergency response and the community at large)
5. Documenting system recovery and repairs and seismic improvement measures already carried out
6. Collecting detailed information on the physical characteristics of the water supply system and its operation

Information was obtained from academic, commercial and public sector sources relating to damage at various locations across the affected region. The town of Düzce was identified as a suitable candidate for a detailed case study on the seismic performance of water supply pipelines. The local municipality provided information covering all of the areas listed above to varying degrees and offered further assistance for any subsequent work planned.

Approximately 12 months later, a follow-up investigation was carried out with the assistance of the municipality and also UNICEF personnel involved in the post-earthquake recovery operations.

The current Chapter and two subsequent Chapters constitute a detailed description of this fieldwork. Chapter 6 is a summary of earthquake effects in and around Düzce. Chapter 7 is a description of a microtremor investigation into the spatial distribution of site effects in the town. Chapter 8 is a detailed analysis of water supply pipeline damage data using GIS.

6.1 Tectonics and seismicity

Düzce is located in one of the most tectonically active regions of Turkey. The tectonic setting of the area covered by Figure 6.1 is illustrated in Figure 6.2. Both the Kocaeli and Düzce earthquakes occurred in a region dominated by the North Anatolian Fault. This fault forms the northern boundary of the Anatolian Plate, which is being squeezed westwards by the collision of the northward moving Arabian Plate with the relatively stable Eurasian Plate. GPS measurements have shown this motion to be at the rate of about 25 mm per year (Jackson, 2001).

The North Anatolian Fault is a right lateral strike-slip fault which stretches over 1000 km from west of the Marmara Sea to its junction with the East Anatolian Fault near the town of Karliova in the east. A detailed 1:1,000,000 scale fault map for the whole of Turkey has been compiled by the Turkish Mineral Research and Exploration General Directorate (MTA) (Saroglu *et al*., 1992). The

structure and kinematics of the North Anatolian Fault zone in the vicinity of Düzce have been described in detail by Neugebauer (1995). The fault passes Düzce approximately 30 km to its south, near Lake Abant (Figure 6.3). In this locality, the fault branches into two, with the main strand extending to the northwest to Lake Sapanca (near Adapazari) and then westwards to the Marmara Sea. The southern branch (no. 2 in Figure 6.3) passes near Geyve and to the south of Lake Iznik, also meeting the Marmara Sea in the west.

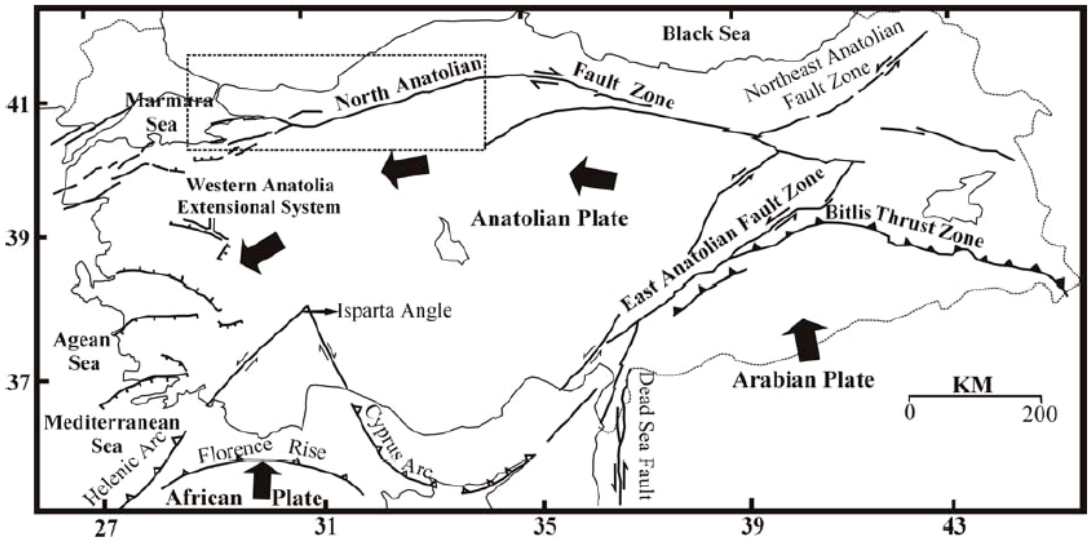

Figure 6.2 Key tectonic features of Turkey (from Utkucu *et al.*, 2003). The boxed region is approximately that shown in Figure 6.1. Thick black arrows show relative plate motions.

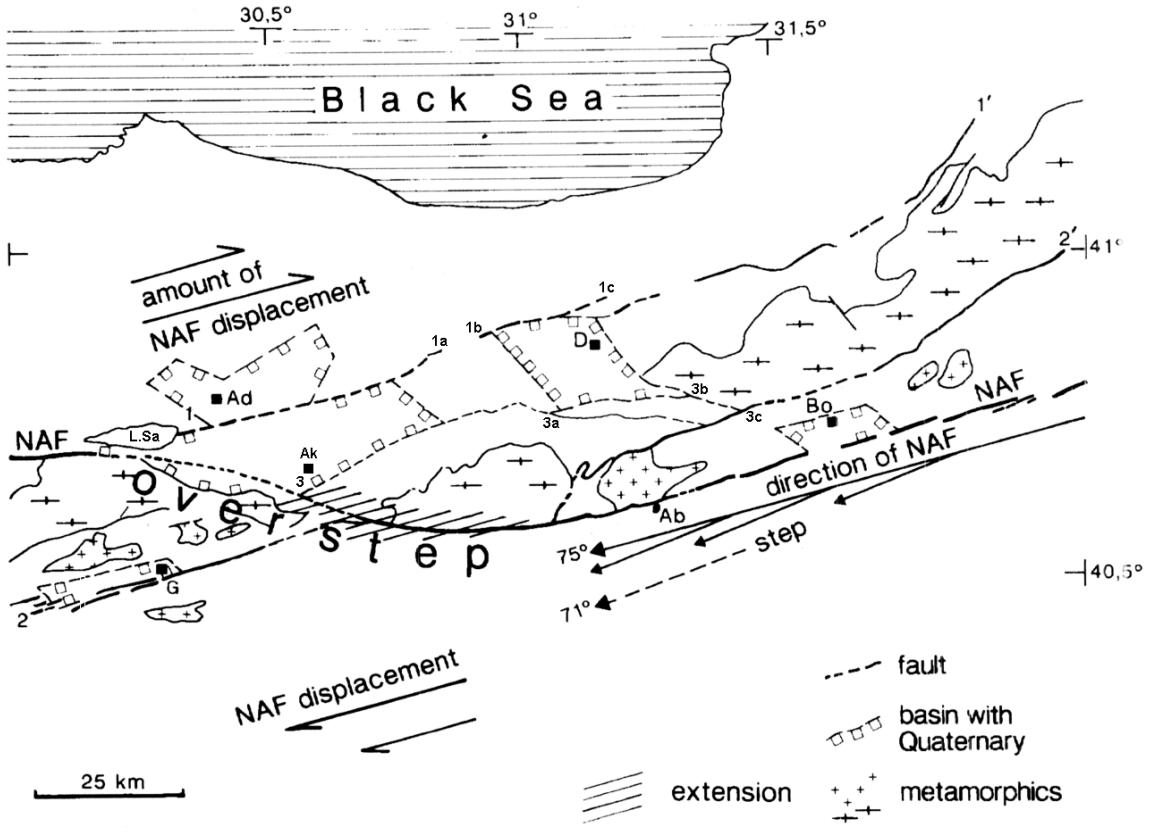

Figure 6.3 Course of the North Anatolian Fault (NAF) in the vicinity of Düzce (D) (Neugebauer, 1995). Ab – Lake Abant; Ad – Adapazari; Ak – Akyazi; Bo – Bolu; G – Geyve; La.S – Lake Sapanca. Numbered fault sections are explained in the text.

The portion of the North Anatolian Fault shown in Figure 6.3 forms a 30 km wide and 70 km long overstep to another, older fault zone (1-1' in Figure 6.3), which includes the Hendek fault (1-1a), stretching some 50 km NE from Lake Sapanca and the shorter Cilimli fault (1b-1c) which marks the northern boundary of the Düzce basin (Aydan *et al.*, 2000).

The Düzce fault (3-3a-3b-3c), activated by the 12/11/1999 earthquake, extends eastwards some 70km from the main branch of the North Anatolian Fault near Akyazi. The fault forms a morphological boundary along the south of the Düzce plain (3a-3b), having its terminus near the village of Kaynasli, to the southeast of Düzce town. The Hendek and Düzce faults are right lateral strike-slip. The morphology of the Cilimli fault also suggests strike-slip characteristics (Aydan *et al.*, 2000).

A recent seismic hazard map for Turkey (published before 1999) shows Düzce's location well-within the highest hazard zone (Figure 6.4). A 100 km width Level I hazard band flanks the North Anatolian Fault for its whole length, which also includes the region of the Kocaeli earthquake.

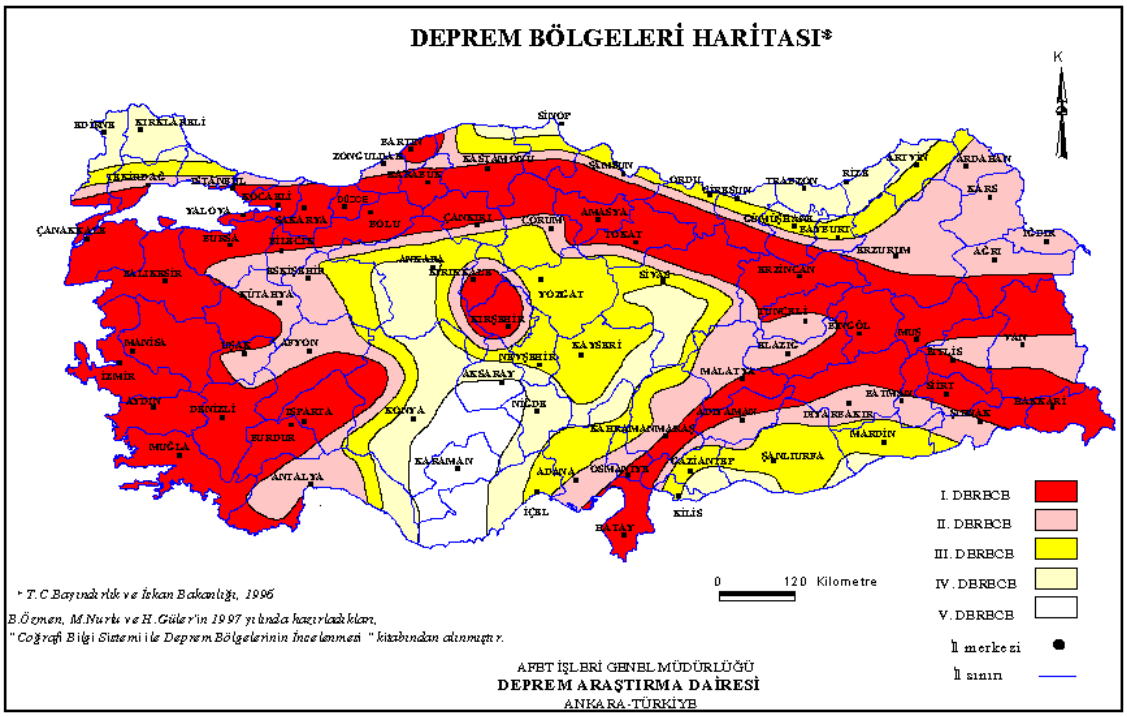

Figure 6.4 Turkey seismic hazard map (http://www.deprem.gov.tr/linkhart.htm). Level I (red) represents the highest hazard whilst level IV (white) represents the lowest hazard.

There have been several large and damaging earthquakes in the Düzce region over the last century. Ambraseys (1988) presents a comprehensive catalogue of events having a magnitude M_s greater than 5.8 for the whole of Turkey from 1899 to 1986. He also includes a number of other smaller events chosen for their importance in location and effects. A sub-catalogue of Ambraseys (1988) is presented in Table 6.1. These are all of the earthquakes occurring within 200 km (latitude and longitude) of the centre of Düzce (here taken as 40.846° N, 31.186° E, the coordinates of the

strong-motion station DZC, from field GPS measurements). This is effectively a rectangular area defined by the limits 39.045 – 42.647° N and 28.815 – 33.557° E. Earthquakes from 1986 – April 2003 have been added from the USGS NEIC online catalogue (http://neic.usgs.gov/) and checked against Ambraseys' recent (2001) reappraisal of significant earthquakes in the Eastern Mediterranean and Middle-East. There were no additional events from Ambraseys (2001). The NEIC search covered all earthquakes with magnitude $M_s > 5.0$ within the specified region and time period. An additional smaller magnitude earthquake, event no. 22 was added due to its proximity to Düzce. Epicentral coordinates and magnitudes for the Kocaeli and Düzce events (Events 18 and 20) are taken from Chapter 5 of the current study. Rupture characteristics for events 18 & 20 are taken from Awata *et al.* (2000), Omer *et al*. (2000) and Ayhan *et al.* (2001). Casualty and damage statistics are taken from Bagci *et al.* (1991) and OECD (2000). The distribution of earthquakes listed in Table 6.1 is illustrated in Figure 6.5.

Most of the significant earthquakes affecting Düzce have been strike-slip events associated with the North Anatolian Fault zone. Six of the earthquakes catalogued in Table 6.1 have been highlighted in bold due to their significance for the town of Düzce. These are the events which are known to have produced macroseismic intensity (MSK) of at least VI in the immediate vicinity of Düzce. For the events taken from Ambraseys (1988), values of I_{Duzce} were obtained from small-scale intensity maps with no distinction between higher values of intensity. Values of I_{Duzce} for these events could therefore have been significantly greater than VI.

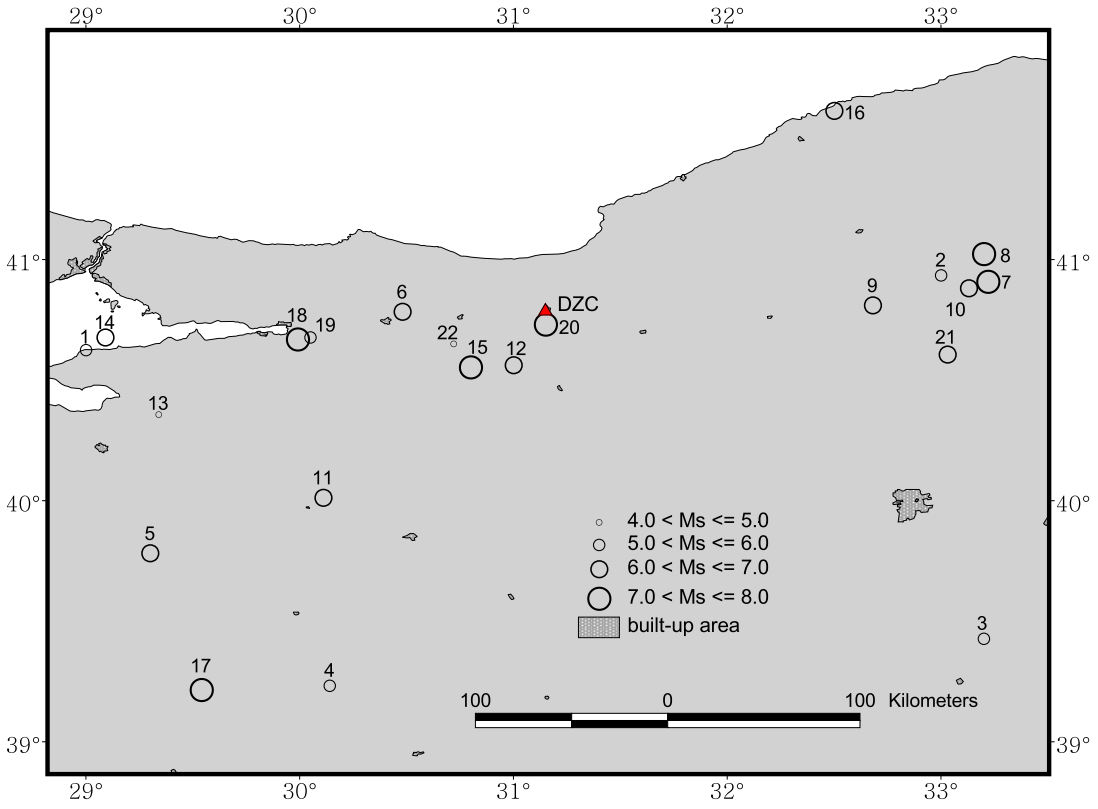

Figure 6.5 Major earthquakes within 200 km of DZC strong-motion station, 1899 - 2003. See Table 6.1 for event identification.

Table 6.1 Catalogue of significant earthquakes near Düzce 1899 – 2003.

Event ID	Origin time		Epicentral Coordinates (Decimal degrees)		M_s	I_0	I_{duzce}	L_{rup} (km)	D_{max} (mm)	$\overline{D}$ (mm)	F	Location	No. of deaths	No. of injured	No. of heavily damaged bdgs
	Date	Time (UTC) hh:mm	N	E											
1	26-May-1903	06:09	40.65	29.00	5.9	VI	-	-	-	-	-	Marmara	-	-	-
2	09-Jun-1919	07:14	41.00	33.00	5.9	VIII	-	-	-	-	-	Çerkeş	-	-	-
3	26-Sep-1921	09:26	39.30	33.20	5.9	VIII	-	-	-	-	-	Argithani	-	-	-
4	20-Nov-1924	20:28	39.08	30.14	6.0	VII	-	-	-	-	-	Altintaş	-	-	-
5	02-May-1928	21:55	39.70	29.30	6.2	VIII	<IV	-	-	-	-	Emet	-	-	-
6	**20-Jun-1943**	**15:33**	**40.83**	**30.48**	**6.4**	**VIII**	**min VI**	**-**	**-**	**-**	**S**	**Hendek**	**336**	**-**	**2240**
7	26-Nov-1943	22:21	40.97	33.22	7.3	IX	IV	265	150	57	SR	Ilgaz	2824	-	25000
8	**01-Feb-1944**	**03:23**	**41.10**	**33.20**	**7.3**	**X**	**min VI**	**175**	**350**	**180**	**SR**	**Bolu-Gerede**	**3959**	**-**	**20865**
9	13-Aug-1951	18:33	40.86	32.68	6.9	IX	IV	62	50	-	SR	Gerede	52	208	3354
10	07-Sep-1953	03:59	40.94	33.13	6.1	VII	-	-	-	-	-	Çerkeş	2	-	230
11	20-Feb-1956	20:32	39.96	30.11	6.1	VIII	IV	-	-	-	-	Söğüt	2	-	1219
12	**26-May-1957**	**06:33**	**40.58**	**31.00**	**7.0**	**X**	**min VI**	**40**	**165**	**55**	**SR**	**Abant**	**52**	**100**	**4201**
13	02-Apr-1959	04:34	40.35	29.34	4.7	VII	-	-	-	-	-	Gölçük	-	-	-
14	18-Sep-1963	16:58	40.71	29.09	6.4	VIII	IV	-	-	-	-	Yalova	1	26	230
15	**22-Jul-1967**	**16:57**	**40.57**	**30.80**	**7.1**	**X**	**min VI**	**80**	**260**	**90**	**SR**	**Mudurnu**	**89**	**235**	**5569**
16	03-Sep-1968	08:20	41.77	32.50	6.5	VIII	-	-	-	-	S	Bartin	29	231	2073
17	28-Mar-1970	21:02	39.06	29.54	7.1	IX	IV	39	225	53	N	Gediz	1086	1260	9452
18	**17-Aug-1999**	**00:01**	**40.70**	**29.99**	**7.8**	**X**	**VIII-IX**	**140**	**500**	**-**	**SR**	**Kocaeli**	**17480**	**43950**	**213840**
19	13-Sep-1999	11:55	40.71	30.05	5.8	-	-	-	-	-	-	Kocaeli (aftershock)	-	-	-
20	**12-Nov-1999**	**16:57**	**40.77**	**31.15**	**7.3**	**IX**	**IX**	**43**	**530**	**376**	**SR**	**Düzce**	**900**	**4950**	**97850**
21	06-Jun-2000	02:41	40.63	33.03	6.1	-	-	-	-	-	SL	Orta	-	-	-
22	23-Aug-2000	13:41	40.68	30.72	4.9	-	-	-	-	-	-	Hendek	-	-	-

Notes: Data are from Ambraseys (1988) unless otherwise specified in the text. M_s – surface-wave magnitude; I_0 – epicentral intensity (MSK); I_{Duzce} – approximate intensity (MSK) in Düzce; L_{rup} - length of fault break associated with earthquake; D_{max} - maximum observed relative displacement on fault (resultant of horizontal and vertical motion); $\overline{D}$ – average displacement along rupture length; F - type of faulting: S - strike slip, SR - Right lateral strike slip, SL – Left lateral strike slip, N - normal slip. A hyphen indicates data unavailable.

The 1943 Hendek earthquake (event no. 6) caused heavy damage in the region between Adapazari, Hendek, Akyazi and Arifiye, destroying over 2000 buildings and causing over 300 deaths.

Event numbers 7 and 8 were the two largest pre-1999 earthquakes to occur in the study area, both having magnitudes M_s = 7.3. Although the epicentres were very close to each other, their effects in Düzce were very different due to the direction of fault-rupture. Event no. 7, the Ilgaz-Ladik earthquake was associated with a 265 km-long fault-break extending from the epicentre eastwards, causing huge damage to buildings and loss of life in this area. The intensity in Düzce was only around IV. The epicentre of the 1944 Bolu-Gerede earthquake (event no. 8) was towards the eastern limit of the fault rupture. This earthquake was associated with a 175 km surface-break along the North Anatolian Fault. Many villages within a 200 km-long and 25 km-wide zone spreading from Ilgaz through Bolu to Abant were completely destroyed. Casualties reached almost 4000 and upwards of 20000 buildings were heavily damaged or destroyed. The damage in Düzce was worsened by a significant aftershock centred on the town.

Faulting during the M_s 7.0 1957 Abant earthquake (event no. 12) began where surface-rupturing ended in the 1944 Bolu-Gerede event. The Abant earthquake was associated with 40 km of surface rupturing along the Elmacik and Mudurnu River valleys, causing numerous landslides.

The M_s 7.1 1967 Mudurnu earthquake (event no. 15) was the result of an 80 km-long rupture that overlapped the fault zone associated with the Abant earthquake. Almost 6000 houses were damaged or destroyed and nearly 100 people were killed.

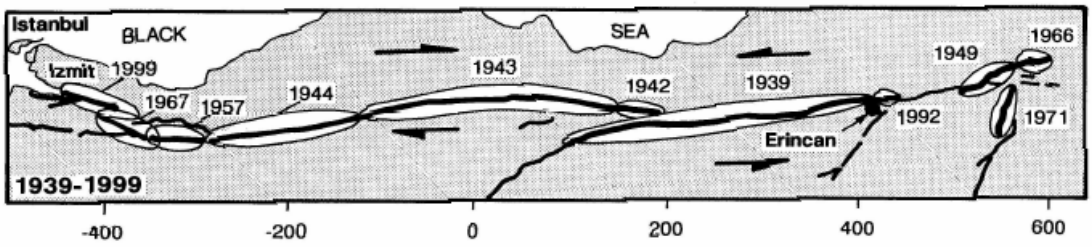

Figure 6.6 Sequence of major earthquakes occurring along the North Anatolian Fault zone between 1939 and 1999 (Jackson, 2001).

Events 7, 8, 12 and 15 in 1943, 1944, 1957 and 1967 respectively represent a westward progression of large earthquakes along the North Anatolian Fault. This pattern, which started with the 1939 Erzincan and 1942 Erbaa-Niksar earthquakes, has been interpreted as being the result of stress transfer to adjacent portions of the Fault following stress release along a given ruptured segment (Stein *et al.*, 1997). The migration of earthquakes westward continued in 1999 with the Kocaeli (Izmit) earthquake. Figure 6.6 shows the sequence of earthquakes between 1939 and August 1999.

Toda *et al.* (1999) used the methodology of Stein *et al.* (1997) to compute the stress state induced by the Kocaeli earthquake and concluded that the Düzce earthquake three months later was a consequence of stress triggering. Whether the 1999 events could have been predicted based upon a stress-transfer model or another GPS-based technique (Aydan *et al*., 2000) is currently the topic of

much discussion. This issue is made even more important because of the proximity of Istanbul to the current western limit of recent fault rupture. Parsons *et al*. (2000) argue, based on stress transfer theory, that the progress westward of faulting on the NAF implies heightened probabilities for earthquakes to the west of Kocaeli, in the Sea of Marmara. However, Bommer *et al*. (2002) question whether the earthquake catalogue upon which Parsons *et al.* (2000) base their research is sufficiently complete or reliable to assign heightened probabilities to earthquakes in this region.

6.2 Geological setting

Düzce is located in a basin which developed under the control of the North Anatolian Fault beginning at the end of the Miocene. The movement responsible for this is accommodated in the overstep illustrated in Figure 6.3 between Lake Sapanca in the west and Abant in the east. The amount and direction of displacement on this portion of the Fault since the Miocene is indicated and is of the order of 30 km.

A detailed geological map of the Düzce basin is shown in Figure 6.7. The following description is based mainly on Simsek & Dalgic (1997) but has supplemental details from Aydan *et al.* (2000) and an unpublished 1:50000 geological map obtained from Düzce Municipality.

6.2.1 Basement lithology

The oldest rocks in the area are the Dirgine Granotoids, which outcrop to the south of Düzce town along the Düzce fault near the village of Beykoy. These consist of metagranite and granodiorite of Paleozoic or Precambrian origin. This unit forms the basement of the plain in its southern part. To the north, the basement consists of the Eregli formation, silicatic shale, sandstones and siltstone alternations of Devonian origin. These are nonconformably overlain by the Cretaceous Akveren formation consisting of conglomerate, sandstone, clayey limestone and marl alternations. These outcrop to the east of the town. To the southwest are Dikmen volcanites, comprising of andesite, spilite and agglomerates. More recent, Tertiary features are observed to the north and northwest: the Kusuri formation that consists of sandstone-mudstone, agglomerate and pyroclastics. All of these units are covered by the Quaternary age Orencik formation, which is composed of loosely-cemented, subrounded, well sorted pebble-sands and silts.

6.2.2 Alluvial deposits

The Quaternary alluvial deposits which fill the basin are classified into three groups:

a. River alluviums (Qal1)

The Buyukmelen, Kucukmelen, Asarsuyu and Ugursuyu rivers deposit materials of various sizes as they pour into the plain. These alluvia are well sorted, rounded, oriented and highly resistant, consisting of sand-pebble and blocks mainly derived from limestone and magmatic rocks.

Examples of such deposits are the alluvial fans formed by the Kucukmelen and Ugursuyu rivers to the north and south of Düzce respectively. Fine-grained pebble, sand, silt and deposits consisting of thinly bedded clay alternations are observed in river beds as they meander across the plain.

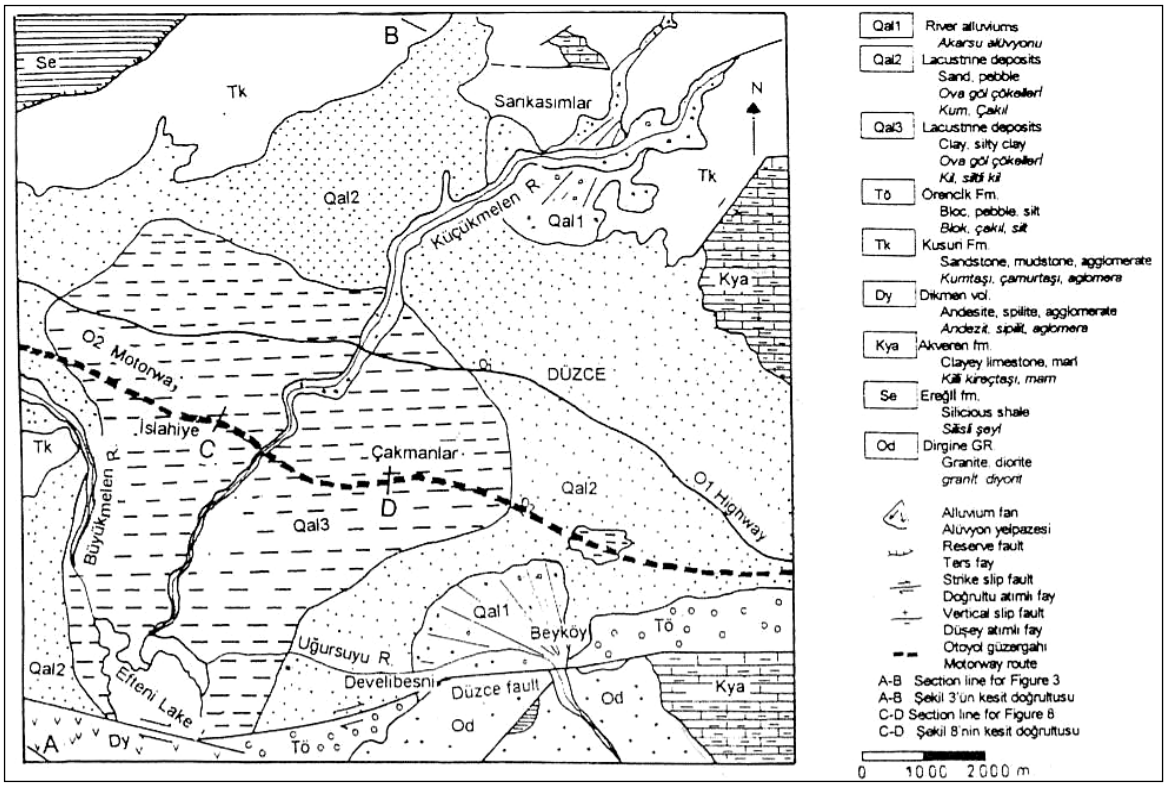

Figure 6.7 Geological map of Düzce and its environs (Simsek & Dalgic, 1997)

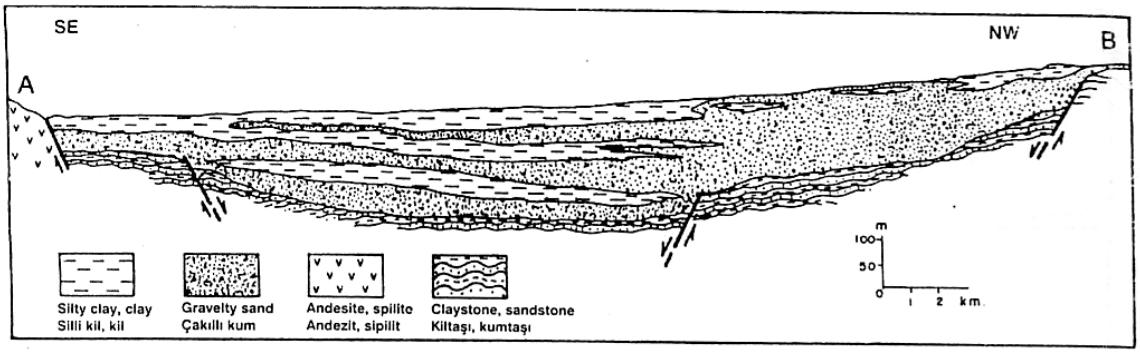

Figure 6.8 Geological section A-B through the Düzce basin (Simsek & Dalgic, 1997)

b. Lacustrine deposits (sand-pebble levels: Qal2)

The Qal2 unit dominates the basin to the north, northeast and east, covering the majority of the town of Düzce. These deposits are generally brown to grey coloured and mostly composed of clayey-silty sand and pebble levels.

c. Lacustrine deposits (clay, silty clay and clayey silt levels: Qal3)

To the south west of Düzce, the basin is dominated by clay, silty clay, clayey silt and sandy silt layers containing a significant amount of shell fragments. This unit, Qal3, changes colour from brown at the surface to grey at the base.

A geological profile (A-B in Figure 6.7) across the basin, extending northeast from near Efteni Lake, is shown in Figure 6.8. The clay layers in this area are up to 40 m thick, whilst the basin depth is over 250 m. The variation of alluvium thickness across the Düzce basin is presented in Chapters 7 and 8.

6.3 Earthquake source characteristics and faulting

Earthquake source characteristics for the Kocaeli and Düzce earthquakes are summarised in Table 6.2. The data are generally taken from MCEER (2000), which quotes official USGS and KOERI values. Dip value for the Düzce earthquake is from the Harvard Centroid Moment Tensor solution, as reported in Ayhan *et al*. (2001). Epicentres and times are those of ISESD (Ambraseys *et al.*, 2002).

Table 6.2 Summary of earthquake source characteristics for the Kocaeli and Düzce earthquakes

	Kocaeli	Düzce
Origin time (UTC)	17 August 1999 00:01:39	12 November 1999 16:57:20
Origin time (local)	3 am	8 pm
Epicentral coordinates	40.702°N 29.987°E	40.768°N 31.148°W
Focal depth	17 km	14 km
Surface-wave magnitude, M_s	7.8	7.3
Body-wave magnitude, m_b	6.3	6.5
Moment magnitude, M_w	7.4	7.1
Seismic moment, M_0	1.4×10^{20} Nm	4.5×10^{19} Nm
Fault mechanism	Right lateral strike-slip	Right lateral strike-slip
Strike, φ_s	91°	276°
Dip, δ_f	76°	54°
Rake, λ_f	179°	-167°

6.3.1 17 August 1999 Kocaeli earthquake

The Kocaeli earthquake was associated with a surface rupture of approximately 140 km of the North Anatolian Fault, extending from Yalova in the west to Lake Eften in the east. Awata *et al.* (2000) divided the surface breaks into eight sections based on geometry and slip characteristics (Figure 6.9).

The westernmost strand, the Taskopru section (labelled A in Figure 6.9), intersected the Catol Peninsula about 10 km east of Yalova. This was an E-W striking, normal-right-oblique rupture which extended for about 3 km, with a maximum displacement of only 0.24 m. The next ruptured segment was not observed until almost 40 km to the east, along the shoreline of Golcuk. No rupture appeared on the intervening Helsek Peninsula.

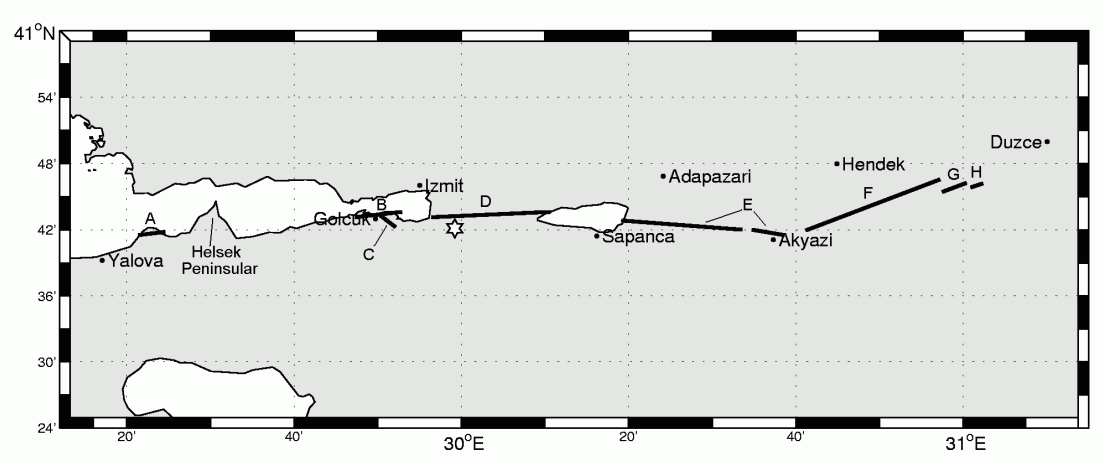

Figure 6.9 Surface fault rupture associated with the 17/08/1999 Kocaeli earthquake. The epicentre is shown as a star. Rupture segments are indicated by letters A-H (described in the text).

The Golcuk section (B), trending E-W, exhibited right-lateral displacement of over 4 m. Part of this strike-slip fault transferred into the N70°W trending normal-right-oblique Kazikli section (C). This 4-5 km segment was responsible for regional subsidence in the Golcuk area of up to 3 m, causing flooding of 4 km of coastline along Izmit Bay.

The rupture continued from the eastern shore of Izmit Bay to the northwest shore of Lake Sapanca (the Tepatarla section - D), a distance of almost 20 km. Right-lateral displacement along this portion was uniformly 2.9 m ± 0.5 m.

Projection of the fault trace though Lake Sapanca requires a right overstep of approximately 2 km to the Arifiye section (E) on the eastern shore (USGS, 1999). This segment then extends 27 km to the town of Akyazi. The ESE-trending fault exhibited right-lateral displacements of up to 4.9 m in the west, reducing gradually to 0.35 m in the east. The rupture then steps to the left for a 5 km strand with right-lateral displacements between 0.2 – 0.55 m. The Arifiye section forms a right overstep between the Kocaeli 1999 rupture and the western portion of fault that broke during the 1967 Mudurnu Valley earthquake.

The Karadere section (F) follows the ENE-trending Düzce fault for a length of 11 km, having predominantly right-lateral displacement of 0.8 – 1.65 m, with a maximum of 2.1 m. The fault had a significant vertical component of between 0.15 and 0.55 m, south side downthrown. The Karadere and Arifiye sections are separated by a 6 km gap.

Following the surface breaks away from the epicentre, the 8-km long Aksu section (G) forms a 0.5 km-wide right overstep with the Karadere section. This is an ENE-trending right-lateral fault with a strike slip of between 1 and 1.7 m and a vertical component of up to 0.3 m.

The Golyaka section (H) marks the termination of surface faulting to the east. This final strand extended almost as far as Lake Eften and had right-lateral displacements of 0.3 m, with a vertical movement of 0.15 m (north side down).

Additional surface ruptures were observed near to the eight main sections described, details of which can be found in Awata *et al.* (2000) and USGS (2000).

The rupture process of the Kocaeli earthquake was shown from joint inversion of near-field strong-motion data and teleseismic body wave data to be asymmetric and bilateral (Yagi & Kikuchi, 2000). The first rupture propagated upward and westward from the hypocentre, followed by a second, much more extensive rupture which propagated to the east.

Aftershocks continued 50 km beyond the Hersek Peninsular (Wright *et al.*, 2001), considerably further than the observed surface rupture. This may indicate the activation of faulting into the Sea of Marmara although the extent of aftershocks does not necessarily coincide with the extent of coseismic rupture (Yagi & Kikuchi, 2000).

6.3.2 12 November 1999 Düzce earthquake

The Düzce fault consists of three distinct segments (Saroglu *et al.*, 1992). Two of these, the Karadere and Golyaka segments, which form the western half of the fault, ruptured during the Kocaeli earthquake, as described in the previous section. The 12/11/1999 event occurred mainly along the eastern half of the Düzce fault, the Beykoy segment, but also involved rupturing of the Golyaka segment, forming a 5 km overlap with the 17/08/1999 rupture. The total rupture length involved in the Düzce earthquake was 43 km, from Golyaka in the west to Kaynasli in the east. A detailed map of surface faulting, including slip distribution is given in Figure 6.10 (after Omer *et al.*, 2000).

The 5 km long Golyaka segment trends N80°E. In the Lake Eften region, rupturing extended N65°W for a length of 6.5 km. A bifurcation approximately half way along aligns with the main Beykoy segment, trending ENE-WSW. Omer *et al.* (2000) identify four sub-segments within the 32 km long Beykoy segment, named Aydinpinar, Dagdibi, Kaynasli and Asarsuyu, from west to east. The first three sub-segments overlap each other, forming left oversteps. At the first of these oversteps, in the region of Beykoy, the rupture zone has a width of over 800 m, details of which are shown separately in the insert in Figure 6.10. The right-stepping 4 km long Asarsuyu sub-segment marks the eastern terminus of surface faulting.

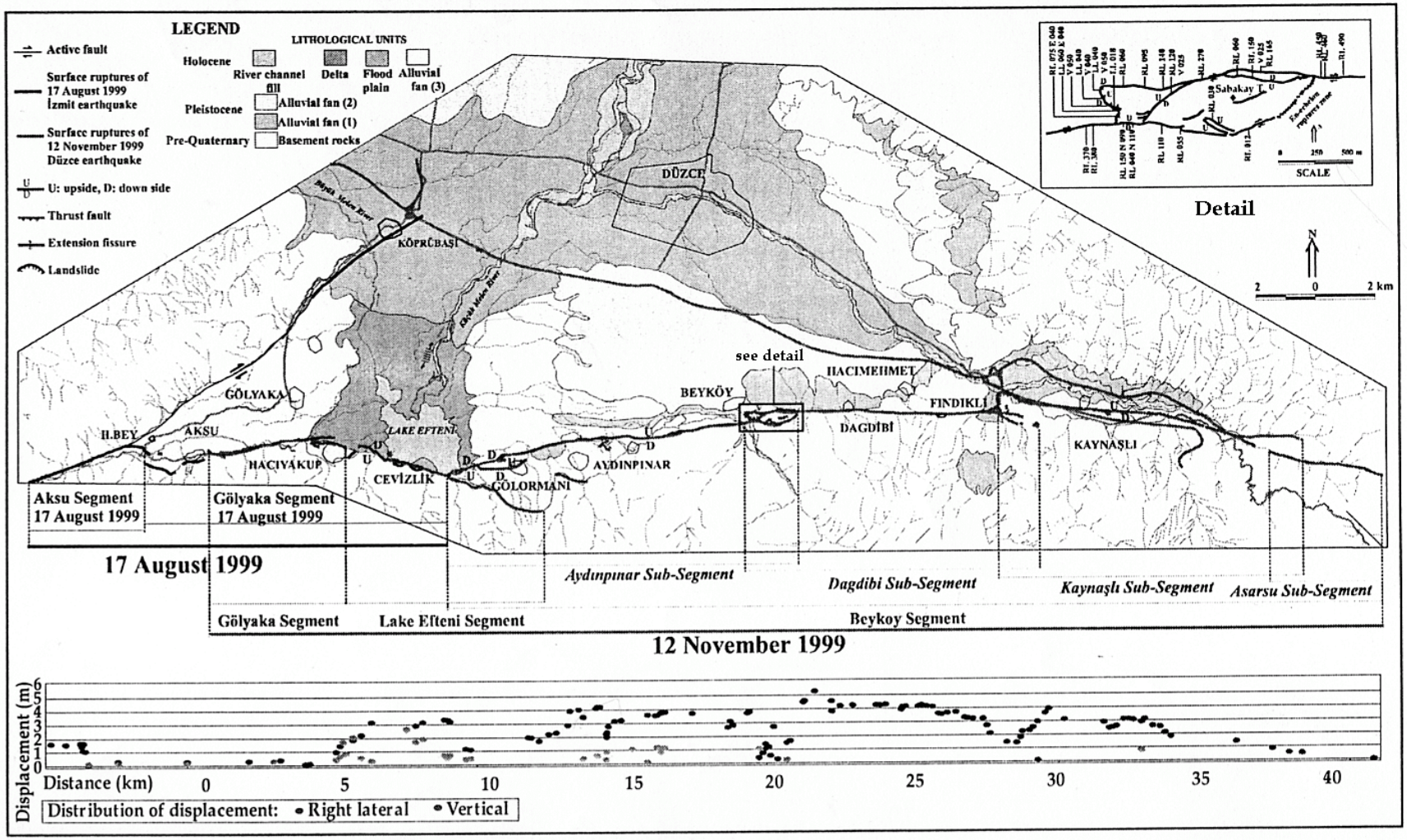

Figure 6.10 Map of faulting and slip distribution associated with the 12/11/1999 Düzce earthquake (Omer *et al.*, 2000)

Slip distribution along the 12/11/1999 rupture is indicated beneath the map in Figure 6.10. The dominant sense of movement was right-lateral strike–slip over the whole length of the fault. However, in the Lake Eften region, the maximum dip slip (2.6 m) is comparable to the maximum strike slip (3.1 m). Greatest slip was observed along the Dagdibi sub-segment, with mean and maximum values of 4.5 and 5.3 m respectively. The Aydinpinar sub-segment exhibited an average slip of 3.5 m and a maximum slip of 4.2 m. Displacement was also large on the Kaynasli sub-segment, with values of up to 3.6 m in the west, reducing to 0.5 m in the east. The Golyaka and Asarsuyu segments, representing the western and eastern limits of fault rupture, exhibited displacements of 0.4 m and 0.5 m respectively.

The Düzce earthquake has the highest slip-to-rupture-length ratio of any historic earthquake along the North Anatolian fault (Ayhan *et al.,* 2001). Ayhan *et al.* (2001) suggest that this is evidence that the Düzce earthquake was effectively part of a composite rupture with the preceding Kocaeli event, with a combined rupture length of around 160 km.

Investigators of the rupture process agree that the Düzce earthquake nucleated near the bottom centre of a northward dipping fault and propagated bilaterally east and west (Yagi & Kikuchi, 1999; Ayhan *et al.*, 2001; Tibi *et al.*, 2001). Tibi *et al.* (2001) calculate rupture duration to be about 14 s, which compares to about 25 s for the Kocaeli main shock.

6.4 Strong-motion data and macroseismic intensity

As explained in Chapters 2 and 3, the nature of strong ground-shaking is influenced by the relative proportions of body and surface waves present at any particular location. Empirical formulae (Equations 2.2 and 2.3) give conditions for the domination of surface waves according to the ratio of epicentral distance to focal depth, d_e/h. Data from the 1999 earthquakes (Table 6.3) suggest that the strong motion at DZC was dominated by surface waves during the Kocaeli earthquake and body waves during the Düzce event.

Table 6.3 Ratio of epicentral distance to focal depth at DZC for the Kocaeli and Düzce earthquakes. Surface waves are likely to dominate strong-motion at $d_e/h > 1.5$ (Equation 2.2).

Earthquake	d_e (km)	h (km)	d_e/h
Kocaeli, 17/8/1999	101	17	5.9
Düzce, 12/11/1999	9	14	0.6

The Kocaeli and Düzce earthquakes produced at least 30 and 48 strong-motion records respectively (Durukal, 2002). Most of these records originate from the networks of permanent stations operated by ERD, KOERI and ITU. However, some of the Düzce records are the result of aftershock

monitoring observations carried out by teams from Turkey, the USA and France following the Kocaeli event.

Table 6.4 Summary of horizontal strong-motion parameters from records made in the vicinity of Düzce.

EQ	Station comp	d_s [1] [km]	d_f [2] [km]	Soil	PGA [g]	PGV [cm/s]	PGD [cm]	I_a [3] [cm/s]	d_{eff} [4] [s]	T_{eq} [5] [s]	f_{eq} [6] [Hz]
Kocaeli	DZC-NS	0	14	Soft	0.31	41	15	102	10	0.85	1.18
	DZC-EW	0	14	Soft	0.36	54	15	131	9	0.96	1.04
	SKR-NS	66	3	Stiff	-[7]	-[7]	-[7]	-[7]	-[7]	-[7]	-[7]
	SKR-EW	66	3	Stiff	0.38	70	94	166	21	1.18	0.85
Düzce	DZC-NS	0	1	Soft	0.38	37	16	257	12	0.62	1.61
	DZC-EW	0	1	Soft	0.51	84	47	289	12	1.05	0.95
	BOL-NS	40	18	Stiff	0.74	56	26	363	13	0.48	2.08
	BOL-EW	40	18	Stiff	0.81	65	11	238	12	0.51	1.96
	SKR-NS	66	47	Stiff	0.02	5	9	1	0	1.60	0.63
	SKR-EW	66	47	Stiff	0.02	5	6.5	1	0	1.60	0.63

Notes: Station codes are DZC (Düzce), SKR (Sakarya) and BOL (Bolu). 1- distance of station to DZC; 2 - closest distance to surface projection of fault (although station DZC lies directly above the surface projection of the 12/11/1999 rupture, it is assigned a nominal value of d_f = 1 km); 3 - Arias intensity, 4 - effective duration (Bommer & Martinez-Pereira, 1999), 5 – Period of an equivalent harmonic wave, $T_{eq}=2\pi(PGV/PGA)$; 6 - $f_{eq}=1/T_{eq}$; 7 - component not measured due to instrument malfunction.

21 of the Kocaeli records and 16 of the Düzce records were included in the catalogue used to derive predictive relationships for strong-motion peaks in Chapter 5. As shown in Table F1 (Appendix F), this dataset includes four records from the Kocaeli earthquake recorded within 20 km of the surface projection of the fault rupture and two such records from the Düzce earthquake. These give an indication of the characteristics of near-field ground motion for these two events.

The availability of such an extensive set of strong-motion records has stimulated several in-depth studies (eg. Idriss *et al.*, 2000; Durukal, 2002; Sucuoglu, 2002; Gulkan & Kalkan, 2002). The current section focuses on the strong-motion observed in and around the town of Düzce.

A summary of some key strong-motion parameters from the records made nearest to the town of Düzce is given in Table 6.4. Values of PGA, PGV, PGD and I_a are taken from corrected strong-motion time-histories, as presented in Figures 6.12 and 6.13. These records are from the dataset used in Chapter 5. Here, details are given of the strong-motion data correction procedure, along with low frequency cut-offs selected for each record (Appendix G).

The relative locations of stations SKR, DZC and BOL is shown in Figure 6.11, along with the surface fault projection for the 12/11/1999 rupture. Strong-motion data are only available for station BOL for the Düzce earthquake due to instrument malfunction during the Kocaeli event (Menkiti *et al.*, 2000).

Peak parameters for DZC are almost invariably larger for the Düzce earthquake than for the Kocaeli earthquake. This is not unexpected due to closer proximity of fault rupture in the former case. A surprising feature of the data for the 12/11/1999 event is the presence of very high values

of strong-motion from the station at Bolu (BOL), some of which exceed those recorded at DZC, which has a considerably smaller value of d_f. This issue was investigated by a team of engineers and geologists working on a nearby tunnelling project (Menkiti *et al.*, 2000). They document the existence of an additional surface rupture associated with the 12/11/1999 event to the east of the Asarsuyu sub-segment. This section passes to the north of the BOL strong-motion station and continues eastwards to a point approximately 20 km beyond the mapped surface rupturing shown in Figure 6.10. The closest distance from this surface break to BOL is reported as 6 km, which is considerably less than the value of 18 km given in Table 6.4, and slightly less than the distance between DZC and its closest portion of surface break (8 km). This reduced distance value would readily account for the high values of strong-motion parameters associated with the BOL record.

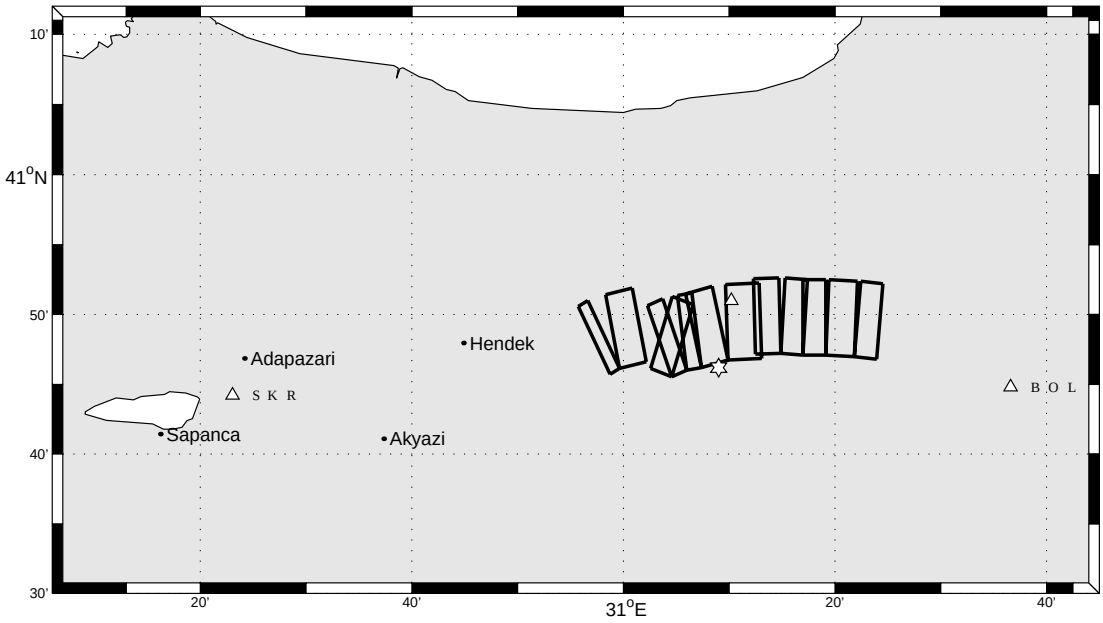

Figure 6.11 Strong-motion stations in the vicinity of Düzce. DZC station, situated in the centre of the town of Düzce, is shown as a triangle north of the 12/11/1999 Düzce earthquake epicentre (star). Black rectangles represent the surface projection of the Düzce fault rupture, based on the source parameters in Table 6.2 and rupture segments described in Section 6.3.2.

Further investigation of the possible extension of the surface fault rupture to the Bolu region is necessary. It is perhaps surprising that this additional segment was not mapped by any other investigators, or at least inferred from aftershock studies. However, the existence of the Bolu rupture segment is supported by the permanent offset obtained following appropriate (Graizer, 1979) processing of the digital BOL strong-motion record. This extended fault could also help explain the unusually large slip-to-rupture-length ratio mentioned by Ayhan *et al.* (2001).

The effective duration of strong-motion at BOL and DZC stations for the 12/11/1999 earthquake (12 -13 s) is comparable to the 14 s rupture duration calculated by Tibi *et al.* (2001). Records from stations closer to the epicentre of the Kocaeli event showed a similar pattern.

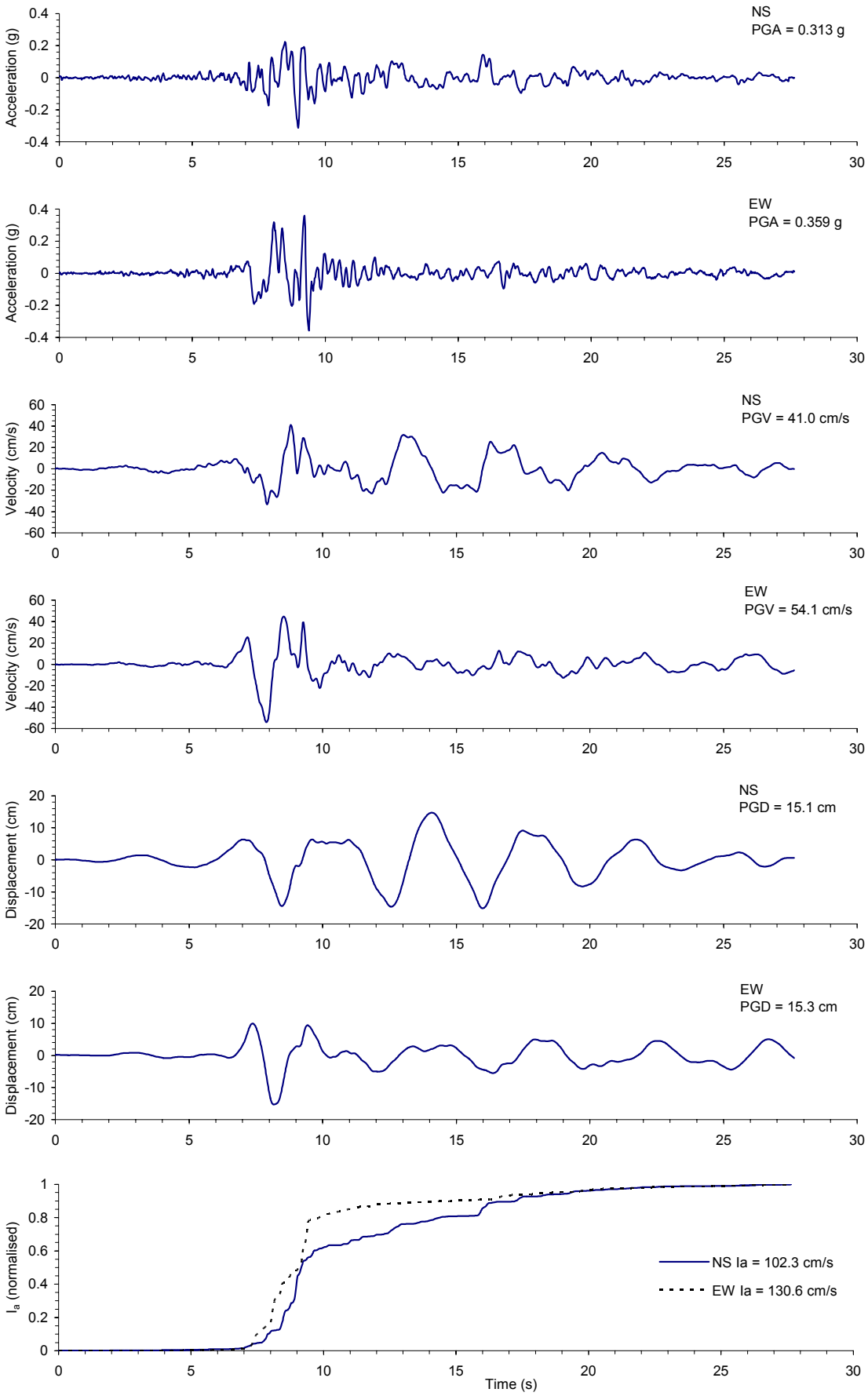

Figure 6.12 Strong-motion time histories recorded at DZC during the Kocaeli earthquake

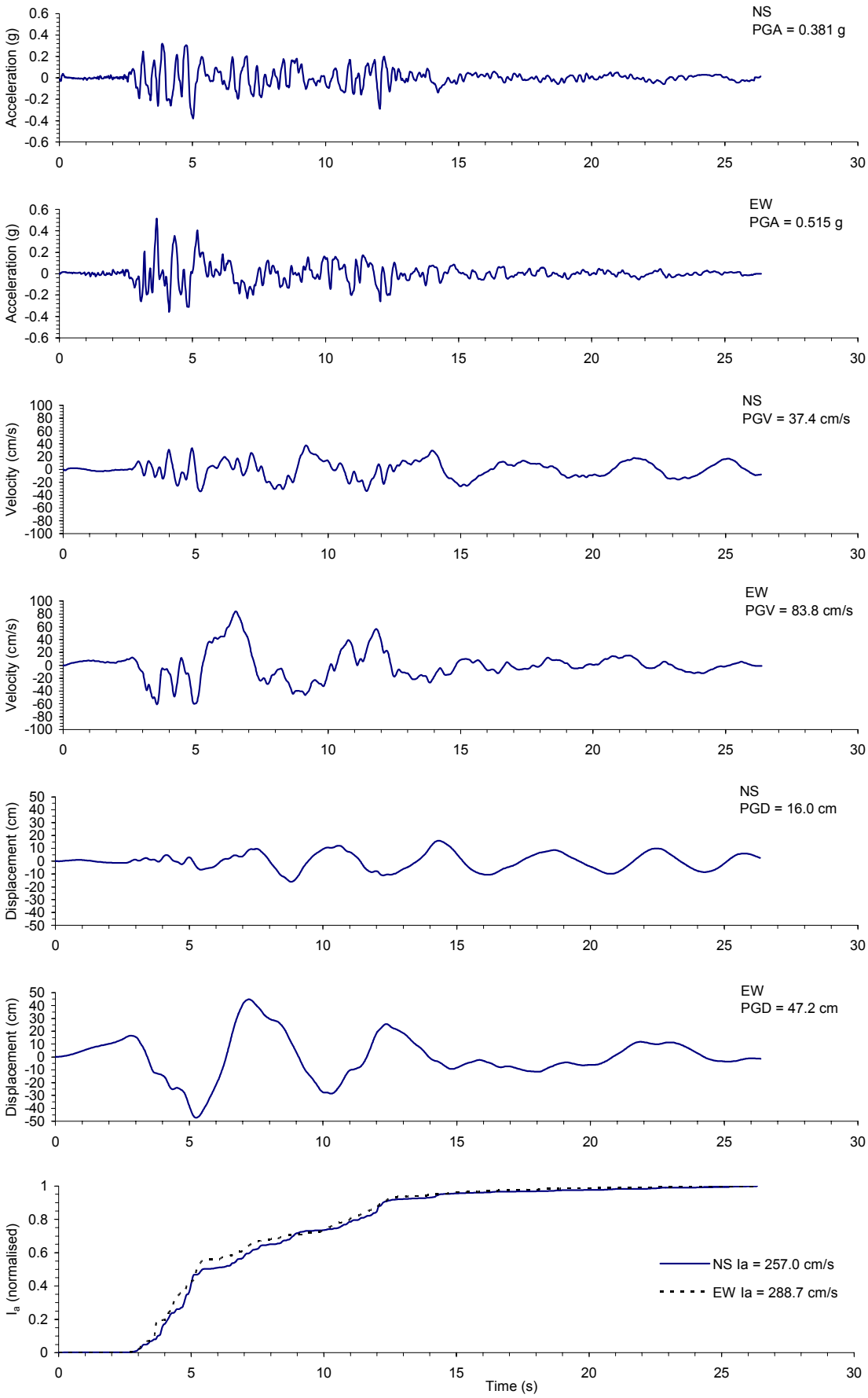

Figure 6.13 Strong-motion time histories recorded at DZC during the Duzce earthquake

The Husid plot (time-history of Arias intensity) for the Düzce earthquake (Figure 6.13) is indicative of bilateral rupture, having two distinct plateaus, evidenced in both fault-normal and fault-parallel plots.

5% damped acceleration response spectra for DZC records from the Kocaeli and Düzce earthquakes are shown in Figure 6.14. Amplitudes associated with records from the Düzce earthquake are generally much larger than those from the Kocaeli event, as would be expected. The presence of significantly more energy between periods of 0.5 and 1 s contributed towards the greater building damage experienced during the Düzce earthquake. This issue is elaborated upon in Chapters 7 and 8.

Both sets of response spectra have common peaks at around 0.4 s. This may indicate a characteristic site response. Another common feature between the two earthquakes is the enhanced response in the EW component at around 1.3s. In the case of the Kocaeli earthquake, this might be partly a consequence of forward directivity effects, considering that about 75 % of the 17/8/1999 fault ruptured towards DZC (Figure 6.9). Comparisons between spectra from near-field stations from the Kocaeli event (eg. Sakarya, Yarimca and Izmit) have confirmed the presence of enhanced long-period motions at DZC (Sucuoglu, 2002). However, amplification at long periods is also indicative of the kind of site conditions encountered at DZC. Both Idriss *et al.* (2000) and Sucuoglu (2002) stress the need for further investigation to separate out these two effects. This issue is addressed in more detail in the context of the investigation into site effects in Chapters 7 and 8.

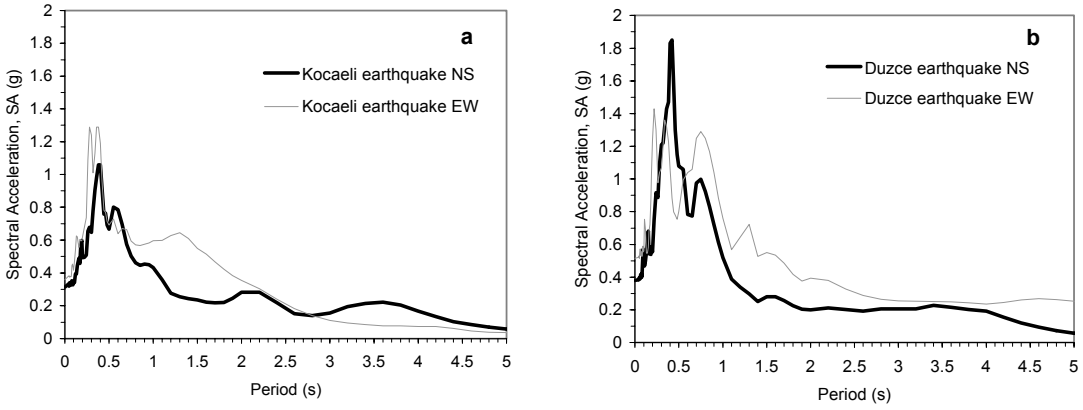

Figure 6.14 5% damped acceleration spectra for a. 17/081999 Kocaeli earthquake and b. 11/12/1999 Düzce earthquake

In Figure 6.15, attenuation characteristics are presented for PGA, PGV and PGD for records drawn from the Chapter 5 study having the same broad site classification type as DZC. There are eight such 'soft-soil' sites from the Kocaeli earthquake and six from the Düzce earthquake. These observed values are compared with predictions from the attenuation relationships derived in Chapter 5. The reasonable agreement is partly due to the fact that these data form a subset of the

dataset used to derive the relationships. However, records from the Kocaeli and Düzce events do not completely dominate the regression, accounting for only 37 out of the total 249 records used. It is notable that the dataset contains an additional 19 records from other Turkish earthquakes.

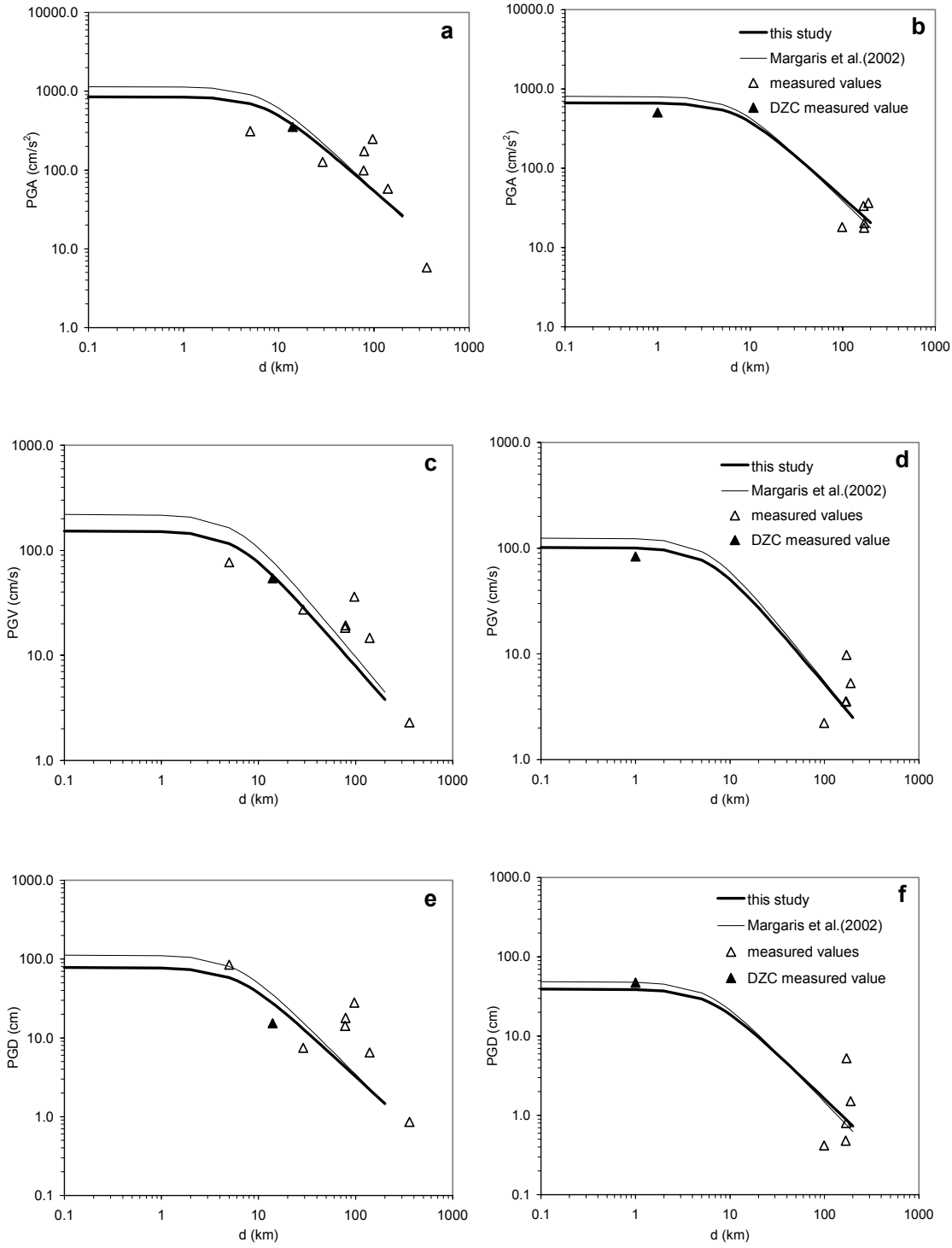

Figure 6.15 Peak strong-motion parameters recorded on soft soil sites compared with predictions from attenuation relations. (a), (c) & (e) show data from the Kocaeli earthquake (M_s 7.8, M_w 7.86); (b), (d) & (f) show data from the Düzce earthquake (M_s 7.3, M_w 7.36). The attenuation relations derived in Chapter 5, 'this study', use M_s whilst values from Margaris *et al*. (2002) are calculated using an equivalent M_w calculated from Ekstrom & Dziewonski (1988).

Figure 6.15 also includes the relationships of Margaris *et al.* (2002). These are the most recent alternative predictive relationships for all three peak strong-motion parameters derived from mainly European data. The relationships of Margaris *et al.* (2002) were derived specifically from data from Greek earthquakes. Gulkan & Kalkan (2002) have recently derived attenuation relationships using solely Turkish data. However, this only covers PGA and 5 percent damped pseudo acceleration response spectra (PSA) and only uses 47 records, over half of which are from the Kocaeli and Düzce earthquakes.

Comparisons between data from the Kocaeli and Düzce earthquakes and North American attenuation relationships have shown over-prediction in the near-field (Idriss *et al.,* 2000; Bommer *et al.,* 2002; Gulkan & Kalkan, 2002). The relationships derived by Gulkan & Kalkan (2002) also seem to indicate that North American relationships underpredict PGA and PSA for Turkey at large distances. As shown in Chapter 5, the attenuation relationships derived for the current study are generally less conservative in the near-field than other relationships, especially for soil sites. This is possibly influenced by the significant number of Turkish records which make up the near-field dataset.

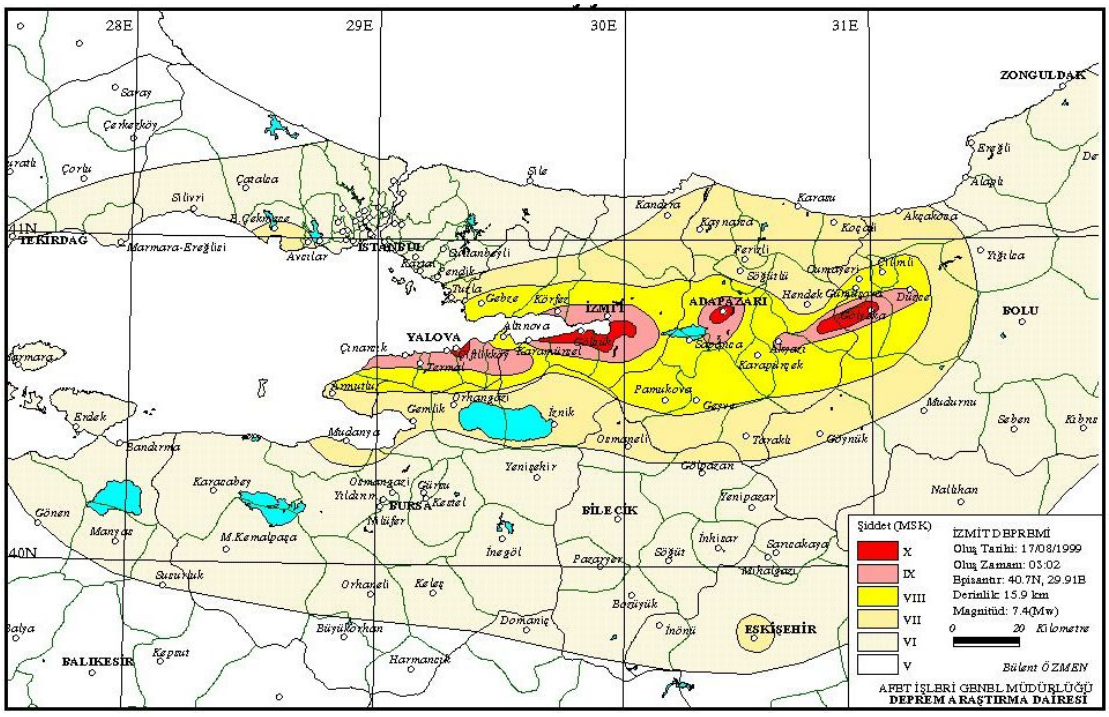

Figure 6.16 Macroseismic intensity for Kocaeli earthquake. Intensity scale shown is MSK (from http://www.deprem.gov.tr/main_e.htm).

A macroseismic intensity map for the Kocaeli earthquake has been published by the Turkish Government and is shown in Figure 6.16; it is based on the MSK intensity scale. The maximum intensity of X was observed in the epicentral area and three additional areas near to observed surface fault ruptures. These are, from west to east, Yalova, Adapazari and Golyaka; Düzce appears on the boundary between intensities VIII and IX.

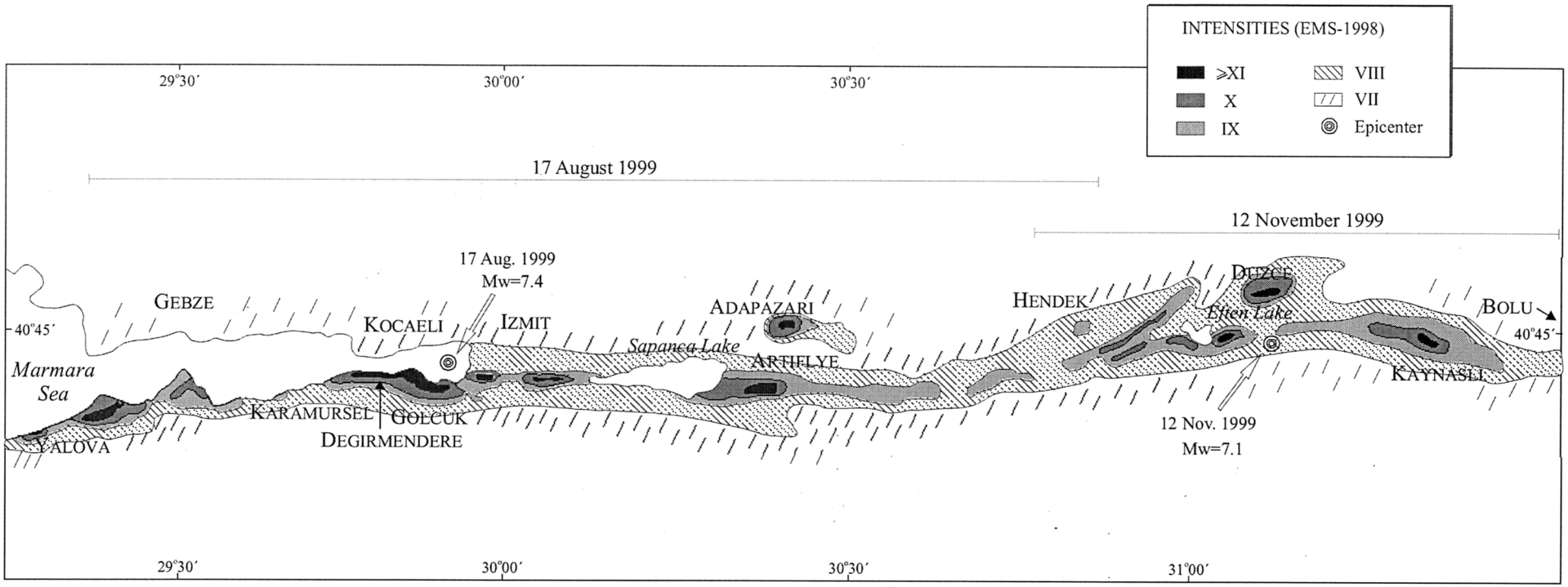

Figure 6.17 Intensity distribution (EMS-98) for the 17/08/1999 Kocaeli and 12/11/1999 Düzce earthquakes (Lekkas, 2000)

No official intensity maps exist for the Düzce earthquake due to the difficulty in distinguishing between the effects of the two events (Durukal, 2002). However, Lekkas (2000) has compiled an intensity distribution for a combination of the Kocaeli and Düzce earthquakes based on the 1998 European Macroseismic Scale, EMS-98 (Grunthal, 1998) (Figure 6.17). During compilation, he tried to separate out the participation of each earthquake in damage manifestation. However, for the region between Adapazari and Düzce, this was not possible. Lekkas' (2000) maximum intensities for the Kocaeli earthquake exceed the official Government figures by as many as two degrees in certain regions whilst his boundary for intensity VIII coincides more closely with the intensity IX boundary of Figure 6.16

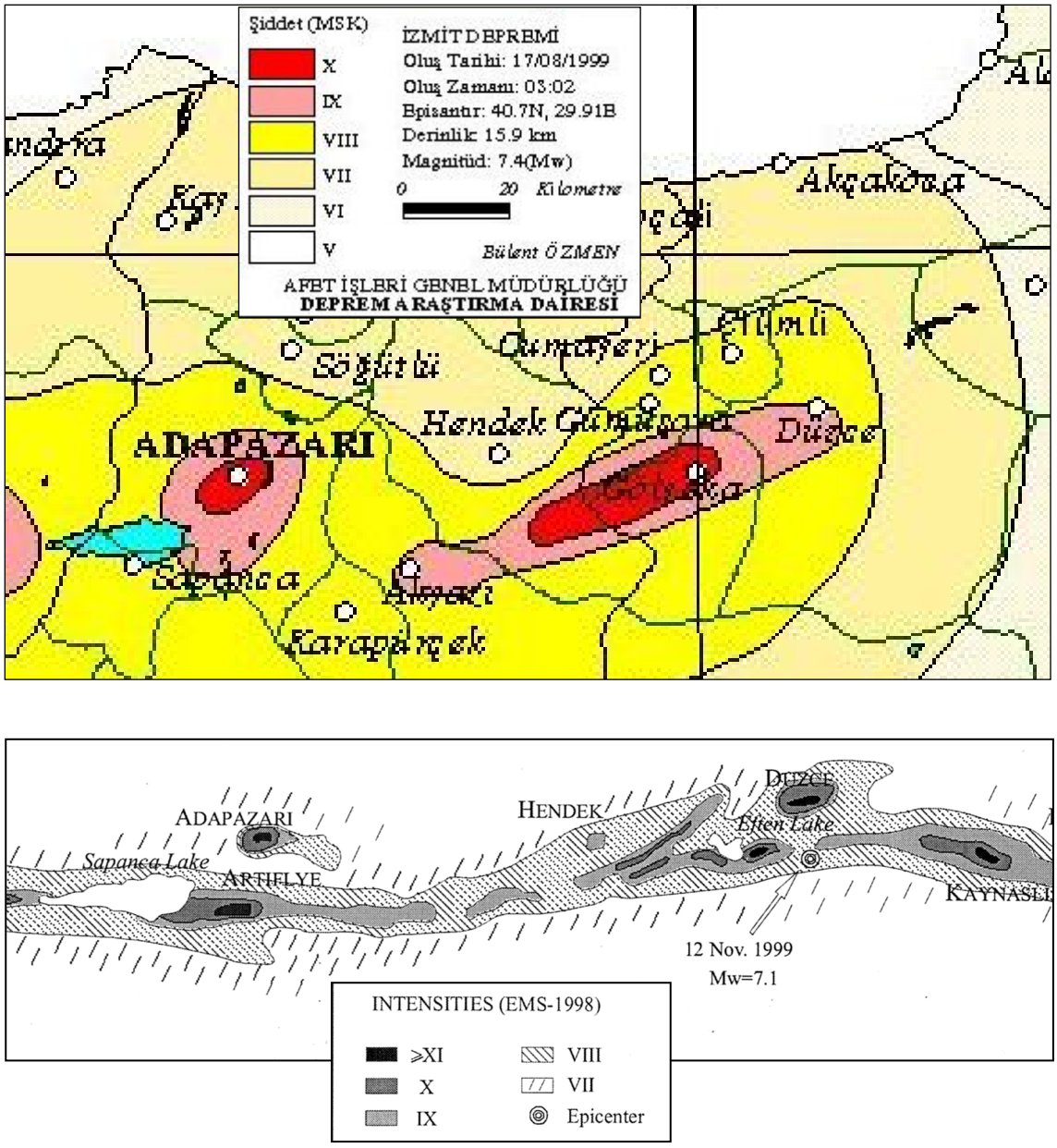

Figure 6.18 Available intensity maps for Düzce and surrounding area for the Kocaeli and Düzce earthquakes. The first map (top) is an extract from Figure 6.16, giving MSK intensities for the Kocaeli earthquake. The second map (bottom) is an extract from Figure 6.17, giving intensities according to EMS-98 based on the combined effects of both the Kocaeli and Düzce earthquakes. Maps have been scaled to ease comparison.

Such significant differences are surprising considering that the EMS-98 scale is intended to give results equivalent to the MSK scale. It is difficult to explain the discrepancies without knowing more about the derivation of the two maps than was available for the current study. However, it seems likely that the map created by Lekkas (2000), which was based on a grid size of 500 x 500 m, was at a higher resolution than the official Government map, allowing isolated regions of higher intensity to be mapped. This is supported by the suggestion of Akkar & Gulkan (2002) that the official Government intensity map under-rates the intensity by one-half degree in isolated pockets around Yalova.

It is believed that the EMS-98 map gives a better understanding of the intensities in the isolated built-up areas close to the surface fault break, as it is based largely on satellite image data, although probably over-estimates the intensity in some areas. The MSK map, however, is thought to be more reliable in outlying rural areas. Figure 6.18 shows the intensities estimated by the two studies in the immediate vicinity of Düzce

In the current Chapter, results are presented of a microtremor field investigation into site effects in the town of Düzce, Turkey. In Section 7.1, details of the measurement procedure are given. Data processing is explained in Section 7.2 and results are presented in Section 7.3 along with a discussion of various factors influencing the measurements. Consideration of the spatial distribution of site effects is given in Chapter 8.

7.1 Instrument selection and data collection

7.1.1 Instrument selection

There are few established guidelines on instrument selection for ambient noise recording for site response studies. In response to this, Mucciarelli (1998) carried out a series of tests to compare three commonly used sensors, summarised in Table 7.1. HVSRs calculated using the same technique for all three sensors (all connected to the same high resolution (24 bit) PRAXS-10 digital acquisition unit) indicated that the two seismometers had greater resolution than the accelerometer at low frequencies. The seismometers gave very similar results to each other over a broad frequency band (0.1 – 20 Hz). Results from the accelerometer, however, diverged significantly from those of the seismometers below about 1.5 Hz, leading to Mucciarelli (1998) suggesting that seismometers be selected in preference to accelerometers for ambient noise recordings for site response studies.

Table 7.1 Sensors included in the comparison by Mucciarelli (1998)

Sensor type	Model
Seismometer	Lennartz LE 3D-Lite
Seismometer	Mark L4C-3D
Accelerometer	Kinemetrics FBA 23

Microtremor investigation of site effects requires that measurements be taken at many locations for a matter of minutes at each location. After sensitivity, portability and ease of installation are therefore the most important instrument characteristics. For the current investigation, information was gathered from a number of instrument suppliers, resulting in a short-list of three seismometer-digitiser pairings, all of which met the key specifications outlined above. The list is given in Table 7.2.

The final selection was determined by cost and technical support considerations. The 'CityShark' instrument was not available on a rental basis and was therefore outside of the project budget. The other two instruments were offered for loan and included technical support from the supplier. Guralp Systems Ltd offered more comprehensive technical support, available both in the UK in the run-up to the fieldwork and in Turkey during the investigation itself. The Guralp instrument was

therefore selected on this basis, with the added benefit of a higher resolution data acquisition system (and therefore greater sensitivity) than that provided with the Lennartz instrument.

Table 7.2 Short-list of seismometers considered for the current investigation

Seismometer	Digitiser / data acquisition system	Supplier
Lennartz LE 3D-Lite	REF TEK 72A-02 (16 bit)	Geophysical Equipment Pool NERC, Grant Institute of Technology West Mains Rd Edinburgh EH9 3JW, UK (http://www.glg.ed.ac.uk/gep)
'CityShark'	Integral (24 bit)	LEAS, 38 Rue des Dauphins 38330 St Ismier, France (http://www.lab-leas.fr) (Chatelain *et al.*, 2000)
Guralp CMG-40TD-1	Integral CMG DM-24 (24 bit)	Guralp Systems Limited, 3 Midas House Calleva Park, Aldermaston, Reading, Berks RG7 8EA, UK (http://www.guralp.com)

Figure 7.1 Guralp CMG-40TD-1 set up to measure ambient noise at a rock site just outside Düzce, Turkey.

Guralp seismometers have been used for ambient noise recording for several recent site response studies (eg. Lachet *et al.*, 1996; Bodin *et al.*, 2001). The Guralp CMG-40TD-1 (Figure 7.1) consists of three orthogonal miniature sensors controlled by force feedback to give velocity and mass position electrical outputs. The basic response of the system is flat to velocity from a specified corner frequency of 1 Hz to 80 Hz. The instrument has a number of features that make it particularly suitable for its purpose:

a) **Portability.** Small size and easy to carry (instrument weight 7.5 kg). Low power consumption (seismometer - 0.46 W, digitiser - 1.7 W, global positioning system - 0.9 W).

b) **Simplicity of set-up**. Instrument only requires levelling. Unlike some longer-period instruments designed for more permanent installation, it does not require sensor mass-unlocking or mass-centring prior to each reading. Data acquisition can begin as soon as the sensor has been powered up. In addition, the instrument does not require precise levelling, being able to operate with up to +/- 2.5 degrees of tilt.

c) **Integrated digitiser.** Apart from simplifying instrument installation, this protects the sensor analogue outputs from contamination by external analogue noise.

d) **Ease of integration with MATLAB for data processing.** Guralp Systems Ltd. have developed a suite of MATLAB scripts to aid data processing. MATLAB is particularly suitable for signal processing, having high level commands for Fourier analysis.

Following instrument selection, a dummy microtremor survey was carried out in the UK under supervision from Guralp staff to familiarise users with the equipment and ensure all needs were addressed before shipment. A full hardware list is presented in Table 7.3. Equipment configuration is illustrated in Figure 7.2. The laptop computer provides a user-interface with the instrument via Guralp's SCREAM (Seismometer Configuration, REaltime Acquisition and Monitoring) software, allowing sample rates and other sensor parameters to be remotely controlled. The software also allows any data streams to be viewed in real time.

Table 7.3 Microtremor survey hardware list

Qty	Item
2	Guralp CMG 40 TD-1 with integral CMG DM-24 digitiser module
2	External Global Positioning System (GPS) - Guralp CMG-GPS2
2	Pentium laptop PC with SCREAM v.3.1 (Seismometer Configuration, REaltime Acquisition and Monitoring) software installed
1	Portable CD-writer
2	Solid state 12V battery with charger
2	Cabling for in-car charging of battery
2	Cabling for instrument-PC-battery interfacing
1	Garmin GPS12 handheld personal navigator

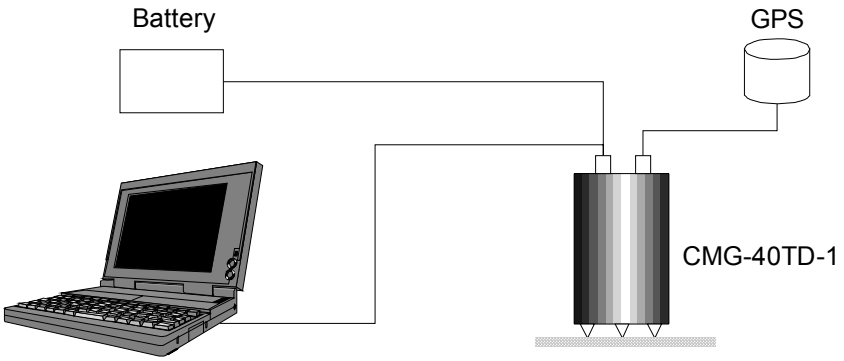

Figure 7.2 Microtremor equipment configuration.

The CMG-GPS2 receivers provide accurate time and location information from satellites and facilitate synchronisation between data recorded on different instruments. A separate handheld GPS was also included for convenience. It was decided to take two sets of equipment to speed up data collection, reduce the risk of instrument downtime in the field and to allow simultaneous monitoring at selected sites to investigate the effects of various factors on the stability of the HVSR calculated from the microtremor data. True reference-site measurements were considered unfeasible for Düzce due to the lack of any suitable rock reference site within a distance appropriate for the frequencies of interest. As explained by Bard (1998), soil-site-to-reference-site distance for frequencies greater than 1 Hz (which is within the range of interest for the Düzce study) should not exceed 500 m, whereas the distance between the centre of Düzce and the nearest rock site is around 6 km (Figure 6.7).

Batteries were selected to ensure adequate power provision for the estimated maximum number of daily measurements, whilst minimising weight. Facilities for overnight battery recharging from the mains and emergency in-car charging were included. Data backup was carried out nightly using a portable CD-writer.

7.1.2 Measurement site selection

Detailed street maps of Düzce (1:1,000) obtained from the Municipality allowed a preliminary grid of microtremor measurements to be defined prior to the fieldwork. The density of measurements was dictated by the resolution of earthquake damage data available. As detailed in Chapter 8, pipeline repair data and building damage data had been provided by the Municipality at the district level. Characterising site conditions at a spatial resolution much beyond the district level would therefore not be justified. Regarding microtremor survey coverage, priority was given to the most built-up areas within the Municipality. Some of the outlying districts were rural and had very low spatial densities of water distribution pipelines and buildings and were therefore not included in the investigation. Exclusion criteria have been defined using GIS and are explained in Chapter 8.

Precise microtremor measurement locations could only be selected on-site. A set of site-selection guidelines was drawn up based on the findings of previous investigators (eg. Bard, 1998; Mucciarelli, 1998) and on the prevailing conditions in Düzce, to ensure consistency of measurements and thereby minimise random errors. This was especially important because of the sensitivity of the instruments being used. The guidelines are listed below:

a) **Maintain consistent instrument-ground interface.** There is no clear, consistent advice in the literature regarding the coupling between the instrument and the ground. Asphalt or concrete surfaces were avoided due to their unknown effects on the ground response. Compact soil was considered the best interface, offering a direct link to the soil and a level surface for easy set-up. Where necessary, loose stones were swept away to enable a stable

contact between instrument and soil. Areas of ground with significant cracking were avoided. A crack creates a vertical free surface, which could affect the dynamic characteristics of the ground. Locations immediately adjacent to ditches or cuttings were also avoided for this reason.

b) **Avoid unusual subsurface conditions.** Due to the extensive post-earthquake demolition work, there were many open areas recently occupied by buildings and awaiting re-development. These were avoided where unusual subsurface conditions (eg. buried basement levels) were anticipated. Longer-established areas of open-space (eg. road verges, gardens, fields, parks) were selected in preference to areas of recently disturbed ground. Measures were taken to avoid known services (sewer or water pipes, etc.)

c) **Avoid excessively windy conditions**. Wind acting on the seismometer can cause distortions in the horizontal components of motion at low frequencies (below about 1.5 Hz).

d) **Avoid rainy conditions or wet ground.** Rain falling on or near the instrument would disturb measurements. Furthermore, increased water content of surface soil layers could modify ground response.

e) **Avoid strong local sources of noise**. No measurements were taken immediately adjacent to main roads to avoid strong, persistent transient vibrations caused by heavy traffic.

In a more established town, some of these criteria might have to be relaxed in order to find sufficient sites to constitute a survey.

7.1.3 Measurement procedure

For consistency, the same setting up and measurement procedure was followed for each microtremor location. Details are given below:

1. **Instrument set up.** Level instrument, trail cables (with slack to minimise spurious vibrations). Set up laptop as far as possible from instrument to minimise user-induced ground disturbance. Initiate data acquisition software and then power up instrument. A typical set-up is shown in Figure 7.3.

2. **Field notes.** Log instrument ID and location coordinates (from GPS), draw a simple schematic location plan highlighting significant local features and to enable repeatability of measurements. Record any significant events or unusual disturbances (especially from nearby sources) *eg*. pedestrians, livestock, vehicles, machinery.

3. **Data monitoring.** Monitor data in real time using SCREAM software to identify any instrument malfunctions or unusual disturbances. Example output is shown in Figure 7.4.

Figure 7.3 Typical field set-up for microtremor measurement. The photograph was taken at location 7.

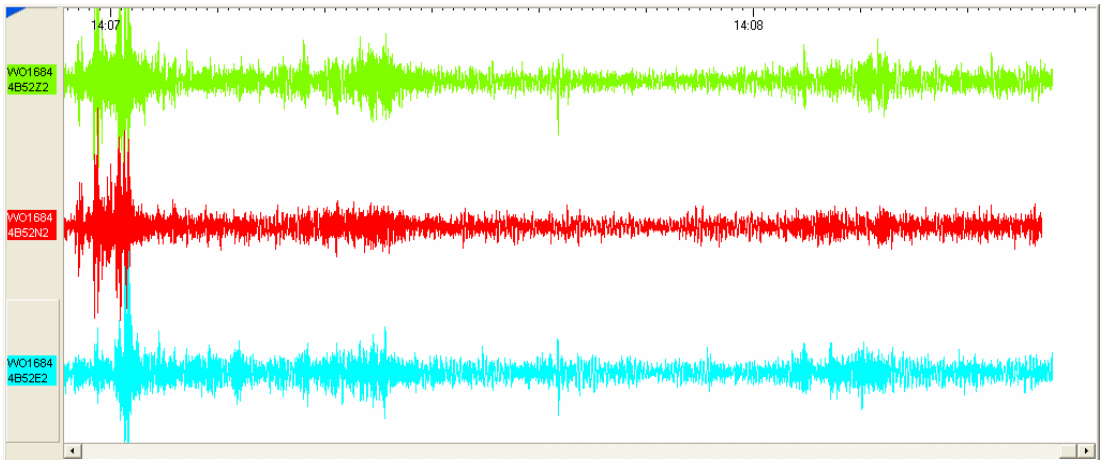

Figure 7.4 Typical screen output of real-time monitoring of ambient noise data. The example shows about a minute's worth of data for all three components of motion (vertical component on top, n-s component in the middle and e-w component on the bottom).

7.2 Data processing and analysis

Following some basic pre-processing, Fourier spectra and horizontal-to-vertical spectral ratios were computed for measurements made at each location using MATLAB. A flow chart of the MATLAB script written for this purpose is given in Figure 7.5. The program consists of nine key stages, each of which is explained in detail in a separate appendix (Appendix H). Details of pre-processing and the program listing are also presented in Appendix H. Example output from the MATLAB script is presented in Figure 7.6. The HVSR illustrated is for measurement location 086, the DZC strong-motion station (see Figure 7.9). The HVSR reveals a clear, predominant frequency, f_p of 0.73Hz with amplitude 3.97.

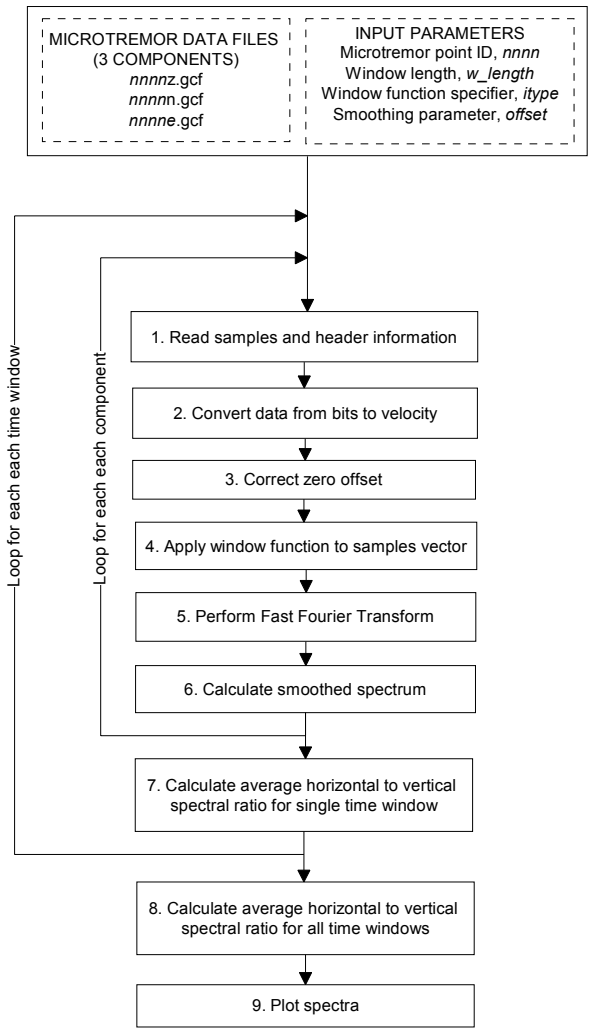

Figure 7.5 Flow chart for MATLAB routine to calculate the average HVSR of microtremor data.

Microtremor point: 086b, Set−up time (UTC): 12−Jun−2001 13:30:00, StreamID: 3A45

Adjacent averaging: 16 points (0.09766 Hz bandwidth), window length 40.96s, no of windows 20

FFT vector length 32768. Window function code 4.

Legend: Average HVSR (thick blk); +/− 1 standard deviation (thin grey)

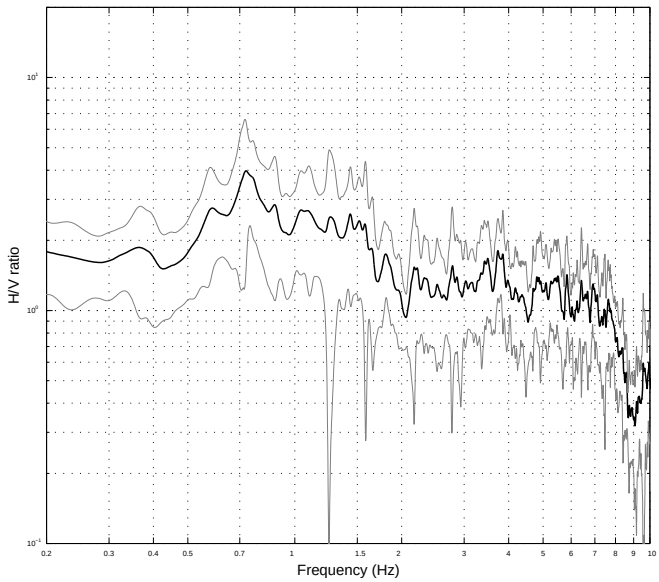

Figure 7.6 Example HVSR output (calculation took 32.9 s on AMD Athlon XP 2000+ with 256 MB memory)

Average HVSR amplifications were calculated for different frequency ranges for each record in the microtremor dataset. The frequency bins were selected by visual inspection of all HVSR plots and consideration of the likely resonant response of different classes of buildings found in Düzce and for which earthquake damage data was available. The frequency ranges are summarised below:

a) 0.5 - 2 Hz

A trough is often observed at around 0.5 Hz in a high proportion of the HVSR plots presented in Appendix I. This defines the lower limit of the first frequency band, which is also well below the predominant frequency observed at all sites and well above the reliable frequency defined by the spectral smoothing bandwidth.

The upper limit is set to correspond with the threshold between the natural frequency of buildings with 4 or more storeys and the natural frequency of buildings with 3 or fewer storeys. This frequency, 2 Hz, is also the point at which many of the HVSR spectra are observed to drop below unity.

A distinction was made between buildings with 4 or more storeys and those with 3 or fewer storeys based on building damage statistics obtained from Sucuoglu & Yilmaz (2001). As shown in Figure 7.7, the first category of buildings suffered considerably more damage as a result of the Kocaeli and Düzce earthquakes than the second category.

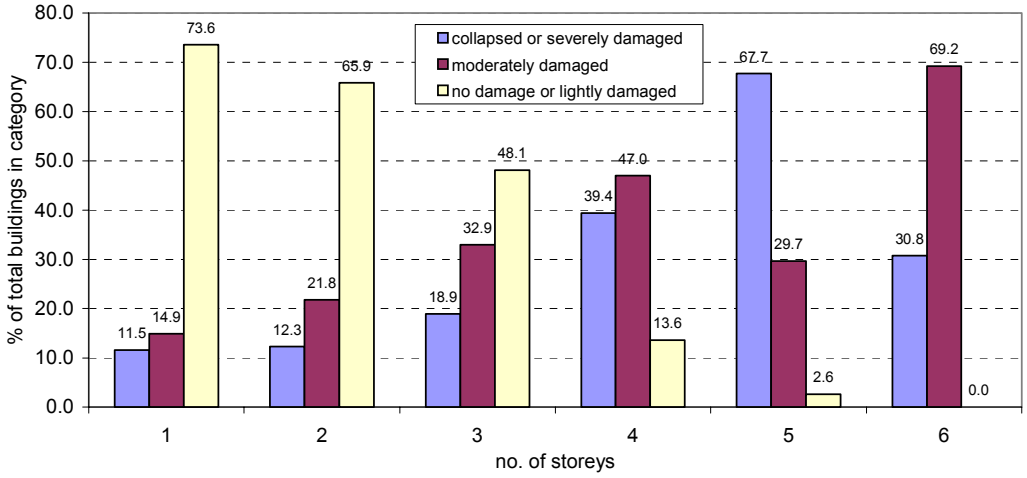

Figure 7.7 Building damage rates in Düzce according to building height. Statistics are from Sucuoglu & Yilmaz (2001) and are aggregated over both Kocaeli and Düzce earthquakes.

Building fundamental frequencies, f_B were estimated using the Eurocode 8 formula, in which the frequency is calculated from building height, H_B:

$$\frac{1}{f_B} = T_B = 0.075 H_B^{3/4} \tag{7.1}$$

where T_B is the building fundamental period (s).

Assuming a ground floor height of 4 m, and 3 m for any additional floors (Aschheim *et al.,* 2000), estimates were made of f_B for building height categories found in Düzce prior to the destructive earthquakes of 1999 (Table 7.4).

Table 7.4 Building fundamental frequencies for heights of buildings found in Düzce

No. of storeys	1	2	3	4	5	6
Building height, *H* (m)	4	7	10	13	16	19
f_B (Hz)	4.71	3.10	2.37	1.95	1.67	1.47

b) 2-5 Hz

This band covers the natural frequencies of buildings of 1, 2 and 3 storeys (Table 7.4). Many HVSR plots show deamplification in this frequency range.

c) 5-10 Hz

The third frequency bin covers the upper range of engineering interest for the current study. Certain very stiff, low-rise buildings can be sensitive to ground motions in this range.

7.3 Results

A total of 121 microtremor measurements were made in and around Düzce over a period of about two weeks. Fieldwork was carried out in May and June 2001. The spatial distribution of measurements is shown in Figure 7.8. Most measurements were made in the central part of the town, with locations indicated in Figure 7.9. A complete list of measurement locations is provided in Appendix I, Table I1. For each location (specified by the point ID), GPS coordinates, instrument ID (StreamID) and measurement time and date are given. For measurements made within district boundaries, a district ID is specified. These correspond to the district names given in Table 7.5, whose locations are shown in Figure 7.9. Field notes made during measurement are summarised into three columns in Table I1: ground contact, location category and location description, explanations of which are given with the table.

Spectra calculated for each location are presented in Appendix I, Figures I1 – I121. In each case, Figure (a) (left hand side) gives the average HVSR with an indication of the scatter (+/- 1 standard deviation) and Figure (b) (right hand side) gives the average FAS at the same location for each of the three components of motion. The FAS have been instrument-corrected.

A summary of spectral parameters obtained from the HVSR plots is presented in Table I2. In most cases, the predominant frequency, f_p is fairly clearly defined by a single peak. Where a peak is unclear, the corresponding data point is excluded from the GIS-based analysis (see Chapter 8). These cases are indicated in the table.

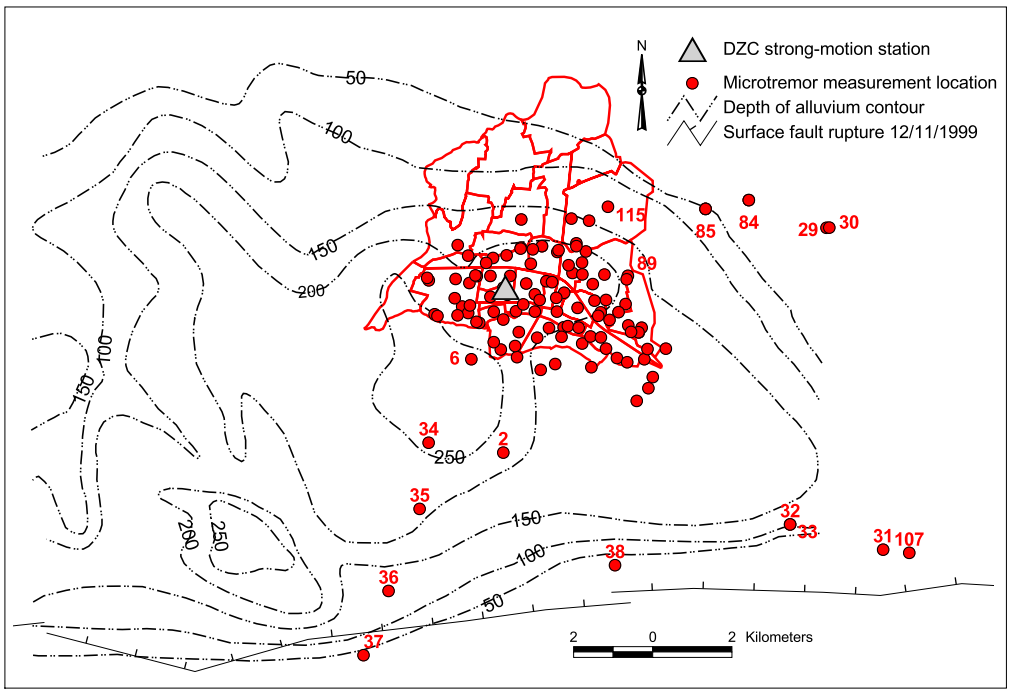

Figure 7.8 Distribution of microtremor measurement locations in and around Düzce. District boundaries are shown in red. Contours of alluvium depth are given in metres.

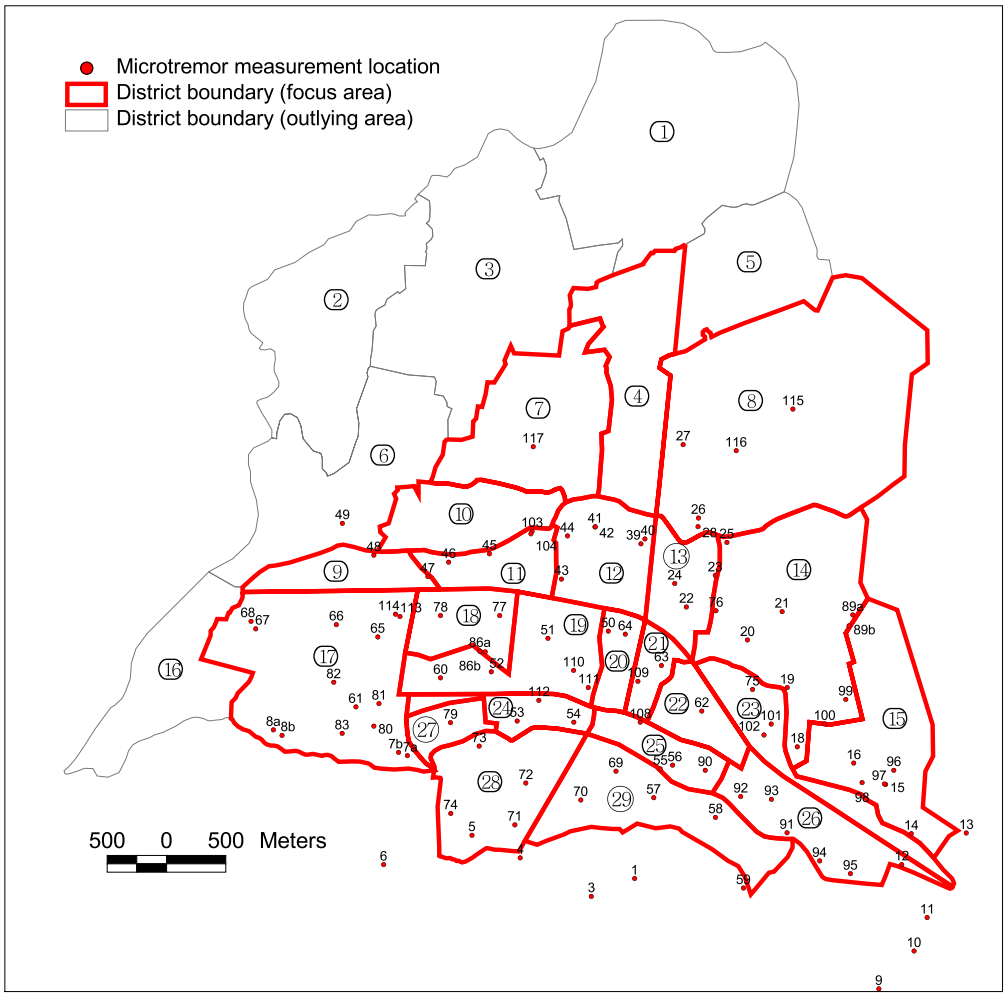

Figure 7.9 Distribution of microtremor measurement locations in central Düzce. Large numbers are defined in Table 7.5.

Table 7.5 Districts (Mahalle) of Düzce Municipality. Alternative district names are given in brackets.

District ID	District name (Mahalle)
1	Çamköyü
2	Sarayyeri
3	Bostanyer (Arapçifliği)
4	Sancaklar
5	Çavuşlar
6	Akınlar (Beslanbey)
7	Körpeşler
8	Beyciler
9	Fatih
10	Karacahacımusa
11	Yeni
12	Hamidiye
13	Karaca
14	Metek (Koçyazı)
15	Dereli (Tütüncü)

District ID	District name (Mahalle)
16	Mergic (Esen)
17	Aziziye (Günlü)
18	Uzunmustafa
19	Kültür
20	Şerefiye
21	Burhaniye
22	Nusrettin
23	Cumhuriyet
24	Camikebir
25	Cedidiye
26	Fevzicakmak
27	Kiremitocağı
28	Çay
29	Azmimilli (Darıcı Köyü)

7.3.1 Comparison between instruments

At an early stage in the fieldwork, the two CMG-40TD-1 instruments were set up adjacent to each other at a quiet semi-rural site (location 7, shown in Figure 7.3) to compare their response to the same ambient noise input. Average HVSRs for 15 identical time windows were calculated for each record, the results of which are shown in Figure 7.10. The similarity in the spectral ratios over the whole frequency range of interest (0.2 – 10 Hz) and beyond (Figure 7.10 is plotted over $0.1 \leq f \leq$ 20 Hz) confirms the consistency of microtremor measurements over the whole dataset.

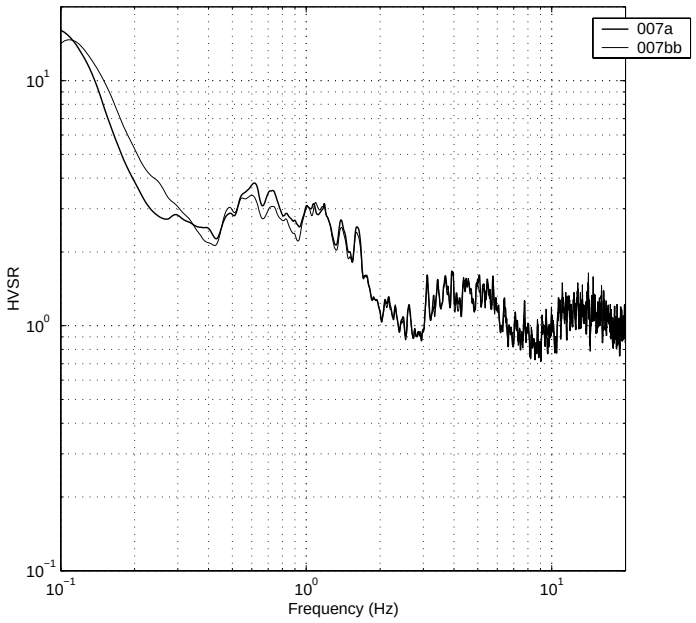

Figure 7.10 Comparison of HVSR for the two CMG-40TD-1 instruments recording simultaneously at the same site (location 7). 007a refers to instrument ID 4B47; 007bb refers to instrument ID 4B52.

Seismometer sensitivity is frequency dependent, the nature of the dependency being defined by an instrument's transfer function. The CMG-40TD-1 is a 1-second instrument and has a flat frequency response over the range 1 – 80 Hz, with sensitivity tailing off for frequencies below about 1 Hz. This affects the reliability of spectral amplitudes in the range of frequencies of interest for the current study. A series of measurements using a more sensitive long-period (30 s) seismometer (the Guralp CMG-3ESP) was therefore carried out to verify the reliable range of the short period instrument. Instrument transfer functions are compared in Figure 7.11.

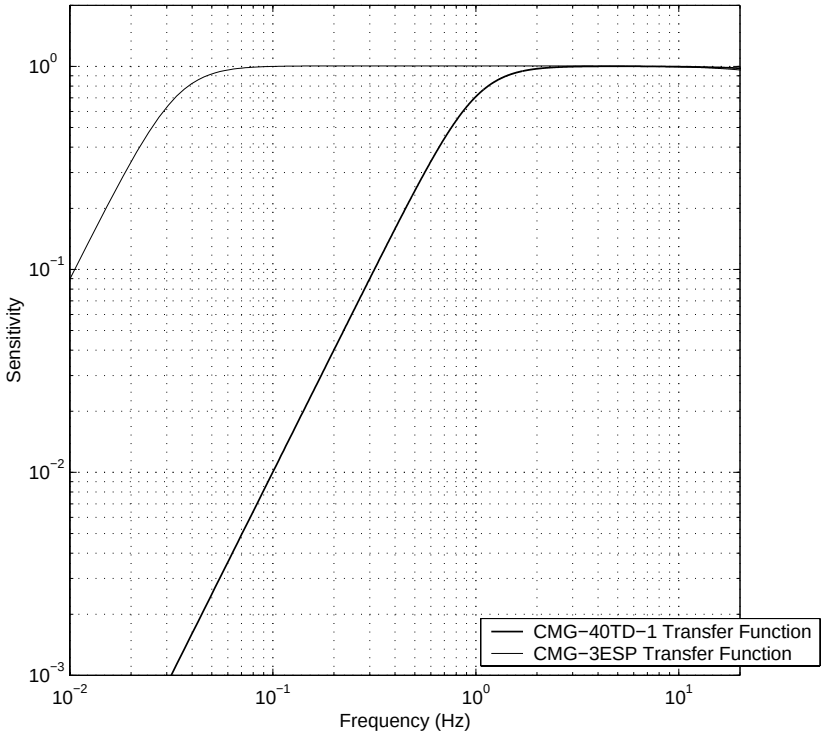

Figure 7.11 Comparison of instrument transfer functions for the 1 s and 30 s instruments

Simultaneous ambient noise measurements were made with the 1 s and 30 s instruments at Düzce's strong-motion station, DZC. Spectral ratios between the two instruments were calculated from FAS for each of 5 sample windows (of 40.96 s duration), results of which are shown in Figure 7.12. Spectral ratios are shown for all three components of motion. Average spectral ratios across all 5 windows are plotted in Figure 7.12f along with the transfer function of the 1-second instrument. The spectral ratios are seen to follow the instrument transfer function down to approximately 0.2 Hz. This confirms that Fourier amplitudes obtained from the 1-second instruments are reliable down to 0.2 Hz, which in any case is the frequency limit defined by the smoothing algorithm employed. Reliable results may be possible at even lower frequencies by using a narrower smoothing bandwidth.

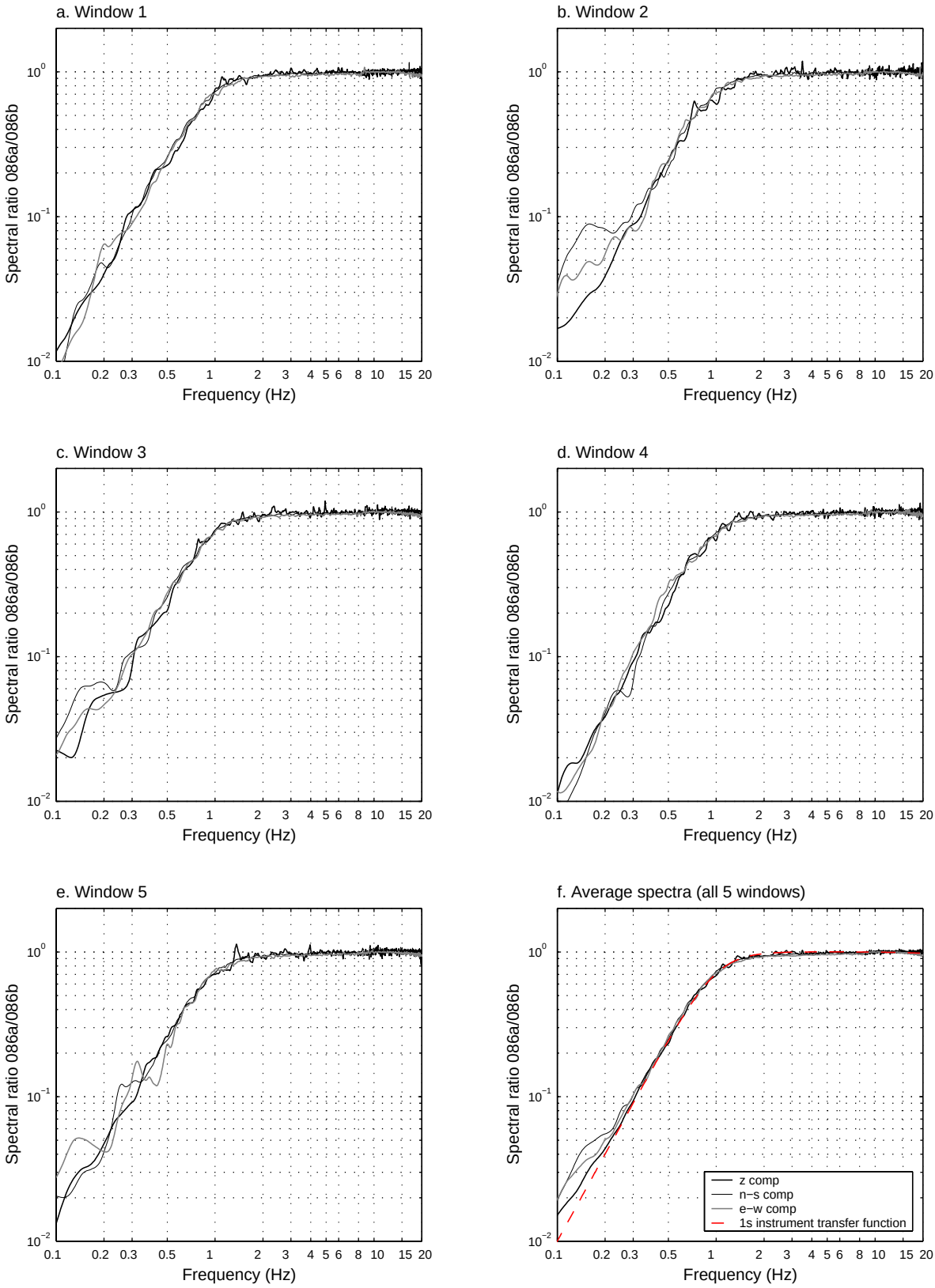

Figure 7.12 Spectral ratios of measurements made at points 086a and 086b to illustrate the sensitivity of the 1-second instrument.

7.3.2 Effect of ambient noise levels on HVSR

Amplitudes of Fourier spectra are seen to vary hugely from site to site in and around Düzce (Appendix I). For spectra from any given pair of sites, the variation will be due to differences in both noise source characteristics and site conditions. At each location, spectra can also vary significantly with time due to the changing nature of ambient noise levels throughout the day. At location 63, ambient noise amplitudes during the first half of the record were dominated by large-scale building demolition works being carried out at a distance of about 130 m. Separate Fourier spectra were calculated for samples taken during the demolition works and after (Figure 7.13). The increased noise levels are seen to affect spectral amplitudes from 0.5 Hz upwards, with differences most marked between 3 and 10Hz. In this frequency band, amplitudes for the noisier samples are up to an order of magnitude greater.

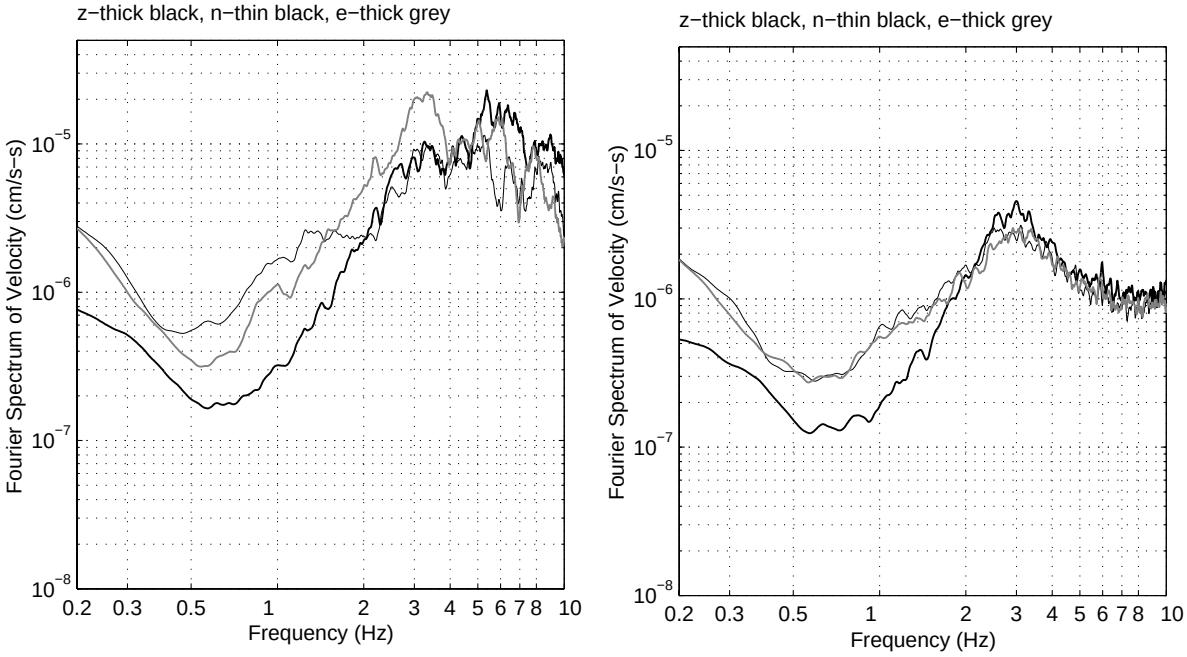

Figure 7.13 Average FAS over 20 windows at the same location (point 63) for very different ambient noise levels. The left hand graph (measurement 063) is dominated by the effect of nearby building demolition works; the right hand graph (measurement 063a) is for the same location but during a pause in the demolition works.

The single station HVSR was calculated for both sets of data represented in Figure 7.13. These are plotted for comparison in Figure 7.14. It is immediately apparent that the variation in HVSR between the two sets of measurements is much less than the variation in FAS. This has been observed in many other microtremor studies (Bard, 1998). Both HVSRs have a similar form up to around 2.5 Hz. Above this, the HVSR of the noisier record has several significant peaks and troughs which are absent in the HVSR of the quieter record. The predominant HVSR peak at around 1 Hz has a similar shape in both records. The coordinates [f_p, A_{fp}] of predominant peaks for measurements 063a and 063 are [0.98, 3.76] and [0.78, 5.41] respectively. The increased noise levels associated with measurement 063 appear to have increased the amplitude of the predominant peak by about 40 % and reduced its frequency by about 25 %.

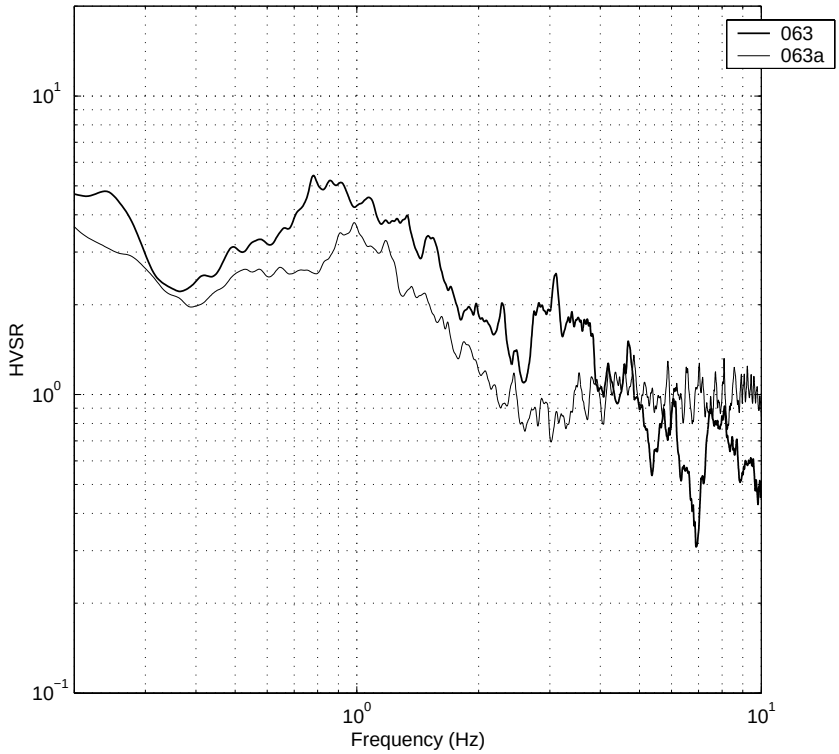

Figure 7.14 Average HVSR over 20 windows at the same location (point 63) for noisy conditions (063) and relatively quiet conditions (063a).

The observations made at location 63 show that the level of ambient noise experienced at a site can influence HVSR amplitudes and, to a lesser extent, the location of the predominant peak, f_p. The general shape of the HVSR is, however relatively insensitive to the nature of the incident noise wave field. It should be noted that the variation in noise levels experienced at location 63 is exceptional for the dataset. Uncertainties in f_p and HVSR amplitudes for the majority of other points in the investigation are therefore, by implication, likely to be smaller.

7.3.3 Effect of wind on HVSR

Mucciarelli (1998) and Bard (1998) have both mentioned the effects of wind on HVSR amplitudes at low frequencies. For most of the measurements taken in Düzce, wind was negligible. However, several data points listed in Table I2 have had to be excluded from the subsequent GIS-based analysis (see Chapter 8) due to adverse effects of wind on HVSR amplitudes in the frequency range of interest (indicated by the comment, "H/V peak obscured").

Some examples of wind-affected HVSRs are shown in Figure 7.15. Amplitudes below about 1.5 Hz are increased, which in many cases has the effect of obscuring the predominant peak. HVSR amplitudes are augmented because wind affects the horizontal components of FAS more than the vertical component (see, for example Figures I42b, I75b and I81b).

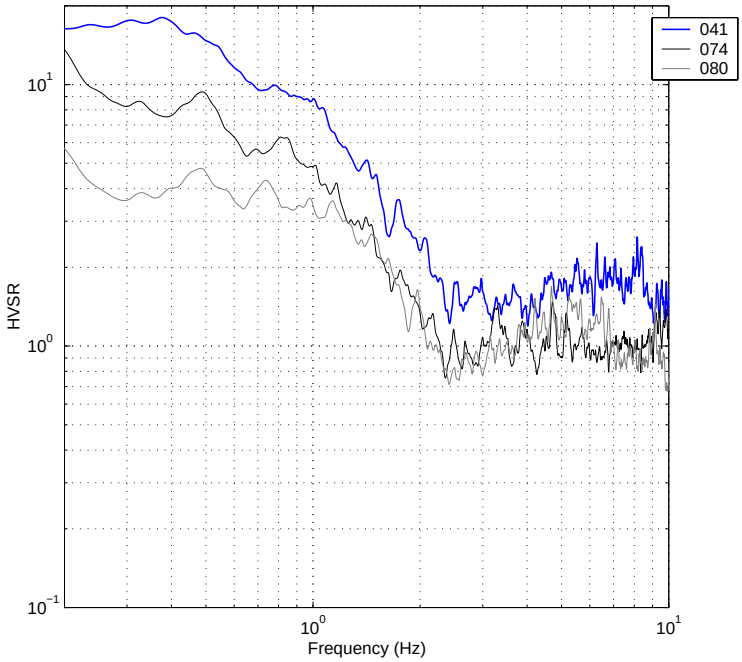

Figure 7.15 Examples of HVSRs adversely affected by windy conditions.

7.3.4 Comparison between microtremor HVSR and earthquake HVSR

A single-station microtremor technique has been used in Düzce to characterise site response due to a lack of any nearby rock reference sites. Non-reference-site techniques are also available for weak and strong-motion data, meaning that earthquake data recorded by the Düzce (DZC) and Bolu (BOL) strong-motion instruments can be used to verify the microtremor results. The method employed here involves computation of the HVSR, or *receiver function* (Langston, 1977), of an earthquake record and is based on an approach suggested by Lermo & Chavez-Garcia (1993) and Field & Jacob (1995). The overall frequency dependence of site response is found by computing HVSRs from the intense S-wave portion of accelerograms, based on the assumption that the local site conditions are relatively transparent to the motion that appears on the vertical component. Zare *et al.* (1998) have used a similar approach for characterising site effects for the Iranian strong-motion network in the absence of adequate reference sites.

Receiver functions have been calculated for six accelerograms obtained from five different earthquakes (Table 7.6). The records are all from ISESD (Ambraseys *et al.*, 2002) and include the Düzce main shock from stations BOL and DZC and the Kocaeli main shock from DZC. The other records are for smaller magnitude events recorded at DZC.

For each record, the S-wave window was estimated from inspection of the strong-motion time-histories. HVSR was computed using MATLAB, following a similar procedure to that used for the microtremor data. For each component of motion, the S-wave sample was tapered using a Hanning window, zero-padded to a length of 32,768 samples and Fourier transformed. FAS smoothing and combination of the horizontal spectra prior to calculation of the HVSR were employed as for the microtremor data.

Table 7.6 Earthquake parameters for strong-motion records used to calculate receiver functions.

Event ID	Origin time		Epicentral Coordinates		Focal Depth	M_s	Strong-motion record ID	
	Date	Time (UTC)	N	E	(km)		BOL	DZC
1	17-Aug-99	00:01:39	40.702	29.987	17	7.8	-	001226
2	13-Sep-99	11:55:28	40.709	30.045	13	5.8	-	001239
3	12-Nov-99	16:57:19	40.768	31.148	10	7.3	001560	001703
4	14-Feb-00	06:56:34	41.016	31.757	10	4.8	-	004458
5	23-Aug-00	13:41:28	40.680	30.720	15	4.9	-	004477

Earthquake receiver functions are compared with the relevant microtremor HVSR in Figure 7.16 (measurement 106a for BOL and measurement 086b for DZC). Receiver functions for the Kocaeli and Düzce main shocks recorded at DZC are remarkably similar in form to the microtremor HVSR (Figures 7.16 b & d). Both receiver functions exhibit a clear predominant peak within about 0.1 Hz of the microtremor predominant peak. Receiver function amplitudes tail off at higher frequencies in a similar way to the microtremor HVSR, including a characteristic deamplification between about 7 and 10 Hz, which probably reflects the influence on the records of the building housing the accelerograph. Receiver function amplitudes for these two earthquakes, particularly at the predominant frequency, are generally much greater than microtremor HVSR amplitudes. Receiver functions for events 2, 4 and 5 (Figures 7.16 c, e & f) all have significant peaks within about 0.1 Hz of the microtremor predominant peak but exhibit greater amplitudes at higher frequencies than the microtremor HVSR. Higher receiver-function amplifications at frequencies beyond the predominant frequency of the ground have been observed in other studies (Bard, 1998).

The microtremor HVSR for BOL is much flatter than that for DZC and does not exhibit such a clear predominant peak. The predominant frequency appears to be at around 1.3 Hz. The receiver function is much more erratic than the microtremor HVSR. It reaches its maximum at around 2 Hz, having an amplitude an order of magnitude greater than the microtremor HVSR at the same frequency.

HVSRs of earthquake records from DZC confirm the predominant frequency obtained from microtremor measurements made at the same location. This adds weight to the reliability of the predominant frequencies obtained at other locations throughout Düzce in the current study. No consistent correlation has been found between the amplitudes obtained using the two approaches. Results obtained at BOL are less conclusive than at DZC, even for estimates of the predominant frequency.

A detailed investigation into the meaning of HVSR from earthquake records is beyond the scope of this study. As with the microtremor method (see Chapter 4), its interpretation is still the subject of much debate (*eg.* Lachet *et al.*, 1996; Satoh *et al.*, 2001).

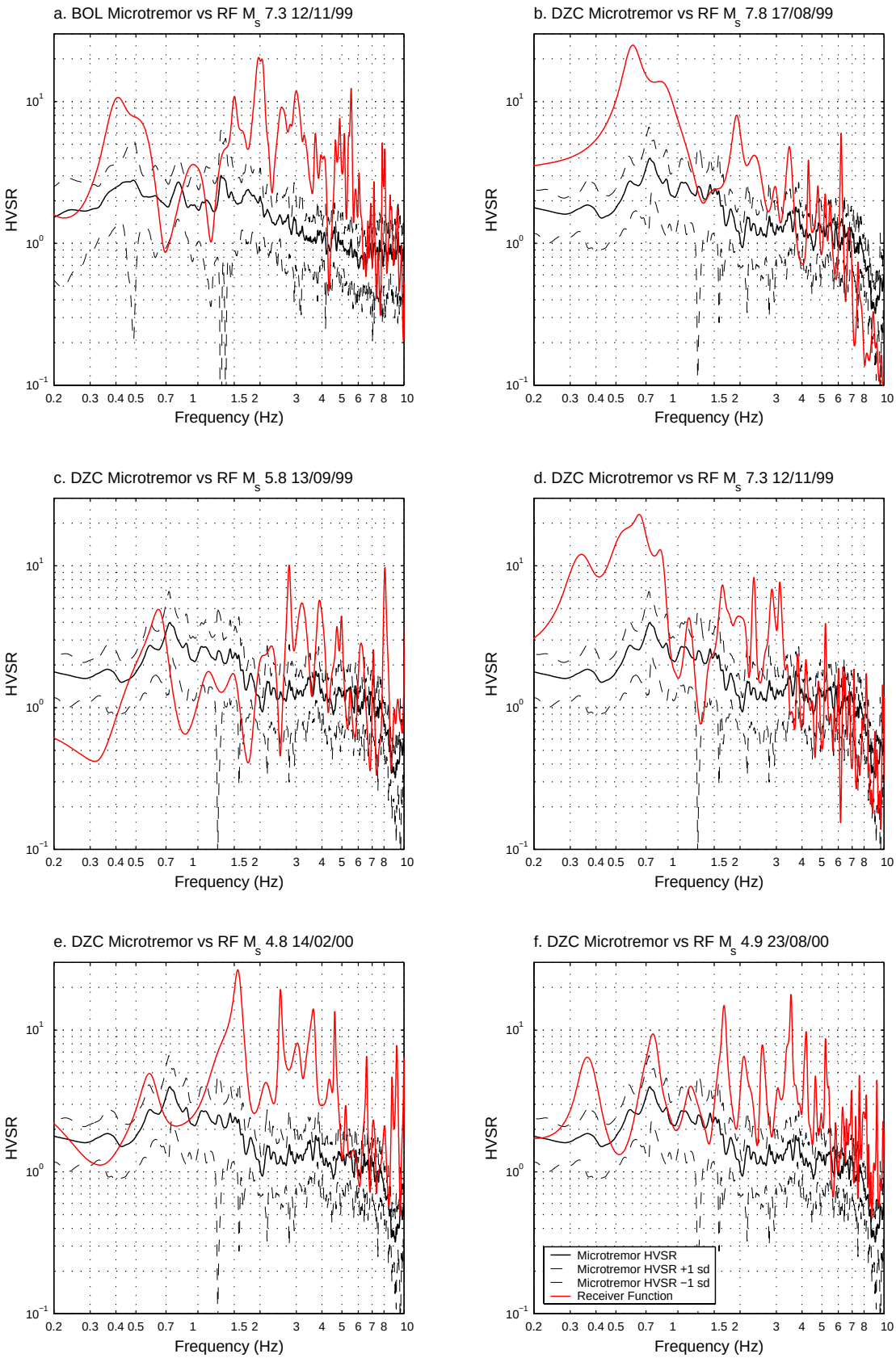

Figure 7.16 Comparison between receiver functions and microtremor HVSR at (a) Bolu strong-motion station (BOL) and (b-f) Düzce strong-motion station (DZC).

8.1 Introduction

A GIS provides an ideal tool for analysing relationships amongst spatial datasets. GIS is increasingly used in lifeline earthquake engineering for post-earthquake investigation of damage (eg. Shirozu *et al.,* 1996; O'Rourke & Toprak, 1997) and for risk assessment (eg. Hwang & Lin, 1997). Indeed, GIS forms the backbone of the United States National Loss Estimation Methodology, HAZUS (FEMA, 1999).

In the current chapter, GIS is used to investigate factors influencing the spatial distribution of water pipeline damage in Düzce as a result of the Kocaeli and Düzce earthquakes. The influence of site conditions is investigated using the microtremor dataset described in the previous chapter. Comparisons are made between the distribution of pipeline damage and building damage.

8.2 Database

As outlined in Section 6.1, data for the current investigation were obtained following field trips to Düzce conducted in May 2000 and May 2001. At the time of the first visit, the Düzce Municipality were beginning to implement their own GIS database for the town as part of the post-earthquake recovery process. The GIS division provided digital map data at 1:1000 scale to the author of this thesis. For the purposes of the current investigation, this data was imported into an ArcView GIS environment (ESRI, 1999) to create a base reference map. Over the course of the two field visits, data were collected to characterise pipeline damage rates, building damage levels and site characteristics across the town, all of which have been added to the GIS database. In the following three sections, each dataset is described in detail.

8.2.1 Pipeline damage rate

8.2.1.1 Water distribution network

The water supply system in Düzce dates back to the 1940's. The only known maps available are those created by the Engineering Department of the Bank of the Provinces (Iller Bankası), which has been responsible for design, finance and construction of Düzce's water supply system since 1985. Düzce Municipality's Water Division provided copies of the most recent Iller Bankası maps, covering the whole town at a scale of 1:2000. These maps, dated July 1997, are design drawings for a new network and therefore differ somewhat from the existing system. Out of a total length of 435 km of pipe, approximately 280 km had been laid by September 2000 (Tadday & Sahin, 2001), although there is no indication which pipes these are. The pre-existing network is thought to be about 500 km in length, although no maps exist to confirm this (Tadday & Sahin, 2001). This older network was still in use at the time of the field work and was connected to the new system via

a series of bypasses. The total length of the pipe network as of September 2000 is therefore estimated to be around 780 km.

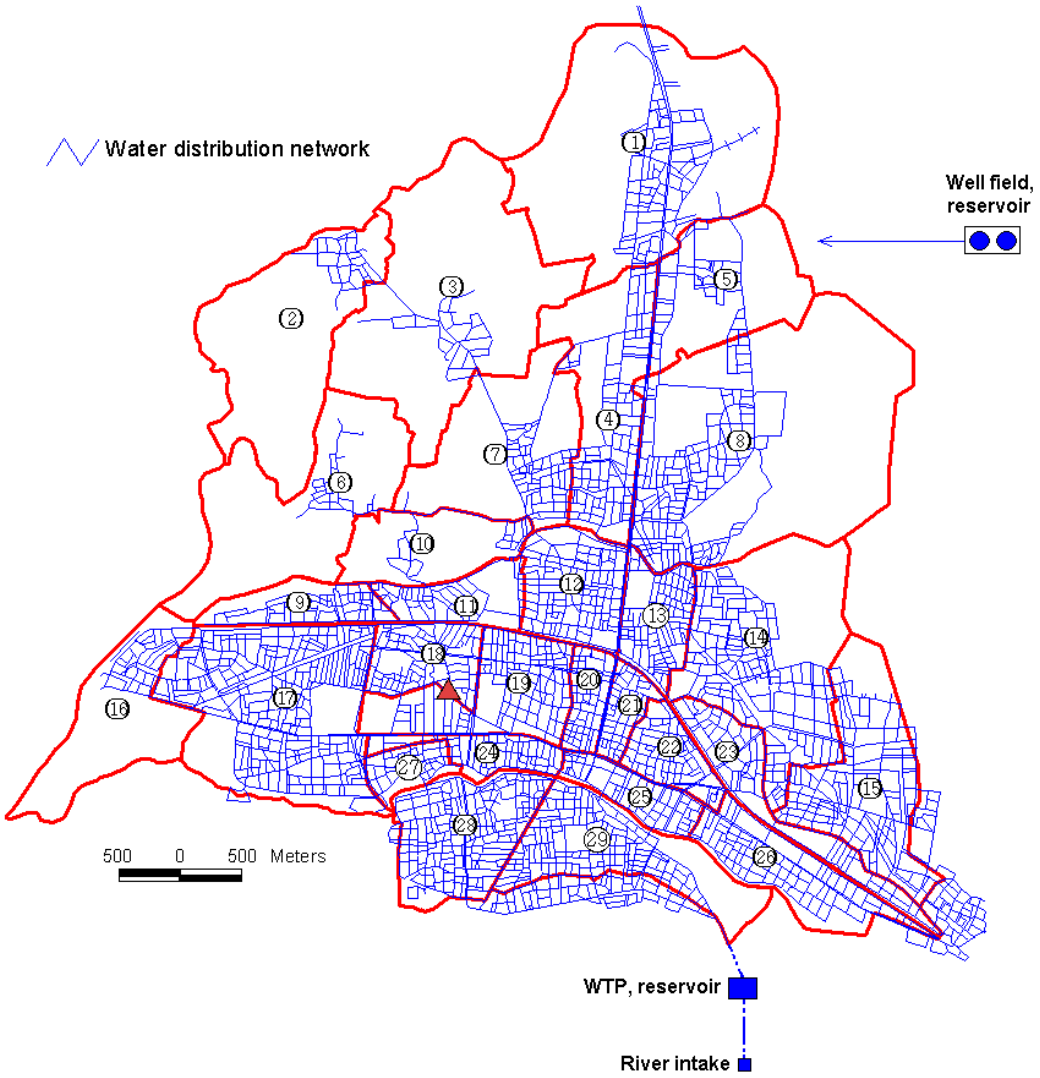

Figure 8.1 Düzce's water supply system, digitised from the 1:2000 scale maps of the Bank of the Provinces. District boundaries are given in red. District IDs were specified in Table 7.5. The red triangle shows the location of the DZC strong-motion station.

For the purposes of the current study, the full 435 km network as designed by Iller Bankası was assumed to be representative of the whole network (new and old combined) and was therefore digitised into the GIS database. Pipeline repair rates calculated from lengths based on this network could then be multiplied by a factor (435/780) to account for the difference. Such uncertainty relating to buried infrastructure is common. In the absence of reliable maps, one study of earthquake damage to buried pipelines took road length (multiplied by a factor of 0.75) as a surrogate measure of pipe length (Shih *et al.*, 1999). In another study (Trifunac & Todorovska, 1997), the variation of pipeline damage across a city relied on the assumption that the spatial density of pipes was constant within the area under investigation. For the town of Düzce, it was decided that the new network would better represent the actual system than either of these

estimation methods. Pipeline lengths per district were calculated within the GIS using ArcView's 'GeoProcessing' tools. A summary of the data is given along with pipeline repair data in Table J5 (Appendix J).

The full digitised network is illustrated in Figure 8.1. No distinction is made between different pipe materials or diameters as this information was not available, although it is known that most of the new network consists of PVC pipes with diameters between 100 and 200 mm. The old network is mainly CI (cast iron), with some AC (Asbestos cement) pipes. The whole distribution network is therefore made up of pipes normally classed as brittle (see Chapter 3). A 600 mm diameter AC pipe conveys raw water from the main source, the River Ugur, to the water treatment plant which lies to the south of the town. A 1m diameter steel pipe then carries the treated water to the distribution network, joining the town in the Azmimilli District (district ID 29). Twin CI pipes, of diameter 125 mm, transport water from a well-field and reservoir to supplement the main river water supply; these pipes join the town in the north-east. Both main water sources are illustrated in Figure 8.1, although the precise connection point of the 125 mm CI pipes to the distribution network is not known.

8.2.1.2 Network repair data

Düzce Municipality's Water Division summarises work carried out on the water network in the form of a daily logbook. An extract from the logbook, giving entries made for 29 December 1999, is shown in Appendix J, Table J1. A translation of this portion into English is given in Table J2. This logbook system had been used by the Municipality since the 1970's. A copy of the logbook entries for the post-earthquake period 16/8/1999 – 11/5/2000 (269 days) was obtained from the Municipality. The details were translated and entered into a spreadsheet for analysis. A computer file summarising a longer period, 25/01/1999 – 20/01/2001 (726 days) and including a significant amount of pre-earthquake data, was subsequently obtained from UNICEF. This had been prepared in collaboration with staff in the Water Division as part of an initiative to improve record keeping following the earthquakes.

These data were in a more usable form, as shown by the example in Table J3. Jobs are classified according to four types: excavations, service connections, network repairs and pump repairs. Job totals and monthly averages for the full 726 days are summarised in Table 8.1. Network repairs and service connections are the most frequent job types and are also the most important datasets for the current study. Each job includes location information, usually in the form of the district name but sometimes including the street or building name. In order to be included in the GIS model, this information was standardised with the aid of the 1:1000 scale map (which included street names). Each job was geo-coded according to the categories given in Table J4. Approximately 75% of all jobs (and 90% of all repairs) could be assigned to one of Düzce's 29 districts (the locations of

which have been given in Figure 7.9). Several additional categories were included for jobs carried out in outlying villages or if location details were unclear.

Table 8.1 Job types and totals recorded in the Water Division logbook. The term 'man power' refers to one person occupied in any single task.

Job type	Total number recorded in logbook 25/01/1999 – 20/01/2001 (726 days)	Average monthly job rate
Network repair	2638	111
Service connection	1793	75
Excavation	1088	46
Pump repair	20	0.8
Man power	8327	349

8.2.1.3 Identification of earthquake-related repairs

Entries made in the water supply system logbook do not include any information on the nature or cause of pipeline damage. The amount of time required to restore a water network following an earthquake varies from earthquake to earthquake and depends on the amount of damage caused and the availability of the workforce. In deriving fragility relations using pipeline damage data obtained from the 1989 Loma Prieta earthquake, Eidinger *et al.* (1995, 1998) used repairs made in the two weeks following the earthquake. Repair of earthquake-related pipeline damage in Mexico City following the 1985 Michoacan earthquake, however, took several months (Ayala & O'Rourke, 1989). The situation in Düzce is complicated by the fact that two destructive earthquakes occurred within three months, the second event occurring whilst repairs were still underway of damage from the first event. In order to identify earthquake-related pipeline repairs in Düzce, it is therefore necessary to plot a time-line of the available data.

The full UNICEF dataset covers three distinct periods, separated by the Kocaeli and Düzce earthquakes:

1 - **pre-earthquake data**: repairs made between 25 Jan 1999 and 17 Aug 1999 (203 days),

2 - **inter-earthquake data**: repairs made between 18 Aug 1999 and 12 Nov 1999 (87 days),

3 - **post-earthquake data**: repairs made between 13 Nov 1999 and 20 Jan 2001 (435 days).

It was decided to aggregate the data according to nominal monthly periods. As time between the Kocaeli and Düzce earthquakes corresponds to exactly three 29-day periods, this was taken as the nominal month length. There are seven full intervals of pre-earthquake data, three intervals of inter-earthquake data and fifteen full intervals of post-earthquake data, making a total of 25 intervals. The temporal variation in network repairs for all districts and outlying areas is summarised in Table J5. The data for districts 1 – 29 is plotted in Figure 8.2.

Prior to the Kocaeli earthquake, the network repair rate is seen to be very stable from month to month. Immediately after the earthquake, there was a marked increase in pipeline repairs. A monthly repair rate about twice the pre-earthquake level was sustained for 2 months, which reflects the response of the Municipality to the extensive earthquake damage to the water network. A sharp drop in repair rates to almost pre-earthquake levels occurred in the month immediately following the Düzce earthquake. This corresponds to the two week period during which the majority of water division staff were repairing the 600 mm diameter AC transmission line which suffered extensive damage where it crossed the Düzce fault zone (ASCE/TCLEE, 1999b). Once this work had been completed, attention was returned again to the water distribution network, evidenced in the sharp increase in numbers of repairs carried out in the period ending 9 January 2000. This was followed by a sharp decrease for a period of four months to an average repair rate around a quarter of pre-earthquake levels. A UNICEF field report dated 13 March 2000 (UNICEF, 2000c) stated that 90% of mains pipes in Düzce were reported to be functioning following the extensive post-earthquake repair works. The trend observed in the repair rate suggests that the majority of repairs to the most important pipes had already been completed some time between 9 January and 7 February 2000. This conclusion is also supported by the trend observed in the time line of service connections ("new connections" in Figure 8.2). The sharp reduction in mains repairs between January and February coincided with a sharp increase in service connection jobs. Such a shift in focus in work carried out by the Water Division staff is only likely to have happened once the mains network had been largely re-established.

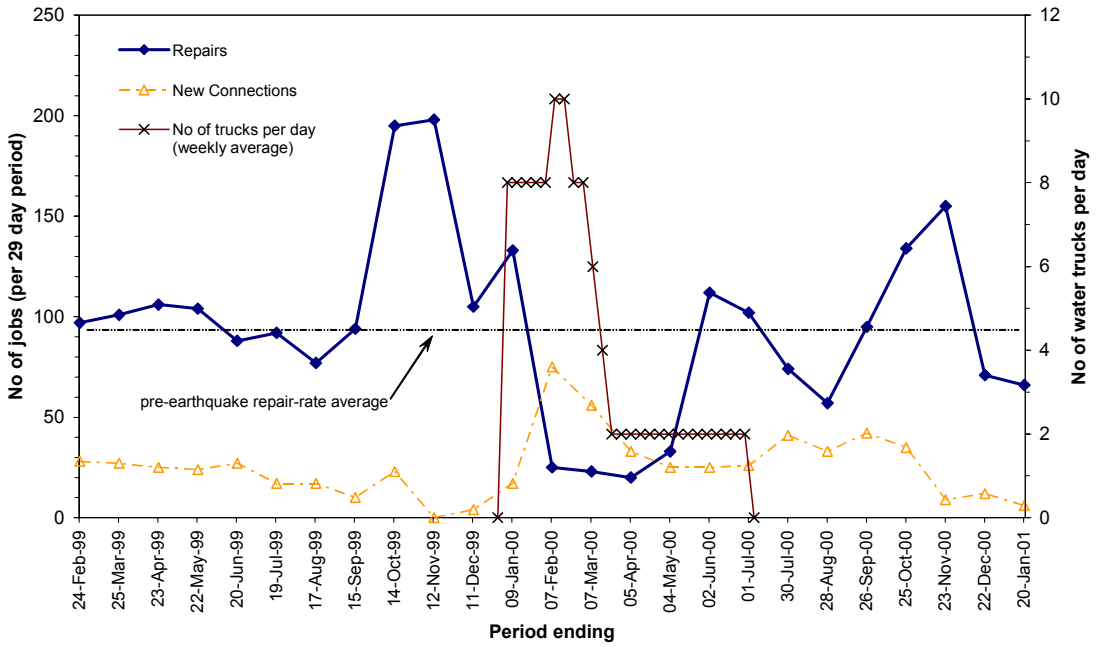

Figure 8.2 Temporal variations of network repairs, service connections and provision of potable water by truck within Düzce (district IDs 1 – 29).

Figure 8.2 also includes data relating to the provision of water by truck, which formed part of the UNICEF-funded post-earthquake rehabilitation of Düzce (UNICEF 1999a, b, 2000a, b & c). Potable water was provided by truck as long as Düzce's water demands were not being met by the town's water distribution network. The UNICEF programme made use of private truck contractors in order to release the Municipality staff to attend to network repairs and service connections. Trucked water supply began on 30 December 1999 with the provision of 600 m^3 water per day (equal to 8 trucks each supplying 75 m^3), enough for 30,000 people (assuming 20 litres per person per day). This provision rose to a maximum of 10 trucks per day for a short period at the start of February 2000, with a graduated reduction over the following five weeks corresponding to a reduction in the number of new connections. Trucked water provision, at 150 m^3 per day, was sustained until July. UNICEF reports indicate that many people in Düzce continued to use trucked water in preference to piped water due to concerns about water quality, even in areas where piped water had been restored.

From the trends observed in the time lines in Figure 8.2, it was decided to aggregate the monthly post-earthquake repair data from Table J5 according to four time-frames. These datasets, along with the pre-earthquake repair data, formed the basis of the spatial analysis. The time-frames, descriptions of the quantities mapped and the corresponding figure numbers are summarised in Table 8.2.

Table 8.2 Summary of time frames used for aggregation of pipeline repair data and quantities mapped for the investigation of the spatial variation of pipeline repairs in Düzce.

Time frame	Explanation	Quantity mapped (incl. description)	Figure
27 Jan 1999 – 17 Aug 1999	Pre-earthquake repairs	*R30_pre* Average repair rate per km length of pipe adjusted to a 30-day average (based on all 7 months of pre-earthquake data)	8.3
18 Aug 1999 – 12 Nov 1999	Damage caused by Kocaeli earthquake	*R_pK3* Post-earthquake repair rate per km length of pipe (data aggregated post Kocaeli earthquake 3 months)	8.4
13 Nov 1999 – 9 Jan 2000	Damage caused by Düzce earthquake	*R_pD2* Post-earthquake repair rate per km length of pipe (data aggregated post Düzce earthquake 2 months)	8.5
18 Aug 1999 – 9 Jan 2000	Combined damage caused by both earthquakes	*R_pK5* Post-earthquake repair rate per km length of pipe (data aggregated post Kocaeli earthquake 5 months)	8.6
18 Aug 1999 – 20 Jan 2001	Combined damage caused by both earthquakes including long-term effects on monthly repairs	*R30_pK18* Repair rate per km length of pipe adjusted to a 30-day average (based on all 18 months of post Kocaeli data)	8.7

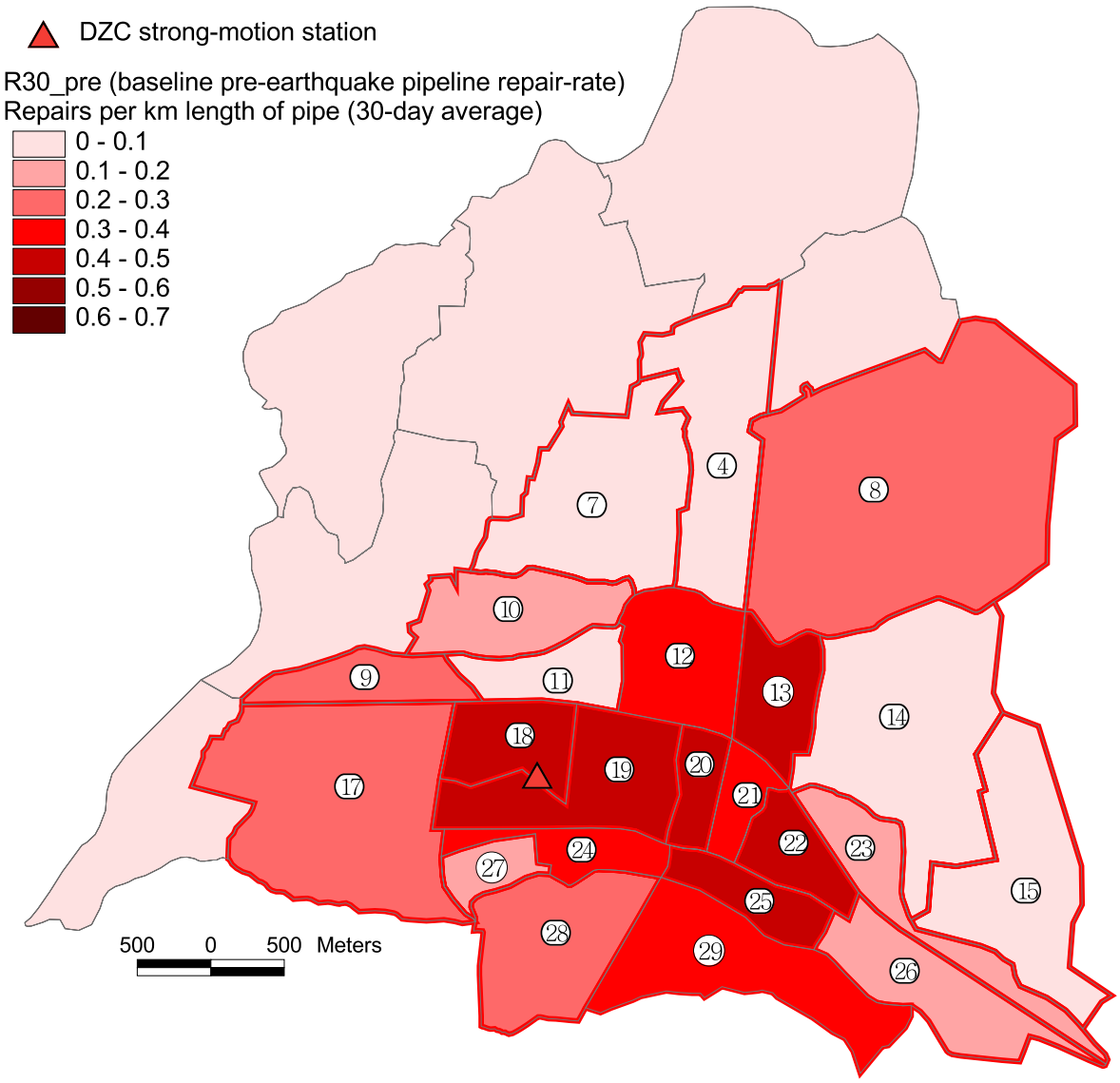

Figure 8.3 Baseline pre-earthquake pipeline repair rates, *R30_pre* (repairs per km adjusted to a 30-day average)

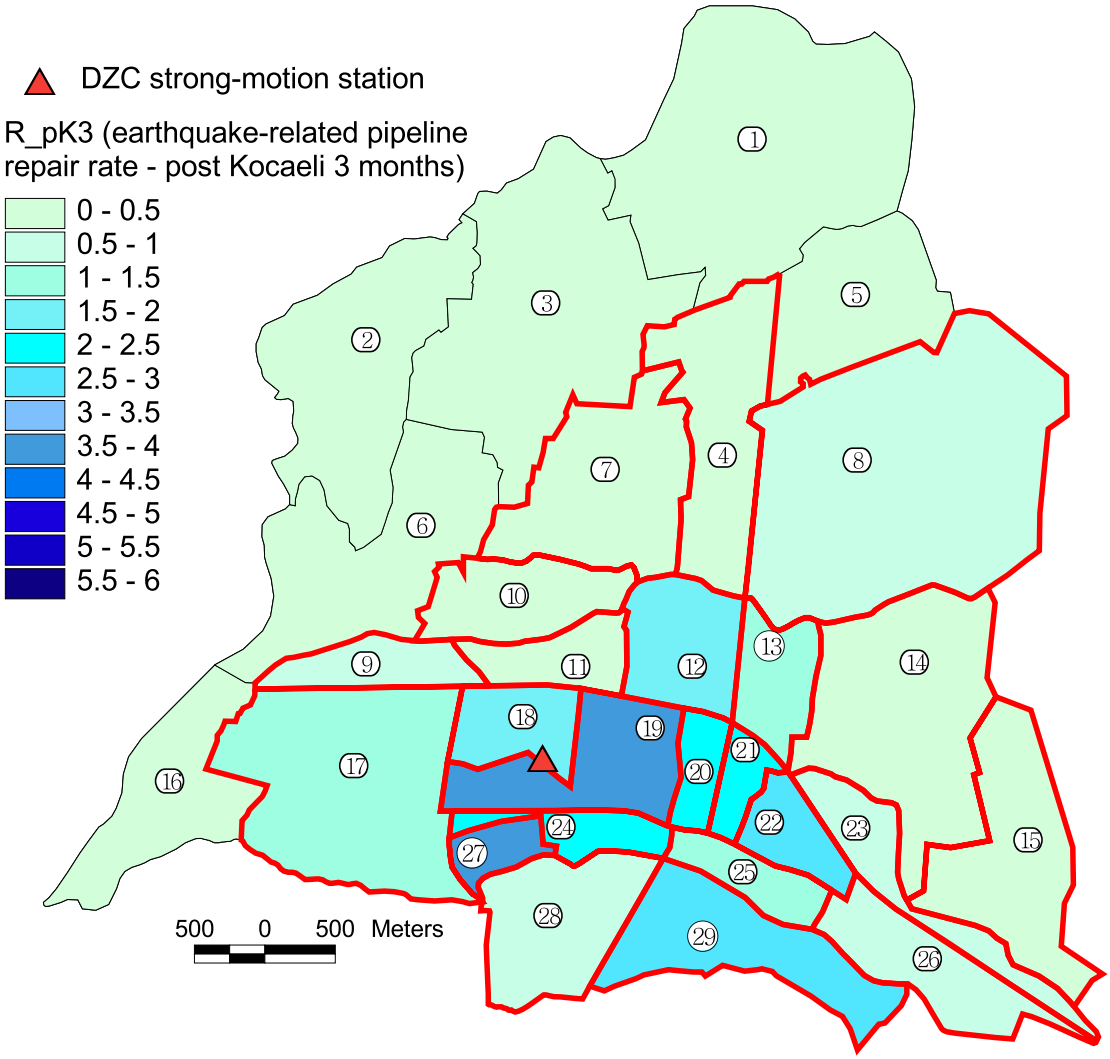

Figure 8.4 Post-earthquake pipeline repairs (per km of pipe) summed over the 3 months immediately following the Kocaeli earthquake, *R_pK3*.

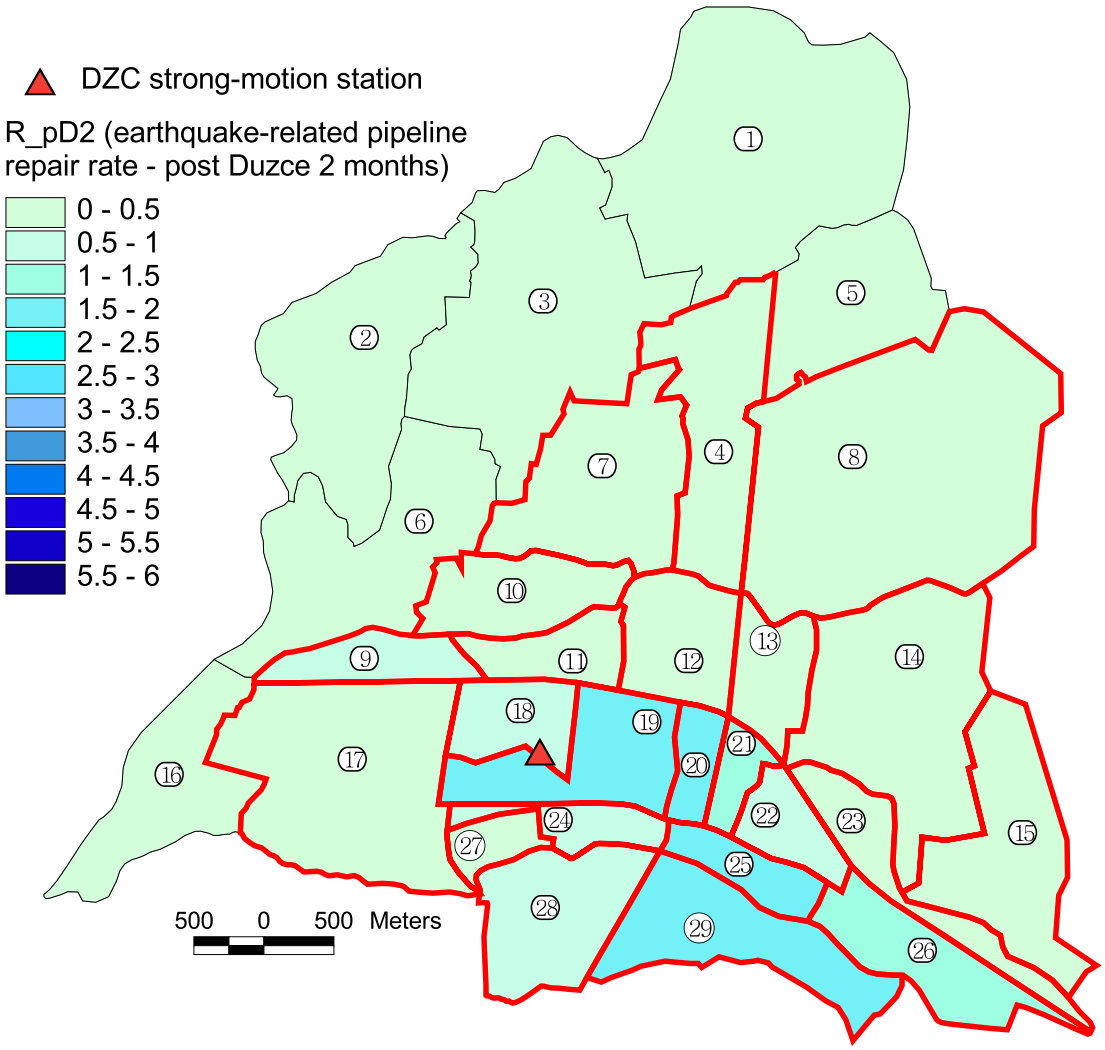

Figure 8.5 Post-earthquake pipeline repairs (per km of pipe) summed over the 2 months immediately following the Düzce earthquake, *R_pD2*.

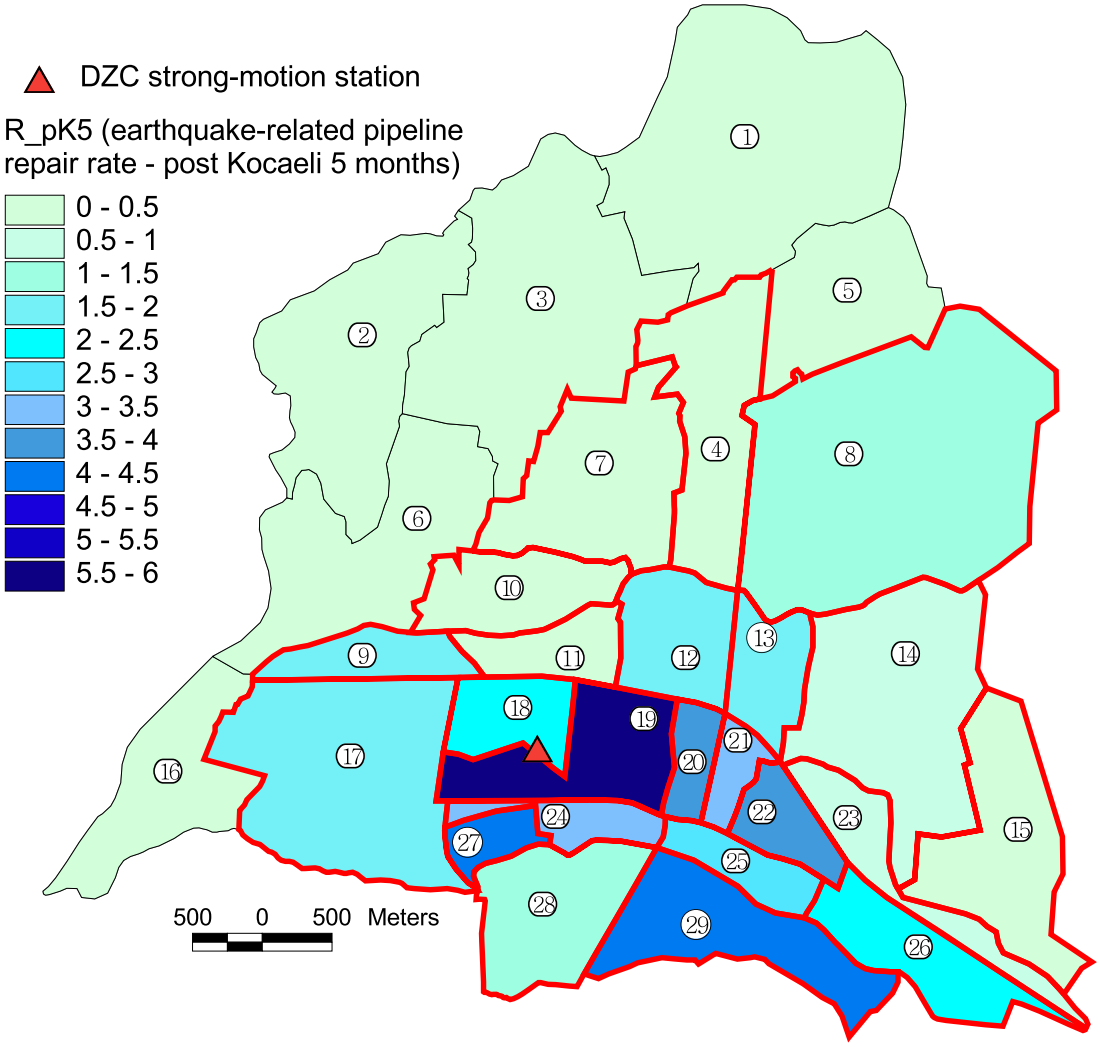

Figure 8.6 Post-earthquake pipeline repairs (per km of pipe) summed over the 5 months immediately following the Kocaeli earthquake, *R_pK5*.

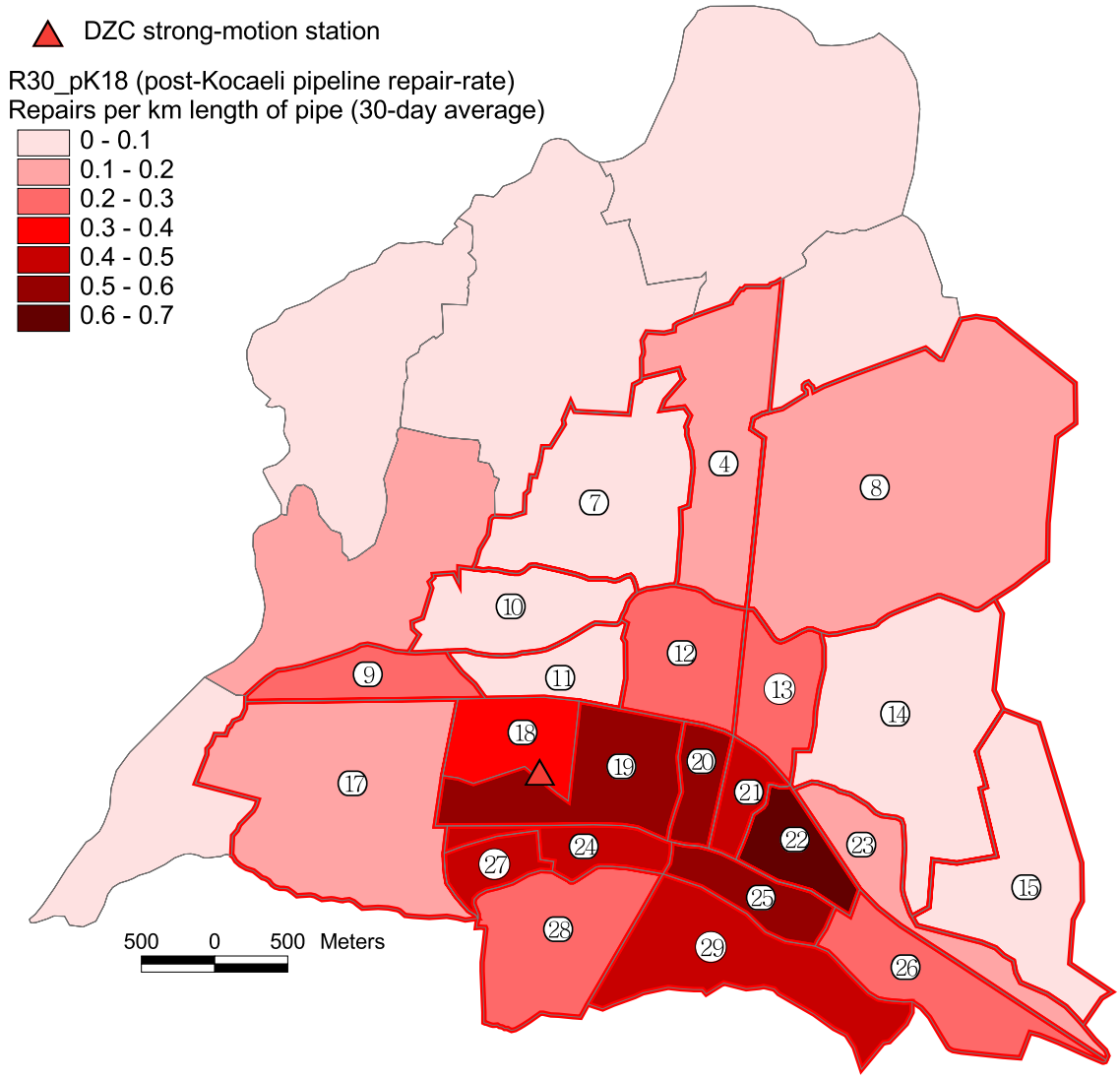

Figure 8.7 Post-earthquake pipeline repair rates for the 18 months following the Kocaeli earthquake, *R30_pK18* (repairs per km adjusted to a 30-day average).

All quantities mapped are based on pipe lengths obtained from the Iller Bankası maps. These values should be multiplied by the pipe length adjustment factor, C_{PL} = 435/780, to compare with values obtained in studies of other earthquake-damaged pipe systems. District boundaries shown in red in these figures and in subsequent maps of Düzce constitute the focus area for the current investigation. This area consists of the most built-up districts of Düzce. Several of the outlying districts are very rural and were excluded from the GIS analysis as damage statistics were considered less reliable. The focus area was defined according to the spatial density of buildings, details of which are given in Section 8.2.2.

The pre-earthquake repair rate, *R30_pre*, varies considerably across the town (Figure 8.3). Six districts in the central region required between 0.4 and 0.5 repairs per km per month (*i.e.* 0.22 – 0.28 repairs per km per month adjusted by C_{PL}) whereas the average for the whole town is 0.23 repairs per km per month (0.13 after adjustment). In Table 8.3, equivalent annual repair rates for Düzce (adjusted by C_{PL}) are compared with typical values for water distribution networks in Western Europe, as reported by Twort *et al.* (2000). Repair rates in Düzce are, on average, about six times greater than those observed in water distribution networks in the UK or Germany (Table 8.3). This is evidence of the poor condition of Düzce's water distribution system prior to the earthquakes and is an important consideration when interpreting the post-earthquake repair statistics.

Table 8.3 Comparison between pre-earthquake distribution main pipeline repair (fracture) rates for UK , Germany and Düzce.

Description	Average number per km per annum		
	UK	Germany	Düzce
Distribution main fracture rate (lowest)	0.1 – 0.15	0.14	0
Distribution main fracture rate (average)	0.2 – 0.35	not given	1.54
Distribution main fracture rate (above average)	0.4 – 0.55	not given	3.38

Figure 8.4 suggests that pipeline damage caused by the Kocaeli earthquake was greatest in districts 19 and 27, exceeding 3.5 breaks per km length of pipe. Two other districts (22 and 29) suffered damage rates in excess of 2.5 breaks per km.

A comparison between Figures 8.4 and 8.5 suggests that more pipeline damage occurred as a result of the Kocaeli earthquake than as a result of the Düzce earthquake, for almost every district in Düzce. The spatial variation in the combined damage as a result of both earthquakes is shown in Figure 8.6.

A summary of results from Figures 8.4 – 8.6 for selected regions is presented in Table 8.4. The DZC strong-motion station is situated just within the boundary of district 18 and adjacent to district 19. Results are therefore summarised for both of these districts. Average repair rates over these two districts are calculated due to the significant differences between the individual values. Average repair rates for the whole town are also included. Repair rates immediately following the

Düzce earthquake are, on average, about half the value of repair rates immediately following the Kocaeli earthquake.

Table 8.4 Summary of observed pipeline repair rates for Düzce following the Kocaeli and Düzce earthquakes

Location	Repairs per km pipe, R_R (unadjusted)			Repairs per km pipe, R_R (adjusted by C_{PL})		
	Kocaeli earthquake *R_pK3*	Düzce earthquake *R_pD2*	Both earthquakes *R_pK5*	Kocaeli earthquake *R_pK3*	Düzce earthquake *R_pD2*	Both earthquakes *R_pK5*
District 18 (*Uzunmustafa*)	1.55	0.52	2.06	0.86	0.29	1.15
District 19 (*Kültür*)	3.66	1.95	5.61	2.04	1.09	3.13
Average (districts 18 & 19)	2.82	1.38	4.20	1.57	0.77	2.34
Average (whole focus area)	1.27	0.62	1.88	0.71	0.34	1.05

It is useful to compare these observed pipeline repair rates with predicted values based on empirical pipeline fragility relations, as reviewed in Chapter 3. PGV values obtained from strong-motion data recorded at DZC during the Kocaeli and Düzce earthquakes are summarised in Table 8.5. Predictions of pipeline repair rate based on these values have been summarised in Table 8.6.

Table 8.5 Strong-motion values recorded at DZC and used in the predictions in Table 8.6. PGV_L is the largest of the two horizontal components of PGV, as used in the HAZUS fragility relation; PGV_G is the geometric average of the two horizontal components of PGV, as used in the ALA (2001) fragility relation.

	Kocaeli earthquake	Düzce earthquake
PGV - NS component (cm/s)	41	37
PGV - EW component (cm/s)	54	84
PGV_L (cm/s)	54	84
PGV_G (cm/s)	47	56

Table 8.6 Summary of predicted pipeline repair rates for Düzce based on the HAZUS and ALA (2001) fragility relations and using PGV values from Table 8.5.

	Pipeline repair rate, R_R (per km)		
	Kocaeli earthquake	Düzce earthquake	Both earthquakes
HAZUS prediction	0.79	2.14	2.93
ALA (2001) prediction	0.11	0.13	0.25

As discussed in Chapter 3, different pipeline fragility relations can give very different predictions of pipeline damage rate for the same strong-motion values. The values calculated in Table 8.6 are from the HAZUS and ALA (2001) fragility relations (Equations 3.33 and 3.36 respectively). The HAZUS relation assumes brittle pipes, as found in Düzce. The ALA (2001) relation was used with a modification factor, $K_{1ALA} = 1.0$, chosen to reflect the typical pipe-joint conditions found in Düzce (see Table 3.5). The HAZUS predictions are significantly larger than the ALA (2001) predictions for both earthquakes. What is more striking is the fact that the ALA (2001) fragility relation predicts very similar damage rates for both earthquakes whereas the HAZUS fragility relation

predicts almost three times more damage from the Düzce earthquake than from the Kocaeli earthquake. This is a result of the different ways in which these fragility relations use the horizontal components of PGV. The differences are emphasised in the case of the Düzce strong-motion record because the EW component of PGV is more than twice as large as the NS component, leading to greater differences between the quantities PGV_L and PGV_G (Table 8.5).

The difference between the ALA (2001) and HAZUS predictions is best understood with reference to the Kocaeli earthquake. The ratio of PGV_L to PGV_G for this earthquake at the DZC strong-motion station is 0.87, which is similar to average values of this ratio used to derive the ALA (2001) fragility relation (see Section 3.3.1.8). PGV_L/PGV_G for the Düzce earthquake at the same station is much lower (0.67) and therefore unrepresentative of the ALA (2001) dataset. The pipeline damage rate predicted by the ALA (2001) relation for the Kocaeli earthquake is around seven times lower than that predicted by the HAZUS relation. Some of this difference can be explained by the difference in the method used to derive these relations. The ALA (2001) relation is based on the median slope of all points in the dataset, resulting in a linear relationship (Equation 3.36), whereas the HAZUS relation assumes a power relationship between PGV and pipeline repair rate. A median slope method used on the HAZUS dataset (obtained from O'Rourke & Ayala, 1993) yields the following alternative fragility relation:

$$R_R = 0.005833 PGV_L \tag{8.1}$$

where R_R is the pipeline repair rate (per km), PGV_L (cm/s). This relation predicts a repair rate of 0.315 /km as a result of the Kocaeli earthquake, which suggests that the use of different data fitting methods accounts for about half of the difference in the predicted values in the case of the Kocaeli earthquake. The remaining difference can be explained by differences in pipeline vulnerability and seismic action.

The HAZUS predictions are closer to the actual values observed in Düzce than the ALA (2001) predictions. The sum of the predicted damage for the two earthquakes using the HAZUS relation is very similar to the value of *R_pK5* observed in the region immediately surrounding the DZC strong-motion station (and highlighted in Table 8.4). The main difference between the HAZUS predictions and the observed values is in the relative damage attributed to each earthquake. The predictions indicate 2.7 times more damage during the Düzce earthquake than during the Kocaeli earthquake, whereas the opposite is the case for the observed damage; damage caused by the Kocaeli earthquake appears to have exceeded the damage caused by the Düzce earthquake by a factor of about 2.0.

It was suggested in Chapter 6 that the strong motion experienced in Düzce during the Kocaeli earthquake may have been dominated by surface waves whereas body waves are likely to have dominated the motion during the Düzce earthquake. If this were the case, peak ground strains induced in Düzce by the Kocaeli earthquake may actually have been higher than those induced by

the Düzce earthquake, even though the PGV was lower, which would help explain the differences between the observed and predicted levels of pipeline damage. The different levels of strain induced by different seismic wave types, even for the same level of PGV, was explained in Chapter 3. This explanation however is not satisfactory as significant surface waves are likely to have been generated in Düzce as a result of the Düzce earthquake, due to the location of the town in the centre of an alluvial basin.

From a closer inspection of the strong-motion records, the Düzce earthquake would be expected to produce greater levels of damage than the Kocaeli earthquake. Husid plots are presented in Figure 8.8 to compare the time variation in Arias intensity between the two earthquakes at the DZC strong-motion station. The Arias intensity associated with the Düzce earthquake is more than twice the value associated with the Kocaeli earthquake, for both horizontal components of motion. The rate of arrival of energy at DZC, as indicated by the gradient of the Husid plot, was also much higher during the Düzce earthquake, again indicating greater damage potential. Finally, longer duration of ground shaking during the Düzce earthquake (as indicated in Figure 8.8) is another factor likely to have contributed to greater damage levels. Energy-equivalent velocity spectra presented by Sucuoglu & Yilmaz (2001) also support the assertion that strong motion during the Düzce earthquake caused greater damage in Düzce than strong motion during the Kocaeli earthquake.

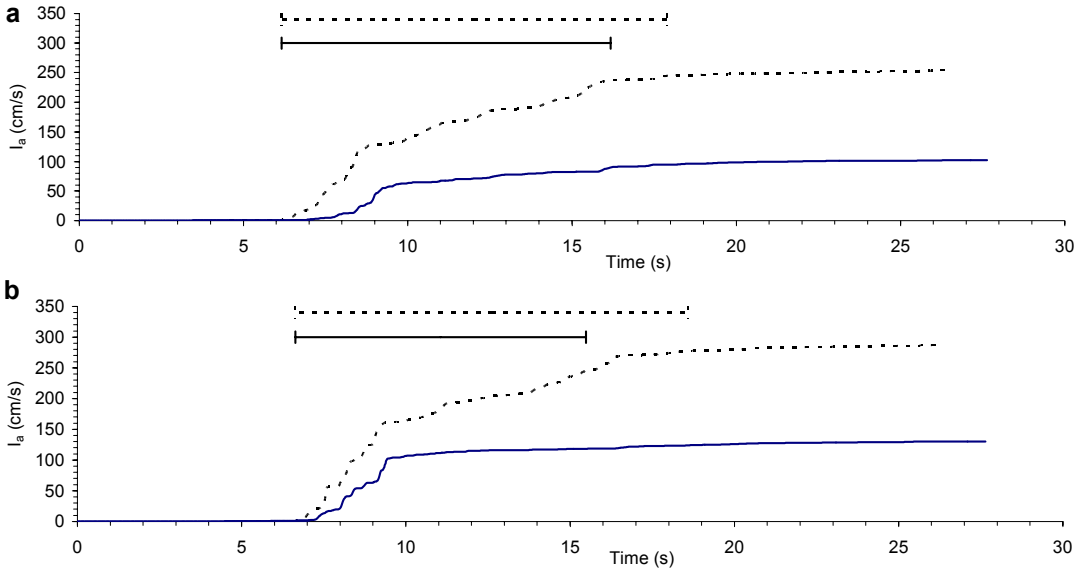

Figure 8.8 Comparison between Husid plots for accelerograms recorded at DZC strong-motion station during the Kocaeli and Düzce earthquakes. Figure a shows NS components for both earthquakes. Figure b shows EW components for both earthquakes. Data from the Kocaeli earthquake is indicated with a solid line; data from the Düzce earthquake is indicated with a dotted line. For each Husid plot, the effective duration, d_{eff} (Bommer & Martinez-Pereira, 1999) is indicated. For each pair of components, the Düzce record has been shifted in time so that the start times, t_0 are the same.

The most likely explanation for the lower levels of pipeline damage observed following the Düzce earthquake is incomplete documentation of repairs carried out in the period immediately after the earthquake. Restoration of an adequate water supply will have taken precedence over systematic

record keeping at this time. Some of the repairs carried out by third parties assisting in the post-earthquake restoration (eg. Iller Bankası, as reported in Efendioglu, 2001) may not have been recorded in the Municipality logbook used in the current study.

Another possible explanation is that significant numbers of repairs of earthquake-related pipeline damage were carried out more than two months after the Düzce earthquake. The significant increase in pipeline repair rates observed in June-July 2000 and especially October and November 2000 (Figure 8.2) could be interpreted as continued recovery from earthquake damage. It is not known whether this is indeed the case.

In September 2000, UNICEF carried out a leakage survey of Düzce's water distribution system. The results, published in Tadday & Sahin (2001) suggest that unaccounted for water, UFW (defined by Equation 8.2) ten months after the Düzce earthquake exceeded 80 %.

$$UFW = \frac{W_P - W_B}{W_P} \tag{8.2}$$

where: W_P is the volume of water produced and introduced to the distribution network and
W_B is the volume of water billed or consumed.

The value quoted is probably an overestimate, as it was based on the assumption that the rate of leakage during the day was the same as that observed during the night, without accounting for the reduced daytime water pressures. Rather than multiplying the hourly night leakage ("nightline") by 24 to obtain total daily water losses, it is in fact more accurate to multiply the nightline by 20 hours (PWA, 2002). Recalculating the UFW based on this modified approach gives a value of 69.6%. This reduced estimate of UFW is still extremely high compared to typical values observed in many towns or cities in Western Europe, but is still within the limits of UFW estimates for many other parts of the world. This is illustrated in Table 8.7 using data from other parts of Eastern Europe. The high post-earthquake level of UFW in Düzce therefore does not necessarily indicate that significant numbers of network repairs of earthquake-related pipeline damage had still to be done ten months after the Düzce earthquake.

Table 8.7 Comparison of water distribution network losses for several locations

Town / city	UFW (%)	Date	Source
Düzce, Turkey	70	2000	This study
Bursa, Turkey	54	1998	Halperin (1998)
Kutahya, Turkey	65	2000	Merzi (2001)
Tbilisi, Georgia	84	1997	Halperin (1998)
Odessa, Ukraine	≈ 80	1997	Halperin (1998)

In conclusion, average repair rates in districts 18 and 19 due to the Kocaeli earthquake exceed HAZUS estimates by about a factor of two. Repair rates observed in district 18 and across the whole of Düzce (focus area average) are very similar to the HAZUS predictions. The quantity *R_pK3* is considered to be a good indicator of pipeline damage levels as a result of the Kocaeli earthquake.

Consideration of the damage potential of strong-motion recorded at DZC suggests that the quantity *R_pD2* underestimates pipeline damage as a result of the Düzce earthquake. The most likely explanation for this underestimation is incompleteness in the pipeline repair log in the immediate aftermath of the Düzce earthquake. Some of the repairs carried out more than two months after the Düzce earthquake may have been related to earthquake damage. Trends observed in the time line presented in Figure 8.2 and the results of a UNICEF leakage survey are inconclusive in this regard.

8.2.2 Building damage index

Data relating to Düzce's building stock and damage caused to buildings as a result of the Kocaeli and Düzce earthquakes were obtained from the Municipality's GIS Division. Data are summarised in Table K1 (Appendix K). Data were available at the district level, although no data were given for District ID 5 (Cavuslar).

The distribution in the spatial density of buildings (designated S_b) was used to define the area of interest for the current investigation, for reasons already explained. This dataset is mapped in Figure 8.9. As indicated in Table K1, there is a natural break in the data covering the range 99.6 - 131.4 buildings per km^2. It was therefore decided to exclude from the analysis all districts having $S_b < 100$ buildings per km^2.

As shown in Figure 8.10, the region defined using this building spatial density criterion is very similar to the region defined by districts having a pipeline spatial density, S_p of at least 10 km per km^2. However, the S_b criterion was selected over the S_p criterion as data pertaining to above-ground structures was considered more reliable than data pertaining to buried structures.

Building damage data in Table K1 is given in terms of the number of buildings in each district, N_{Di} having a certain level of damage, i. Building damage was defined according to a four-level classification scheme, details of which are summarised in Table 8.8. These data refer to the situation following the second earthquake. The available data do not make any distinction between damage caused by the two earthquakes.

Table 8.8 Building damage classification for Düzce (translated from Kajitani *et al.*, 2002). Approximate equivalence to EMS-98 damage grades is also from Kajitani *et al.* (2002).

Damage grade	Description	Details	Approximate equivalence to EMS-98 (Grunthal, 1998) damage grade
1	No damage	No visible damage.	-
2	Light damage	No damage to main supporting system of building (foundation or main pillars). Cracks visible in non-structural walls. Building habitable.	1 & 2
3	Medium damage	Some damage and weakening of main supporting system. Cracks visible in beams or shallow cracks visible in columns. Partial collapse of non-structural walls.	3
4	Heavy damage	Significant destruction of main supporting system. Columns or structural walls split or collapsed. Building toppled or partially or totally collapsed.	4 & 5

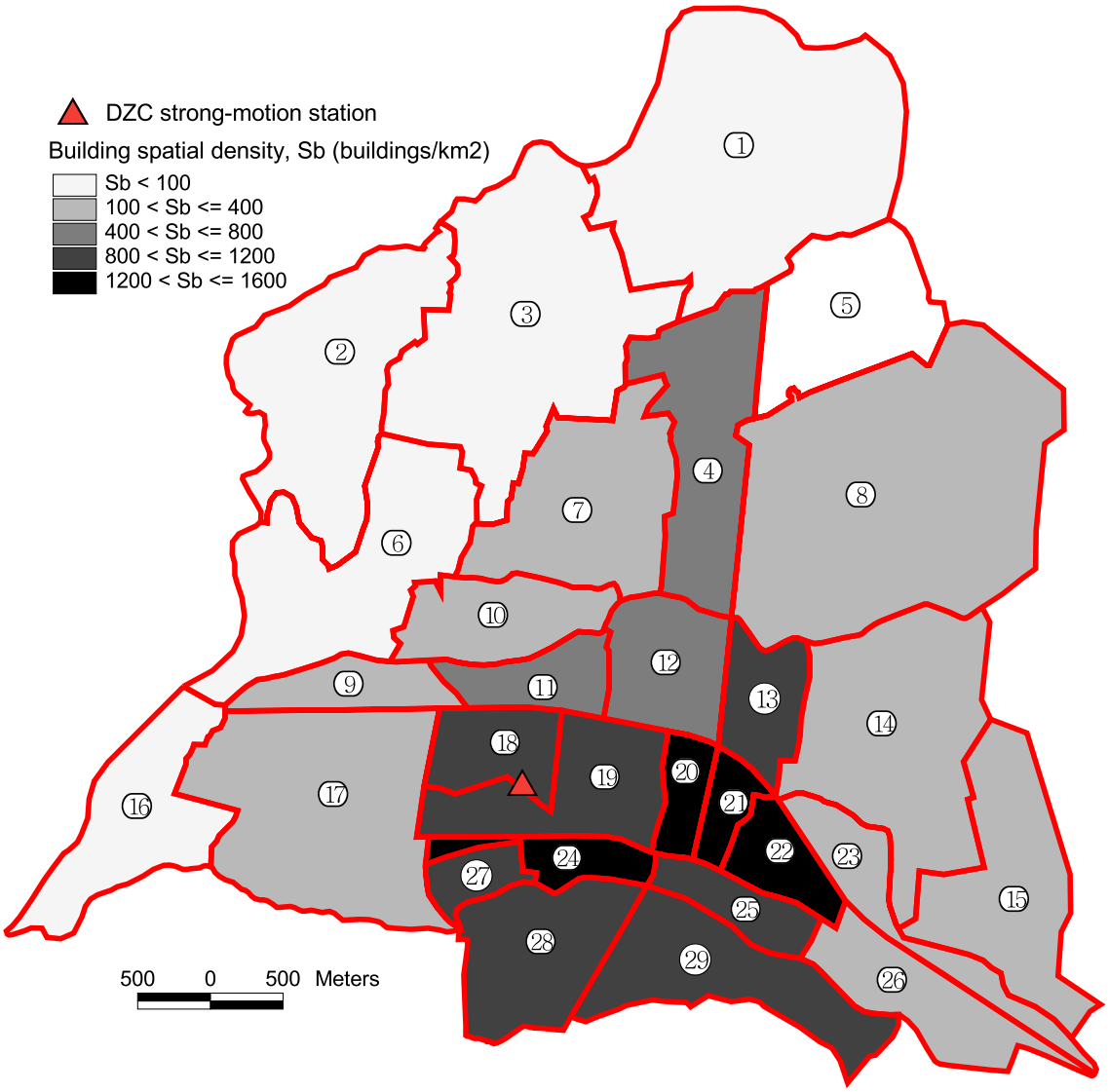

Figure 8.9 Spatial density of buildings across Düzce, S_b

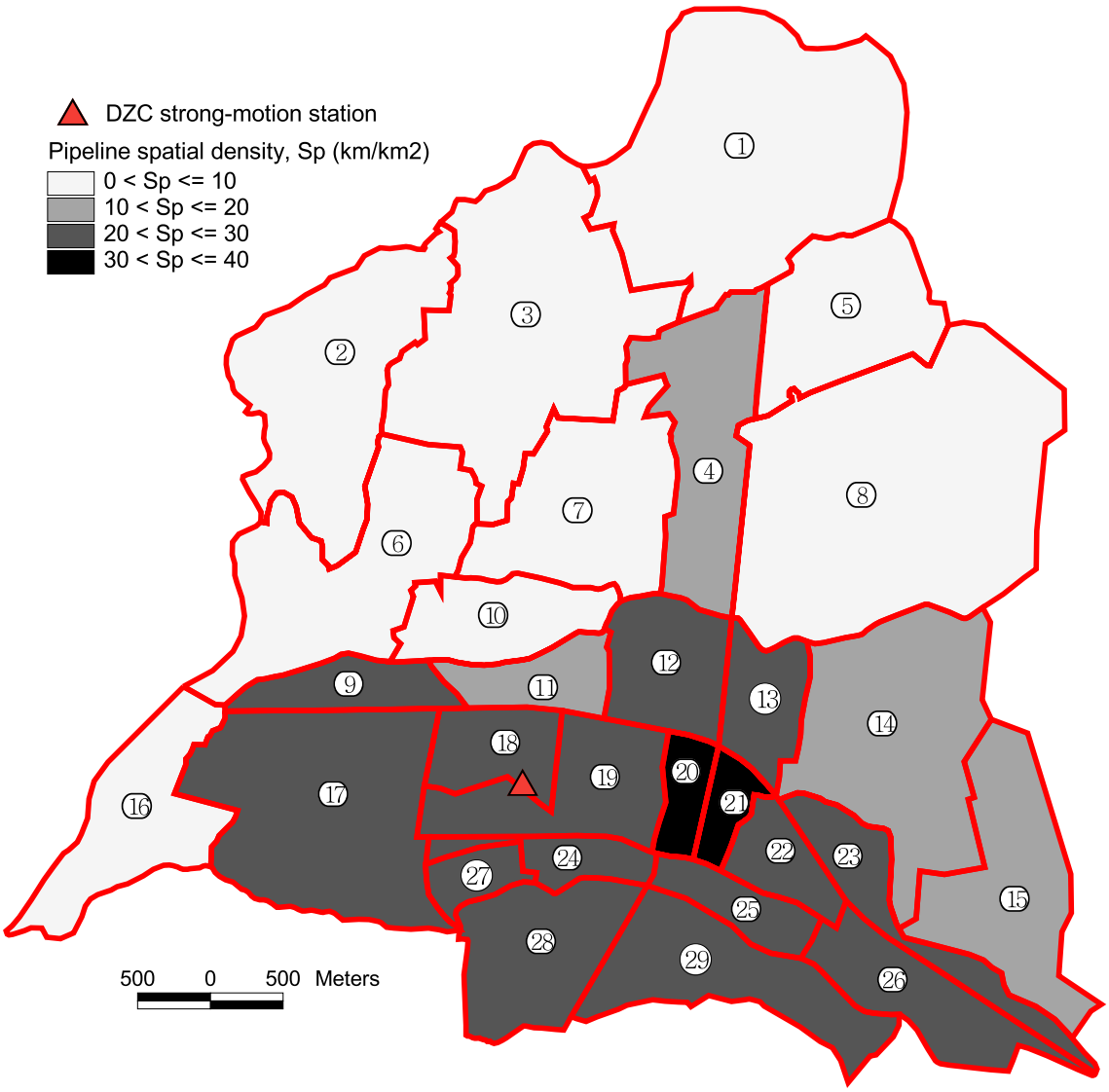

Figure 8.10 Spatial density of pipelines across Düzce, S_p

The building stock in each district was also classified by the number of storeys. The number of buildings of i storeys is given by N_{Si}. Summing N_{Di} and N_{Si} reveals that some buildings in most districts have not been classified according to the number of storeys. This generally only affects less than 10% of the total number of buildings in each district and does not significantly affect the analysis in the current investigation.

In order to quantify total damage, it is common to combine data for different damage grades into a single damage index, D_1, using a weighted average, as expressed in Equation (8.3):

$$D_1 = \frac{\sum_{i=1}^{n} \left(W_i N_{Di} / N_{Btot} \right)}{\sum_{i=1}^{n} W_i} \tag{8.3}$$

where: W_i are damage grade weighting coefficients, as given in Table 8.9,
N_{Di} is the number of buildings at a given damage grade for a particular district,
N_{Btot} is the total number of buildings in a particular district

Table 8.9 Building damage classification and weighting scheme

Damage Grade, i	Description	Weighting Coefficient, W_i	
		Damage index D_1	Damage index D_2
1	No damage	0	0
2	Light damage	0.25	0.2
3	Medium damage	0.5	0.5
4	Heavy damage	1	1

For the current study, the damage index, D_1 was found using the same weighting scheme as used by the Municipality, which is summarised in Table 8.9. This is very similar to the scheme used by Gueguen *et al.* (1998) in an investigation into building damage distribution following the 1996 Pujili, Ecuador earthquake (D_2 in Table 8.9). Both schemes give almost identical results for the Düzce data.

The spatial distribution of the quantity D_1 is illustrated in Figure 8.11. The area experiencing the worst building damage ($D_1 > 0.28$) is a continuous region in the central part of the town made up of six districts (19, 20, 21, 22, 25 and 25).

As already mentioned in Chapter 7, the damage to buildings of four storeys or more was significantly greater than the damage to buildings having fewer storeys. This was illustrated in Figure 7.8 using damage data aggregated for the whole town. The spatial variation in the percentage of buildings of four storeys or more is illustrated in Figure 8.12. Districts in the centre of Düzce have the highest percentage of tall buildings, up to a value of 51 % in the case of District 25 (Cedidiye). The districts experiencing the worst building damage and the districts containing the highest proportion of tall buildings are generally the same. The correlation between these two quantities for all districts of Düzce is remarkable, as illustrated in Figure 8.13.

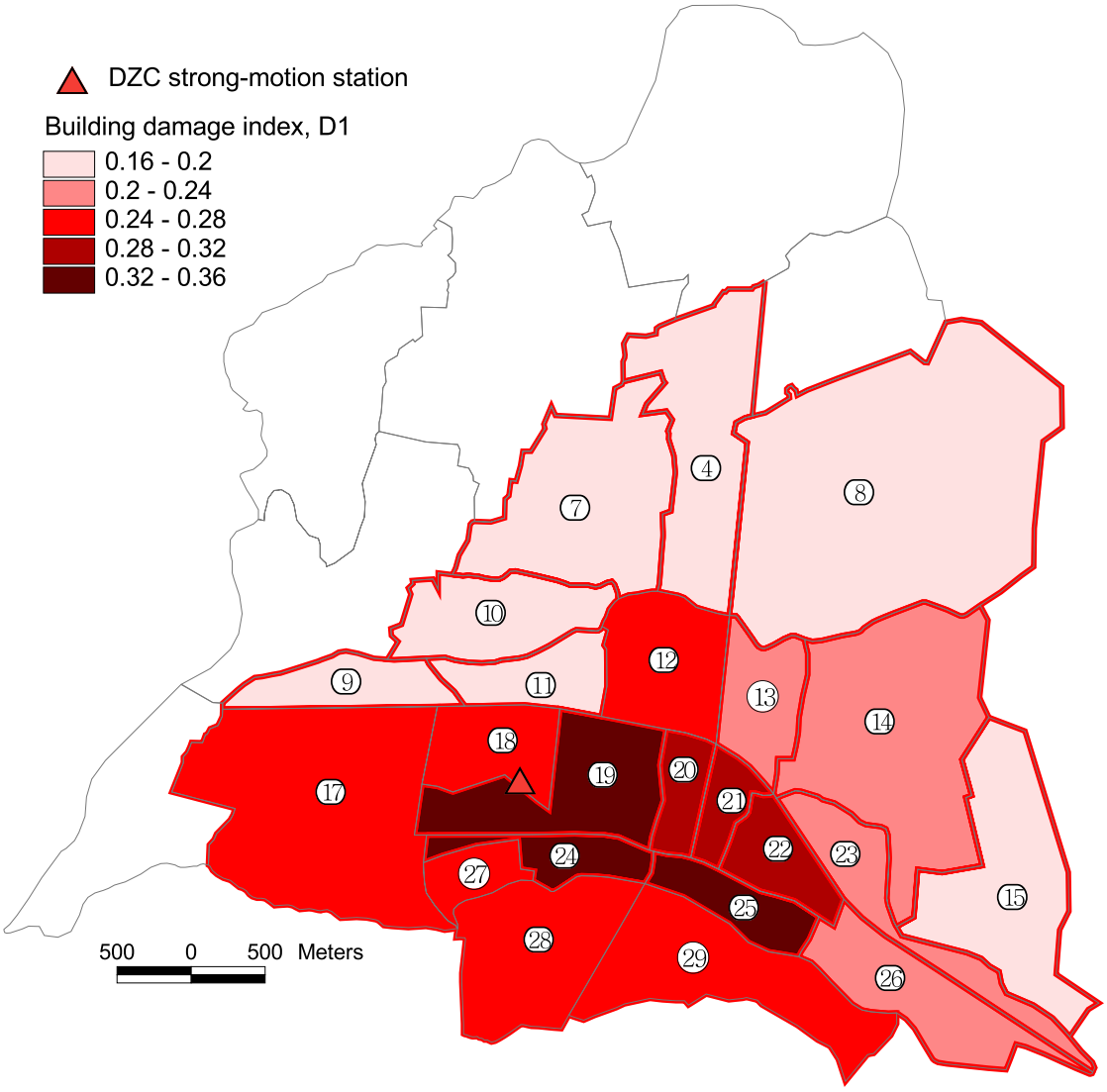

Figure 8.11 Distribution of building damage index, D1

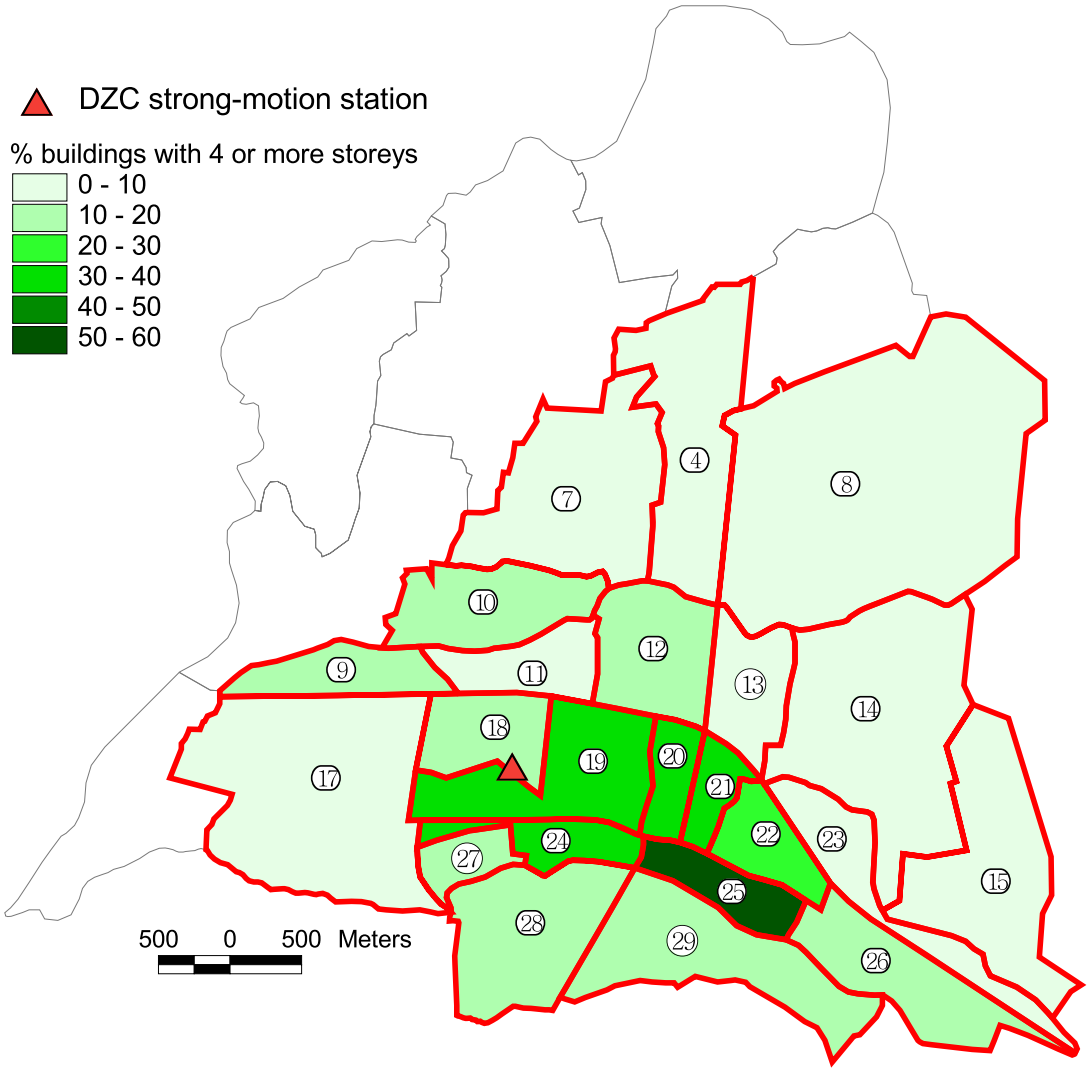

Figure 8.12 Percentage of buildings with 4 or more storeys

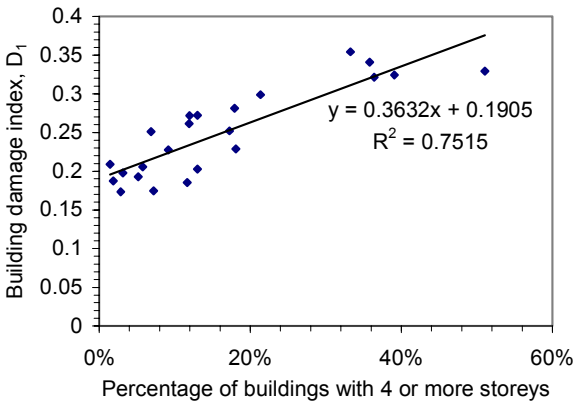

Figure 8.13 Correlation between the percentage of buildings per district having at least 4 storeys and building damage index, D_1.

Another factor known to have influenced damage levels is building construction type. Reinforced concrete structures generally suffered much worse than traditional wood-framed buildings with stone or brick infill panels (Yoshikawa *et al.*, 2001). Detailed information on Düzce's building inventory, however, was not available to the author.

The quality of construction is also known to have played a significant role in the high levels of building damage observed (Thompson, 1999). The influence of construction quality on the damage statistics for Düzce cannot be quantified, due to lack of data. Ansal *et al.* (1999) in their study of building damage distribution following the 1995 Dinar earthquake, suggest that the structural characteristics of buildings in Dinar were reasonably uniform since for a small town, most of the design and construction tends to be performed by a small number of engineers, architects and builders. The same assumption can be made for the town of Düzce. The total level of damage in Düzce *will* have been influenced by construction quality. Variations in building damage levels from district to district, however, are more likely to have been caused by variations in the proportion of tall buildings and variations in ground motion, influenced by site conditions.

The building damage statistics obtained from Düzce Municipality and presented in Table K1 do not shed any light on the relative damage caused by the Kocaeli and Düzce earthquakes, as they make no distinction between these two events. Sucuoglu & Yilmaz (2001), however, have presented statistics of the proportion of households in Düzce having different levels of damage following each of the two events. These data are summarised in Figure 8.14. It should be noted that households and buildings are not the same thing; Düzce has about 20,000 households in a total of around 10,000 buildings as much of its population lives in multi-occupancy apartment blocks.

Few households survived both earthquakes without damage. The proportion of households suffering each of three different levels of damage was significantly greater as a result of the second earthquake than the first, with the greatest increase relating to the high damage category. These statistics indicate that both earthquakes caused significant damage to Düzce's building stock.

However, it is difficult to make inferences about the relative levels of ground motion experienced during these two earthquakes as few of the households damaged by the Kocaeli earthquake had been repaired prior to the Düzce event. The building stock experiencing the Düzce earthquake was therefore much more vulnerable than the building stock which experienced the Kocaeli earthquake.

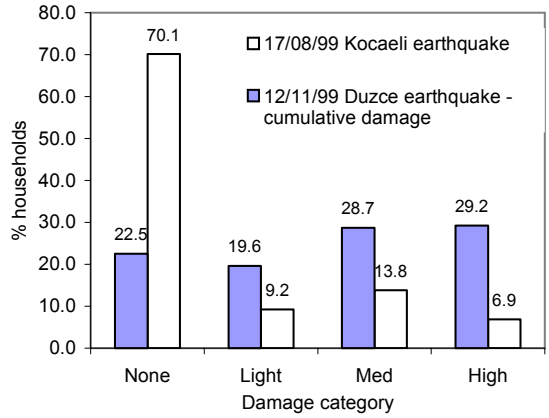

Figure 8.14 Comparison between damage to households in Düzce following the Kocaeli and Düzce earthquakes

Lekkas (2000) used damage surveys, aerial photos and satellite data to establish the macroseismic intensity distribution as a result of the Kocaeli and Düzce earthquakes, as already presented in Chapter 6. In the region between Adapazari and Düzce intensity was estimated from the combined effects of the two earthquakes. Based on damage observed to reinforced concrete structures, Lekkas (2000) attributed about 30% of the damage to the first earthquake and 70% to the second earthquake.

8.2.3 Site effects from HVSR of microtremor data

Site effects across the town of Düzce have been characterised using the HVSR obtained from microtremor measurements, as described in the previous chapter. In the current section, the spatial variations in four HVSR parameters are presented and discussed.

The full microtremor dataset consists of 121 measurements made at 114 different locations, as summarised in Table I2. The majority of these measurements were taken within, or just outside the district boundaries defined in the previous section (the 'focus area'). Several additional measurements were taken at locations slightly further afield in order to help interpret the results obtained within Düzce. These locations are shown in Figure 7.8. The GIS-based analysis is restricted to the points falling within or close to the district boundaries, as mapped in Figure 7.9 and highlighted in grey in Table I2. At a few of these locations more than one measurement was made within a distance of a few metres. These dual or triple instrument set-ups were carried out in order to help interpret the main dataset and are indicated in Table I1 in the first column of data. For each of these locations, a single measurement was selected for inclusion in the GIS dataset.

Coordinates for each microtremor measurement location were obtained using the handheld GPS (Garmin GPS 12). In several instances, GPS coordinates differed from measurement point locations identified from features on the Düzce base reference map by up to 140 m. These inconsistencies were due to limitations in the accuracy of the GPS (which has a maximum horizontal accuracy of 15 m assuming good satellite reception conditions, as stated in Garmin Corporation, 1999 & Garmin Corporation, 2002) and difficulties in transforming map data provided by Düzce Municipality from an unknown local coordinate system to a standard global coordinate system. Where necessary, measurement point locations were re-digitised with reference to features on the base map to give a location accuracy of at least 5 m within the mapped part of Düzce.

In order to help identify spatial trends in the microtremor data, each dataset was interpolated to create a parameter surface extending over the whole focus area. Interpolation was carried out within the GIS environment using the ArcView 3D Analyst Extension. A tension spline interpolation algorithm (based on a 5 m grid spacing, a weighting parameter of 20 and a fit to the nearest 6 grid points) was judged to give the best results. The parameter surfaces for all four HVSR quantities are presented in Figures 8.15-8.18. In order to investigate the influence of these parameters on pipeline damage rates, mean values of each parameter were computed at the district level using the ArcView Spatial Analyst Extension. Maps of these quantities are presented in Figures 8.19 and 8.21-8.23. Figure numbers of all microtremor quantities mapped are summarised in Table 8.10.

Table 8.10 Summary of microtremor quantities mapped.

Quantity mapped	Details	Figure No.
f_p	Predominant HVSR frequency	8.15
$A_{0.5\text{-}2}$	Average HVSR amplification (0.5 – 2 Hz)	8.16
$A_{2\text{-}5}$	Average HVSR amplification (2 – 5 Hz)	8.17
$A_{5\text{-}10}$	Average HVSR amplification (5 – 10 Hz)	8.18
Mean f_p	Predominant HVSR frequency – district mean	8.19
Mean f_p	Predominant HVSR frequency – district mean	8.20
Mean $A_{0.5\text{-}2}$	Average HVSR amplification (0.5 – 2 Hz) – district mean	8.21
Mean $A_{2\text{-}5}$	Average HVSR amplification (2 – 5 Hz) – district mean	8.22
Mean $A_{5\text{-}10}$	Average HVSR amplification (5 – 10 Hz) – district mean	8.23

Contours of soil depth (surface-to-bedrock) have been superimposed on each of the Figures summarised in Table 8.10. This information is from a geophysical investigation carried out by the Turkish General Directorate of Mineral Research and Exploration and Ankara University (MTA/AU, 1999), as presented in Aydan *et al.* (2000). Soil depths vary significantly, from around 50 m in the north-east to over 250 m in the south-west.

Figure 8.15 shows the predominant frequency, f_p, within Düzce varying between 0.56 Hz (at location 82) and 1.40 Hz (locations 99 and 100). There appears to be a general trend of increasing f_p from the western and central parts of the town towards the east and northeast. The trend is more

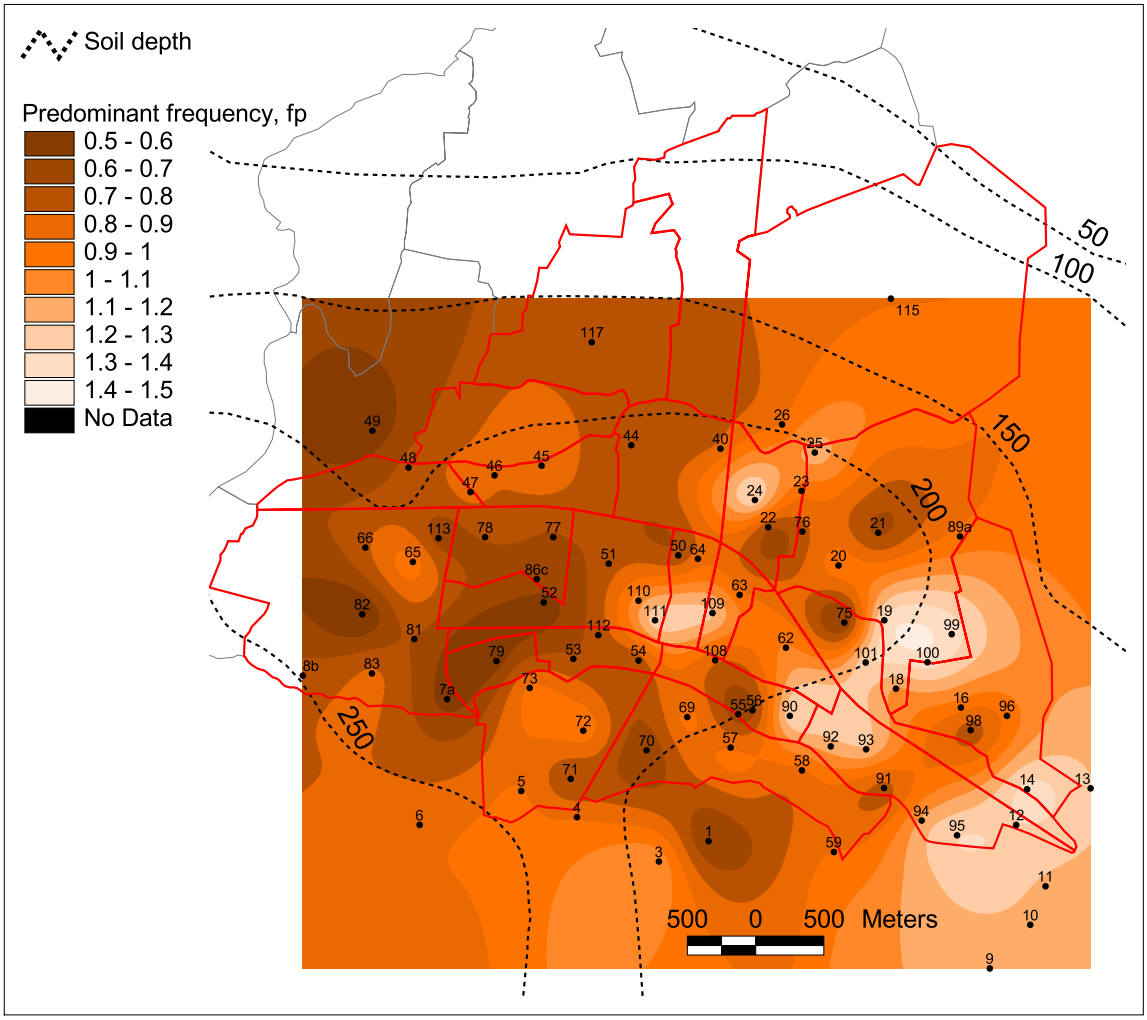

Figure 8.15 Contours of predominant frequency, f_p (Hz).

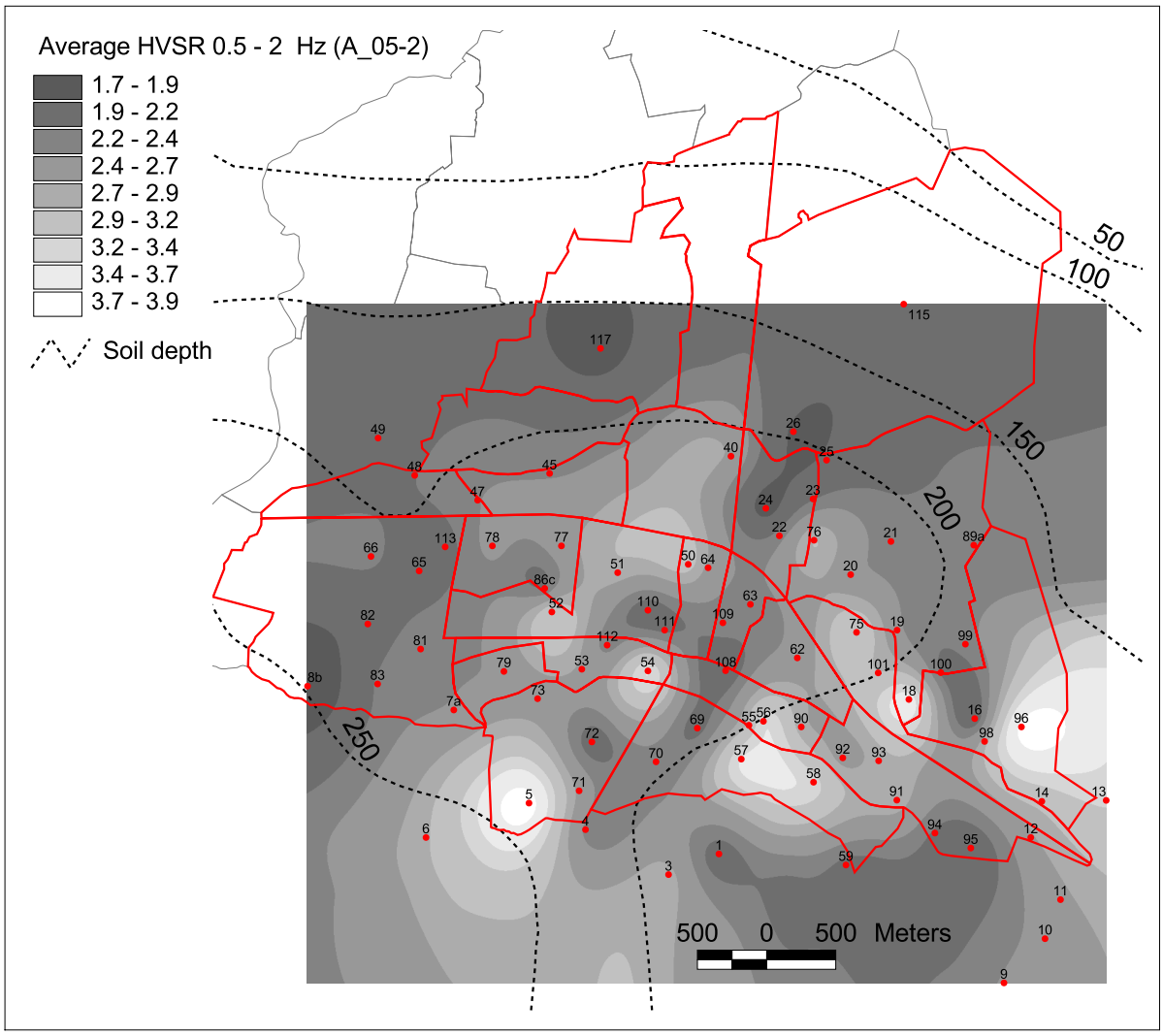

Figure 8.16 Contours of average HVSR amplification (0.5 – 2 Hz), $A_{0.5\text{-}2}$

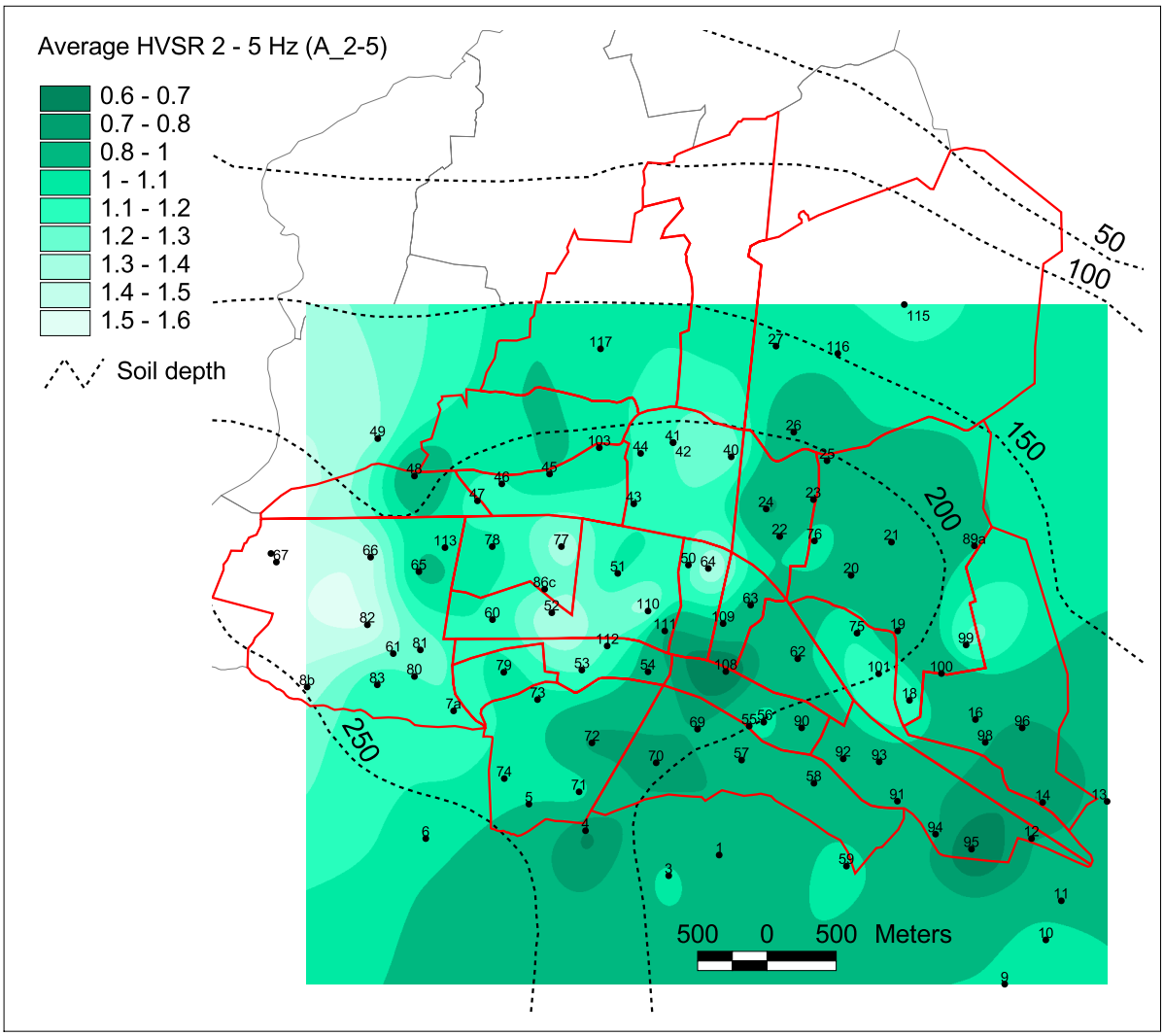

Figure 8.17 Contours of average HVSR amplification (2 -5 Hz), $A_{2\text{-}5}$

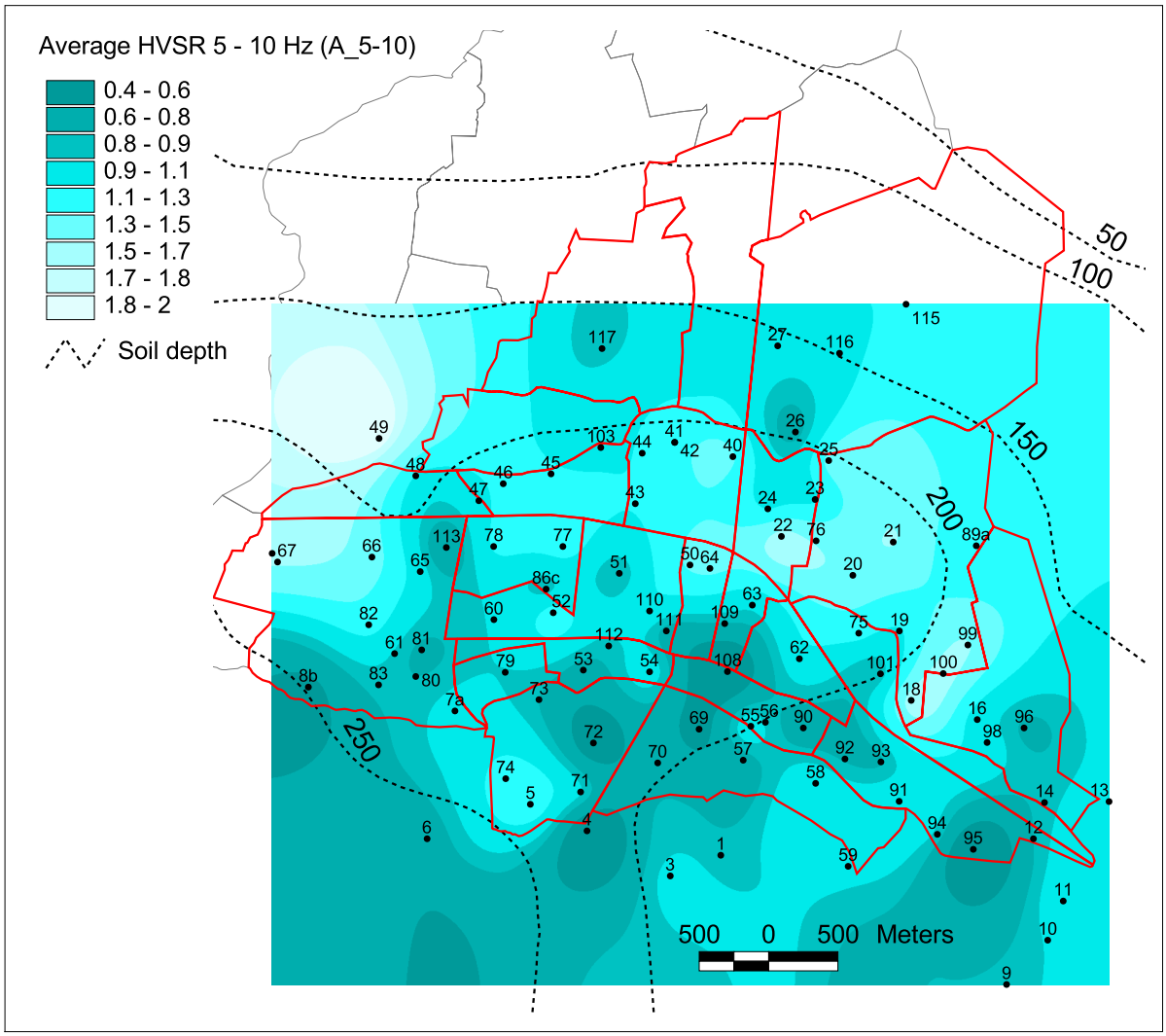

Figure 8.18 Contours of average HVSR amplification (5 – 10 Hz), $A_{5\text{-}10}$

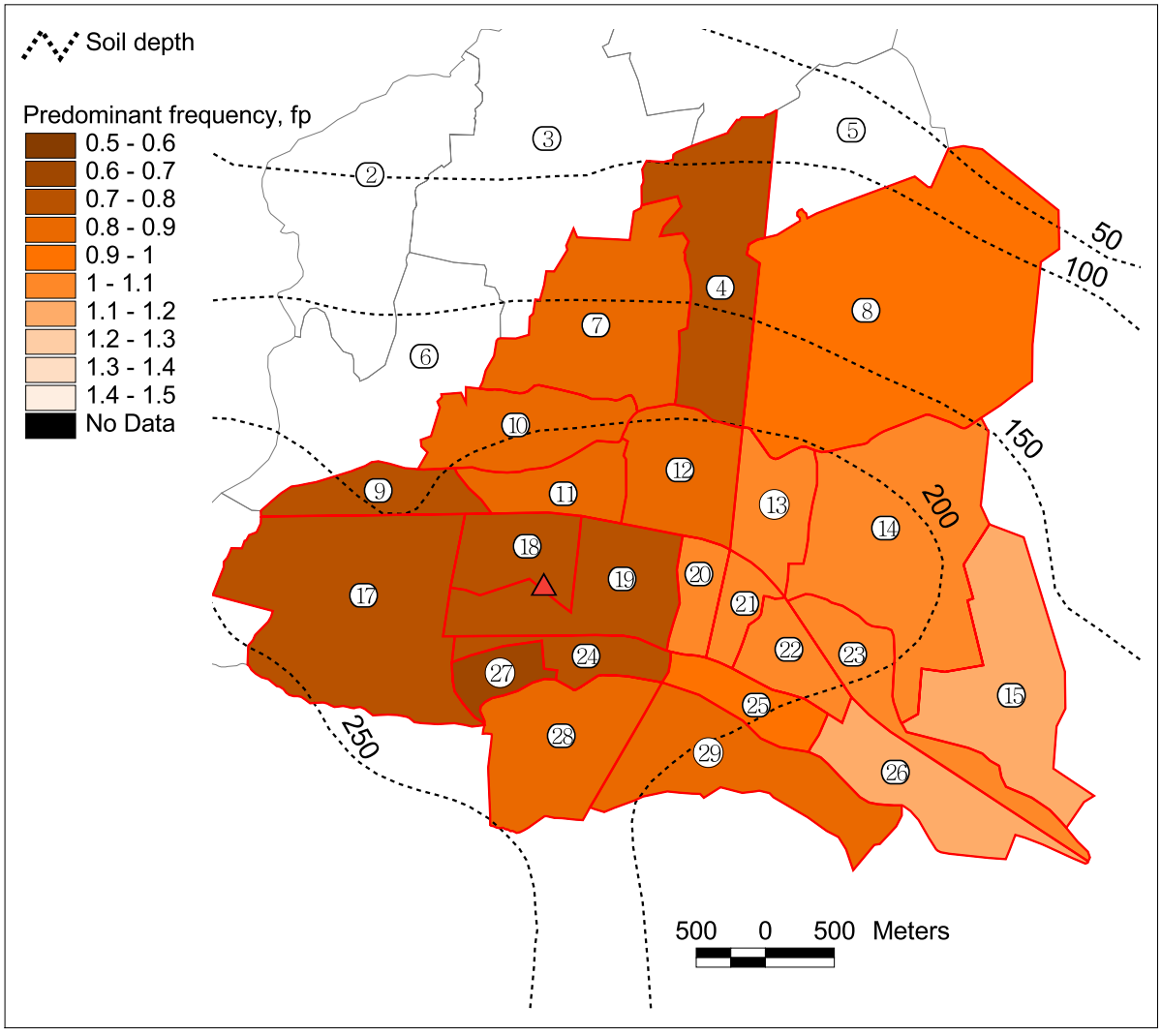

Figure 8.19. Spatial distribution of mean HVSR predominant frequency.

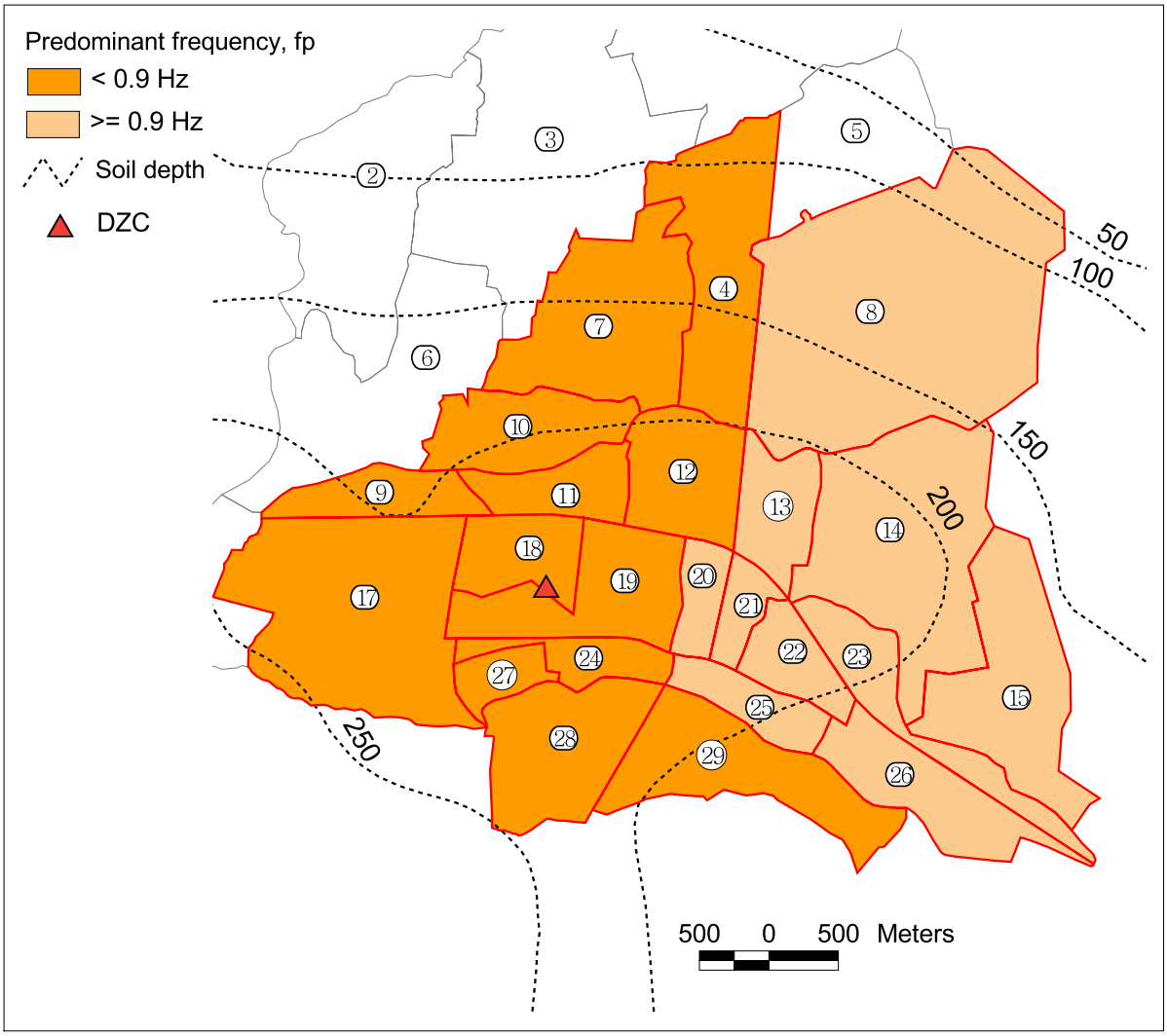

Figure 8.20 Simplified microzonation based on the mean value of f_p. obtained from the HVSR of microtremor measurements.

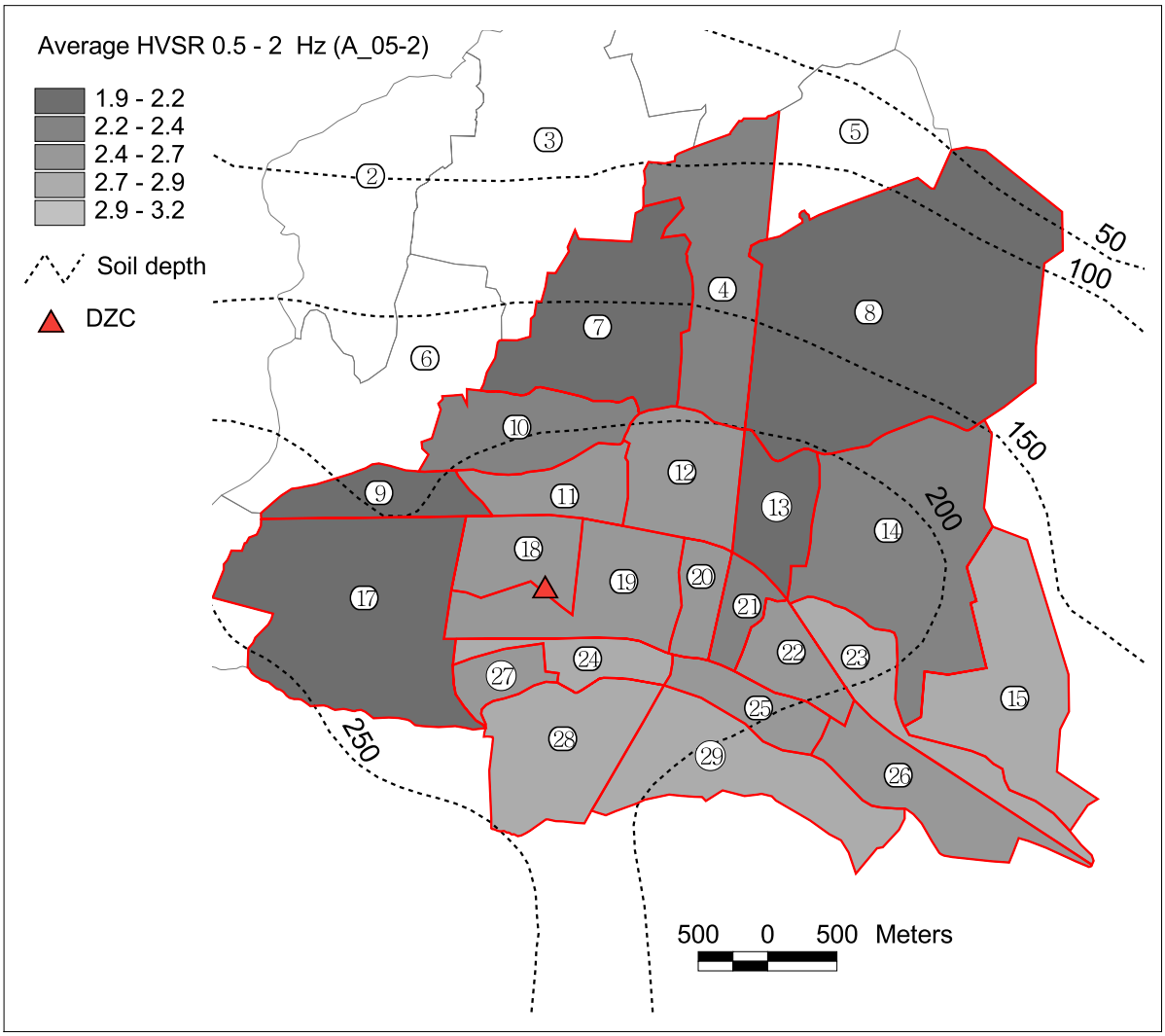

Figure 8.21 Spatial distribution of mean $A_{0.5\text{-}2}$

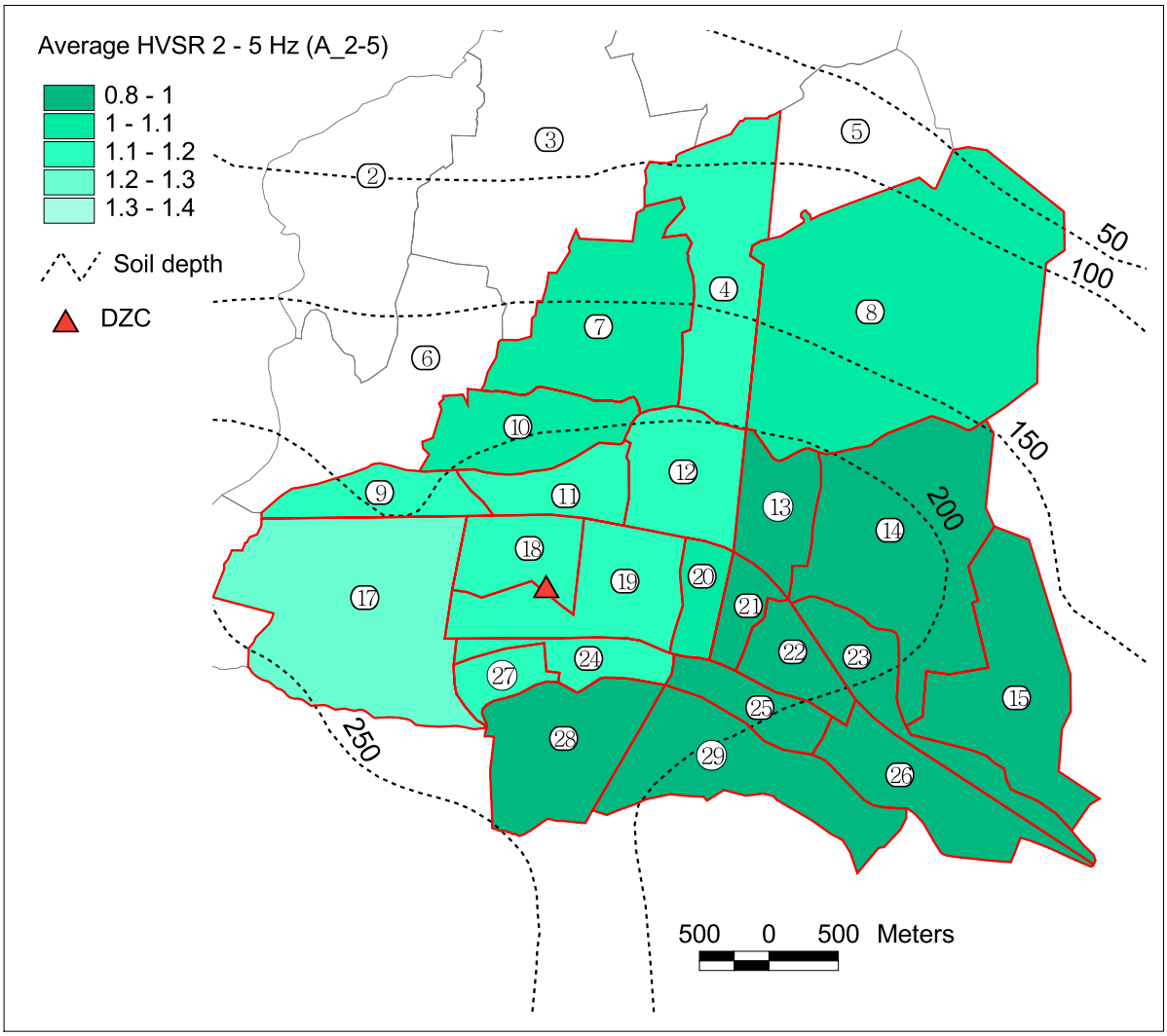

Figure 8.22 Spatial distribution of mean $A_{2\text{-}5}$

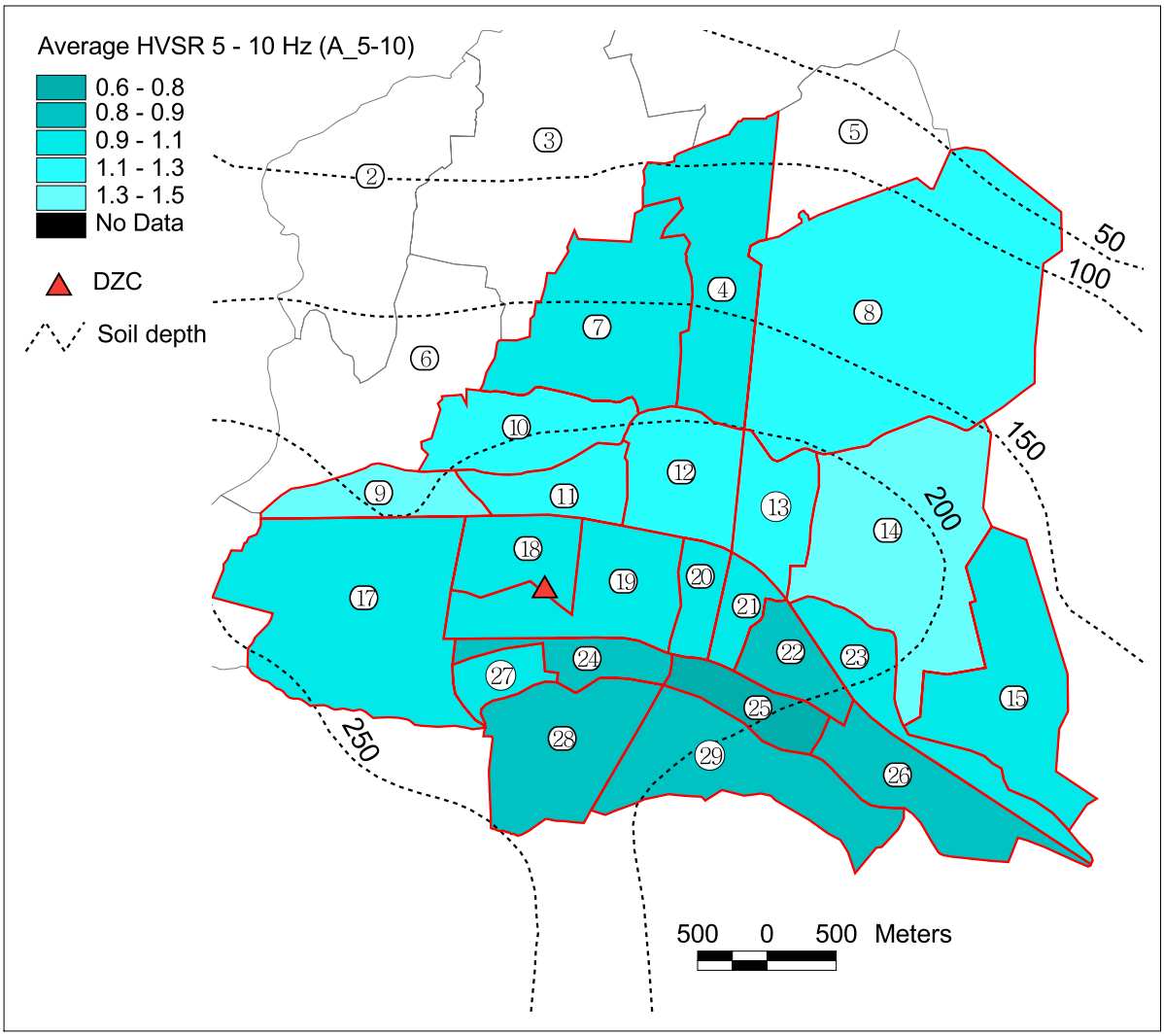

Figure 8.23 Spatial distribution of mean $A_{5\text{-}10}$

apparent in the mean values presented in Figure 8.19. This observation is interpreted as the influence of soil depth on the ground response since a reduction in soil depth is generally expected to lead to an increase in f_p, as expressed through Equation (2.4). Additional microtremor measurements taken at locations further to the east (as shown in Figure 7.8), where soil depths are even smaller, confirm this interpretation. The predominant frequency at location 13, the most easterly point shown in Figure 8.15, which has a soil depth in the range 150 – 175 m, is 1.3 Hz. A measurement made to the northeast of Düzce (location 85), coinciding with the 50 m soil-depth contour, indicates a predominant frequency of about 2.9 Hz. A measurement taken on rock, at location 30, showed very little HVSR amplification over the whole frequency range other than between about 4 and 5 Hz. HVSRs for these three locations are compared in Figure 8.24.

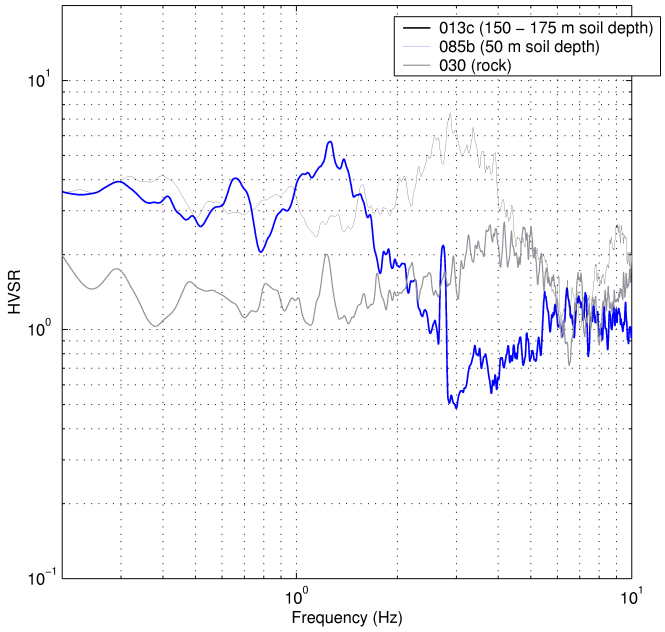

Figure 8.24 Comparison of HVSR from microtremor measurements made at three different locations to illustrate the effect of soil depth on the frequency of the predominant peak, f_p.

Figure 8.15 shows quite significant variations in f_p for similar soil depths. Some of these differences can be attributed to variations in the soil conditions, as characterised by the shear-wave velocity, v_s, giving rise to genuine variations in the resonant frequencies at different locations. The dependency of the resonant frequency on shear-wave velocity was expressed in Equation (2.4). Some of the variations, however, are indicative of the uncertainties associated with the frequency of the predominant HVSR peak obtained from microtremor measurements.

The variations in f_p for similar soil depths do not mask the general trend of increasing f_p towards the east and northeast of the town. The spatial distribution in the mean value of f_p per district shown in Figure 8.19 can be simplified to the microzonation given in Figure 8.20. This microzonation distinguishes between districts having mean $f_p < 0.9$ Hz and districts having mean $f_p \geq 0.9$ Hz,

effectively dividing the town in half. The classifications for district numbers 7 and 4 are not considered as reliable as those for the other districts due to sparse coverage of the microtremor investigation in this area (Figure 8.15). Additional observations are required to confirm the trends observed in the northern part of the town.

Consideration of the spatial variations observed in the other microtremor parameters is reserved for the following section.

8.3 Comparison amongst datasets

In the previous sections, each GIS dataset was presented in some detail, along with a discussion of the associated uncertainties. In the current section, regressions are performed between selected datasets in order to interpret the spatial distribution of pipeline damage observed in Düzce. All analyses are performed at the district level.

8.3.1 Influence of site characteristics on damage distribution

In order to investigate the influence of site characteristics on the distributions of pipeline and building damage, regressions were performed of each of the five damage parameters on each of the four microtremor parameters. The microtremor parameters used were the mean values per district, as presented in Figures 8.19 and 8.21-8.23. The damage parameters consisted of four measures of pipeline repair rate (*R_pK3*, *R_pD2*, *R_pK5* and *R30_pK18*) and the building damage index, D_1.

Table 8.11 Summary of figures showing regressions between site characteristics obtained from microtremor data and various damage parameters.

Site characteristic, X	Damage parameter	Figure No. Mean (X)	Figure No. Std (X)
f_p (Hz)	*R_pK3* (Pipeline repairs per km)	8.25a	8.25b
	R_pD2 (Pipeline repairs per km)	8.25c	8.25d
	R_pK5 (Pipeline repairs per km)	8.25e	8.25f
	R30_pK18 (Monthly pipeline repairs per km)	8.25g	8.25h
	D_1	8.25i	8.25j
$A_{0.5\text{-}2}$	*R_pK3* (Pipeline repairs per km)	8.27a	-
	R_pD2 (Pipeline repairs per km)	8.27b	-
	R_pK5 (Pipeline repairs per km)	8.27c	-
	R30_pK18 (Monthly pipeline repairs per km)	8.27d	-
	D_1	8.27e	-
$A_{2\text{-}5}$	*R_pK3* (Pipeline repairs per km)	8.28a	-
	R_pD2 (Pipeline repairs per km)	8.28b	-
	R_pK5 (Pipeline repairs per km)	8.28c	-
	R30_pK18 (Monthly pipeline repairs per km)	8.28d	-
	D_1	8.28e	-
$A_{5\text{-}10}$	*R_pK3* (Pipeline repairs per km)	8.29a	-
	R_pD2 (Pipeline repairs per km)	8.29b	-
	R_pK5 (Pipeline repairs per km)	8.29c	-
	R30_pK18 (Monthly pipeline repairs per km)	8.29d	-
	D_1	8.29e	-

Additional regressions were performed using the standard deviation (designated "std" in the figures) of f_p in place of the mean value. The value, calculated for each district was taken as a measure of the non-uniformity of site conditions within that district. As explained in Chapter 3, the degree of non-uniformity of site conditions is an important consideration in the seismic behaviour of buried structures. Pipes buried in regions having significant lateral variations in ground conditions will generally be subject to greater strains during earthquakes than pipes buried in more uniform ground.

A summary of the regressions performed, together with relevant figure numbers is presented in Table 8.11.

8.3.1.1 Influence of f_p on damage distribution

In Figure 8.25, regressions are presented for f_p. From the theoretical investigation carried out in Chapter 3, it was anticipated that districts having low average values of f_p would experience greater pipeline damage rates than districts with higher average values of f_p. Figure 8.25a, which represents damage from just the Kocaeli earthquake, does show such a trend. However, the r^2 value for this dataset is very low (approximately 0.06), calling in to question the significance of any apparent trend. The correlations between mean f_p and the three other measures of pipeline damage are even less significant.

The districts of Düzce have mean values of f_p ranging from 0.65 to 1.16 Hz. Likely values of peak ground strain experienced in Düzce during either of the Kocaeli or Düzce earthquakes can be estimated from f_p using expressions from the Japanese seismic design code for buried pipelines (JWWA, 1997) (see Section 3.2). In Figure 8.26, the variation of peak ground strain, ε_p, with f_p is illustrated for two different soil depths, H = 250 m and H = 150 m corresponding with the range of depths covering most of Düzce. The ground strain in these Figures can be assumed to be equivalent to the strain induced in a buried pipeline. Higher values of ground strain are therefore expected to give rise to higher pipeline damage rate.

For a fixed depth of soil, a reduction in f_p (brought about by a reduction in shear-wave velocity of the surface layer, v_{Ssoil}) gives rise to an increase in ε_p. Figure 8.26b illustrates the range of ground strains associated with the range of values of f_p in Düzce. Peak ground strains estimated for a district with mean f_p = 0.65 Hz exceed those for a district with mean f_p = 1.16 Hz by approximately 50 %. The variation in mean f_p across Düzce, however, is caused by a combination of changes in soil depth and changes in the shear-wave velocity of the ground. If changes in f_p are mainly caused by variations in soil depth (with v_{Ssoil} remaining almost constant), the estimated variation in peak ground strains using the JWWA (1997) expressions is actually much less. Peak ground strain for soil having f_p = 0.65 Hz, with H = 250 m (Figure 8.26 (a)), is only about 5 % greater than the peak ground strain for soil having f_p = 1.16 Hz with H = 150 m (Figure 8.26 (b)).

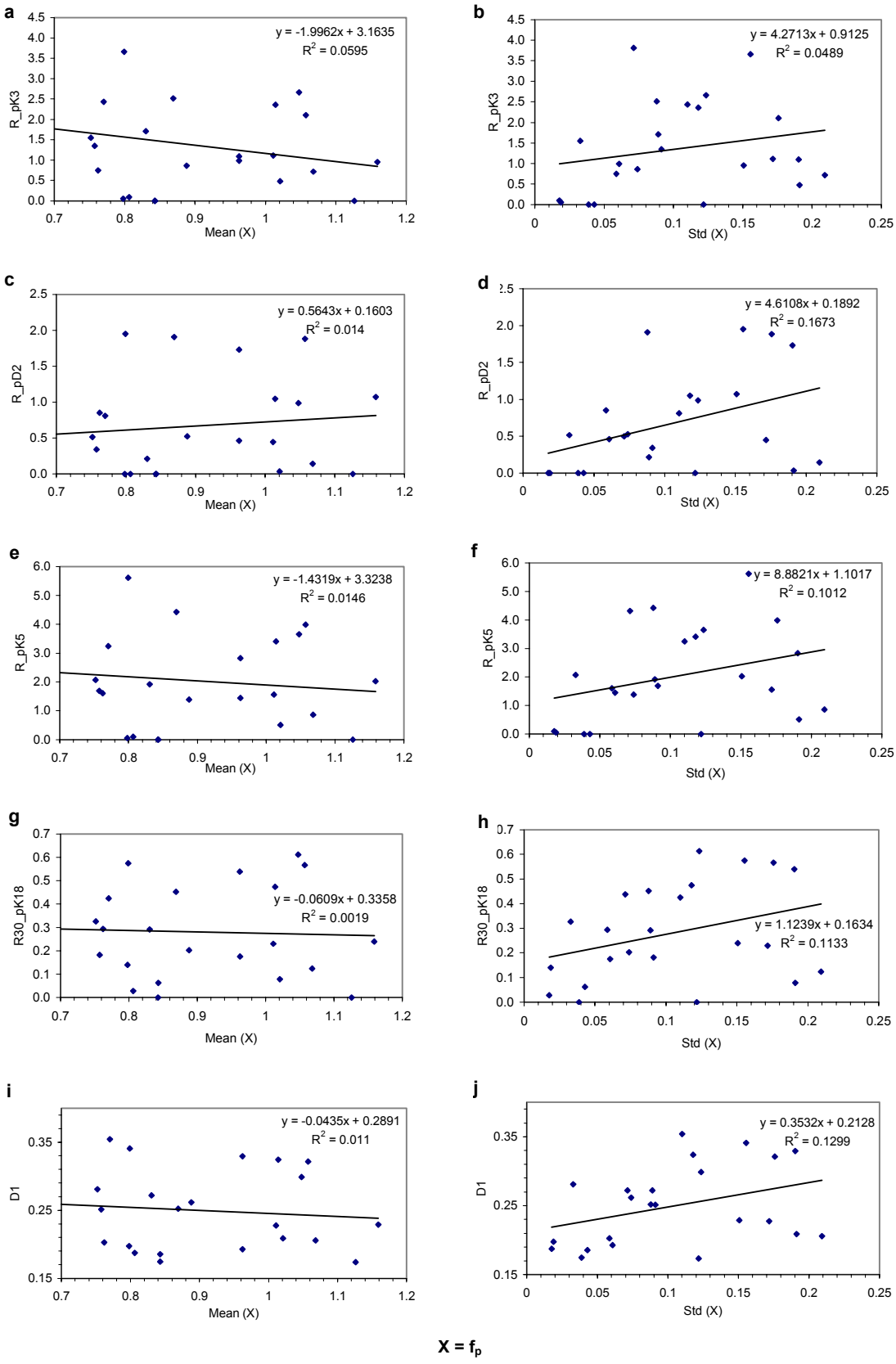

Figure 8.25 Relationship between mean (X) and various damage parameters (left); relationship between standard deviation of (X) ("std (X)") and various damage parameters (right). X = f_p.

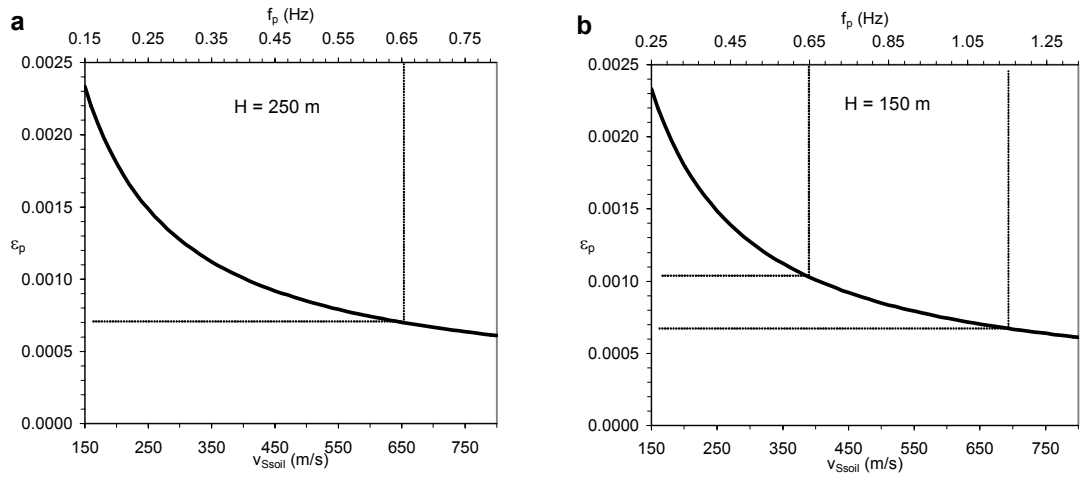

Figure 8.26 Dependency of ground strain, ε_p on the predominant frequency of the ground, f_p for a single soil layer of thickness H overlying bedrock having shear wave velocity of 1500 m/s. Strains are calculated for a 'Level 2' seismic motion using the Japanese seismic design code (JWWA, 1997), as expressed in Section 3.2.

These results confirm the significance of f_p in the seismic behaviour of buried pipelines. However, they also suggest that f_p by itself cannot be used to explain the full variation in ground strains, and therefore the variation in pipeline damage rates, observed in Düzce. It is expected that measurements of shear-wave velocity for soil profiles in each district would help in the interpretation of the pipeline damage data. However, such information is not available for the town of Düzce.

Figure 8.25 also includes regressions performed between the standard deviation of f_p for each district, σ_{fp}, and pipeline damage rates. The quantity σ_{fp} is similar to the quantity used in a method proposed by Shinozuka & Kawakami (1977) to estimate ground strains arising from spatial variability in the predominant frequency of the ground. They applied the method to estimate ground strains for the Metropolitan Tokyo area and found a reasonable correlation between these strains and the distribution of pipeline damage caused by the 1923 Kanto earthquake. In the current study, a positive correlation is found between σ_{fp} and each of the pipeline damage parameters, which appears to confirm the effect of soil non-uniformity on the earthquake performance of buried pipelines as described in Chapter 3. However, none of the corresponding r^2 values exceeds about 0.17. The fact that a similar level of positive correlation is found between σ_{fp} and the building damage index, D_1, lessens the significance of any apparent trends between σ_{fp} and pipeline damage parameters as the level of variability in f_p is not thought to be as significant to the seismic behaviour of above-ground structures as it is to the seismic behaviour of buried pipelines.

8.3.1.2 Influence of average HVSR amplification on damage distribution

Figures 8.27, 8.28 and 8.29 show regressions performed amongst the three average HVSR amplification factors and each of the damage parameters. The trends observed between mean $A_{0.5\text{-}2}$ and earthquake damage in Figure 8.27 are all positive, although r^2 values are all very low. The

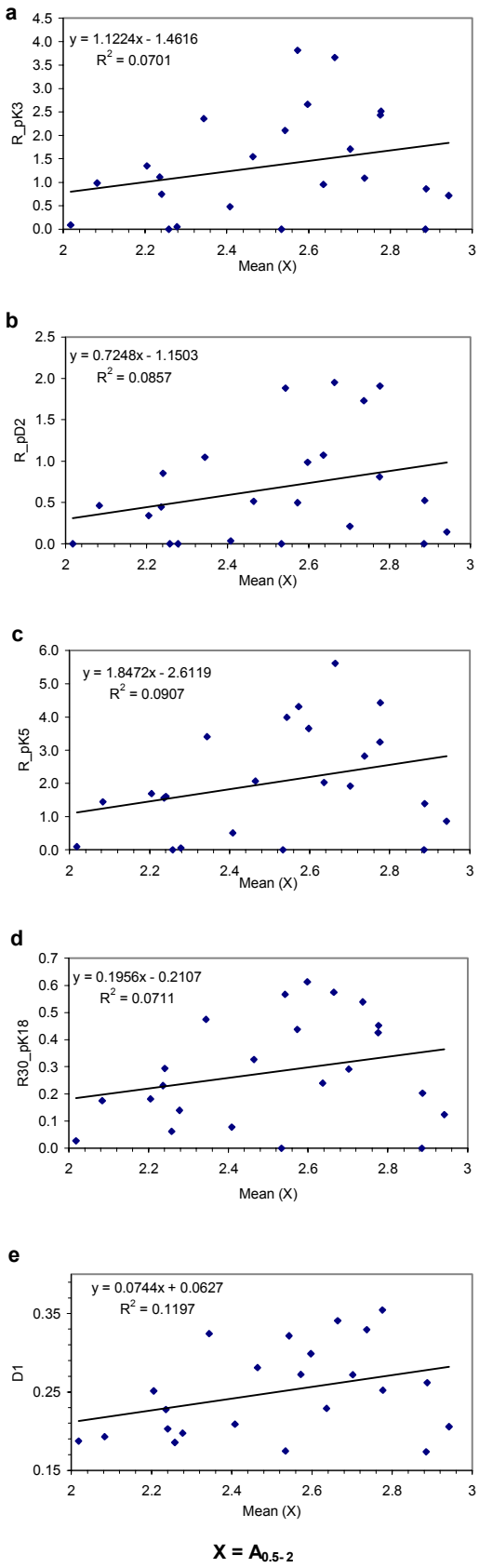

Figure 8.27 Relationship between mean (X) and various damage parameters. X = $A_{05\text{-}2}$ (defined in Table 8.10).

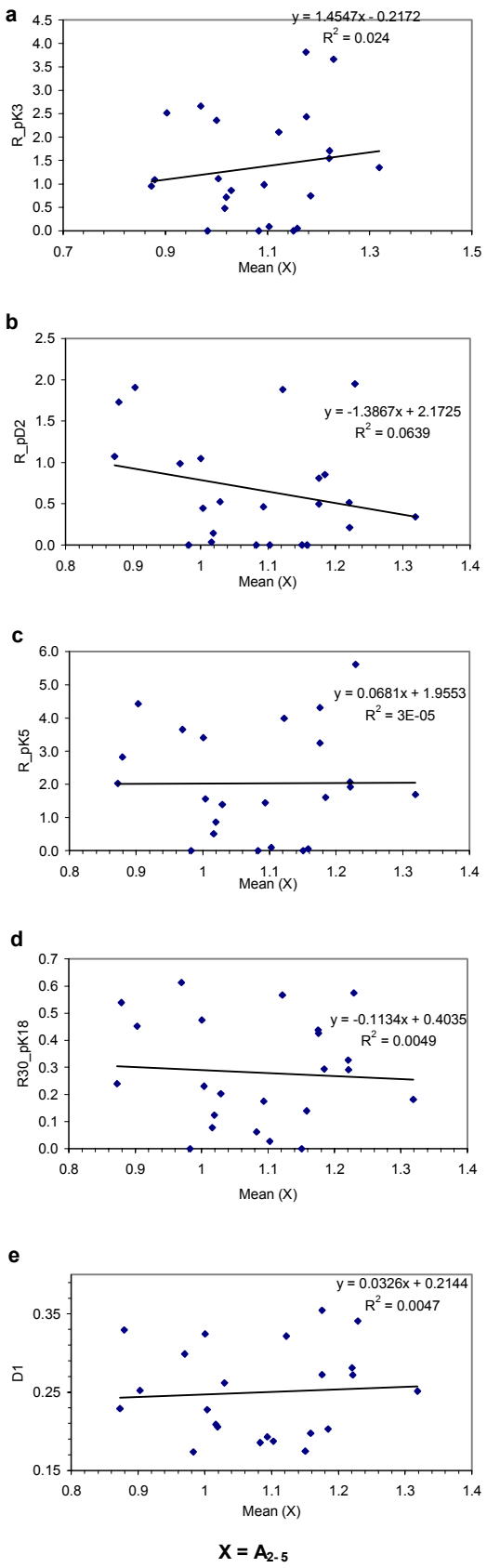

Figure 8.28 Relationship between mean (X) and various damage parameters. X = $A_{2\text{-}5}$ (defined in Table 8.10).

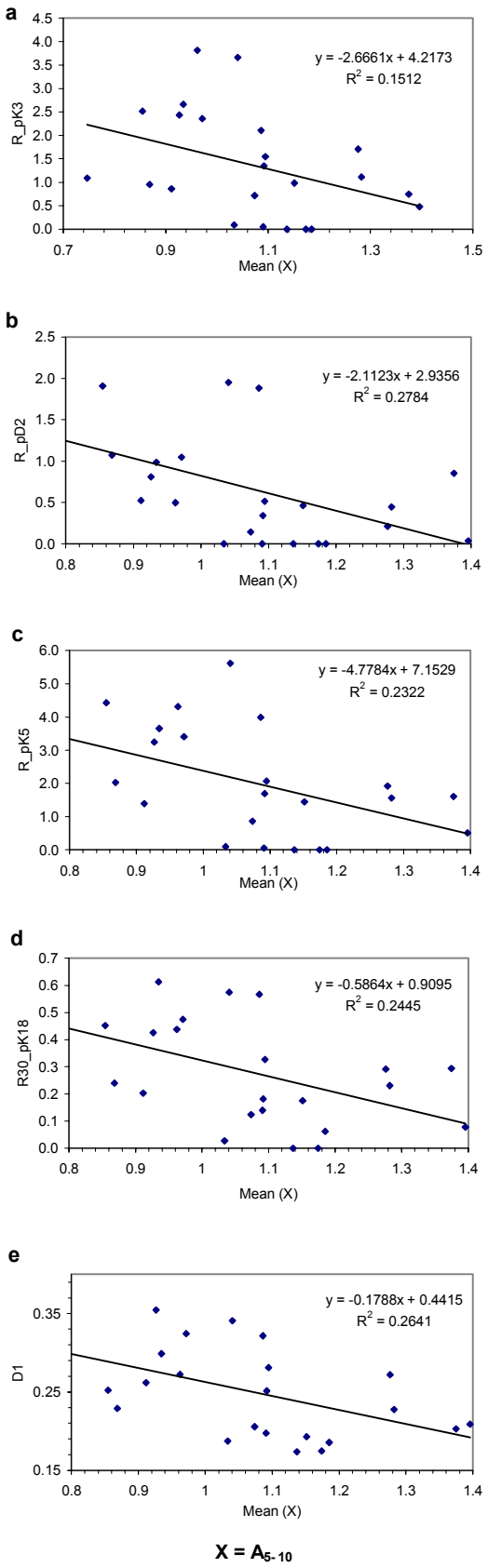

Figure 8.29 Relationship between mean (X) and various damage parameters. X = $A_{5\text{-}10}$ (defined in Table 8.10).

most significant correlation observed is between mean $A_{0.5\text{-}2}$ and the building damage index, D_1, which has an r^2 value of 0.12. As explained in Chapter 7, the frequency band 0.5 – 2 Hz was defined to correspond with estimations of the resonant frequencies of buildings having 4 storeys or more. As implied by Figure 8.11, this category of buildings suffered greater levels of damage than buildings with fewer storeys. It was therefore anticipated that districts with greater HVSR amplification in the frequency range 0.5 – 2 Hz would have experienced higher building damage, as quantified by D_1.

The two most likely explanations for the poor correlation observed between these two quantities are given below:

1. HVSR amplification is not a good measure of earthquake site amplification in the case of Düzce.
2. The HVSR does provide a reasonable measure of earthquake site amplification but the influence of $A_{0.5\text{-}2}$ on D_1 is unclear due to the limited range of values of mean $A_{0.5\text{-}2}$ within Düzce (2.0 - 2.9).

The usefulness of amplification factors obtained from the HVSR of microtremor data is still a matter of much debate. The results in Düzce are not conclusive.

No significant correlations are observed between $A_{2\text{-}5}$ and any of the damage parameters included in Figure 8.28. This parameter might be expected to correlate with damage to 1, 2 and 3-storey buildings because of the frequency range covered. However, building damage aggregated by building height in each district was not available for the current study.

The trends observed between $A_{5\text{-}10}$ and the damage parameters in Figure 8.29 are notable inasmuch as they are all negative and have r^2 values in the range 0.15 – 0.28, generally greater than r^2 values observed for the datasets presented in Figures 8.25, 8.27 and 8.28. The trends observed in Figure 8.29 are counter-intuitive in that they imply greater pipeline and building damage rates for reduced amplification in the frequency range 5 – 10 Hz. This could be evidence of the HVSR in this frequency range being governed more by ambient noise source characteristics than measurement location site characteristics. The vertical component of the Fourier amplitude spectrum of noise in this frequency range appears to be systematically greater in the central, built-up regions of Düzce (which tended to suffer greater levels of earthquake damage) than the outlying areas of the town (which generally suffered less damage). This could explain the trends observed in Figure 8.29.

The poor correlations observed in Figures 8.25 and 8.27-8.29 do not necessarily imply failure of the microtremor method to characterise site effects across Düzce. Trifunac & Todorovska (1998b) investigated the spatial distributions of severely damaged buildings and of breaks in the water distribution system following the 1994 Northridge earthquake and found no simple correlations with various generalised categories of surficial geology. More investigation is required into the relative influence on site effects of near-surface ground conditions and deeper ground conditions.

8.3.2 Comparison between pipeline damage and building damage

Comparisons between measures of pipeline damage and the building damage index, D_1, are presented in Figure 8.30. All four measures of pipeline damage are seen to correlate closely with building damage, with r^2 values ranging from 0.51 – 0.79. It is notable that the best correlations are seen for parameters *R_pK5* and *R30_pK18* (Figures 8.30c & d), which include the combined effects of both the Kocaeli and Düzce earthquakes (as is the case for the building damage statistics).

The fact that districts experiencing a high level of pipeline damage also experienced a high level of building damage implies that damage patterns were dominated by the influence of variations in strong motion from district to district. It is assumed that there was no strong regional correlation between pipeline vulnerability and building vulnerability, which is reasonable at the district level, although would not be so reasonable if considering damage variations between individual town blocks. The significant range in levels of damage observed across the districts of Düzce (as evidenced in Figures 8.4 – 8.7 and Figure 8.11) is therefore believed to be the result of significant variations in the intensity of ground shaking.

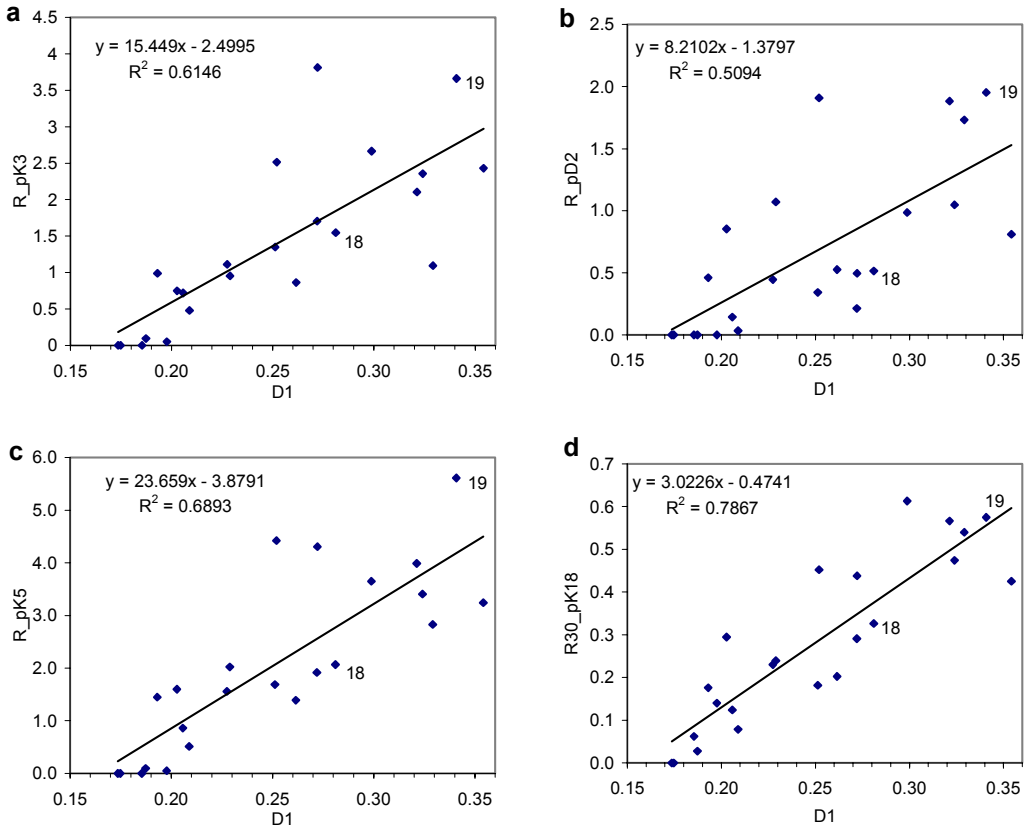

Figure 8.30 Comparison between pipeline damage rates and building damage rates for all districts of Düzce. Data points referring to districts 18 and 19, in the vicinity of DZC strong-motion station, are highlighted.

None of the trends shown in Figure 8.30 passes through the origin. This implies that a greater level of ground motion is required to cause pipeline damage than building damage. O'Rourke *et al.*

(1998) observed no pipeline damage in areas with PGV < 10 cm/s as a result of the 1994 Northridge earthquake. Isoyama *et al.* (2000), in deriving their pipeline fragility relations based on data from the 1995 Hyogoken-nanbu earthquake, suggested strong-motion thresholds of PGV = 15 cm/s and PGA = 100 cm/s^2 for pipeline damage to occur.

The DZC strong-motion station is situated in district 18 (Uzunmustafa). As indicated in Figure 8.30, this district experienced average levels of both pipeline and building damage (regardless of the pipeline damage parameter considered). The average strong ground-motion in other districts could be scaled according to the level of damage relative to this district. It is, however, possible that the strong-motion recorded at DZC was more representative of the ground motion experienced in district 19 (Kültür) as the strong-motion station is very close to the boundary of this district. In this case, the values recorded at DZC would have been amongst the highest experienced anywhere in the town, as inferred from the high levels of pipeline and building damage in district 19.

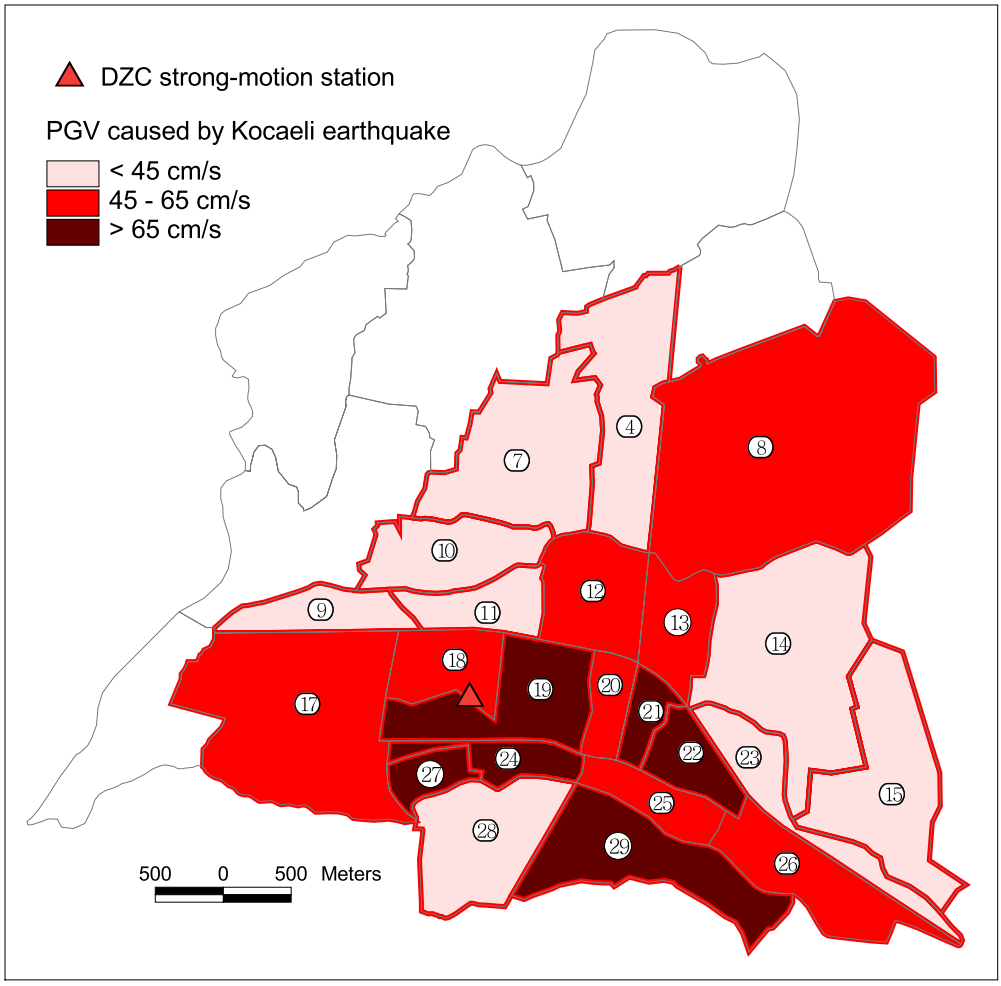

Figure 8.31 Estimated distribution of PGV in Düzce as a result of the Kocaeli earthquake, inferred from pipeline damage distribution. Predictions are in terms of PGV_L, the largest of the two horizontal components of PGV.

Figure 8.31 shows the distribution of PGV as a result of the Kocaeli earthquake, inferred from pipeline damage data. This map is based on the assumption that the strong-motion experienced at

DZC was representative of the district in which it is located (district 18). PGV was calculated using the HAZUS fragility relationship (Equation 3.33), which predicted a pipeline damage rate in district 18 very similar to the observed value (see Tables 8.4 and 8.6). Due to the uncertainties associated with the data, predictions have been restricted to three levels of PGV:

1. Districts with PGV similar to the value recorded at the DZC strong-motion station (defined by the range 45–65 cm/s, which is approximately 10 cm/s either side of the recorded value).
2. Districts with PGV less than the value recorded at DZC (PGV < 45 cm/s).
3. Districts with PGV greater than the value recorded at DZC (PGV > 65 cm/s).

One factor which might have contributed to the close correlations observed between pipeline and building damage levels is the effect of building collapse on buried structures. Some pipes may have survived the passage of seismic waves only to have been damaged by the collapse of a nearby building. It is known from discussions with Municipality Water Division staff that some pipe damage was caused during post-earthquake reconstruction works. The toppling of a damaged minaret, for example, resulted in damage to buried water pipes leading to 10,000 people being without water for three days (Tadday, 2001).

9.1 Summary

The behaviour of buried water supply pipelines subject to various earthquake effects has been investigated, with particular emphasis on ground shaking. Key factors affecting transient ground motion and pipeline vulnerability have been identified from both theory and evidence from the field.

Behaviour of buried pipelines subject to ground shaking is dependent on ground strains induced by the passage of seismic waves. A travelling-wave model has illustrated the dependency of peak ground strains on PGV and the apparent wave propagation velocity of the seismic wave. The effects of different seismic wave types and site conditions on transient ground strains have been investigated. In particular, the influence of the predominant period of the ground on peak ground strains has been illustrated using expressions from the Japanese seismic design guidelines for buried pipelines.

The earthquake performance of buried pipelines has been investigated by means of a detailed review of existing pipeline fragility relations. Specific emphasis was placed on identifying the size, origin and reliability of the datasets used. Improvements were made to the recently compiled dataset of the American Lifelines Alliance (ALA, 2001).

Post-earthquake investigation of factors influencing pipeline damage and prediction of future earthquake damage both require characterisation of the spatial variation in ground shaking. A summary has been presented of some common methods used to characterise site effects. Detailed consideration was given to characterisation of site effects using microtremor data as this was the method selected for subsequent field work in Turkey.

Prediction of damage in future earthquakes requires reliable strong-motion estimates. New strong-motion records from recent significant crustal earthquakes provided the opportunity to expand an existing database of European strong-motion data for the derivation of new predictive relationships for horizontal PGA, PGV and PGD. The new equations were derived from 249 strong-motion records obtained from 51 European earthquakes with surface-wave magnitudes between 5.5 and 7.9. This is believed to be the most extensive Europe-wide strong-motion dataset used for the unified derivation of relationships for PGA, PGV and PGD. The sensitivity of each dataset to the record processing technique was investigated.

Results were presented of a post-earthquake investigation into water pipeline damage in the town of Düzce, Turkey, caused by two destructive earthquakes in 1999. The influence of various factors on the spatial distribution of water pipeline damage was examined using a Geographical Information System. Temporal variations in pipeline repair statistics before and after the earthquakes were analysed to identify earthquake-related pipe breaks. Spatial variations in pipeline damage rates were then identified following data aggregation at the district level. In the absence of

detailed geological data, site conditions in Düzce were characterised using ambient noise measurements taken at over one hundred locations in and around the town. The spatial distributions of site conditions and building damage were used to help interpret the spatial distribution of pipeline damage.

9.2 Conclusions

The work summarised has led to a number of conclusions which help in understanding the performance of buried pipelines in past earthquakes and permit more reliable damage prediction in the event of a future earthquake. Contributions can be summarised in three main areas:

9.2.1 Post-earthquake investigation of pipeline damage in Düzce, Turkey

- A close correlation was observed between the spatial distributions of pipeline damage and building damage. This is interpreted as evidence that damage patterns were dominated by the influence of variations in strong motion from district to district. Building damage data, aggregated over both the Kocaeli and Düzce earthquakes, obscured earthquake-specific damage patterns. However, the variation in pipeline damage levels from district to district assigned to the Kocaeli earthquake was used to infer the spatial distribution of characteristics of the strong motion, based on the existing HAZUS pipeline fragility relation.
- Anecdotal evidence suggests that the close correlation between the spatial distributions of pipeline damage and building damage may have been influenced by the impact of building collapse on buried pipelines. Further investigation is required to quantify the significance of this effect in Düzce.
- Comparison between building damage rates and pipeline damage rates across Düzce implies that the onset of pipeline damage requires a greater level of ground motion than the level needed to cause building damage. This confirms the findings of previous studies in Japan and the US.
- Reasonable results have been obtained of the predominant frequency of the ground, f_p, from the horizontal-to-vertical spectral ratio (HVSR) of microtremor data. For measurements made at the DZC strong-motion station, this is supported by receiver-function estimates of f_p from strong-motion data. It is suggested that shear-wave velocity profiles at a selection of microtremor measurement sites would further improve validation of the microtremor dataset.
- In the case of Düzce, no significant correlation was found between the spatial distributions of pipeline damage and f_p. Further investigation is needed to identify the influence of local

variations in the shear-wave velocity structure of the ground on the relationship between f_p and peak earthquake-induced ground strains.

- Lateral variations in ground conditions, as characterised by the quantity σ_{fp} (the standard deviation of f_p in a given district) did not show any significant correlation with pipeline damage. It is believed that this quantity is useful for characterising non-uniformity of ground conditions but that the geological features whose lateral variation is of significance to the earthquake behaviour of buried pipelines need to be characterised on a more local scale, requiring a greater density of microtremor measurements.
- No significant correlation was found between average HVSR amplification factors obtained from microtremor and pipeline or building damage levels. Comparison of microtremor HVSR for different ambient noise levels indicates that the HVSR amplitude is a less stable quantity than f_p. Strong-motion data in Düzce is inadequate to verify whether HVSR amplification from microtremor provides a reliable measure of strong-motion amplification.

9.2.2 Detailed review of pipeline fragility relations

- Comparison between different pipeline fragility relations and their associated scatter confirms that PGV is better than PGA as a predictor parameter for earthquake damage to buried pipelines.
- Improved characterisation of the seismic action in the ALA (2001) dataset was shown to reduce scatter significantly, although there was little change in the original fragility expression.
- It is suggested that some of the scatter associated with pipeline fragility relations is a result of differences in the apparent propagation velocity of seismic waves for different earthquakes or for different regions affected by the same earthquake. In particular, it is proposed that the systematically higher pipeline damage rates (for the same level of PGV) observed in Kobe during the 1995 Hyogoken-nanbu earthquake compared to pipeline damage rates observed in Northridge during the 1994 earthquake is evidence of systematic differences in the average apparent propagation velocity of seismic waves generated during these two events. Further investigation using strong-motion data is warranted.

9.2.3 Development of new predictive relationships for peak strong-motion parameters

- The newly derived predictive equations are of particular application to seismic hazard analysis and earthquake-resistant design of structures in Europe. Predictions of PGV can be used in conjunction with pipeline fragility relations to predict earthquake-induced pipeline damage rates.
- The supplementary records added to the existing database have constrained the predictive relationships better for large magnitude earthquakes ($M_s > 7$) and for distances less than 10 km.
- Comparisons between the new equations and the equations of Bommer *et al.* (2000), derived from the original dataset, indicate only small changes in magnitude-dependence and site-dependence. Changes in scatter are negligible in the equations for PGA and PGV, although there is an increase in the scatter associated with the new PGD equation. This is most likely related to slight differences in the criteria used for selection of the low-frequency filter cut-off when processing the supplementary strong-motion records, as compared to the original strong-motion records.
- Values of PGV, and particularly PGD, were shown to be inherently more uncertain than values of PGA due to their sensitivity to the strong-motion record processing technique. Peak strong-motion values obtained from digital records were shown to be significantly more reliable than values obtained from analogue records.

9.3 Recommendations

In light of these conclusions, further work is recommended in two main areas:

9.3.1 Recommendations for improved interpretation of pipeline damage distribution in Düzce

- **Improve characterisation of ground conditions from shear-wave velocity data**. Ongoing post-earthquake investigations by academic and governmental organisations may yield data to help characterise the near-surface deposits. Shear-wave velocity data extending down to bedrock in the Düzce area, however would be very costly.
- **Improve estimation of earthquake-related pipeline repair rates**. Areas of uncertainty in estimations of pipeline repair rates could be reduced in liaison with Düzce Municipality and third parties involved in the post-earthquake recovery (notably, UNICEF and Iller Bankası).
- **Improve characterisation of building damage**. It is known that building damage data was gathered at a greater level of detail than that available for the current study. Data

which helps distinguish between damage caused by the two earthquakes would be of particular use.

- **Compare Düzce study with other detailed case studies of earthquake-induced pipeline damage.** Further investigation is required into the correlations between ground conditions and pipeline damage as a result of other earthquakes. In particular, investigations are needed into the influence of f_p and ground non-uniformity on pipeline damage distributions.

9.3.2 Recommendations for improved prediction of pipeline damage rates

- **Reduce uncertainties associated with existing pipeline fragility relations.** Uncertainties in pipeline repair rates and seismic action need to be quantified for each data point in the existing dataset. More rigorous criteria need to be defined to exclude less reliable data points.
- **Improve water utility record-keeping.** More detailed and consistent recording of earthquake damage to buried pipelines is necessary to improve the characterisation of factors influencing pipeline vulnerability.
- **Improve prediction of PGV**. Greater availability of digital strong-motion records in the future is likely to lead to improvements in the reliability of subsequently derived attenuation relationships for PGV, leading to improved PGV predictions.
- **Improve characterisation of seismic action in pipeline fragility relations.** In order to significantly improve characterisation of the seismic action due to ground shaking, new fragility relations need to be developed which use transient ground strain directly rather than via its association with PGV since strain is influenced by the apparent propagation velocity of seismic waves. This represents a formidable task, requiring reliable estimates of ground strains from previous earthquakes as well as reliable predictions of ground strains in the event of a future earthquake. One possible way forward is to derive separate predictive relationships for PGV caused by body waves and surface waves.

REFERENCES

ABRAHAMSON, N. (2001). "Incorporating effects of near fault tectonic deformation into design ground motions," Webcast presentation at University of Buffalo, http://civil.eng.buffalo.edu/webcast/abrahamson/.

ABRAHAMSON, N.A., SCHNEIDER, J.F. & STEPP, J.C. (1991). "Empirical spatial coherency functions for application to soil-structure interaction analyses," *Earthquake Spectra*, **7** (1), 1-27.

AIJ (1999). "Progress report on damage investigation after Kocaeli earthquake by Architectural Institute of Japan," *Proceedings of the ITU – IAHS International Conference on the Kocaeli Earthquake, 17 August 1999*, Istanbul Technical University, Istanbul, Turkey, 239 – 270.

AKI, K. (1993). "Local site effects on weak and strong ground motion," *Tectonophysics,* **218**, 93-111.

AKKAR, S. & GULKAN, P. (2002). "A critical examination of near-field accelerograms from the Sea of Marmara region earthquakes," *Bulletin of the Seismological Society of America*, **92** (1), 428-447.

AKTAR, M., ERGIN, M., OZALAYBEY, S., TAPIRDAMAZ, C., YORUK, A. & BICMEN, F. (2000) "A lower-crustal event in the northeastern Mediterranean: the 1998 Adana earthquake (M_w=6.2) and its aftershocks," *Geophysical Research Letters,* **27** (16), 2361-2364.

ALA (2001). *Seismic fragility formulations for water systems*, ALA, 327pp., http://www.americanlifelinesalliance.org.

AMATO, A.., AZZARA, R., CHIARABBA, C., CIMINI, G.B., COCCO, M., DI BONA, M., MARGHERITI, S., MAZZA, S., MELE, F., SELVAGGI, G., BASILI, A., BOSHI, E., COURBOULEX, F., DESCHAMPS, A., GAFFET, S., BITTARELLI, G., CHIARALUCE, L., PICCININI, D., & RIPEPE, M. (1998). "The 1997 Umbria-Marche, Italy, earthquake sequence: a first look at the main shocks and aftershocks," *Geophysical Research Letters*, **25** (15), 2861-2864.

AMBRASEYS, N.N. (1988). "Engineering seismology," *Earthquake Engineering & Structural Dynamics*, **17**, 1-105.

AMBRASEYS, N.N. (1995). "The prediction of earthquake peak ground acceleration in Europe," *Earthquake Engineering and Structural Dynamics*, **24** (4), 467-490.

AMBRASEYS, N.N. (2001). "Reassessment of earthquakes, 1900-1999, in the Eastern Mediterranean and the Middle East," *Geophysical Journal International*, **145**, 471-485.

AMBRASEYS, N.N. & BOMMER, J.J. (1990). "Uniform magnitude re-evaluation for the strong-motion database of Europe and adjacent areas," *European Earthquake Engineering,* **4** (2), 3-16.

AMBRASEYS, N.N. & BOMMER, J.J. (1991). "The attenuation of ground accelerations in Europe," *Earthquake Engineering and Structural Dynamics*, **20** (12), 1179-1202.

AMBRASEYS, N.N. & BOMMER, J.J. (1995). "Attenuation relations for use in Europe: an overview." *In:* Elnashai, A. (ed.) *European seismic design practice.* Balkema, Rotterdam. 67-74.

AMBRASEYS, N.N., SIMPSON, K.A. & BOMMER, J.J. (1996). "Prediction of horizontal response spectra in Europe," *Earthquake Engineering and Structural Dynamics,* **25**, 371-400.

AMBRASEYS, N.N., SIMPSON, K.A. & BOMMER, J.J. (1997). "Authors' reply," *Earthquake Engineering and Structural Dynamics,* **26**, 295-300.

AMBRASEYS, N., SMIT, P., SIGBJORNSSON, R., SUHADOLC, P. AND MARGARIS, B. (2002), *Internet-Site for European Strong-Motion Data*, European Commission, Research-Directorate General, Environment and Climate Programme, http://www.isesd.cv.ic.ac.uk/

ANDO, H., SATO, S. & TAKAGI, N. (1992). "Seismic observation of a pipeline buried at the heterogeneous ground," *Proceedings of the Tenth World Conference on Earthquake Engineering*, Balkema, Rotterdam, 5563-5567.

ANDRUS, R.D. (1997). “Surface wave method – a tool for lifeline earthquake engineering,” *Proceedings of Research Needs Workshop, Earthquake Engineering Site Characterisation*, Miscellaneous Paper GK-97-21, Appendix G, U.S. Army Corps of Engineers, pp G1-G14.

ANSAL, A.M., IYISAN, R. & GULLU, H. (2001). “Microtremor measurements for the microzonation of Dinar,” *Pure and Applied Geophysics*, **158**, 2525-2541.

ARIAS, A. (1970). "A measure of earthquake intensity," in *Seismic Design for Nuclear Power Plants*, ed. Hansen, R. (MIT Press, Cambridge, Massachusetts), pp. 438-483.

ARPAT, E., HERECE, E., KOMUT, T., OZGUL, N. (1999). “Duzce earthquake of October (*sic*) 12, 1999: Preliminary evaluation of the first 3 days’ field data”, Department of Geophysics, Bogazici University, Turkey, http://www.koeri.boun.edu.tr/jeofizik/duzing1.html.

ASCE/TCLEE (1991). “Seismic loss estimation for a hypothetical water system,” *ASCE/TCLEE Monograph No.2*, C.E. Taylor *(ed.)*.

ASCE/TCLEE (1997). "Guide to post-earthquake investigation of lifelines" *ASCE/TCLEE Monograph No.11*, Anshel J. Schiff *(ed.)*.

ASCE/TCLEE (1999a). “ASCE preliminary report on the Izmit, Turkey earthquake,” *ASCE/TCLEE,*13 September, 1999, http://www.asce.org/peta/tech/tclee0999.html.

ASCE/TCLEE (1999b). “Lifelines performance, Düzce, Turkey earthquake,” *Technical Council on Lifeline Earthquake Engineering,* http://www.asce.org/peta/tech/tclee0999.html.

ASCE/TCLEE (2000). “Izmit (Kocaeli), Turkey, earthquake of August 17, 1999 including Düzce earthquake of November 12th, 1999,” *ASCE TCLEE Monograph No. 17,* Alex K. Tang (ed), Reston, Virginia, 290pp.

ASCHHEIM, M., GULKAN, P. & SEZEN, H. (2000). “Performance of buildings.” *In:* T.L. Youd, J-P. Bardet & J.D. Bray, ed. “Kocaeli, Turkey, earthquake of August 17, 1999: reconnaissance report,” *Earthquake Spectra*, Supplement A to Volume 16, 237-279.

ATAKAN, K. & FIGUEROA, J.C. (1993). “Local site response in San Salvador: Comparison between the synthetics and the observed ground motion of the October 10, 1986 earthquake,” *Reduction of Natural Disasters in Central America: Earthquake Preparedness and Hazard Mitigation Report No. 8*, Institute of Solid Earth Physics, University of Bergen, Norway.

AWATA,Y. et al (2000) "Segment structures of the surface ruptures associated with the August 17, 1999 Izmit earthquake, Turkey." *Proceedings of the 27th General Assembly, European Seismological Commission*, 149-153.

AWATA,Y., YOSHIOKA, T., EMRE, O., DUMAN, T.Y., DOGAN, A. & TSUKUDA, E. (2000). “Segment structures of the surface ruptures associated with the August 17, 1999 Izmit earthquake, Turkey,” *Proceedings of the 27th General Assembly, European Seismological Commission*, 149-153.

AYALA, A.G. & O'ROURKE, M. J. (1989). “Effects of the 1985 Michoacan Earthquake on Water Systems in Mexico,” *Technical Report NCEER-89-0009*, National Center for Earthquake Engineering Research, State University of New York at Buffalo, Buffalo, NY.

AYHAN, M.E., BURGMANN, R., MCCLUSKY, S., LENK, O., AKTOG, B., HERECE, E. & REILINGER, R.E. (2001). "Kinematics of the M_w=7.2, 12 November 1999, Düzce, Turkey earthquake." *Geophysical Research Letters*, **28** (2), 367-370.

AYDAN, O., ULUSAY, R., KUMSAR, H. & TUNCAY, E. (2000). “Site investigation and engineering evaluation of the Düzce-Bolu earthquake of November 12, 1999,” TDV, 220 pp.

AYHAN, M.E., BURGMANN, R., MCCLUSKY, S., LENK, O., AKTUG, B., HERECE, E., REILINGER, R.E. (2001). “Kinematics of the Mw = 7.2, 12 November 1999, Duzce, Turkey earthquake,” *Geophysical Research Letters,* **28** (2), 367-370.

BAGCI, G., YATMAN, A., OZDEMIR, S. & ALTIN, N. (1991). “Turkiye’de hasar yapan depremler,” *Deprem Arastirma Bulteni,* **69**, 113-126.
http://www.deprem.gov.tr/yikicidepremler.htm.

BAKIR, S. (2000). Personal communication.

BALLANTYNE, D. “Minimising earthquake damage,” *World Water and Environmental Engineering*, September, 30-31

BALLANTYNE, D.B., BERG, E., KENNEDY, J., RENEAU, R., & WU, D. (1990). “Earthquake loss estimation modelling for the Seattle water system: report to US Geological Survey under Grant 14-08-0001-G1526,” *Technical Report,* Kennedy/Jenks/Chilton, Federal Way, WA.

BARD, P.-Y. (1997). “Local effects on strong ground motion: basic physical phenomena and estimation methods for microzoning studies,” SERINA [Seismic Risk: An Integrated Seismological, Geotechnical and Structural Approach], ITSAK, Thessaloniki.

BARD, P.-Y. (1998). "Microtremor measurements: a tool for site effect estimation?" *Second International Symposium on the effects of surface geology on seismic motion,* Yokohama, Japan, December 1-3, 1998.

BARD P.-Y. (2001). “Ground motion variability and interpretation of sparse strong motion records,” *Proceedings of the Earthquake Geotechnical Engineering Satellite Conference, XVth International Conference on Soil Mechanics & Geotechnical Engineering,* Istanbul, Turkey, August 23-25, 113-116.

BARD, P.-Y. & RIEPL-THOMAS, J. (2000). “Wave propagation in compex geological structures and their effects on strong motion.” *In:* Kausel & Manolis (eds.) *Wave Motion in Earthquake Engineering,* 37-95.

BARENBERG, M.E. (1988). "Correlation of pipeline damage with ground motions." *Journal of Geotechnical Engineering,* ASCE, June, **114** (6), 706-711.

BARTLETT, S.F. & YOUD, T.L. (1992). “Empirical analysis of horizontal ground displacement generated by liquefaction-induced lateral spreads,” *Technical Report NCEER-92-0021*, National Center for Earthquake Engineering Research, State University of New York at Buffalo, Buffalo, NY.

BAZIAR, M.H., FALLAH, H., RAZEGHI, H.R. & KHORASANI, M.M. (1998). “The relation of shear wave velocity and SPT for soils in Iran,” *Proceedings of the Eleventh European Conference on Earthquake Engineering,* Balkema, Rotterdam.

BINDI, D., PAROLAI, S., SPALLAROSSA, D. & CATTENEO, M. (2000). “Site effects by H/V ratio: comparison of two different procedures,” *Journal of Earthquake Engineering*, **4** (1), 97-113.

BODIN, P., SMITH, K., HORTON, S. & HWANG, H. (2001). “Microtremor observations of deep sediment resonance in metropolitan Memphis, Tennessee,” *Engineering Geology,* **62**, 159-168.

BOLT, B.A. (1989). “The nature of earthquake ground motion,” *In*: F.Naeim (ed.) *The Seismic Design Handbook*, Van Nostrand Reinhold, New York.

BOLT, B.A. (1993). *Earthquakes,* W.H. Freeman and Company, New York, 331pp.

BOMMER, J.J., ELNASHAI, A.S., CHLIMINTZAS, G.O. & LEE, D. (1998). "Review and development of response spectra for displacement-based seismic design," *ESEE Report No. 98-3.* Imperial College of Science, Technology and Medicine, University of London, 163pp.

BOMMER, J.J., ELNASHAI, A.S. & WEIR, A.G. (2000). "Compatible acceleration and displacement spectra for seismic design codes," *Proceedings of the Twelfth World Conference on Earthquake Engineering*.

BOMMER, J.J., GEORGALLIDES, G. & TROMANS, I.J. (2001). "Is there a near-field for small-to-moderate magnitude earthquakes?" *Journal of Earthquake Engineering*, **5** (3), 395-423.

BOMMER, J.J. & MARTÍNEZ-PEREIRA, A. (1999). "The effective duration of earthquake strong motion." *Journal of Earthquake Engineering,* **3** (2), 127-172.

BOMMER, J.J. & MARTÍNEZ-PEREIRA, A. (2000). “Strong-motion parameters: definition, usefulness and predictability.” *Proceedings of the 12th World Conference on Earthquake Engineering*, CD-ROM Paper No. 0206.

BOMMER, J., SPENCE, R., ERDIK, M., TABUCHI, S., AYDINOGLU, N., BOOTH, E., DEL RE, D. & PETERKEN, O. (2002). "Development of an earthquake loss model for Turkish catastrophe insurance," *Journal of Seismology*, **6**, 431-446.

BOORE, D. M. (2001). "Effect of baseline corrections on displacements and response spectra for several recordings of the 1999 Chi-Chi, Taiwan, earthquake," *Bulletin of the Seismological Society of America,* **91** (5), 1199-1211.

BOORE, D.M., JOYNER, W.B., & FUMAL, T.E. (1993). "Estimation of response spectra and peak accelerations from western North American earthquakes: An interim report," *Open-File Report 93-509*. U.S. Geological Survey.

BOORE, D.M., JOYNER, W.J., OLIVER, A.A. & PAGE, R.A. (1980). "Peak acceleration, velocity and displacement from strong-motion records," *Bulletin of the Seismological Society of America*, **70**, 305-321.

BORCHERDT, R.D. (1970). "Effects of local geology on ground motion near San Francisco Bay," *Bulletin of the Seismological Society of America,* **60** (1), 29-62.

BORCHERDT, R.D. & GIBBS, J.F. (1976). "Effects of local geological conditions in the San Francisco Bay Region on ground motions and the intensities of the 1906 earthquake," *Bulletin of the Seismological Society of America*, **66**, 467-500.

BORCHERDT, R.D., WENTWORTH, C.M., JANSSEN, A., FUMAL, T. & GIBBS, J. (1991). "Methodology for predictive GIS mapping of special study zones for strong ground shaking in the San Francisco Bay region," *Proceedings of the Fourth International Conference on Seismic Zonation*, **3**, 545-552.

BOUR, M., FOUISSAC, D., DOMINIQUE, P. & MARTIN, C. (1998). "On the use of microtremor recordings in seismic microzonation." *Soil Dynamics and Earthquake Engineering*, **17**, 465-474.

BRESKO, D. (1980). "Seismic risk analysis of a water system," *Research Report NSF-RANH, ENV-75-20977*, Department of Civil Engineering, Carnegie-Mellon University – GAI Consultants Inc., Pittsburgh, PA, June 1980.

BROWN, L.T., DIEHL, J.G. & NIGBOR, R.L. (2000). "A simplified method to measure average shear-wave velocity in the top 30 m (vs30)," *Proceedings of the Sixth International Conference on Seismic Zonation*, Palm Springs, CA, EERI, November.

BRUNE, J.N. (1970). "Tectonic stress and the spectra of seismic shear waves from earthquakes," *Journal of Geophysical Research*, **75**, 4997-5009.

BRUNE, J.N. & OLIVER, J. (1959). "The seismic noise of the Earth's surface," *Bulletin of the Seismological Society of America,* **49**, 349-353.

CAE. (1991). *Lifelines in earthquakes: Wellington case study.* University of Canterbury, New Zealand, 210pp.

CAJINA, A. (1973). "The Managua earthquake and its effects on the water supply system." *Proceedings, Managua, Nicaragua earthquake of December 23, 1972.* California: EERI, **2**, 768-790.

CAMPBELL, K.W. (1997). "Empirical near-source attenuation relatioships for horizontal and vertical components of peak ground acceleration, peak ground velocity and pseudo-absolute acceleration response spectra," *Seismological Research Letters*, **68** (1), 154-179.

CHANG, S.W., BRAY, J.D. & SEED, R.B. (1996). "Engineering implications of ground motions from the Northridge earthquake," *Bulletin of the Seismological Society of America*, **86** (1B), S270-S288.

CHATELAIN, J.-L., GUEGUEN, P., GUILLIER, B., FRECHET, J., BONDOUX, F., SARRAULT, J., SULPLICE, P., NEUVILLE, J.-M. (2000) "CityShark: a user-friendly instrument dedicated to ambient noise (microtremor) recording for site and building response studies," *Seismological Research Letters*, **71** (6), 698-703.

CHAVEZ-GARCIA, F.J. & CARDENAS-SOTO, M. (2002). "The contribution of the built environmanet to the 'free-field' ground motion of Mexico City," *Soil Dynamics and Earthquake Engineering,* **22**, 773-780.

CHEN, W., SHIH, B.-J., CHEN, Y.-C., HUNG, J.-H. & HWANG, H. (2002). "Seismic response of natural gas and water pipelines in the Ji-Ji earthquake," *Soil Dynamics and Earthquake Engineering,* **22**, 1209-1214.

CHUO KAIHATSU CO. LTD. (1995). *The reconnaissance report on the Hyogoken-nanbu earthquake* [in Japanese].

COBURN, A. & SPENCE, R. (1992) *Earthquake Protection*, John Wiley

CSOES (1973). "The Managua, Nicaragua earthquake of December, 23, 1972: an emergency response evaluation." *Proceedings, Managua, Nicaragua earthquake of December 23, 1972.* California: EERI, **2**, 955-975.DARRAGH, R.B. & SHAKAL, A.F. (1991). "The site response of two rock and soil station pairs to strong and weak ground motion," *Bulletin of the Seismological Society of America,* **85**, 440-451.

DARRAGH, R.B. & SHAKAL, A.F. (1991). "The site response of two rock and soil station pairs to strong and weak ground motion," *Bulletin of the Seismological Society of America,* **85**, 440-451.

DATTA, T.K. (1999). "Seismic response of buried pipelines: a state-of-the-art review," *Nuclear Engineering and Design*, **192**, 271-284.

DEWEY, J.W., REAGOR, B.G., DENGLER, L. & MOLEY, K. (1995). "Intensity distribution and isoseismal maps for the Northridge, California, earthquake of January 17, 1994," *US Geological Survey Open-File Report 95-92.* US Department of the Interior, Washington, DC, 1995.

DOBRY, R., OWEIS, I. & URZUA, A. (1976). "Simplified procedures for estimating the fundamental period of a soil profile," *Bulletin of the Seismological Society of America,* **66** (4), 1293-1321.

DODO, J. (1998). "The damage of waterworks in Hyogo prefecture and lessons of emergency management in the Great Hanshin-Awaji Earthquake," *Proceedings of the IWSA International Workshop on Anti-seismic Measures on Water Supply, 'Water & Earthquake '98 Tokyo',* Tokyo, Japan, 15-18 November, 125-130.

DOUGLAS, J. (2001a). "A comprehensive world-wide summary of strong-motion attenuation relationships for peak ground acceleration and spectral ordinates (1969-2000)," *ESEE Report No. 01-1.* Imperial College of Science, Technology and Medicine, University of London, 138pp, http://www.esee.cv.ic.ac.uk/reports.htm.

DOUGLAS, J. (2001b). "A critical reappraisal of some problems in engineering seismology," *PhD Thesis*, University of London.

DUKE, C.M. & MATTHIESEN, R.B. (1973). "Earthquakes, lifelines and ASCE." *Civil Engineering,* ASCE, December 1973, 65-67.

DUKE, C.M. & MORAN, D.F. (1975). "Guidelines for evolution of lifeline earthquake engineering." *Proceedings of the US National Conference on Earthquake Engineering,* EERI, 367-376.

DURUKAL, E. (2000). Personal communication.

DURUKAL, E. (2002). "Critical evaluation of strong motion in Kocaeli and Düzce (Turkey) Earthquakes," *Soil Dynamics and Earthquake Engineering,* **22**, 589 – 609.

DURUKAL, E., ERDIK, M., AVCI, O., YUZUGULLU, Y., ALPAY, B., AVAR, B., ZULFIKAR, C., BIRO, T. & MERT, A. (1998). "Analysis of the strong motion data of the 1995 Dinar, Turkay earthquake," *Soil Dynamics and Earthquake Engineering*, **17**, 557-578.

EERI (1999). "The Izmit (Kocaeli), Turkey Earthquake of August 17, 1999." *EERI Special Earthquake Report - October 1999,*
http://www.eeri.org/Reconn/Turkey0899/Turkey0899.html

EFENDIOGLU, M.E. (2001). “Studies done in Düzce before and after the earthquake,” *Proceedings of the Symposium on Water Supply Situation in Earthquake Affected Region*, Düzce Municipality/UNICEF, Koru Hotel, Düzce, Turkey, 4 – 5 April, 55 – 57.

EGUCHI, R.T. (1983). “Seismic vulnerability models for underground pipes,” *Proceedings of Earthquake Behavior and Safety of Oil and Gas Storage Facilities, Buried Pipelines and Equipment,* PVP-77, ASME, New York, June, 368-373.

EGUCHI, R.T. (1991). “Seismic hazard input for lifeline systems,” *Structural Safety,* **10**, 193-198.

EIDINGER, J. (1998). "Water distribution system." *In:* Anshel J. Schiff (ed.) *The Loma Prieta, Californai, Earthquake of October 17, 1989 - Lifelines*. USGS Professional Paper 1552-A, US Government Printing Office, Washington, A63-A78.

EIDINGER, J., MAISON, B, LEE, D. & LAU, B. (1995). "East Bay Municipal District water distribution damage in 1989 Loma Prieta earthquake". *Proceedings of the Fourth US Conference on Lifeline Earthquake Engineering,* ASCE, TCLEE, Monograph No. 6, 240-247

EKSTROM, G. & DZIEWONSKI, A.M. (1988). “Evidence of bias in estimation of earthquake size,” *Nature*, 332, 319-323.

EQE International (1999). "An EQE briefing - 1999 Izmit, Turkey Earthquake," http://www.eqe.com.

ERDIK, M. (2000). “Report on 1999 Kocaeli and Düzce (Turkey) earthquakes.” Department of Earthquake Engineering, Boğaziçi University, Istanbul, Turkey, http://www.koeri.boun.edu.tr/earthq/Kocaelireport.pdf

ESRI (1999). ArcView GIS, Version 3.2a.

EVERNDEN, J.F. & THOMPSON, J.M. (1985). “Predicting seismic intensities,” *U.S. Geological Survey Professional Paper 1360,* 151-202.

FAH, D., KIND, F. & GIARDINI, D. (2001). “A theoretical investigation of average H/V ratios,” *Geophysical Journal International,* **145**, 535-549.

FALCONER, R. (1999). "The frightening force of nature." *Water & Environment Manager*. November 1999, p15.

FARLEY, M. (2001) *Leakage Management and Control - A Best Practice Training Manual*, WHO, http://www.who.int/docstore/water_sanitation_health/leakage/begin.html.

FEMA (1999). *Earthquake Loss Estimation Methodology HAZUS 99 Service Release 2: Technical Manual,* FEMA, Washington DC, http://www.fema.gov/hazus.

FIELD, E.H., HOUGH, S.E. & JACOB, K.H. (1990). “Using microtremors to assess potential earthquake site response: a case study in Flushing Meadows, New York,” *Bulletin of the Seismological Society of America,* **80**, 1456-1480.

FIELD, E.H. & JACOB, K.H. (1995). “A comparison and test of various site-response estimation techniques including three that are not reference-site dependent,” *Bulletin of the Seismological Society of America*, **85** (4), 1127-1143.

GARMIN CORPORATION (1999). “GPS12 Personal Navigator: Owner’s Manual and Reference,” http://www.garmin.com/products/gps12/manual.html

GARMIN CORPORATION (2002). “How accurate is a Garmin GPS?” http://www.garmin.com/support/faqs/8.html.

GAULL, B.A., KAGAMI, H., TANIGUCHI, H. (1995). "The microzonation of Perth, Western Australia, using microtremor spectral ratios." *Earthquake Spectra* **11** (2), 173-191.

GELI, L., BARD, P.-Y. & JULIEN, B. (1988). “The effect of topography on earthquake ground motion: a review and new results.” *Bulletin of the Seismological Society of America,* **78**, 42-63.

GEOGRAPHICAL SURVEY INSTITUTE (1996). *1:10,000 Earthquake Disaster Prevention Land Condition Map*.

GRAIZER, V.M. (1979). “Determination of the true ground displacement by using strong motion records”, *Izvestiya Academy of Sciences, USSR, Physics of the Solid Earth,* **15** (12), 875-885.

GREGOR, N.J. (1995). "The attenuation of strong ground motion displacements." *Earthquake Engineering Research Center, Report No. UCB/EERC-95/02.*

GREGOR, N.J. & BOLT, B.A. (1997). "Peak strong motion attenuation relations for horizontal and vertical ground displacements." *Journal of Earthquake Engineering*, **1** (2), 275-292.

GRUNTHAL, G. (ed.) (1998). “European Macroseismic Scale 1998”, Conseil de l’Europe, **15**, 99p.

GUEGEN, P., CHATELAIN, J-L., GUILLIER, B., YEPES, H. & EGRED, J. (1998). "Site effect and damage distribution in Pujili (Ecuador) after the 28 March 1996 earthquake." *Soil Dynamics and Earthquake Engineering,* **17**, 329-334.

GULKAN, P. & KALKAN, E. (2002). “Attenuation modelling of recent earthquakes in Turkey,” *Journal of Seismology*, **6**, 397-409.

GUPTA, V.K., NIELSEN, S.R.K. & KIRKEGAARD, P.H. (2001). “A preliminary prediction of seismic damage-based degradation in RC structures,” *Earthquake Engineering and Structural Dynamics,* **30** (7), 981-993.

HADJIAN, A.H. (2002). “Fundamental period and mode shape of layered soil profiles,” *Soil Dynamics and Earthquake Engineering*, **22**, 885-891.

HALPERIN (1998). “Living by serving: new directions for the transition economies,” *Report No. 18426 ECA*, Europe and Central Asia Infrastructure Sector Unit, World Bank, September 25, http://www.gaps2.atomnet.pl/infrawb.htm.

HANKS, T.C. & KANAMORI, H. (1979). “A moment magnitude scale,” *Journal of Geophysical Research*, **84**, 2348-2350.

HAMADA, M. (1991). “Estimation of earthquake damage to lifeline systems in Japan,” *Proceedings of the Third Japan-US Workshop on Earthquake Resistant Design of Lifeline Facilities and Countermeasures for Soil Liquefaction,* San Francisco, CA, December 17-19, 1990, *Technical Report NCEER-91-0001*, NCEER, State University of New York at Buffalo, Buffalo, NY, 5-22.

HAMADA, M. (1997). “Lessons learned from the 1995 Hyogoken-Nanbu (Kobe) earthquake: JSCE’s proposals on measures against future earthquakes.” http://www.jsce.or.jp/e/ce_jsce/jsce97/97jsce2/97jsce2.htm.

HAMADA, M., YASUDA, S., ISOYAMA, R. & EMOTO, K. (1986). "Study on liquefaction induced permanent ground displacements." Association for the Development of Earthquake Prediction in Japan, Tokyo, Japan.

HASHASH, Y.M.A., HOOK, J.J., SCHMIDT, B. & YAO, J.I-C. (2001). “Seismic design and analysis of underground structures,” *Tunneling and Underground Space Technology*, **16**, 247-293.

HASKELL, N.A. (1953). “The dispersion of surface waves in multi-layered media,” *Bulletin of the Seismological Society of America*, **43** (1), 17-34.

HASKELL, N.A. (1969). “Elastic displacements in the near field of a propagating fault,” *Bulletin of the Seismological Society of America,* **59**, 865-908.

HO, C.L. (1991). "Ground motion model for Puget Sound cohesionless soil sites", E*arthquake Spectra* **7** (2), 1991.

HWANG, H. & LIN, H. (1997). “GIS-based evaluation of seismic performance of water delivery systems,” *Technical Report,* CERI, the University of Memphis, Memphis, TN, 110pp.

IASPEI. 1967. “Recommendations of the committee on magnitudes,” *Comptes rendu*s, **15**, 65.

ICBO (1997). “Uniform Building Code – 1997,” *International Conference of Building Officials*, Whittier, California.

ICHIHARA, M. & YAMADA, K. (1982). “Application of microzonation for the damage of water pipelines,” *Proceedings of the Third International Conference on Microzonation*, Seattle, 1665-1676.

IDRISS, I.M. (1978). "Characteristics of earthquake ground motions," *Proceedings of the ASCE Geotechnical Engineering Division Speciality Conference: Earthquake Engineering and Soil Dynamics*, vol. III, 1151-1265.

IDRISS, I.M. (1985). “Evaluating seismic risk in engineering practice,” *Proceedings of the Eleventh International Conference on Soil Mechanics and Foundation Engineering*, San Francisco, **1**, 255-320.

IDRISS, I.M, RATHJE, E. & SOMERVILLE, P. (2000). “Strong ground motions and site effects,” *In:* Youd, T.L. *et al.*(ed.) *Kocaeli, Turkey, Earthquake of August 17, 1999: Reconnaissance Report. Supplement A to Volume 16, Earthquake Spectra,* EERI. 65-96.

INADA, H. (2000). Personal communication.

ISENBERG, J. (1979). "Role of corrosion in water pipeline performance in three US earthquakes." *Proceedings of the 2nd US National Conference on Earthquake Engineering, 1979.* EERI, 683-692.

ISOYAMA, R., ISHIDA, E., YUNE, K. & SHIROZU, T. (2000). “Seismic damage estimation procedure for water supply pipelines,” *Proceedings of the Twelfth World Conference on Earthquake Engineering,* CD-ROM Paper No. 1762, 8pp.

ISOYAMA, R. & KATAYAMA, T. (1982). “Reliability evaluation of water supply systems during earthquakes,” *Report of the Institute of Industrial Science, University of Tokyo,* **30** (1) (Serial No. 194).

IWAMOTO, T., INADA, H. & NEMOTO, Y. (1992). "Observation on behaviours of buried pipelines and ground strain during earthquakes." *Proceedings of the 10th World Conference on Earthquake Engineering,* 5575-5579.

IYISAN, R. (1996). “Correlations between shear-wave velocity and in-situ penetration test results,” *Technical Journal of the Turkish Chamber of Civil Engineers,* **7** (2), 1187-1199.

JACKSON, J. (2001). "Living with earthquakes: know your faults." *Journal of Earthquake Engineering,* **5**, Special Issue 1, 5-123.

JDIPA (1998). *Ductile iron pipe with earthquake-proof joint.*

JOHNSON, A.M., JOHNSON, K.M., DURDELLA, J., SÖZEN, M. & GÜR, T. (2002). “An emendation of elastic rebound theory: Main rupture and adjacent belt of right-lateral distortion detected by Viaduct at Kaynasli, Turkey 12 November 1999 Düzce Earthquake,” *Journal of Seismology,* **6**, 329-346.

JOYNER, W.B. & BOORE, D.M. (1981). "Peak horizontal acceleration and velocity from strong-motion records including records from the 1979 Imperial Valley, California, earthquake," *Bulletin of the Seismological Society of America*, **71** (6), 2011-2038.

JOYNER, W.B. & BOORE, D.M. (1988). "Measurement, characterisation and prediction of strong ground motion," *Proceedings of Earthquake Engineering and Soil Dynamics II, GT Division, ASCE,* Park City, Utah, 43-102.

JOYNER, W.B. & FUMAL, T. (1984). “Use of measured shear-wave velocity for predicting geological site effects on strong motion,” *Proceedings of the Eighth World Conference on Earthquake Engineering*, **2**, 777-783.

JWWA (1998). *Seismic Design and Construction Guidelines for Water Supply Facilities - English edition.* JWWA.

KACHADOORIAN, R. (1976). "Earthquake: correlation between pipeline damage and geologic environment." *Journal of American Waterworks Association*, **68**, 165-167.

KAJITANI, Y., KAKUMOTO, S., HAYASHI, Y., YOSHIKAWA, K., HATAYAMA, M. & USUI, M. (2002). "Damages and recovery status in Düzce city after the 1999 Turkey earthquakes," *Area Safety Academic Essay Collection*, (4), 6pp. [in Japanese], http://zeisei5.dpri.kyoto-u.ac.jp/~hayashi/paper/2002kajitani.pdf

KAMIYAMA, M., O'ROURKE, M.J. & FLORES-BERRONES, R. (1992). "A semi-empirical analysis of strong-motion peaks in terms of seismic source, propagation path and local site conditions," *Technical Report NCEER-92-0023,* NCEER, Buffalo, New York.

KANAI, K. & TANAKA, T. (1961). "On microtremors. VII," *Bulletin of the Earthquake Research Institute,* Tokyo University, **31**, 457.

KATAYAMA, T. (1996). "Lessons from the 1995 Great Hanshin earthquake of Japan with emphasis on urban infrastructure systems." *Proceedings of the 15th Congress on Structural Engineering in Consideration of Economy, Environment and Energy.* Copenhagan, Denmark, 187-200, http://incede.iis.u-tokyo.ac.jp/kobenet/report/pub1/pub1-6.html

KATAYAMA, T., KUBO, K. & SATO, N. (1975). "Earthquake damage to water and gas distribution systems," *Proceedings of the U.S. National Conference on Earthquake Engineering.,* EERI, Oakland, CA, 396-405.

KAWASHIMA, K., AIZAWA, K. & TAKAHASHI, K. (1983). "Effects of composition of two horizontal components on attenuation of maximum earthquake ground motions and response spectra," *Proceedings of the Japan Society of Civil Engineers,* (329).

KAWASHIMA, K., AIZAWA, K. & TAKAHASHI, K. (1986). "Attenuation of peak ground acceleration, velocity and displacement based on multiple regression analysis of Japanese strong motion records," *Earthquake Engineering and Structural Dynamics,* **14**, 199-215.

KEEFER, D.K. (1984). "Landslides caused by earthquakes." *Geological Society of America Bulletin,* **95**, 406-421.

KITAURA, M. & MIYAJIMA, M. (1996). "Damage to water supply pipelines," *Special Issue of Soils & Foundations,* Japanese Geotechnical Society, Japan, January, 325-333.

KOBAYASHI, M., ANDO, H. & WATANABE, T. (2000). "Amplification of ground strain in irregular surface layers during strong ground motion," *Proceedings of the Twelfth World Conference on Earthquake Engineering*, CD-ROM Paper No. 2182.

KONNO, K. & OHMACHI, T. (1998). "Ground-motion characteristics estimated from spectral ratio between horizontal and vertical components of microtremor," *Bulletin of the Seismological Society of America*, **88** (1), 228-241.

KRAMER, S. L. (1996). *Geotechnical Earthquake Engineering.* New Jersey: Prentice Hall.

KUDO, K. (1995). "Practical estimates of site response: state-of-the-art report," *Proceedings of the Fifth International Conference on Seismic Zonation*, Nice, France, Ouest Editions Nantes, **3**, 1878-1907.

KUDO, K., KANNO, T., OKADA, H., OZEL, O., ERDIK, M., TAKAHASHI, M., SASATANI, T., HIGASHI, S. & YOSHIDA, K. (2002). "Site-specific issues on strong ground motion during the Kocaeli, Turkey earthquake of August 17, 1999, as inferred from array observations of microtremors and aftershocks," *Bulletin of the Seismological Society of America,* **92** (1), 448-465.

LACHET, C. & BARD, P-Y. (1994). "Numerical and theoretical investigations on the possibilities and limitations of Nakamura's technique," *Journal of Physics of the Earth*, **42**, 377-397.

LACHET, C., HATZFELD, D., BARD, P.-Y., THEODULIDIS, N., PAPAIOANNOU, C. & SAVVAIDIS, A. (1996). "Site effects and microzonation in the city of Thessaloniki (Greece): comparison of different approaches." *Bulletin of the Seismological Society of America,* **86** (6), 1692-1703.

LANGSTON, C.A. (1977). "Corvallis, Oregon, crustal and upper mantle receiver structure from teleseismic P and S waves," *Bulletin of the Seismological Society of America,* **67**, 713-724.

LEBRUN, B., HATZFELD, D. & BARD, P.Y. (2001). “Site effect study in urban area: experimental results in Grenoble (France).” *Pure and Applied Geophysics*, **158**, 2543-2557.

LEE, V.W., TRIFUNAC, M.D., TODOROVSKA, M.I. & NOVIKOVA, E.I. (1995). "Empirical equations describing attenuation of peaks of strong ground motion, in terms of magnitude, distance, path effects and site conditions," *Report No. CE 95-02*, University of Southern California, Department of Civil Engineering..

LEKKAS, E.L. (2000). “Intensity distribution and controlling factors at the Izmit and Düzce earthquakes (Turkey),” *Proceedings of the CRAAG Symposium 2000*, Algiers, Algeria, 9-11 October, 9pp.

LERMO, J. & CHAVEZ-GARCIA, F.J. (1993). “Site effect evaluation using spectral ratios with only one station,” *Bulletin of the Seismological Society of America*, **83** (5), 1574 – 1594.

LERMO, J.M., RODRIGUEZ, M. & SINGH, S.K. (1988). “Natural periods of sites in the valley of Mexico from microtremor measurements of strong-motion data,” *Earthquake Spectra*, **4** (4), 805-814.

LIANG, J. & SUN, S. (2000). “Site effects on seismic behaviour of pipelines: a review.” *Journal of Pressure Vessel Technology*, ASME, **122**, 469-475.

MANSINHA, L. & SMYLIE, D.E. (1971). "The displacement fields of inclined faults." *Bulletin of the Seismological Society of America,* **61** (5), 1433-1440.

MARGARIS, B., PAPAZACHOS, C., PAPAIOANNOU, C., THEODULIDIS, N., KALOGERAS, I. & SKARLATOUDIS, A. (2002). “Ground motion attenuation relations for shallow earthquakes in Greece,” *Proceedings of the Twelfth European Conference on Earthquake Engineering,* CD-ROM Paper Reference 385, 10p.

MARTINEZ-PEREIRA, A. (1996). "The characterisation of near-field earthquake ground motions for engineering design." *PhD Thesis*, University of London.

MATSUSHITA, M., MORITA, S. & OGURA. (1998). “Post-earthquake reconstruction of Kobe water system based on the lessons from the 1995 Hanshin-Awaji (Kobe) earthquake.” *Proceedings of the IWSA International Workshop on Anti-seismic Measures on Water Supply, 'Water & Earthquake '98 Tokyo',* Tokyo, Japan, 15-18 November, 119-124.

MCEER [Multidisciplinary Center for Earthquake Engineering Research] (2000). “The Marmara, Turkey Earthquake of August 17, 1999: Reconnaissance Report,” *Technical Report MCEER-00-0001*, MCEER, University of Buffalo, New York, 190pp.

MCGUIRE, R.K. (1974). "Seismic structure response risk analysis, incorporating peak response regression on earthquake magnitude and distance," *Report R74-51,* School of Engineering, MIT, Cambridge, Mass.

MCGUIRE, R.K. (1978). "Seismic ground motion parameter relations," *Journal of the Geotechnical Division, ASCE,* **104**, No. GT 4, 481-490.

MEDVEDEV, J. (1962). *Engineering Seismology*, Academia Nauk Press, Moscow, 260pp.

MENKITI, C.O., ISIK, S. & SIMSEK, O. (2002). “Appendix A: Report on site visit to Bolu strong ground motion station,” *Unpublished report, Yuksel Proje/Geotechnical Consulting Group.*

MENU, J.M. (1986). “Engineering study of near-field earthquake ground motions,” *PhD Thesis*, University of London.

MERZI, N. (2001). “Ways of improving leakage in drinking water distribution networks,” *Oral Presentation at the Symposium on Water Supply Situation in Earthquake Affected Region*, Düzce Municipality/UNICEF, Koru Hotel, Düzce, Turkey, 4 April.

MIDORIKAWA, S. (1987). “Prediction of isoseismal map in the Kanto plain due to hypothetical earthquake,” *Journal of Structural Engineering*, **33B**, 43-48 [in Japanese with English abstract].

MIDORIKAWA, S. (1993). "Intensity of earthquake motion." In: The Architectural Institute of Japan, (ed.) *Earthquake motion and ground conditions.* Tokyo: AIJ, 1993. pp. 157-184.

MIYAJIMA, M. & HASHJMOTO, T. (2001). "Damage to water supply system and surface rupture due to fault movement during the 1999 Ji-Ji earthquake in Taiwan." *Proceedings of the Fourth International Conference on Recent Advances in Geotechnical Earthquake Engineering and Soil Dynamics.* San Diego, California, CD-ROM Paper No. 1045.

MOHRAZ, B. & ELGHADAMSI, F.E. (1989). "Earthquake ground motion and response spectra," *In:* Naeim, Farzad (ed.) *The Seismic Design Handbook,* 32-80.

MOLAS, G.L. & YAMAZAKI, F. (1994). "An earthquake damage model using neural networks." *Bulletin of Earthquake Resistant Structure Research Center*, No. 27, March 1994, 89-101.

MTA/AU. (1999). "17 Agustos 1999 Depremi Sonrasi Düzce (Bolu) ilçesi alternatif yerlesim alanlarinin jeolojik incelemesi," *TÜBITAK Yer, Deniz, Atmosfer Bilimleri ve Çevre Arastirma Grubu Raporu*, 59pp.

MUCCIARELLI, M. (1998). "Reliability and applicability of Nakamura's technique using microtremors: an experimental approach." *Journal of Earthquake Engineering*. **2** (4), 625-638.

NAKAJIMA, T., IWAMOTO, T. & TOSHIMA, T. (1998). "Study on the anti-seismic countermeasures for ductile iron pipes," *Proceedings of the IWSA International Workshop on Anti-seismic Measures on Water Supply, 'Water & Earthquake '98 Tokyo',* Tokyo, Japan, 15-18 November, 218-223.

NAKAJIMA, Y., ABEKI, N. & WATANABE, D. (2000). "Study on the stability of H/V spectral ratio of microtremor in short period range for the estimation of dynamic characteristics of surface geology," *Proceedings of the Twelfth World Conference on Earthquake Engineering,* Auckland, New Zealand. CD-ROM, Paper No. 2904.

NAKAMURA, S. (1988). "Prediction of the Characteristics of surface wqave considering irregularity of stratum and application and design." *PhD Thesis,* Tohoku University, 1989.

NAKAMURA, Y. (1989). "A method for dynamic characteristics estimation of subsurface using microtremor on the ground surface," *Quarterly Report of Railway Technical Research Institute,* **30** (1).

NAKAMURA, Y. (1996). "Real-time information systems for seismic hazards mitigation UrEDAS, HERAS and PIC," *Quarterly Report of Railway Technical Research Institute,* **37** (3), 112-127.

NAKAMURA, Y. (2000). "Clear identification of fundamental idea of Nakamura's technique and its applications," *Proceedings of the Twelfth World Conference on Earthquake Engineering,* Auckland, New Zealand. CD-ROM, Paper No. 2656.

NAKANE, H., KODAMA, E. & YOKOI, I. (1992). "New earthquake-induced ground motion severity sensing apparatus for reliable system shutdown." *Proceedings of the Tenth World Conference on Earthquake Engineering*. Balkema, Rotterdam, 5559-5562.

NAZARIAN, S. & STOKOE, K.H. (1984). "In situ shear-wave velocities from spectral analysis of surface waves," *Proceedings of the Eighth World Conference on Earthquake Engineering*, **3**, 31-38.

NEUGEBAUER, J. (1995). "Structures and kinematics of the North Anatolian Fault zone, Adapazari-Bolu region, northwest Turkey," *Tectonophysics*, **243**, 119-134.

NEWMARK, N.M. (1967). "Problems in wave propagation in soil and rocks." *Proceedings of the International Symposium on Wave Propagation and Dynamic Properties of Earth Materials,* University of New Mexico Press, 7-26.

NEWMARK, N.M. & HALL, W.J. (1982). *Earthquake Spectra and Design.* EERI Monograph, Earthquake Engineering Research Institute, Berkeley, California, 103pp.

NEWMARK, N. & ROSENBLEUTH, E. (1971). *Fundamentals of Earthquake Engineering*, Prentice-Hall, Inc.

NIKOLAOS, T. & VASSILIOS, L. (1996). "The Kozani-Grevena, northern Greece, earthquake of May 13, 1995: strong motion data and structural response." *European Earthquake Engineering*, **1**, 3-13.

NISHIO, N., HAMURA, A. & SASE, T. (1988). "Earthquake observation of a buried pipeline in a non-uniform ground," *Proceedings of the Ninth World Conference on Earthquake Engineering*, August 2-9, Tokyo-Kyoto, Japan, **7**, 23-28.

NISHIO, N. (1994). "Damage ratio prediction for buried pipelines based on the deformability of pipelines and the nonuniformity of the ground," *Journal of Pressure Vessel Technology,* **116**, 459-466.

NOGOSHI, M. & IGARASHI, T. (1971). "On the amplitude characteristics of microtremor (Part 2)," *Journal of the Seismological Society of Japan*, **24**, 26-40 [in Japanese].

NUTTLI, O.W. (1973). "Seismic wave attenuation and magnitude relations for eastern North America," *Journal of Geophysical Research*, **78**, 876-885.

OECD (2000). "Economic effects of the 1999 Turkish earthquakes: an interim report." *OECD Economics Department Working Papers No. 247 (ECO/WKP(2000)20),* http://www.oecd.org/eco/eco.

OFWAT (2002). *Security of supply, leakage and the efficient use of water: 2001-2002 report*, October, 60pp., http://www.ofwat.gov.uk/aptrix/ofwat/publish.nsf/Content/navigation-publications-reportsonwatercompanies.

OHNO, S., TAKEMURA, M., NIWA, M. & TAKAHASHI, K. (1996). "Intensity of strong ground motion on Pre-Quaternary stratum and surface soil amplifications during the 1995 Hyogo-ken Nanbu earthquake, Japan," *Journal of the Physics of the Earth*, **44**, 623-648.

OHTA, Y. & GOTO, N. (1978). "Empirical shear wave velocity equations in terms of characteristic soil indexes," *Earthquake Engineering and Structural Dynamics*, **6** (2), 167-187.

OMER, E., YIGIT, D.T., YASUO, A., AHMET, D. & SELIM, O. (2000). "Surface ruptures of November 12 1999 Düzce earthquake, NW Turkey," *Proceedings of the 27th General Assembly, European Seismological Commission*, 247-252.

O'ROURKE, M.J. (1999). "Estimation of post-earthquake water system serviceability," *Proceedings of the Seventh Japan-US Workshop on Earthquake Resistant Design of Lifeline Facilities and Countermeasures for Soil Liquefaction,* MCEER, State University of New York at Buffalo, Buffalo, NY, 391-403.

O'ROURKE, M.J. & AYALA, G. (1993). "Pipeline damage due to wave propagation." *Journal of Geotechnical Engineering.* ASCE. **119** (9), 1490-1498.

O'ROURKE, M.J., BLOOM, M.C. & DOBRY, R. (1982). "Apparent propagation velocity of body waves," *Earthquake Engineering and Structural Dynamics*, **10**, 283-294.

O'ROURKE, M.J., CASTRO, G. & CENTOLA, N. (1980). "Effects of seismic wave propagation upon buried pipelines." *Earthquake Engineering and Structural Dynamics*, **8**, 455-467.

O'ROURKE, M.J., CASTRO, G. & HOSSAIN, I. (1984). "Horizontal soil strain due to seismic waves." *Journal of Geotechnical Engineering*, ASCE, **110**, 9, 1173-1187.

O'ROURKE, M.J. & EL HMADI, K. (1988). "Analysis of continuous buried pipelines for seismic wave effects," *Earthquake Engineering and Structural Dynamics,* **16**, 917-929.

O'ROURKE, M.J. & LIU, X. (1999). *Response of Buried Pipelines Subject to Earthquake Effects.* MCEER Monograph No. 3.

O'ROURKE, T.D. (1985). "Factors affecting the performance of cast iron pipelines: a review of U.S. observations and research investigations," *Final Report to Ground Engineering Division,* TRRL, Crowthorne, UK, May.

O'ROURKE, T.D. (1996). "Lessons learned for lifeline engineering from major urban earthquakes," *Proceedings of the Eleventh World Conference on Earthquake Engineering.* Acapulco, Mexico, June 23-28. Elsevier Science Ltd. CD-ROM, Paper No. 2172.

O'ROURKE, T.D. (1998). "An overview of geotechnical and lifeline earthquake engineering." *Geotechnical Special Publication No. 75,* ASCE, **2**, 1392-1426.

O'ROURKE, T.D., BEAUJON, P.A. & SCAWTHORN, C.R. (1992). "Large ground deformations and their effects on lifeline facilities: 1906 San Francisco earthquake." In: O'Rourke, T.D. & Hamada, M. (eds.) *Case Studies of Liquefaction and Lifeline Performance During Past Earthquakes: Technical Report NCEER-92-0002,* **2**. NCEER, Buffalo, New York.

O'ROURKE, T.D. & JEON, S.-S. (1999). "Factors affecting the earthquake damage of water distribution systems," *Proceedings of the Fifth US Conference on Lifeline Earthquake Engineering*, Seattle, WA, ASCE, Reston, VA, 379-388.

O'ROURKE, T.D. & JEON, S.-S. (2000). "Seismic zonation for lifelines and utilities," *Proceedings of the Sixth International Conference on Seismic Zonation,* CD-ROM Paper No. 168.

O'ROURKE, T.D., STEWART, H.E., GOWDY, T.E. & PEASE, J.W. (1991). "Lifeline and geotechnical aspects of the 1989 Loma Prieta earthquake," *Proceedings of the Second International Conference on Recent Advances in Geotechnical Earthquake Engineering and Soil Dynamics,* St. Louis, MO, 1601-1612.

O'ROURKE, T.D., STEWART, H.E. & JEON, S.-S. (2001). "Geotechnical aspects of lifeline engineering," *Proceedings of the Institution of Civil Engineers: Geotechnical Engineering*, **149**, January 2001, Issue 1, 13-26.

O'ROURKE, T.D. & TOPRAK, S. (1997). "GIS assessment of water supply damage from the Northridge earthquake." In: David Frost, J. (ed.) S*patial Analysis in Soil Dynamics and Earthquake Engineering: Geotechnical Special Publication No.67.* ASCE. 117-131.

O'ROURKE, T.D., TOPRAK, S. & SANO, Y. (1998). "Factors affecting water supply damage caused by the Northridge earthquake." *Proceedings of the Sixth US National Conference on Earthquake Engineering.* [CD-ROM].

PAPADOPOULOS, G.A., DRAKATOS, G., PAPANASTASSIOU, D., KALOGERAS, I. & STAVRAKAKIS, G. (2000). "Preliminary results about the catastrophic earthquake of 7 September 1999 in Athens, Greece." *Seismological Research Letters*, **71** (3), 318-329.

PARSONS, T., TODA, S., STEIN, R.S., BARKA, A. & DIETERICH, J.H. (2000), "Heightened odds of large earthquakes near Istanbul: an interaction-based probability calculation," *Science* **288**, 28 April, 661–665.

PEASE, J.W. & O'ROURKE, T.D. (1997). "Seismic response of liquefaction sites." *ASCE Journal of Geotechnical and Geoenvironmental Engineering,* **123**(1), pp.37-45.

PETERSON, J. (1993). "Observations and modelling of seismic background noise," *United States Department of Interior Geological Survey,* Open-File Report 93-322, Albuquerque, New Mexico, 95pp.

PITILAKIS, K., ANAGNOSTOPOULOS, Ch., MAVRIDIS, G. & TOLIS, St. "An integrated automatic procedure for estimating the aseismic design and vulnerability of buried pipelines crossing areas with seismically induced landslides." *Proceedings of the 5th International Confernece on Seismic Zonation,* October 17-19, 1995, Nice, France, **1**, 76-83.

PSYCHARIS, I., PAPASTAMATIOU, D., TAFLAMBAS, I. & CARYDIS, P. (1999). "The Athens, Greece earthquake of September 7, 1999", *EERI Special Report* http://www.eeri.org/Reconn/Greece1099/Greece1099.html.

PWA (2002). "Case study for a Pacific islands regional leak detection program," PWA, Suva, Fiji, http://www.pwa.org.fj/.

RAPTAKIS, D.G., ANASTASIADIS, A.J., PITILAKIS, K.D. & LONTZETIDIS, K.S. (1995). "Shear wave velocities and damping of Greek natural soils," *Proceedings of the Tenth European Conference on Earthquake Engineering,* Balkema, Rotterdam, 477-482.

REILINGER, R.E., ERGINTAV, S., BURGMANN, R., MCCLUSKY, S., LENK, O., NARKA, A., GURKAN, O., HEARN, L., FEIGL, K.L., CAKMAK, R., AKTUG, B., OZENER, H., TOKSOZ, M.N. (2000). "Coseismic and postseismic fault slip for the 17 August 1999, M=7.5, Izmit, Turkey earthquake." *Science*, **289**, 1519-1524.

REITER, L. (1990). *Earthquake Hazard Analysis: Issues and Insights,* Columbia University Press, New York, 254pp.

RICHTER, C.F. (1935). "An instrumental earthquake magnitude scale," *Bulletin of the Seismological Society of America*, **25**, 1-32.

RINALDIS, D., BERARDI, R., THEODULIDIS, N. & MARGARIS, B. (1998). "Empirical predictive models based on a joint Italian and Greek strong-motion database: I, peak ground acceleration and velocity," *Proceedings of the 11th European Conference on Earthquake Engineering*, A.A.Balkema, Rotterdam.

ROBERTSON, R.K., CAMPANELLA, R.G., WIGHTMAN, A. (1983). "SPT-CPT correlations, *Proceedings of the American Society of Civil Engineers*, **109**, GT11, 1449-1459.

RODRIGUEZ, C.E., BOMMER, J.J. & CHANDLER, R.J. (1999). "Earthquake-induced landslides: 1980-1997." *Soil Dynamics and Earthquake Engineering,* **18**, 325-346.

SABETTA, F. & PUGLIESE, A. (1987). "Attenuation of peak horizontal acceleration and velocity from Italian strong-motion records," *Bulletin of the Seismological Society of America*, **77** (5), 1491-1511.

SADIGH, R.K. & EGAN, J.A. (1998). "Updated relationships for horizontal peak ground velocity and peak ground displacement for shallow crustal earthquakes," *Proceedings of the 6th US National Conference on Earthquake Engineering.* [CD-ROM].

SAFAK, E. (2001). "Local site effects and dynamic soil behaviour," *Soil Dynamics and Earthquake Engineering,* **21**, 453-458.

SAGHIR, J., SCHIFFLER, M. & WOLDU, M. (2000). "Urban water and sanitation in the Middle East and North Africa region: the way forward," The World Bank Middle East and North Africa Region Infrastructure Development Group, January, pp29.

SARIKAYA, H.Z. & KOYUNCU, I. (1999). "Evaluation of the effects of Kocaeli earthquake on water and wastewater systems." *Proceedings of the ITU-IAHS International Conference on the Kocaeli Earthquake of 17 August, 1999.* Dec 2-5, 1999, Istanbul, Turkey, 183-191.

SARMA, S.K. (1971). "Energy flux of strong earthquakes," *Tectonophysics*, **11**, 159-173.

SARMA, S.K. (1994). *Fortran program ATTEN.* ESEE Section, Imperial College, University of London.

SAROGLU, F., EMRE, O. & KUSCU, I. (1992). "Active Fault Map of Turkey," *MTA*, Turkey.

SATO, N., KATAYAMA, T, NAKAMURA, M., IWAMOTO, T & OHBO, N. (1988). "Observation of seismic ground motion and buried pipe strain in a very dense seismometer array." *Proceedings of the Ninth World Conference on Earthquake Engineering*, Tokyo-Kyoto, August 2-9, **7**, 29-34.

SATOH, T., KAWASE, H. & MATSUSHIMA, S. (2001). "Differences between site characteristics obtained from microtremors, S-waves, P-waves and codas," *Bulletin of the Seismological Society of America*, **91** (2), 313-334.

SAVAGE, W.U. (2000). "Commentary on lifeline application of seismic zonation," *Proceedings of the Sixth International Conference on Seismic Zonation*, Palm Springs, CA, EERI, November, 1345-1349.

SCAWTHORN. C. (1999). “Preliminary report: Kocaeli (Izmit) earthquake of 17 August 1999,” MCEER, http://www.mceer.buffalo.edu.

SCHIFF, A., & BOGDANOFF, J. L. (1967). "Analysis of current methods of interpreting strong-motion accelerograms," Bulletin of the Seismological Society of America, **57** (5), 857–874.

SCHNEIDER, J.F., ABRAHAMSON, N.A., SOMERVILLE, P.G. & STEPP, J.C. (1990). “Spatial variation of ground motion from EPRI’s dense accelerograph array at Parkfield, California,” *Proceedings of the Fourth US National Conference on Earthquake Engineering*, Palm Springs, California, Vol 1, 375 – 384.

SEED, H.B., MURARKA, R., LYSMER, J. & IDRISS, I.M. (1976). “Relationships of maximum acceleration, maximum velocity, distance from source and local site conditions for moderately strong earthquakes,” *Bulletin of the Seismological Society of America*, **66** (4), 1323-1342.

SELCUK, A.S. & YUCEMEN, M.S. (2000). “Reliability of lifeline networks with multiple sources under seismic hazard,” *Natural Hazards*, **21**, 1-18.

SELLARS, B. (1999). "Dealing with disaster: special feature - Turkey earthquake". *Water & Environment International*, November 1999, 22-23

SEO, K., HAILE, M., KURITA, K., YAMAZAKI, K. & NAKAMURA, A. (1996). “Study of site effects in Kobe area using microtremors,” *Proceedings of the Eleventh World Conference on Earthquake Engineering,* Acapulco, Mexico, June 23-28. Elsevier Science Ltd. CD-ROM, Paper No. 1656.

SHIH, B., CHEN, W., CHANG, T-C. & LIU, S-Y. (1999). “Water system damages in the Ji-Ji earthquake – a GIS application,” *Proceedings of the 6th International Conference on Seismic Zonation.*

SHIH, B.-J., CHEN, W.W., CHANG, T.-C. & LIU, S.-Y. (2000). "Water system damages in the Ji-Ji earthquake - a GIS application." *Proceedings of the Sixth International Conference on Seismic Zonation.* Palm Springs, California.

SHINOARA, H., JIN, K. & YAMAMOTO, A. (1996). “Local site effects of surface geology on strong earthquake motion during the 1993 Kushiro-Oki earthquake,” *Proceedings of the Eleventh World Conference on Earthquake Engineering.* Acapulco, Mexico, June 23-28. Elsevier Science Ltd. CD-ROM, Paper No. 1641.

SHINOZUKA, M. & KAWAKAMI, H. (1977). “Underground pipe damages and ground characteristics,” *Proceedings, ASCE Specialty Conference on Lifeline Earthquake Engineering*, Los Angeles, 239-307.

SHIROZU, T., YUNE, S., ISOYAMA, R. & IWAMOTO, T. (1996). "Report on damage to water distribution pipes caused by the 1995 Hyogoken-Nanbu (Kobe) earthquake." *Proceedings from the 6th Japan-US Workshop on Earthquake Resistant Design of Lifeline Facilities and Countermeasures Against Soil Liquefaction.* Technical Report NCEER-96-0012. 93-110.

SHYAM SUNDER, S. & CONNOR, J.J. (1982). “A new procedure for processing strong-motion earthquake signals,” *Bulletin of the Seismological Society of America*, **72** (2), 643-661.

SIMPSON, K.A. (1996). “Attenuation of strong ground-motion incorporating near-surface foundation conditions.” *Doctoral Thesis*, University of London.

SIMSEK, O. & DALGIC, S. (1997). “Consolidation properties of the clays at Düzce plain and their relationship with geological evolution,” *Geological Bulletin of Turkey*, **40** (2), 29–38.

SMITH, S.W. (1999). *The Scientist and Engineer’s Guide to Digital Signal Processing.* 2nd ed. California Technical Publishing, San Diego, California, http://www.dspguide.com/.

SMITH, J.O. (2002). *Mathematics of the Discrete Fourier Transform* Centre for Computer Research in Music and Acoustics (CCRMA), Stanford University, California, http://www-ccrma.stanford.edu/~jos/mdft/.

SOMERVILLE, P. (1998b). “Ground motion attenuation relationships and their application to aseismic design and seismic zonation,” *In:* Irikura, Kudo, Okada & Sasatani (eds) *The effects of Surface Geology on Seismic Motion.* pp.35-49.

SOMERVILLE, P.G., SMITH, N.F., GRAVES, R.W.& ABRAHAMSON, N.A. (1997). “Modification of empirical strong ground motion attenuation relationships to include the amplitude and duration effects of rupture directivity,” *Seismological Research Letters,* **68** (1), 199-222.

STEARNS, S.D. & DAVID, R.A. (1996). *Signal processing algorithms in MATLAB*, Prentice-Hall, New Jersey, 372pp.

STEIDL, J.H., TUMARKIN, A.G. & ARCHULETA, R.J. (1996). “What is a reference site?” *Bulletin of the Seismological Society of America,* **86** (6), 1733-1748.

STEIN, R.S., BARKA, A.A. & DIETRICH, J.H. (1997). “Progressive failure on the North Anatolian fault since 1939 by earthquake stress triggering”, *Geophysical Journal International* **128**, 594–604.

STEWART, J.P., LIU, A.H., CHOI, Y. & BATURAY, M.B. (2001). “Amplification factors for spectral acceleration in active regions,” *PEER Report 2001/10*, PEER Center, College of Engineering, University of California, Berkeley, December.

ST. JOHN, C.M. & ZAHRAH, T.F. (1987). “Aseismic design of underground structures”, *Tunneling and Underground Space Technology*, **2** (2), 165-197.

STUART, R. *et al.* (1996). “Seismic and thermal analysis of buried piping,” *Proceedings of the Eleventh World Conference on Earthquake Engineering*, CD-ROM Paper No. 1457.

SUCUOGLU, H. & YILMAZ, T. (2001). “Düzce, Turkey: a city hit by two major earthquakes in 1999 within three months,” *Seismological Research Letters,* **72** (6), 679-689.

SUCUOGLU, H. (2002) “Engineering characteristics of the near-field strong motions from the 1999 Kocaeli and Düzce Earthquakes in Turkey,” *Journal of Seismology*, **6**, 347 – 355.3

SUNDAHL, A.-C.M. (1997). “Geographical analysis of water main pipe breaks in the city of Malmo, Sweden,” *Journal of Water Supply :Research and Technology – Aqua*, **46** (1), 40-47.

SYKORA, D.W. & BASTANI, S.A. (1998). "Distribution of peak horizontal acceleration and peak horizontal particle velocity with depth measured during earthquakes." *Proceedings of the Sixth US National Conference on Earthquake Engineering.* EERI, CD-ROM Paper No 178.

TADDAY, K. (2001). “Situation analysis and recommendations related to improvement measures for drinking water supply system in Düzce,” *Oral Presentation at the Symposium on Water Supply Situation in Earthquake Affected Region*, Düzce Municipality/UNICEF, Koru Hotel, Düzce, Turkey, 4 April.

TADDAY, K. & SAHIN, M. (2001). “Situation analysis and recommendations related to improvement measures for drinking water supply system in Düzce,” *Proceedings of the Symposium on Water Supply Situation in Earthquake Affected Region*, Düzce Municipality/UNICEF, Koru Hotel, Düzce, Turkey, 4 – 5 April, 1-54.

TAKADA, S. (1991). *Lifeline Earthquake Engineering,* Kyoritsu Shuppan Co. [in Japanese]

TAKADA, S., HASSANI, N. & FUKUDA, K. (2002). “Damage directivity in buried pipelines of Kobe city during the 1995 earthquake,” *Journal of Earthquake Engineering*, **6**, 1, 1-15.

TAKADA, S., HASSANI, N., TSUYOSHI, T. & OZAKI, R. (2000). “A new proposal for simplified seismic response analysis of pipes in ground with inclined bed-rock,” *Proceedings of the Twelfth World Conference of Earthquake Engineering*, CD-ROM Paper No. 0930.

TAKADA, S. & TANABE, K. (1988). “Estimation of earthquake induced settlements for lifeline engineering.” *Proceedings of the Ninth World Conference on Earthquake Engineering.* Tokyo, Japan, **7**, 109-114.

TAYLOR, C.L. & CLUFF, L.S. (1977). "Fault displacement and ground deformation associated with surface faulting." *The Current State of Knowledge of Lifeline Earthquake Engineering,* ASCE TCLEE, 338-353.

TAYLOR, C., MITTLER, E. & VAL LUND, L. (1998) *Overcoming Barriers: Lifeline Seismic Improvement Programs.* ASCE TCLEE, Monograph No. 13. ASCE. 292pp.

TC4/ISSMGE (1999). *Manual for zonation on seismic geotechnical hazards.* Tokyo, Japan: Japanese Society of Soil Mechanics and Foundation Engineering, 209pp.

TENG, T.L. & QU, J. (1996). "Long-period ground motions and dynamic strain field of Los Angeles basin during large earthquakes." *Bulletin of the Seismological Society of America.* **86**, 5, 1417-1433.

TEVES-COSTA, P., MATIAS, L. & BARD, P-Y. (1996). "Seismic behaviour estimation of thin alluvium layers using microtremor recordings," *Soil Dynamics and Earthquake Engineering,* **15**, 201-209.

THEODULIDIS, N.P. & PAPAZACHOS, B.C. (1992). "Dependence of strong ground motion on magnitude-distance, site geology and macroseismic intensity for shallow earthquakes in Greece: I, peak horizontal acceleration, velocity and displacement," *Soil Dynamics and Earthquake Engineering*, 11, 387-402.

THOMPSON, R. (1999). "Design failures led to tragedy," *New Civil Engineer*, 16 September, 16-19.

TIBI, R., BOCK, G., XIA, Z., BAUMBACH, M., GROSSER, H., MILKEREIT, C., KARTAKISA, S., ZUNBUL, S. & ZSCHAU, J. (2001). "Rupture processes of the 1999 August 17 Izmit and November 12 Düzce (Turkey) earthquakes," *Geophysical Journal International*, **144**, F1-F7.

TIEDEMANN, H. (1992). *Earthquakes and Volcanoes: a Handbook for Risk Assessment,* Swiss Reinsurance Company, Zurich, Switzerland.

TMG (1995). *Tokyo and earthquakes*, TMG Municipal Library No. 29, Tokyo Metropolitan Governement, pp114.

TODA, S., PARSONS, T. & STEIN, R. (1999). "Coulomb stress state induced by Kocaeli earthquake," http://ncweb-menlo.wr.usgs.gov/study/turkey.

TODOROVSKA, M.I. & TRIFUNAC, M.D (1996). "Hazard mapping of normalised peak strain in soils during earthquakes: microzonation of a metropolitan area," *Soil Dynamics and Earthquake Engineering*, **15**, 321-329.

TOKIMATSU, K., ARAI, H. & ASAKA, Y. (1996). "Three-dimensional soil profiling in Kobe area using microtremors," *Proceedings of the Eleventh World Conference on Earthquake Engineering.* Acapulco, Mexico, June 23-28. Elsevier Science Ltd. CD-ROM, Paper No. 1486.

TOKSOZ, M.N. & LACOSS, R.T. (1968). "Microseisms: mode structure and sources," *Science*, **159**, 872-873.

TRIFUNAC, M.D. (1971). "Zero base-line correction of strong-motion accelerograms," *Bulletin of the Seismological Society of America,* **61**, 1201-1211.

TRIFUNAC, M.D. (1972). "A note on correction of strong-motion ccelerograms for instrument response," *Bulletin of the Seismological Society of America,* **62**, 401-409.

TRIFUNAC, M.D. (1976). "Preliminary analysis of the peaks of strong earthquake ground motion - dependence of peaks on earthquake magnitude, epicentral distance, and recording site conditions," *Bulletin of the Seismological Society of America*, **66** (1), 189-219.

TRIFUNAC, M.D. & BRADY, A.G. (1975). "On the correlation of seismic intensity scales with peaks of recorded strong ground motion." *Bulletin of the Seismological Society of America,* **65**, 139-162.

TRIFUNAC, M.D. & BRADY, A.G. (1976). "Correlations of peak acceleration, velocity and displacement with earthquake magnitude, distance and site conditions," *Earthquake Engineering and Structural Dynamics*, **4** (5), 455-471.

TRIFUNAC, M.D., IVANOVIC, S.S. & TODOROVSKA, M.I. (2001). "Apparent periods of a building. I: Fourier Analysis," *Journal of Structural Engineering,* **127** (5), 517-526.

TRIFUNAC, M.D. & LEE, V.W. (1973). "Routine computer processing of strong-motion accelerograms," *EERL [Earthquake Engineering Research Laboratory] Report 73-03,* California Institute of Technology, Pasadena, California.

TRIFUNAC, M.D. & LEE, V.W. (1974). "A note on the accuracy of computed ground displacements from strong-motion accelerograms," *Bulletin of the Seismological Society of America,* **64**, 1209-1219.

TRIFUNAC, M.D. & LEE, V.W. (1996). "Peak surface strains during strong ground motion," *Soil Dynamics and Earthquake Engineering*, **15**, 311-319.

TRIFUNAC, M.D., LEE, V.W. & TODOROVSKA, M.I. (1999). "Common problems in automatic digitisation of strong motion accelerograms," *Soil Dynamics and Earthquake Engineering*, **18**, 519-530.

TRIFUNAC, M.D. & TODOROVSKA, M.I. (1997). "Northridge, California, earthquake of 1994: density of pipe breaks and surface strains," *Soil Dynamics and Earthquake Engineering,* **16**, 193-207.

TRIFUNAC, M.D. AND TODOROVSKA, M.I. (1998a). "Amplification of strong ground motion and damage patterns during the 1994 Northridge, California, Earthquake", *Proccedings of the ASCE Specialty Conference on Geotechnical Earthquake Engineering. and Soil Dynamics*, Seattle, Washington, Geotechnical Special Publication No. 75, ASCE, **1**, 714-725.

TRIFUNAC, M.D. & TODOROVSKA, M.I. (1998b). "Damage distribution during the 1994 Northridge, California, earthquake relative to generalised categories of surficial geology," *Soil Dynamics and Earthquake Engineering,* **17**, 239 - 253.

TRIFUNAC, M.D. & TODOROVSKA, M.I. (1999). "Reduction of structural damage by nonlinear soil response," *Journal of Structural Engineering*, **125** (1), 89-97.

TRIFUNAC, M.D. & TODOROVSKA, M.I. (2000). "Long period microtremors, microseisms and earthquake damage: Northridge, CA, earthquake of 17 January 1994," *Soil Dynamics and Earthquake Engineering,* **19**, 253-267.

TRIFUNAC, M.D. & TODOROVSKA, M.I. (2001). "A note on the useable dynamic range of accelerographs recording translation," *Soil Dynamics and Earthquake Engineering*, **21**, 275-286.

TRIFUNAC, M.D. & TODOROVSKA, M.I. (2001). "Evolution of accelerographs, data processing, strong-motion arrays and spatial resolution in recording strong earthquake motion," *Soil Dynamics and Earthquake Engineering,* 6, 537-555.

TRIFUNAC, M.D., TODOROVSKA, M.I. & IVANOVIC, S.S. (1996). "Peak velocities and peak surface strains during Northridge, California, earthquake of 17 January 1994," *Soil Dynamics and Earthquake Engineering,* **15**, 301-310.

TRIFUNAC, M.D., UDWADIA, F.E. & BRADY, A.G. (1973). "Analysis of errors in digitised strong-motion accelerograms," *Bulletin of the Seismological Society of America,* **63** (1), 157-187.

TSANGARIS, M. & CHANDLER, A.M. (1998). "A global analysis of earthquake displacement response spectra," *Proceedings of the 6th SECED Conference: Seismic Design Practice into the Next Century - Research and Application*, Balkema, Rotterdam, 253-260.

TSELENTIS, G. & ZAHRADNIK, J. (2000) "Aftershock Monitoring of the Athens Earthquake of 7 September 1999," *Seismological Research Letters*, **71** (3), 330-337.

TSO, W.K., ZHU, T.J. & HEIDEBRECHT, A.C. (1992). "Engineering implication of ground motion A/V ratio." *Soil Dynamics and Earthquake Engineering.* **11**, 133-144.

TWORT, A.C., LAW, F.M., CROWLEY, F.W. & RATNAYAKA, D.D. (1994). *Water Supply*. 5th ed., London: Arnold, 642pp.

UDWADIA, F.E. & TRIFUNAC, M.D. (1973). "Comparison of earthquake and microtremor ground motions," *Bulletin of the Seismological Society of America,* **63** (4), 1227-1253.

UNICEF (1999a). *Situation Report*, 15 December 1999, http://www.unicef.org/turkey/u_in_tr/recovery-dec15.htm

UNICEF (1999b). *Situation Report*, 30 December 1999, http://wwww.reliefweb.int/w/rwb.nsf/480fa8736b88bbc3c12564f6004c8ad5/b600bfd7fa89e256c125685d003d4ccd.

UNICEF (2000a). *Situation Report*, January 2000, http://wwww.reliefweb.int/w/rwb.nsf/480fa8736b88bbc3c12564f6004c8ad5/4a1e2ad2dba8b473c1256872005ab205.

UNICEF, (2000b). "Recovery plan for Turkish children: Situation Report,", 21 February 2000, http://www.unicef.org/emerg/turkey_plan.pdf.

UNICEF, (2000c). "Recovery plan for Turkish children: Situation Report 16", 13 March 2000, http://www.unicef.org/emerg/sitrep16.pdf.

USGS (2000) "Implications for Earthquake Risk Reduction in the United States from the Kocaeli, Turkey, Earthquake of August 17, 1999", *U.S. Geological Survey Circular 1193*, US Department of the Interior, 65pp.

UTKUCU, M., ALPTEKIN, O & PINAR, A. (2003). "A detailed source study of the Orta (Çankiri) earthquake of June 6, 2000, (MS = 6.1): An intraplate earthquake in central Anatolia," *Journal of Seismology* **7**, 193–202

VARNES, D.J. (1978). "Slope movement types and processes," In: *Landslides: Analysis and Control,* Transportation Research Board Special Report 176, National Academy of Sciences, Washington, D.C, 12-33.

VILLACIS, C.A. & KATAYAMA, T. (1992). "Analysis of seismic ground and pipe strains observed in Chiba, Japan," *Proceedings of the Tenth World Conference on Earthquake Engineering*, Balkema, Rotterdam, 5517-5522.

WANG, Y. & LI, H. (1986). "Site dependent attenuation statistics of strong ground motion parameters," Earthquake *Engineering and Engineering Vibration,* **6** (3), 67-77(in Chinese).

WATER UK MAGAZINE (1999). "Earthquake hits Thames' works." 20 August 1999, No. 66, p3.

WELLS, D.L. & COPPERSMITH, K.J. (1994). "New empirical relationships among magnitude, rupture length, rupture width, rupture area, and surface displacement." *Bulletin of the Seismological Society of America,* **84** (4), 974-1002.

WENGSTROM, T.R. (1993). "Comparative analysis of pipe break rates: a literature review." *Chalmers Univ of Technology, Publication 2:93,* 95pp.

WILLS, C.J. & SILVA, W. (1998). "Shear-wave velocity characteristics of geologic units in California," *Earthquake Spectra*, **14** (3), 533-556.

WRIGHT, T., FIELDING, E. & PARSONS, B. (2001). "Triggered slip: observations of the 17 August 1999 Izmit (Turkey) earthquake using radar interferometry," *Geophysical Research Letters*, **28** (6), 1079-1082.

YAGI, Y. & KIKUCHI, M. (1999). "Preliminary results of rupture process for the November 12, 1999 Turkey earthquake," http://wwweic.eri.u-tokyo.ac.jp/yuji/trk2/Turkeyafter.html.

YAGI, Y. & KIKUCHI, M. (2000). "Source rupture process of the Kocaeli, Turkey, earthquake of August 17, 1999, obtained by the joint inversion of near-field data and teleseismic data," *Geophysical Research Letters,* **27** (13), 1969-1972.

YAMAGUCHI, N. & YAMAZAKI, F. (2001). “Estimation of strong motion distribution on the 1995 Kobe earthquake based on building damage data,” *Earthquake Engineering and Structural Dynamics* **30**, 781-801.

YOSHIDA, N. & IAI, S. (1998). “Nonlinear site response and its evaluation and prediction,” *In:* Irikura, Kudo, Okada & Sasatani (eds) *The effects of Surface Geology on Seismic Motion.*

YOSHIKAWA, K., USUI, M. & KAJITANI, Y. (2001). “An application of spatial-temporal GIS for supporting the restoration activities of the Turkey large earthquakes,” 4pp. [in Japanese]. http://www.urban.meijo-u.ac.jp/zyoshika/zemi/gue/ch7/doboku_keikaku_gakkai2001/usui.pdf.

YOUD, T.L. & PERKINS, D.M. (1987). "Mapping of liquefaction severity index." *Journal of Geotechnical Engineering*, ASCE, **113** (11), 1374-1392.

ZARE, M., BARD, P.-Y. & GHAFORY-ASHTIANY, M. (1998). “Site characterisation for the Iranian strong motion network,” *Proceedings of the Eleventh European Conference on Earthquake Engineering,* Balkema, Rotterdam.

ZERVA, A. (2000). “Spatial variability of seismic motions recorded over extended ground surface areas,” *In:* E. Kausel & G.D. Manolis (ed.) *Wave Motion in Earthquake Engineering: Advances in Earthquake Engineering,* MIT Press, 97-139.

A1. Local magnitude, M_L

The local magnitude scale is more commonly known as the Richter magnitude scale. It was originally defined as (Richter, 1935):

$$M_L = \log_{10} A_{seis} - \log_{10} A_0 \tag{A1}$$

where: A_{seis} is the maximum trace amplitude (mm) on a Wood-Anderson seismograph,
A_0 is the amplitude that an earthquake of magnitude zero would produce at the same epicentral distance.

Zero magnitude was defined (arbitrarily) as the size of earthquake that would produce a maximum trace amplitude on a Wood-Anderson seismograph of 0.001 mm at a distance of 100 km. The Richter local magnitude was originally calibrated specifically for southern California and only for recordings made on a specific type of seismograph. Local magnitude scales have since been derived for other parts of the world and using other types of instrument.

A2. Surface-wave magnitude, M_s

Surface-wave magnitude is calculated from the maximum ratio of amplitude, A_g (μm) to period, T (s) of the ground motion caused by long period ($18 \leq T \leq 22$ s) Rayleigh waves and is therefore independent of the type of seismograph used. M_s is calculated using the 'Prague formula':

$$M_s = \log\left(\frac{A_g}{T}\right)_{\max} + 1.66\log\Delta + 3.3 \tag{A2}$$

where: Δ is the epicentral distance in geocentric degrees.

Recommended period ranges corresponding to maximum amplitudes of surface waves at different epicentral distances are given by IASPEI (1967). The surface-wave magnitude is most commonly used to describe the size of shallow (focal depth less than 70 km), distant (epicentral distances greater than 1000 km) moderate-to-large earthquakes.

A3. Body-wave magnitude, m_b

Like M_s, the body-wave magnitude is calculated from the amplitude of ground motion, independent of the recording instrument. m_b is based on the amplitude of the first few cycles of P-waves and is expressed as:

$$m_b = \log\left(\frac{A_g}{T}\right)_{\max} + Q(\Delta, h) \tag{A3}$$

where: A_g is the p-wave amplitude (μm),

T is the period of the p-wave (usually about 1 second),
Q is a function of epicentral distance, Δ and focal depth, h, defined from standard tables and curves.

Body-wave magnitude can also be estimated from the amplitude of one-second period higher-order Rayleigh (Lg) waves (Nuttli, 1973). The resulting magnitude scale, $m_{b,Lg}$ is often used to quantify intraplate earthquakes. In general, body-wave magnitude is less reliable than M_s for describing the size of shallow-focus earthquakes.

A4. Japanese Meteorological Agency magnitude, M_{JMA}

The M_{JMA} scale is based on the amplitude of long-period waves and is the scale most commonly used by Japanese agencies.

A5. Moment magnitude, M_w

The magnitude scales M_L, M_s, m_b and M_{JMA} are all subject to saturation for very large earthquakes. In other words, beyond a certain level, an increase in seismic energy release does not result in an increase in magnitude. This happens because each of these scales is based on the amplitude of waves in a limited period range. As the size of the earthquake source grows, the additional energy release results in waves of longer period rather than an increase in the amplitude of shorter period radiation. The only magnitude scale that is not subject to saturation is the moment magnitude, M_w as it is based on the seismic moment, M_0, which is a direct measure of the work done by the earthquake in rupturing the fault:

$$M_0 = \mu A \overline{D} \tag{A4}$$

where: μ is the rigidity of the crust (usually taken as 3.3×10^{10} N.m^{-2}),
A is the total area of the rupture surface,
$\overline{D}$ is the average displacement on the rupture surface (usually of the order of 10^{-4} of the rupture length for large earthquakes)

If the seismic moment is given in Nm (as expressed in Equation A4), the moment magnitude, M_w (sometimes designated, **M**) can be calculated from the following expression (Hanks & Kanamori, 1979):

$$M_w = \frac{2}{3}\log(M_0) - 6.1 \tag{A5}$$

The relationship between the various magnitude scales is illustrated in Figure A1 by plotting each scale against M_w. The saturation of the instrumental scales is indicated by their flattening at higher magnitudes. Bolt (1989) suggests that M_L or m_b be used for shallow earthquakes of magnitude in the range 3 to 7, M_s for earthquakes of magnitude 5 to 7.5, and M_w for earthquakes with magnitude greater than 7.5.

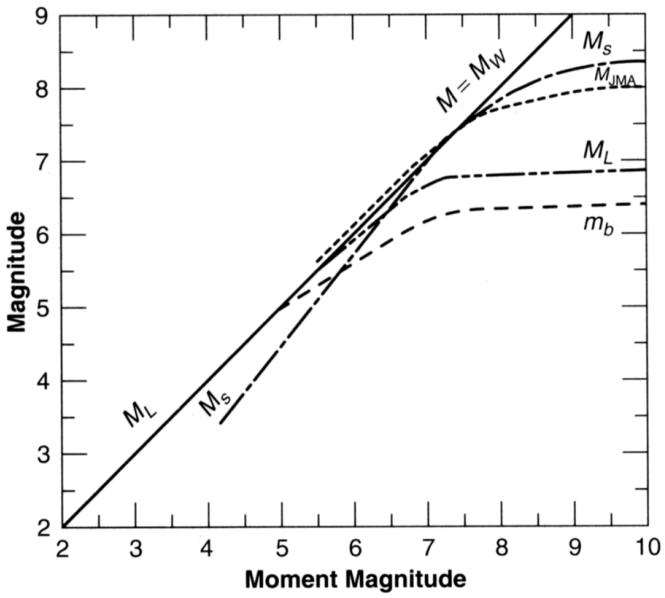

Figure A1 Comparison between moment magnitude and various other magnitude scales (Idriss, 1985). Definitions are given in the accompanying text.

APPENDIX B. MODIFIED MERCALLI INTENSITY (MMI) SCALE AND EFFECTS ON WATER SUPPLY SYSTEMS

Levels in the MMI scale (Reiter, 1990) are defined partially in terms of the effects (both direct and indirect) of an earthquake on water supply systems, as highlighted below:

I. Not felt-or, except rarely under especially favourable circumstances. Under certain conditions, at and outside the boundary of the area in which a great shock is felt: sometimes birds, animals, reported uneasy or disturbed; sometimes dizziness or nausea experienced; ***sometimes*** trees, structures, ***liquids, bodies of water, may sway***-doors may swing, very slowly.

II. Felt indoors by few, especially on upper floors, or by sensitive, or nervous persons. Also, as in grade I, but often more noticeably: sometimes hanging objects may swing, especially when delicately suspended; ***sometimes*** trees, structures, ***liquids, bodies of water, may sway***, doors may swing, very slowly; sometimes birds, animals, reported uneasy or disturbed; sometimes dizziness or nausea experienced.

III. Felt indoors by several, motion usually rapid vibration. Sometimes not recognised to be an earthquake at first. Duration estimated in some cases. Vibration like that due to passing of light, or lightly loaded trucks, or heavy trucks some distance away. Hanging objects may swing slightly. Movements may be appreciable on upper levels of tall structures. Rocked standing motor cars slightly.

IV. Felt indoors by many, outdoors by few. Awakened few, especially light sleepers. Frightened no one, unless apprehensive from previous experience. Vibration like that due to passing of heavy or heavily loaded trucks. Sensation like heavy body striking building or falling of heavy objects inside. Rattling of dishes, windows, doors; glassware and crockery clink and clash. Creaking of walls, frame, especially in the upper range of this grade. Hanging objects swung, in numerous instances. ***Disturbed liquids in open vessels slightly***. Rocked standing motor cars noticeably.

V. Felt indoors by practically all, outdoors by many or most: outdoors direction estimated. Awakened many, or most. Frightened few-slight excitement, a few ran outdoors. Buildings trembled throughout. Broke dishes, glassware, to some extent. Cracked windows-in some cases, but not generally. Overturned vases, small or unstable objects, in many instances, with occasional fall. Hanging objects, doors, swing generally or considerably. Knocked pictures against walls, or swung them out of place. Opened, or closed, doors, shutters, abruptly. Pendulum clocks stopped, started, or ran fast, or slow. Moved small objects, furnishings, the latter to slight extent. ***Spilled liquids in small amounts from well-filled open containers***. Trees, bushes, shaken slightly.

VI. Felt by all, indoors and outdoors. Frightened many, excitement general, some alarm, many ran outdoors. Awakened all. Persons made to move unsteadily. Trees, bushes, shaken slightly to moderately. ***Liquid set in strong motion.*** Small bells rang-church, chapel, school, etc. Damage slight in poorly built buildings. Fall of plaster in small amount. Cracked plaster somewhat, especially fine cracks, chimneys in some instances. Broke dishes, glassware, in considerable quantity, also some windows. Fall of knickknacks, books, pictures. Overturned furniture in many instances. Moved furnishings of moderately heavy kind.

VII. Frightened all-general alarm, all ran outdoors. Some, or many, found it difficult to stand. Noticed by persons driving motor cars. Trees and bushes shaken moderately to strongly. ***Waves on ponds, lakes, and running water. Water turbid from mud stirred up. In caving to some extent of sand or gravel stream banks.*** Rang large church bells, etc. Suspended objects made to quiver. Damage negligible in buildings of good design and

construction, slight to moderate in well-built ordinary buildings, considerable in poorly built or badly designed buildings, adobe houses, old walls (especially where laid up without mortar), spires, etc. Cracked chimneys to considerable extent, walls to some extent. Fall of plaster in considerable to large amount, also some stucco. Broke numerous windows, furniture to some extent. Shook down loosened brickwork and tiles. Broke weak chimneys at the roof-line (sometimes damaging roofs). Fall of cornices from towers and high buildings. Dislodged bricks and stones. Overturned heavy furniture, with damage from breaking. ***Damage considerable to concrete irrigation ditches.***

VIII. Fright general-alarm approaches panic. Disturbed persons driving motor cars. Trees shaken strongly-branches, trunks, broken off, especially palm trees. Ejected sand and mud in small amounts. ***Changes: temporary, permanent; in flow of springs and wells; dry wells renewed flow; in temperature of spring and well waters.*** Damage slight in structures (brick) built especially to withstand earthquakes. Considerable in ordinary substantial buildings, partial collapse: racked, tumbled down, wooden houses in some cases; threw out panel walls in frame structures, broke off decayed piling. Fall of walls. Cracked, broke, solid stone walls seriously. Wet ground to some extent, also ground on steep slopes. Twisting, fall, of chimneys, columns, monuments, also factory stacks, towers. Moved conspicuously, overturned, very heavy furniture.

IX. Panic general. Cracked ground conspicuously. Damage considerable in (masonry) structures built especially to withstand earthquakes: threw out of plumb some wood-frame houses built especially to withstand earthquakes; great in substantial (masonry) buildings, some collapse in large part; or wholly shifted frame buildings off foundations, racked frames; ***serious to reservoirs; underground pipes sometimes broken***.

X. Cracked ground, especially when loose and wet, up to widths of several inches; ***fissures up to a yard in width ran parallel to canal and stream banks. Landslides considerable from river banks and steep coasts.*** Shifted sand and mud horizontally on beaches and flat land. Changed level of water in wells. ***Threw water on banks of canals, lakes, rivers, etc. Damage serious to dams, dikes, embankments.*** Severe to well-built wooden structures and bridges, some destroyed. Developed dangerous cracks in excellent brick walls. Destroyed most masonry and frame structures, also their foundations. Bent railroad rails slightly. ***Tore apart, or crushed endwise, pipelines buried in earth.*** Open cracks and broad wavy folds in cement pavements and asphalt road surfaces.

XI. Disturbances in ground many and widespread, varying with ground material. Broad fissures, earth slumps, and land slips in soft wet ground. Ejected water in large amounts charged with sand and mud. Caused sea waves ("tidal" waves) of significant magnitude. Damage severe to wood frame structures, especially near shock centres. ***Great to dams, dikes, embankments often for long distances.*** Few, if any (masonry) structures remained standing. Destroyed large well-built bridges by the wrecking of supporting piers, or pillars. Affected yielding wooden bridges less. Bent railroad rails greatly, and thrust them endwise. ***Put pipelines buried in earth completely out of service.***

XII. Damage total-practically all works of construction damaged greatly or destroyed. Disturbances in ground great and varied, numerous shearing cracks. Landslides, falls of rock of significant character, slumping of riverbanks, etc., numerous and extensive. Wrenched loose, tore off, large rock masses. Fault slips in firm rock, with notable horizontal and vertical offset displacements. ***Water channels, surface and underground, disturbed and modified greatly. Dammed lakes, produced waterfalls, deflected rivers, etc.*** Waves seen on ground surfaces (actually seen, probably, in some cases). Distorted lines of sight and level. Threw objects upward into the air.

APPENDIX C. TYPES AND CHARACTERISTICS OF EARTHQUAKE-INDUCED LANDSLIDES

Table C1. Types and characteristics of earthquake-induced landslides (Keefer, 1984)

Name	Type of Movement	Internal Disruption[a]	Water content[b]				Velocity[c]	Depth[d]
			D	U	PS	S		
DISRUPTED SLIDES AND FALLS								
Rock falls	Bounding, rolling, free fall	High or very high	Y	Y	Y	Y	Extremely rapid	Shallow
Rock slides	Translational sliding on basal shear surface	High	Y	Y	Y	Y	Rapid to extremely rapid	Shallow
Rock avalanches	Complex, involving sliding and/or flow, as stream of rock fragments	Very high	Y	Y	Y	Y	Extremely rapid	
Soil falls	Bounding, rolling, free fall	High or very high	Y	Y	Y	Y	Extremely rapid	Shallow
Disrupted soil slides	Translational sliding on basal shear surface or zone of weakened, sensitive clay	High	Y	Y	Y	Y	Moderate to rapid	Shallow
Soil avalanches	Translational sliding with subsidiary flow	Very high	Y	Y	Y	Y	Very rapid to extremely rapid	Shallow
COHERENT SLIDES								
Rock slumps	Sliding on basal shear surface with component of headward rotation	Slight or moderate	?	Y	Y	Y	Slow to rapid	Deep
Rock block slides	Translational sliding on basal shear surface	Slight or moderate	?	Y	Y	Y	Slow to rapid	Deep
Soil slumps	Sliding on basal shear surface with component of headward rotation	Slight or moderate	?	Y	Y	Y	Slow to rapid	Deep
Soil block slides	Translational sliding on basal shear surface	Slight or moderate	?	?	Y	Y	Slow to rapid	Deep
Slow earth flows	Translational sliding on basal shear surface with minor internal flow	Slight	N	N	Y	Y	Very slow to moderate with very rapid surges	Generally shallow, occasionally deep
LATERAL SPREADS AND FLOWS								
Soil lateral spreads	Translation on basal zone of liquefied sand, silt or weakened, sensitive clay	Generally moderate, occasionally slight , occasionally high	N	N	Y	Y	Very rapid	Variable
Rapid soil flows	Flow	Very High	?	?	?	Y	Very rapid to extremely rapid	Shallow
Subaqueous landslides	Complex, generally involving lateral spreading and/or flow; occasionally involving slumping and/or block sliding	Generally high or very high, occasionally moderate or slight	N	N	Y	Y	Generally rapid to extremely rapid, occasionally slow to moderate	Variable

[a] Internal disruption: "slight" signifies landslide consists of one or a few coherent blocks
"moderate" signifies several coherent blocks
"high" signifies numerous small blocks and individual soil grains and rock fragments
"very high" signifies nearly complete disaggregation into individual soil grains or small rock fragments.

[b] Water content: D - dry; U - moist, but unsaturated; PS - partly saturated; S - saturated. Y - landslide possible in given ground conditions; ? – landslide occurrence not known but theoretically possible; N – not possible

[c] Velocity:

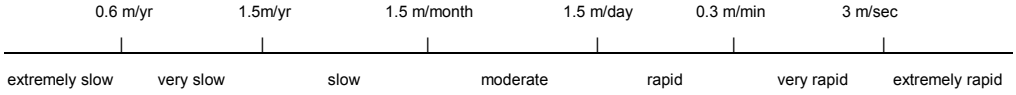

[d] Depth: "shallow" signifies thickness generally < 3 m; "deep" generally > 3 m.

Shading in the first column indicates relative abundance of each landslide phenomenon according to categories defined below (Keefer totalled the estimated numbers of each type of event over 40 earthquakes):

Classification	Estimated number of landslide occurrences, n over 40 earthquakes
Very abundant	100 000 < n
Abundant	10 000 < n < 100 000
Moderately common	1 000 < n < 10 000
Uncommon	100 < n < 1 000

Newmark (1967) and Newmark & Rosenbleuth (1971) derived simple expressions for relative motions of two points on or in the ground based on two assumptions:

1. Propagation of waves is in one direction without interference from other waves travelling in other directions, and
2. The change in shape of the wave between the two points is relatively small.

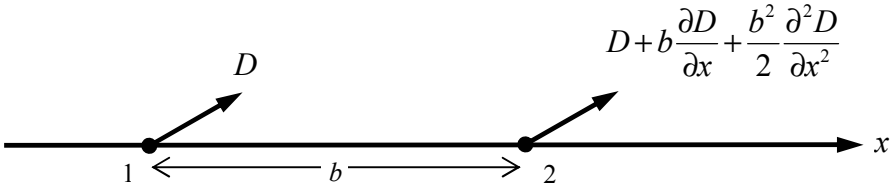

Figure D1 Relative displacements along a line

Consider two points, separated by a distance b (Figure D1). The displacement is D at point 1 and D plus an increment at point 2, as indicated. The second term of the increment, involving $\partial^2 D / \partial x^2$ is important only if b is relatively large. For a wave propagating from point 1 towards point 2, the displacement, D has the form

$$D(x,t) = f(x - ct) \tag{D1}$$

where c is the velocity of the travelling wave and t is the time. Derivatives of displacement with respect to x and t are given by

$$\frac{\partial D}{\partial x} = f'(x - ct) \tag{D2}$$

$$\frac{\partial^2 D}{\partial x^2} = f''(x - ct) \tag{D3}$$

$$\frac{\partial D}{\partial t} = -cf'(x - ct) \tag{D4}$$

$$\frac{\partial^2 D}{\partial t^2} = c^2 f''(x - ct) \tag{D5}$$

From Equations (D2) and (D4), the following result is obtained:

$$\frac{\partial D}{\partial x} = -\frac{1}{c}\frac{\partial D}{\partial t} \tag{D6}$$

In the case where D is parallel to x, Equation (D6) gives the peak ground strain (tension or compression) at point 1, ε_p as a function of the peak particle velocity parallel to the wave propagation, v_p:

$$\varepsilon_p = -\frac{v_p}{c} \tag{D7}$$

Combining Equations (D3) and (D5) gives the following result:

$$\frac{\partial^2 D}{\partial x^2} = \frac{1}{c^2}\frac{\partial^2 D}{\partial t^2} \tag{D8}$$

For the case of D perpendicular to x, either horizontally or vertically, Equation (D8) gives an expression for the maximum curvature at point 1, κ_p in terms of the maximum acceleration, a_p:

$$\kappa_p = \frac{a_p}{c^2} \tag{D9}$$

E1. McGuire (1974) (cited in Tsangaris & Chandler, 1998)

$$\log(PGD) = -0.460 + 0.434M - 0.885\log(d_h + 25) \quad \text{(E1)}$$

where: PGD is measured in cm.

No further details were available for this relationship, being obtained from a secondary source.

E2. Trifunac (1976), Trifunac & Brady (1976)

$$\log X = M + \log A_0(d_e) - \log\begin{Bmatrix} a_0(M,p,s,v) \\ v_0(M,p,s,v) \\ d_0(M,p,s,v) \end{Bmatrix} \quad \text{(E2)}$$

$$\log\begin{Bmatrix} a_0(M,p,s,v) \\ v_0(M,p,s,v) \\ d_0(M,p,s,v) \end{Bmatrix} = \begin{cases} C_1 p + C_2 M + C_3 + C_4 s + C_5 v + C_6 M^2 - f(M - M_{\max})^2 \ldots M \geq M_{\max} \\ C_1 p + C_2 M + C_3 + C_4 s + C_5 v + C_6 M^2 \ldots\ldots\ldots\ldots\ldots\ldots M_{\max} \geq M \geq M_{\min} \\ C_1 p + C_2 M_{\min} + C_3 + C_4 s + C_5 v + C_6 M_{\min}^2 \ldots\ldots\ldots\ldots\ldots M \leq M_{\min} \end{cases}$$

…… (E3)

where: X is the peak strong-motion parameter: PGA (cm/s^2), PGV (cm/s) or PGD (cm),
$\log A_0(d_e)$ is an empirical attenuation function from Richter (1958) for calculation of M_L (not given here due to lack of space),
p is the confidence level,
s is a site parameter, defined in Table E1,
v is an index for component direction (v=0 for horizontal; v=1 for vertical),
C_i are regression coefficients, given in Table E2 along with the magnitude range and number of data points (N_{Data}) used for each regression.

Table E1. Site parameters and distribution of records within dataset for Trifunac (1976)

s	Geological description	Proportion of total database
0	Alluvium or other low velocity 'soft' deposits	63%
1	'Intermediate' type rock	23%
2	Solid 'hard' basement rock	8%

Table E2. Coefficients for the predictive equations of Trifunac (1976)

X	C_1	C_2	C_3	C_4	C_5	C_6	N_{Data}	M_{min}	M_{max}
PGA	-0.898	-1.789	6.217	0.060	0.331	0.186	227	4.80	7.50
PGV	-1.087	-2.059	8.357	0.134	0.344	0.201	227	5.12	7.61
PGD	-1.288	-2.366	9.717	0.205	0.240	0.226	227	5.24	7.45

E3. McGuire (1978)

$$\ln(X) = C_1 + C_2 M + C_3 \ln(d_h) + C_4 Y_s \quad \text{(E4)}$$

where: X is the peak ground-motion parameter: PGA (cm/s^2), PGV (cm/s) or PGD(cm),
C_i are regression coefficients, given in Table E3 along with standard deviation values for both ln$x$ and log$x$ values,
Y_s is a site geology indicator, equal to 0 for 'rock' sites and 1 for 'soil' sites (here defined as being underlain by a minimum of 10m of alluvium or other soft material),

Table E3. Coefficients for the predictive equations of McGuire (1978)

X	C_1	C_2	C_3	C_4	σ_{lnX}	σ_{logX}
PGA	3.40	0.89	-1.17	-0.20	0.62	0.27
PGV	-1.00	1.07	-0.96	0.07	0.64	0.28
PGD	-2.72	1.00	-0.63	0.12	0.69	0.30

E4. Joyner & Boore (1981)

$$\log X = C_1 + C_2 M_w - \log r + C_3 r + C_4 S \quad \text{(E5)}$$

$$r = \left(d_f^2 + h_0^2\right)^{1/2} \quad \text{(E6)}$$

where: X is the peak ground-motion parameter: PGA (g) or PGV (cm/s),
S is a site geology indicator, equal to 0 for 'rock' sites and 1 for 'soil' sites. 'Rock' sites are those described as granite, diorite, gneiss, chert, greywacke, limestone, sandstone or siltstone and sites with soil material less than 4 to 5 m thick. Soil sites are those described as alluvium, sand, gravel, clay, silt, mud, fill or glacial outwash except where soil thickness is less than 4 to 5 m.
C_i and h_0 are regression coefficients, given in Table E4 along with standard deviation values.

Table E4. Coefficients for the predictive equations of Joyner & Boore (1981)

X	C_1	C_2	C_3	C_4	h_0	σ_{logX}
PGA	-1.02	0.249	-0.00255	0	7.3	0.26
PGV	-0.67	0.489	-0.00256	0.17	4.0	0.22

E5. Kawashima *et al.* (1986)

$$\log X = \log C_1 + C_2 M_{JMA} + C_3 \log(d_e + 30) \quad \text{(E7)}$$

where: X is the peak ground-motion parameter: PGA (gals), PGV (cm/s) or PGD (cm),
C_i are regression coefficients, given in Table E5 along with $\sigma_{\log X}$ values for each strong-motion parameter and each of 3 soil classes,
The three distinct site classifications are summarised in Table E6.

Table E5. Coefficients for the predictive equations of Kawashima *et al.* (1986)

X	C_3	Group 1			Group 2			Group 3		
		C_1	C_2	σ_{logX}	C_1	C_2	σ_{logX}	C_1	C_2	σ_{logX}
PGA	-1.218	987.4	0.216	0.216	232.5	0.313	0.224	403.8	0.265	0.197
PGV	-1.222	20.8	0.263	0.236	2.81	0.430	0.239	5.11	0.404	0.243
PGD	-1.254	0.626	0.372	0.262	0.062	0.567	0.258	0.070	0.584	0.262

Table E6. Classifications of site conditions for the predictive equations of Kawashima *et al.* (1986)

Category	Geological definition	Definition by natural period
Group 1	Tertiary or older rock or diluvium less than 10m thick	Period less than 0.2s
Group 2	Diluvium with thickness 10m or more or alluvium less than 25m thick including soft layer less than 5m thick	Period between 0.2 and 0.6s
Group 3	Other than the above, usually soft alluvium or reclaimed land	Period more than 0.6s

E6. Sabetta & Pugliese (1987)

$$\log X = C_1 + C_2 M - \log(d_f{}^2 + h_0{}^2)^{½} + C_3 S \qquad \text{(E8)}$$

where: X is the peak strong-motion parameter: PGA (g) or PGV (cm/s),
C_i and h_0 are regression coefficients, summarised in Table E7 along with sigma values,
S is a site geology indicator, as defined in Table E8,

Table E7. Coefficients for the predictive equations of Sabetta & Pugliese (1987)

X	C_1	C_2	h_0	C_3	σ_{lnX}
PGA	-1.562	0.306	5.8	0.169	0.173
PGV	-0.710	0.455	3.6	0.133	0.215

Table E8. Classifications of site conditions for the predictive equations of Sabetta & Pugliese (1987)

Category	Geological description	S for A	S for V
Stiff soil	classifications such as "limestone", "sandstone", "siltstone", "marl", "shale", "conglomerates" average shear wave velocity > 800m/s	0	0
Shallow soil	classifications such as "alluvium", "sand", "gravel", "clay", "silt" average shear wave velocity between 400 and 800m/s soil layer between 5 and 20m thick	1	1
Deep soil	classifications such as "alluvium", "sand", "gravel", "clay", "silt" average shear wave velocity between 400 and 800m/s soil layer > 20m thick	0	1

E7. Kamiyama *et al.* (1992)

$$X = C_1 \times 10^{C_2 M} \times AMP_i \qquad \text{for } d_h \le 10^{0.014+0.218M} \qquad \text{(E9)}$$

$$X = C_3 \times 10^{C_4 M - 1.64 \log_{10} d_h} \times AMP_i \qquad \text{for } d_h > 10^{0.014+0.218M} \qquad \text{(E10)}$$

where: X is the peak ground-motion parameter: PGA (cm/s^2), PGV (cm/s) or PGD (cm),
C_i are regression coefficients, as given in Table E9.

AMP_i is the amplification factor at the i-th site. The factor is defined individually for each of the 33 sites used in the regression and is different for each peak ground-motion parameter (see table E9). AMP_i(PGA), AMP_i(PGV), AMP_i(PGD) are equal to 1 for rock sites. Since the focus of their investigation is on PGV, Kamiyama *et al.* (1992) derive a more general expression for the amplification factor for PGV (equation E11), where C_{amp} is a function of N-values throughout the soil profile (see Kamiyama *et al.,*1992 for details). Standard deviations for the equations are not stated.

$$AMP_i(PGV) = 1.25 + 0.112C_{amp} \tag{E11}$$

Table E9. Coefficients for the predictive equations of Kamiyama *et al.* (1992)

X	C_1	C_2	C_3	C_4	AMP_i
PGA	518.9	0	547.6	0.358	AMP_i(PGA)
PGV	2.879	0.153	3.036	0.511	AMP_i(PGV)
PGD	0.189	0.236	0.200	0.594	AMP_i(PGD)

E8. Theodulidis & Papazachos (1992)

$$\ln X = C_1 + C_2 M_s - C_3 \ln(d_e + 15) + C_4 S \tag{E12}$$

where: X is the peak ground-motion parameter: PGA (cm/s^2), PGV (cm/s); or PGD (cm),
C_i are coefficients, as given in Table E10, along with standard deviations (for ln$X$ and log$X$),
S is a site geology indicator, equal to 1 at 'alluvium' sites and 0 at 'rock' sites. Classification was by expert opinion due to the lack of detailed geological data.

Table E10. Coefficients for the predictive equations of Theodulidis & Papazachos (1992)

X	C_1	C_2	C_3	C_4	σ_{lnX}	σ_{logX}
PGA	3.88	1.12	1.65	0.41	0.71	0.31
PGV	-0.79	1.41	1.62	-0.22	0.80	0.35
PGD	-5.92	2.08	1.85	-0.97	1.23	0.53

E9. Gregor & Bolt (1997)

$$\log_{10}(PGD) = C_1 + C_2 M_w + C_3 \log_{10}(d_s) \tag{E13}$$

where: PGD (cm) is associated with the S-wave arrival, as distinguished from the peak displacement value measured from the later-arriving surface waves.
C_i are coefficients which are given in Table E11, with corresponding standard errors. The regression was performed separately for data from different earthquake mechanisms, components and site conditions, as shown. SH refers to the horizontal component of motion resolved perpendicularly to a line connecting the site to the location of largest slip on the fault plane. SV refers to the vertical component of motion.
Because different curves were based on different datasets, they are valid for different magnitude and distance ranges as detailed in Table E12.

Table E11. Coefficients for the predictive equations of Gregor & Bolt (1997).

Name	Mechanism	Component	Site condition	C_1	C_2	C_3	σ_{logPGD}
SSHR	Strike-slip	SH	Rock	-13.46 ± 1.48	5.99 ± 0.62	-0.99 ± 0.18	0.37
SSVR	Strike-slip	SV	Rock	-13.50 ± 1.17	6.03 ± 0.49	-1.22 ± 0.15	0.29
SSHS	Strike-slip	SH	Soil	-11.71 ± 0.77	5.56 ± 0.32	-1.22 ± 0.10	0.30
SSVS	Strike-slip	SV	Soil	-11.79 ± 0.63	5.41 ± 0.26	-1.23 ± 0.08	0.24
RSHR	Reverse	SH	Rock	-9.16 ± 1.59	4.59 ± 0.65	-1.51 ± 0.25	0.32
RSVR	Reverse	SV	Rock	-9.98 ± 1.23	4.77 ± 0.50	-1.50 ± 0.19	0.25
RSHS	Reverse	SH	Soil	-9.01 ± 0.91	4.58 ± 0.38	-1.53 ± 0.11	0.27
RSVS	Reverse	SV	Soil	-11.41 ± 0.90	5.26 ± 0.38	-1.31 ± 0.11	0.26

Table E12. Applicability ranges for the attenuation relationships of Gregor & Bolt (1997)

Name	M range	d range (km)
SSHR	5.4 – 7.2	8 - 224
SSVR	5.4 – 7.2	8 - 224
SSHS	5.4 – 7.2	6 - 190
SSVS	5.4 – 7.2	6 - 190
RSHR	5.6 – 6.7	9 - 93
RSVR	5.6 – 6.7	9 - 93
RSHS	5.6 – 6.7	15 - 180
RSVS	5.6 - 6.7	15 - 180

E10. Campbell (1997)

$$\begin{aligned}\ln PGA &= -3.512 + 0.904M - 1.328\ln\sqrt{d_{seis}^2 + [0.149\exp(0.647M)]^2} \\ &+ [1.125 - 0.112\ln d_{seis} - 0.0957M]F + [0.440 - 0.171\ln d_{seis}]S_{SR} \\ &+ [0.405 - 0.222\ln d_{seis}]S_{HR}\end{aligned} \tag{E14}$$

$$\begin{aligned}\ln PGV &= \ln A_H + 0.26 + 0.29M - 1.44\ln[d_{seis} + 0.0203\exp(0.958M)] \\ &+ 1.89\ln[d_{seis} + 0.361\exp(0.576M)] + (0.0001 - 0.000565M)d_{seis} - 0.12F \\ &- 0.15S_{SR} - 0.30S_{SR} + 0.75\tanh(0.51D)(1 - S_{HR}) + f_V(D)\end{aligned} \tag{E15}$$

$$f_v(D) = \begin{cases} 0 & D \geq 1 \\ -0.30(1 - S_{HR})(1 - D) - 0.15(1 - D)S_{SR} & D < 1 \end{cases} \tag{E16}$$

where: PGA is measured in g and PGV is measured in cm/s,
F is an index to distinguish between different styles of faulting. F = 0 for strike-slip faulting and F = 1 for reverse, thrust, reverse-oblique and thrust-oblique faulting.
S_{HR} and S_{SR} are site geology indicators, as indicated in Table E13.
D is the depth to basement rock (km).
Standard deviation values for equations E14 and E15 are given in Table E14. Figures in brackets are standard deviations using $\log_{10}$ rather than ln.
See Campbell (1997) for expressions for vertical components of motion.

Table E13. Classifications of site conditions for the predictive equations of Campbell (1997)

Category	Geological description	S_{SR}	S_{HR}
alluvium or firm soil	firm or stiff Quaternary deposits with depths greater than 10m	0	0
soft rock	primarily Tertiary sedimentary deposits and soft volcanic deposits	1	0
hard rock	primarily Cretaceous and older sedimentary deposits, metamorphic rock, crystalline rock and hard volcanic deposits	0	1

Table E14. Standard deviation for the equations of Campbell (1997)

	PGA < 0.068g	0.068g ≤ PGA ≤ 0.21g	0.21g < PGA
$\sigma_{\ln PGA}$	0.55 (0.24)	0.173-0.140lnPGA	0.39 (0.17)
$\sigma_{\ln PGV}$	0.55 (0.24)	$\sqrt{\sigma_{\ln PGV}^2 + 0.06^2}$	0.39 (0.17)

E11. Rinaldis *et al.* (1998)

$$\ln X = C_1 + C_2 M + C_3 \ln(d_e + 15) + C_4 S + C_5 F \qquad \text{(E17)}$$

where: X is the peak ground-motion parameter: PGA (cm/s^2) or PGV (cm/s),
C_i are regression coefficients, as given in Table E15, along with standard deviation values for both ln$X$ and log$X$,
S is a site geology indicator. S = 0 for 'rock' sites (including 'stiff soil' sites) and S = 1 for 'alluvium' sites (including both 'shallow' and 'deep' soil sites),
F is a fault-type indicator. F = 0 for thrust and strike-slip faulting and F = 1 for normal faulting.

Table E15. Coefficients for the predictive equations of Rinaldis *et al.* (1998)

X	C_1	C_2	C_3	C_4	C_5	σ_{lnX}	σ_{logX}
PGA	5.57	0.82	-1.59	-0.14	-0.18	0.68	0.30
PGV	-0.97	1.34	-1.54	0.16	0.08	0.77	0.33

E12. Sadigh & Egan (1998)

$$\ln X = C_1 + C_2 M + C_3 (8.5 - M)^{C_4} + C_5 \ln\left(d_r + \exp\left(C_6 + C_7 M\right)\right) \qquad \text{(E18)}$$

where: X is the peak ground-motion parameter: PGA (g), PGV (cm/s), PGD (cm),
C_i are coefficients of regression, summarised in Table E16,
No standard deviation values are given,
'Rock' sites are sites with bedrock within about 1 m of the surface. Many such sites are soft rock with $v_s \leq$ 750m/s and a strong velocity gradient because of near-surface weathering and fracturing. 'Deep soil' sites are sites with greater than 20 m of soil over bedrock. Data from very soft sites, such as those on San Francisco Bay Mud, were excluded from the analysis.

Table E16. Coefficients for the predictive equations of Sadigh & Egan *et al.* (1998)

X	Fault Mechanism	Site class	*M range*	C_1	C_2	C_3	C_4	C_5	C_6	C_7
PGA	strike-slip	rock	≥ 6.5	-1.274	1.100	0	-	-2.100	-0.48451	0.524
			< 6.5	-0.949	1.050	0	-	-2.100	1.29649	0.250
PGA	reverse-slip	rock	≥ 6.5	-1.024	1.100	0	-	-2.100	-0.48451	0.524
			< 6.5	0.276	0.900	0	-	-2.100	1.29649	0.250
PGA	strike-slip	soil	≥ 6.5	-1.383	0.917	0	-	-1.75	-0.48451	0.524
			< 6.5	-1.110	0.875	0	-	-1.75	1.29649	0.250
PGA	reverse-slip	soil	≥ 6.5	-1.175	0.917	0	-	-1.75	-0.48451	0.524
			< 6.5	-0.0895	0.750	0	-	-1.75	1.29649	0.250
PGV	strike-slip	rock	≥ 6.5	2.4418	1.10	-0.114	1.85	-1.85	-0.48451	0.524
			< 6.5	2.7668	1.05	-0.114	1.85	-1.85	1.29649	0.250
PGV	reverse-slip	rock	≥ 6.5	2.5918	1.10	-0.114	1.85	-1.85	-0.48451	0.524
			< 6.5	4.3143	0.835	-0.114	1.85	-1.85	1.29649	0.250
PGV	strike-slip	soil	≥ 6.5	3.1934	0.917	-0.114	1.85	-1.65	-0.48451	0.524
			< 6.5	3.4664	0.875	-0.114	1.85	-1.65	1.29649	0.250
PGV	reverse-slip	soil	≥ 6.5	3.3134	0.917	-0.114	1.85	-1.65	-0.48451	0.524
			< 6.5	4.7499	0.696	-0.114	1.85	-1.65	1.29649	0.250
PGD	strike-slip	rock	≥ 6.5	0.8773	1.10	-0.310	1.75	-1.60	-0.48451	0.524
			< 6.5	1.2023	1.05	-0.310	1.75	-1.60	1.29649	0.250
PGD	reverse-slip	rock	≥ 6.5	0.7273	1.10	-0.310	1.75	-1.60	-0.48451	0.524
			< 6.5	2.7618	0.787	-0.310	1.75	-1.60	1.29649	0.250
PGD	strike-slip	soil	≥ 6.5	2.4887	0.917	-0.310	1.75	-1.55	-0.48451	0.524
			< 6.5	2.7617	0.875	-0.310	1.75	-1.55	1.29649	0.250
PGD	reverse-slip	soil	≥ 6.5	2.3387	0.917	-0.310	1.75	-1.55	-0.48451	0.524
			< 6.5	4.0352	0.656	-0.310	1.75	-1.55	1.29649	0.250

Table F1 Characteristics of supplementary records

Event No.	Earthquake Name	Date dd-mm-yyyy	Time (UTC) hh:mm:ss	M_s	Epicentral Coordinates N	Epicentral Coordinates E	Focal depth (km)	Record ID	Station name	Instrument Type	Site Class	Station Coordinates N	Station Coordinates E	Epicentral distance (km)	Fault distance (km)
44	Grevena, Greece	13-V-1995	8:47:13	6.6	40.1673	21.686	14	181	Kozani Prefecture	SMA1	R	40.3	21.79	17	9
45	Dinar, Turkey	1-X-1995	15:57:13	6.1	38.0561	30.152	5	182	Dinar Meteoroloji Mudurlugu	SMA-1	S	38.06	30.155	1	1
								183	Denizli Bayandirlik ve Iskan Mudurlugu	*GSR-16*	A	37.813	29.114	95	87
46	Umbria (a), Italy	26-IX-1997	0:33:16	5.5	43.023	12.892	7	184	Colfiorito	SMA1	A	43.037	12.921	3	3
								185	Nocera Umbra	SMA1	R	43.113	12.785	13	13
								186	Bevagna	SMA1	A	42.932	12.611	25	25
								187	Castelnuovo-Assisi	SMA1	S	43.007	12.591	24	24
								188	Forca Canapine	SMA1	R	42.761	13.21	39	33
								189	Borgo-Cerreto Torre	*D*	R	42.814	12.915	23	17
47	Umbria (b), Italy	26-IX-1997	9:40:30	5.9	43.031	12.862	6	190	Colfiorito	SMA1	A	43.037	12.921	5	3
								191	Nocera Umbra	SMA1	R	43.113	12.785	11	4
								192	Bevagna	SMA1	A	42.932	12.611	23	26
								193	Castelnuovo-Assisi	SMA1	S	43.007	12.591	22	23
								194	Matelica	SMA1	A	43.249	13.007	27	21
								195	Gubbio	SMA1	R	43.357	12.602	42	34
								196	Gubbio-Piana	*D*	R	43.313	12.589	38	30
								197	Peglio	SMA1	R	43.695	12.498	79	71
								198	Borgo-Cerreto Torre	*D*	R	42.814	12.915	24	23
48	Adana, Turkey	27-VI-1998	13:55:53	6.2	36.883	35.55	32	199	Ceyhan Tarim Ilce Mudurlugu	SMA1	S	37.05	35.81	30	4
								200	Mersin Meteoroloji Mudurlugu	SMA1	A	36.83	34.65	80	71
								201	Kahramanmaras Bayindirlik Mudurlugu	*SMACH SM2*	A	37.583	36.9	142	118
49	Kocaeli, Turkey	17-VIII-1999	0:01:39	7.8	40.702	29.987	17	202	Aydin-Hayvan Hastanesi	*GSR-16*	S	37.837	27.838	368	359
								203	Balikesir-Bayindirlik ve Iskan Mudurlugu	*GSR-16*	A	39.65	27.883	213	199
								204	Bursa-Sivil Savunma Mudurluga	*GSR-16*	A	40.183	29.131	92	79
								205	Istanbul-Bayindirlik ve Iskan Mudurlugu	*GSR-16*	A	41.08	29.09	86	71
								206	Kutahya-Sivil Savunma Mudurlugu	*GSR-16*	S	39.419	29.997	142	140
								207	Denizli-Bayindirlik ve Iskan Mudurlugu	*GSR-16*	A	37.813	29.114	329	323
								208	Duzce-Meteoroloji Mudurlugu	SMA-1	S	40.85	31.17	101	14
								209	Gebze-Tubitak Marmara Arastirma Merkezi	SMA-1	A	40.82	29.44	48	32
								210	Goynuk-Devlet Hastanesi	SMA-1	A	40.381	30.734	72	31
								211	Iznik-Karayollari Sefligi Muracaati	SMA-1	S	40.437	29.691	39	29
								212	Izmit-Meteoroloji Istasyonu	SMA-1	R	40.79	29.96	10	8
								213	Sakarya-Bayindirlik ve Iskan Mudurlugu	*GSR-16*	A	40.737	30.384	34	3
								214	Arcelik	*GSR-16*	A	40.824	29.361	54	38
								215	Ambarli-Termik Santrali	*GSR-16*	S	40.981	28.693	113	97
								216	Botas-Gas Terminal	*GSR-16*	A	40.992	27.98	172	156
								217	Bursa-Tofa Fabrikasi	*GSR-16*	S	40.173	29.097	95	78
								218	Kucuk-Cekmece	*GSR-16*	A	41.024	28.759	109	94
								219	Yesilkoy-Havaalani	*GSR-16*	A	40.982	28.82	103	87
								220	Fatih	*GSR-16*	S	41.02	28.95	94	79
								221	Yapi-Kredi Plaza Levent	*GSR-16*	R	41.081	29.011	92	77
								222	Yarimca-Petkim	*GSR-16*	S	40.764	29.762	20	5

Table F1 (cont.)

Event No.	Earthquake Name	Date dd-mm-yyyy	Time (UTC) hh:mm:ss	M_s	Epicentral Coordinates N	Epicentral Coordinates E	Focal depth (km)	Record ID	Station name	Instrument Type	Site Class	Station Coordinates N	Station Coordinates E	Epicentral distance (km)	Fault distance (km)
50	Athens, Greece	7-IX-1999	11:56:51	5.9	38.08	23.58	17	223	N.PSIHIKO	*A800*	A	38	23.77	19	8
								224	Demokritos (Ag. Paraskevi)	*A800*	R	37.99	23.82	23	13
								225	Syngrou-FIX	*A800*	R	37.96	23.73	19	9
								226	Kypseli - ITSAK GYS SMA-1 4123	SMA1	R	37.97	23.703	16	8
								227	ITSAK CHALANDRI SMA-1 4117	SMA1	A	38.017	23.787	19	9
								228	ITSAK KEDESMA-1 4115	SMA1	R	37.969	23.702	16	8
								229	Papagos	*A800*	A	38	23.79	20	10
								230	Syntagma A	*A800*	R	37.98	23.74	18	8
								231	Syntagma B	*A800*	R	37.98	23.74	18	8
								232	Sepolia A	*A800*	S	38	23.71	14	5
								233	Sepolia B	*A800*	S	38	23.71	14	5
51	Duzce, Turkey	1999-XI-12	16:57:20	7.3	40.768	31.148	14	234	Arcelik	*GSR-16*	A	40.824	29.361	150	132
								235	Ambarli-Termik Santrali	*GSR-16*	S	40.981	28.693	207	189
								236	Botas-Gas Terminal	*GSR-16*	A	40.992	27.98	267	249
								237	Bursa-Tofa Fabrikasi	*GSR-16*	S	40.261	29.068	184	170
								238	Kucuk-Cekmece	*GSR-16*	A	41.024	28.759	202	184
								239	Yesilkoy-Havaalani	*GSR-16*	A	40.982	28.82	197	178
								240	Fatih	*GSR-16*	S	41.02	28.95	187	168
								241	Yapi-Kredi Plaza Levent	*GSR-16*	R	41.081	29.011	183	164
								242	Yarimca-Petkim	*GSR-16*	S	40.764	29.762	117	99
								243	Balikesir-Bayindirlik ve Iskan Mudurlugu	*GSR-16*	A	39.65	27.883	303	291
								244	Bolu-Bayindirlik ve Iskan Mudurlugu	*GSR-16*	A	40.747	31.61	39	18
								245	Bursa-Sivil Savunma Mudurluga	*GSR-16*	A	40.183	29.131	182	169
								246	Istanbul-Bayindirlik ve Iskan Mudurlugu	*GSR-16*	A	41.08	29.09	176	157
								247	Kutahya-Sivil Savunma Mudurlugu	*GSR-16*	S	39.419	29.997	179	171
								248	Sakarya-Bayindirlik ve Iskan Mudurlugu	*GSR-16*	A	40.737	30.384	64	47
								249	Duzce-Meteoroloji Mudurlugu	SMA1	S	40.85	31.17	9	1

Notes:

- **Station Coordinates** are given to the same number of decimal places as the source data - which varies from source to source and from station to station
- **Instrument type**: digital instruments are indicated by italics. "*D*" refers to a digital instrument but of unknown type

Table F2 Summary of data sources used for supplementary records

Event No.	Earthquake Name	M_s, time	Epicentre and focal depth	Fault plane projection	Strong-motion data	Station coordinates	Site classification
44	Grevena, Greece	ISC, Nikolaos & Vassilios (1996)	ISC	Nikolaos & Vassilios (1996)	ITSAK	Nikolaos & Vassilios (1996)	Nikolaos & Vassilios (1996)
45	Dinar, Turkey	ISC, Durukal et al (1998)	ISC	ISESD	ISESD, Durukal (2000), KOERI	ISESD	ISESD
46	Umbria (a), Italy	ISESD	ISESD, Amato et al. (1998)	ISESD, Amato et al. (1998)	ISESD	ISESD	ISESD
47	Umbria (b), Italy	ISESD	ISESD, Amato et al. (1998)	ISESD, Amato et al. (1998)	ISESD	ISESD	ISESD
48	Adana, Turkey	ISESD	ISESD	Aktar et al. (2000)	ISESD, ITSAK	ISESD	Unpublished data, Imperial College
49	Kocaeli, Turkey	ISESD, ISC, MCEER (2000)	ISESD, Erdik (2000)	Awata et al. (2000), USGS (2000)	ISESD	ISESD, IISEE	ISESD, Idriss et al (2000), Bakir (2000)
50	Athens, Greece	ISESD	ISESD, P et al. (2000)	T & Z (2000)	ISESD, ITSAK	ISESD, P et al. (2000)	P et al. (2000), Psycharis et al (1999)
51	Duzce, Turkey	ISESD	ISESD	ISESD, Arpat et al. (1999)	ISESD	ISESD, IISEE	ISESD, Idriss et al (2000)

Notes:

ISESD	Internet Site for European Strong-Motion Data (Ambraseys *et al.* , 2002)
IISEE	International Institute for Seismology and Earthquake Engineering earthquake report web site [http://iisee.kenken.go.jp/quakes/kocaeli/index.htm]
ISC	International Seismological Centre, Thatcham, UK [http://www.isc.ac.uk/]
ITSAK	Institute of Engineering Seismology and Earthquake Engineering (Thessaloniki, Greece)
KOERI	Kandilli Observatory and Earthquake Research Institute ftp site [ftp://ftp.boun.edu.tr/kandilli/dinar_eq/]
P et al. (2000)	Papadopoulos et al. (2000)
T & Z (2000)	Tselentis & Zahradnik (2000)

APPENDIX G: INPUT FILE FOR REGRESSION ANALYSIS OF EUROPEAN STRONG-MOTION DATA

```
 1    1969      2      28   024033     30        7.9
        1    A    LSB            331    260      26.97      2.97      0.58 PGL      LISBON        az02   L: 0.500  T: 0.400

 2    1973     11       4   155212      7        5.7
        2    S    LEF1            15     11     516.71     57.39     11.62 GRE      LEFKAS 1&2    gr17   L: 0.200  T: 0.200

 3    1976      5       6   200013      6        6.5
        3    R    TLM1            27      6     347.15     32.49      3.00 ITA      TOLMEZZO1     fr11   L: 0.333  T: 0.333
        4    A    CDR             47     26      85.71      6.86      1.22 ITA      CODROIPO      fri5   L: 0.500  T: 0.400
        5    S    BRC             61     40      30.30      1.54      0.23 ITA      BARCIS        fri3   L: 0.364  T: 0.500
        6    A    CON             92     69      72.96      4.19      0.55 ITA      CONEGLIANO    fri6   L: 0.500  T: 0.500
        7    A    COR             95     74      15.89      1.99      0.32 ITA      CORTINA       fri7   L: 0.500  T: 0.500
        8    R    FEL            113     91      40.70      1.65      0.26 ITA      FELTRE        fri8   L: 0.500  T: 0.500
        9    A    LJU2            96     92      20.10      1.11      0.13 YUG      LJUBLJANA2    fr82   L: 0.500  T: 0.500
       10    R    LJU1            96     92      36.87      1.73      0.15 YUG      LJUBLJANA1    fr81   L: 0.500  T: 0.500
       11    A    CAS            130    107      26.87      2.47      0.55 ITA      CASTELFRAN    fri4   L: 0.400  T: 0.667
       12    R    ASI            151    128      28.93      2.45      0.30 ITA      ASIAGO        fri2   L: 0.400  T: 0.400
       13    S    MON            171    148      19.12      1.15      0.09 ITA      MONSELICE     fr10   L: 0.800  T: 0.800
       14    R    TRE            190    167      29.52      1.61      0.15 ITA      TREGNAGO      fr12   L: 0.500  T: 0.500
       15    A    MAL            199    177      33.44      1.62      0.17 ITA      MALCESINE     fri9   L: 0.667  T: 0.667

 4    1976      5      17   025841     13        7.1
       16    L    KAR             19      3     651.55     45.74      8.44 USR      GAZLI         gaz1   L: 0.400  T: 0.500

 5    1976      9      11   163110      6        5.5
       17    S    BUI             14             44.62      3.38      0.32 ITA      BUIA          f106   L: 0.333  T: 0.333
       18    A    BRE             16     15     168.38      4.65      0.34 YUG      BREGINJ       fr84   L: 0.500  T: 0.400
       19    A    SRC             20             66.59      2.06      0.10 ITA      S. ROCCO      f103   L: 1.667  T: 1.250
       20    A    FRC             20            104.34      4.06      0.18 ITA      FORGARIA      f102   L: 0.667  T: 0.667
       21    A    KOB             27     27      92.87      3.90      0.32 YUG      KOBARID       fr83   L: 0.400  T: 0.400

 6    1976      9      11   163503     16        5.5
       22    S    BUI             11      7     223.59     21.67      2.36 ITA      BUIA          f113   L: 0.200  T: 0.200
       23    A    SRC             16     16      90.02      4.67      0.29 ITA      S. ROCCO      f110   L: 0.667  T: 0.667
       24    A    FRC             16     16     229.57     11.85      0.78 ITA      FORGARIA      it45   L: 0.308  T: 0.333
       25    A    KOB             31     31      96.01      3.47      0.23 YUG      KOBARID       fr85   L: 0.500  T: 0.500
       26    S    BRC             50     48      13.93      0.48      0.05 ITA      BARCIS        f107   L: 0.500  T: 0.800
       27    A    CON             82             12.45      1.08      0.17 ITA      CONEGLIANO    f108   L: 0.333  T: 0.333
       28    R    TRE            180              7.75      0.48      0.09 ITA      TREGNAGO      f111   L: 0.333  T: 0.500

 7    1976      9      15   031519     15        6.1
       29    S    BUI             11      9     105.81     10.93      2.51 ITA      BUIA          f122   L: 0.200  T: 0.200
       30    A    SRC             17     12     120.23      7.71      2.15 ITA      S. ROCCO      f120   L: 0.250  T: 0.250
       31    A    FRC             17     12     255.27     10.05      1.90 ITA      FORGARIA      it47   L: 0.200  T: 0.222
       32    A    BRE             18     14     494.55     27.10      2.27 YUG      BREGINJ       fr86   L: 0.250  T: 0.308
       33    R    ROB             24     19     101.79      2.59      0.45 YUG      ROBIC         fr88   L: 0.333  T: 0.333
       34    A    KOB             30     25     118.07      6.90      0.76 YUG      KOBARID       fr87   L: 0.333  T: 0.333
       35    A    CDR             40     35      27.85      2.38      0.48 ITA      CODROIPO      f117   L: 0.667  T: 0.500
       36    A    CON             82     77      20.10      0.76      0.12 ITA      CONEGLIANO    f118   L: 0.500  T: 0.500
       37    R    TRE            180    175       9.71      0.38      0.04 ITA      TREGNAGO      f121   L: 0.400  T: 0.500
       38    A    GEM              6      6     662.93     71.15     13.36 ITA      GEMONA        gem1   L: 0.200  T: 0.250

 8    1976      9      15   092119     12          6
       39    R    TRC             11      6     126.70      6.77      1.15 ITA      TARCENTO      f135   L: 0.200  T: 0.200
       40    A    BRE             22      7     406.29     11.97      0.95 YUG      BREGINJ       fr91   L: 0.250  T: 0.267
       41    S    BUI             12      8      88.85      7.99      2.00 ITA      BUIA          f137   L: 0.200  T: 0.222
       42    A    SRC             16      9     235.36     17.98      2.79 ITA      S. ROCCO      f133   L: 0.250  T: 0.250
       43    A    FRC             17      9     339.41     23.15      3.75 ITA      FORGARIA      f132   L: 0.200  T: 0.200
       44    R    ROB             28     12      83.85      2.74      0.25 YUG      ROBIC         fr92   L: 0.400  T: 0.400
       45    A    KOB             34     19     135.63      8.03      0.64 YUG      KOBARID       fr90   L: 0.333  T: 0.400
       46    S    BRC             49     35      25.69      1.39      0.17 ITA      BARCIS        f127   L: 0.400  T: 0.444
       47    A    CDR             42     38      42.95      2.66      0.39 ITA      CODROIPO      f128   L: 0.500  T: 0.500
       48    A    CON             82     70      27.26      2.14      0.21 ITA      CONEGLIANO    f129   L: 0.444  T: 0.500
       49    A    COR             83     70      11.67      1.24      0.21 ITA      CORTINA       f130   L: 0.500  T: 0.500
       50    R    FEL            101     88      21.57      0.40      0.03 ITA      FELTRE        f131   L: 0.667  T: 0.800
       51    R    TRE            179    167      21.08      0.58      0.08 ITA      TREGNAGO      f136   L: 0.667  T: 0.500
       52    A    MAL            187    173      25.10      0.85      0.07 ITA      MALCESINE     f134   L: 0.500  T: 0.667

 9    1976     11      24   122216     10        7.3
       53    R    MAK             50     44      96.20      6.17      0.74 IRA      MAKU          maku   L: 0.286  T: 0.333

10    1977      4       6   133637     10          6
       54    A    NAG1             5      4     728.34     46.07      4.18 IRA      NAGHAN        nghn   L: 0.444  T: none

11    1978      4      15   233348     15        5.8
       55    L    PAT             16     11     156.61     15.38      2.53 ITA      PATTI         it49   L: 0.250  T: 0.250
       56    A    NAS             18     16     149.55      7.90      0.73 ITA      NASO          it50   L: 0.250  T: 0.250
       57    A    MLZ             34     30      71.29      3.46      0.53 ITA      MILAZZO       it52   L: 0.333  T: 0.333
       58    R    MSS             58     52      36.97      2.00      0.20 ITA      MESSINA       it51   L: 0.250  T: 0.250

12    1978      6      20   200321      8        6.4
       59    S    THE3            27     17     142.29     15.06      2.14 GRE      THESSALONI    grk3   L: 0.250  T: 0.250

13    1978      9      16   153557      5        7.3
       60    S    TAB             54      3     913.58    106.62     72.04 IRA      TABAS         taba   L: 0.100  T: 0.100
       61    A    DAY             11     11     376.48     22.53      5.69 IRA      DAYHOOK       day1   L: 0.250  T: 0.250
       62    S    BOS             57     34     100.42     10.77      2.36 IRA      BOSHROOYEH    bosh   L: 0.400  T: 0.400
       63    S    FER             99     94      95.81      5.01      0.52 IRA      FERDOWS       ferd   L: 0.500  T: 0.500
       64    A    BAJ            143    132      88.06      4.78      0.51 IRA      BAJESTAN      baje   L: 0.500  T: 0.400
       65    A    KHE            146    145      25.99      3.69      1.02 IRA      KHEZRI        khez   L: 0.250  T: 0.250
```

	66	A	SED		166	166	27.75	3.02	0.52	IRA	SEDEH	sede	L: 0.364	T: 0.364
	67	A	BRJ		173	170	18.83	1.89	0.34	IRA	BIRJAND	birj	L: none	T: 0.666
	68	S	KAS		233	212	37.36	7.52	2.03	IRA	KAASHMAR	kaas	L: 0.286	T: 0.250
14	1979		4	15	061941	12	7							
	69	R	ULA		20	9	217.90	24.98	7.48	YUG	ULCINJ-2	mon3	L: 0.200	T: 0.200
	70	A	ULO		22	9	287.43	48.09	12.75	YUG	ULCINJ-1	mon2	L: 0.167	T: 0.167
	71	A	BAR		15	12	358.73	51.76	14.49	YUG	BAR-1	mon4	L: 0.200	T: 0.200
	72	A	PET		25	12	438.94	38.97	6.62	YUG	PETROVAC	mon1	L: 0.200	T: 0.200
	73	R	HRZ		65	29	238.69	13.29	1.79	YUG	HERCEG-NOV	mon5	L: 0.222	T: 0.222
	74	R	TIG		56	46	55.51	4.30	1.08	YUG	TITOGRAD-1	mon8	L: 0.286	T: 0.286
	75	R	TIT		56	46	30.60	3.58	0.92	YUG	TITOGRAD-2	mn12	L: 0.250	T: 0.250
	76	R	DUB		101	65	74.82	3.69	0.65	YUG	DUBROVN-1	mon7	L: 0.333	T: 0.333
	77	A	DEB		137	108	58.06	2.78	0.59	YUG	DEBAR	mo10	L: 0.333	T: 0.333
	78	A	GAC		138	110	54.52	3.82	0.82	YUG	GACKO	mon9	L: 0.250	T: 0.250
15	1979		4	15	144306	7	5.8							
	79	R	HRZ		22	22	89.93	4.25	0.23	YUG	HERCEG-NOV	mn27	L: 0.250	T: 0.286
	80	A	PET		24		96.50	6.13	0.71	YUG	PETROVAC	mn16	L: 0.200	T: 0.200
	81	A	BAR		41		80.12	5.29	0.63	YUG	BAR-1	mn24	L: 0.182	T: 0.182
	82	A	ULO		42		44.42	1.70	0.16	YUG	ULCINJ-1	mn19	L: 0.167	T: 0.222
16	1979		5	24	172318	5	6.3							
	83	A	PETR		16	7	268.31	16.59	3.13	YUG	PETROVAC-2	mn37	L: 0.167	T: 0.167
	84	A	BUD		9	9	264.88	27.24	4.03	YUG	BUDVA	mn38	L: 0.167	T: 0.167
	85	A	BAR		32	12	257.03	16.42	1.88	YUG	BAR-1	mn36	L: 0.167	T: 0.167
	86	A	TIV		23	15	150.43	8.35	1.69	YUG	TIVAT	mn39	L: 0.200	T: 0.200
	87	R	HRZ		30	18	73.84	6.02	0.96	YUG	HERCEG-NOV	mn42	L: 0.250	T: 0.250
	88	A	KOTZ		21	19	57.27	4.04	1.04	YUG	KOTOR-2	mn40	L: 0.250	T: 0.250
	89	R	KOTN		21	19	147.79	8.02	1.33	YUG	KOTOR-1	mn41	L: 0.250	T: 0.250
	90	A	ULO		53	30	31.77	3.33	0.54	YUG	ULCINJ-1	mn35	L: 0.250	T: 0.250
17	1979		9	19	213537	4	5.8							
	91	R	CSC		6	6	195.54	13.60	1.85	ITA	CASCIA-A	it22	L: 0.250	T: 0.250
	92	R	ARQ		21	21	76.10	4.26	0.64	ITA	ARQUATA	it26	L: 0.308	T: 0.286
	93	R	SPL		25	21	42.07	2.05	0.28	ITA	SPOLETO	it27	L: 0.333	T: 0.308
	94	A	BVG		39	33	39.42	2.11	0.32	ITA	BEVAGNA	it24	L: 0.666	T: 0.666
	95	A	MSC		37	37	37.56	2.12	0.24	ITA	MASCIONI	it28	L: 0.666	T: 0.666
	96	A	NCR		43	38	76.00	3.15	0.15	ITA	NOCERA	it25	L: 0.666	T: 0.500
	97	R	SVT		47		18.53	1.12	0.30	ITA	VITTORINO	it23	L: 0.250	T: 0.286
18	1980		1	1	164239	5	7							
	98	A	HOR			80	53.35	3.92	0.53	AZO	HORTA	az01	L: 0.333	T: 0.333
19	1980		11	23	183452	10	6.9							
	99	R	BGI		23	8	174.95	32.03	10.64	ITA	BAGNOLI-IR	ir02	L: 0.143	T: 0.143
	100	A	CLT		18	15	166.91	29.59	8.92	ITA	CALITRI	ir06	L: 0.143	T: 0.143
	101	R	STR		32	16	305.57	59.09	19.55	ITA	STURNO	ir05	L: 0.167	T: 0.167
	102	R	BSC		26	22	93.75	19.35	7.06	ITA	BISACCIA	ir10	L: 0.167	T: 0.167
	103	R	ALT		27	23	59.53	6.01	1.97	ITA	AULETTA	ir08	L: 0.200	T: 0.200
	104	A	RNR		33	30	97.77	13.86	3.60	ITA	RIO.IN.VUL	ir09	L: 0.200	T: 0.200
	105	A	BRN		43	33	212.41	11.49	2.37	ITA	BRIENZA	ir03	L: 0.250	T: 0.238
	106	A	MRT		48	33	133.27	12.27	2.52	ITA	MER.S.SEV.	ir04	L: 0.182	T: 0.182
	107	A	BNV		58	41	54.13	8.29	2.71	ITA	BENEVENTO	ir11	L: 0.222	T: 0.200
	108	S	BVN		53	46	46.29	3.79	1.27	ITA	BOVINO	ir17	L: 0.235	T: 0.235
	109	R	ARN		77	60	35.70	3.17	0.68	ITA	ARIENZO	ir01	L: 0.308	T: 0.308
	110	A	TRR		72	63	44.03	5.62	2.12	ITA	TRICARICO	ir14	L: 0.200	T: 0.200
	111	R	TDG		80	65	60.90	4.93	0.80	ITA	TOR. GRECO	ir12	L: 0.286	T: 0.308
	112	R	LRS		92	82	15.30	2.07	0.52	ITA	LAURIA	it56	L: 0.286	T: 0.250
	113	A	SSV		100	88	23.83	1.86	0.37	ITA	SAN SEVERO	ir18	L: 0.286	T: 0.286
	114	S	RCC		126	109	31.09	4.58	1.60	ITA	ROCCAMONFI	it57	L: 0.167	T: 0.182
	115	S	GRC1		136	119	32.26	6.07	1.45	ITA	GARIGLIANO	ir15	L: 0.500	T: 0.500
	116	A	VSS		140	135	34.72	1.46	0.35	ITA	VIESTE	ir19	L: 0.286	T: 0.400
	117	R	sSGR		64	48	17.55	2.05	0.38	ITA	S. GIORGIO	it58	L: 0.308	T: 0.333
20	1981		2	24	205337	10	6.7							
	118	S	KOR1		19	13	304.40	23.38	6.49	GRE	KORINTHOS	gr16	L: 0.111	T: 0.111
	119	S	XYL1		18	4	291.06	24.30	7.35	GRE	XYLOKASTRO	gr69	L: 0.125	T: 0.125
21	1981		2	25	023551	8	6.4							
	120	S	KOR1		24	24	116.21	14.00	4.92	GRE	KORINTHOS	gr18	L: 0.143	T: 0.125
22	1981		7	23	533	20	5.6							
	121	S	REZ1		50		65.90	5.95	0.95	IRA	FARMONDARI	farm	L: 0.286	T: 0.286
	122	S	REZ2		50		46.68	3.96	0.57	IRA	OROUMIYEH	orm1	L: 0.222	T: 0.286
23	1983		1	17	124130	14	7							
	123	S	LEF3		93	87	64.33	6.53	1.12	GRE	LEFKAS 3	gr27	L: 0.125	T: 0.100
24	1983		3	23	235105	10	6.2							
	124	S	LEF3		76	70	25.01	2.51	0.33	GRE	LEFKAS 3	gr30	L: 0.125	T: 0.125
25	1983		7	5	120127	7	6							
	125	A	GNN		45		44.33	3.46	0.71	TUR	GONEN	tur8	L: 0.308	T: 0.667
	126	R	EDN		55		50.41	5.10	0.82	TUR	EDINCIK	tur6	L: 0.250	T: 0.667
	127	A	EDR		83		23.93	1.25	0.16	TUR	EDREMIT	tur7	L: 0.500	T: 0.500
	128	A	BLK		95		22.06	1.68	0.28	TUR	BALIKES	tu22	L: 0.500	T: 0.500
26	1983		10	30	041228	14	6.7							
	129	A	HRS		33	17	151.81	26.89	10.80	TUR	HORASAN	tu11	L: 0.286	T: 0.333
27	1984		5	7	174943	8	5.8							
	130	R	ATN		15	12	106.01	3.70	0.88	ITA	ATINA	lz02	L: 0.167	T: 0.182

	131	A	CSS	23	17	142.20	11.05	1.83	ITA	CASSINO	lz44	L: 0.133	T: 0.143
	132	R	PNT	31		66.88	5.52	0.70	ITA	PONTECORVO	lz05	L: 0.154	T: 0.154
	133	S	ORT	33		82.67	3.76	0.56	ITA	ORTUCCHIO	lz11	L: 0.167	T: 0.167
	134	S	LMP	39		75.81	4.56	0.52	ITA	LIMA DP	lz15	L: 0.308	T: 0.250
	135	A	ISR	46		67.86	3.68	0.50	ITA	AGAPITO	lz03	L: 0.167	T: 0.167
	136	S	RCC	49		42.85	4.60	0.82	ITA	ROCCAMONFI	lz06	L: 0.167	T: 0.167
	137	R	BSS	51		22.85	1.18	0.21	ITA	BUSSI	it81	L: 0.308	T: 0.308
	138	S	GRG1	52		59.13	6.42	1.05	ITA	GARIG CN1	lz12	L: 0.200	T: 0.182
	139	S	GRG2	52		60.02	6.56	0.89	ITA	GARIG CN2	lz13	L: 0.222	T: 0.200
	140	A	RIP	65		17.06	1.12	0.16	ITA	RIPA	lz14	L: 0.250	T: 0.250
	141	A	CSN	67		28.05	1.88	0.27	ITA	CASTELNUOV	lz04	L: 0.286	T: 0.286
	142	S	BRSC	71		12.26	0.39	0.05	ITA	BARISCIANO	lz08	L: 0.400	T: 0.500
	143	A	P0G	72		16.38	0.82	0.10	ITA	POGGIO	lz07	L: 0.333	T: 0.333
	144	R	MAN	59		132.10	9.01	0.81	ITA	MANOPELLO	lz09	L: 0.286	T: 0.250
28	1986		5	5	033538	4	5.9						
	145	R	GOLB	23	27	53.74	7.30	1.67	TUR	GOLBASI	tu12	L: 0.333	T: 0.333
29	1986		6	6	103947	11	5.7						
	146	R	GOLB	34		30.60	3.74	0.62	TUR	GOLBASI	tu13	L: 0.400	T: 0.400
30	1986		9	13	172431	8	5.8						
	147	A	KAL3	8	5	268.31	31.68	6.95	GRE	KALAMATA1	kal1	L: 0.167	T: 0.167
	148	A	KAL1	8	5	290.18	32.43	7.33	GRE	KALAMATA3	gr46	L: 0.167	T: 0.167
31	1988		10	16	123405	12	5.6						
	149	S	ZAK4	19	11	142.78	9.89	1.24	GRE	ZAKYNTHOS	kill	L: 0.222	T: 0.250
	150	A	AMA	28		151.81	8.41	1.26	GRE	AMALIAS	grk1	L: 0.200	T: 0.182
32	1988		12	7	074124	6	6.8						
	151	S	GUK	36	20	181.91	23.82	7.12	USR	GUKASIAN	guk1	L: 0.125	T: 0.125
33	1988		12	7	074545	11	5.8						
	152	S	GUK	35	10	141.41	10.61	2.89	USR	GUKASIAN	guk2	L: 0.200	T: 0.200
34	1989		10	29	190913	6	5.7						
	153	R	ALG	55	61	35.60	1.51	0.20	ALG	BOUZAREAH	tpz3	L: 0.500	T: 0.667
35	1990		6	20	210008	19	7.3						
	154	A	QAZ	99	51	183.78	15.35	4.27	IRA	QAZVIN	mj02	L: 0.222	T: 0.333
	155	S	RUD	85	65	94.73	15.31	6.19	IRA	RUDSAR	mj07	L: 0.235	T: 0.222
	156	S	ABH	94	67	191.43	15.65	2.66	IRA	ABHAR	mj01	L: 0.333	T: 0.364
	157	S	TON	118	78	131.60	18.03	4.49	IRA	TONEKABUN	mj08	L: 0.308	T: 0.400
	158	R	GCR	201	151	103.26	4.30	1.50	IRA	GACHSAR	mj09	L: 0.222	T: 0.222
36	1991		4	29	091248	6	6.9						
	159	R	,AKH	111	108	11.18	0.98	0.21	USR	AKHALK	sw03	L: 0.280	T: 0.308
	160	A	,BGD	125	122	8.14	0.49	0.10	USR	BOGDANOVKA	sw11	L: 0.500	T: 0.333
37	1991		6	15	005920	6	6.2						
	161	A	,IRI	39		110.91	7.59	0.81	USR	IRI	sw17	L: 0.167	T: 0.167
	162	A	,BAZ	50		34.91	1.93	0.33	USR	ONI-BASE	sw25	L: 0.222	T: 0.222
	163	A	,ONS	50		68.74	2.80	0.41	USR	ONI	sw31	L: 0.125	T: 0.133
	164	A	,ZMB	59		60.31	4.62	0.83	USR	ZEMO-BARI	sw45	L: 0.154	T: 0.143
	165	A	,AMB	71		16.38	1.66	0.34	USR	AMBROLAURI	sw05	L: 0.200	T: 0.200
38	1992		3	13	171840	10	6.8						
	166	A	ERC	11	4	492.49	104.44	29.58	TUR	ERZINCAN	erz1	L: 0.167	T: 0.143
	167	A	TER	67		29.32	4.37	1.60	TUR	TERCAN	erz2	L: 0.200	T: 0.200
	168	A	REF	75		68.65	5.40	1.78	TUR	REFAHIYE	erz3	L: 0.200	T: 0.200
39	1992		3	15	161625	10	5.8						
	169	A	ERC	45		103.36	3.50	0.50	TUR	ERZINCAN	erz4	L: 0.400	T: 0.250
	170	A	ERS	45		38.54	4.67	0.86	TUR	ERZINCAN-S	sw16	L: 0.280	T: 0.280
40	1992		11	6	190809	17	6						
	171	A	IZM	30		38.15	6.69	1.52	TUR	IZMIR2	tk02	L: 0.182	T: 0.182
	172	A	KUS	40		79.43	5.03	0.61	TUR	KUSADASI	tk03	L: 0.222	T: 0.250
41	1992		11	18	211941	15	5.7						
	173	S	AIG	25		35.60	1.30	0.30	GRE	AIGION2	gr76	L: 0.250	T: 0.250
	174	R	MRN1	36		20.79	1.17	0.22	GRE	MORNOS1	gr99	L: 0.222	T: 0.280
42	1993		7	14	123149	15	5.6						
	175	A	PAT1	8		185.15	10.46	1.07	GRE	PATRAS1	g106	L: 0.125	T: 0.154
	176	S	NAF	25		49.23	4.52	0.40	GRE	NAFPAK	g102	L: 0.182	T: 0.182
	177	S	AIG	29		49.43	2.28	0.28	GRE	AIGION2	gr77	L: 0.250	T: 0.250
	178	S	MSL1	36		29.81	2.13	0.38	GRE	MESOLONGI	g101	L: 0.125	T: 0.125
	179	A	AMA	55		25.10	1.06	0.12	GRE	AMALIAS	gr88	L: 0.222	T: 0.286
43	1995		6	15	001630	17	6.1						
	180	S	AIG	26	10	520.44	49.18	7.22	GRE	AIGION2	aig1	L: 0.200	T: 0.200
44	1995		5	13	084713	14	6.6						
	181	R	KOZ	17	9	204.37	8.82	1.65	GRE	KOZANI PR	gv05	L: 0.200	T: 0.300

45	1995		10		1	155713	5	6.1						
	182	S				1	1	318.13	43.48	10.03	TUR	DINAR MET	dn01	L: 0.200 T: 0.100
	183	A				95	87	14.91	3.85	1.37	TUR	DENIZLI	dn04	L: 0.100 T: 0.080
46	1997		9		26	003316	7	5.5						
	184	A				3	3	394.32	22.49	3.96	ITA	COLFIORIT	um10	L: 0.200 T: 0.150
	185	R				13	13	564.08	19.47	1.91	ITA	NOCERA UM	um11	L: 0.200 T: 0.200
	186	A				25	25	50.31	6.07	1.26	ITA	BEVAGNA	um12	L: 0.300 T: 0.300
	187	S				24	24	97.67	5.98	2.25	ITA	CASTELNUO	um13	L: 0.250 T: 0.100
	188	R				39	33	63.94	2.50	0.25	ITA	FORCA CAN	um14	L: 0.400 T: 0.300
	189	R				23	17	177.70	4.43	0.50	ITA	BORGO-CER	um16	L: 0.350 T: 0.350
47	1997		9		26	094030	6	6.1						
	190	A				5	3	258.40	17.06	2.89	ITA	COLFIORIT	um20	L: 0.250 T: 0.250
	191	R				11	4	530.34	31.03	3.07	ITA	NOCERA UM	um21	L: 0.250 T: 0.300
	192	A				23	26	77.28	8.49	1.03	ITA	BEVAGNA	um22	L: 0.350 T: 0.350
	193	S				22	23	168.87	14.63	4.21	ITA	CASTELNUO	um23	L: 0.150 T: 0.100
	194	A				27	21	113.95	7.09	1.05	ITA	MATELICA	um24	L: 0.300 T: 0.300
	195	R				42	34	82.18	3.26	1.36	ITA	GUBBIO	um25	L: 0.200 T: 0.300
	196	R				38	30	90.81	17.75	5.84	ITA	GUBBIO PI	um26	L: 0.023 T: 0.025
	197	R				79	71	68.06	2.68	0.21	ITA	PEGLIO	um28	L: 0.600 T: 0.600
	198	R				24	23	104.15	4.58	0.39	ITA	BORGO-CER	um31	L: 0.300 T: 0.300
48	1998		6		27	135553	32	6.2						
	199	S				30	4	267.23	29.26	7.22	TUR	CEYHAN	ad01	L: 0.100 T: 0.150
	200	A				80	71	122.68	11.79	1.07	TUR	MERSIN	ad04	L: 0.350 T: 0.200
	201	A				142	118	7.94	1.30	0.44	TUR	KAHRAMAN	ad07	L: 0.200 T: 0.200
49	1999		8		17	000139	17	7.8						
	202	S	AYD			368	359	5.79	2.29	0.86	TUR	AYDIN-HAY	kc02	L: 0.150 T: 0.150
	203	A	BLK			213	199	15.59	3.31	1.40	TUR	BALIKESIR	kc03	L: 0.300 T: 0.200
	204	A	BRS			92	79	53.54	9.12	4.87	TUR	BURSA-SIV	kc05	L: 0.100 T: 0.100
	205	A	IST			86	71	57.27	8.71	9.38	TUR	IST-BAYIN	kc07	L: 0.050 T: 0.100
	206	S	KUT			142	140	57.96	14.69	6.52	TUR	KUTAHYA	kc08	L: 0.080 T: 0.100
	207	A	DNZ			329	323	5.69	1.51	0.45	TUR	DENIZLI	kc14	L: 0.300 T: 0.350
	208	S	DZC			101	14	351.96	54.08	15.34	TUR	DUZCE	kc15	L: 0.200 T: 0.200
	209	A	GBZ			48	32	247.13	35.97	29.15	TUR	GEBZE-TUB	kc17	L: 0.080 T: 0.080
	210	A	GYN			72	31	130.23	9.65	2.07	TUR	GOYNUK	kc18	L: 0.400 T: 0.400
	211	S	IZN			39	29	126.51	27.28	7.45	TUR	IZNIK-KAR	kc19	L: 0.200 T: 0.200
	212	R	IZT			10	8	209.86	17.81	3.59	TUR	IZMIT-MET	kc20	L: 0.300 T: 0.400
	213	A	SKR			34	3	374.02	69.83	94.29	TUR	SAKARYA	kc22t	L: none T: 0.023
	214	A	ARC			54	38	207.02	41.40	44.33	TUR	ARCELIK	kc23	L: 0.023 T: 0.030
	215	S	ATS			113	97	248.21	36.25	28.12	TUR	AMBARLI	kc24	L: 0.030 T: 0.050
	216	A	BTS			172	156	97.67	10.76	2.86	TUR	BOTAS	kc25	L: 0.200 T: 0.200
	217	S	BUR			95	78	98.85	18.22	14.20	TUR	BURSA-TOF	kc26	L: 0.050 T: 0.080
	218	A	CNA			109	94	173.97	16.89	19.73	TUR	KUCUK-CEK	kc27	L: 0.023 T: 0.023
	219	A	DHM			103	87	87.97	24.76	27.10	TUR	YESILKOY	kc28	L: 0.023 T: 0.040
	220	S	FAT			94	79	173.77	19.27	17.93	TUR	FATIH	kc29	L: 0.023 T: 0.023
	221	R	YKP			92	77	40.31	9.27	10.71	TUR	YAPI-KRED	kc31	L: 0.023 T: 0.065
	222	S	YPT			20	5	311.95	77.04	84.83	TUR	YARIMCA	kc32	L: 0.023 T: 0.023
50	1999		9		7	000139	17	5.9						
	223	A	ATHA			19	8	91.99	7.55	1.23	GRE	N.PSIHIKO	at01	L: 0.200 T: 0.200
	224	R	DMK1			23	13	62.37	2.35	0.62	GRE	DEMOKRITO	at03	L: 0.200 T: 0.400
	225	R	FIX1			19	9	121.80	21.72	7.57	GRE	SYNGROU	at04	L: 0.100 T: 0.080
	226	R	ATH0			16	8	118.66	8.84	1.76	GRE	KYPSELI	at05	L: 0.200 T: 0.250
	227	A	ATH0			19	9	156.71	6.91	1.11	GRE	ITSAK CHA	at06	L: 0.400 T: 0.300
	228	R	ATH0			16	8	303.71	15.42	2.41	GRE	ITSAK KED	at07	L: 0.200 T: 0.150
	229	A	PNT1			20	10	85.12	15.04	6.26	GRE	PAPAGOS	at09	L: 0.080 T: 0.100
	230	R	SMGA			18	8	235.16	28.19	8.59	GRE	SYNTAGMAA	at10	L: 0.100 T: 0.200
	231	R	SMGB			18	8	109.64	20.77	6.90	GRE	SYNTAGMAB	at11	L: 0.120 T: 0.120
	232	S	SPLA			14	5	244.18	17.71	2.80	GRE	SEPOLIA-A	at12	L: 0.170 T: 0.150
	233	S	SPLB			14	5	316.66	22.58	2.50	GRE	SEPOLIA-B	at13	L: 0.200 T: 0.200
51	1999		11		12	165720	14	7.3						
	234	A	ARC			150	132	7.06	1.43	0.56	TUR	ARCELIK	du01	L: 0.150 T: 0.150
	235	S	ATS			207	189	36.58	5.30	1.51	TUR	AMBARLI	du02	L: 0.300 T: 0.300
	236	A	BOT			267	249	3.82	1.06	0.40	TUR	BOTAS	du03	L: 0.200 T: 0.200
	237	S	BUR			184	170	17.75	3.55	0.80	TUR	BURSA-TOF	du04	L: 0.300 T: 0.250
	238	A	CNA			202	184	16.57	1.81	0.62	TUR	KUCUK-CEK	du05	L: 0.200 T: 0.250
	239	A				197	178	17.85	4.17	1.55	TUR	YESILKOY	du07	L: 0.200 T: 0.200
	240	S	FAT			187	168	33.34	3.53	0.48	TUR	FATIH	du08	L: 0.250 T: 0.200
	241	R	YKP			183	164	4.90	1.05	0.29	TUR	YAPI-KRED	du12	L: 0.300 T: 0.300
	242	S	YPT			117	99	18.14	2.23	0.42	TUR	YARIMCA	du13	L: 0.350 T: 0.350
	243	A	BLK			303	291	1.96	0.30	0.07	TUR	BALIKESIR	du15	L: 0.300 T: 0.350
	244	A	BOL			39	18	790.41	65.15	26.25	TUR	BOLU	du16	L: 0.030 T: 0.050
	245	A	BRS			182	169	8.43	1.82	0.41	TUR	BURSA-SIV	du17	L: 0.300 T: 0.300
	246	A	IST			176	157	7.75	1.55	0.40	TUR	IST-BAYIN	du19	L: 0.350 T: 0.350
	247	S	KUT			179	171	20.30	9.79	5.26	TUR	KUTAHYA	du20	L: 0.075 T: 0.030
	248	A	SKR			64	47	23.34	5.23	9.12	TUR	SAKARYA	du22	L: 0.010 T: 0.010
	249	S	DZC			9	1	504.94	83.83	47.21	TUR	DUZCE	du28	L: 0.180 T: 0.050

Notes on table format:

For each block of data, the first line gives earthquake characteristics:

Event No.	Year	Month	Day	Time	h (km)	M_s

where h is focal depth

Subsequent lines give characteristics of accelerograms:

Record No.	Soil Class	Station Code	d_e (km)	d_f (km)	PGA (cm/s^2)	PGV (cm/s)	PGD (cm)	Country	Station name	File name	f_{LL} (Hz)	f_{LT} (Hz)

where f_{LL} and f_{LT} are the lower frequency filter cut-offs for the longitudinal and transverse components respectively

Country codes are as follows:

Code	Country/region
ALG	Algeria
AZO	Azores
GRE	Greece
IRA	Iran
ITA	Italy

Code	Country/region
PGL	Portugal
TUR	Turkey
USR	Former USSR
YUG	Former Yugoslavia

H1. Pre-processing

Prior to analysis, data underwent two stages of pre-processing:

1. **File splicing and renaming.** Velocity data were acquired in a binary compressed format, with each channel (component) of data automatically being given a time-dependent file name by the data acquisition system. Consecutive blocks of data were spliced together in order to create a single file per component. For two instruments recording at the same time, automatically generated file names were identical. In order to avoid confusion, files were renamed to correspond with the measurement point number. An example is given in Figure H1.

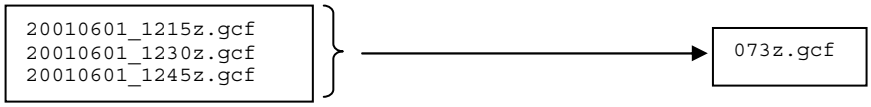

Figure H1 Splicing and renaming of velocity channel data prior to data processing. Filename suffix z indicates vertical component. Procedure repeated for two horizontal components e and n. File extension '.gcf' stands for Guralp Compressed Format.

2. **Error checking.** The analysis method requires that all three components for a given point have an identical start time and that the data streams are continuous. Each set of files was inspected using SCREAM and corrected for these problems wherever encountered. Occasional gaps in data streams or short delays in the start of one or more of the components generally corresponded with disruption of power to the instrument.

H2. MATLAB analysis for calculation of HVSR

The MATLAB script written for calculation of the Fourier spectra and HVSR consists of nine stages:

1. Read samples and header information

Binary .gcf files are read in, a component at a time, using a standard proprietary routine, readgcffile.m. This returns the samples, the streamID (which identifies the recording instrument and component), the number of samples per second (sps) and the instrument start time (ist). All measurements were taken at a sample rate of 100 Hz.

The full sample length is divided into shorter windows of duration, w_length, whose value is dictated by the period bandwidth of interest. As a rule of thumb, Bard (1998) suggests an optimum window length of around 10 cycles of the longest period (T_m) about which reliable information is required. For the current study, T_m was assumed to be around 4 s, which suggests an optimum sample window duration of around 40 s, or 4000 samples (assuming 100 samples per second). The

FFT (Fast Fourier Transform) algorithm used by MATLAB operates most effectively for sample lengths equal to an integer power of 2. The closest integer power of 2 to 4000 is 2^{12}, or 4096. Therefore, w_length was taken as 40.96s for the current study.

2. Convert data from bits to velocity

Raw data are recorded as bits and need converting to velocity using the appropriate conversion factor, which is instrument and component dependent. This is illustrated using a portion of a microtremor time-history (Figure H2). The amplitude markers show typical peak-to-peak values of around 9,984 bits. For the data stream shown, the conversion factor is $799.320*10^{-12}$ m/s/bit. Typical ambient noise amplitudes are therefore around 4 microns/s.

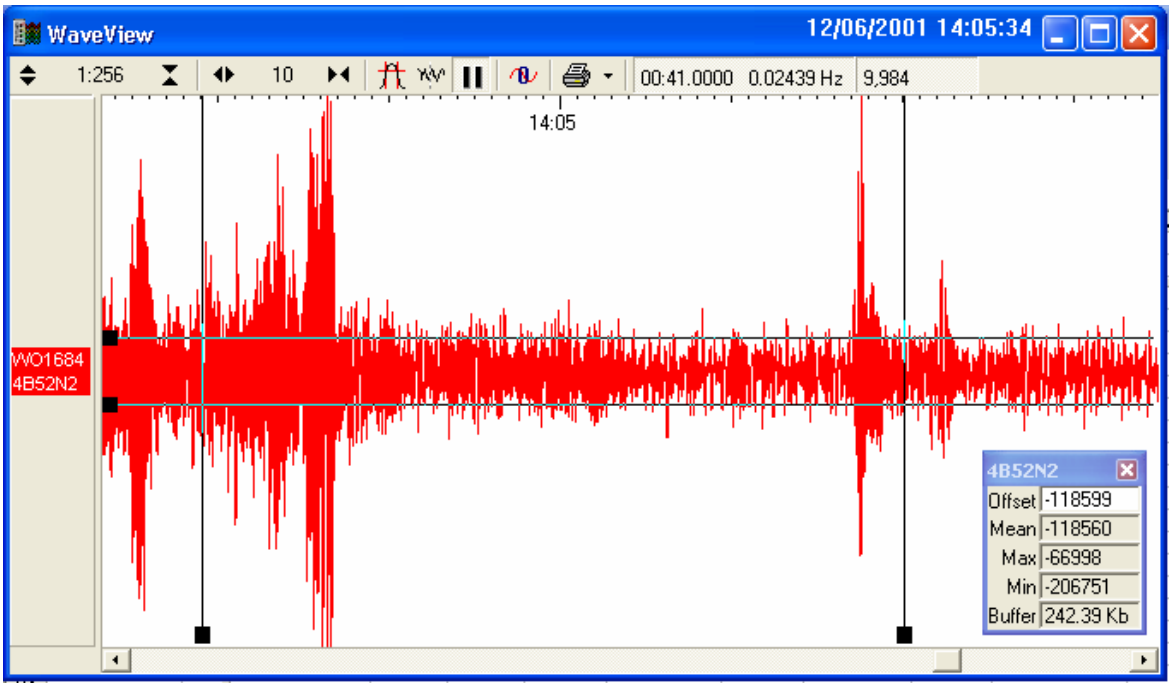

Figure H2. Typical microtremor time history, viewed within SCREAM. The data shown is the N-S component of point 86c (streamID 4B52N2). Marks along the top indicate seconds.

3. Correct zero offset

Raw data have a zero offset, which is corrected by subtracting the mean amplitude from each sample point.

4. Apply window function to samples vector

A window function is applied to the samples vector in order to gradually taper the record at both ends. This reduces spectral leakage caused by Discrete Fourier Transform (DFT) of an abruptly truncated sample. Windowing subroutines are from Stearns & David (1996). Various different windowing functions (Figure H3a) were applied to the data, with little difference observed in the resulting microtremor HVSRs. The Hanning (or raised cosine) window was selected due to its

observed use in other microtremor investigations (eg. Bour *et al.*, 1998). The effect of a Hanning window on a simple sinusoidal wave is illustrated in Figure H3b.

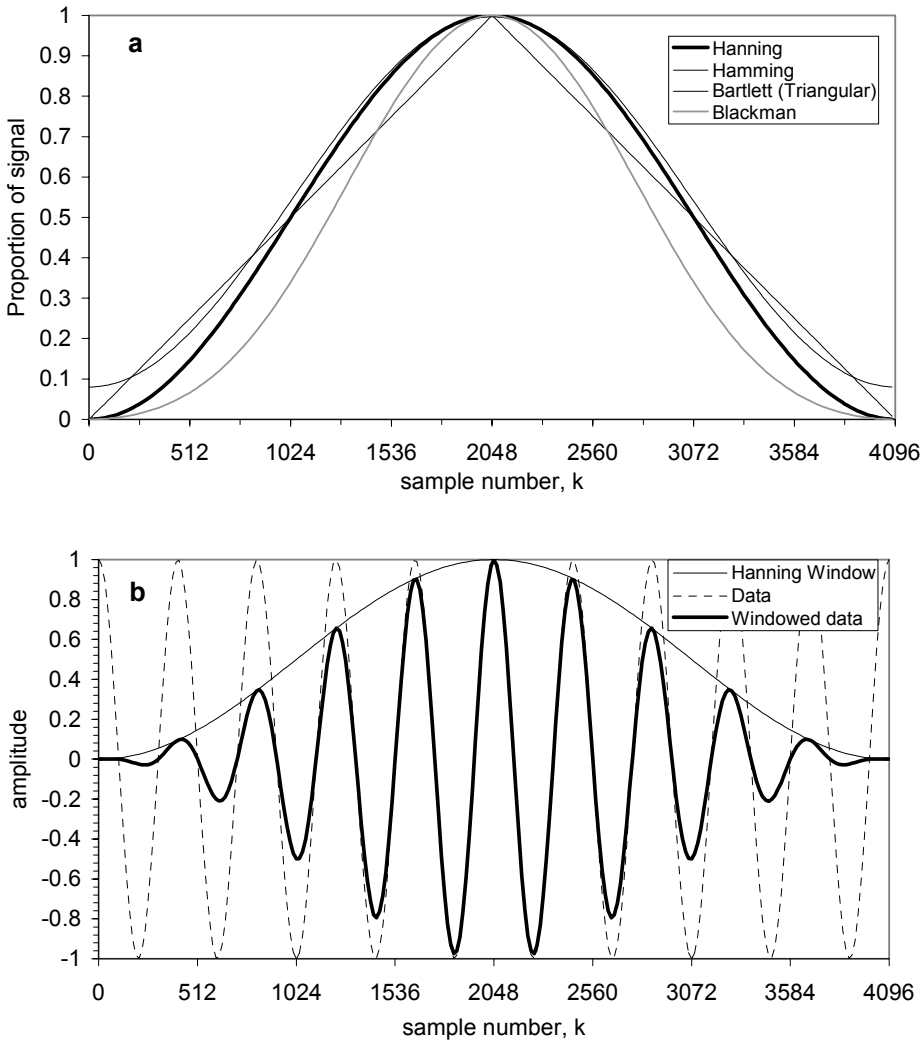

Figure H3. a. Shape of various windowing functions, b. Effect of Hanning window function on a simple sinusoidal wave of 4096 samples length.

5. Perform Fast Fourier Transform (FFT)

MATLAB calculates the DFT using an efficient FFT (Fast Fourier Transform) algorithm. An explanation of the DFT can be found in various standard mathematics or signal processing texts (eg. Smith, 1999; Smith, 2002).

The windowed sample is appended with zeroes ("zero-padded") in order to increase the resolution of the spectrum obtained through DFT. In MATLAB, this is achieved by specifying a sample length, *N*, greater than the value defined by w_length in stage 1. *N* was taken as 2^{15} = 32,768, selected to be long enough to use for subsequent DFT of strong-motion data (see section 7.3.4). A strong-motion signal can continue for well over a minute, especially in the case of digital records. Using the same value of *N* for DFT of both strong-motion and microtremor data simplifies comparison of resultant spectra as they will be identical in length.

6. Calculate smoothed spectrum

Smoothing of Fourier spectra is carried out prior to calculation of spectral ratios. If no smoothing is performed, the ratio of two FAS tends to give unrealistically high amplitudes (Safak, 2001). Selection of the smoothing bandwidth has an effect on the reliability of spectral amplitudes. As pointed out by Bard (1998), a smoothing bandwidth of b Hz means that amplitudes below about $2b$ Hz are unrepresentative. For the current study, b = 0.1 Hz was considered small enough not to interfere with frequencies of interest (down to 0.2 Hz), whilst being large enough to remove spurious peaks and allow identification of distinct features in the spectra.

To achieve a smoothing bandwidth as close as possible to 0.1 Hz, each point is averaged with 16 points either side ($b = \Delta f \times 16 \times 2 = 0.09765$ Hz) where Δf is the frequency resolution of the DFT (0.0030517 Hz), calculated from the sampling interval, Δt and the DFT length, N using Equation (H1):

$$\Delta f = \frac{1}{N\Delta t} \tag{H1}$$

where: $N = 32768$ and $\Delta t = 0.01$ s.

The smoothing method applied to the spectra is a simple adjacent averaging algorithm, obtained from MATLAB's online file repository, http://www.mathtools.net/MATLAB/. Although Hanning or triangular smoothing windows are more commonly used in the literature (eg. Bindi *et al.*, 2000), the adjacent averaging method is computationally much quicker and for the bandwidth used, gives almost identical HVSR amplitudes to a Hanning window of bandwidth 0.15 Hz. Experiments were also conducted using a smoothing window having a constant bandwidth on a logarithmic scale (Konno & Ohmachi, 1998). Whilst this method gave clearer HVSR at higher frequencies (which is useful for identifying predominant frequencies at the few rock or shallow soil sites included in the current study), it was computationally much more intensive than the adjacent averaging approach, which was an important factor considering the large number of spectra requiring smoothing.

7. Calculate average horizontal to vertical spectral ratio for single data sample

The average HVSR is calculated from the root-mean-square average HVSR for the two horizontal components.

8. Calculate average horizontal to vertical spectral ratio for all sample windows

The final HVSR for a given site is calculated from an average over several sample windows. If a feature is not present in the spectra from most of the windows, it is not considered typical of the response at a given site. Bard (1998) suggests the use of around 10 sample windows. For the current study, the measurement duration at each site was generally long enough to permit averaging over 20 windows. The standard deviation in HVSR is calculated at each frequency.

9. Plot spectra

The average HVSR +/- 1 standard deviation is plotted for each point. The spectrum is plotted over the frequency range $0.2 \leq f \leq 10$ Hz. The lower limit was dictated by the smoothing bandwidth used in stage 6. Frequencies above 10 Hz were not considered relevant to the current study.

A separate routine, stationary.m outputs the coordinates of stationary points in the data, assisting identification of the predominant peak. The predominant frequency was selected as the frequency corresponding to the highest amplitude in the average HVSR within the reliable range of frequencies. As explained in Chapter 7, some HVSR plots were affected at low frequencies by wind. In a few cases, this was enough to obscure identification of the predominant peak (as indicated in Appendix I, Table I2). At some measurement locations, the operation of heavy machinery near to the instrument gave rise to spurious peaks in the average HVSR corresponding to source effects rather than site effects. Such measurements were excluded from the dataset unless they could be validated using sample windows corresponding to periods of time during which machinery was not operating.

The program listing for the MATLAB routine described is presented below:

```
function hvsr(point_no,w_length,numwin,itype,offset,outfig)

% HVSR.M CALCULATE AND PLOT AVERAGE HVSR OF MICROTREMOR DATA
% ------------------------------------------------------------------------------------------
%
% ARGUMENTS:
%  point_no -   microtremor measurement point number
%  w_length -   length of sample window (s)
%  numwin   -   number of consecutive time windows
%  itype    -   specifies type of window function applied to time-history
%                   1=rectangular (i.e. no window); 2=tapered rectangular; 3=triangular;
%                   4=Hanning; 5=Hamming; 6=Blackman
%  offset   -   specifies smoothing offset for spectral smoothing
%  outfig   -   MATLAB figure number
%
% ADDITIONAL MATLAB SCRIPTS CALLED:
%  readgcffile.m   courtesy of Guralp Systems Ltd., http://www.guralp.com/
%  spmask.m        included in software bundled with Stearns & David (1996)
%  spwndo.m        included in software bundled with Stearns & David (1996)
%  smooth.m        courtesy of Olof Liungman, http://www.mathtools.net/MATLAB/Filtering/
%  stationary.m    courtesy of James Rooney, http://www.mathtools.net/MATLAB/
%
% INPUT FILES REQUIRED:
%  Data files in GCF (Guralp Compressed Format) Format.
%  For a given measurement point number, point_no, there is a separate file for each of
%  the 3 component directions, with names specified below:
%  [point_no,'z.gcf']  up-down component
%  [point_no,'n.gcf']  n-s component
%  [point_no,'e.gcf']  e-w component
%
% COMMAND LINE EXAMPLE:
%  hvsr('086b',40.96,20,4,16,1)
%
%  This will select files: 086bz.gcf, 086bn.gcf & 086be.gcf
%  Window length is 40.96s
%  Hanning window function is applied to the time-history (option 4)
%  Adjacent averaging smoothing offset is 16 points
%  This effectively means a bandwidth of ((2*16)*df)Hz where df is the frequency interval
%
% FILE HISTORY:
%  24.01.2002  Written by Iain Tromans (i.tromans@ic.ac.uk)
% ------------------------------------------------------------------------------------------

% Assign filename strings to all three component data files

filename1=[point_no,'z.gcf'];
```

```
filename2=[point_no,'n.gcf'];
filename3=[point_no,'e.gcf'];

% Loop for each window

for window=1:numwin

   % Loop for each component
   % -----------------------

   for i=1:3

      % Select relevant component data file (up-down component first)

      if (i== 1);
         filename=filename1;
      elseif (i== 2);
         filename=filename2;
      elseif (i== 3);
         filename=filename3;
      end;

      % 1. Read samples and header information
      % --------------------------------------
      % Call readgcffile.m
      % [samples,streamID,sps,ist]=readgcffile(filename)
      % INPUT:
      %  filename      component data file in GCF format
      % OUTPUT:
      %  samples       an array of all samples in file
      %  streamID      string up to 6 characters
      %  sps           Samples Per Second (sample rate of data in 'samples')
      %  ist           Instrument Start Time (start time of data, as serial date number)

      [samples,streamID,sps,ist]=readgcffile(filename);

      % On 1st pass, check that there are enough samples in the record for the required
      % number of time windows
      window=window
      samplength(i)=length(samples);
      if (window==1)&(i==1);
         reqsamplelength=numwin*sps*w_length;
         if (samplength(1)<(numwin*sps*w_length))
            error('not enough samples to perform analysis');
         end;
      end;

      if (window==1);
         ignore=0;
         samples=samples(ignore+1:1:samplength(i));
                                        % ignore initial block of data (each comp)
         i=i
         lengthofsamples=length(samples)
      end;

      % Define window of samples as a subset of the full sample set
      % Window starts at a given sample number, w_start and ends w_length seconds later

      w_start=1+((window-1)*w_length*sps);
      w_end=w_start+(w_length*sps)-1;
      x=samples(w_start:1:w_end);

      % 2. Convert data from bits to velocities
      % ---------------------------------------
      % Conversion is instrument dependent.  Insrument is identified from streamID

      if streamID=='4B47Z2';
         vperbit=802.288e-12;
      elseif streamID=='4B47N2';
         vperbit=788.983e-12;
      elseif streamID=='4B47E2';
         vperbit=797.645e-12;
      elseif streamID=='4B52Z2';
         vperbit=796.519e-12;
      elseif streamID=='4B52N2';
         vperbit=799.320e-12;
      elseif streamID=='4B52E2';
         vperbit=791.603e-12;
      elseif streamID=='3A45Z2';
         vperbit=429.790e-12;
```

```
elseif streamID=='3A45N2';
   vperbit=428.344e-12;
elseif streamID=='3A45E2';
   vperbit=428.704e-12;
else return;
end;

x=x*vperbit;

% 3. Correct for zero offset
% --------------------------

meanx=mean(x);
x=x-meanx;


% 4. Apply window function to samples vector
% ------------------------------------------
% Call spmask.m
% [y,tsv]=spmask(x,itype)
% INPUT:
%  x         data (row vector)
%  itype     window type (1-6)
% OUTPUT:
%  y         masked version of x
%  tsv       sum of squared window values i.e. energy of window vector (not used)
%
% spmask.m calls spwndo.m

[x,tsv]=spmask(x',itype);
x=x';

% 5. Perform Fast Fourier Transform
% ---------------------------------

% Define length of FFT
N=32768;
% Interval between samples
dt=1/sps;
% Total sample time (s)
T=N*dt;
% Frequency interval
df=1/T;
% Nyquist frequency
nyqfreq=sps/2;

% Use MATLAB built-in command X=FFT(x,N)
% This calculates the N-point FFT, padded with zeros if x has less than N points
% and truncated if it has more
X=fft(x,N);
amp=abs(X);

% Construct a frequency axis
freq=0:df:(nyqfreq);

% 6. Calculate smoothed spectra
% -----------------------------
% Carry out smoothing using a running mean over ((2*offset)+1) successive points,
% (offset) points either side of the current point. At the ends of the series skewed
% or one-sided  means are used.
% Call smooth.m
% yout=smooth(yin,offset)
% INPUT:
%  yin       unsmoothed spectrum for a given time window
%  offset    offset value for adjacent averaging
% OUTPUT:
%  yout      smoothed spectrum

% For each component, store FAS in column corresponding to window number
if (i==1);
   zfft(:,window)=amp;
elseif (i==2);
   nfft(:,window)=amp;
   [nfft_saa(:,window)]=smooth(nfft(:,window),offset);
   [zfft_saa(:,window)]=smooth(zfft(:,window),offset);
   nvsr_saa(:,window)=nfft_saa(:,window)./zfft_saa(:,window);
elseif (i==3);
   efft(:,window)=amp;
   [efft_saa(:,window)]=smooth(efft(:,window),offset);
   evsr_saa(:,window)=efft_saa(:,window)./zfft_saa(:,window);
```

```
            % 7. Calculate average HVSR for single time window
            % ------------------------------------------------
            avhvsr_saa(:,window)=(nvsr_saa(:,window).^2+evsr_saa(:,window).^2).^0.5/sqrt(2);
        end;
    end; % End component loop
end; % End time window loop

% 8. Calculate average HVSR over all time windows
% -----------------------------------------------
av=sum(avhvsr_saa,2)/numwin;

% Calculate standard deviation of HVSR values over all windows
sigma=std(avhvsr_saa');

avplussigma=av'+sigma;
avminussigma=av'-sigma;

% Option to save average spectra to external file
savespec=0;

if savespec==1
   outfile1=['c:\mt\data\',point_no,'_evsr.dat'];
   fid = fopen(outfile1,'w');
   fprintf(fid,'%10.6f %10.6f %10.6f %10.6f %10.6f\n',evsr_saa(1:N/2,1:5)');
   fclose(fid);
   outfile2=['c:\mt\data\',point_no,'_nvsr.dat'];
   fid = fopen(outfile2,'w');
   fprintf(fid,'%10.6f %10.6f %10.6f %10.6f %10.6f\n',nvsr_saa(1:N/2,1:5)');
   fclose(fid);
end;

% 9. Plot spectra
% ---------------
figure(outfig);
set(outfig,'PaperType','a4letter');
set(outfig,'PaperPosition',[0.55 0.25 7.5 10]); % Units in inches
set(outfig,'PaperOrientation','Portrait');

loglog(freq(1:(N/2)),av(1:(N/2)),'k-','LineWidth',0.5); hold on;
loglog(freq(1:(N/2)),avminussigma(1:(N/2)),'k-','LineWidth',0.1); hold on;
loglog(freq(1:(N/2)),avplussigma(1:(N/2)),'k-','LineWidth',0.1); hold on;

%  Call stationary.m to identify candidates for fundamental frequency
%  [ind]=stationary(x,y,type)
%  INPUT:
%  x           x-variable
%  y           y-variable
%  type     'max' or 'min' for peaks or troughs respectively
% OUTPUT:
%  ind      vector of stationary points

upperval=3; % Set upper frequency search limit (Hz)
upperf=floor(upperval/df);
type='max';
[indmax]=stationary(freq(1:upperf),av(1:upperf),type);
peaks=[indmax' freq(indmax)' av(indmax)];

% Sort peaks in descending order of magnitude and output first 's' values to screen
s=5
sortedpeaks=sortrows(peaks,3);
[q,r]=size(sortedpeaks);
sortedpeaks=[sortedpeaks(q:-1:1)' sortedpeaks(2*q:-1:q+1)' sortedpeaks(3*q:-1:(2*q)+1)'];
sprintf('Index    Freq    HVSR peak\n%5d, %8.4f, %8.4e\n',sortedpeaks(1:s,:)')

% Identify troughs to help in identification of fundamental frequency
upperval=2*upperval; % Upper frequency search limit for troughs twice that for peaks
upperf=floor(upperval/df);
type='min'
[indmin]=stationary(freq(1:upperf),av(1:upperf),type);
troughs=[indmin' freq(indmin)' av(indmin)];

% Sort troughs in ascending order of amplitude and output first 's' values to screen
sortedtroughs=sortrows(troughs,3);
sprintf('Index    Freq    HVSR trough\n%5d, %8.4f, %8.4e\n',sortedtroughs(1:s,:)')

% Option to highlight peak values on plot
plotpeaks=0;
if plotpeaks==1;
   loglog(freq(indmax),av(indmax),'X'); hold on;
end;
```

```
% Specify plot axes and header information
grid on;
axis ([0.1 20 1e-1 1e2]);
set(gca,'Position',[0.2,0.3,0.6,0.4]); % Position given by [left,bottom,width,height]
xlabel('Frequency (Hz)','FontSize', 8);
ylabel('H/V ratio','FontSize', 8);
A=[0.1,0.2,0.3,0.4,0.5,0.7,1,1.5,2,3,4,5,6,7,8,9,10,12,15,20];
set (gca, 'XTick',A);
set (gca, 'XTickLabel',A,'FontSize', 4);

line1=sprintf('Microtremor point: %s, Set-up time (UTC): %s, StreamID: %s',...
   point_no,datestr(ist,0),streamID(1:4));
line2=sprintf('Adjacent averaging: %d points (%8.5f Hz bandwidth), window length %6.2fs, no
of windows %d',...
   offset, offset*2*df,w_length,numwin);
line3=sprintf('FFT vector length %d. Window function code %d.',N,itype);
line4=sprintf('Legend: Average HVSR (thick blk); +/- 1 standard deviation (thin black)');
text(-.2,1.3,line1,'Fontsize',10,'Units','normalized');
text(-.2,1.22,line2,'Fontsize',10,'Units','normalized');
text(-.2,1.14,line3,'Fontsize',10,'Units','normalized');
text(-.2,1.06,line4,'Fontsize',10,'Units','normalized');
```

APPENDIX I. MICROTREMOR DATA

Table I1 Summary of microtremor measurement locations

ID	Coordinates N	Coordinates E	Height (m)	StreamID	UTC	Date	District	Ground contact	Location category	Location description
1	40.82617	31.16348	?	4B52	14:42:05	30-May-01	N/A	CS	V	Darci Koyu - just south of Duzce - adjacent to tree
2	40.80613	31.14977	159	4B52	16:28:05	30-May-01	N/A	CS	V	nr. TEM OB10 (km 18+404) - surrounded by trees
3	40.82480	31.15913	?	4B52	09:15:11	31-May-01	N/A	CS	V	Darci Koyu - just south of Duzce - next to farmhouse
4	40.82777	31.15203	153	4B52	10:13:53	31-May-01	N/A	LS	OS	adjacent to open area with rubble piles
5	40.82962	31.14727	156	4B52	11:01:54	31-May-01	28	CS	OS	edge of fields, quiet rural setting, person on swing in adjacent compound (@10 m)
6	40.82745	31.13843	143	4B52	12:00:36	31-May-01	30	CS	V	uncompleted buildings in most of block
7a	40.83573	31.14090	147	4B47	15:27:31	31-May-01	17	CS	V	quiet cul de sac adjacent to vegetable garden and wood
7b	40.83573	31.14091	147	4B52	15:21:12	31-May-01	17	CS	V	quiet cul de sac adjacent to vegetable garden and wood
8a	40.83725	31.12835	144	4B52	17:08:20	31-May-01	17	A	Rd	extreme s.w corner of Duzce (Mergic/Esen Koyu)
8b	40.83725	31.12836	144	4B47	16:52:05	31-May-01	17	CS	V	extreme s.w corner of Duzce (Mergic/Esen Koyu)
9	40.81758	31.18750	?	4B47	06:15:47	01-Jun-01	N/A	CS	V	pull-in for shop and café; adjacent to wall
10	40.82035	31.19128	178	4B52	06:48:18	01-Jun-01	N/A	CS	V	adjacent to triangle of land with bus stop
11	40.82280	31.19235	?	4B47	07:28:25	01-Jun-01	N/A	CS	OS	open area
12	40.82690	31.19012	175	4B52	07:48:05	01-Jun-01	26	CS	OS	makeshift car park adjacent to brick yard (east) & garden (north); 40m south of D100
13	40.82922	31.19662	178	4B47	08:46:14	01-Jun-01	N/A	CS	V	opposite Haci Osman Yesil Kent Mosque, small village, adjacent to walled garden
14	40.82923	31.19090	222	4B52	08:43:28	01-Jun-01	15	CS	OS	dust track adjacent to agric land (north), adjacent 1-storey house
15	40.83408	31.18960	196	4B47	09:24:01	01-Jun-01	15	CS	W	adjacent to veneer factory - soil [cf. 096, 097]
16	40.83478	31.18502	176	4B52	09:33:43	01-Jun-01	15	CS	V	quiet lane, rural setting, beneath tree canopy
17	40.83413	31.18312	?			01-Jun-02				INSTRUMENT MALFUNCTION
18	40.83605	31.17990	162	4B52	12:47:20	01-Jun-01	14	CS	OS	grassed open area with patches of uncovered soil, used as a dumping ground
19	40.84016	31.17743	?	4B47	14:56:27	01-Jun-01	14	CS	V	adjacent to electricity sub-station
20	40.84427	31.17497	162	4B52	09:17:53	02-Jun-01	14	CS	OS	open area adjacent to 4-way junction
21	40.84552	31.17197	?	4B47	09:27:38	02-Jun-01	14	?	?	no notes
22	40.84677	31.16897	?	4B47	09:33:05	03-Jun-01	13	CS	G	garden in densely populated residential area
23	40.84905	31.17195	154	4B52	09:48:22	03-Jun-01	13	CS	OS	near school
24	40.84905	31.16795	?	4B47	10:33:14	03-Jun-01	13	CS	V	adjacent to damaged house
25	40.85170	31.17298	153	4B52	11:09:36	03-Jun-01	14	CS	OS	near canal; adjacent to lorry driver's house
26	40.85340	31.17033	159	4B52	14:36:41	03-Jun-01	8	CS	V	quiet residential area
27	40.85893	31.16885	155	4B47	14:37:08	03-Jun-01	8	?	?	cul de sac - near to Akcakoca Road
28	40.85340	31.17033	155	4B52	15:01:34	03-Jun-01	8	Conc	V	concrete plinth (20cm from each of 2 edges)
29	40.85873	31.24510	326	4B47	17:01:15	03-Jun-01	N/A	R	OS	ROCK outcrop overlooking Nalbantoglu
30	40.85880	31.24595	331	4B52	17:19:28	03-Jun-01	N/A	R	OS	ROCK outcrop overlooking Nalbantoglu
31	40.78583	31.26397	188	4B47	11:43:39	04-Jun-01	N/A	CS	V	nr. TEM bridge/viaduct 5 (obstructed GPS coverage)
32	40.79113	31.23597	?	4B52	15:23:01	04-Jun-01	N/A	CS	OS	nr. TEM OB17, established agricultural land
33	40.79113	31.23597	?	4B47	15:16:14	04-Jun-01	N/A	CS	OS	nr. TEM OB17, rough ground (filled for motorway construction)
34	40.80802	31.12738	230	4B52	11:34:12	05-Jun-01	N/A	CS	OS	nr. TEM UB2/UB2A, motorway bridge beam factory/storage area
35	40.79293	31.12510	?	4B47	13:44:47	05-Jun-01	N/A	CS	V	2km south of Duzce (Duraklar village)
36	40.77413	31.11635	160	4B52	14:01:28	05-Jun-01	N/A	CS	V	4km south of Düzce, quiet rural setting 250m east of main Beykoy - Duzce road

Table I1 (cont.)

ID	Coordinates N	E	Height (m)	StreamID	UTC	Date	District	Ground contact	Location category	Location description
37	40.75938	31.10925	178	4B47	15:23:18	05-Jun-01	N/A	CS	G	Aydinpinar Koyu (near fault trace)
38	40.78105	31.18388	218	4B52	17:45:41	05-Jun-01	N/A	CS	OS	agricultural land 200 m south of water treatment plant
39	40.85200	31.16467	155	4B47	09:15:51	08-Jun-01	12	CS	AL	wasteland adjacent to Akcakoca Road
40	40.85200	31.16468	155	4B52	09:15:43	08-Jun-01	12	GC	AL	wasteland adjacent to Akcakoca Road
41	40.85322	31.16005	147	4B47	10:23:44	08-Jun-01	12	CS	G	adjacent to partly-built house, soil
42	40.85322	31.16006	147	4B52	10:23:32	08-Jun-01	12	Conc	G	adjacent to partly-built house, concrete overlying soil
43	40.84905	31.15665	148	4B47	12:59:50	08-Jun-01	12	CS	OS	open area adjacent to access track
44	40.85230	31.15715	?	4B52	13:20:46	08-Jun-01	12	CS	G	near blackberry tree
45	40.85095	31.14943	146	4B47	14:13:39	08-Jun-01	11	CS	V	dense residential area, opposite school
46	40.85027	31.14520	133	4B47	14:50:09	08-Jun-01	11	CS	OS	long, narrow open area, slightly cracked soil
47	40.84932	31.14315	146	4B47	15:27:50	08-Jun-01	9	CS	W	wooded area to rear of car park of D100 service station, opposite cemetery
48	40.85093	31.13780	146	4B47	16:18:35	08-Jun-01	9	CS	OS	open area immediately south of river bund; adjacent to new building foundation
49	40.85337	31.13477	154	4B52	16:31:45	08-Jun-01	6	CS	V	very quiet rural setting (nw corrner of Duzce - Beslanbey Koy)
50	40.84495	31.16112	?	4B47	07:21:16	09-Jun-01	20	CS	W	adjacent to open area with hardcore base now used as lorry park
51	40.84452	31.15515	?	4B47	08:17:37	09-Jun-01	19	CS	G	front walled garden of damaged building, adjacent to driveway
52	40.84193	31.14945	?	4B47	08:59:25	09-Jun-01	19	CS	G	sheltered back garden of 1-storey house
53	40.83828	31.15180	152	4B47	09:37:19	09-Jun-01	24	LS	G	soil patch in garden (crumbly surface), (nearby main sewer pipe?)
54	40.83808	31.15768	157	4B52	10:27:15	09-Jun-01	24	CS	G	walled garden of 2-storey building; n of large 4-storey "Durmazlar Mobilya Sarayi"
55	40.83450	31.16615	165	4B47	11:41:51	09-Jun-01	25	CS	R	in river channel sediments, dry, silty soil
56	40.83475	31.16732	158	4B52	11:49:03	09-Jun-01	25	CS	OS	within 100m of 055 - bushy area adjacent to all weather sports ground
57	40.83228	31.16547	169	4B47	12:27:01	09-Jun-01	29	CS	V	next to doctors' house, near location of (collapsed) oldest workshop in Duzce
58	40.83063	31.17165	169	4B47	13:07:33	09-Jun-01	29	CS	OS	farm land, small trees
59	40.82523	31.17433	175	4B47	13:45:22	09-Jun-01	N/A	LS	W	south-east extremity of Duzce; adjacent to pile of dumped building rubble
60	40.84150	31.14440	147	4B47	14:27:57	09-Jun-01	19	LS	OS	"Orman Isletme Mudurlugu", extensive, apparently abandoned region
61	40.83937	31.13588	152	4B47	15:10:12	09-Jun-01	17	CS	G	front garden of Tugba and family
62	40.83872	31.17030	162	4B47	07:03:16	10-Jun-01	22	CS	V	access track off main road
63	40.84227	31.16637	160	4B47	07:42:10	10-Jun-01	21	CS	V	nr building demolition works
64	40.84465	31.16290	157	4B47	08:27:17	10-Jun-01	20	CS	V	adjacent to large open area to north, verge of footpath
65	40.84468	31.13813	158	4B47	09:04:31	10-Jun-01	17	CS	V	adjacent to appartment block
66	40.84568	31.13412	144	4B47	09:43:49	10-Jun-01	17	CS	OS	grassed field (grazing land for cows)
67	40.84547	31.12588	145	4B47	10:20:37	10-Jun-01	17	CS	OS	western-most measurement - dust-track - wide open space
68	40.84547	31.12589	145	4B52	10:24:59	10-Jun-01	17	CS	OS	western-most measurement - dust-track - wide open space
69	40.83415	31.12838	179	4B47	11:37:30	10-Jun-01	29	CS	V	adjacent to new (still-under-construction) 5-storey building
70	40.83235	31.15810	168	4B47	12:09:07	10-Jun-01	29	CS	V	adjacent to gap in buildings (evidnce of collapse), opposite corner to shop
71	40.83030	31.15160	153	4B47	12:41:03	10-Jun-01	28	CS	G	garden in residential area; mainly 1 and 2-storey houses
72	40.83358	31.15268	151	4B47	13:11:23	10-Jun-01	28	CS	V	Ms 5.3 EQ @ 540 km picked up during measurement
73	40.83638	31.14807	143	4B47	13:46:07	10-Jun-01	28	CS	V	near to Asar Suyu and damaged school
74	40.83138	31.14522	147	4B47	14:20:07	10-Jun-01	28	CS	OS	soil between trees in orchard, adjacent to temporary village

Table I1 (cont.)

ID	Coordinates N	E	Height (m)	StreamID	UTC	Date	District	Ground contact	Location category	Location description
75	40.84012	31.17542	153	4B47	12:04:59	11-Jun-01	23	CS	OS	field/garden adjacent to house, tent pitched nearby
76	40.84637	31.17232	166	4B52	12:22:58	11-Jun-01	14	CS	W	edge of footpath through wood, soil slightly undulating/slightly cracked
77	40.84632	31.15023	158	4B47	13:30:52	11-Jun-01	18	CS	OS	open area just off dual carriageway
78	40.84637	31.14442	154	4B52	13:48:27	11-Jun-01	18	CS	V	broad verge on bend in quiet road, rural setting, small holdings nearby
79	40.83803	31.14527	150	4B47	14:43:33	11-Jun-01	27	CS	G	in grounds of mosque
80	40.83792	31.13750	149	4B47	15:14:25	11-Jun-01	17	CS	OS	school yard (some trees nearby)
81	40.83972	31.13812	149	4B52	15:26:06	11-Jun-01	17	CS	V	adjacent to demolished factories/warehouses
82	40.84133	31.13360	153	4B47	16:17:59	11-Jun-01	17	CS	V	driveway to residential area
83	40.83743	31.13437	150	4B52	16:35:56	11-Jun-01	17	CS	V	adjacent to driving school
84a	40.86467	31.22168	206	4B47	09:21:55	12-Jun-01	N/A	CS	V	Nalbantoglu (6km ne of Düzce centre) - 1s instrument
84b	40.86467	31.22169	206	3A45	09:45:00	12-Jun-01	N/A	CS	V	Nalbantoglu (6km ne of Düzce centre) - 30s instrument
85a	40.86248	31.20878	160	4B47	11:32:47	12-Jun-01	N/A	CS	V	Kazikoglu (5km ne of Düzce centre), access road to farm - 1s instrument
85b	40.86248	31.20879	160	3A45	11:34:52	12-Jun-01	N/A	CS	V	Kazikoglu (5km ne of Düzce centre), access road to farm - 30s instrument
86a	40.84358	31.14880	155	4B47	13:25:31	12-Jun-01	18	Conc	IB	DZC strong-motion station - 1s instrument inside, next to s-m instrument
86b	40.84358	31.14881	155	3A45	13:30:00	12-Jun-01	18	Conc	IB	DZC strong-motion station - 30s instrument inside, next to s-m instrument
86c	40.84358	31.14882	155	4B52	13:39:06	12-Jun-01	18	CS	G	DZC strong-motion station - 1s instrument outside in garden
89a	40.84608	31.18562	164	4B47	15:46:59	12-Jun-01	14	CS	OS	Metek-Yahyalar road (3km ne of Düzce centre), farmer's field - 1s instrument
89b	40.84608	31.18562	164	3A45	15:53:22	12-Jun-01	14	CS	OS	Metek-Yahyalar road (3km ne of Düzce centre), farmer's field - 30s instrument
90	40.83425	31.17045	171	4B47	07:54:57	13-Jun-01	25	CS	OS	derelict (badly damaged area) near pipe installation works
91	40.82945	31.17875	167	4B47	08:25:28	13-Jun-01	26	CS	V	edge of track running alongside Asar Suyu river
92	40.83233	31.17418	173	4B52	08:36:47	13-Jun-01	26	CS	V	many prefabs for post-earthquake housing
93	40.83220	31.17728	163	4B47	09:20:13	13-Jun-01	26	CS	G	quiet residential area; end of cul de sac; communal garden/open area
94	40.82727	31.18187	169	4B47	10:03:23	13-Jun-01	26	CS	V	adjacent to dirt track access road to large house alongside Asar Suyu river
95	40.82635	31.18505	173	4B52	10:12:25	13-Jun-01	26	A	V	temporary prefab village built on fill area adjacent to Asar Suyu river
96	40.83410	31.18947	170	4B47	12:06:36	13-Jun-01	15	CS	W	adjacent to veneer factory - soil
97	40.83410	31.18948	96	4B52	12:06:24	13-Jun-01	15	A	Rd	adjacent to veneer factory - asphalt
98	40.83332	31.18633	173	4B47	12:43:09	13-Jun-01	15	CS	V	tree-lined track through centre of farmer's field (line of old river?)
99	40.83960	31.18478	170	4B47	13:29:00	13-Jun-01	14	CS	V	isolated cluster of houses; access tricky due to nearby construction work
100	40.83768	31.18278	167	4B47	14:00:22	13-Jun-01	15	CS	V	end of farm access road
101	40.83765	31.17733	170	4B47	14:39:57	13-Jun-01	23	CS	V	adjacent to ploughed fields
102	40.83765	31.17734	170	4B52	14:39:36	13-Jun-01	23	LS	OS	in ploughed field
103	40.85258	31.15365	160	4B47	16:31:59	13-Jun-01	11	CS	OS	Near canal; near telegaph pole
104	40.85258	31.15366	160	4B52	16:31:39	13-Jun-01	11	GC	OS	Near canal; near tree
105	40.74605	31.60722	760	4B47	09:26:00	14-Jun-01	N/A	CS	G	BOL strong-motion station - outside building in garden
106	40.74605	31.60723	760	4B52	09:25:24	14-Jun-01	N/A	Conc	IB	BOL strong-motion station - inside building, on plinth next to s-m instrument
107	40.78522	31.27177	252	4B47	12:06:25	14-Jun-01	N/A	CS	V	adjacent to TEM embankment (nr UB4/OB18), nr 1-storey house
108	40.83803	31.16423	165	4B47	13:01:19	14-Jun-01	25	H	V	outside Duzce Municipality; noisy central location
109	40.84117	31.16407	183	4B47	14:15:04	14-Jun-01	21	H	V	off side road
110	40.84200	31.15763	162	4B47	14:52:45	14-Jun-01	19	CS	OS	Duzce Park

Table I1 (cont.)

ID	Coordinates N	Coordinates E	Height (m)	StreamID	UTC	Date	District	Ground contact	Location category	Location description
111	40.84072	31.15897	164	4B47	15:27:48	14-Jun-01	19	GC	G	back garden of house # 8
112	40.83978	31.15412	160	4B47	16:05:31	14-Jun-01	24	CS	G	back garden of house near main intersection
113	40.84625	31.14030	161	4B47	12:22:13	15-Jun-01	17	CS	V	quiet side street; adjacent to house #5 - soil
114	40.84625	31.14031	161	4B52	12:31:43	15-Jun-01	17	A	Rd	quiet side street; adjacent to house #5 - asphalt
115	40.86163	31.17985	164	4B47	15:06:29	15-Jun-01	8	LS	OS	southern edge of tent village - Beyciler Town; very open area
116	40.85860	31.17412	161	4B52	15:25:43	15-Jun-01	8	CS	V	Adjacent to flour mill; rural setting; edge of track
117	40.85908	31.15347	158	4B47	16:20:35	15-Jun-01	7	CS	G	rural area - edge of small village

Notes
ID - microtremor measurement locations; simultaneous set-ups are indicated by a box
Coodinates obtained from field GPS measurements
Height - height above sea level; ? - not recorded
StreamID - see Table 7.1
UTC - measurement time (+3h to convert to local time)
District - see Table 7.2 for details
Ground contact specifies interface between instrument and ground: CS - compact soil; LS - loose soil; A - asphalt; Conc - concrete; H - hardcore; ? - not recorded
Location category: V - road verge; OS - open space; Rd - road; W - wooded area; IB - inside building; G - residential garden; ? - not recorded
Location description - abbrevs: TEM - Trans-European Motorway; OB - Overbridge; UB - Underbridge; D100 - main dual carriageway running E-W through Düzce

Table I2 Microtremor data summary

Point ID	f_p (Hz)	T_p (s)	A_{fp}	$A_{0.5-2}$	A_{2-5}	A_{5-10}	Notes
1	0.66	1.51	3.61	2.13	0.87	0.91	
2	0.76	1.31	3.92	2.34	1.59	0.85	
3	1.11	0.90	4.48	2.83	1.07	1.00	
4	0.94	1.06	3.37	2.42	0.76	0.42	
5	0.96	1.04	6.86	3.88	1.05	1.30	
6	0.92	1.09	4.71	2.92	1.10	0.74	
7a	0.62	1.62	3.82	2.48	1.24	1.02	
7b	1.05	0.95	2.97	2.26	1.24	1.02	point 7a has clearer peak
8a	0.73	1.38	2.29	1.63	1.29	0.57	very similar to point 8b
8b	0.79	1.27	2.51	1.69	1.40	0.58	
9	0.80	1.25	2.99	1.85	0.99	0.87	
10	1.23	0.82	3.80	2.54	1.13	0.97	
11	1.24	0.81	4.05	2.68	0.94	1.10	
12	1.35	0.74	4.39	2.72	0.84	0.86	
13	1.26	0.79	5.68	3.29	0.91	1.09	
14	1.39	0.72	6.60	3.04	0.76	0.90	
15				2.32	0.79	0.94	redundant measurement (same location as point 96)
16	0.99	1.01	2.85	2.11	0.87	1.04	
17							instrument malfunction
18	1.14	0.87	5.34	3.58	1.22	1.64	
19	1.36	0.73	4.49	2.54	0.91	1.14	
20	1.01	0.99	4.20	2.54	0.96	1.49	
21	0.73	1.37	3.32	2.36	0.94	1.56	
22	0.78	1.29	3.27	2.35	1.00	1.63	
23	0.99	1.01	3.59	2.23	0.98	1.14	
24	1.32	0.76	2.56	1.86	0.84	1.15	
25	1.19	0.84	2.89	1.99	1.02	1.40	
26	0.96	1.04	2.96	1.92	0.92	0.80	
27	0.69	1.46	2.45	1.60	1.12	1.22	H/V peak obscured
28	0.82	1.22	3.86				building foundation (open face)
29	4.97	0.20	3.50	2.70	2.24	2.34	spurious peaks in time-history (use point 30)
30	4.17	0.24	2.69	1.32	1.95	1.35	
31	5.59	0.18	6.32	9.70	4.61	3.37	likely soil-structure interaction from bridge
32	0.63	1.58	5.37	2.36	1.30	1.33	
33	0.63	1.58	4.13	1.96	1.19	1.15	
34	1.20	0.84	3.38	2.19	0.91	1.42	
35	1.21	0.83	2.58	1.78	1.61	1.52	
36	1.57	0.64	3.95	2.86	1.22	1.52	
37				1.60	1.14	1.24	no clear H/V peak
38				1.03	0.98	1.39	no clear H/V peak
39	0.88	1.14	4.22	2.80	1.30	1.47	point 40 has clearer peak
40	0.88	1.13	4.22	2.70	1.29	1.37	
41				6.48	1.59	1.72	H/V peak obscured
42	0.80	1.26		5.02	1.36	1.45	H/V peak obscured
43	0.77	1.30	6.31	3.79	1.26	1.21	H/V peak obscured
44	0.75	1.33	7.58	4.64	1.17	1.61	H/V peak obscured
45	0.92	1.08	3.80	2.43	1.06	1.17	
46	0.86	1.16	5.85	3.77	1.19	1.28	H/V peak obscured
47	0.89	1.13	4.02	2.44	1.20	1.10	
48	0.78	1.28	3.42	2.24	0.92	1.15	
49	0.59	1.69	4.53	2.05	1.34	1.95	
50	0.78	1.28	5.04	3.05	1.22	1.38	
51	0.80	1.25	6.11	2.86	1.15	0.88	
52	0.62	1.62	6.56	3.15	1.43	1.23	
53	0.77	1.30	4.05	2.70	1.26	0.78	
54	0.80	1.25	6.58	3.44	0.98	1.03	
55	0.70	1.42	5.23	3.03	1.04	1.06	
56	0.72	1.39	5.05	3.40	1.11	0.93	
57	0.95	1.06	4.39	3.46	0.92	0.78	
58	0.93	1.07	4.75	3.35	0.93	1.08	
59	0.95	1.05	3.03	2.17	1.09	1.00	
60	0.67	1.50	4.58	2.91	1.33	1.53	H/V peak obscured
61	0.93	1.07	4.21	3.11	1.39	1.51	H/V peak obscured
62	1.06	0.94	3.87	2.59	1.01	1.08	
63	0.98	1.02	3.76	2.35	0.99	0.99	
64	0.90	1.11	4.16	2.69	1.43	1.40	
65	0.99	1.01	3.02	2.15	1.04	1.03	
66	0.83	1.20	3.37	2.28	1.47	1.45	
67	0.75	1.34	5.23	3.15	1.20	1.34	H/V peak obscured
68	0.89	1.12		3.03	1.18	1.40	H/V peak obscured
69	0.97	1.03	2.97	2.18	0.86	0.57	
70	0.67	1.48	4.13	2.37	0.82	0.81	
71	0.77	1.31	4.17	2.70	1.09	0.96	
72	1.00	1.00	5.08	2.14	0.83	0.50	
73	0.52	1.94	4.55	2.62	1.12	0.86	
74	0.81	1.24	6.30	3.75	1.04	1.04	H/V peak obscured
75	0.67	1.50	5.77	3.20	1.13	1.22	
76	0.82	1.22	4.95	2.95	1.09	1.53	
77	0.74	1.35	5.76	2.63	1.40	1.25	

Table I2 (cont.)

Point ID	f_p (Hz)	T_p (s)	A_{fp}	$A_{0.5-2}$	A_{2-5}	A_{5-10}	Notes
78	0.76	1.32	5.77	2.51	1.12	1.17	
79	0.60	1.66	4.07	2.51	1.11	0.95	
80	0.73	1.37	4.30	2.80	1.04	1.05	H/V peak obscured
81	0.75	1.34	3.20	2.36	1.31	0.82	
82	0.56	1.78	3.25	2.09	1.54	1.23	
83	0.87	1.15	3.20	2.27	1.17	0.89	
84a				3.83	1.58	1.51	H/V peak appears between 15 & 20 Hz - poorly defined
84b				3.23	1.55	1.45	H/V peak appears between 15 & 20 Hz - poorly defined
85a				5.72	4.37	1.76	H/V peak obscured - point 85b gives clearer peak
85b	2.88	0.35	7.41	3.02	4.19	1.71	
86a	0.74	1.34	3.64	2.20	1.32	0.86	recorded inside building (use point 86c)
86b	0.73	1.38	3.97	2.25	1.28	0.85	recorded inside building (use point 86c)
86c	0.71	1.40	3.64	2.27	1.26	0.91	
89a	0.98	1.02	3.31	2.34	1.05	1.17	
89b	0.97	1.03	3.46	2.31	1.08	1.19	use point 89a
90	1.30	0.77	4.46	2.85	0.87	0.78	
91	0.81	1.23	4.50	2.86	0.87	1.09	
92	1.20	0.83	4.43	2.67	0.91	0.84	
93	1.23	0.81	5.48	2.85	0.95	0.85	
94	1.17	0.85	2.90	2.21	0.86	0.91	
95	1.35	0.74	3.52	2.03	0.67	0.40	
96	0.99	1.01	7.08	3.83	0.83	0.83	measurement on soil (peak at 1.5 Hz influenced by machinery)
97	0.78	1.29		3.54	0.74	0.68	measurement on asphalt - use point 96
98	0.81	1.24	5.19	2.88	0.86	1.06	
99	1.40	0.72	3.40	2.35	1.24	1.56	
100	1.40	0.72	3.29	2.24	0.88	1.61	
101	1.32	0.76	4.31	2.97	1.22	0.90	
102	1.09	0.92	4.82	3.13	1.21	1.33	loose, ploughed soil
103	0.75	1.33	2.73	1.93	1.24	1.42	peak unclear
104	0.76	1.32	3.14	2.23	1.25	1.53	peak unclear
105	1.36	0.74	3.72	2.76	1.37	1.20	broadband H/V amplification - no distinct peak
106	1.30	0.77	3.01	2.12	1.22	0.87	broadband H/V amplification - no distinct peak
107	5.63	0.18	4.22	3.66	3.11	1.87	broadband H/V amplification between 3.5 and 6.5 Hz
108	0.87	1.15	4.52	2.05	0.65	0.41	
109	1.26	0.80	3.18	2.36	1.02	0.84	
110	1.10	0.91	2.93	2.10	1.34	1.10	
111	1.30	0.77	3.55	2.21	0.88	0.80	
112	0.80	1.26	3.68	2.38	1.25	0.92	
113	0.72	1.39	3.45	2.16	1.08	0.71	
114	0.71	1.40	3.58	2.15	1.06	0.74	measurement on asphalt - use point 113
115	0.95	1.06	3.58	2.01	1.18	1.18	
116	0.67	1.50	3.18	1.85	1.20	1.29	peak unclear
117	0.80	1.25	3.51	1.82	1.09	0.92	

Notes

Point IDs highlighted in grey represent points within central Düzce

f_p Predominant frequency of ground

T_p Predominant period of ground (reciprocal of f_p)

A_{fp} HVSR amplification at predominant frequency

$A_{0.5-2}$ average HVSR amplification (0.5 - 2.0 Hz)

A_{2-5} average HVSR amplification (2 - 5 Hz)

A_{5-10} average HVSR amplification (5 - 10 Hz)

Values highlighted in grey are included in the GIS-based analysis.

Where readings made in the centre of Düzce have been omitted, reasons are summarised in the Table.

Notable features or problems with the data are also summarised in the Table.

Figure I.1a Point 001 average HVSR +/− 1 sd

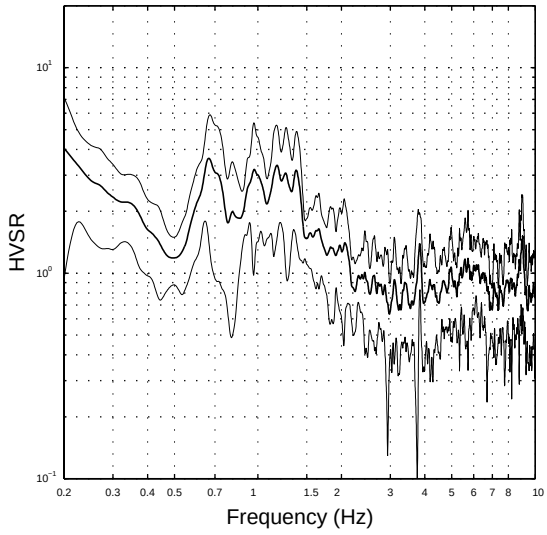

Figure I.1b Point 001 average FAS of velocity

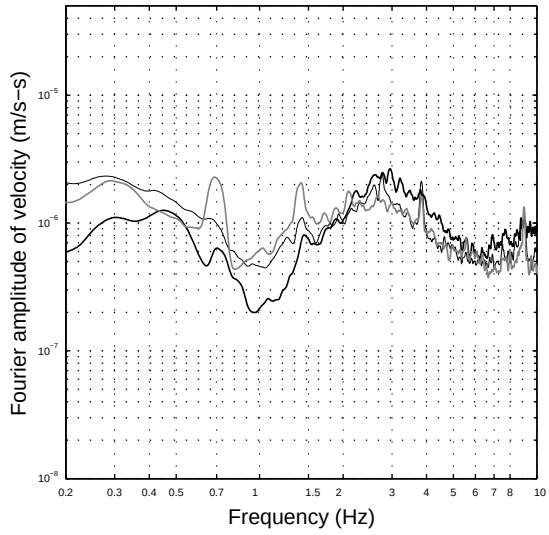

Figure I.2a Point 002 average HVSR +/− 1 sd

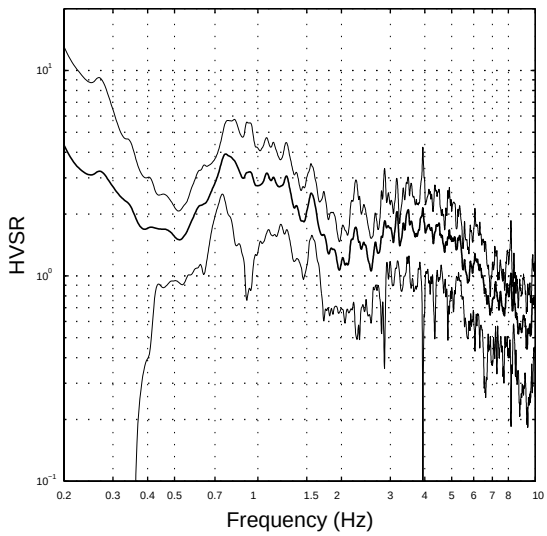

Figure I.2b Point 002 average FAS of velocity

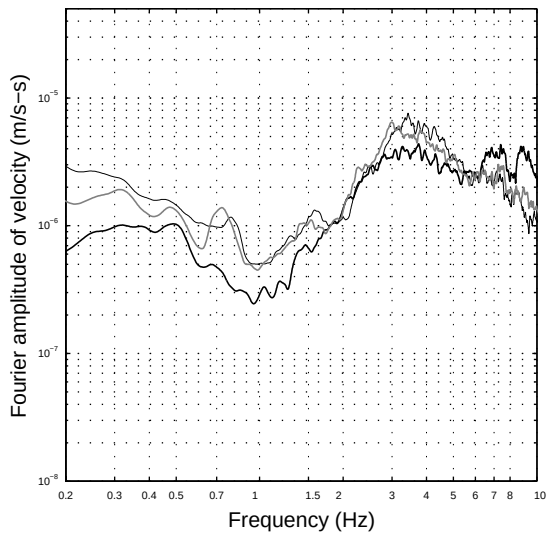

Figure I.3a Point 003 average HVSR +/− 1 sd

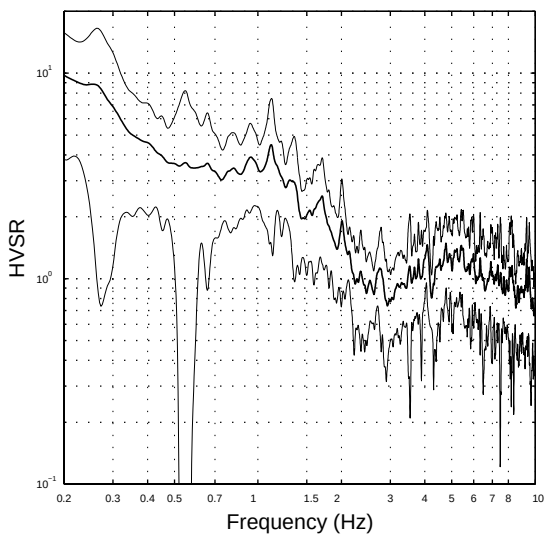

Figure I.3b Point 003 average FAS of velocity

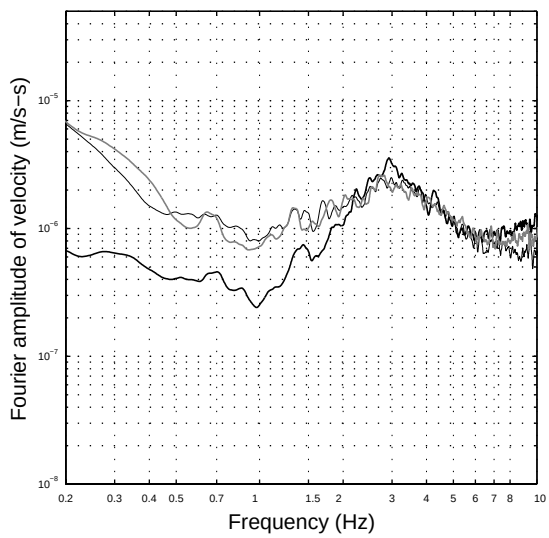

Average FAS plots: thick black − z−comp; thin black − n−s comp; thick grey − e−w comp

Figure I.4a Point 004 average HVSR +/− 1 sd

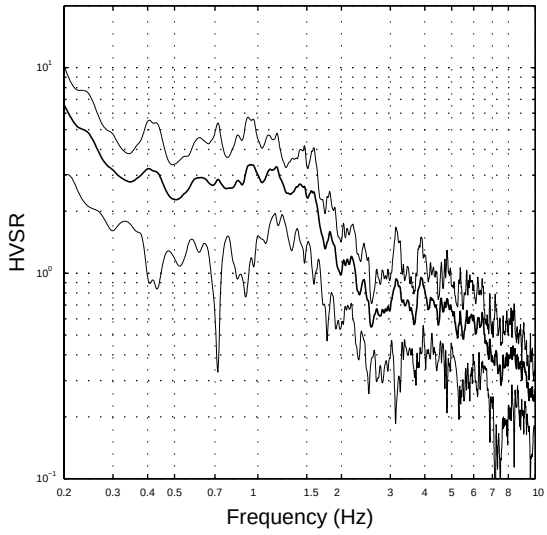

Figure I.4b Point 004 average FAS of velocity

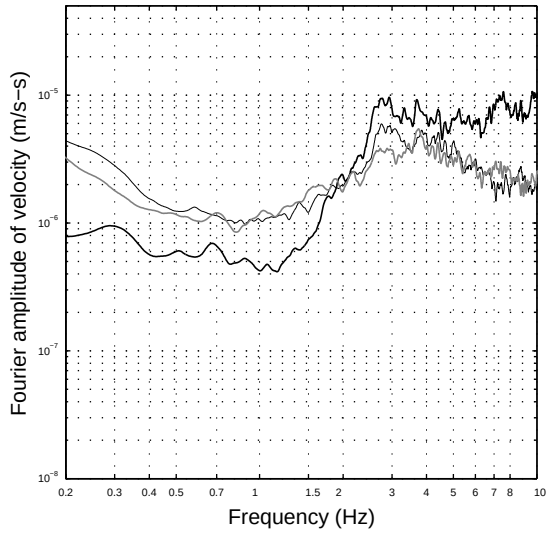

Figure I.5a Point 005 average HVSR +/− 1 sd

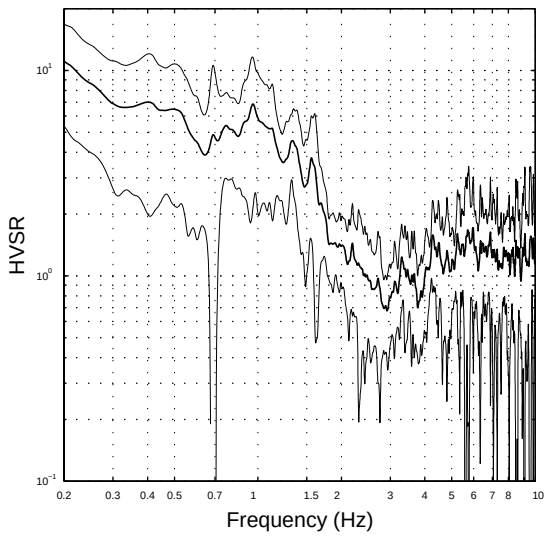

Figure I.5b Point 005 average FAS of velocity

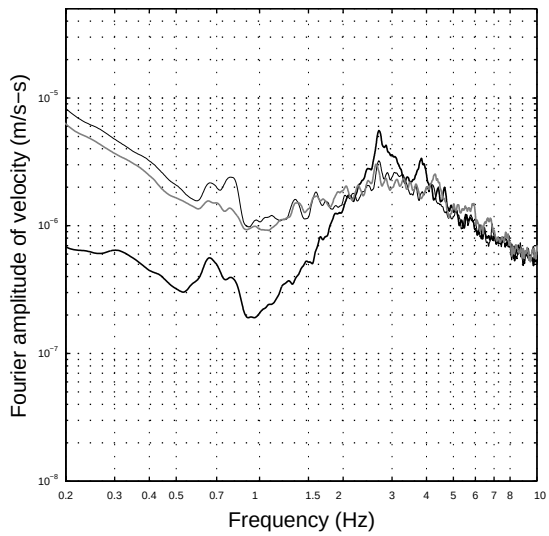

Figure I.6a Point 006 average HVSR +/− 1 sd

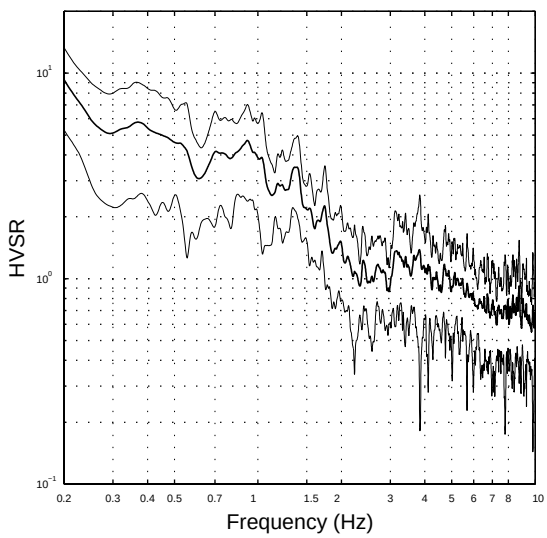

Figure I.6b Point 006 average FAS of velocity

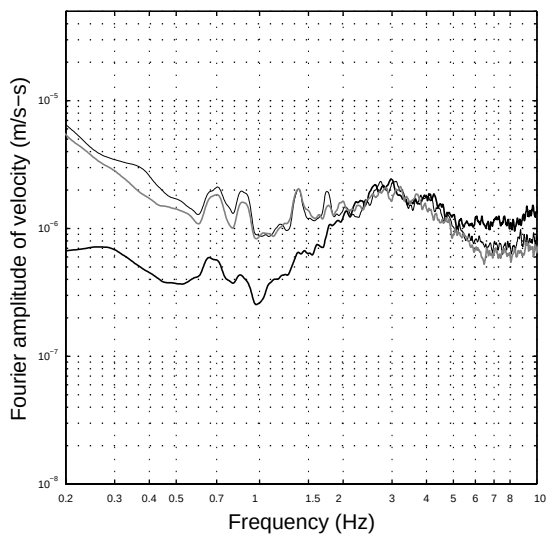

Average FAS plots: thick black − z−comp; thin black − n−s comp; thick grey − e−w comp

Figure I.7a Point 007a average HVSR +/− 1 sd

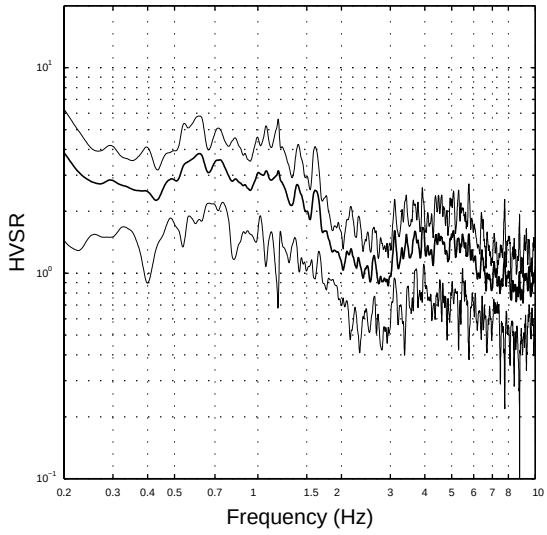

Figure I.7b Point 007a average FAS of velocity

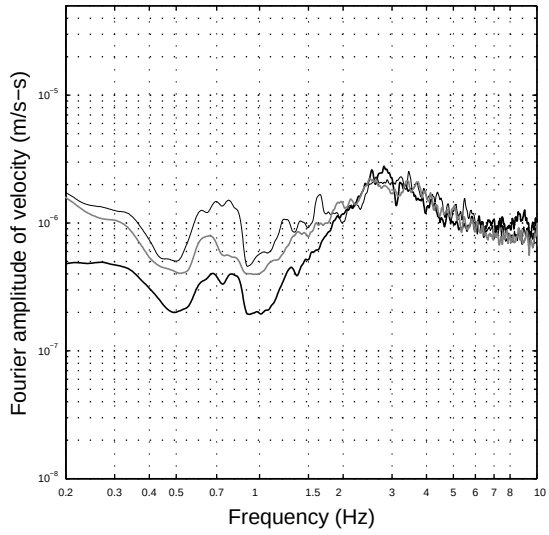

Figure I.8a Point 007b average HVSR +/− 1 sd

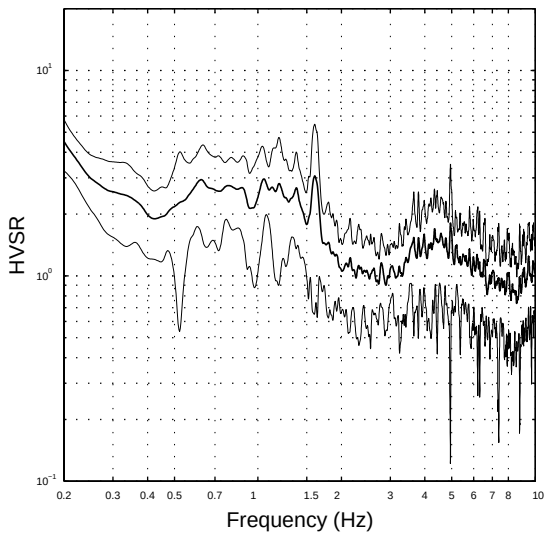

Figure I.8b Point 007b average FAS of velocity

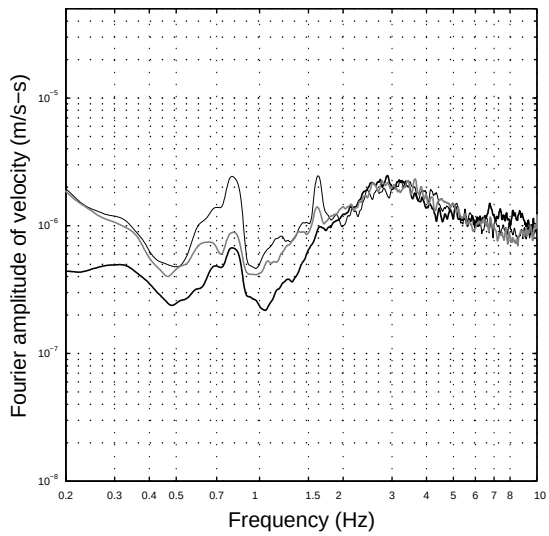

Figure I.9a Point 008a average HVSR +/− 1 sd

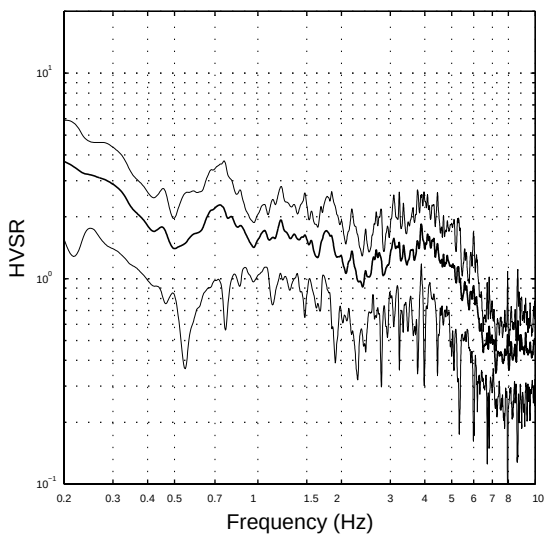

Figure I.9b Point 008a average FAS of velocity

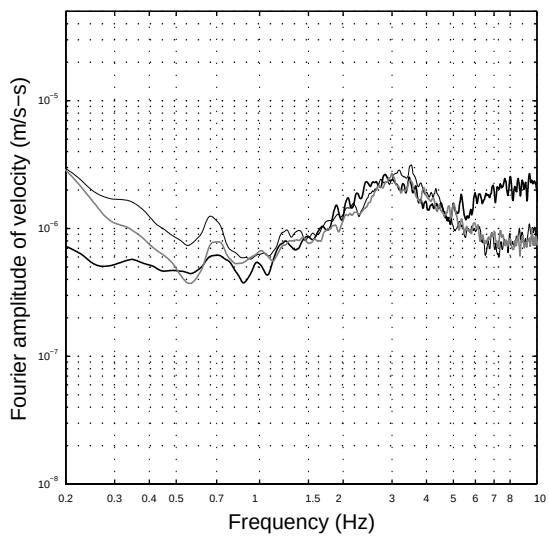

Average FAS plots: thick black − z−comp; thin black − n−s comp; thick grey − e−w comp

Figure I.10a Point 008b average HVSR +/− 1 sd

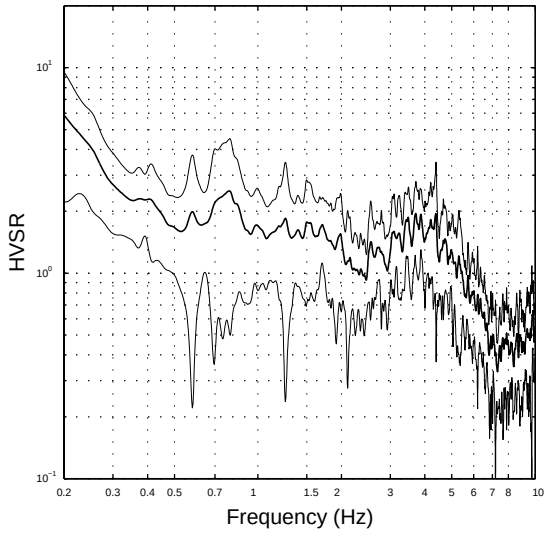

Figure I.10b Point 008b average FAS of velocity

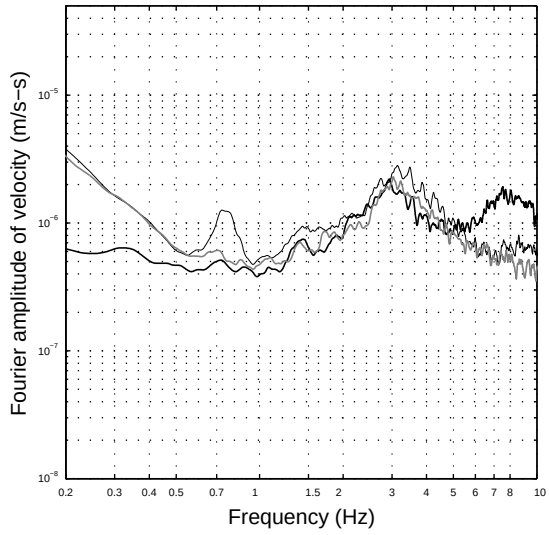

Figure I.11a Point 009 average HVSR +/− 1 sd

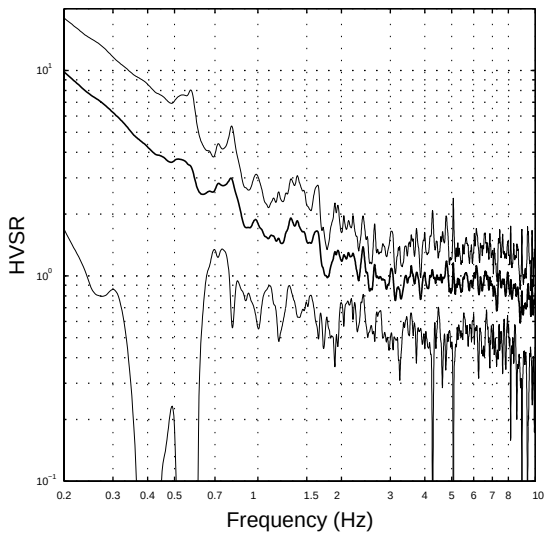

Figure I.11b Point 009 average FAS of velocity

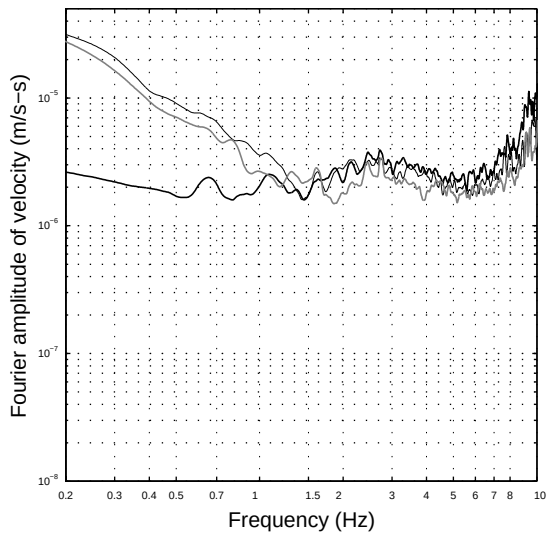

Figure I.12a Point 010 average HVSR +/− 1 sd

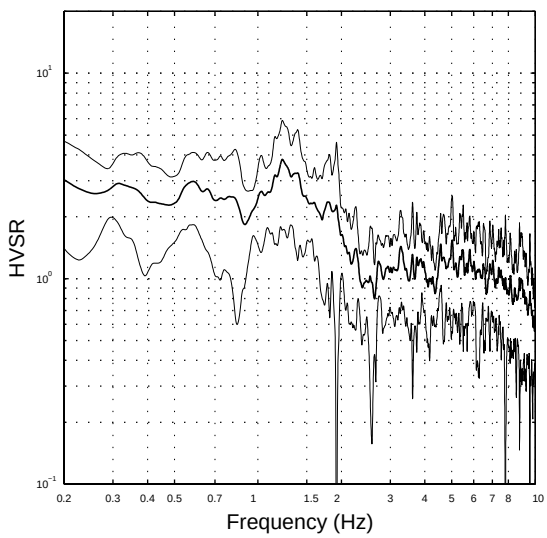

Figure I.12b Point 010 average FAS of velocity

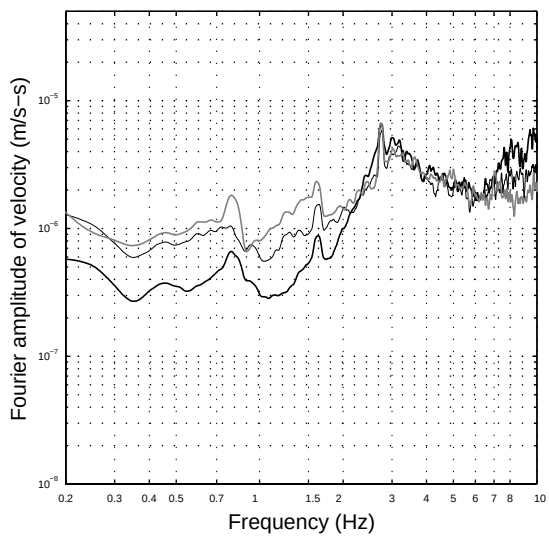

Average FAS plots: thick black − z−comp; thin black − n−s comp; thick grey − e−w comp

Figure I.13a Point 011 average HVSR +/− 1 sd

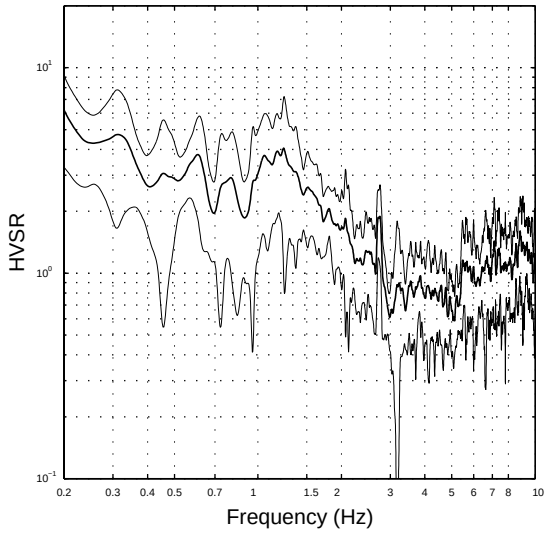

Figure I.13b Point 011 average FAS of velocity

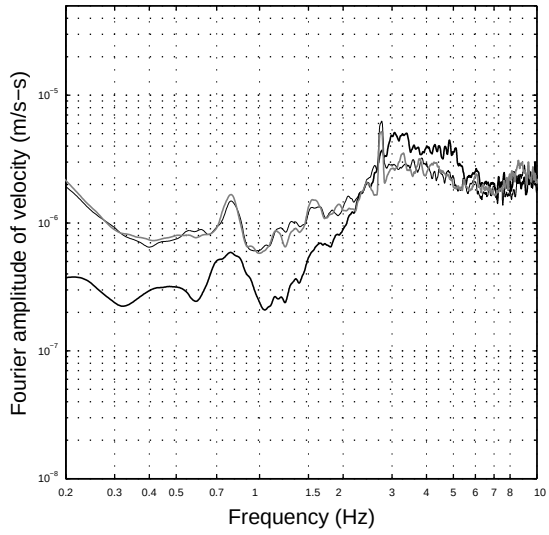

Figure I.14a Point 012 average HVSR +/− 1 sd

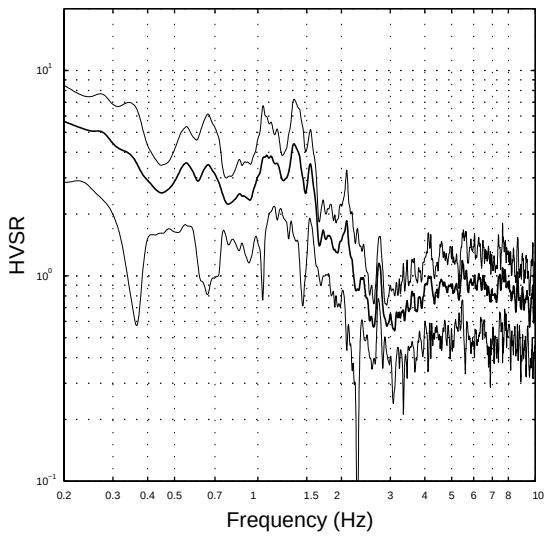

Figure I.14b Point 012 average FAS of velocity

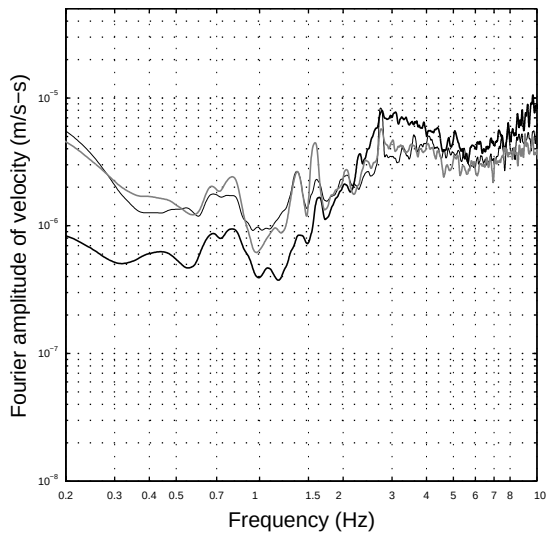

Figure I.15a Point 013c average HVSR +/− 1 sd

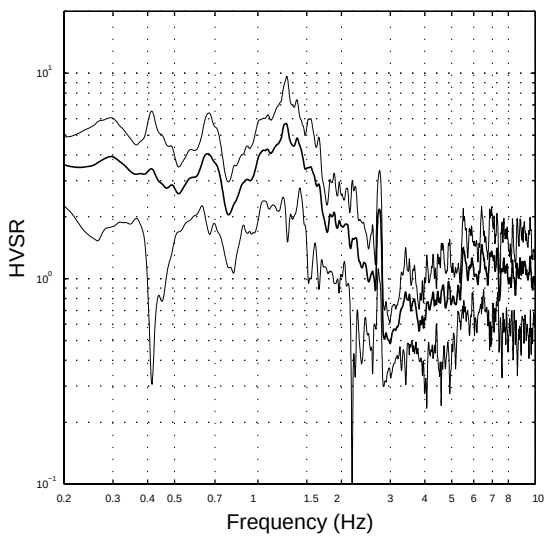

Figure I.15b Point 013c average FAS of velocity

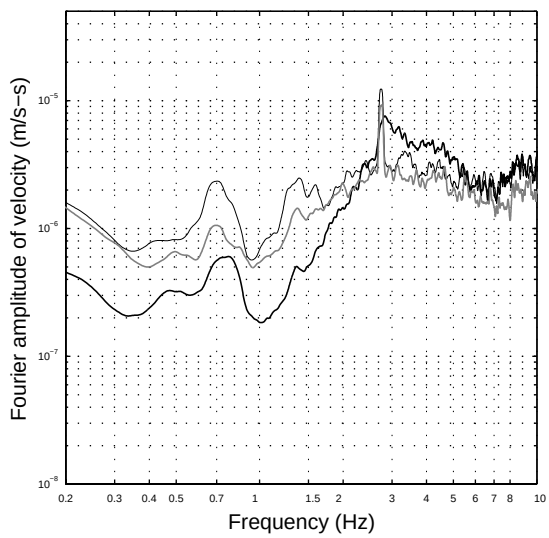

Average FAS plots: thick black − z−comp; thin black − n−s comp; thick grey − e−w comp

Figure I.16a Point 014 average HVSR +/− 1 sd

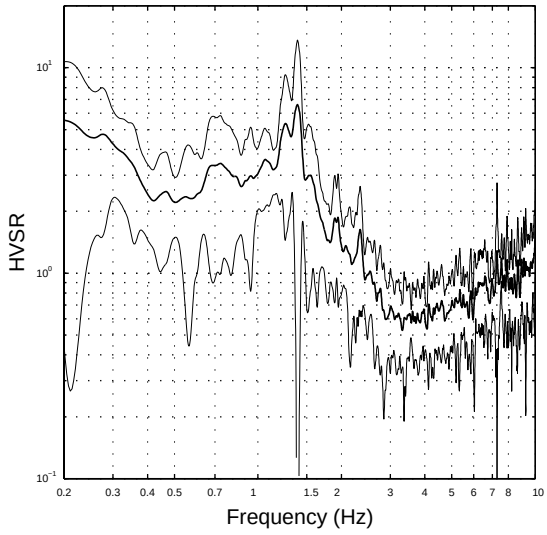

Figure I.16b Point 014 average FAS of velocity

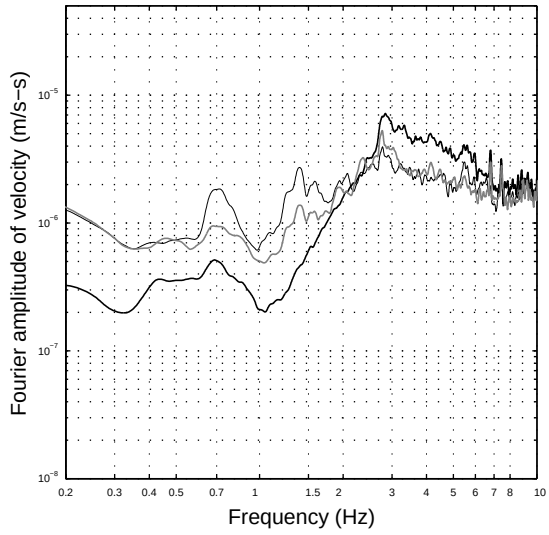

Figure I.17a Point 015 average HVSR +/− 1 sd

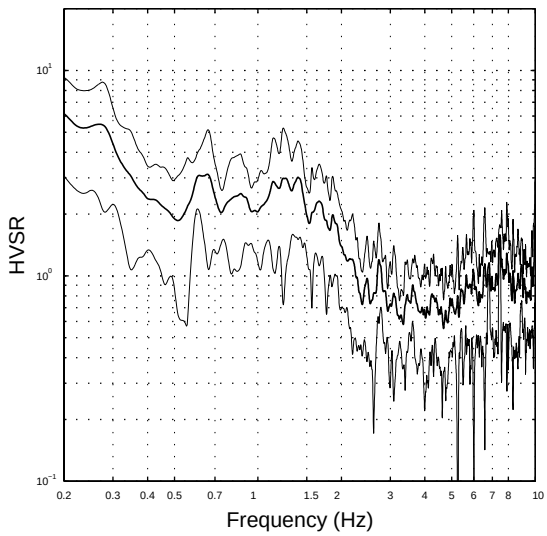

Figure I.17b Point 015 average FAS of velocity

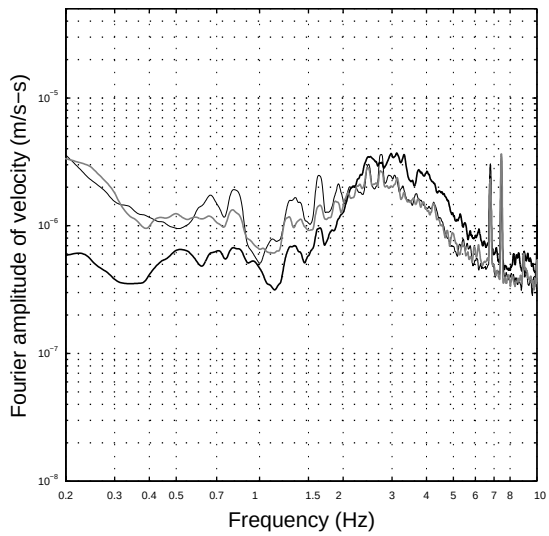

Figure I.18a Point 016 average HVSR +/− 1 sd

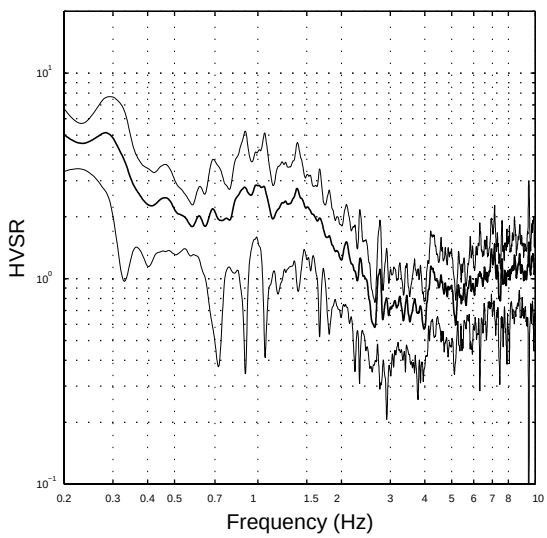

Figure I.18b Point 016 average FAS of velocity

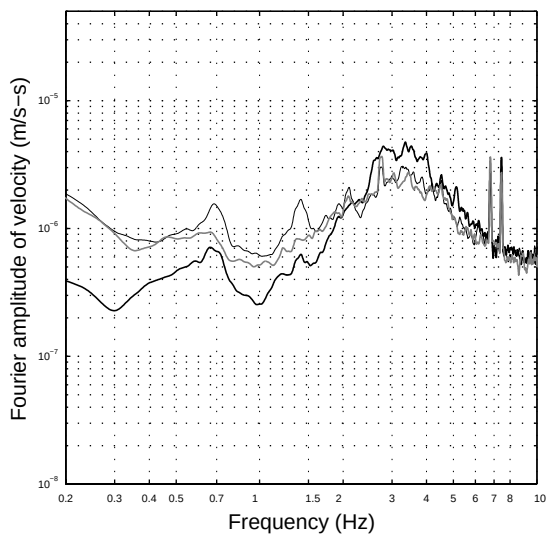

Average FAS plots: thick black − z−comp; thin black − n−s comp; thick grey − e−w comp

Figure I.19a Point 018 average HVSR +/− 1 sd

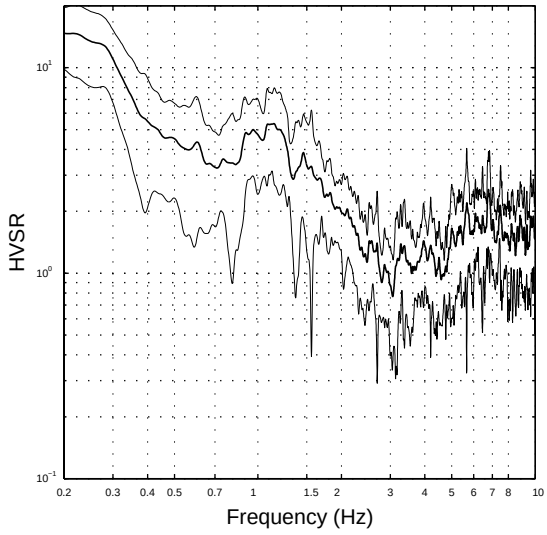

Figure I.19b Point 018 average FAS of velocity

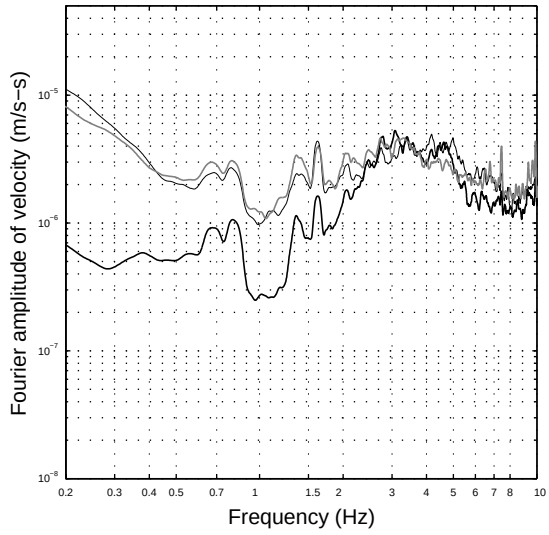

Figure I.20a Point 019 average HVSR +/− 1 sd

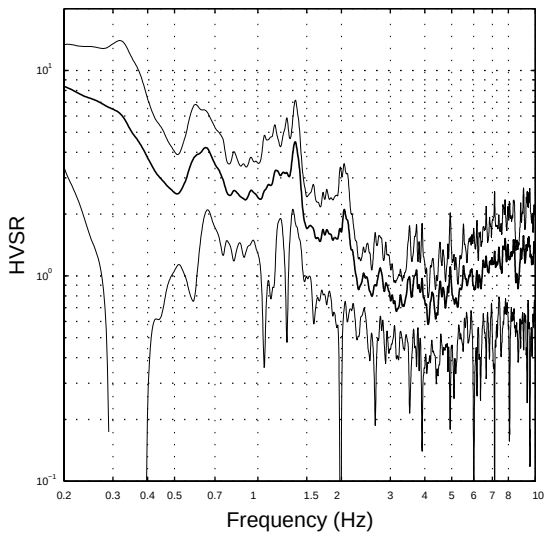

Figure I.20b Point 019 average FAS of velocity

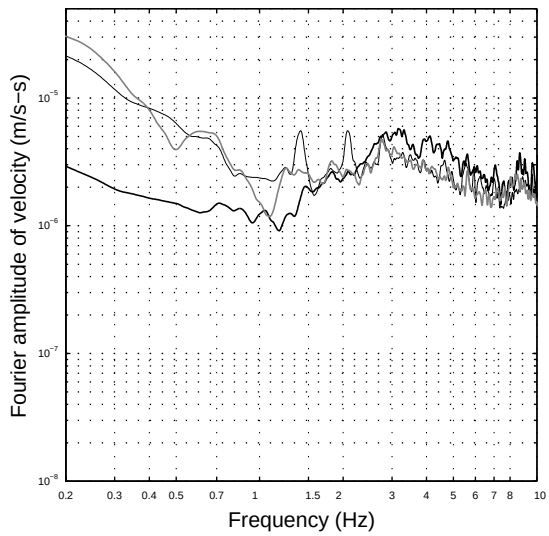

Figure I.21a Point 020 average HVSR +/− 1 sd

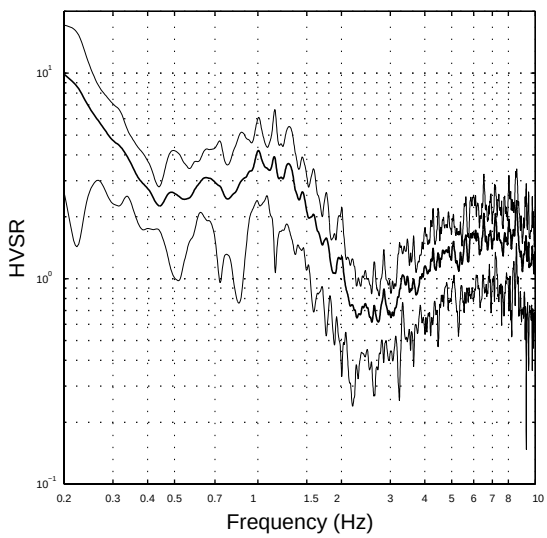

Figure I.21b Point 020 average FAS of velocity

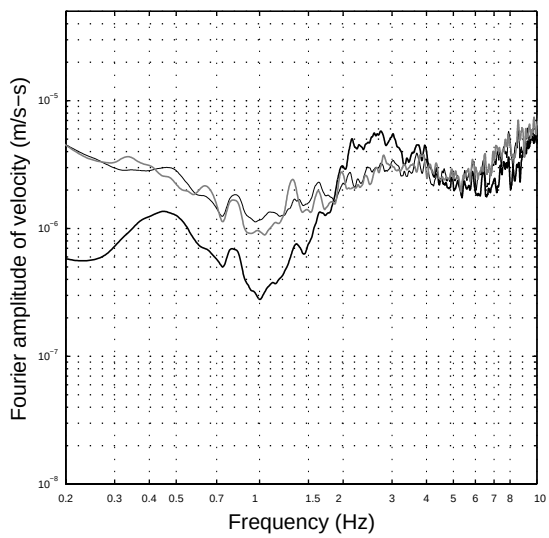

Average FAS plots: thick black − z−comp; thin black − n−s comp; thick grey − e−w comp

Figure I.22a Point 021 average HVSR +/− 1 sd

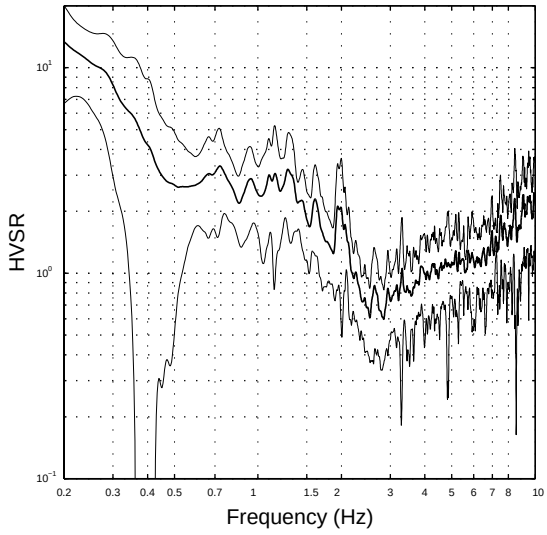

Figure I.22b Point 021 average FAS of velocity

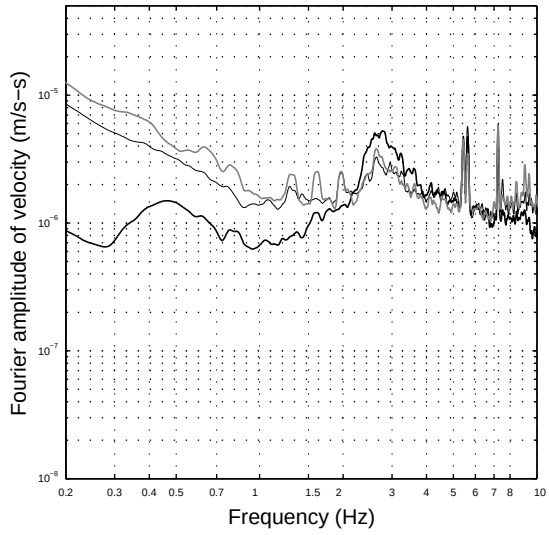

Figure I.23a Point 022 average HVSR +/− 1 sd

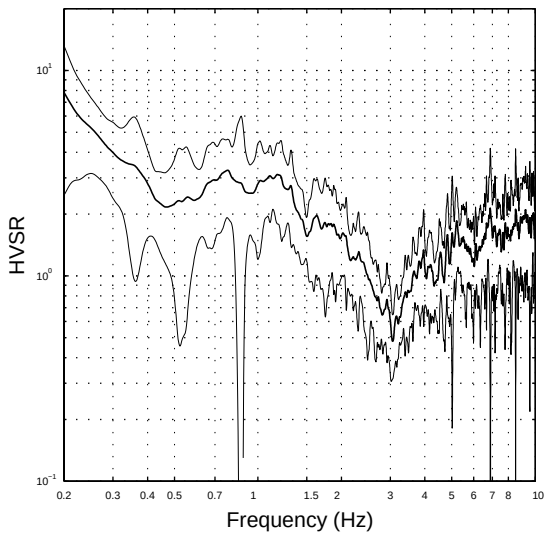

Figure I.23b Point 022 average FAS of velocity

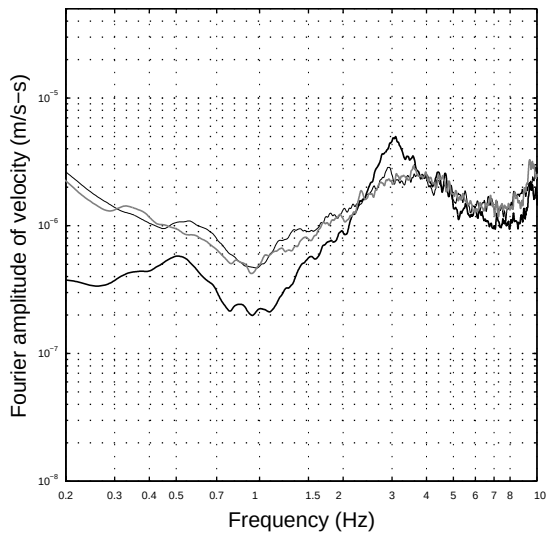

Figure I.24a Point 023 average HVSR +/− 1 sd

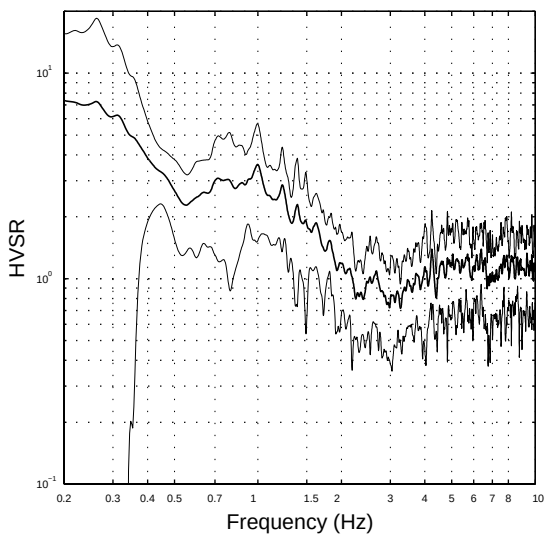

Figure I.24b Point 023 average FAS of velocity

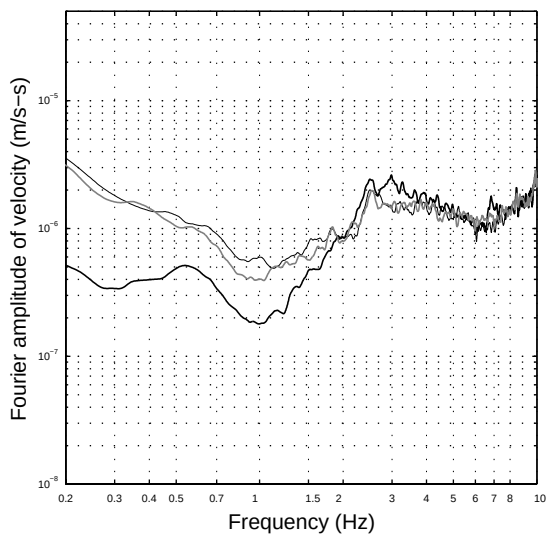

Average FAS plots: thick black − z−comp; thin black − n−s comp; thick grey − e−w comp

Figure I.25a Point 024 average HVSR +/− 1 sd

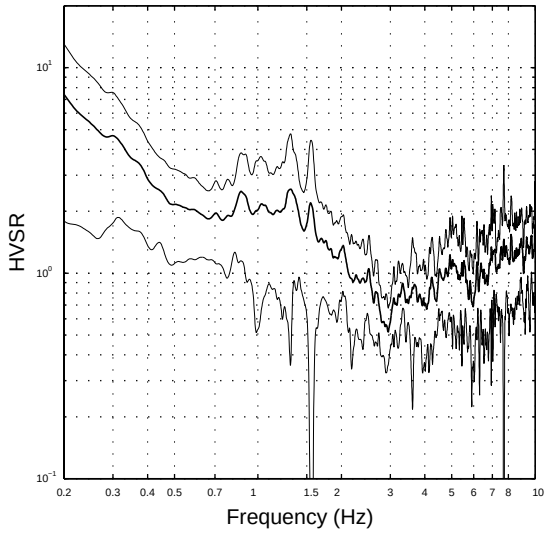

Figure I.25b Point 024 average FAS of velocity

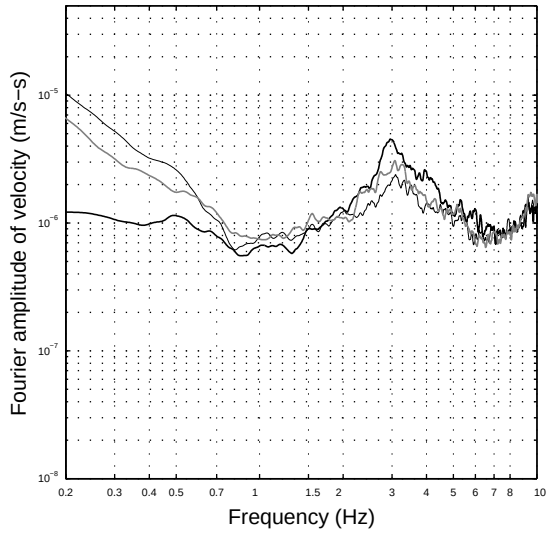

Figure I.26a Point 025 average HVSR +/− 1 sd

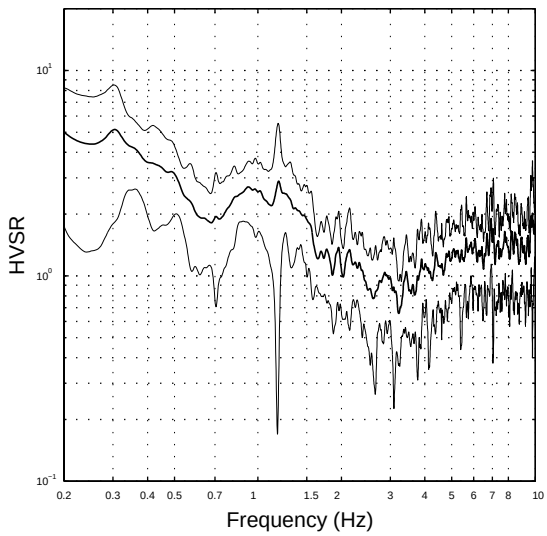

Figure I.26b Point 025 average FAS of velocity

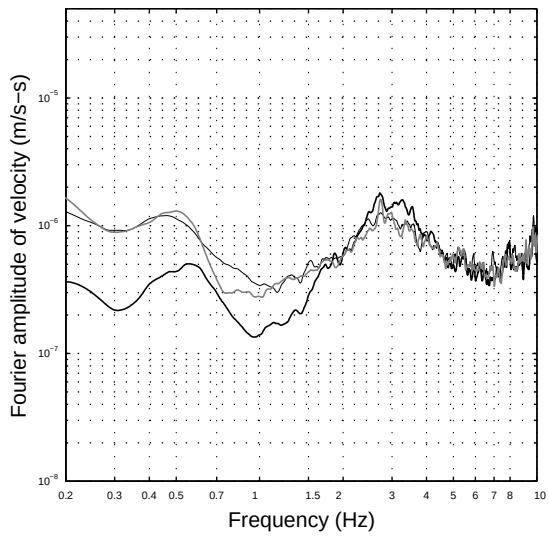

Figure I.27a Point 026 average HVSR +/− 1 sd

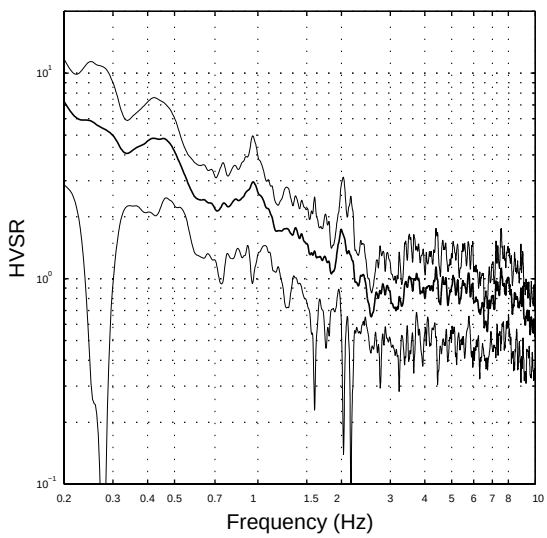

Figure I.27b Point 026 average FAS of velocity

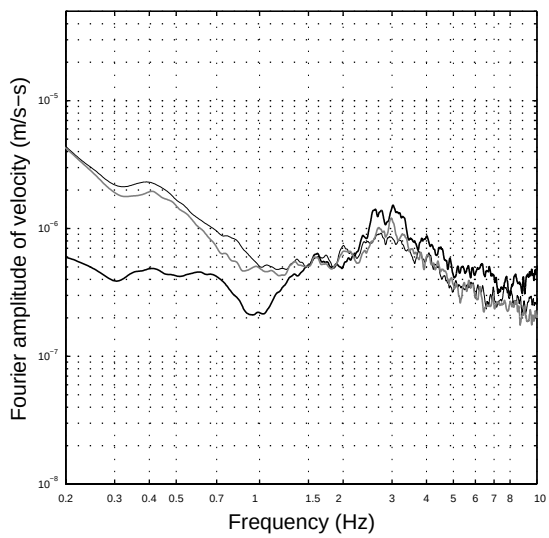

Average FAS plots: thick black − z−comp; thin black − n−s comp; thick grey − e−w comp

Figure I.28a Point 027 average HVSR +/− 1 sd

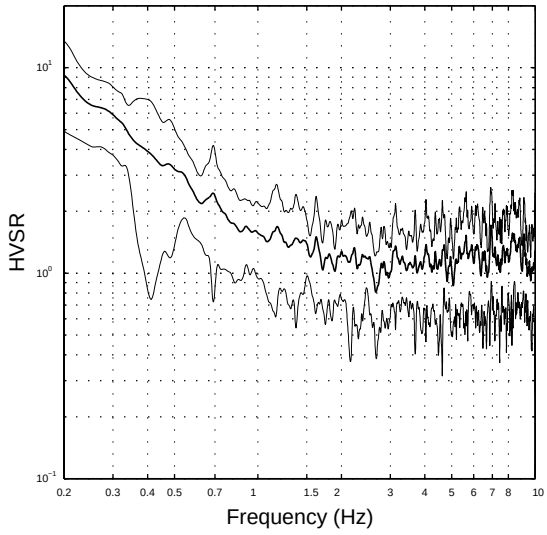

Figure I.28b Point 027 average FAS of velocity

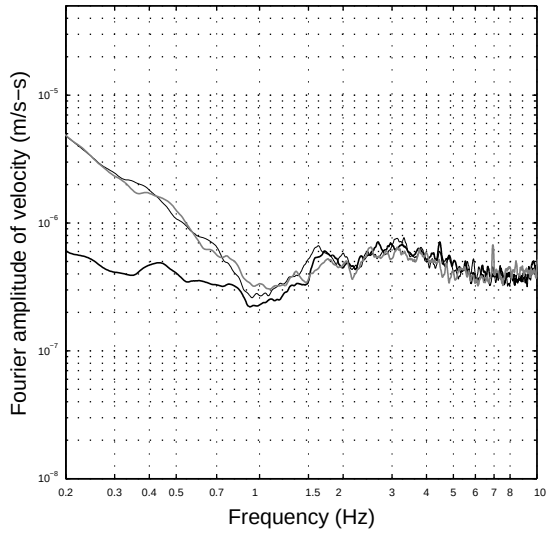

Figure I.29a Point 028 average HVSR +/− 1 sd

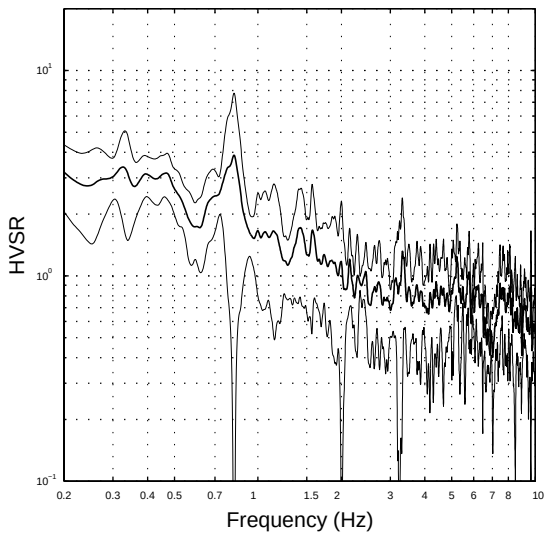

Figure I.29b Point 028 average FAS of velocity

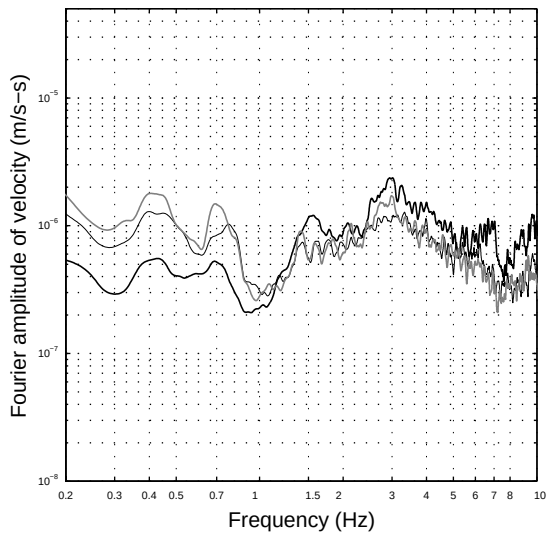

Figure I.30a Point 029 average HVSR +/− 1 sd

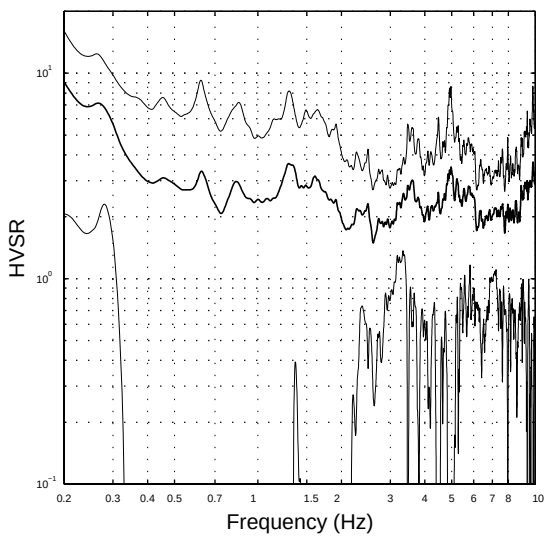

Figure I.30b Point 029 average FAS of velocity

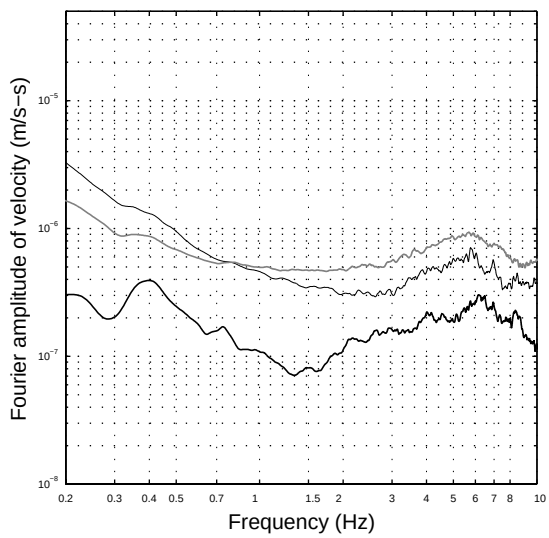

Average FAS plots: thick black − z−comp; thin black − n−s comp; thick grey − e−w comp

Figure I.31a Point 030 average HVSR +/− 1 sd

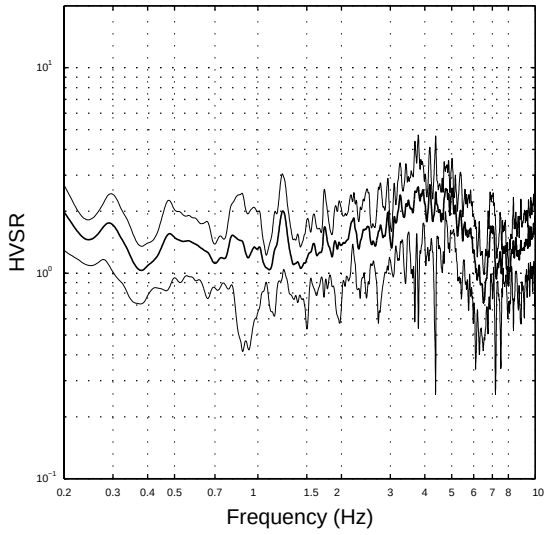

Figure I.31b Point 030 average FAS of velocity

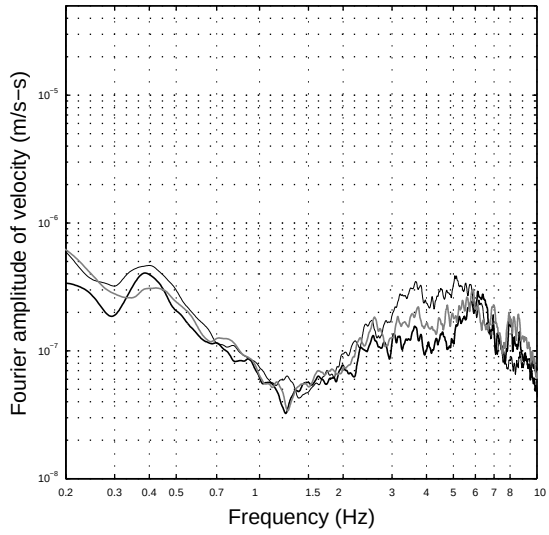

Figure I.32a Point 031 average HVSR +/− 1 sd

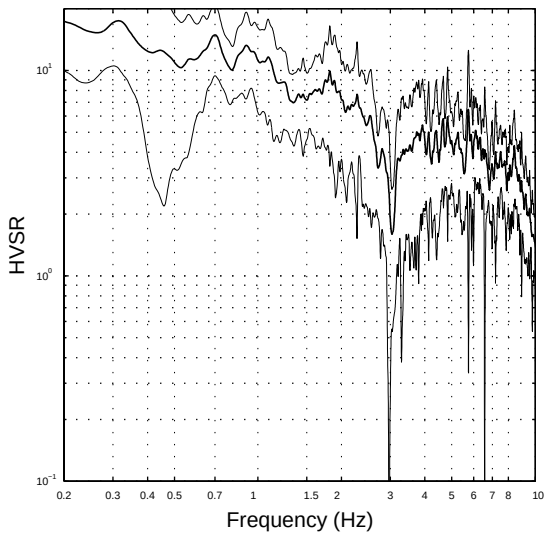

Figure I.32b Point 031 average FAS of velocity

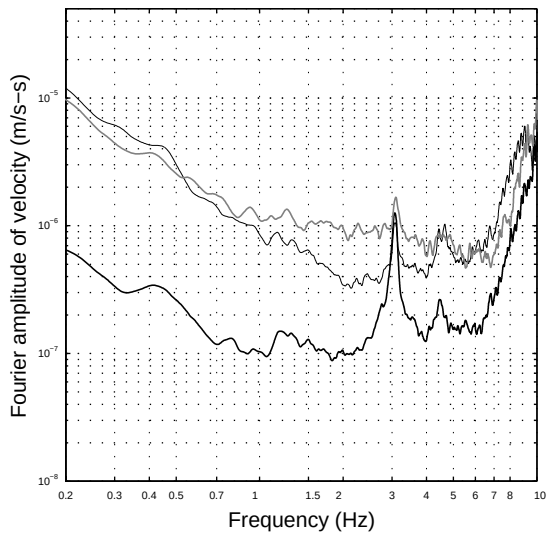

Figure I.33a Point 032 average HVSR +/− 1 sd

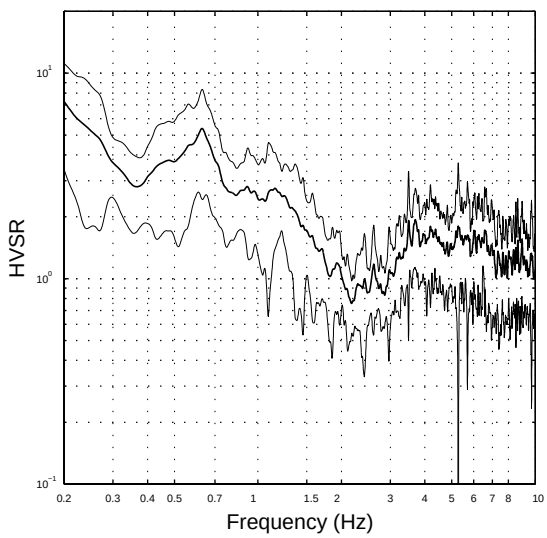

Figure I.33b Point 032 average FAS of velocity

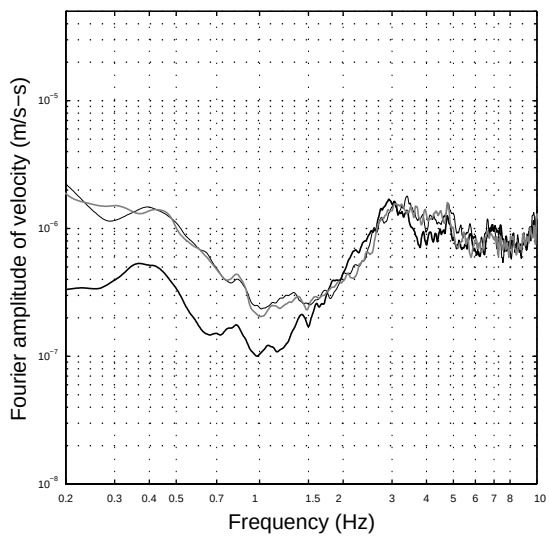

Average FAS plots: thick black − z−comp; thin black − n−s comp; thick grey − e−w comp

Figure I.34a Point 033 average HVSR +/− 1 sd

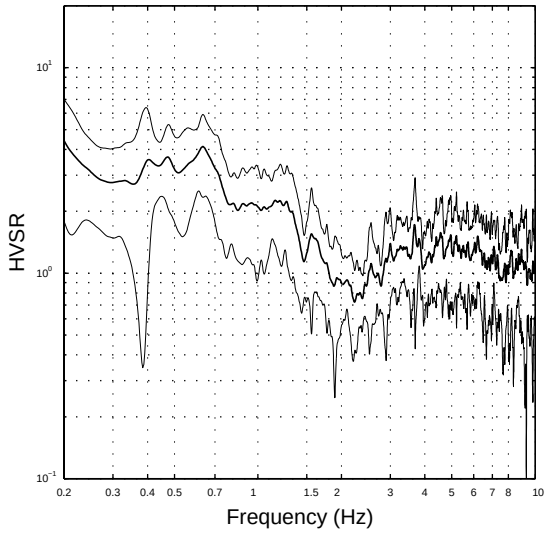

Figure I.34b Point 033 average FAS of velocity

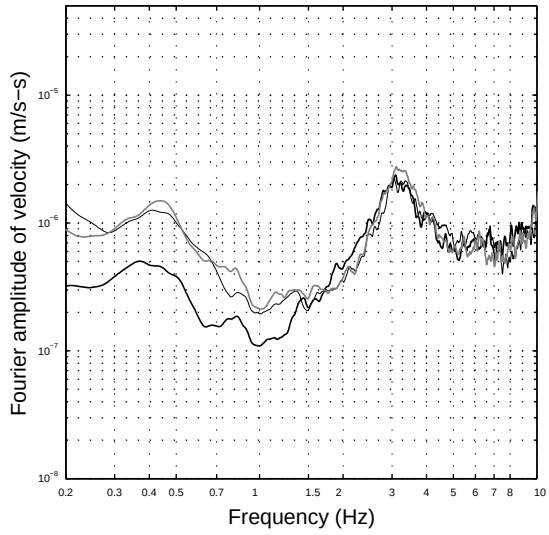

Figure I.35a Point 034 average HVSR +/− 1 sd

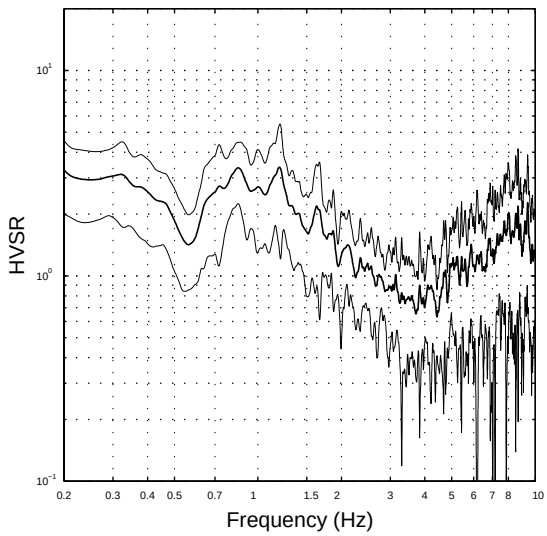

Figure I.35b Point 034 average FAS of velocity

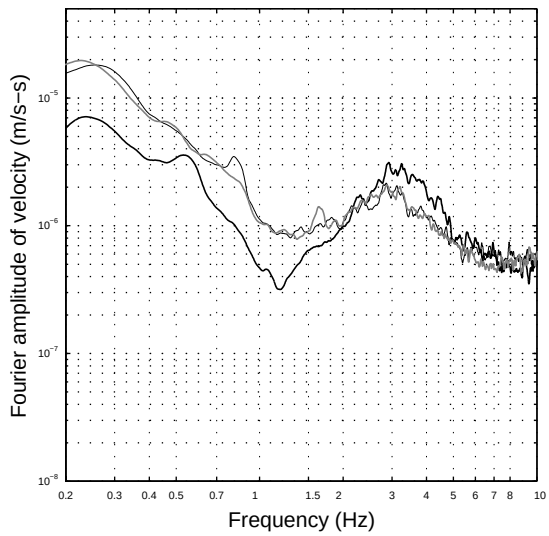

Figure I.36a Point 035a average HVSR +/− 1 sd

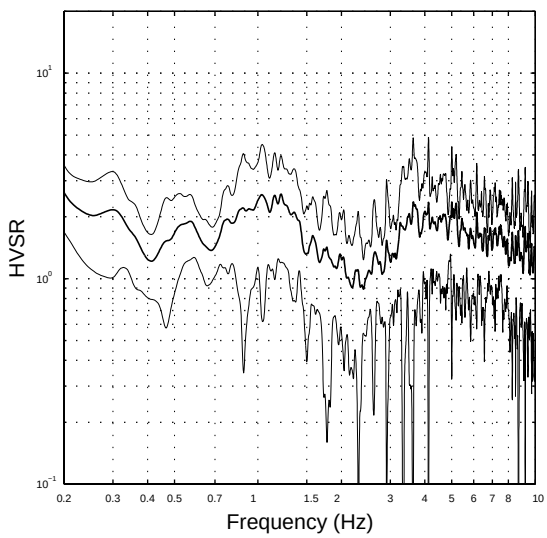

Figure I.36b Point 035a average FAS of velocity

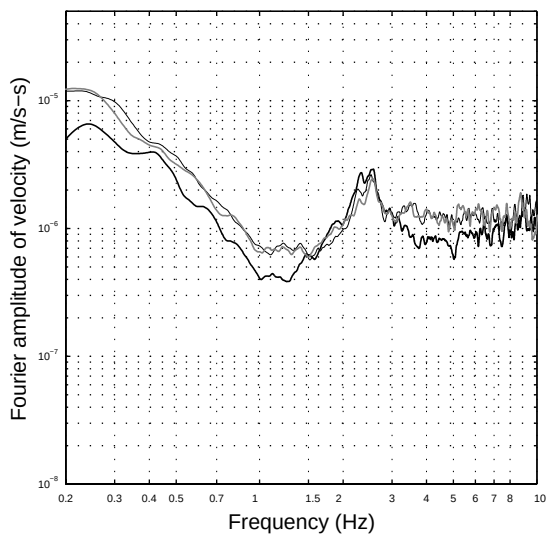

Average FAS plots: thick black − z−comp; thin black − n−s comp; thick grey − e−w comp

Figure I.37a Point 036 average HVSR +/− 1 sd

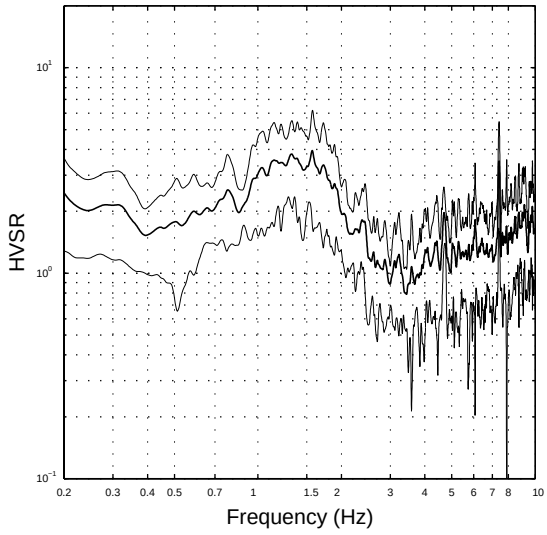

Figure I.37b Point 036 average FAS of velocity

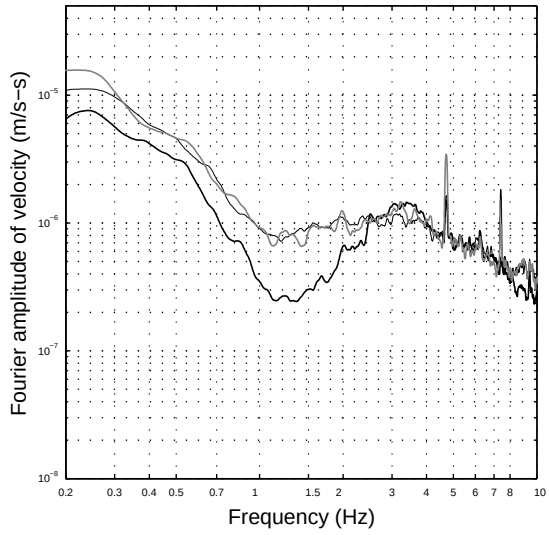

Figure I.38a Point 037 average HVSR +/− 1 sd

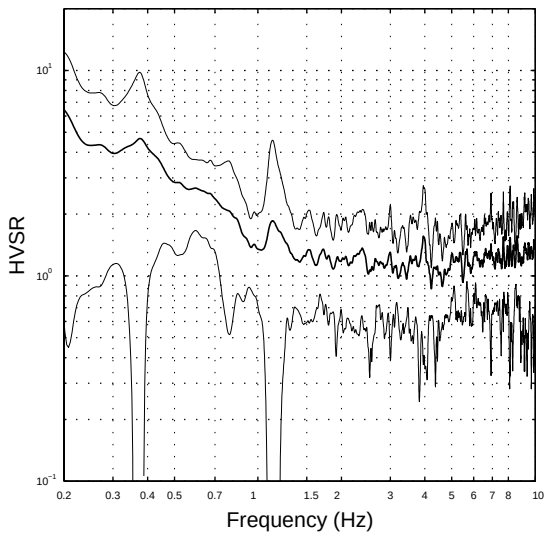

Figure I.38b Point 037 average FAS of velocity

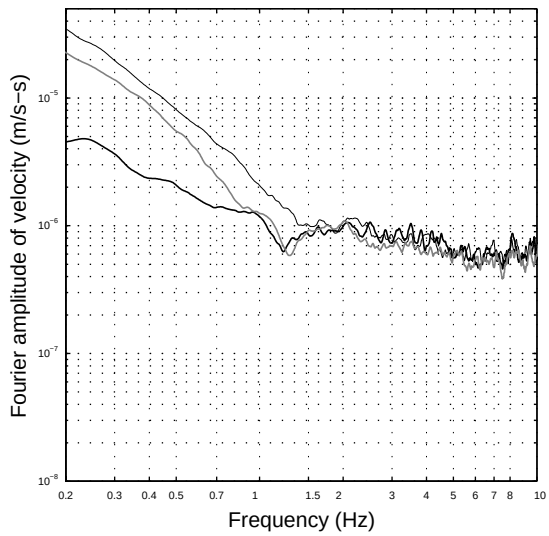

Figure I.39a Point 038 average HVSR +/− 1 sd

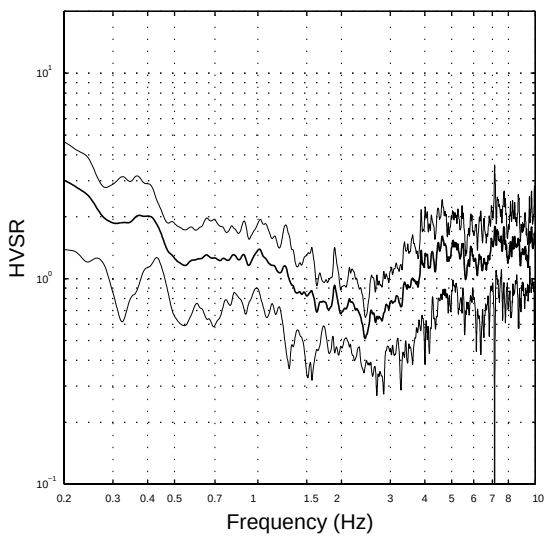

Figure I.39b Point 038 average FAS of velocity

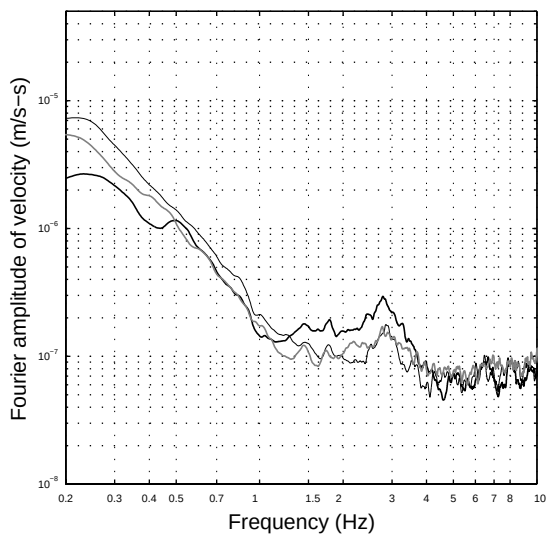

Average FAS plots: thick black − z−comp; thin black − n−s comp; thick grey − e−w comp

Figure I.40a Point 039 average HVSR +/− 1 sd

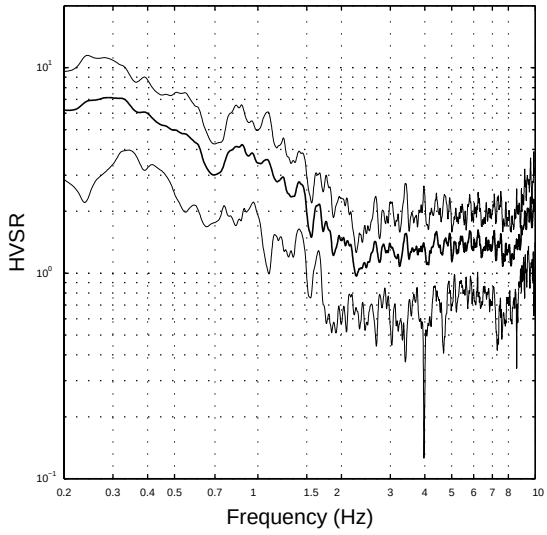

Figure I.40b Point 039 average FAS of velocity

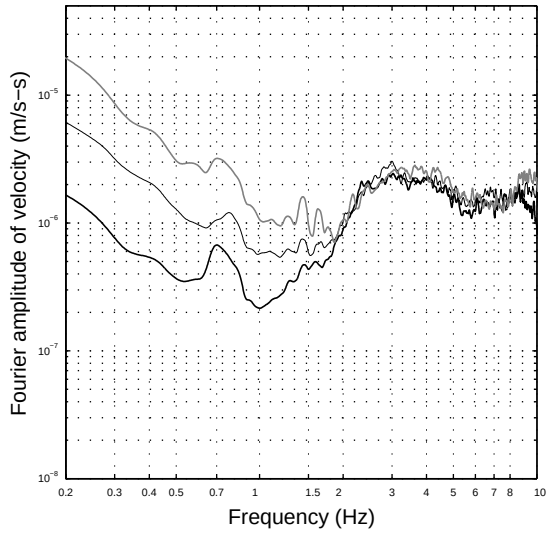

Figure I.41a Point 040 average HVSR +/− 1 sd

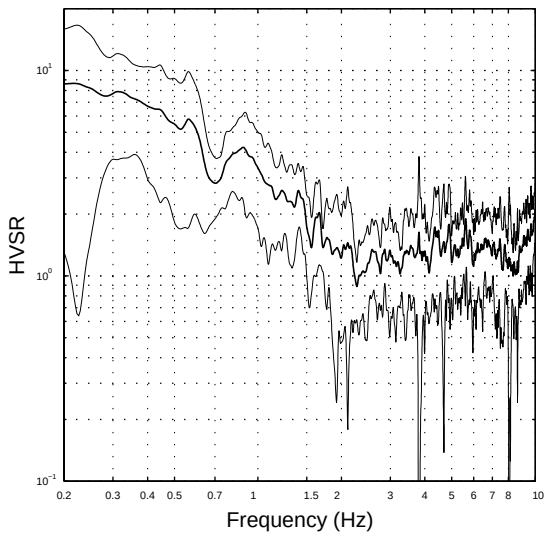

Figure I.41b Point 040 average FAS of velocity

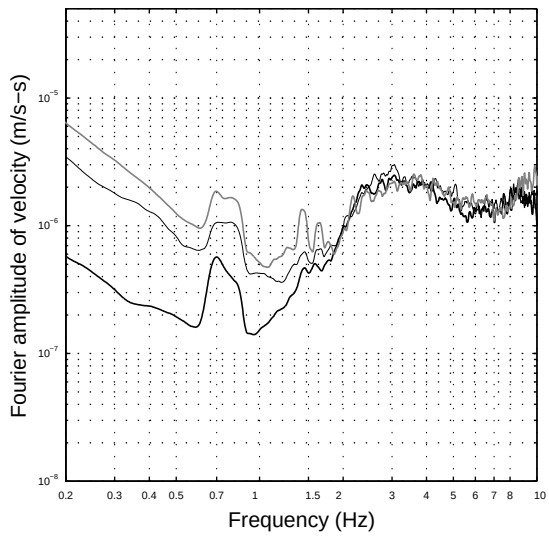

Figure I.42a Point 041 average HVSR +/− 1 sd

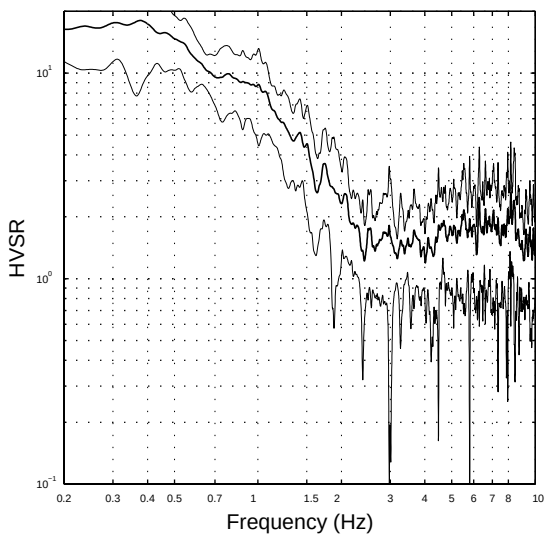

Figure I.42b Point 041 average FAS of velocity

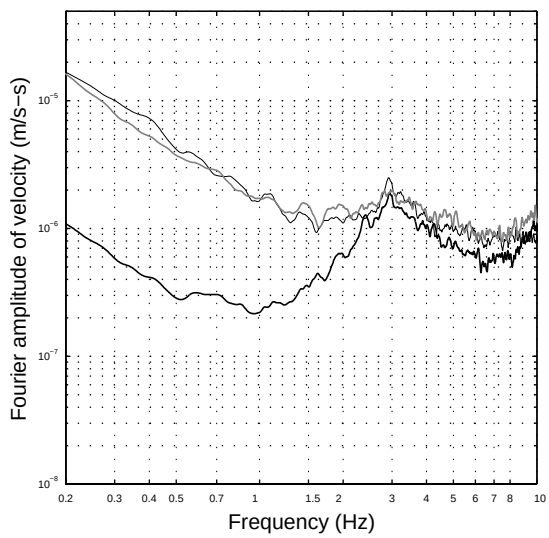

Average FAS plots: thick black − z−comp; thin black − n−s comp; thick grey − e−w comp

Figure I.43a Point 042 average HVSR +/− 1 sd

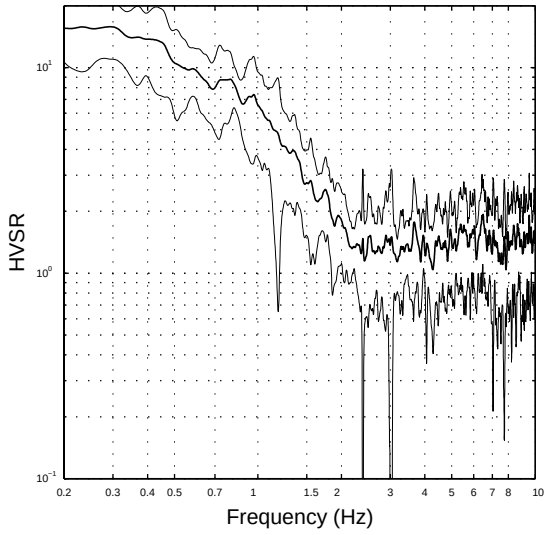

Figure I.43b Point 042 average FAS of velocity

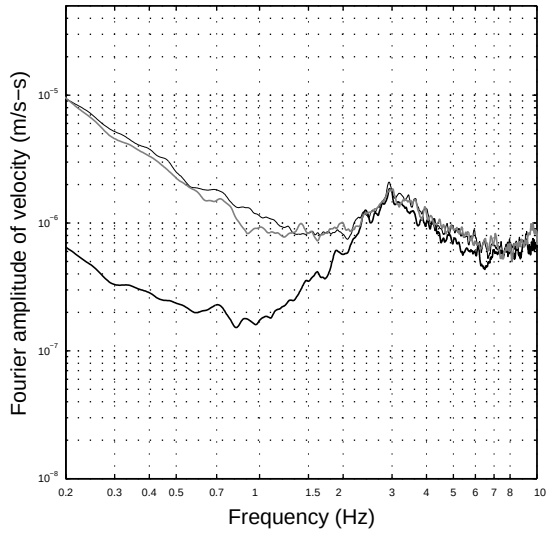

Figure I.44a Point 043 average HVSR +/− 1 sd

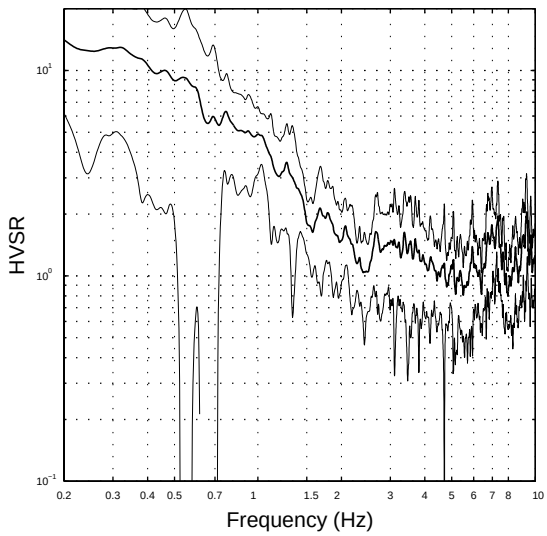

Figure I.44b Point 043 average FAS of velocity

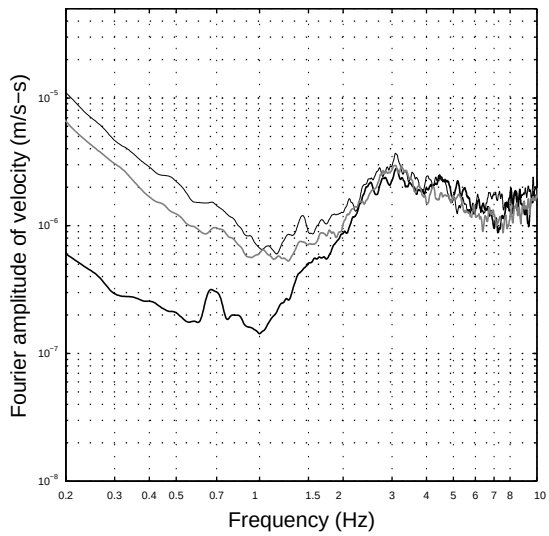

Figure I.45a Point 044 average HVSR +/− 1 sd

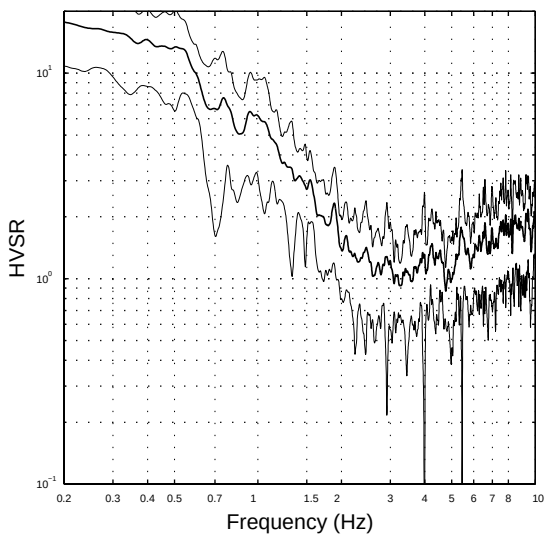

Figure I.45b Point 044 average FAS of velocity

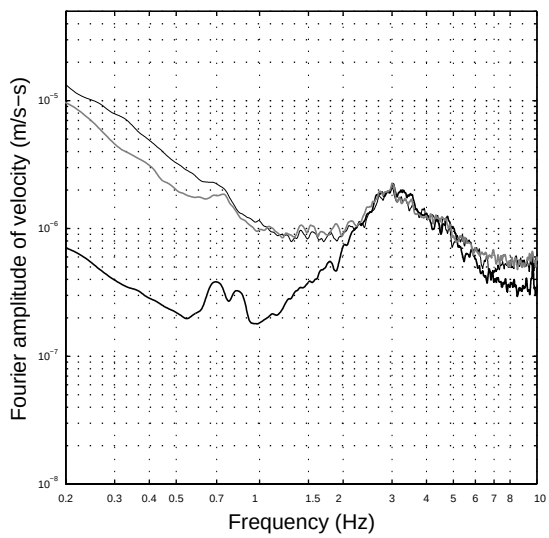

Average FAS plots: thick black − z−comp; thin black − n−s comp; thick grey − e−w comp

Figure I.46a Point 045 average HVSR +/− 1 sd

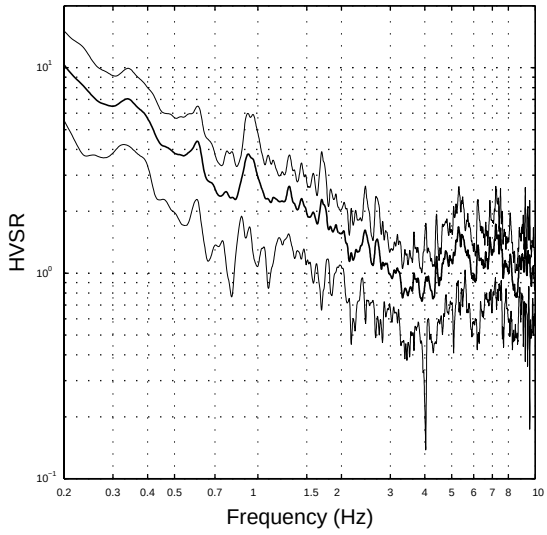

Figure I.46b Point 045 average FAS of velocity

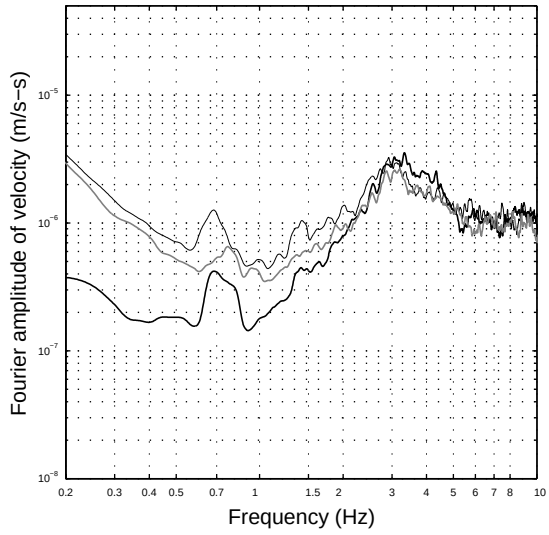

Figure I.47a Point 046 average HVSR +/− 1 sd

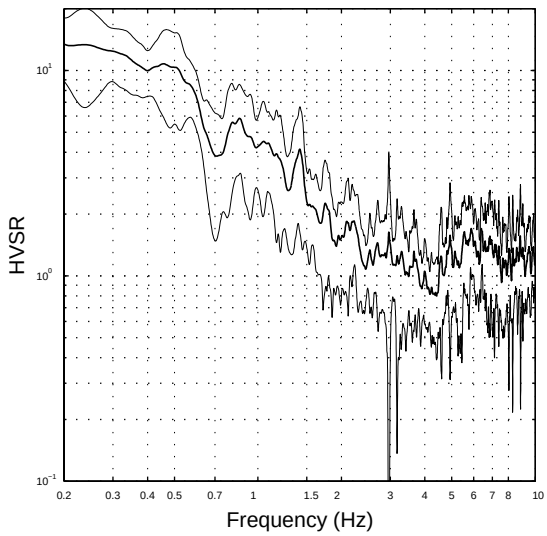

Figure I.47b Point 046 average FAS of velocity

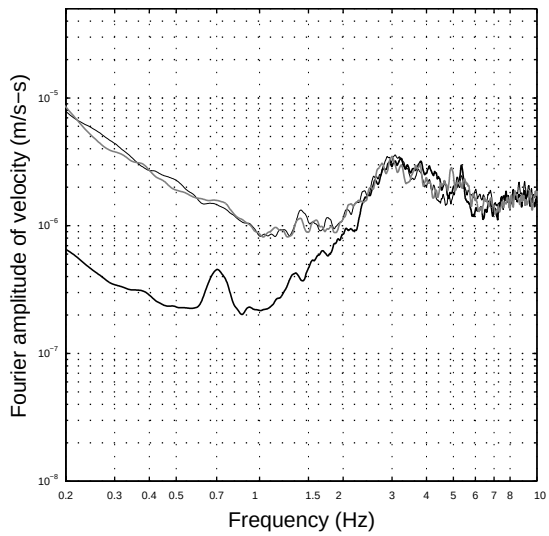

Figure I.48a Point 047 average HVSR +/− 1 sd

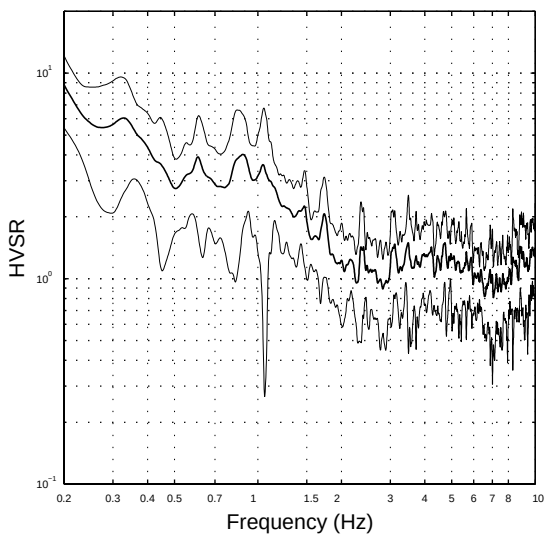

Figure I.48b Point 047 average FAS of velocity

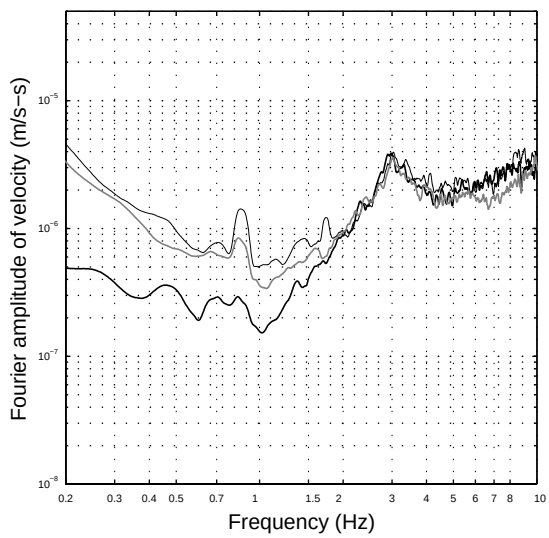

Average FAS plots: thick black − z−comp; thin black − n−s comp; thick grey − e−w comp

Figure I.49a Point 048 average HVSR +/− 1 sd

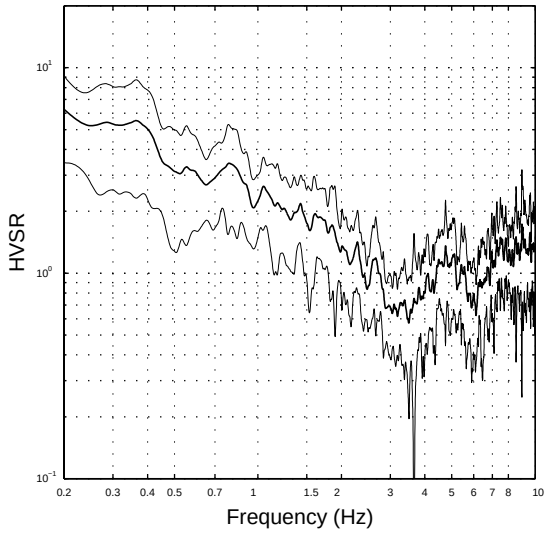

Figure I.49b Point 048 average FAS of velocity

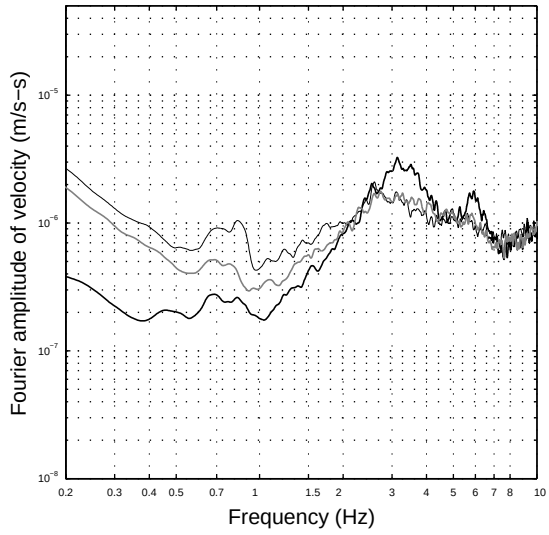

Figure I.50a Point 049 average HVSR +/− 1 sd

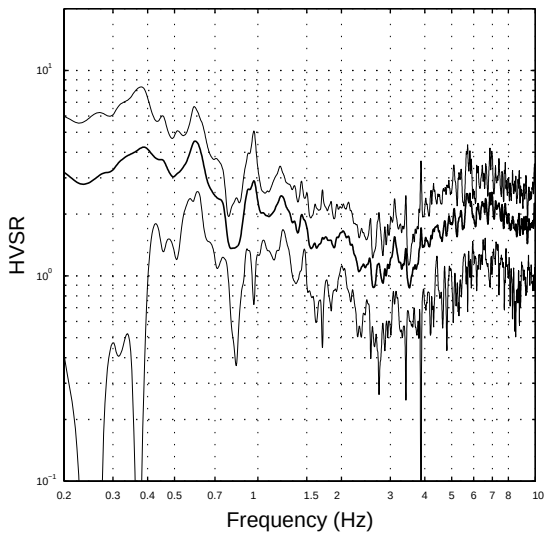

Figure I.50b Point 049 average FAS of velocity

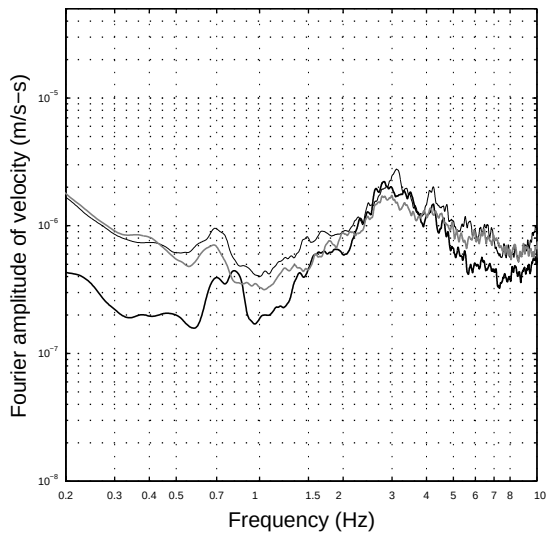

Figure I.51a Point 050 average HVSR +/− 1 sd

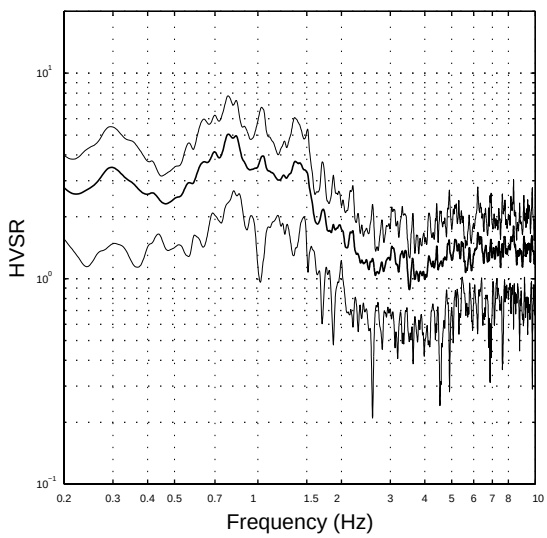

Figure I.51b Point 050 average FAS of velocity

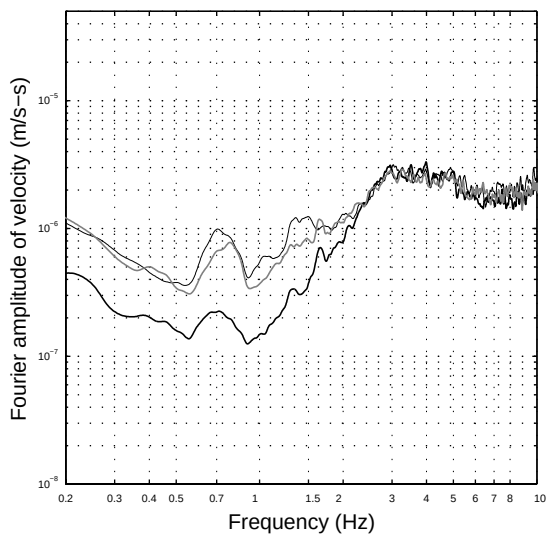

Average FAS plots: thick black − z−comp; thin black − n−s comp; thick grey − e−w comp

Figure I.52a Point 051 average HVSR +/− 1 sd

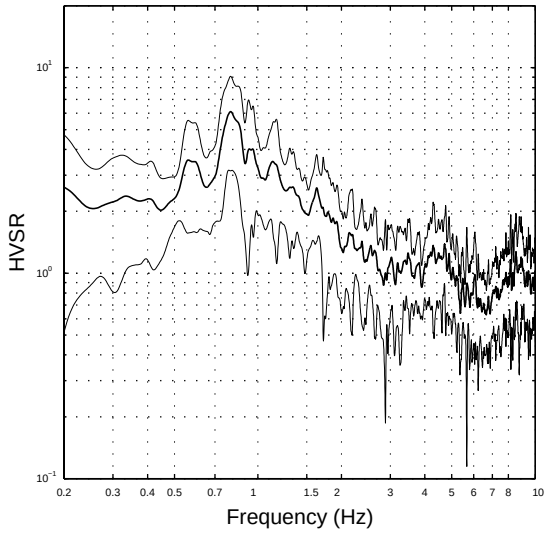

Figure I.52b Point 051 average FAS of velocity

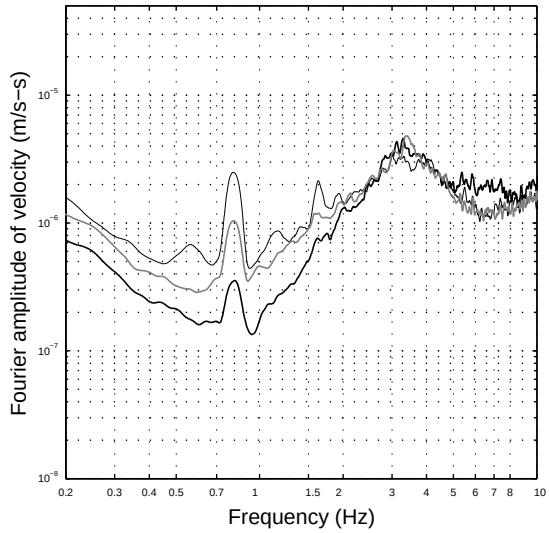

Figure I.53a Point 052 average HVSR +/− 1 sd

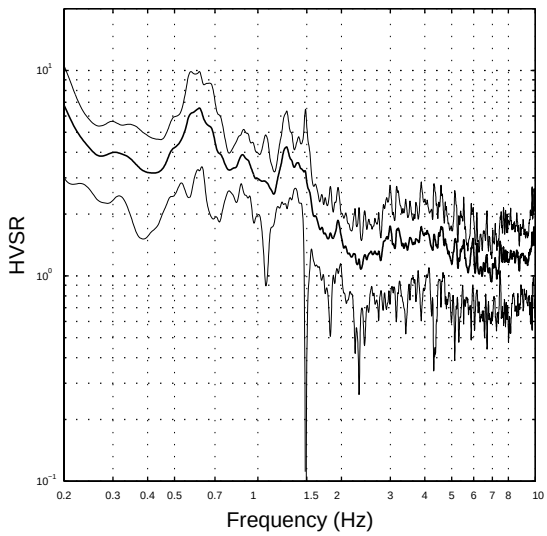

Figure I.53b Point 052 average FAS of velocity

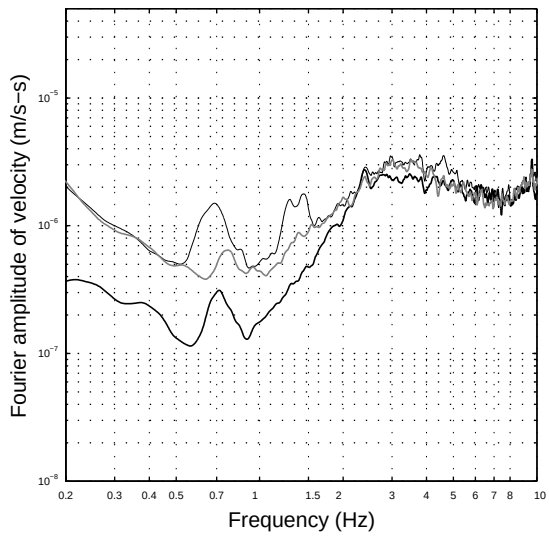

Figure I.54a Point 053 average HVSR +/− 1 sd

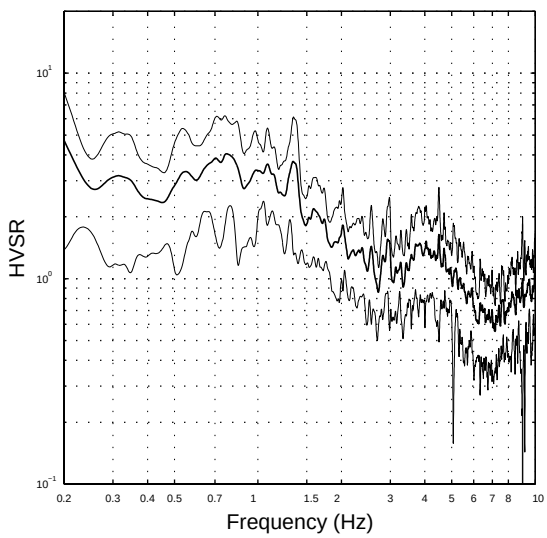

Figure I.54b Point 053 average FAS of velocity

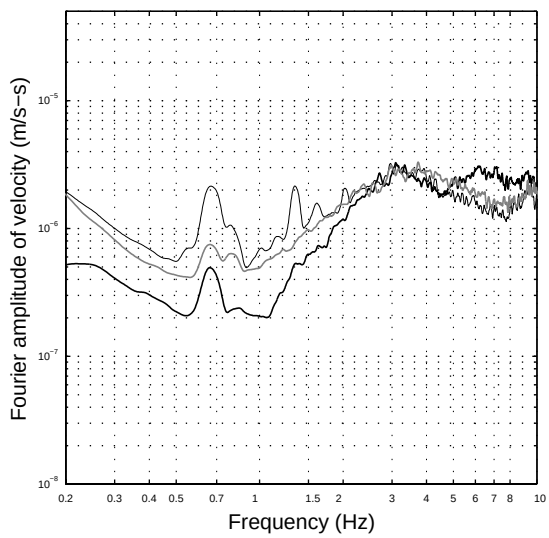

Average FAS plots: thick black − z−comp; thin black − n−s comp; thick grey − e−w comp

Figure I.55a Point 054 average HVSR +/− 1 sd

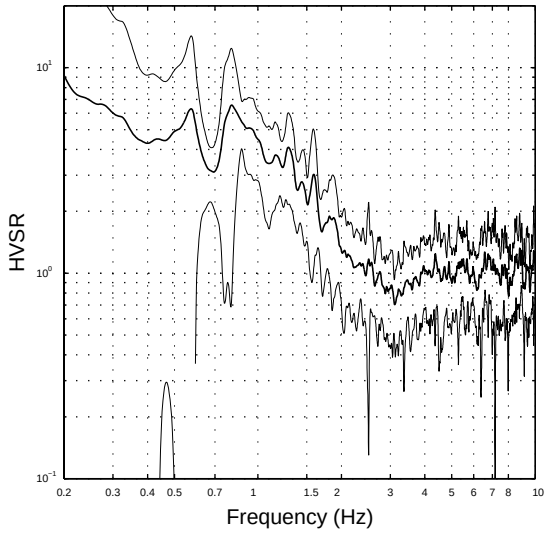

Figure I.55b Point 054 average FAS of velocity

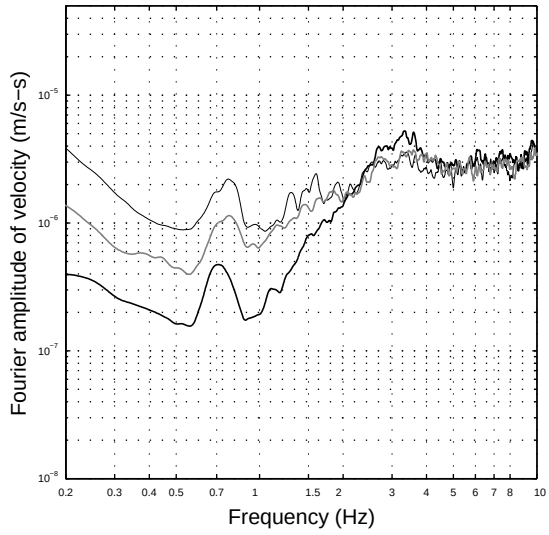

Figure I.56a Point 055 average HVSR +/− 1 sd

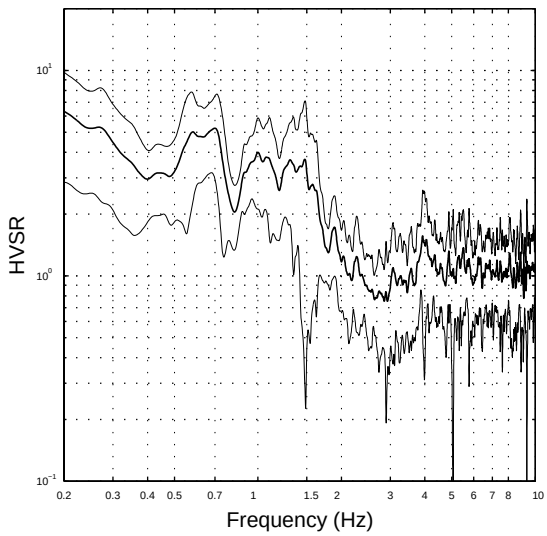

Figure I.56b Point 055 average FAS of velocity

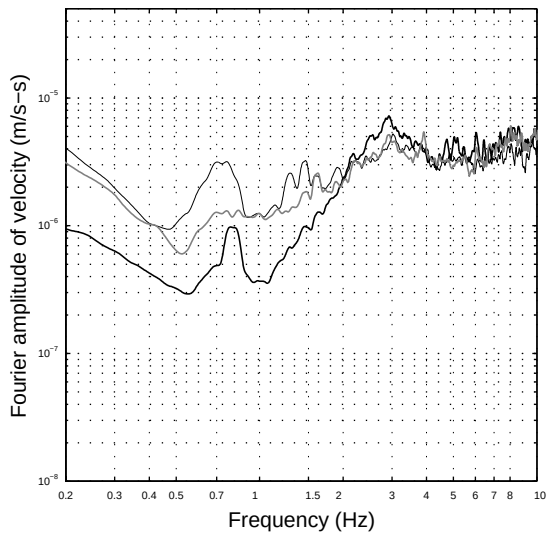

Figure I.57a Point 056 average HVSR +/− 1 sd

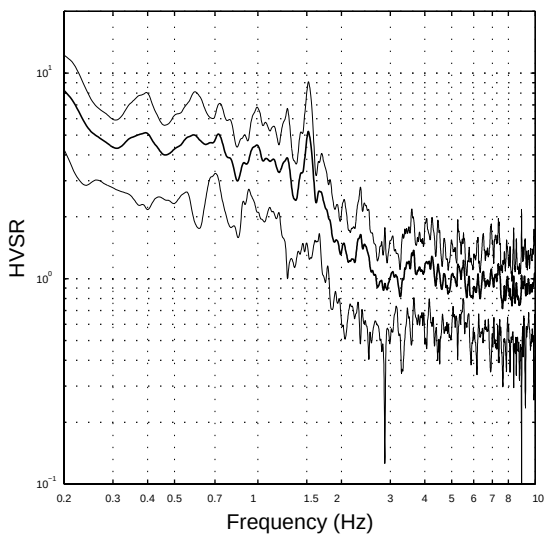

Figure I.57b Point 056 average FAS of velocity

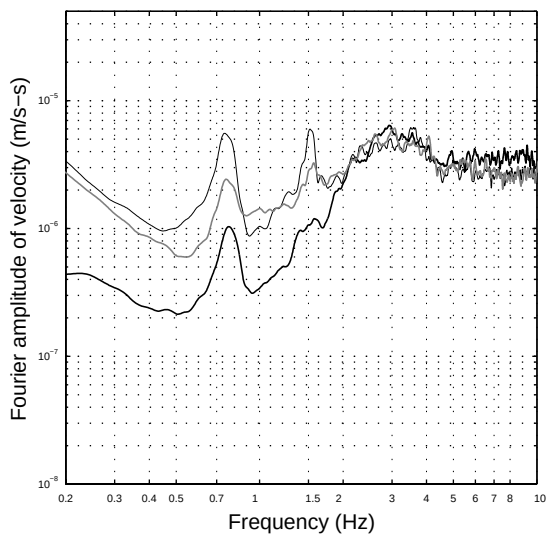

Average FAS plots: thick black − z−comp; thin black − n−s comp; thick grey − e−w comp

Figure I.58a Point 057 average HVSR +/− 1 sd

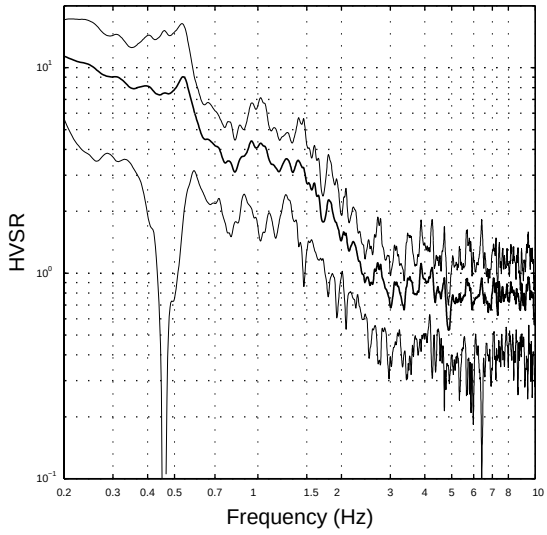

Figure I.58b Point 057 average FAS of velocity

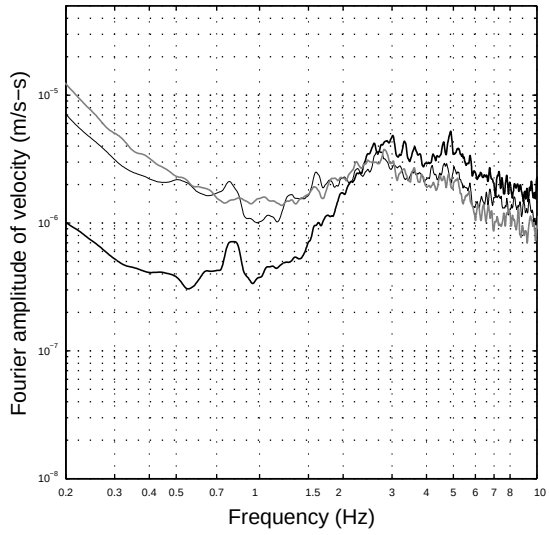

Figure I.59a Point 058 average HVSR +/− 1 sd

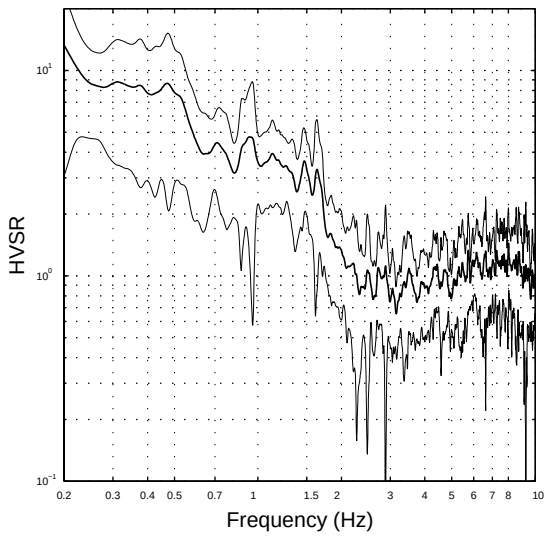

Figure I.59b Point 058 average FAS of velocity

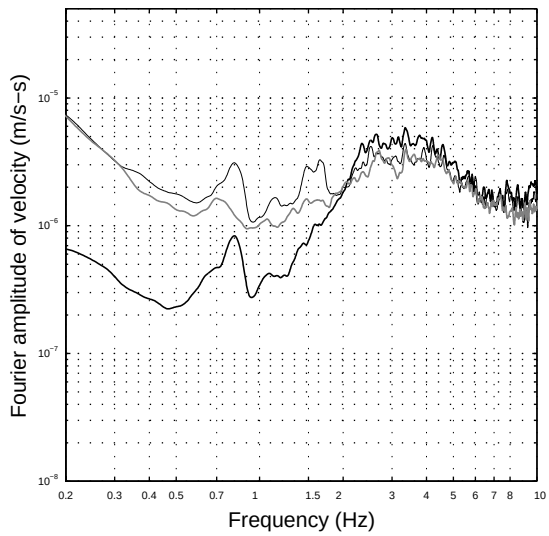

Figure I.60a Point 059 average HVSR +/− 1 sd

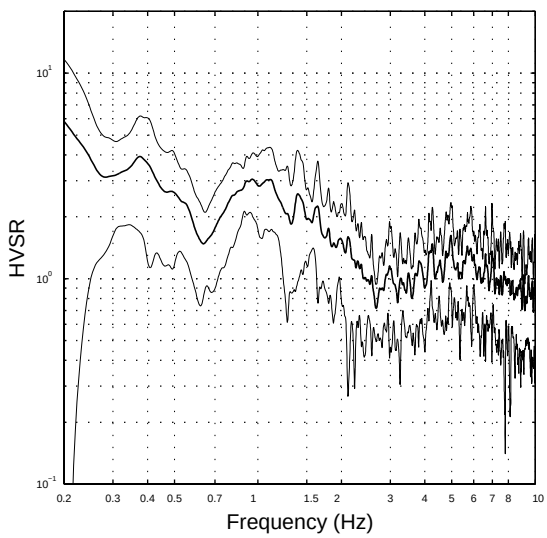

Figure I.60b Point 059 average FAS of velocity

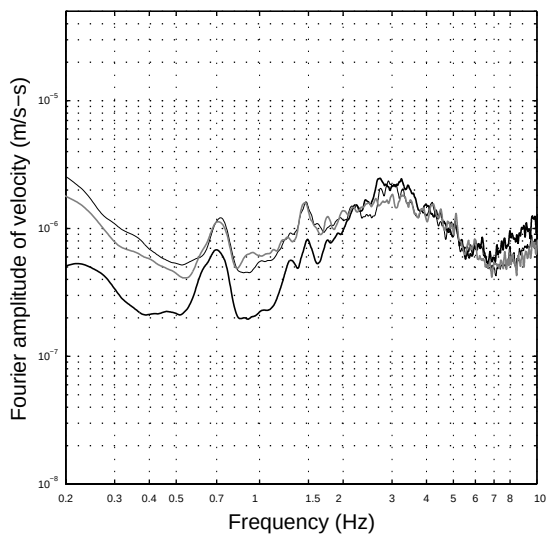

Average FAS plots: thick black − z−comp; thin black − n−s comp; thick grey − e−w comp

Figure I.61a Point 060 average HVSR +/− 1 sd

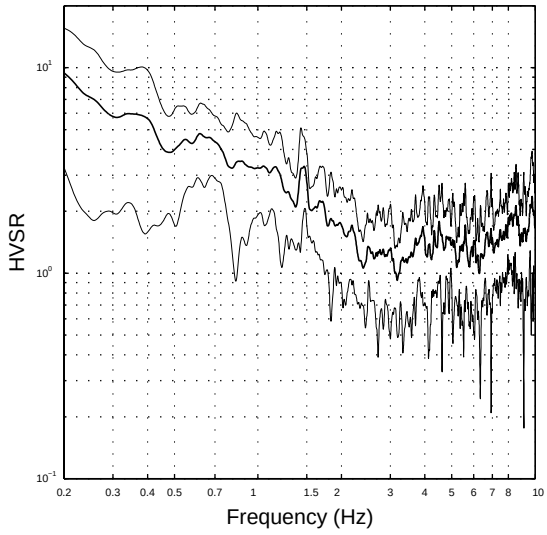

Figure I.61b Point 060 average FAS of velocity

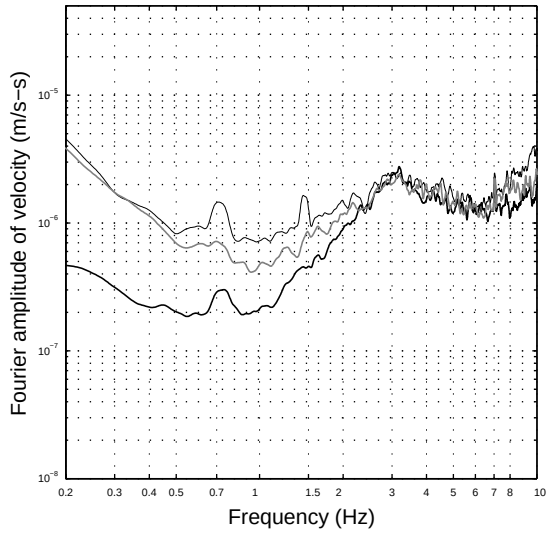

Figure I.62a Point 061 average HVSR +/− 1 sd

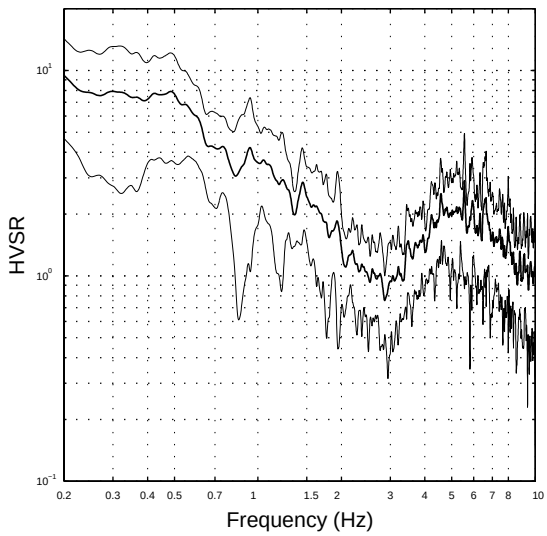

Figure I.62b Point 061 average FAS of velocity

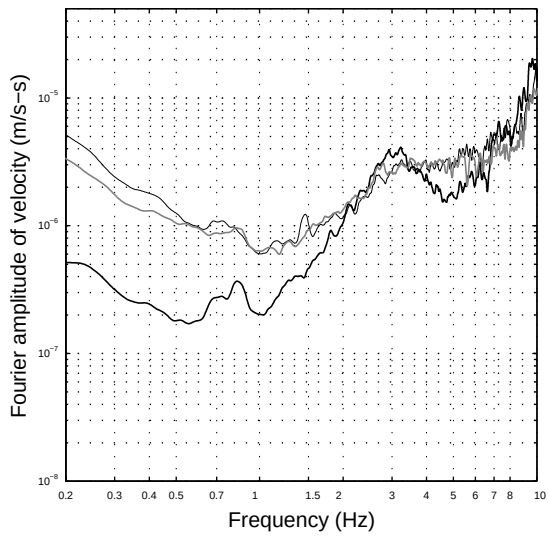

Figure I.63a Point 062 average HVSR +/− 1 sd

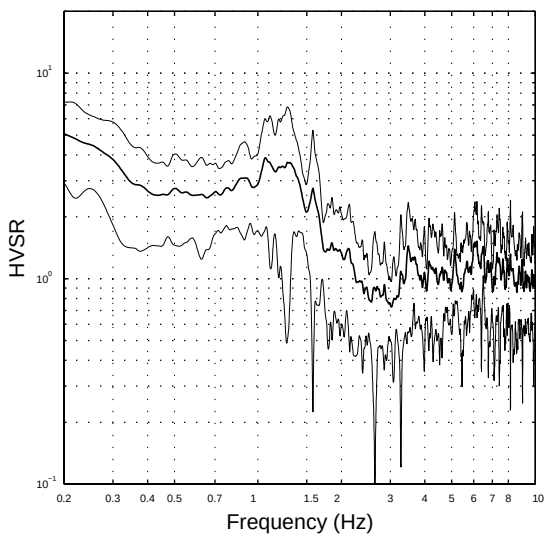

Figure I.63b Point 062 average FAS of velocity

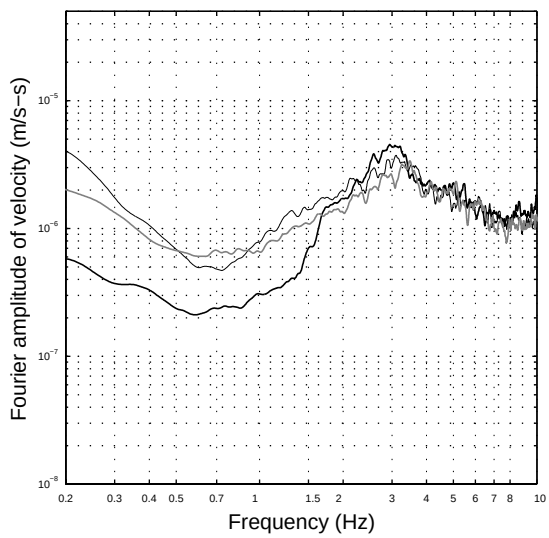

Average FAS plots: thick black − z−comp; thin black − n−s comp; thick grey − e−w comp

Figure I.64a Point 063a average HVSR +/− 1 sd

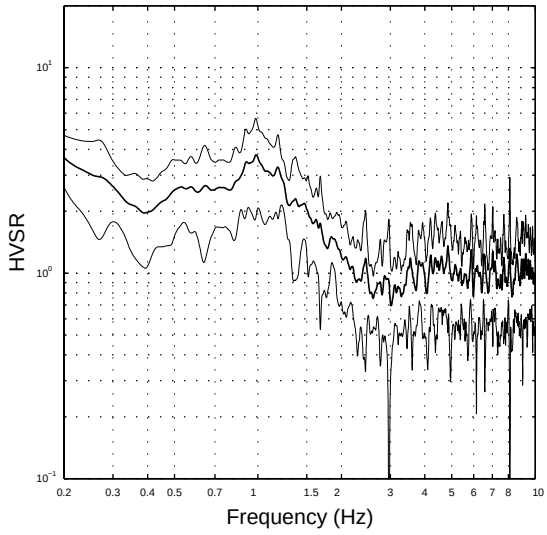

Figure I.64b Point 063a average FAS of velocity

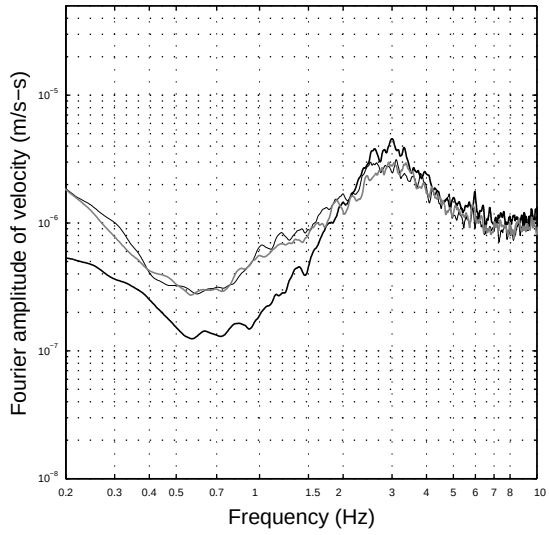

Figure I.65a Point 064 average HVSR +/− 1 sd

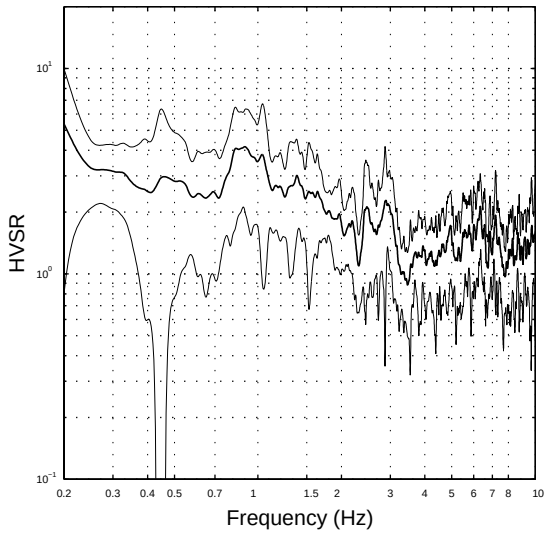

Figure I.65b Point 064 average FAS of velocity

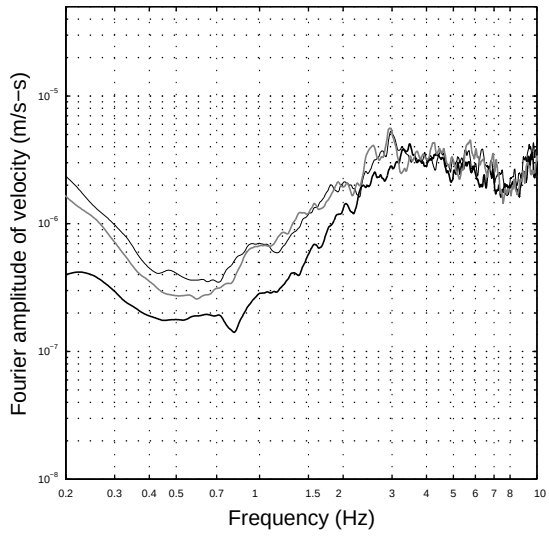

Figure I.66a Point 065 average HVSR +/− 1 sd

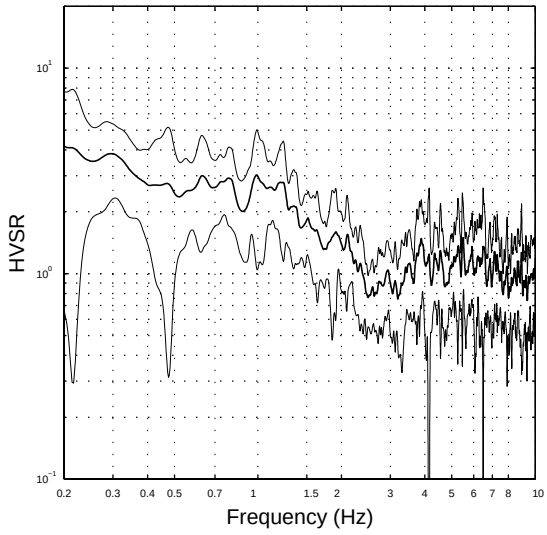

Figure I.66b Point 065 average FAS of velocity

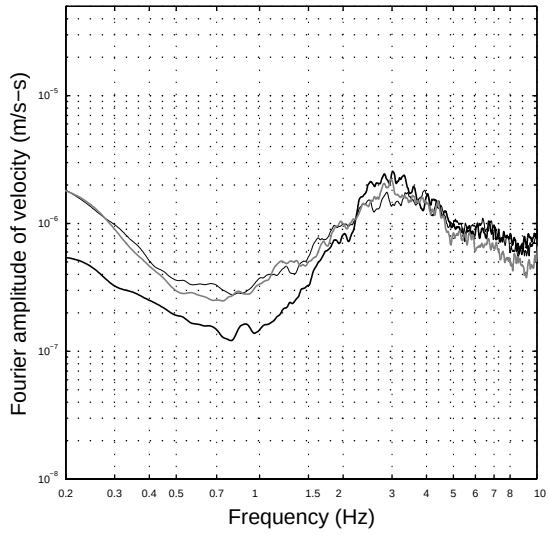

Average FAS plots: thick black − z−comp; thin black − n−s comp; thick grey − e−w comp

Figure I.67a Point 066 average HVSR +/− 1 sd

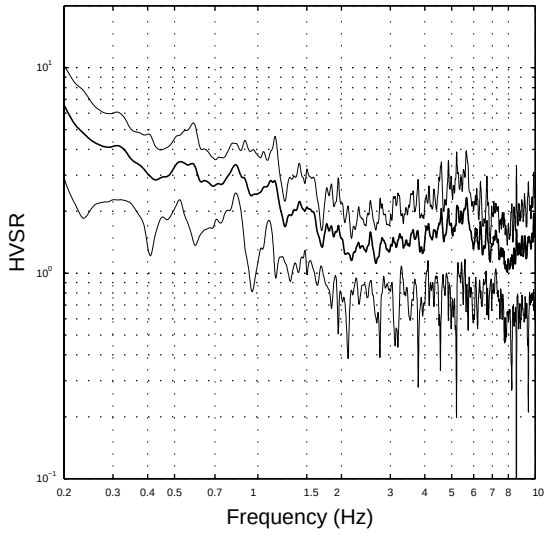

Figure I.67b Point 066 average FAS of velocity

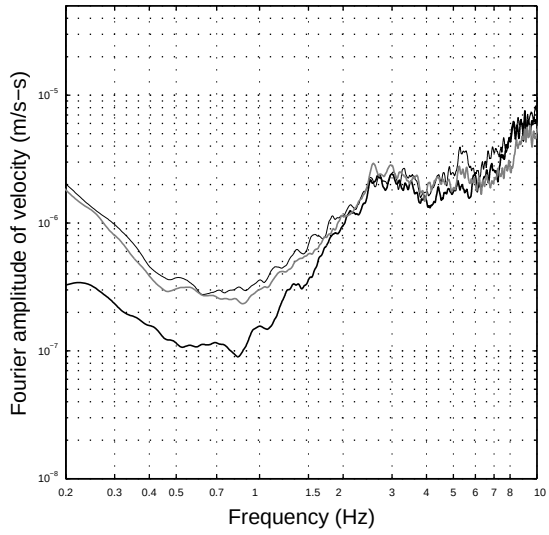

Figure I.68a Point 067 average HVSR +/− 1 sd

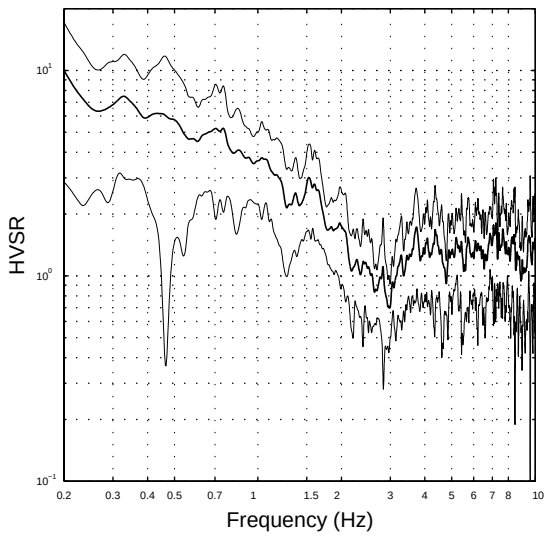

Figure I.68b Point 067 average FAS of velocity

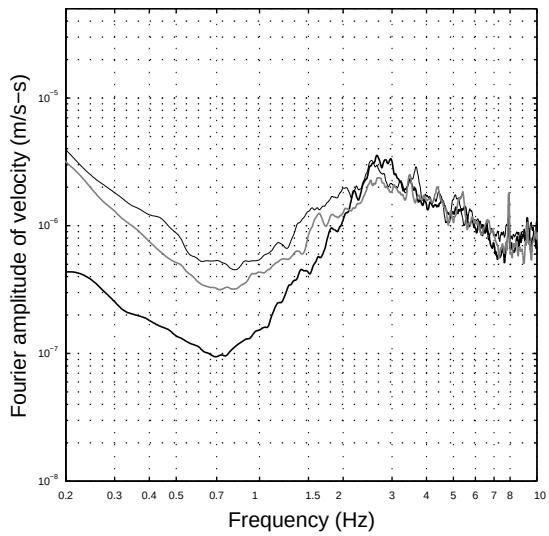

Figure I.69a Point 068 average HVSR +/− 1 sd

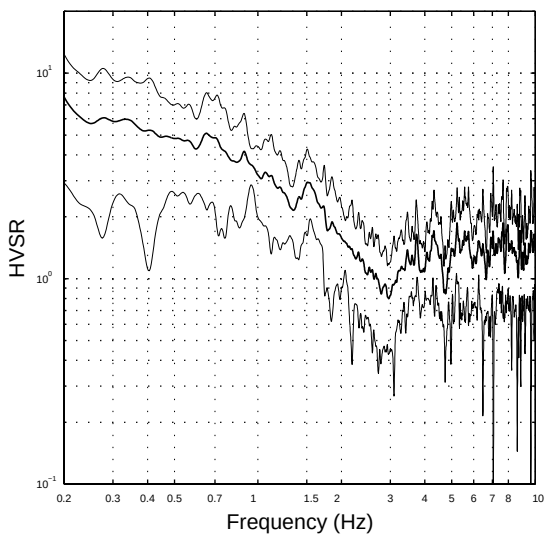

Figure I.69b Point 068 average FAS of velocity

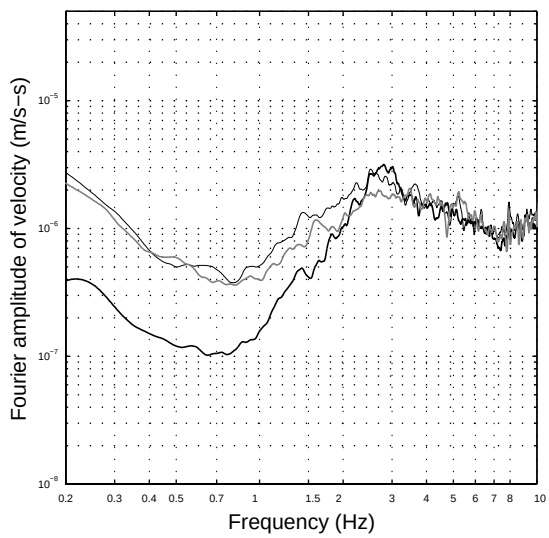

Average FAS plots: thick black − z−comp; thin black − n−s comp; thick grey − e−w comp

Figure I.70a Point 069 average HVSR +/− 1 sd

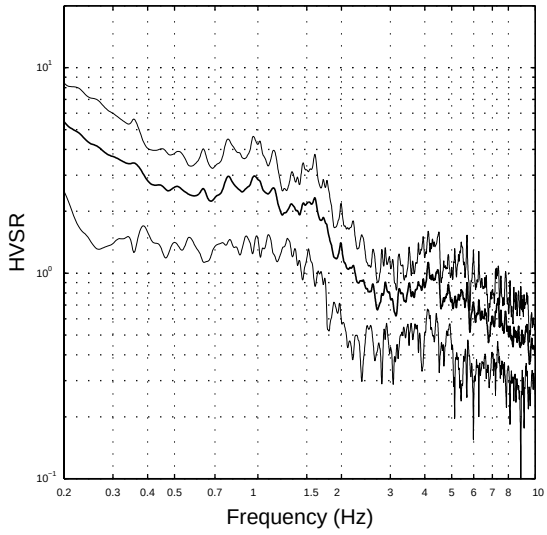

Figure I.70b Point 069 average FAS of velocity

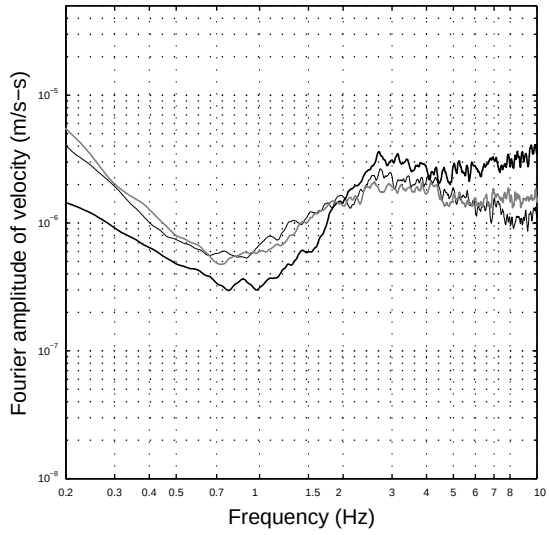

Figure I.71a Point 070 average HVSR +/− 1 sd

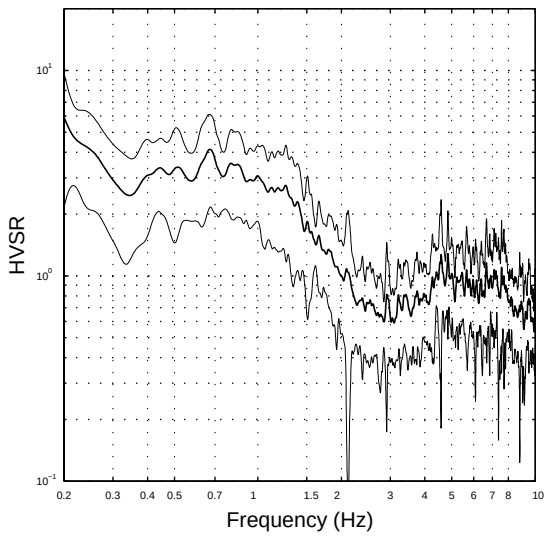

Figure I.71b Point 070 average FAS of velocity

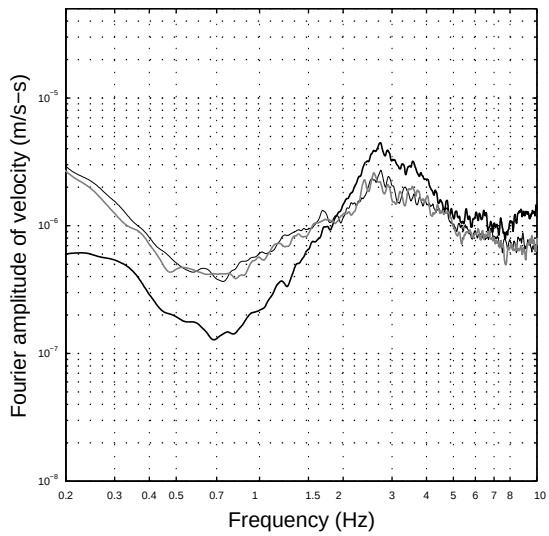

Figure I.72a Point 071 average HVSR +/− 1 sd

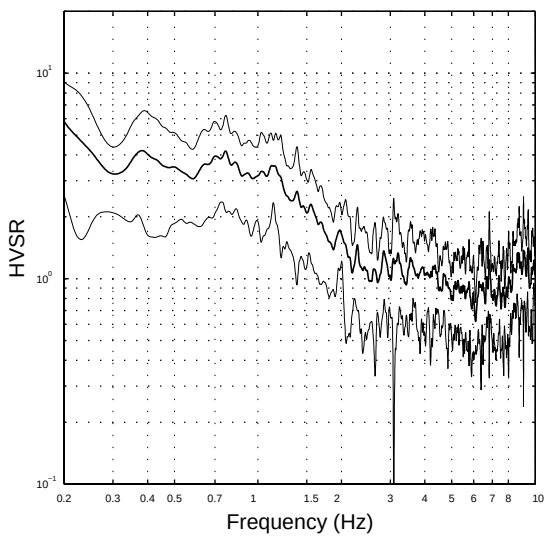

Figure I.72b Point 071 average FAS of velocity

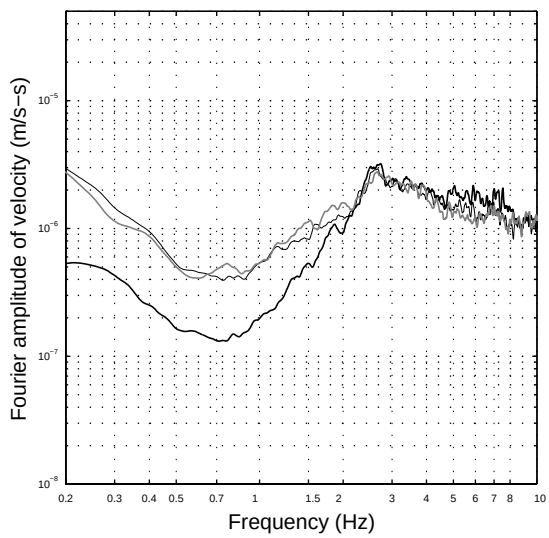

Average FAS plots: thick black − z−comp; thin black − n−s comp; thick grey − e−w comp

Figure I.73a Point 072e average HVSR +/− 1 sd

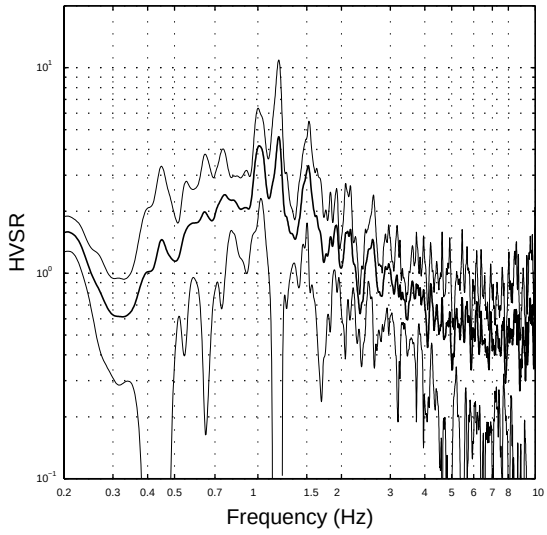

Figure I.73b Point 072e average FAS of velocity

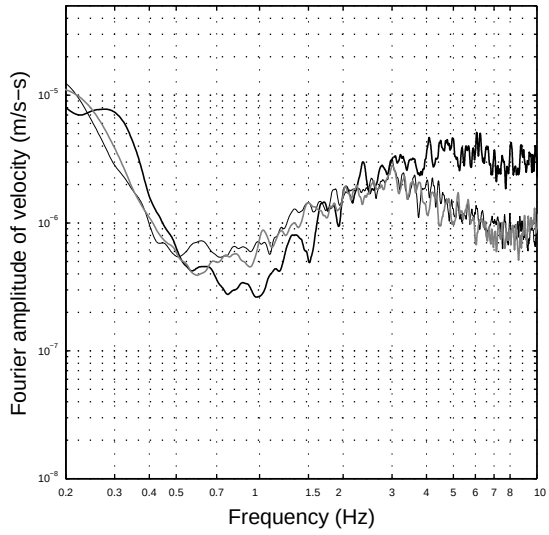

Figure I.74a Point 073 average HVSR +/− 1 sd

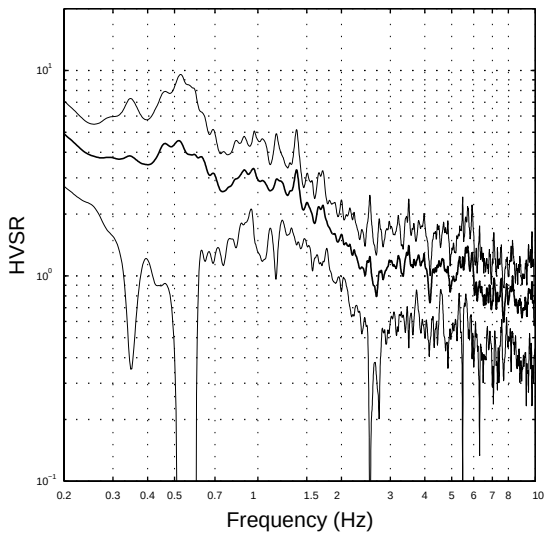

Figure I.74b Point 073 average FAS of velocity

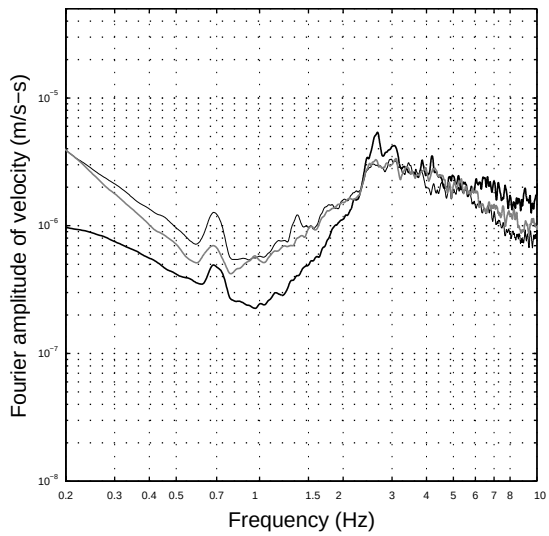

Figure I.75a Point 074 average HVSR +/− 1 sd

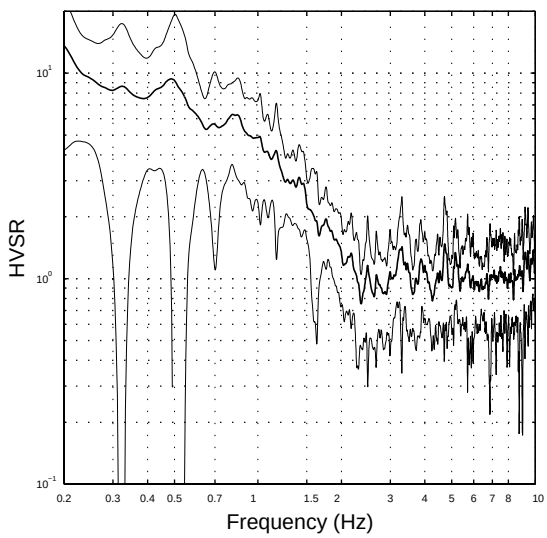

Figure I.75b Point 074 average FAS of velocity

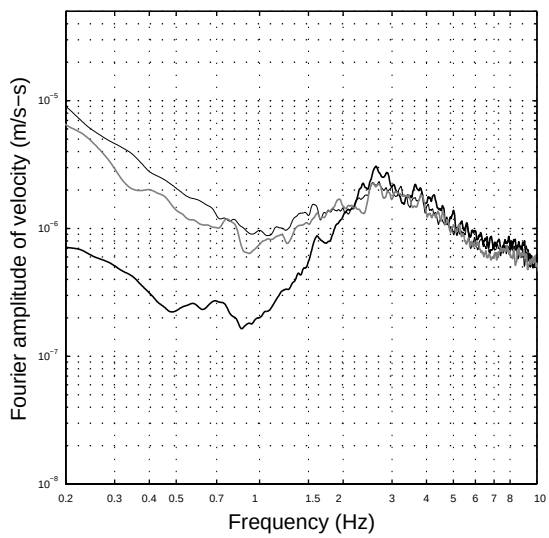

Average FAS plots: thick black − z−comp; thin black − n−s comp; thick grey − e−w comp

Figure I.76a Point 075 average HVSR +/− 1 sd

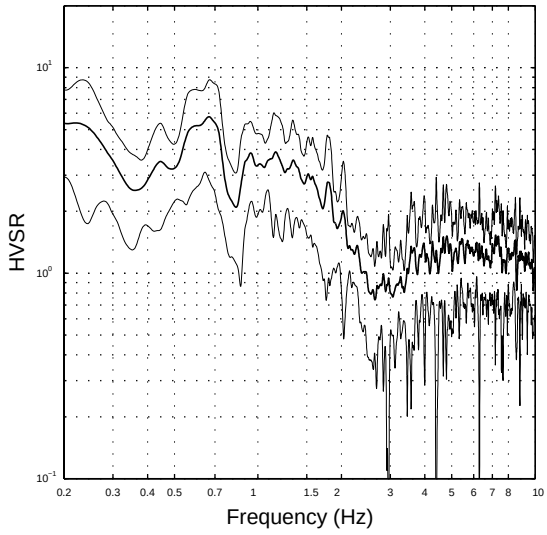

Figure I.76b Point 075 average FAS of velocity

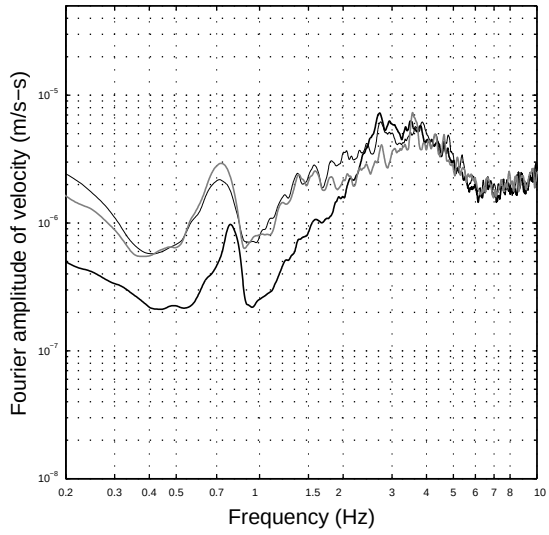

Figure I.77a Point 076 average HVSR +/− 1 sd

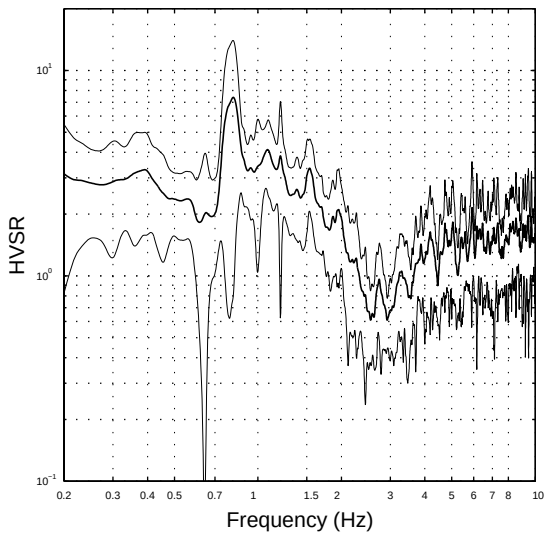

Figure I.77b Point 076 average FAS of velocity

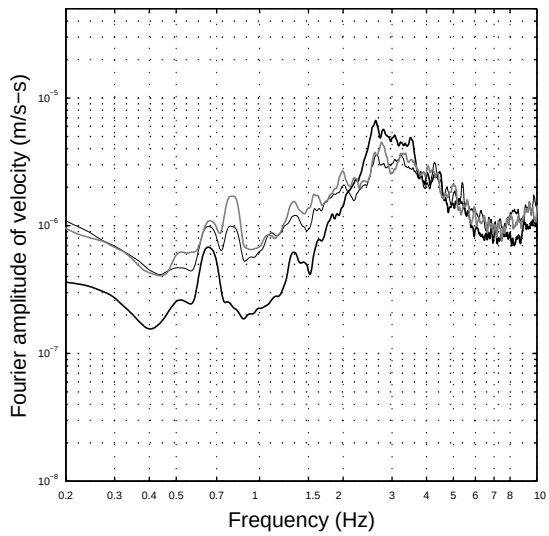

Figure I.78a Point 077 average HVSR +/− 1 sd

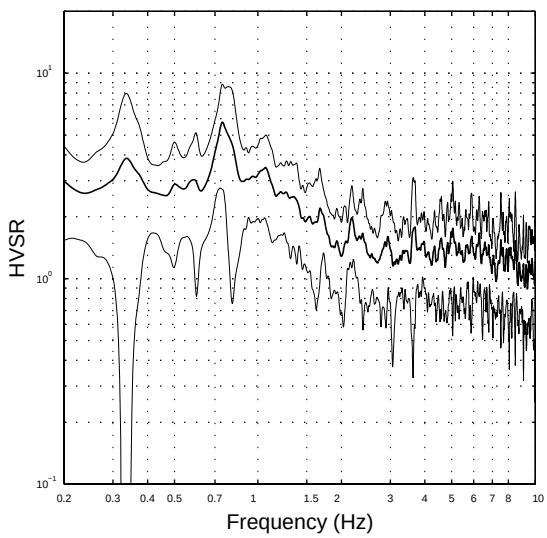

Figure I.78b Point 077 average FAS of velocity

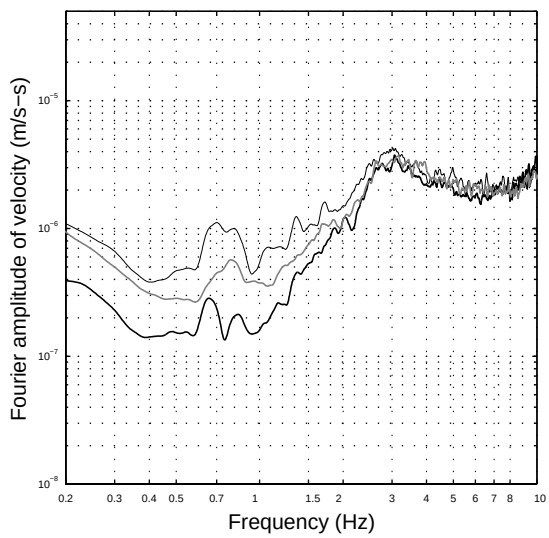

Average FAS plots: thick black − z−comp; thin black − n−s comp; thick grey − e−w comp

Figure I.79a Point 078 average HVSR +/− 1 sd

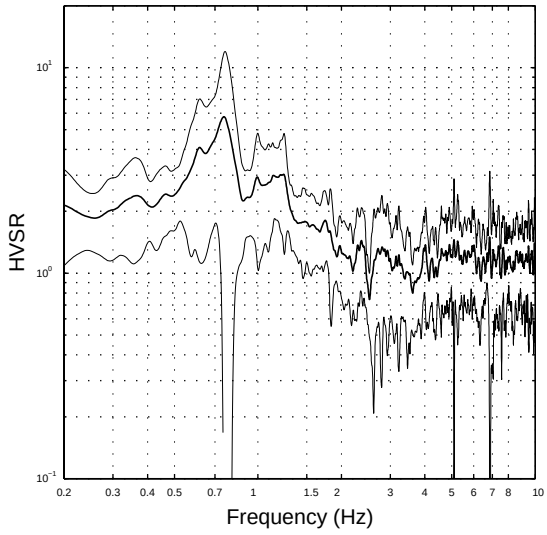

Figure I.79b Point 078 average FAS of velocity

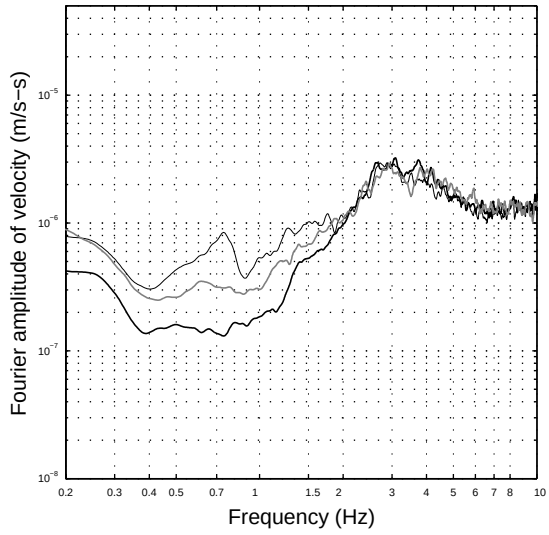

Figure I.80a Point 079 average HVSR +/− 1 sd

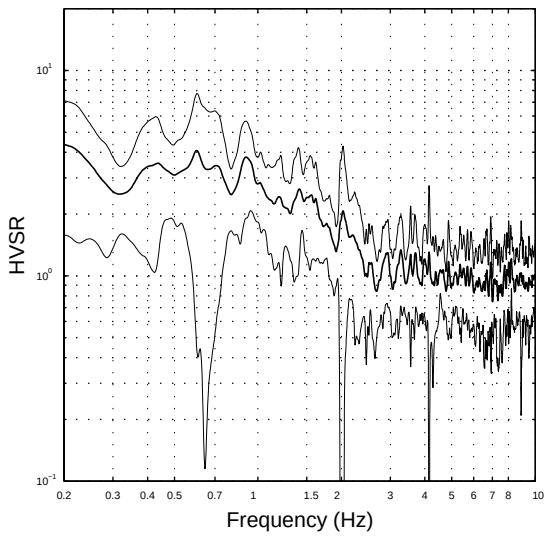

Figure I.80b Point 079 average FAS of velocity

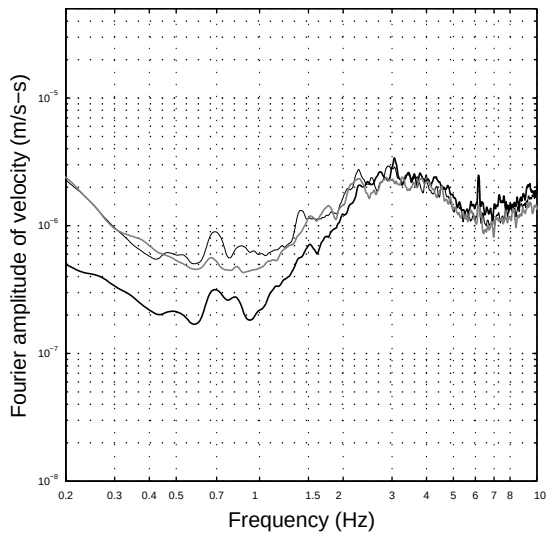

Figure I.81a Point 080 average HVSR +/− 1 sd

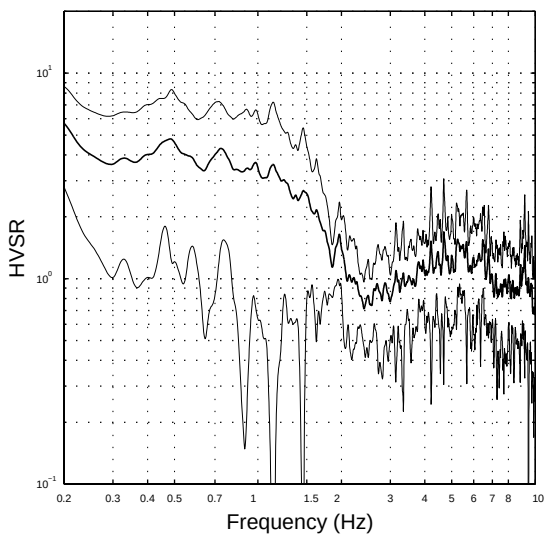

Figure I.81b Point 080 average FAS of velocity

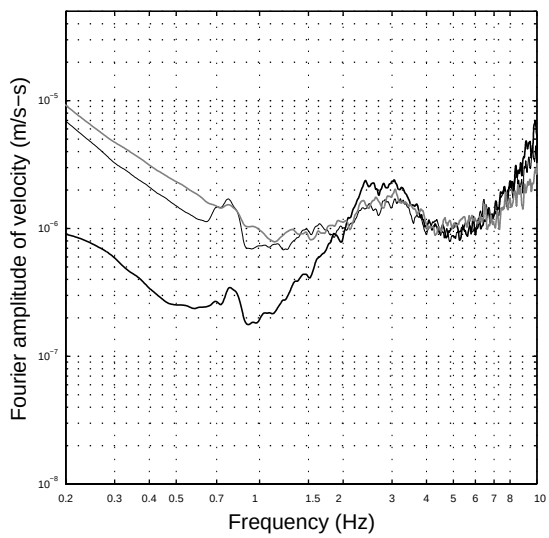

Average FAS plots: thick black − z−comp; thin black − n−s comp; thick grey − e−w comp

Figure I.82a Point 081 average HVSR +/− 1 sd

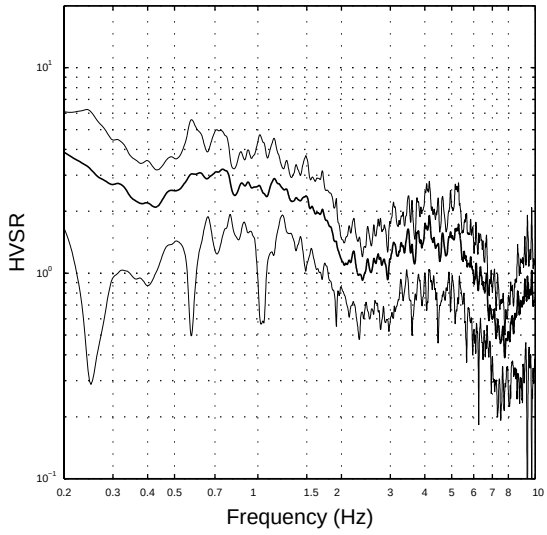

Figure I.82b Point 081 average FAS of velocity

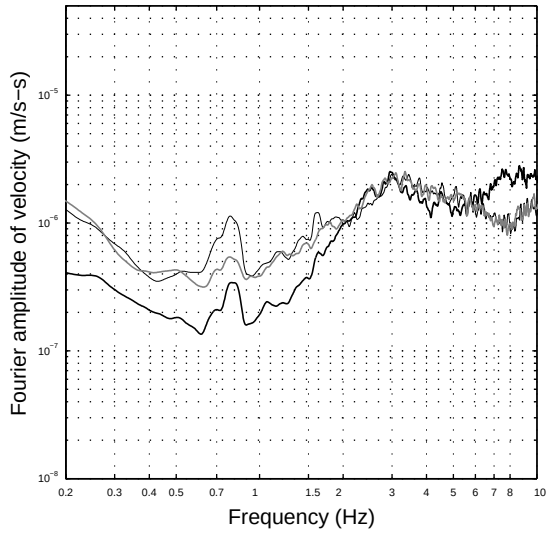

Figure I.83a Point 082 average HVSR +/− 1 sd

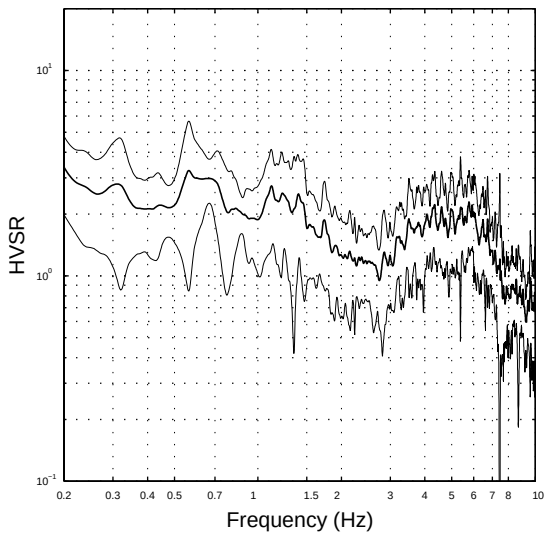

Figure I.83b Point 082 average FAS of velocity

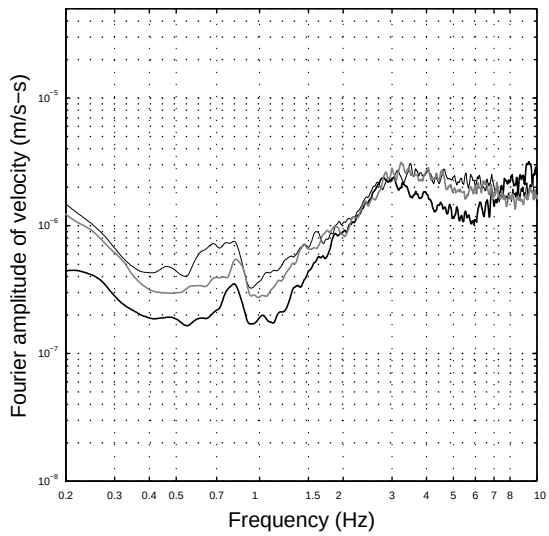

Figure I.84a Point 083 average HVSR +/− 1 sd

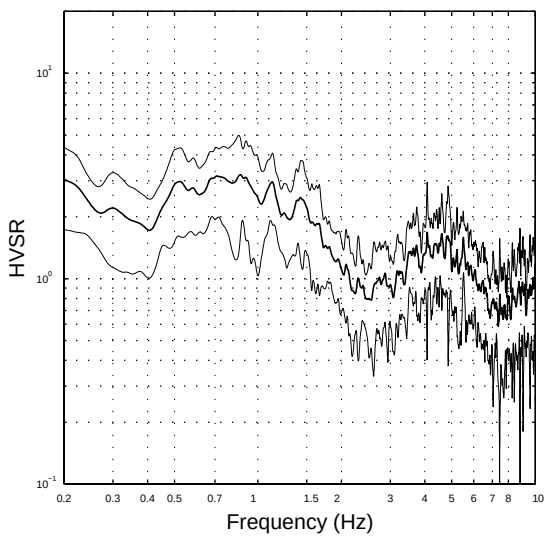

Figure I.84b Point 083 average FAS of velocity

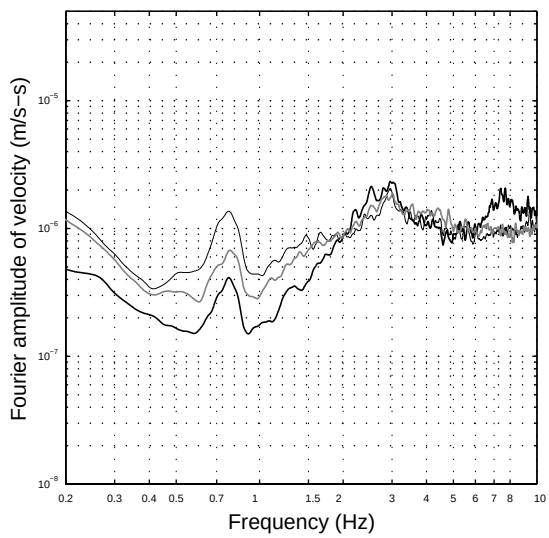

Average FAS plots: thick black − z−comp; thin black − n−s comp; thick grey − e−w comp

Figure I.85a Point 084aa average HVSR +/− 1 sd

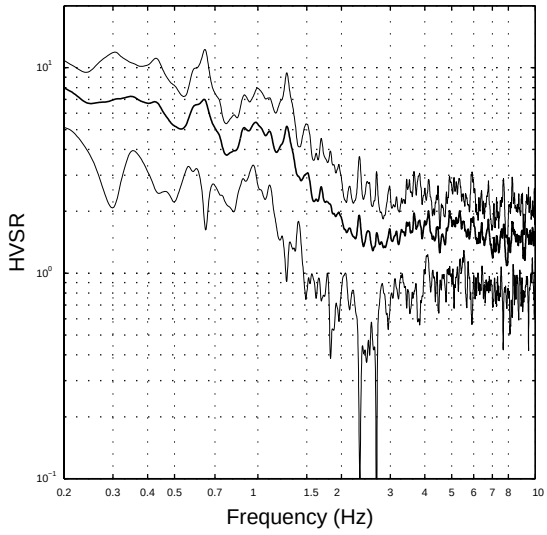

Figure I.85b Point 084aa average FAS of velocity

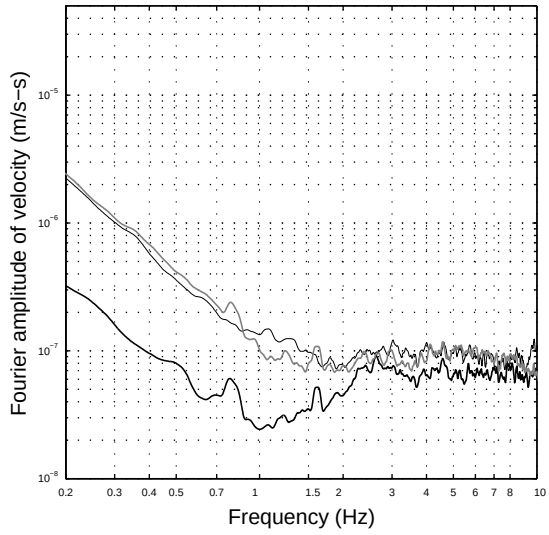

Figure I.86a Point 084ba average HVSR +/− 1 sd

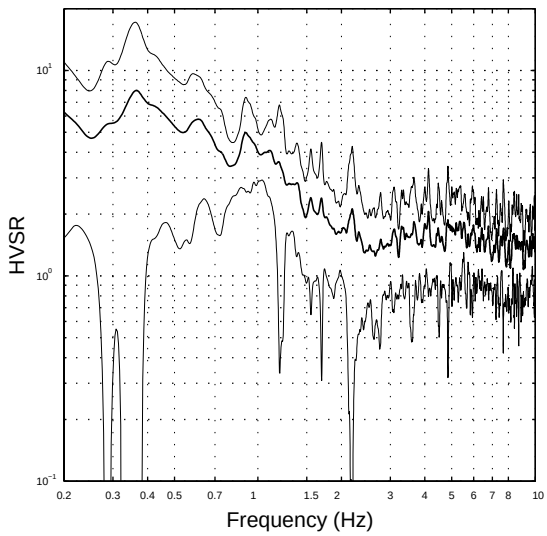

Figure I.86b Point 084ba average FAS of velocity

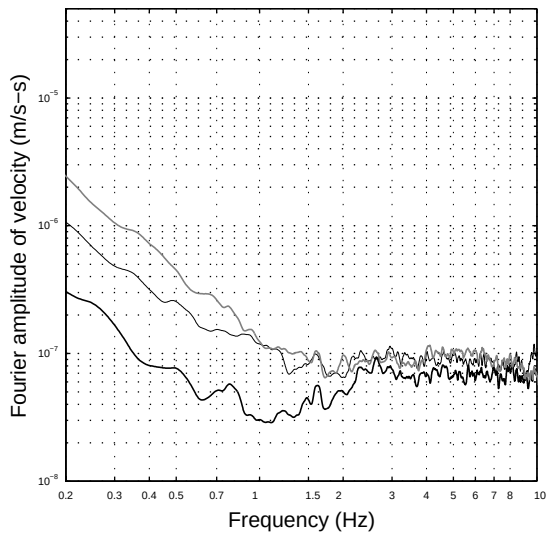

Figure I.87a Point 085a average HVSR +/− 1 sd

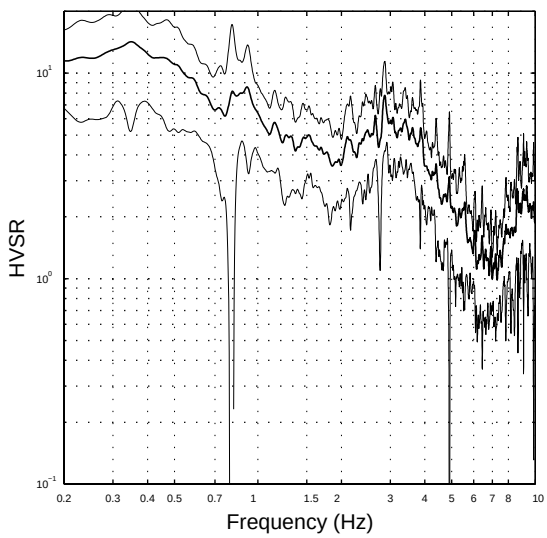

Figure I.87b Point 085a average FAS of velocity

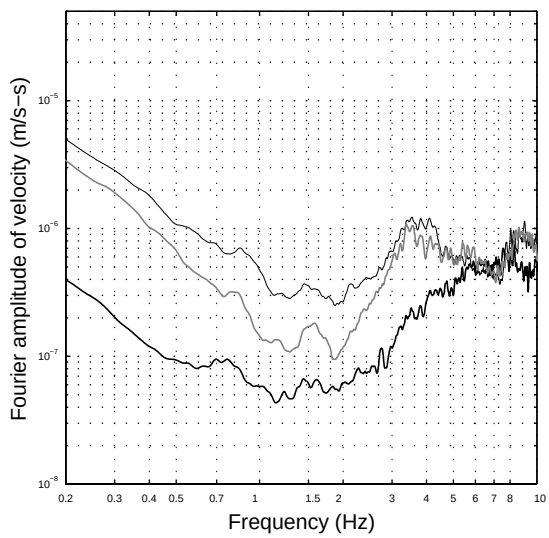

Average FAS plots: thick black − z−comp; thin black − n−s comp; thick grey − e−w comp

Figure I.88a Point 085b average HVSR +/− 1 sd

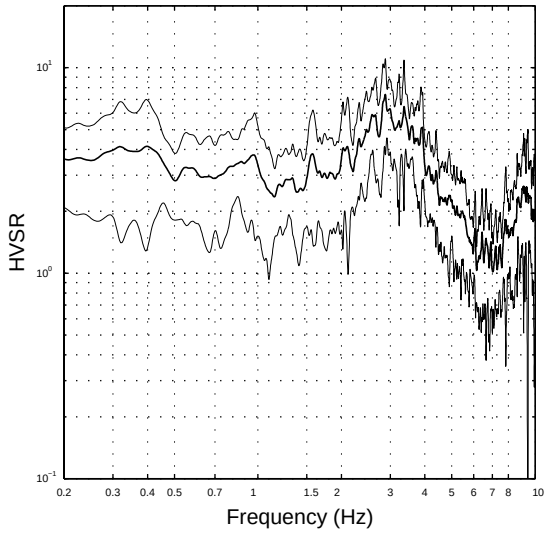

Figure I.88b Point 085b average FAS of velocity

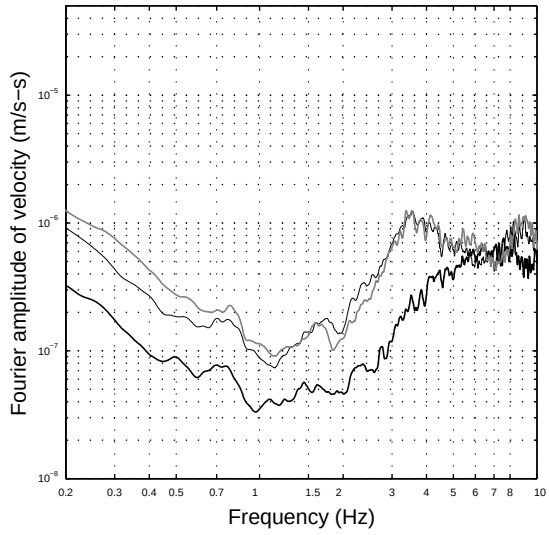

Figure I.89a Point 086a average HVSR +/− 1 sd

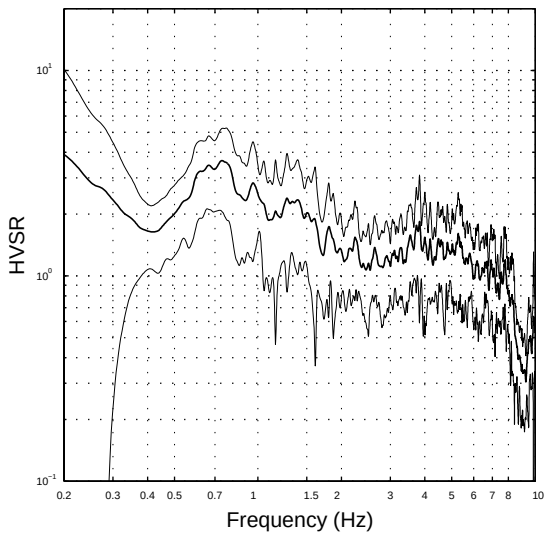

Figure I.89b Point 086a average FAS of velocity

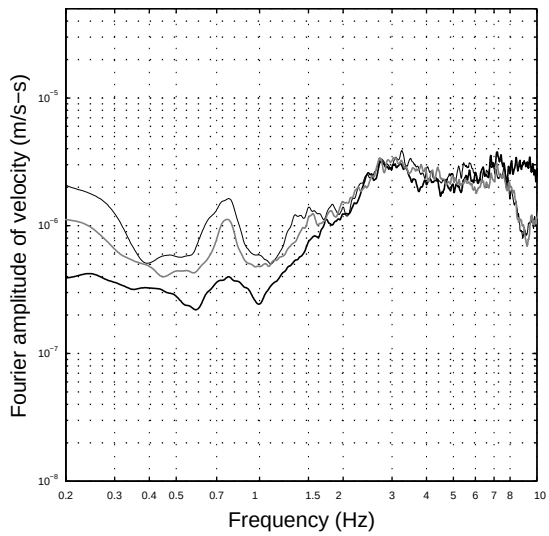

Figure I.90a Point 086b average HVSR +/− 1 sd

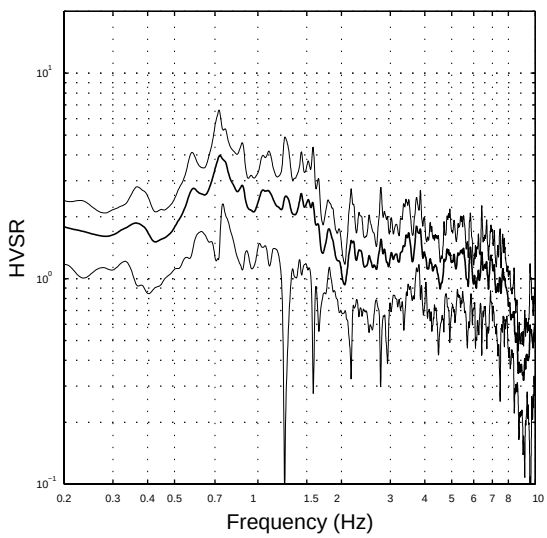

Figure I.90b Point 086b average FAS of velocity

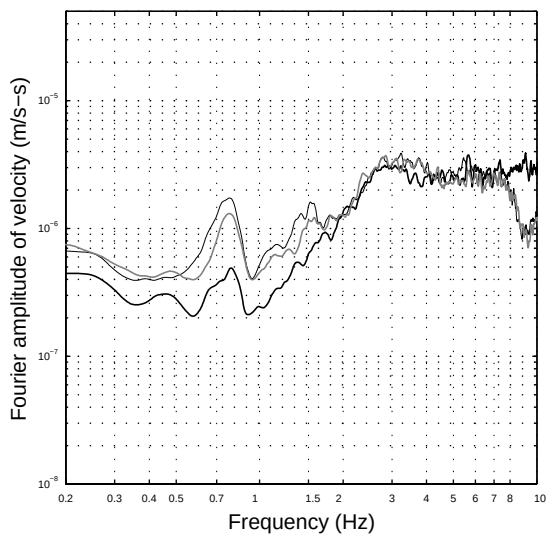

Average FAS plots: thick black − z−comp; thin black − n−s comp; thick grey − e−w comp

Figure I.91a Point 086c average HVSR +/− 1 sd

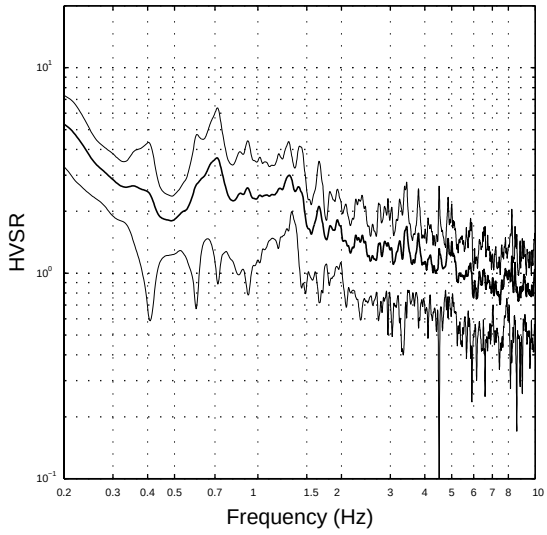

Figure I.91b Point 086c average FAS of velocity

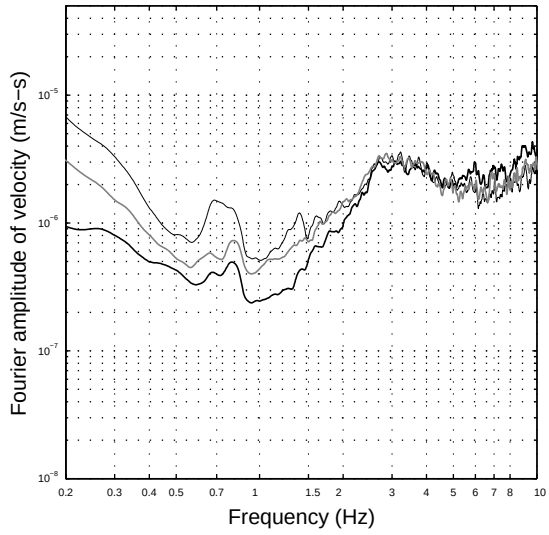

Figure I.92a Point 089a average HVSR +/− 1 sd

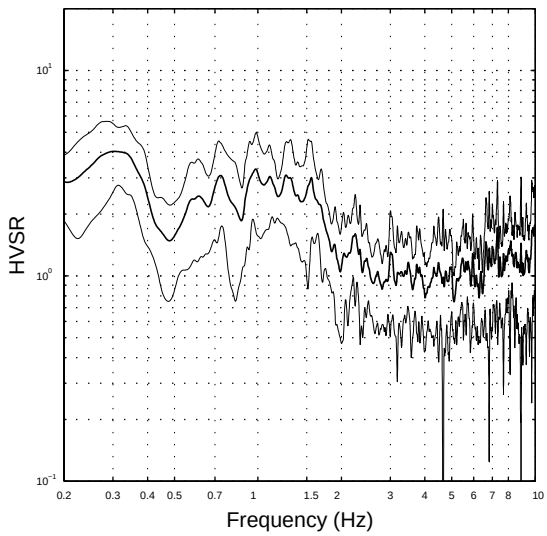

Figure I.92b Point 089a average FAS of velocity

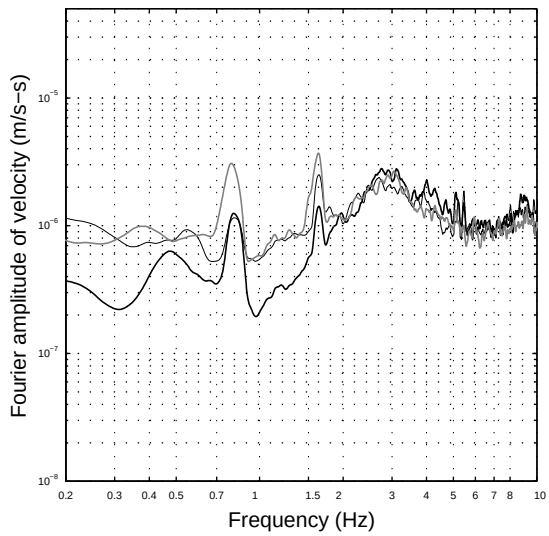

Figure I.93a Point 089b average HVSR +/− 1 sd

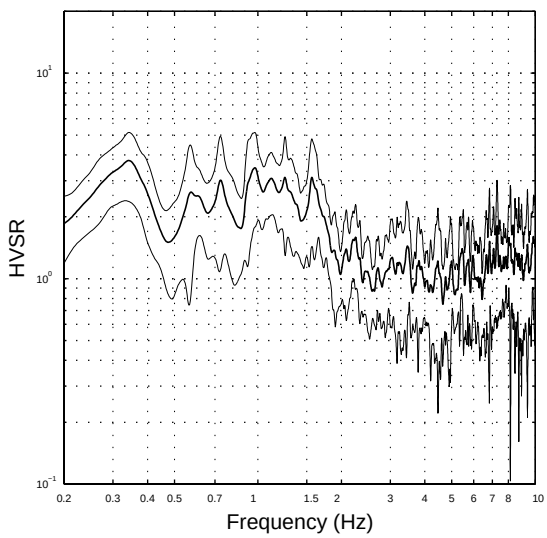

Figure I.93b Point 089b average FAS of velocity

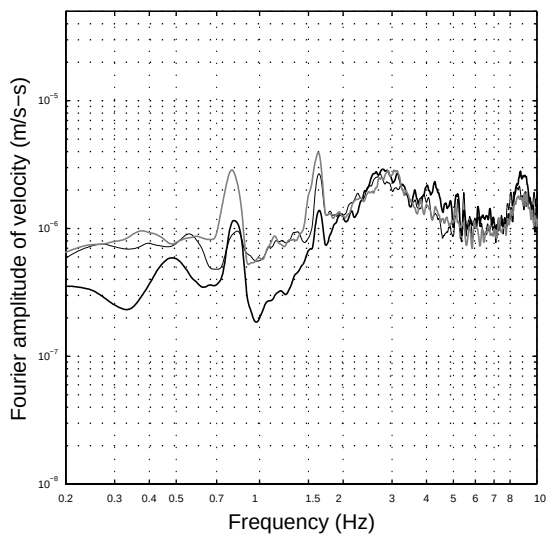

Average FAS plots: thick black − z−comp; thin black − n−s comp; thick grey − e−w comp

Figure I.94a Point 090 average HVSR +/− 1 sd

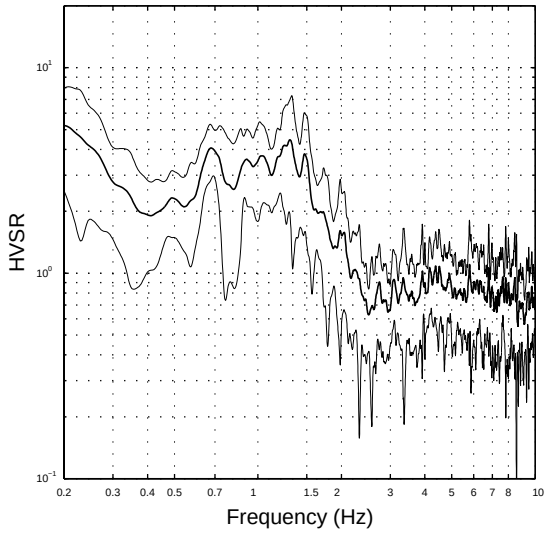

Figure I.94b Point 090 average FAS of velocity

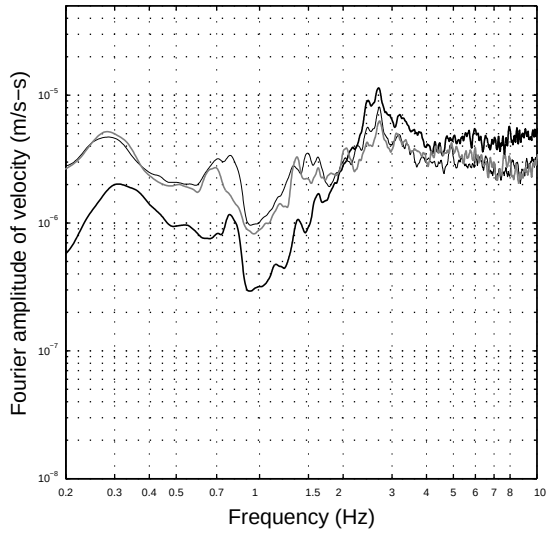

Figure I.95a Point 091 average HVSR +/− 1 sd

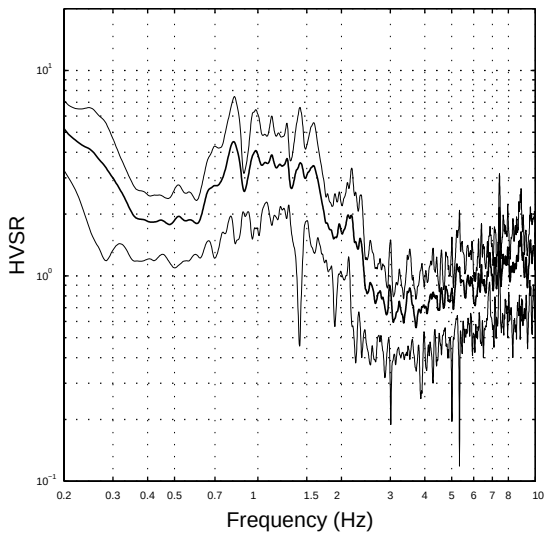

Figure I.95b Point 091 average FAS of velocity

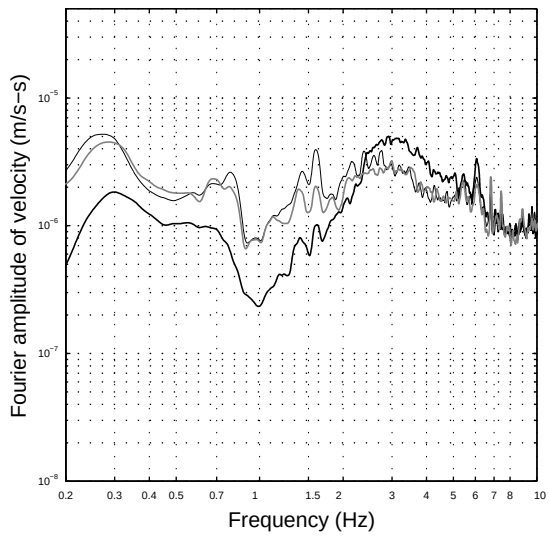

Figure I.96a Point 092a average HVSR +/− 1 sd

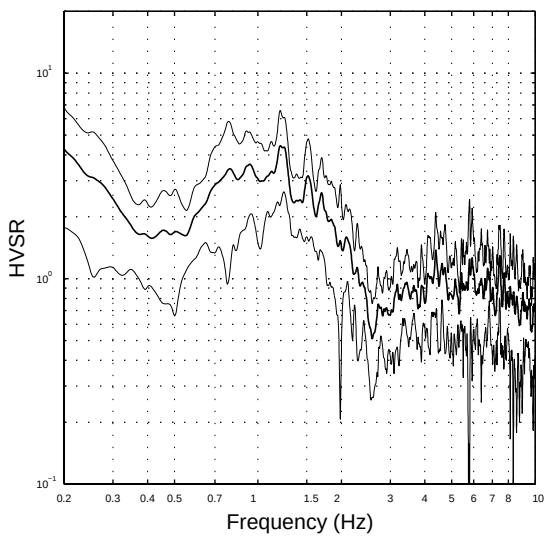

Figure I.96b Point 092a average FAS of velocity

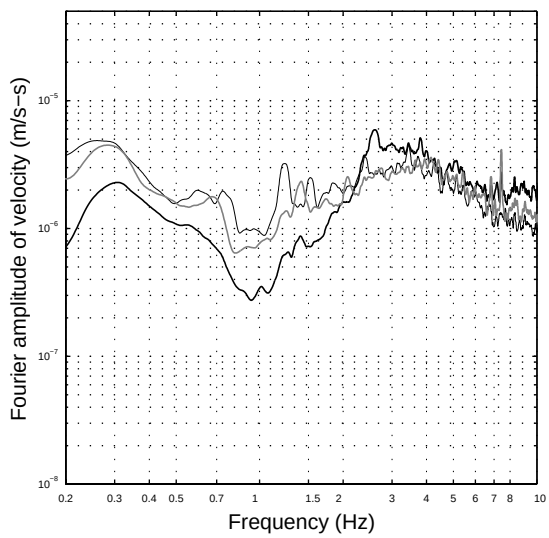

Average FAS plots: thick black − z−comp; thin black − n−s comp; thick grey − e−w comp

Figure I.97a Point 093 average HVSR +/− 1 sd

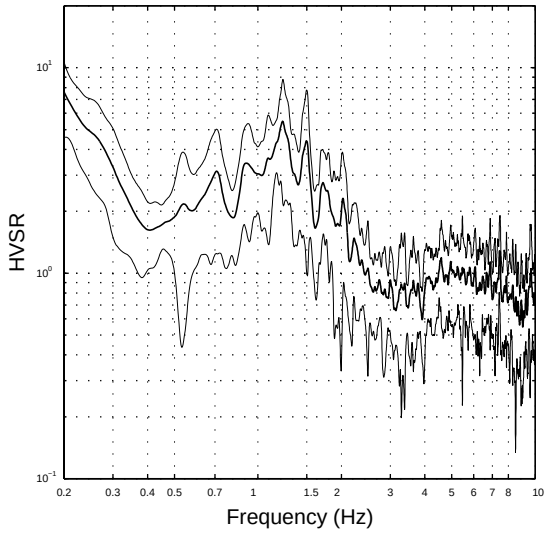

Figure I.97b Point 093 average FAS of velocity

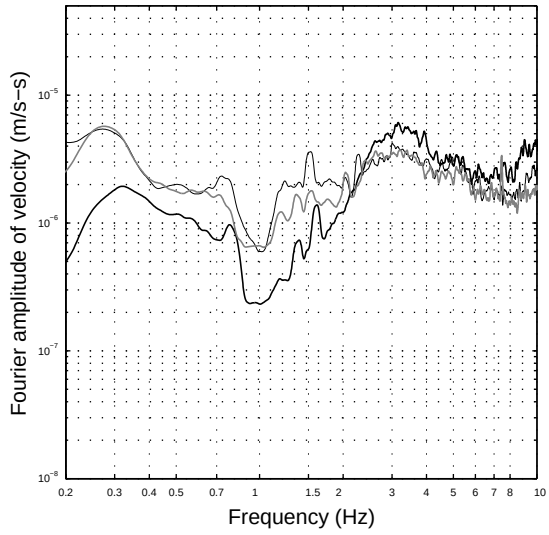

Figure I.98a Point 094 average HVSR +/− 1 sd

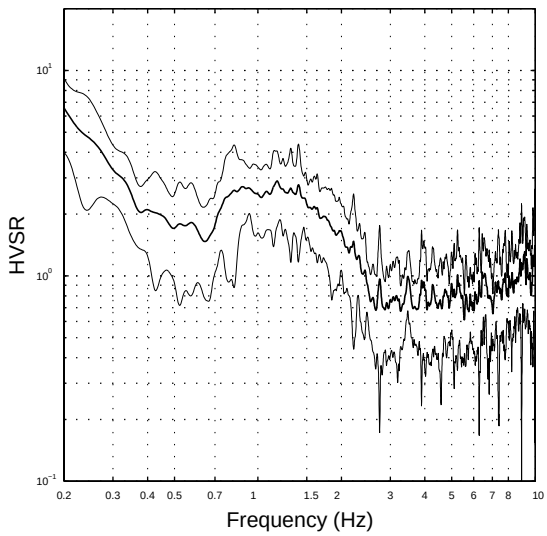

Figure I.98b Point 094 average FAS of velocity

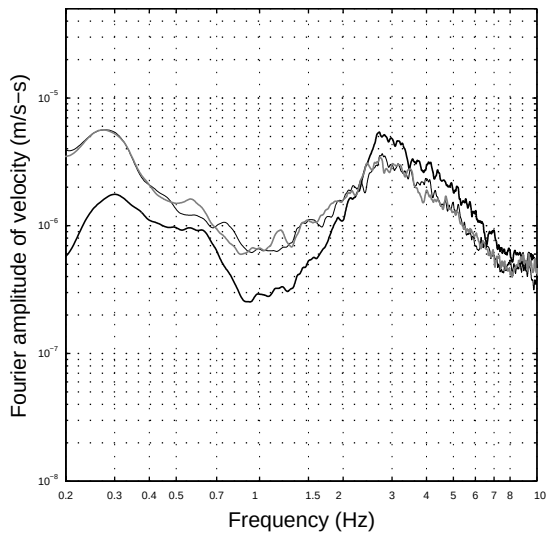

Figure I.99a Point 095 average HVSR +/− 1 sd

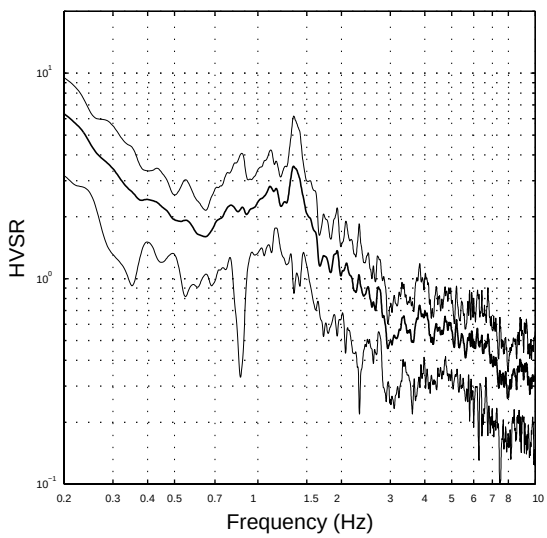

Figure I.99b Point 095 average FAS of velocity

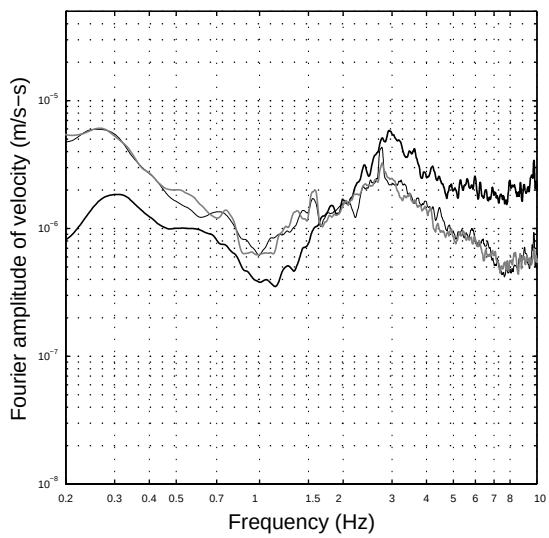

Average FAS plots: thick black − z−comp; thin black − n−s comp; thick grey − e−w comp

Figure I.100a Point 096a average HVSR +/− 1 sd

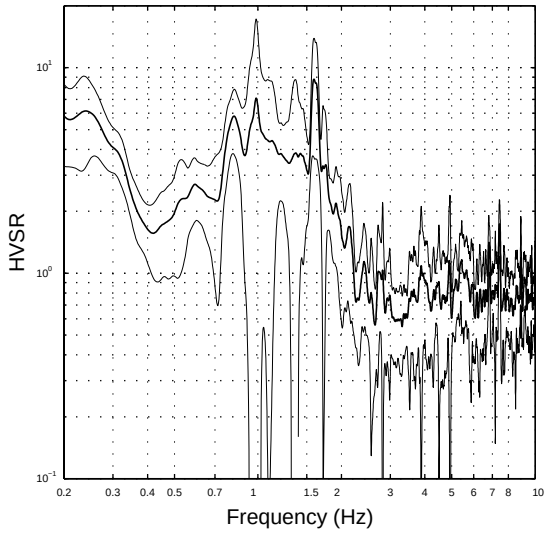

Figure I.100b Point 096a average FAS of velocity

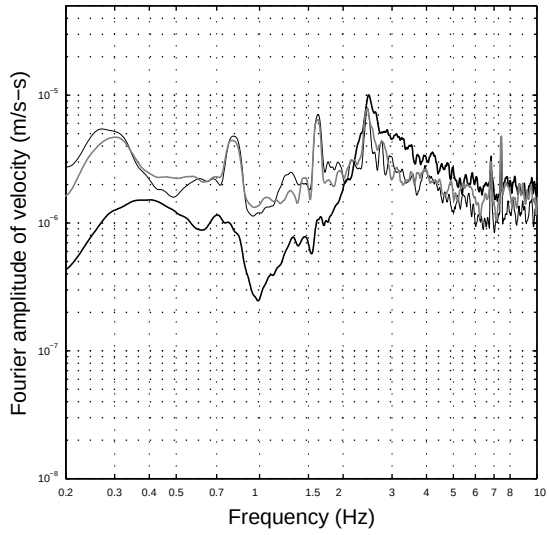

Figure I.101a Point 097a average HVSR +/− 1 sd

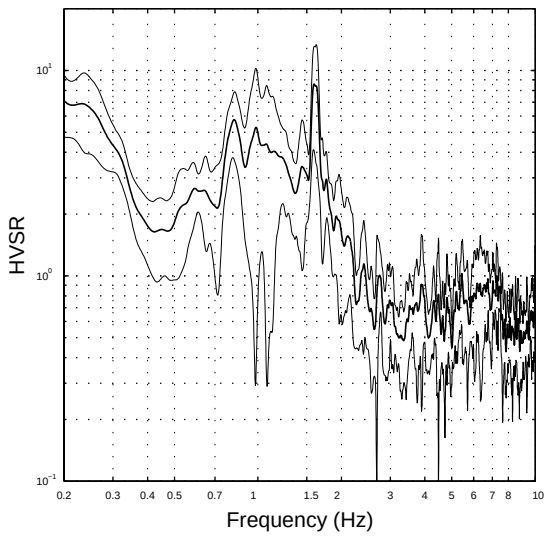

Figure I.101b Point 097a average FAS of velocity

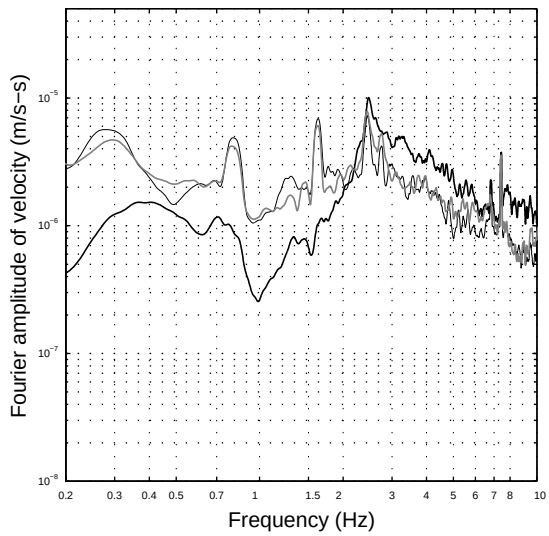

Figure I.102a Point 098 average HVSR +/− 1 sd

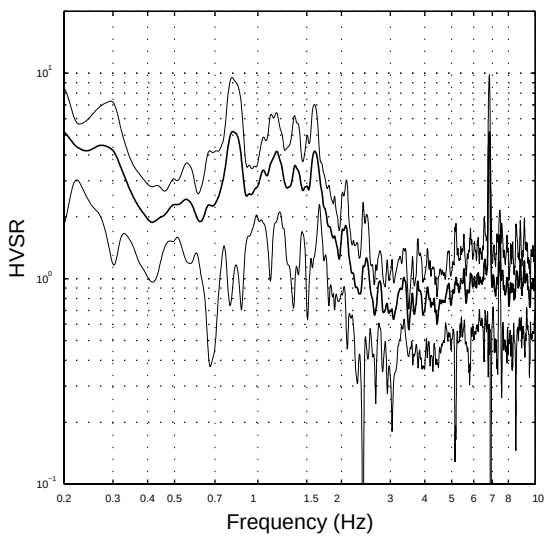

Figure I.102b Point 098 average FAS of velocity

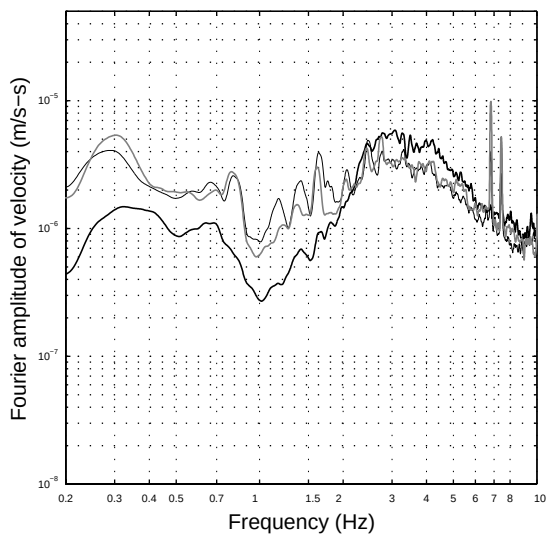

Average FAS plots: thick black − z−comp; thin black − n−s comp; thick grey − e−w comp

Figure I.103a Point 099 average HVSR +/− 1 sd

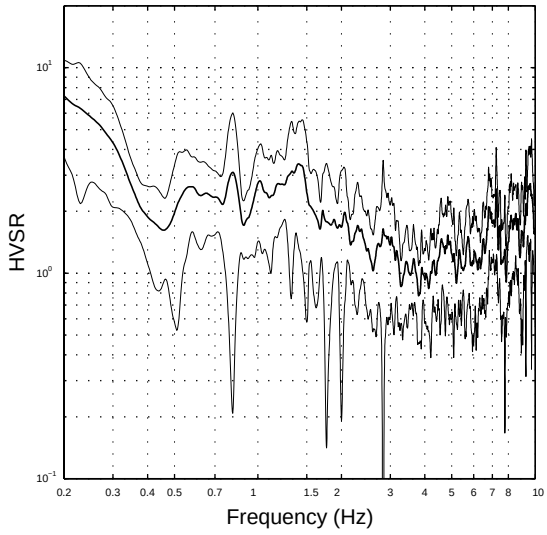

Figure I.103b Point 099 average FAS of velocity

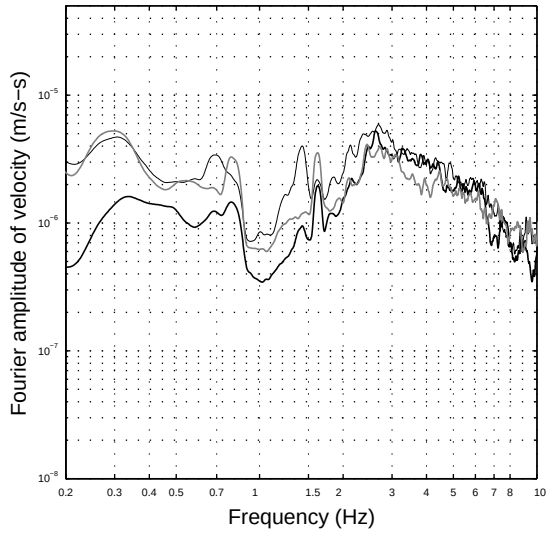

Figure I.104a Point 100 average HVSR +/− 1 sd

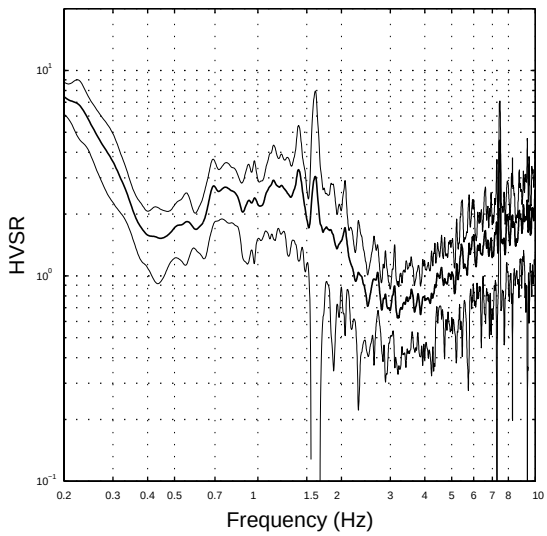

Figure I.104b Point 100 average FAS of velocity

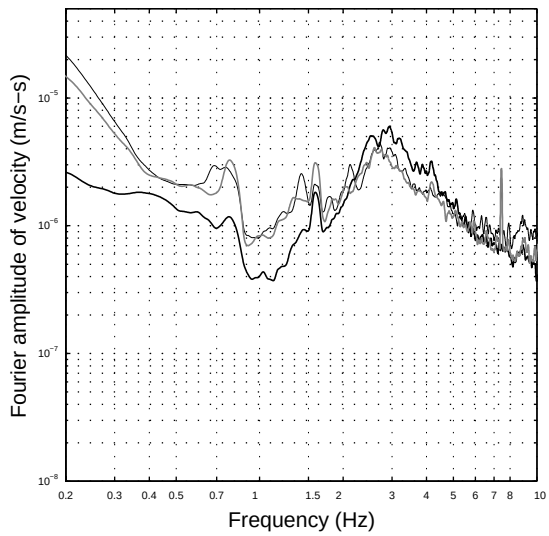

Figure I.105a Point 101 average HVSR +/− 1 sd

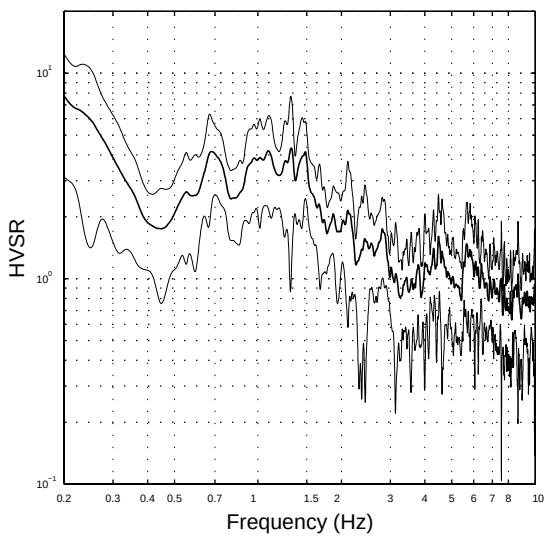

Figure I.105b Point 101 average FAS of velocity

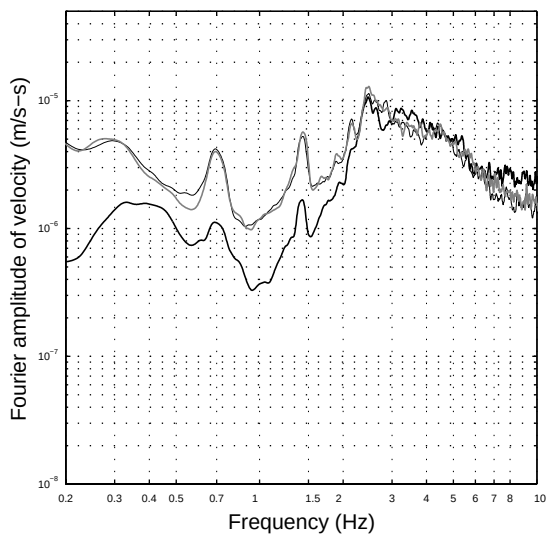

Average FAS plots: thick black − z−comp; thin black − n−s comp; thick grey − e−w comp

Figure I.106a Point 102 average HVSR +/− 1 sd

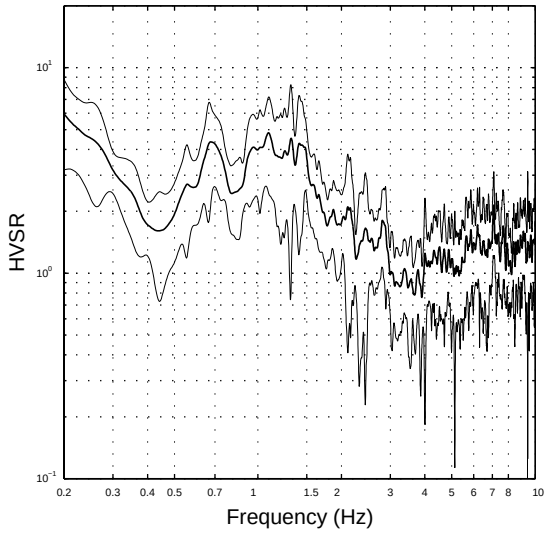

Figure I.106b Point 102 average FAS of velocity

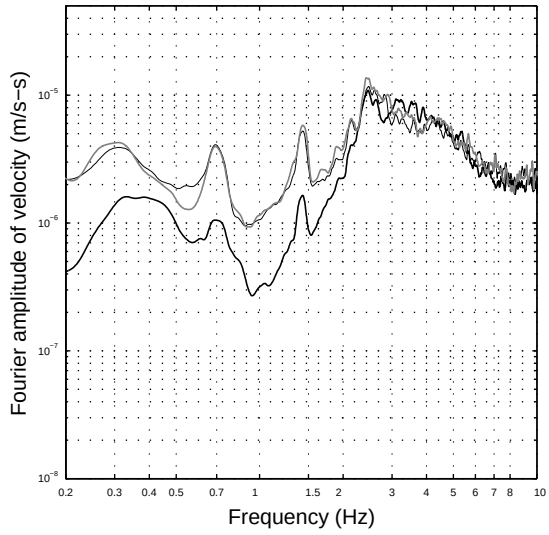

Figure I.107a Point 103 average HVSR +/− 1 sd

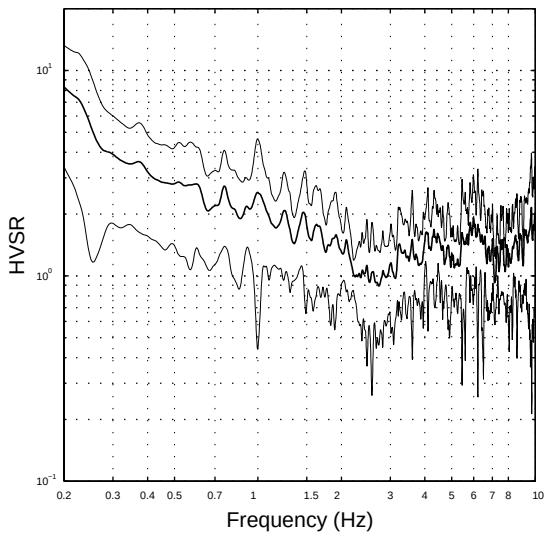

Figure I.107b Point 103 average FAS of velocity

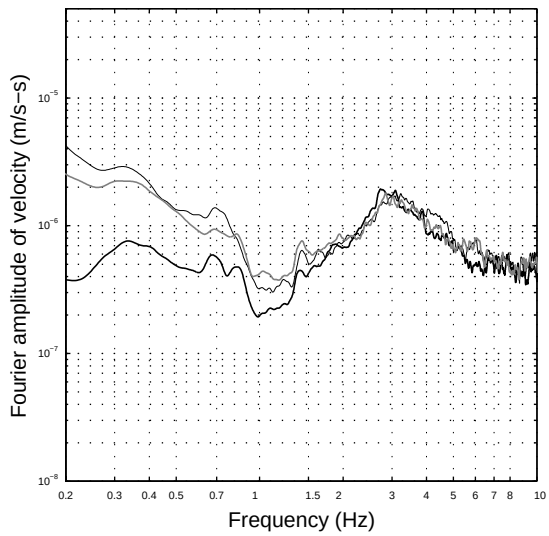

Figure I.108a Point 104 average HVSR +/− 1 sd

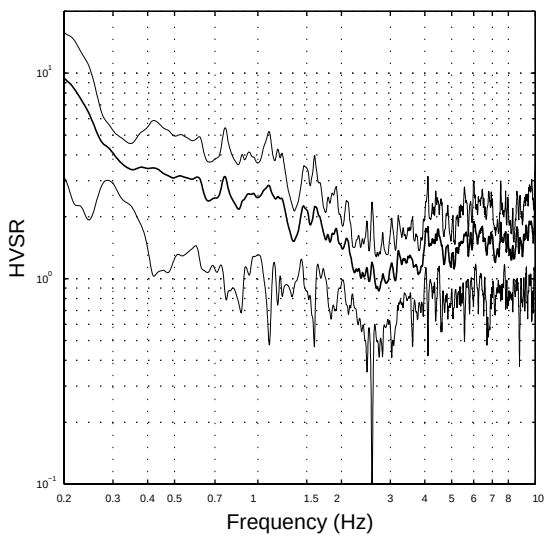

Figure I.108b Point 104 average FAS of velocity

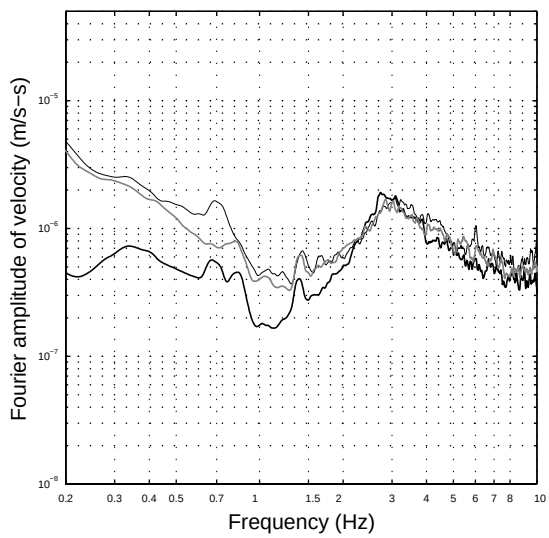

Average FAS plots: thick black − z−comp; thin black − n−s comp; thick grey − e−w comp

Figure I.109a Point 105a average HVSR +/− 1 sd

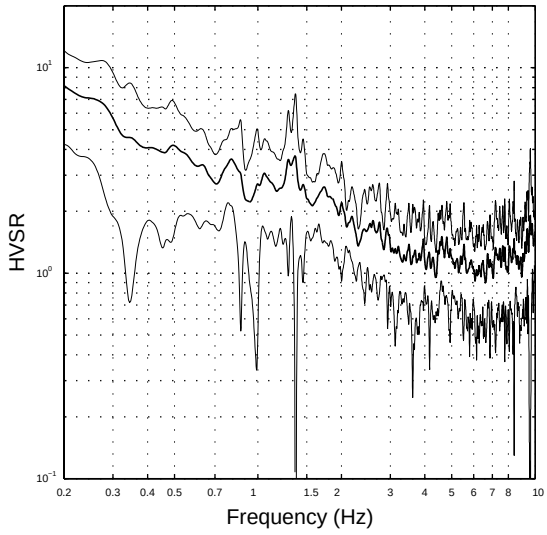

Figure I.109b Point 105a average FAS of velocity

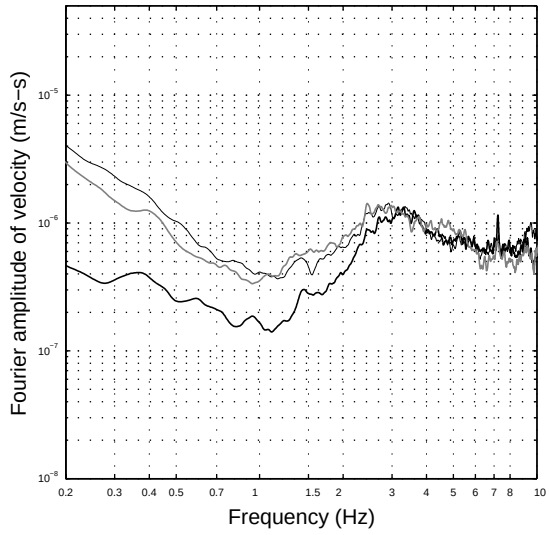

Figure I.110a Point 106a average HVSR +/− 1 sd

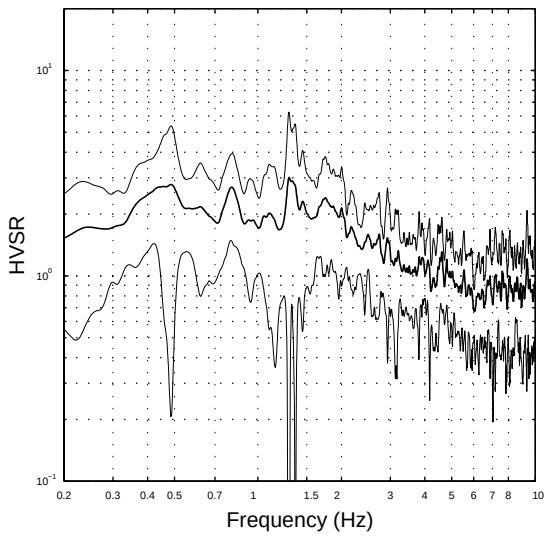

Figure I.110b Point 106a average FAS of velocity

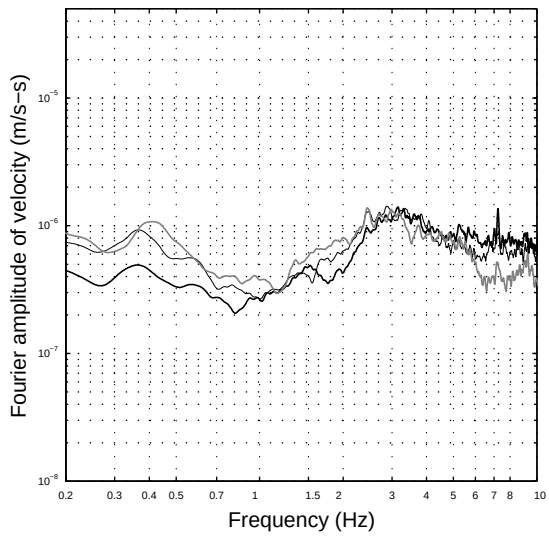

Figure I.111a Point 107 average HVSR +/− 1 sd

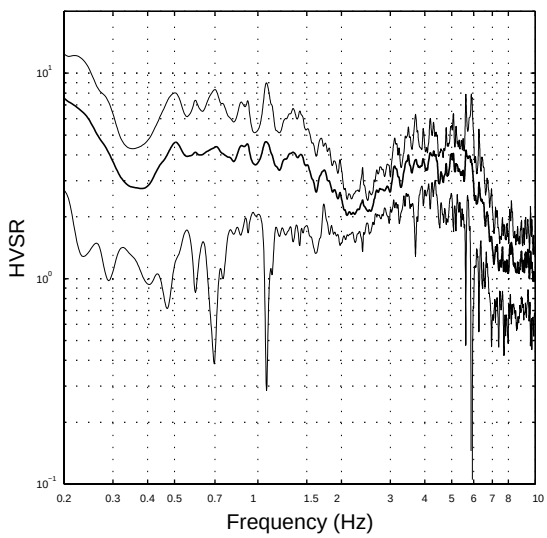

Figure I.111b Point 107 average FAS of velocity

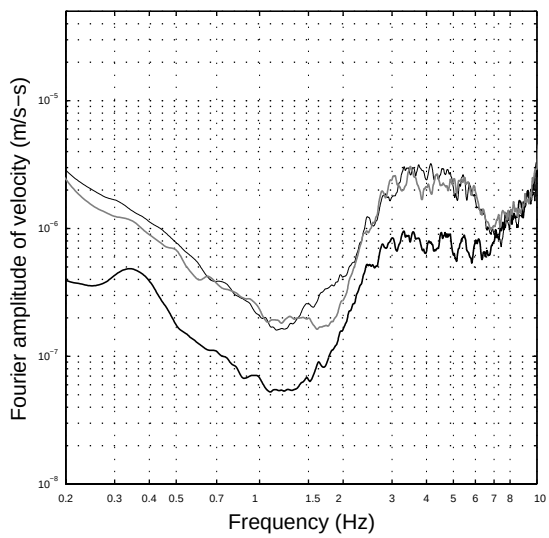

Average FAS plots: thick black − z−comp; thin black − n−s comp; thick grey − e−w comp

Figure I.112a Point 108 average HVSR +/− 1 sd

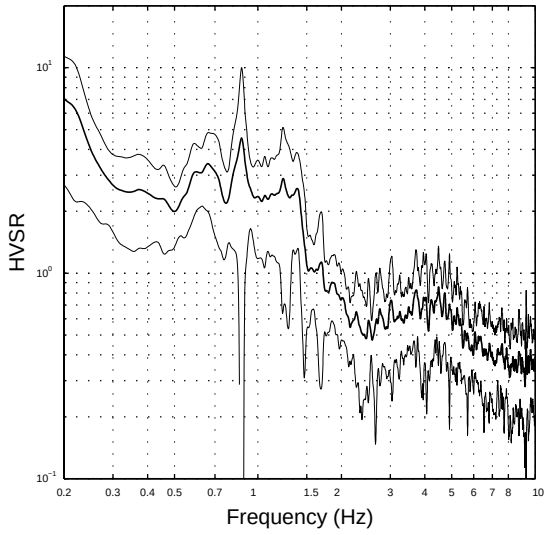

Figure I.112b Point 108 average FAS of velocity

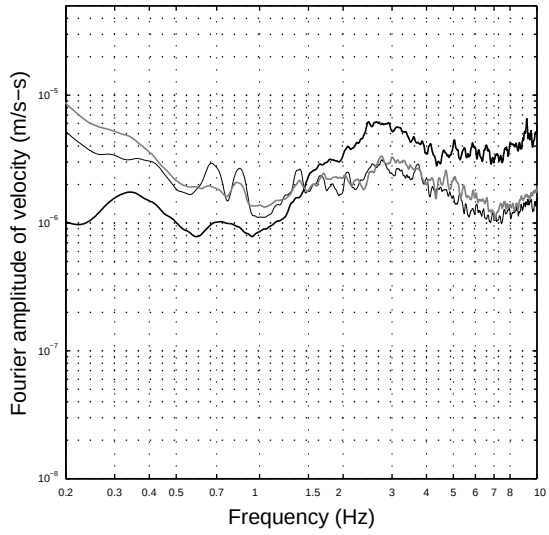

Figure I.113a Point 109 average HVSR +/− 1 sd

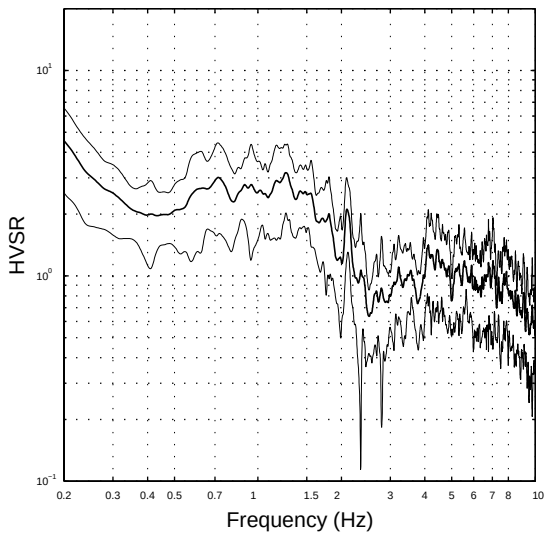

Figure I.113b Point 109 average FAS of velocity

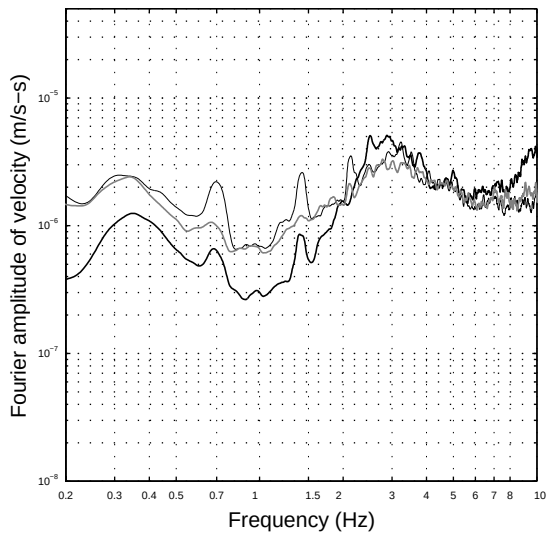

Figure I.114a Point 110 average HVSR +/− 1 sd

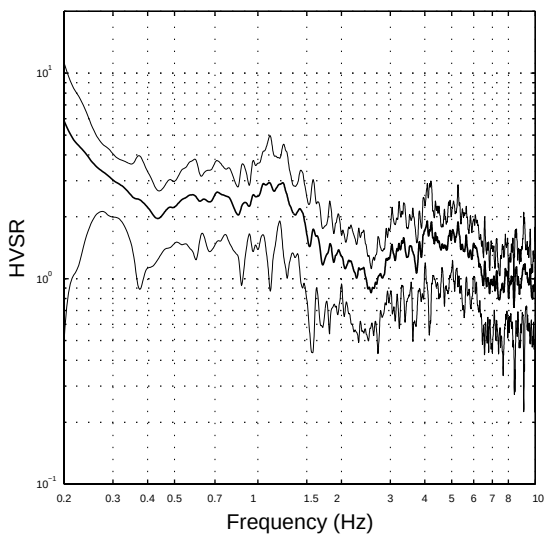

Figure I.114b Point 110 average FAS of velocity

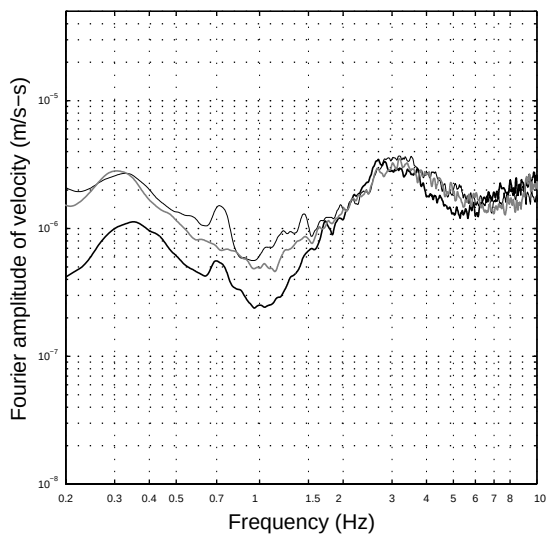

Average FAS plots: thick black − z−comp; thin black − n−s comp; thick grey − e−w comp

Figure I.115a Point 111 average HVSR +/− 1 sd

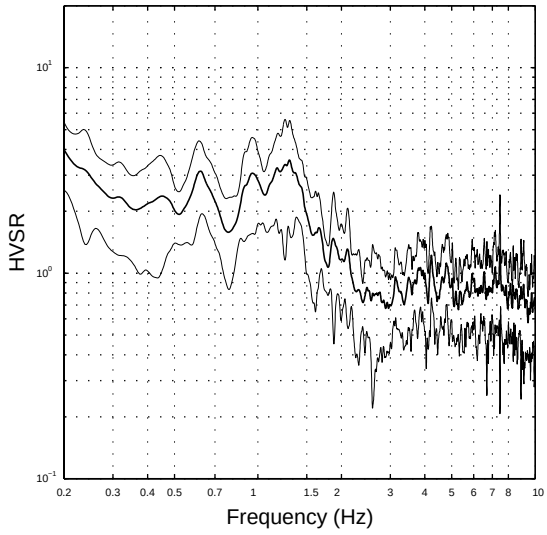

Figure I.115b Point 111 average FAS of velocity

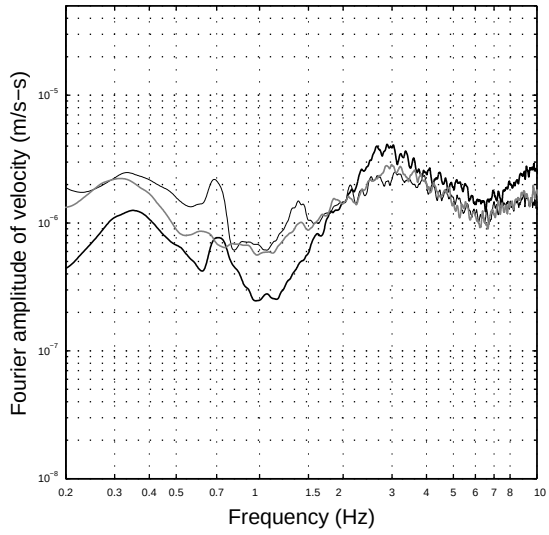

Figure I.116a Point 112 average HVSR +/− 1 sd

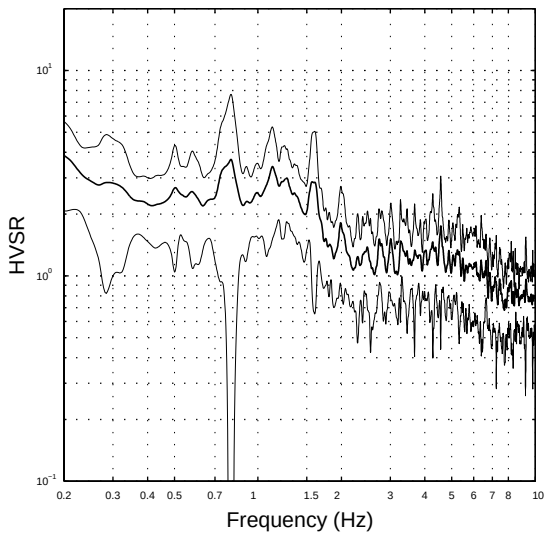

Figure I.116b Point 112 average FAS of velocity

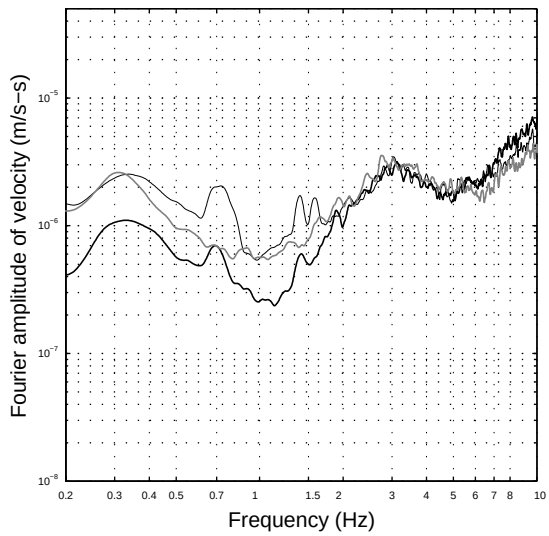

Figure I.117a Point 113a average HVSR +/− 1 sd

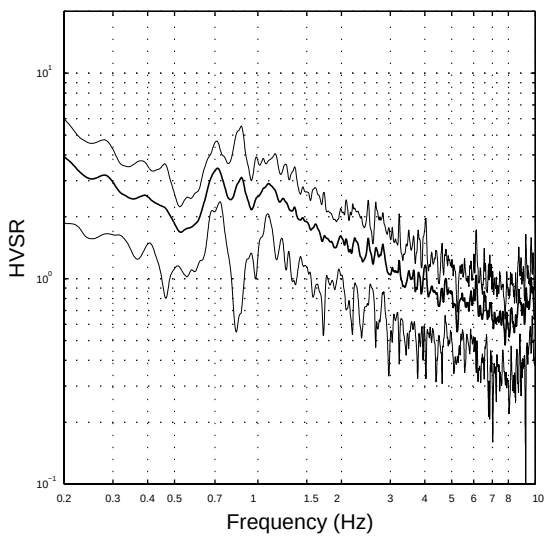

Figure I.117b Point 113a average FAS of velocity

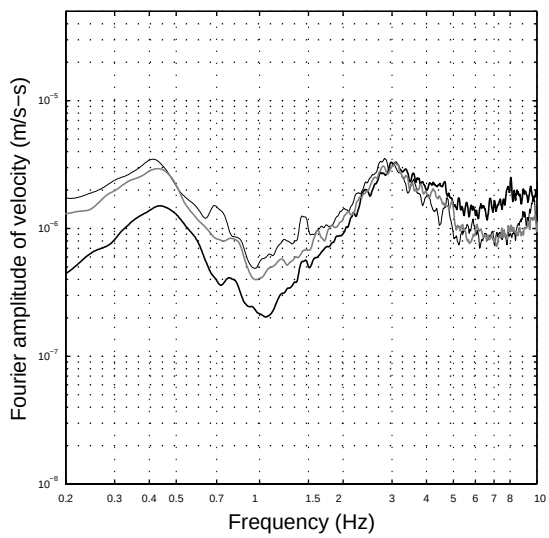

Average FAS plots: thick black − z−comp; thin black − n−s comp; thick grey − e−w comp

Figure I.118a Point 114a average HVSR +/− 1 sd

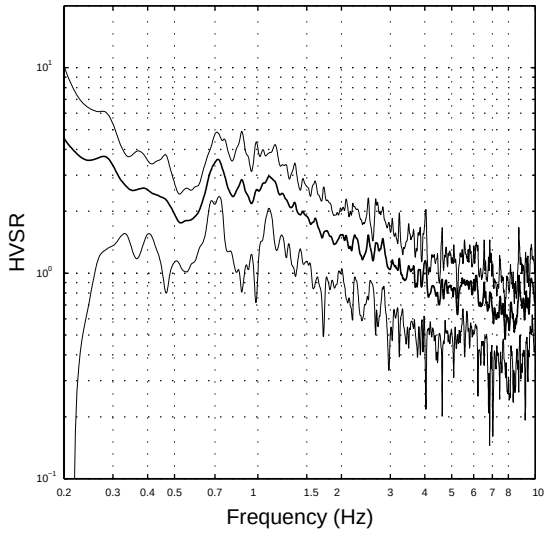

Figure I.118b Point 114a average FAS of velocity

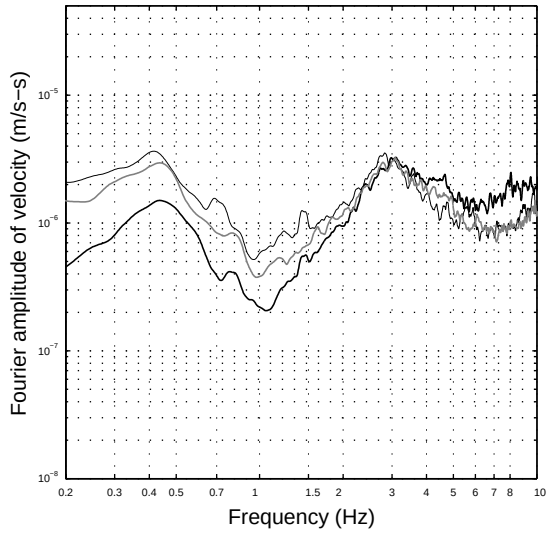

Figure I.119a Point 115 average HVSR +/− 1 sd

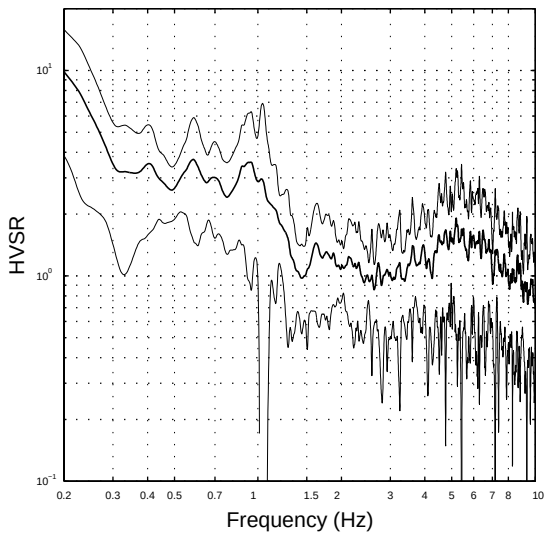

Figure I.119b Point 115 average FAS of velocity

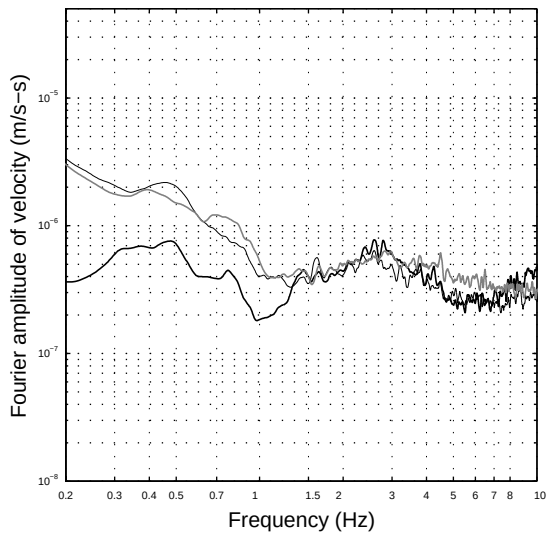

Figure I.120a Point 116 average HVSR +/− 1 sd

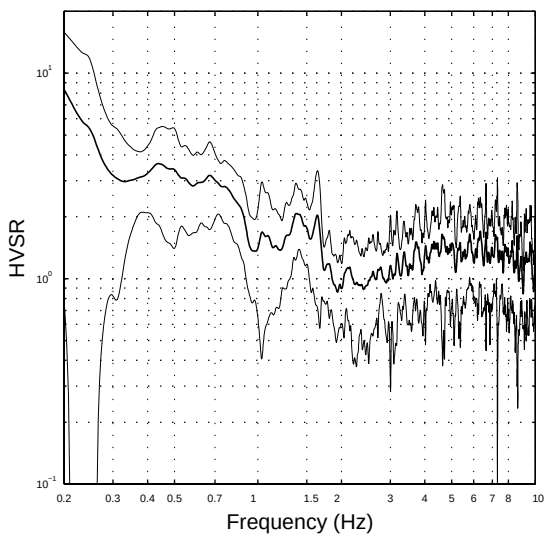

Figure I.120b Point 116 average FAS of velocity

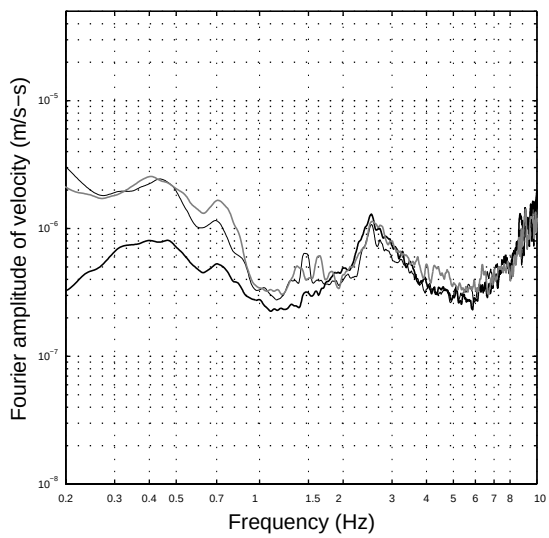

Average FAS plots: thick black − z−comp; thin black − n−s comp; thick grey − e−w comp

Figure I.121a Point 117 average HVSR +/− 1 sd

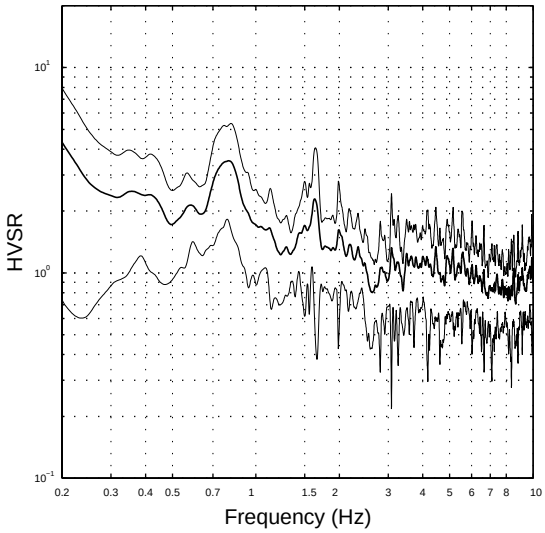

Figure I.121b Point 117 average FAS of velocity

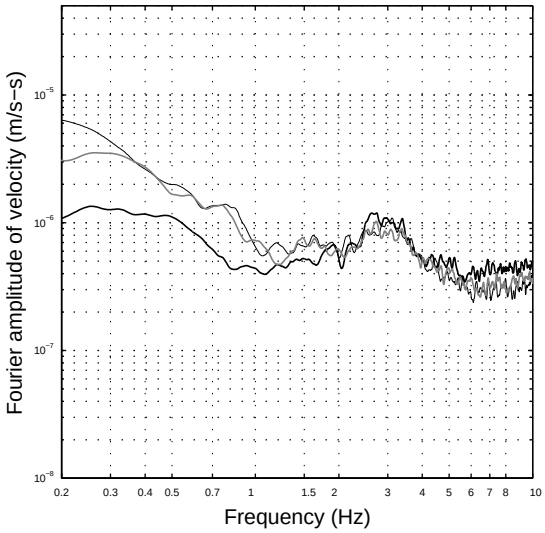

Average FAS plots: thick black – z-comp; thin black – n-s comp; thick grey – e-w comp

Table J1 Sample Düzce Municipality Water Division logbook entry for 29 December 1999 summarising work carried out on the water network. Table J2 gives a translation into English.

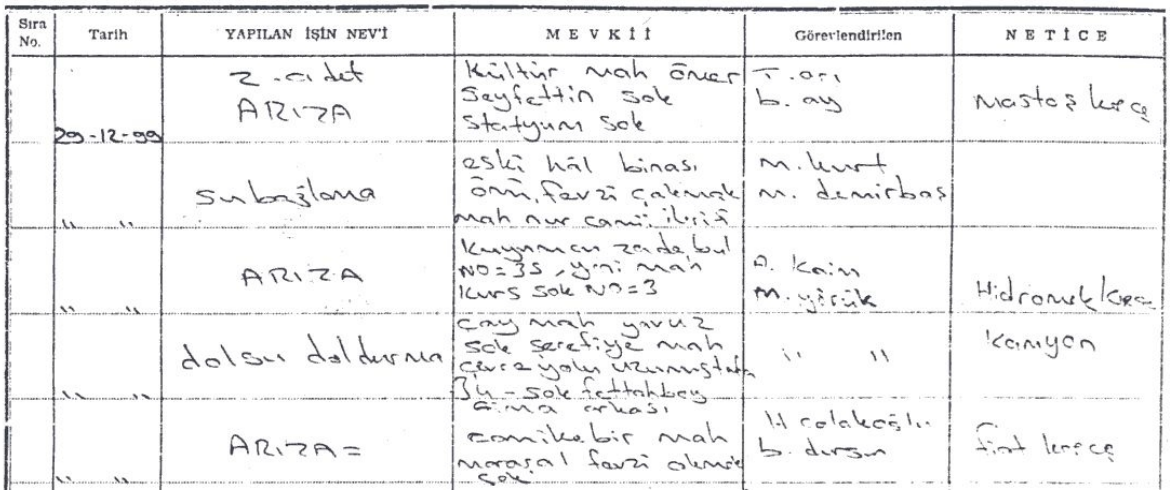

Sıra No.	Tarih	YAPILAN İŞİN NEVİ	M E V K İ İ	Görevlendirilen	N E T İ C E
	29-12-99	2 adet ARIZA	Kültür mah Ömer Seyfettin Sok Stadyum Sok	T. arı b. ay	Mastaş kepçe
	" "	Su bağlama	eski hal binası Ömr. fevzi çakmak mah cami ilerisi	M. kurt m. demirbaş	
	" "	ARIZA	Kuyumcu zade bul NO=35, yeni mah kurs sok NO=3	A. kaim M. yörük	Hidrome. kepçe
	" "	dolgu doldurma	çay mah yavuz sok şerefiye mah çev: yolu uzunmustafa 34 sok fettahbey arkası	" "	kamyon
	" "	ARIZA=	camikebir mah mareşal fevzi çakmak sok	H. colakoğlu b. dursun	fiat kepçe

Table J2 Translation of excerpt from logbook shown above

Order No.	Date	Type of work	Location	Personnel carrying out work	Machinery used
	29.12.99	2 x failure	Kültür District Ömer Seyfettin Street, Stadyum Street	T. Arı B. Ay	Mastaş shovel
	29.12.99	Water network connection	In front of the former market building, Fevzi Çakmak District near to the Mosque	M. Kurt M. Demirbaş	
	29.12.99	Failure	35 Kuyumcuzade Boulevard, Yeni District, 3 Kurs Street	A. Kaim M. Yörük	Hydro-mechanical shovel
	29.12.99	Filling with material	Çay District Yavuz Street, Şerefiye District Çevre Road, Uzunmustafa District 34 Fettahbey Street behind Gima store	A. Kaim M. Yörük	Lorry
	29.12.99	Failure	Camikebir District Mareşal Street, Fevzi Çakmak District	H. Colakoğlu B. Dursun	Fiat shovel

Table J3 Water network repair log format initiated by UNICEF

No	Date	Job type				Location	Man power	Excavator
		Excavation	Service connection	Network repair	Pump repair			
1	25/01/99				1	Zirai Donatim	4	1
2				1		Istanbul street	4	1
3				1		Zaferi Milli	2	
4			1			City	3	
5			1			City	4	
6				1		Serefiye	2	
7				1		Karaca	2	

Table J4 Georeferences for districts/villages in and immediately adjacent to Düzce Municipality. Düzce town itself is split into 29 districts ('*Mahalle*' in Turkish), referenced 1 – 29. Locations 30 – 37 are additional outlying villages/small towns. Entries in brackets are alternative district names.

District ID	District name (Mahalle)
1	Çamköyü
2	Sarayyeri
3	Bostanyer (Arapçifliği)
4	Sancaklar
5	Çavuşlar
6	Akınlar (Beslanbey)
7	Körpeşler
8	Beyciler
9	Fatih
10	Karacahacımusa
11	Yeni
12	Hamidiye
13	Karaca
14	Metek (Koçyazı)
15	Dereli (Tütüncü)
16	Mergic (Esen)
17	Aziziye (Günlü)
18	Uzunmustafa
19	Kültür

District ID	District name (Mahalle)
20	Şerefiye
21	Burhaniye
22	Nusrettin
23	Cumhuriyet
24	Camikebir
25	Cedidiye
26	Fevzicakmak
27	Kiremitocağı
28	Çay
29	Azmimilli (Darıcı Köyü)
30	Ağaköyü
31	Akpınar
32	Sinirci Köyü
33	Şıralık Köyü
34	Tokuşlar
35	"Şehir civarı"
36	Kirazlı köyü
37	Beykoy
99	Unknown

Table J5 Water distribution network repairs covering 26 nominal monthly periods for Düzce and outlying districts. Pre-earthquake periods are indicated by blue; inter-earthquake periods are indicated by yellow; post-earthquake periods are indicated by red. Pipe length is given for each district, derived from the Iller Bankası maps.

District ID	District Name	Pipe length, Lp (km)	Period ending: 24-Feb-1999	25-Mar-1999	23-Apr-1999	22-May-1999	20-Jun-1999	19-Jul-1999	17-Aug-1999	15-Sep-1999	14-Oct-1999	12-Nov-1999	11-Dec-1999	9-Jan-2000	7-Feb-2000	7-Mar-2000	5-Apr-2000	4-May-2000	2-Jun-2000	1-Jul-2000	30-Jul-2000	28-Aug-2000	26-Sep-2000	25-Oct-2000	23-Nov-2000	22-Dec-2000	20-Jan-2001	Totals
1	Çamköyü	20.59	0	0	0	0	0	0	0	0	0	0	0	0	0	0	0	0	0	0	0	0	0	3	2	0	1	6
2	Sarayyeri	4.49	0	3	0	0	0	0	0	0	0	0	0	0	0	0	0	0	0	0	0	0	0	0	0	0	0	3
3	Arapçiftliği	6.14	0	0	0	0	0	0	0	0	0	0	0	0	1	0	0	0	0	0	1	0	0	0	0	0	0	2
4	Sancaklar	19.72	0	0	1	1	0	1	0	0	1	0	0	0	0	0	1	0	2	3	2	3	9	5	8	2	12	51
5	Çavuşlar	8.97	1	0	2	0	0	0	1	0	0	1	2	0	1	0	2	0	0	0	0	0	1	0	1	0	0	12
6	Akınlar	4.18	0	1	1	0	0	0	0	0	0	1	0	0	0	0	0	0	0	0	0	0	2	2	2	3	3	15
7	Körpeşler	10.51	0	1	0	0	1	1	0	0	0	1	0	0	0	0	0	1	0	1	0	1	0	0	0	0	1	8
8	Beyciler	30.38	8	17	9	3	6	3	1	2	16	12	6	8	0	1	2	3	2	3	8	4	4	10	4	4	4	140
9	Fatih	9.37	0	5	2	4	3	2	3	1	2	4	4	4	1	2	0	0	11	3	2	0	0	1	8	1	2	67
10	Karacahacımusa	4.64	0	1	0	1	0	2	0	0	0	0	0	0	0	0	0	0	1	1	2	0	0	1	0	0	0	9
11	Yeni	8.15	5	0	0	0	0	0	0	0	0	0	0	0	0	0	0	0	0	0	0	0	0	1	0	0	0	5
12	Hamidiye	18.76	12	5	8	7	3	6	5	7	7	18	2	2	1	0	1	2	8	10	4	3	13	5	7	2	3	141
13	Karaca	13.49	6	3	11	12	5	2	5	3	3	9	2	4	0	0	0	1	5	1	1	1	6	5	6	5	2	98
14	Koçyazı	29.36	1	7	1	2	2	2	0	6	4	4	1	0	1	2	0	2	0	6	1	1	1	1	3	4	3	55
15	Dereli	24.95	0	0	0	0	0	0	0	0	0	0	0	0	0	0	0	0	0	0	0	0	0	0	0	0	0	0
16	Mergic	6.54	1	0	0	0	0	0	0	0	0	0	0	0	0	0	0	1	7	5	2	0	10	14	17	3	4	235
17	Aziziye	46.77	11	15	18	9	10	15	9	11	23	29	13	3	4	1	1	1	7	5	2	0	1	2	12	7	0	122
18	Uzunmustafa	13.56	5	5	5	4	11	3	12	10	9	2	4	3	0	0	3	3	7	8	5	1	1	2	11	9	2	274
19	Kültür	20.49	8	8	4	16	10	17	6	12	32	31	9	31	3	4	2	4	12	4	8	9	10	11	12	9	2	119
20	Şerefiye	9.03	0	4	7	2	3	9	5	6	13	0	6	11	2	3	1	0	8	5	1	1	3	12	14	1	2	83
21	Burhaniye	7.63	3	4	2	2	1	1	7	0	11	7	5	3	3	0	1	1	5	2	3	5	3	4	6	1	3	142
22	Nusrettin	10.13	11	5	6	4	3	3	2	4	8	15	8	2	1	4	1	0	6	7	14	5	7	6	12	6	2	46
23	Cumhuriyet	13.93	1	5	1	4	1	1	3	0	7	3	2	0	0	0	0	0	2	3	0	0	3	4	1	1	4	97
24	Camikebir	9.87	0	3	4	9	3	2	3	2	9	13	6	2	0	0	1	3	3	7	1	6	6	6	5	2	1	135
25	Cedidiye	10.97	5	1	3	7	1	10	5	2	5	5	9	10	2	1	1	5	20	10	7	3	3	7	6	2	5	84
26	Fevzicakmak	16.81	3	2	4	1	1	2	1	7	7	2	6	12	3	2	0	0	2	8	1	0	2	5	6	2	5	53
27	Kiremitocağı	6.03	0	0	0	3	0	3	1	1	12	10	1	2	0	0	1	0	1	1	0	3	1	3	3	3	4	137
28	Çay	26.65	10	2	8	6	9	6	2	3	9	11	5	9	1	2	0	4	7	6	2	2	6	11	9	6	1	217
29	Azmimilli	21.48	6	4	9	7	15	2	5	17	17	20	14	27	1	1	2	3	3	8	9	7	4	16	11	7	2	2357
	Totals	433.60	97	101	106	104	88	92	77	94	195	198	105	133	25	23	20	33	112	102	74	57	95	134	155	71	66	
30	Ağaköyü		2	0	0	0	0	2	1	0	3	0	1	5	0	0	0	2	1	5	0	1	3	2	1	7	0	36
31	Akpınar		0	0	0	0	2	0	0	0	1	2	1	0	0	0	0	0	0	1	0	1	0	0	0	0	0	8
32	Sinirci Köyü		0	0	0	0	0	0	0	0	0	0	0	0	0	0	0	0	0	0	0	0	0	0	0	0	0	0
33	Şıralık Köyü		0	0	0	0	0	0	0	0	0	0	0	0	0	0	0	0	0	0	0	0	0	1	2	5	0	8
34	Tokuşlar		0	1	0	0	0	0	0	0	0	0	0	0	0	0	0	0	0	0	1	0	0	1	0	0	0	3
35	Şehir civarı		0	0	4	1	9	10	1	8	21	10	13	25	13	17	6	22	14	4	1	4	4	7	2	10	0	206
36	Kirazlı köyü		0	0	0	0	0	0	0	0	0	0	0	0	0	0	0	0	0	0	0	0	0	0	2	0	1	3
37	Beykoy		0	0	1	0	0	0	0	0	0	0	1	0	0	0	0	1	0	0	0	0	0	0	0	0	0	3
99	Unknown		5	0	1	0	0	0	0	0	0	0	0	0	0	0	0	0	0	0	0	0	0	0	1	0	0	7
																										Total (Düzce + environs)->		2631

Table K1 Building damage data. No building-related data were available for District ID 5 – Çavuşlar.

District ID	Name	No. buildings by damage grade					No. buildings by storeys						% buildings unclassified	% buildings having 4 - 6 storeys	District area (km²)	Spatial density of buildings, S_b (per km²)	Building damage index	
		N_{D4}	N_{D3}	N_{D2}	N_{D1}	ΣN_{DI}	N_{S1}	N_{S2}	N_{S3}	N_{S4}	N_{S5}	N_{S6}	ΣN_{SI}					D_1	D_2
1	Çamköyü	69	54	183	2	308	154	130	14	0	0	0	298	3.2%	0.0%	3.093	99.6	0.263	0.253
2	Sarayyeri	17	20	63	0	100	70	24	6	0	0	0	100	0.0%	0.0%	1.802	55.5	0.244	0.233
3	Arapçiftliği	4	33	124	0	161	95	53	8	1	1	0	158	1.9%	1.3%	2.667	60.4	0.183	0.166
4	Sancaklar	36	108	387	9	540	225	221	51	15	1	0	513	5.0%	3.1%	1.241	***435.1***	0.198	0.182
5	Çavuşlar															1.117			
6	Akınlar	16	17	124	2	159	89	58	7	3	0	0	157	1.3%	1.9%	1.711	92.9	0.199	0.182
7	Körpeşler	9	43	169	1	222	111	80	23	2	2	0	218	1.8%	1.8%	1.392	***159.5***	0.187	0.170
8	Beyciler	29	114	411	5	559	170	244	101	26	2	0	543	2.9%	5.2%	3.625	***154.2***	0.193	0.177
9	Fatih	9	31	95	1	136	45	51	18	10	7	0	131	3.7%	13.0%	0.443	***306.7***	0.203	0.188
10	Karacahacımusa	11	2	74	7	94	43	25	8	3	7	0	86	8.5%	11.6%	0.715	***131.4***	0.185	0.168
11	Yeni	12	6	165	1	184	59	78	31	13	0	0	181	1.6%	7.2%	0.443	***415.5***	0.175	0.153
12	Hamidiye	122	141	298	0	561	208	199	64	36	28	0	535	4.6%	12.0%	0.715	***784.9***	0.272	0.264
13	Karaca	71	23	302	1	397	175	119	44	17	17	0	372	6.3%	9.1%	0.493	***805.3***	0.227	0.212
14	Koçyazı	42	51	281	3	377	152	163	33	5	0	0	353	6.4%	1.4%	1.932	***195.1***	0.209	0.193
15	Dereli	12	13	203	0	228	96	92	16	6	0	0	210	7.9%	2.9%	1.297	***175.8***	0.174	0.152
16	Mergic	10	20	59	0	89	48	32	5	0	0	0	85	4.5%	0.0%	1.052	84.6	0.223	0.210
17	Aziziye	160	130	512	1	803	280	326	86	27	24	0	743	7.5%	6.9%	2.098	***382.8***	0.251	0.240
18	Uzunmustafa	109	124	231	1	465	130	136	92	46	32	0	436	6.2%	17.9%	0.487	***954.8***	0.281	0.275
19	Kültür	280	381	208	7	876	176	273	82	126	168	2	827	5.6%	35.8%	0.901	***971.8***	0.341	0.344
20	Şerefiye	106	100	125	2	333	50	102	54	56	62	0	324	2.7%	36.4%	0.257	***1293.7***	0.321	0.320
21	Burhaniye	92	116	101	0	309	60	90	31	42	73	1	297	3.9%	39.1%	0.221	***1398.5***	0.324	0.324
22	Nusrettin	128	175	207	1	511	168	185	41	61	46	0	501	2.0%	21.4%	0.379	***1349.5***	0.299	0.296
23	Cumhuriyet	18	28	137	1	184	62	67	34	8	2	0	173	6.0%	5.8%	0.618	***297.9***	0.206	0.190
24	Camikebir	163	125	127	0	415	56	112	65	48	65	3	349	15.9%	33.2%	0.331	***1255.5***	0.354	0.356
25	Cedidiye	114	146	107	4	371	42	81	42	70	98	4	337	9.2%	51.0%	0.367	***1010.8***	0.329	0.330
26	Fevzicakmak	27	84	163	0	274	93	90	30	34	13	0	260	5.1%	18.1%	0.768	***357.0***	0.229	0.218
27	Kiremitocağı	49	45	116	1	211	97	53	11	6	18	0	185	12.3%	13.0%	0.232	***908.0***	0.272	0.264
28	Çay	189	172	524	2	887	317	289	135	63	37	0	841	5.2%	11.9%	0.978	***906.5***	0.262	0.252
29	Azmimilli	158	236	533	1	928	184	329	174	83	60	0	830	10.6%	17.2%	1.074	***864.3***	0.252	0.243
	TOTALS (all 29 districts):	2062	2538	6029	53	10682	3455	3702	1306	807	763	10	10043			32.450			
	TOTALS (Focus area):	1946	2394	5476	49	9865	2999	3405	1266	803	762	10	9245			21.007			